water

Special Issue Reprint

Climate Change and Hydrological Processes

Edited by
Alina Bărbulescu, Romulus Costache and Cristian Ștefan Dumitriu

mdpi.com/journal/water

MDPI

Climate Change and Hydrological Processes

Climate Change and Hydrological Processes

Guest Editors

Alina Bărbulescu
Romulus Costache
Cristian Ștefan Dumitriu

MDPI

Basel • Beijing • Wuhan • Barcelona • Belgrade • Novi Sad • Cluj • Manchester

Guest Editors

Alina Bărbulescu
Department of Civil Engineering Transilvania University of Brașov
Brașov
Romania

Romulus Costache
Flash-Flood Forecast Department
National Institute of Hydrology and Water Management
Bucharest
Romania

Cristian Ștefan Dumitriu
Faculty of Mechanical Engineering and Robotics in Constructions
Technical University of Civil Engineering of Bucharest
Bucharest
Romania

Editorial Office

MDPI AG
Grosspeteranlage 5
4052 Basel, Switzerland

This is a reprint of the Special Issue, published open access by the journal *Water* (ISSN 2073-4441), freely accessible at: https://www.mdpi.com/journal/water/special_issues/170L79L494.

For citation purposes, cite each article independently as indicated on the article page online and as indicated below:

Lastname, A.A.; Lastname, B.B. Article Title. *Journal Name* **Year**, *Volume Number*, Page Range.

ISBN 978-3-7258-5753-1 (Hbk)
ISBN 978-3-7258-5754-8 (PDF)
https://doi.org/10.3390/books978-3-7258-5754-8

Contents

Preface

Climate change has become one of the most defining forces shaping the behavior of hydrological systems worldwide. Rising temperatures, altered precipitation regimes, and the increasing frequency of hydrological extremes are transforming the spatial and temporal dynamics of water resources. These changes challenge long-standing assumptions of hydrological stationarity and pose new questions regarding the sustainability, reliability, and resilience of water systems.

This reprint contains articles devoted to advancing understanding of how hydrological processes respond to changing climatic conditions, with particular emphasis on the occurrence, magnitude, and distribution of extreme events such as floods and droughts. It combines studies on quantitative modeling, statistical analysis, and scenario-based assessments to identify trends, evaluate uncertainties, and derive implications for risk management and adaptation strategies.

The subject centers on the interactions between climate variability and hydrological processes across multiple scales. Its scope extends from methodological developments—such as improved modeling frameworks and nonstationary analyses—to applied case studies that explore the implications of projected hydrological shifts for water management, hazard assessment, and policy design. Its aim and purpose are twofold: (i) to contribute to the scientific understanding of hydroclimatic responses under future climate scenarios, and (ii) to provide practical insights that support evidence-based decision making in water resources planning. By quantifying the influence of climate drivers on hydrological extremes and assessing related uncertainties, this study seeks to bridge the gap between climate modeling, hydrological science, and applied water management.

The motivation for undertaking this research arises from the urgent need to adapt to an evolving climate reality. Conventional hydrological models and design standards—often founded on historical data and assumptions of stability—are increasingly inadequate for predicting future risks. Enhancing the accuracy and interpretability of hydrological projections is essential to inform sustainable adaptation measures, safeguard critical water infrastructure, and reduce the socio-economic impacts of climate-induced extremes.

This reprint is addressed to a broad audience of researchers, practitioners, and decision-makers in the fields of hydrology, climatology, environmental engineering, and water policy. It is also intended for early-career scientists seeking to engage with the complex challenges at the intersection of climate change and hydrological science. Ultimately, its purpose is not only to advance scientific knowledge but also to support the development of resilient and adaptive water management strategies.

Alina Bărbulescu, Romulus Costache, and Cristian Ștefan Dumitriu
Guest Editors

water

MDPI

Editorial

Climate Change and Hydrological Processes

Alina Bărbulescu [1,*], Romulus Costache [2] and Cristian Ștefan Dumitriu [3,*]

[1] Department of Civil Engineering, Transilvania University of Brașov, 5 Turnului Street, 500152 Brașov, Romania
[2] National Institute of Hydrology and Water Management, București-Ploiești Road, 97E, 1st District, 013686 Bucharest, Romania; romuluscostache2000@yahoo.com
[3] Faculty of Mechanical Engineering and Robotics in Constructions, Technical University of Civil Engineering, Calea Plevnei 59, 021242 Bucharest, Romania
* Correspondence: alina.barbulescu@unitbv.ro (A.B.); cristian.dumitriu@utcb.ro (C.Ș.D.)

1. Introduction

In recent decades, many regions have experienced a noticeable increase in the frequency and intensity of extreme events, posing serious challenges to water resource management [1,2]. Changes in hydrological patterns—manifesting as prolonged periods of drought, devastating floods, rapid glacial melting, and the ominous rise in sea levels—are fundamentally reshaping the dynamics of water security and ecological stability [3–5].

Climate change affects virtually all components of the hydrological cycle, particularly through changes in temperature and precipitation. These climatic variables directly influence evaporation, evapotranspiration, runoff, and groundwater recharge, altering water availability and distribution [5]. As global temperatures continue to rise, the hydrological cycle is expected to intensify, leading to faster and more variable water movement across the Earth's surface and atmosphere [6–9].

Precipitation is a key connector between the atmospheric and hydrological systems, making its variability a critical concern for water management strategies in the face of climate-related stressors. The interplay between water and climate is fundamentally cyclical: water contributes to climate regulation through the exchange of heat and mass among the ocean, atmosphere, and land, while climate factors dictate the behavior of water systems [9,10]. Furthermore, this variability substantially impacts the runoff and the development of flooding, which are increasingly difficult to predict and manage [11,12].

Quantifying specific processes remains a complex challenge due to their sensitivity to multiple meteorological factors and anthropogenic activities [13,14]. To achieve resilience in the face of climate change and to promote sustainable development, it is essential to develop integrated strategies focused on the efficient utilization of water resources [15]. These strategies should also aim to mitigate the effects of extreme weather events and create adaptive frameworks for water management that can adjust to evolving conditions [16,17].

This Special Issue was dedicated to deepening the knowledge on effects of climate change on hydrological processes. The contributions within it include cutting-edge research that examines the implications of climate change on water runoff, evaluates the risks and uncertainties associated with hydro-meteorological events, assesses flood susceptibility, investigates the appropriateness of existing methodologies for evaluating the intensity and duration of these events, explores the impact of human activities on watershed dynamics, and proposes innovative mitigation and adaptation strategies with which to address the effects of climate change.

2. Main Contributions to the Special Issue

Eleven articles were accepted for publication after the peer review process. In the following, we shall summarize the main findings and contributions to advancements in the study area.

Babaousmail and Ojara [1] analyzed rainfall patterns over Uganda's Lake Kyoga Basin from 1981 to 2017 using ground-recorded and satellite data. They applied CDI, RAI, and rainfall frequency metrics to identify trends in droughts and floods. The study found a general decrease in seasonal rainfall over the years, followed by a rising trend during 2006–2017 in both MAM and SOND seasons. Northeastern areas experienced dry days more frequently than other parts of the basin. These rainfall fluctuations pose risks to agriculture and livelihoods. The authors recommend using localized climate information to support adaptive planning and development.

Xu et al. [2] have examined runoff changes during the freeze–thaw period in the Changbai Mountains. Using long-term hydrological and climate data, the authors identified strong seasonal and spatial variability in runoff patterns, influenced primarily by snowmelt accumulation and its dynamics. While potential evapotranspiration has limited impact due to cold and frozen conditions, subsurface changes, such as permafrost degradation and land-use shifts, play a growing role in runoff variability. The research underscores the need to consider both climatic and subsurface processes for effective water management in cold-region basins facing environmental change.

The article "*Multiscale Factors Driving Extreme Flooding in China's Pearl River Basin During the 2022 Dragon Boat Precipitation Season*" [3] offers an in-depth analysis of the extreme flooding that occurred in the Pearl River Basin during the 2022 Dragon Boat Festival period, investigating multiscale atmospheric factors that contributed to this unique event. The authors identify several key atmospheric systems operating on different temporal and spatial scales that played a role in the extreme rainfall and flooding. These include large-scale phenomena such as the South Asian High (SAH), the Western Pacific Subtropical High (WPSH), and the South China Sea summer monsoon, which directly influenced precipitation patterns in the region.

A significant factor identified in the research is the Boreal Summer Intraseasonal Oscillation (BSISO), a subseasonal atmospheric oscillation, whose phase stagnation enhanced the intensity and persistence of rainfall during this period. The study also draws attention to the role of the La Niña phenomenon, which, although not directly responsible for the flooding, influenced the atmospheric dynamics by modulating the monsoon and affecting the propagation of the BSISO, further amplifying the precipitation events.

Zheng et al. [3] proposed a conceptual model that highlights the interactions between various factors, illustrating how their combined effects resulted in extreme rainfall and subsequent flooding. They underscore the importance of understanding these interactions for improving flood prediction and management. The authors call for more integrated forecasting systems that can account for these complex atmospheric interactions and provide more accurate early warnings to mitigate the impacts of such hydrological disasters in the future.

The study titled "*Intercomparison of Runoff and River Discharge Reanalysis Datasets at the Upper Jinsha River, an Alpine River on the Eastern Edge of the Tibetan Plateau*" [4] compares the output of four reanalysis datasets in evaluating the hydrologic processes in a hydrographic basin in Tibet. The research shows that model calibration significantly influences the accuracy of runoff and discharge estimates, with calibrated datasets like GloFAS and GRFR generally outperforming uncalibrated ones. However, GRFR's river discharge estimates were overestimated due to suboptimal river routing configurations. The evaluation was substantially improved when rerouted using the Muskingum–Cunge

method. The study also notes that vector-based river routing models offer advantages over grid-based models in representing river networks and catchment areas. These findings underscore the importance of proper model calibration and routing configurations in hydrological modeling, especially in data-scarce and topographically complex regions like the Tibetan Plateau.

The article of Monges et al. [5] presents the results of a Random Forest (RF) model enhanced with time-lagged hydrometeorological inputs for daily streamflow forecasting and compares its performance with the physically based SWAT model across diverse catchments. The RF model outperformed the SWAT model in daily simulations, achieving higher Nash–Sutcliffe Efficiency values, particularly where short-term dynamics dominate. The RF approach required a fraction of the computational time compared to the SWAT approach—under 12 s versus up to 24 h—highlighting its suitability for rapid assessment, especially in data-limited regions. Conversely, the SWAT model demonstrated superior performance for monthly predictions in catchments with irregular flow, leveraging its process-based structure. However, both models exhibited reduced accuracy in snow-influenced basins, particularly for peak flow estimation. These findings support the use of time-lag-informed RF models for efficient, short-term hydrological forecasting while reinforcing the SWAT model's value for long-term planning and in-depth watershed analysis.

In the study "*Intelligent Methods for Estimating the Flood Susceptibility in the Danube Delta, Romania*", Costache et al. [6] evaluate the susceptibility to flood based on eight geographic factors. Various machine learning models are employed, including Gradient Boosting Machine, Random Forest, and Support Vector Machine, to assess and predict flood-prone areas in the Danube Delta (Romania). They found that all factors contribute to flood susceptibility, the most significant predictors being elevation, topographic wetness index, and distance from rivers. The models demonstrated high accuracy in predicting flood-prone zones, with the Random Forest model outperforming the others in terms of predictive performance. The study's results underscore the effectiveness of integrating machine learning approaches with geographic information system data to enhance flood risk assessment and management. By identifying areas with higher flood susceptibility, the research provides valuable insights for policymakers and stakeholders to develop targeted flood mitigation strategies and improve disaster preparedness in the Danube Delta region.

The paper by Stancu et al. [7] examines the influence of various factors on the navigability in one of the Danube channels (in Romania), using hydrological and hydrodynamic models. The rapid sediment build-up indicates the necessity of frequent dredging to maintain navigability in the channel. The study further indicates that ships with deeper drafts, specifically those around 11.5 m, generate propeller-induced currents that significantly erode the seabed, exacerbating the sedimentation problem. Moreover, the research highlights the significant role of the prevailing northeastern marine waves and currents, which contribute to the movement of sediments into the Sulina channel, further complicating the sedimentation challenges. The study confirms that the current dikes remain robust, despite these natural forces' actions. In conclusion, the research provides valuable insights into the complex interactions between marine dynamics and shipping activities in the Sulina channel, offering a deeper understanding of the challenges associated with maintaining safe and efficient navigation. It underscores the importance of ongoing sediment management and infrastructure maintenance in safeguarding this critical maritime route.

The authors of [8] indicate that the Emirate of Sharjah in the United Arab Emirates (UAE) has experienced several such events, most notably the severe urban flooding that occurred on 17 April 2024. These developments highlight the urgent need to reassess existing hydrological tools, particularly Intensity–Duration–Frequency curves, which serve as critical inputs for flood risk assessment, stormwater design, and urban drainage planning.

They applied the Gumbel distribution to annual maximum rainfall data, supplemented by a neural network-based extension technique using Self-Organizing Maps (SOMs), which improves data continuity and accuracy for IDF curve updates. Given the implications of outdated IDF models on flood resilience and infrastructure safety, this work underscores the necessity of incorporating recent climatic variability into hydrological design frameworks.

The article by Dimond et al. [9] explores how uncertainties in climate models influence adaptation pathways in managing the water resources. The authors demonstrate that different climate models can lead to varying adaptation decisions, highlighting the importance of considering a range of scenarios. They advocate for flexible adaptive management strategies that can be adjusted as new information becomes available. The study emphasizes the need for decision-making frameworks that account for uncertainty to ensure resilient and sustainable water management practices.

The study "*Water Management Instructions as an Element of Improving the State of the Pakoski Reservoir (Central–Western Poland)*" by Nowak et al. [10] addresses the growing challenges of managing the Pakoski Reservoir, which has been a vital water resource in the region for over five decades. The reservoir faces deteriorating conditions due to a combination of factors, including climate change, human activities, and the increasing pressure on water resources in its catchment area. The study emphasizes the need for more effective management strategies that consider both hydrological data and environmental considerations. A key proposal is the development of comprehensive water management instructions, which would provide guidelines for water quality improvement, sustainable use, and the prevention of ecological degradation in the reservoir. The authors stress that these measures would help maintain the balance of the reservoir's ecosystems while supporting biodiversity and ensuring a stable water supply for local communities. The article also highlights the importance of adaptive management approaches, where water management practices are flexible and can be adjusted in response to changing conditions, particularly in uncertain future climate patterns.

Article [11] presents the development and implementation of a cheap system for the hydrological monitoring of a protected area in Colombia, which is affected by climate change. Despite the simplicity of the tools, the collected data provided valuable insights into the hydrological behavior of the lagoon. The study emphasizes the importance of understanding water exchange processes between the lagoon and the sea, especially considering the potential impacts of climate change.

3. Concluding Remarks

As its editors, we are particularly happy with the balance struck in this collection—between theoretical depth and applied relevance; between global overviews and locally rooted case studies. The inclusion of perspectives from both data-rich and data-scarce regions ensures that the Special Issue remains globally relevant while recognizing the specific challenges of local contexts.

We are deeply grateful to the authors for their high-quality contributions and to the reviewers for their critical, constructive feedback. We also thank the editorial team for their support in the production of this Special Issue. It is our hope that the knowledge shared within these pages will inspire further research, strengthen cross-disciplinary collaboration, and ultimately contribute to building more resilient hydrological systems and societies.

We invite readers from across disciplines—hydrology, climatology, environmental science, engineering, and beyond—to engage with the work presented here. The challenges we face in adapting to hydrological change are formidable, but through scientific innovation, collaborative action, and sustained dialogue, meaningful progress is possible.

Author Contributions: Writing—original draft preparation, A.B.; writing—review and editing, A.B., R.C. and C.Ș.D. All authors have read and agreed to the published version of the manuscript.

Funding: This research received no external funding.

Conflicts of Interest: The authors declare no conflicts of interest.

List of Contributions:

1. Babaousmail, H.; Ojara, M.A. Evaluation of Historical Dry and Wet Periods over Lake Kyoga Basin in Uganda. *Water* **2025**, *17*, 1044. https://doi.org/10.3390/w17071044.
2. Xu, M.; Chen, Y.; Liu, D.; Qi, P.; Sun, Y.; Guo, L.; Zhang, G. Characteristics of Runoff Changes during the Freeze–Thaw Period and the Response to Environmental Changes in a High-Latitude Water Tower. *Water* **2024**, *16*, 2735. https://doi.org/10.3390/w16192735.
3. Zheng, J.; Wu, N.; Ren, P.; Deng, W.; Zhang, D. Multiscale Factors Driving Extreme Flooding in China's Pearl River Basin During the 2022 Dragon Boat Precipitation Season. *Water* **2025**, *17*, 1013. https://doi.org/10.3390/w17071013.
4. Chen, S.; Yang, H.; Zheng, H. Intercomparison of Runoff and River Discharge Reanalysis Datasets at the Upper Jinsha River, an Alpine River on the Eastern Edge of the Tibetan Plateau. *Water* **2025**, *17*, 871. https://doi.org/10.3390/w17060871.
5. Moges, D.M.; Virro, H.; Kmoch, A.; Cibin, R.; Rohith, R.A.N.; Martínez-Salvador, A.; Conesa-García, C.; Uuemaa, E. Streamflow Prediction with Time-Lag-Informed Random Forest and Its Performance Compared to SWAT in Diverse Catchments. *Water* **2024**, *16*, 2805. https://doi.org/10.3390/w16192805.
6. Costache, R.; Crăciun, A.; Ciobotaru, N.; Bărbulescu, A. Intelligent Methods for Estimating the Flood Susceptibility in the Danube Delta, Romania. *Water* **2024**, *16*, 3511. https://doi.org/10.3390/w16233511.
7. Stancu, M.V.; Cheveresan, M.I.; Sârbu, D.; Maizel, A.; Soare, R.; Bărbulescu, A.; Dumitriu, C.Ș. Influence of Marine Currents, Waves, and Shipping Traffic on Sulina Channel Fairway at the Mouth of the Black Sea. *Water* **2024**, *16*, 2779. https://doi.org/10.3390/w16192779.
8. Almheiri, K.B.; Rustum, R.; Wright, G.; Adeloye, A.J. The Necessity of Updating IDF Curves for the Sharjah Emirate, UAE: A Comparative Analysis of 2020 IDF Values in Light of Recent Urban Flooding (April 2024). *Water* **2024**, *16*, 2621. https://doi.org/10.3390/w16182621.
9. Dimond, J.; Roose, W.; Beevers, L. Making Different Decisions: Demonstrating the Influence of Climate Model Uncertainty on Adaptation Pathways. *Water* **2025**, *17*, 1366. https://doi.org/10.3390/w17091366.
10. Nowak, B.; Dumieński, G.; Ławniczak-Malińska, A. Water Management Instructions as an Element of Improving the State of the Pakoski Reservoir (Central–Western Poland). *Water* **2025**, *17*, 403. https://doi.org/10.3390/w17030403.
11. Nardini, A.G.C.; Escobar Villanueva, J.R.; Pérez-Montiel, J.I. Hydrological Monitoring System of the Navío-Quebrado Coastal Lagoon (Colombia): A Very Low-Cost, High-Value, Replicable, Semi-Participatory Solution with Preliminary Results. *Water* **2024**, *16*, 2248. https://doi.org/10.3390/w16162248.

References

1. IPCC. Sixth Assessment Report (AR6). Intergovernmental Panel on Climate Change, 2021. Available online: https://www.ipcc.ch/assessment-report/ar6/ (accessed on 1 May 2025).
2. Bărbulescu, A.; Dumitriu, C.S.; Maftei, C. On the Probable Maximum Precipitation Method. *Rom. J. Phys.* **2022**, *67*, 1–8.
3. Lindersson, S.; Brandimarte, L.; Mård, J.; Di Baldassarre, G. A review of freely accessible global datasets for the study of floods, droughts and their interactions with human societies. *Wiley Interdiscip. Rev. Water* **2020**, *7*, e1424. [CrossRef]
4. Payne, A.E.; Demory, M.E.; Leung, L.R.; Ramos, A.M.; Shields, C.A.; Rutz, J.J.; Siler, N.; Villarini, G.; Hall, A.; Ralph, F.M. Responses and impacts of atmospheric rivers to climate change. *Nat. Rev. Earth Environ.* **2020**, *1*, 143–157. [CrossRef]
5. Hattermann, F.F.; Krysanova, V. Impact attribution: Exploring the contribution of climate change to recent trends in hydrological processes—An editorial introduction. *Clim. Chang.* **2024**, *177*, 172. [CrossRef]

6. Terskii, P.N.; Kuleshov, A.A.; Chalov, S.R. Water Balance Assessment Using Swat Model. Case Study on Russian Subcatchment of Western Dvina River. In *Climate Change Impacts on Hydrological Processes and Sediment Dynamics: Measurement, Modelling and Management*; Chalov, S., Golosov, V., Li, R., Tsyplenkov, A., Eds.; Springer Proceedings in Earth and Environmental Sciences; Springer: Cham, Switzerland, 2019; pp. 83–87. [CrossRef]
7. Jiang, C.; Zhang, L.; Tang, Z. Multi-temporal scale changes of streamflow and sediment discharge in the headwaters of Yellow River and Yangtze River on the Tibetan Plateau, China. *Ecol. Eng.* **2017**, *102*, 240–254. [CrossRef]
8. Huang, S.C.; Kumar, R.; Rakovec, O.; Aich, V.; Wang, X.Y.; Samaniego, L.; Liersch, S.; Krysanova, V. Multimodel assessment of flood characteristics in four large river basins at global warming of 1.5, 2.0 and 3.0 K above the preindustrial level. *Environ. Res. Lett.* **2018**, *13*, 124005. [CrossRef]
9. Kundzewicz, Z.W. Climate change impacts on the hydrological cycle. *Ecohydrol. Hydrobiol.* **2008**, *8*, 195–203. [CrossRef]
10. Wang, Q.; Deng, H.; Jian, J. Hydrological Processes under Climate Change and Human Activities: Status and Challenges. *Water* **2023**, *15*, 4164. [CrossRef]
11. Clarke, B.J.; Otto, F.E.; Jones, R.G. Inventories of extreme weather events and impacts: Implications for loss and damage from and adaptation to climate extremes. *Clim. Risk Manag.* **2021**, *32*, 100285. [CrossRef]
12. Xue, P.; Zhang, C.; Wen, Z.; Yu, F.; Park, E.; Nourani, V. Climate variability impacts on runoff projection in the 21st century based on the applicability assessment of multiple GCMs: A case study of the Lushi Basin, China. *J. Hydrol.* **2024**, *638*, 131383. [CrossRef]
13. Bărbulescu, A. Modeling the impact of the human activity, behavior and decisions on the environment. Marketing and green consumer. *J. Environ. Manag.* **2017**, *204 Pt 3*, 813. [CrossRef]
14. Bărbulescu, A.; Barbeş, L. Statistical methods for assessing water quality after treatment on a sequencing batch reactor. *Sci. Total Environ.* **2021**, *752*, 141991. [CrossRef] [PubMed]
15. Li, P.; Wu, J. Water Resources and Sustainable Development. *Water* **2024**, *16*, 134. [CrossRef]
16. Brown, C.; Boltz, F.; Freeman, S.; Tront, J.; Rodriguez, D. Resilience by design: A deep uncertainty approach for water systems in a changing world. *Water Secur.* **2020**, *9*, 100051. [CrossRef]
17. Herman, J.D.; Quinn, J.D.; Steinschneider, S.; Giuliani, M.; Fletcher, S. Climate adaptation as a control problem: Review and perspectives on dynamic water resources planning under uncertainty. *Water Resour. Res.* **2020**, *56*, e24389. [CrossRef]

water

MDPI

Article

Evaluation of Historical Dry and Wet Periods over Lake Kyoga Basin in Uganda

Hassen Babaousmail [1] and Moses A. Ojara [2,3,*]

[1] School of Atmospheric Science and Remote Sensing, Wuxi University, Wuxi 214105, China; baw.hassan47@gmail.com
[2] Division of Station Network and Observations, Department of Meteorological Services, Plot 21, 28 Port Bell Rd, Kampala P.O. Box 7025, Uganda
[3] Green Life Research Initiative Uganda Limited, Namulonge-Nabalanga, Wakiso P.O. Box 1179, Uganda
* Correspondence: ojacksmoz@gmail.com; Tel.: +256-70-249-3588

Abstract: Rainfall datasets from the Uganda National Meteorological Authority (UNMA) for 1981–2017 and two reanalysis datasets (Climate Hazards Group Infrared Precipitation with Stations data (CHIRPS) and Tropical Applications of Meteorology using Satellite data (TAMSAT) were used to compute drought and flood tendencies from 1981 to 2017. The cumulative departure index (CDI) and rainfall anomaly index (RAI) were computed to show drought and flood tendencies in the region. Meanwhile, dry days (DD) and wet days (WD) were computed based on the definition as a day of the season with rainfall amounts less than 1.0 mm and greater than 1.0 mm, respectively. The CDI graphics indicated below-average rainfall during 1981–1987 and relatively wetter conditions during 1989–1995 for all stations in the region. Generally, seasonal rainfall declined over the first 27 years but an increasing trend in both MAM (March–April–May) and SOND (September–October–November–December) was observed in most stations during 2006–2017. The highly variable seasonal rainfall in the region is expected to impact the livelihoods of the communities. This study recommends that the use of tailor-made weather and climate information for planning economic development programs such as agriculture will play a critical role in improving the livelihood of the communities in the region.

Keywords: rainfall variability; rainfall anomaly index (RAI); cumulative departure index (CDI); Lake Kyoga Basin; Uganda

1. Introduction

African countries are expected to be the most affected by climate change and variability yet are the least prepared to deal with the effects [1–6]. Climate change is also emerging as one of the main challenges humankind will have to face for many years to come. It could become a major threat to world food security, as it has a strong impact on food production, access, and distribution [7]. Across East Africa (EA), rainfall is predicted to increase by 5–20% during the December to February rainy season and by 5–10% between the June and August rainy seasons [8]. In Uganda, it is stated that current average temperatures are expected to increase by between 0.7 °C and 1.5 °C by the 2020s [9]; however, this will be interrupted by the naturally variable climate by high spatial and temporal variability of rainfall largely explained by natural phenomena such as the El Niño and Southern Oscillation (ENSO) [10,11].

Climate variability and recent changes have exposed most parts of the East African region to poverty and hunger [12,13], starvation, and death, as seen recently in northeastern

Uganda. This is exacerbated by the impact of unreliable weather patterns, usually resulting in worse food insecurity in the region [14]. Precipitation variability is expected to intensify the magnitude and frequency of flood and drought events that negatively affect agricultural sectors in most countries of EA [4,15], yet the increasing human population continues to exert pressure on food security, worsening the already fragile situation [16].

Climate variability impacts have the potential to undermine and even undo the progress made in improving the socio-economic well-being of countries, especially those that rely on natural weather systems for agriculture, like Uganda [17]. Furthermore, given an estimate that 80% of farmers produce food primarily to meet their family needs, rural poverty in Uganda could worsen with climate change, and due to their low income and lower technological and capital stocks, households are predicted to have limited options to adapt to climate change [6,18,19].

In the recent study to determine climate change trends in the Lake Kyoga Basin using standardized precipitation and anomaly indexes, significant changes in precipitation were revealed at some stations during the period 1981–2020, and the frequency of severe wet weather events was more than for dry weather events in many stations, further indicating that precipitation was increasing over the Lake Kyoga Basin [20].

Similarly, studies using long-term (1948–2016) changes in gridded ($0.25^\circ \times 0.25^\circ$) Princeton Global Forcing (PGF) precipitation and potential evapotranspiration (PET) data over two sub-catchments in the Lake Kyoga Basin revealed negative trends ($p < 0.05$) in annual precipitation and positive anomalies in the early 2000s through 2016, which forms part of this current study period of 1981–2017. Negative anomalies existed between 1960 and 2000. Both were seasonal [18]. Additionally, analysis of extreme precipitation events over the Lake Kyoga Basin using the same gridded ($0.25^\circ \times 0.25^\circ$) PGF precipitation dataset and period (1948–2016 from Princeton Global Forcing (PGF)) showed that the number of wet days decreased, although insignificantly ($p > 0.05$), and less frequent rains were received over the Lake Kyoga Basin, although some events had high intensity [17].

Using CenTrends gridded precipitation (1961–2015), the March to May (MAM) precipitation was shown to have insignificantly decreased ($p > 0.05$) in most parts of the Lake Kyoga Basin, while in the second season of September to November (SON), precipitation revealed a positive trend [17]. The variability of seasonal and annual precipitation over the Lake Kyoga Basin also showed an abrupt change in rainfall in the MAM season in 1982; the SON season did not show a significant abrupt change but a significant ($p < 0.05$) increase in rainfall above the upper limit from 1994 to date [19].

The impacts of highly uncertain rainfall patterns in the Lake Kyoga Basin provide major challenges to rural communities that consist of subsistence and nomadic farmers, as issues of water shortages for agriculture are common. This is usually due to drier conditions experienced in the areas with occasionally wet periods due to erratic rainfall. Economic losses have not been reliably quantified, but physical damages include crop failures due to droughts or floods, destruction to crops by hailstones during wet periods, livestock death due to lack of water or lightning strikes, and damages to physical infrastructures such as roads and buildings, among others. In order to minimize such losses and destruction reliably, location-specific weather and climate information need to be available.

There have been general studies that generated climate change and variability information in Uganda [17,19–21], but these cannot be used for adaptation at the local level. Further, recent trends in rainfall, weather, and climate information need to be frequently generated to aid in making both strategic and tactical decisions. There is a need for proper planning of agricultural activities around the Lake Kyoga Basin based on reliable weather and climate information to adapt to climate variability with its associated implications on food security, poverty, and health-related challenges.

The remaining sections of this study are structured as follows. Section 2 describes the study area. Section 3 is reserved for data and methods, while Section 4 presents the main results. Section 5 is for discussion. The conclusions and recommendations are highlighted in Section 6.

2. Study Area

The study area lies along geographical latitude and longitude of 0°13′ N, 3°41 N and longitude 32°02′ E, 34°52′ E. The Lake Kyoga Basin is among the largest basins in Uganda (Figure 1).

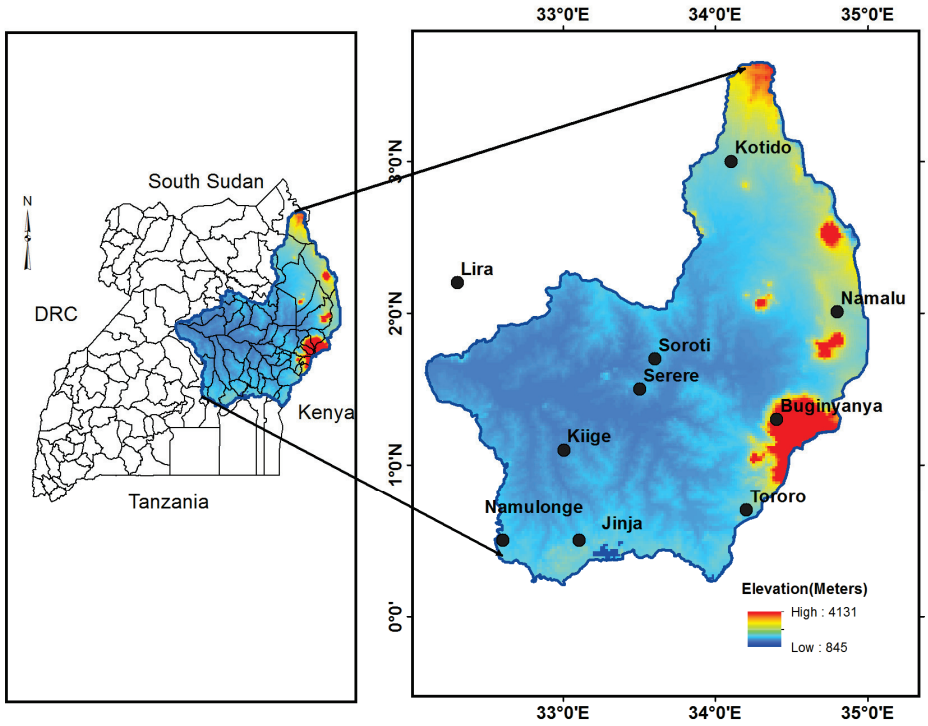

Figure 1. Map of the Lake Kyoga Basin in Uganda (inset) showing the elevation of the Lake Kyoga Basin and the weather stations (black dots).

Generally, the Lake Kyoga Basin is a low laying area with an elevation ranging between 450 m and 867 m as per the Shuttle Radar Topography Mission digital model (SRTM) released in 2004. The climate of the basin is modified by the large swampy surrounding area. The basin has a rainy season from March to November, with a marked minimum in June and marked peaks in April to May and August to October, while December and January are the driest months.

3. Materials and Methods

3.1. Materials

3.1.1. Observed Station Climate Data

The in situ daily and monthly rainfall climate data were obtained from the Uganda National Meteorological Authority for Namulonge, Tororo, Soroti Jinja, Lira, Serere, Kiige, Buginyanya, Kotido, and Namalu stations. The duration for all datasets was taken in the range of 1981 to 2017 and collected from manual instruments. The stations are presented in Figure 1 and Table 1. The quality control measures for the observed rainfall dataset included checks control to identify the negative precipitation values, typing errors to identify gaps in the dataset, and false zeros [22]. All the rainfall data were processed through an extensive series of quality control procedures to ensure erroneous values, such as errors in manual

keying. Negative daily precipitation amounts were removed and/or identified. Some stations, such as Namulonge, Tororo, Soroti, Jinja, and Lira, had daily rainfall datasets, which are required for the determination of critical phenomena like the onset and cessation of rainfall. The remaining stations had only monthly rainfall totals; these included Jinja, Nakasongola, Serere, Kiige, Buginyanya, Kotido, and Namalu. Thus, we are unable to determine the onset and cessation in these rainfall stations and zones. Almost none of the stations had complete temperature datasets (except for Soroti and Jinja, both located at the airfield).

Table 1. Detailed geographical information of meteorological stations in the Lake Kyoga Basin.

Stations	Longitude (Degree)	Latitude (Degree)	Elevation (Meters)	Data Period (Years)	Rainfall Zones
Namulonge	32.6	0.5	1128.3	1981–2017	B
Tororo	34.2	0.7	1176	1981–2017	D
Soroti	33.6	1.7	1115.8	1981–2017	E
Jinja	33.1	0.5	1175.1	1981–2017	A2
Lira	32.3	2.2	1120.2	1981–2017	I
Serere	33.5	1.5	1098	1961–2017	E
Kiige	33	1.1	1089.4	1981–2017	B
Buginyanya	34.4	1.3	1875	1981–2017	F
Kotido	34.1	3	1219.5	1981–2017	G
Namalu	34.8	2	1274.4	1981–2017	L

3.1.2. Climate Hazards Group Infrared Precipitation with Stations Data (CHIRPS)

The gridded precipitation of the spatial resolution of $0.05^\circ \times 0.05^\circ$ for 1981 to 2017 was sourced from the Climate Hazards Group Infrared Precipitation with Stations data (CHIRPS). CHIRPS is a product developed by merging three types of high-resolution data, including global climatology, satellite estimates, and in situ observations, employing a combination of interpolation techniques that improves rainfall products [23]. Funk et al. [23] provide an elaborated detail of CHIRPS data. Over EA, the lack of well-distributed and managed rain gauges is a challenge to the spatial analysis of climate data [24] that can only be overcome by the use of satellite or reanalysis datasets. Data can be accessed through the webpage https://data.chc.ucsb.edu/products/CHIRPS-2.0/global_daily/netcdf/p25/ (accessed on 20 October 2024).

3.1.3. TAMSAT Precipitation Data

The TAMSAT (Tropical Applications of Meteorology using Satellite data) precipitation dataset is widely used for monitoring and studying rainfall patterns in Africa. The data have a spatial resolution of $0.0375^\circ \times 0.0375^\circ$ (approximately 4 km $\times$ 4 km) and temporal resolution of daily, 10-day, and monthly [25]. TAMSAT precipitation data are available from 1983 to the present and can be accessed through the links:

https://data.tamsat.org.uk/data-download/rainfall/ (accessed on 25 October 2024) and https://research.reading.ac.uk/tamsat/regridded-files/ (accessed on 25 October 2024).

TAMSAT precipitation data are derived from a combination of satellite and ground-based observations, such as geostationary satellite images from the European Organisation for the Exploitation of Meteorological Satellites (EUMETSAT), rain gauge data from ground-based rainfall measurements from national meteorological agencies and research institutions, and finally, Tropical Rainfall Measuring Mission (TRMM) satellite data (to 2015). The TAMSAT algorithm uses a combination of techniques to estimate rainfall from

satellite data, including Cold Cloud Duration (CCD) and Rainfall Estimation Algorithm (REA) [25].

A Taylor diagram was used to evaluate these datasets, CHIRPS and TAMSAT, against the observed monthly rainfall datasets based on correlation (r), the RMSD, and the fraction of their variances [26].

3.2. Methods

3.2.1. Descriptive Statistics and Mann–Kendall Trend Analysis

For all the stations, monthly observed rainfall data were computed into annual rainfall and the two main rainfall seasons of March–May (MAM) and September–December (SOND) following the well-established seasons in the region [20]. Descriptive statistics were computed to mean, minimum, and maximum rainfall over the annual and seasonal basis in the region.

The trend analysis was performed using a rank-based non-parametric Mann–Kendall test (MK) [27,28]. The MK test was selected because it allows the existence of a trend in any data to confirm the null hypothesis of no trend. It does not require the sample to conform to any specific probability distribution since it works well even with insufficient or abnormal values.

The advantage of this technique is that it does not require any hypothesis about the variables and is more powerful than a parametric test. The Mann–Kendall (MK) test statistic was computed at a 5% significance level. In recent years, the MK statistical approach for trend analysis in climate studies has been employed [8,29]. Further discussion and the mathematical expression used to calculate MK trend statistics can be referred to in several studies [8,29].

3.2.2. Sen's Slope Methods

To show the rate of change within the annual and seasonal rainfall, Sen's slope test [30,31] was employed. The test gives a more robust estimation of the direction, especially when the trend cannot be estimated by other statistical approaches like Kendall's test statistics or regression. This method is considered adequate due to its robust handling of outliers in the datasets. It is not affected by any extreme distributions and does not entail any normal distribution of the residuals. It has been generally employed in various studies to examine the linear tendencies of hydro/climatic variables across multiple domains, e.g., [8,32].

The Sen's slope test is illustrated by Equations (1) and (2) below:

$$t_i = \frac{Y_j - K_k}{j - k} \tag{1}$$

where Y_j and K_k represent data values at the time, respectively. However, considering the expression of S in the Equation (2) below:

$$S = \begin{cases} T_{M+1/2} & M = odd \\ \left((T_{\frac{(M)}{2}} + (T_{\frac{(M+2)}{2}} \right)_{M = even} \end{cases} \tag{2}$$

The median of these M values of S is a Sen's estimator of the slope. If M is odd, then Sen's estimator is computed by the top part of Equation (2), and if M is even, Sen's estimator is calculated by the lower part of Equation (1). Finally, S is tested by a two-sided test at a 100% (1-α) confidence interval, and the actual slope is obtained.

3.2.3. Number of WET/DRY Days over MAM and SOND Rainfall Seasons

For the two well-known rainfall seasons over Uganda and EA (MAM and SOND), wet and dry days are generated by the common definition that a rainy day must experience at least 1.0 mm of rainfall, while a dry day is a day with less than 1.0 mm of rainfall [33,34]. When recorded over a concessive period, the two variables are referred to as wet and dry spells, respectively. Analyzing the number of wet and dry days is crucial for understanding rainfall variability, managing water resources, planning agricultural activities, studying climate change impacts, and maintaining ecosystem health.

The onset (start) and the cessation (end) of the rainy season were calculated based on the condition that a place must receive 20 mm of rainfall over 2 successive days and should not be followed by a dry spell of 9 days in the next 30 days at the time of the overhead appearance of the sun (March and September). The end of the season was described as being the first 9 days of a dry spell after May 1st and November 1st for the cessation of the first and second seasons, respectively. Consideration for the water balance failing to zero is observed as well. This helped to identify the season length or growing period and amount of rainfall each year in consideration.

3.2.4. Cumulative Departure Index (CDI) for 1981–2017

The MAM and SOND seasonal rainfall variability was further assessed by the cumulative departure index (CDI). The CDI involves the estimation of the arithmetic mean of seasonal rainfall for the period of record. The means of seasonal rainfall were then normalized by Equation (3) below:

$$CDI = (r_1 - R_1)/S \tag{3}$$

where r_1 represent the actual seasonal rainfall of a given year. R_1 is the mean rainfall of the total length of the period and S the standard deviation of the total length of the period. Results of the values were cumulatively added to each other for the period of record and plotted to achieve long-term trends for seasonal as used [33,34].

3.2.5. Rainfall Anomaly Index (RAI) for 1981–2017

Further, the rainfall anomaly index (RAI) was analyzed to show the variability of annual rainfall (frequency and intensity of dry and wet years) and presented through graphical plots for visual interpretation. The RAI is suggested to be very effective in detecting the persistence of drought periods [33]. Rainfall variability indices were used to establish drought periods and to show some haphazard values for drought indication [33]. These simple indices, which use rainfall as the only input, perform comparatively well compared with more complicated indices in depicting periods and intensity of droughts [33,35]. RAI was used to describe annual rainfall variability and it is currently used by many authors [36].

The RAI is calculated from Equation (4) for positive anomalies and Equation (5) for negative anomalies.

$$\text{RAI} = +3\left(\frac{R_f - M_{Rf}}{MH_{10} - M_{Rf}}\right) \tag{4}$$

$$\text{RAI} = -3\left(\frac{R_f - M_{Rf}}{ML_{10} - M_{Rf}}\right) \tag{5}$$

where RAI represents the annual rainfall anomaly index, R_f the actual rainfall for a given year, M_{Rf} the mean of the total length of the record, MH_{10} the mean of the ten highest values of rainfall on record, and ML_{10} the lowest values of rainfall on record.

4. Results

4.1. Relationship Between CHIRPS and TAMSAT and Observed Station Rainfall Data

Figure 2 shows Taylor diagrams for 4 main rainfall stations in the Lake Kyoga Basin, showing the relationship between the two reanalysis datasets (CHIRPS and TAMSAT) with observed datasets. Results showed a strong positive correlation coefficient between the observed station datasets and reanalysis ranging from +0.5 to 0.8 across the four stations, with TAMSAT being a better performer than CHIRPS. TAMSAT and CHIRPS are high-resolution reanalysis datasets that have been blended with station-observed datasets; their quality in the African region has been highly discussed [23]. This is represented by a strong positive correlation that provides confidence in using these datasets to present the ground-based observations in the region with scarcely populated observation stations.

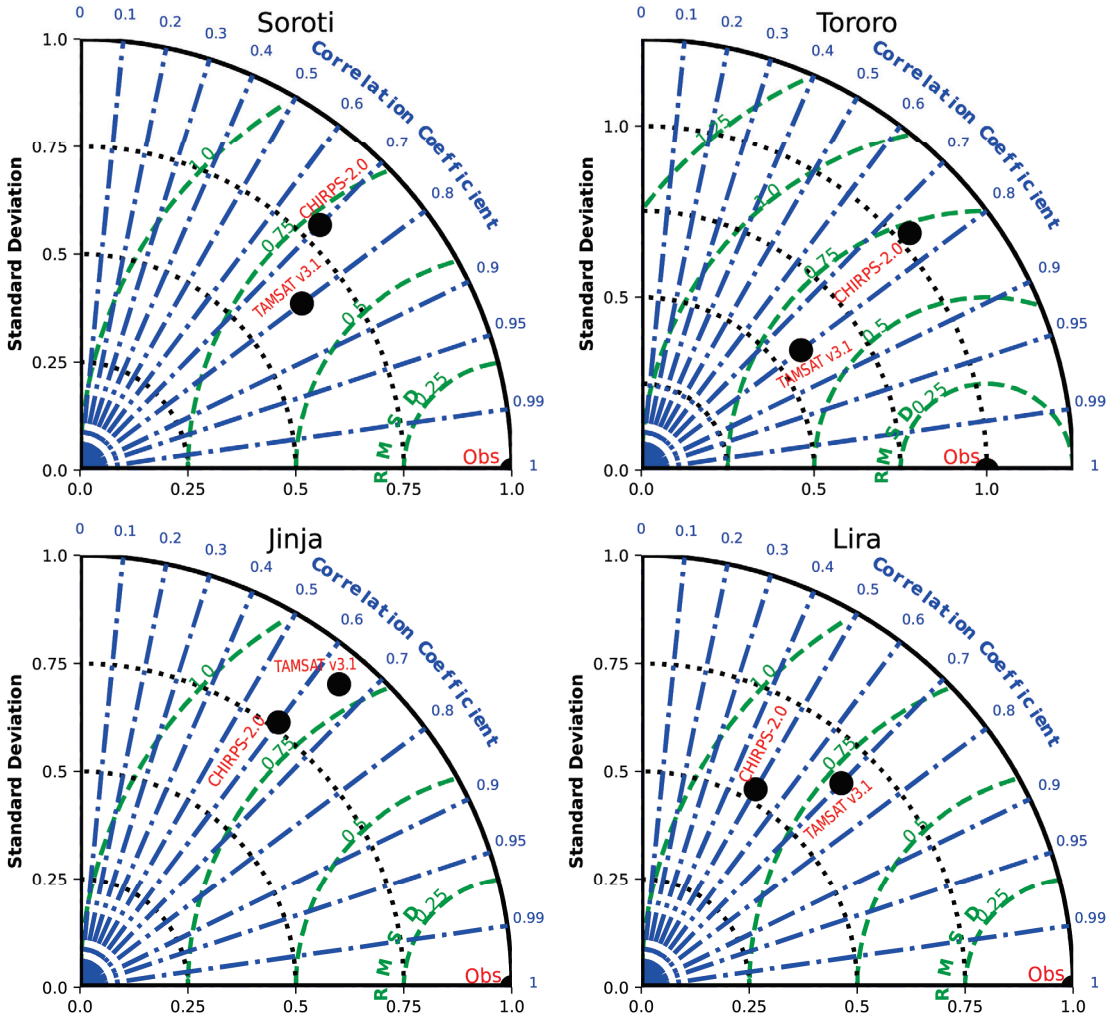

Figure 2. Taylor diagram showing the performance of CHIPRS and TAMSAT datasets against station observed rainfall values.

4.2. Mean Monthly Annual Rainfall Cycles over Different Stations

Figure 3 presents the mean monthly annual rainfall for 9 stations in the Lake Kyoga Basin during the period 1981–2017. Results reveal unimodal rainfall at all the stations within the Lake Kyoga Basin but show a slight decline in June. This result is in agreement with previous studies on the region [37]. Several factors usually contribute to rainfall in the Lake Kyoga Basin, including the north/south movement of ITCZ and the Congo air mass, and rainfall is modified by topographic features [36–38].

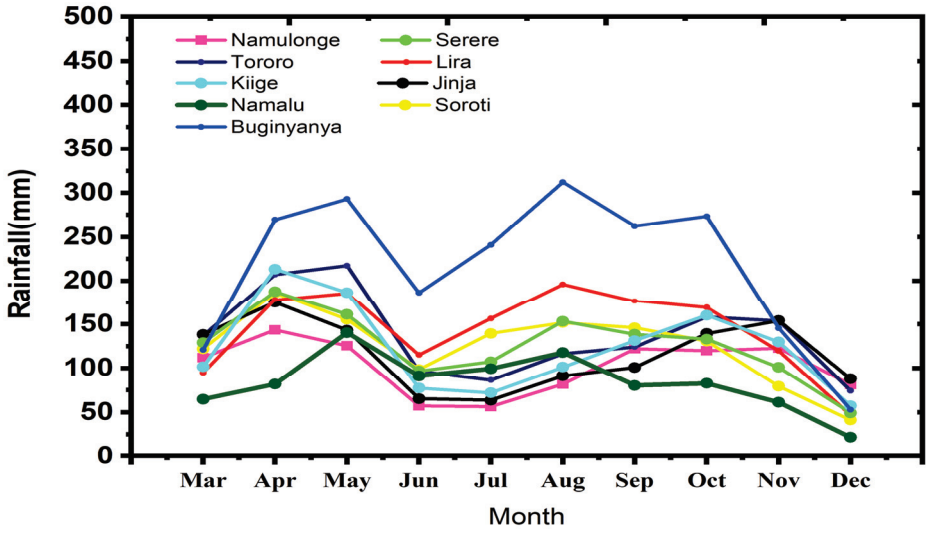

Figure 3. Mean monthly rainfall cycle for different stations for the period 1981–2017.

The results showed high values of seasonal rainfall recorded during the months of March–April–May (MAM) and September–October–November–December (SOND), coinciding with two main modal rainfall regimes (MAM) and (SOND) reported by other studies over the regions [39,40]. In this study, these two main rainy periods, MAM and SOND, are considered the major seasons for subsequent use in the seasonal analysis. The main rainfall season from March to May (MAM) is usually referred to as the "long rains" and September to December as the "short rains" in EA [39–41].

4.3. Descriptive Statistics and Trends of Seasonal Annual Rainfall

A descriptive statistical analysis of seasonal annual rainfall is presented in Table 2. The results show that the highest annual rainfall of 3179.4 mm was recorded at the Buginyanya station in the Mount Elgon area, followed by 2015.7 mm recorded at the Namulonge station located near Lake Victoria. The annual rainfall over the region showed positive trends at all the stations, but statistically significant trends were observed at some stations, including the Namalu, Tororo, and Jinja stations. At these stations, the rate of change is 87.8, 8.6, and 50.4 (mm/decade), respectively.

Table 2. Shows a statistical description of annual and seasonal rainfall and MK trend and Sen's slope for four major stations in the Lake Kyoga Basin in Uganda. The stations with an asterisk (*) mark show a statistically significant trend; Min and Max show minimum and maximum values in millimeters (mm). Negative Sen's slope values show a decreasing trend, while a positive Sen's slope indicates a positive trend.

	Annual					MAM					SOND				
Station	**Mean (mm)**	**Max (mm)**	**Min (mm)**	***p*-v (MK)**	**Sen's Slope (mm/ Decade)**	**Mean (mm)**	**Max (mm)**	**Min (mm)**	***p*-v (MK)**	**Sen's Slope (mm/ Decade)**	**Mean (mm)**	**Min (mm)**	**Max (mm)**	***p*-v (MK)**	**Sen's Slope (mm/ Decade)**
Namalu	1180.6	1633.5	765.0	0.01 *	87.8	385.0	534.3	236.5	0.539	11.8	346.5	184.7	673.1	0.00	5.9
Buginyanya	1719.6	3179.4	2064	0.11	63.9	526.7	681.7	337.0	0.539	9.9	560.1	224.4	861.5	0.04	4.9
Kiige	1272.4	1530.7	958.5	0.16	32.6	467.1	645.1	364.7	0.685	−4.7	460.6	180.3	723.8	0.09	3.4
Namulonge	1719.6	2015.7	1240.5	0.27	52.9	470.7	615.4	326.3	0.647	4.3	452.8	140.9	772.6	0.72	12.3
Soroti	1411.9	1813.9	1148.0	0.25	30.3	484.8	660.0	366.5	0.969	−7.0	455.0	244.0	740.2	0.34	32
Tororo	1573.3	2203.5	1191.8	0.01 *	8.6	578.1	773.9	411.2	0.410	7.8	532.9	153.8	955.1	0.01	68.7
Jinja	1331.9	1739.1	1073.5	0.02 *	50.4	476.8	612.5	318.9	0.244	12.7	489.7	167.0	863.2	0.41	29.1
Lira	1405.6	1698.0	997.3	0.38	19.6	425.8	534.1	296.6	0.302	−10.5	484.8	202.0	707.4	0.23	30.1

Further, results also revealed that MAM seasonal rainfall had both decreasing and increasing trends, although both are statistically insignificant at all the stations. In terms of rainfall amount, MAM revealed between 236.5 mm at Namalu station and 773.9 mm at Tororo station. SOND seasonal rainfall over the region ranged from 184.7 to 707.4 mm at Namalu and Tororo stations. Overall, there was an increasing trend in the SOND seasonal rainfall amount, with statistically significant trends at some stations, including the Namalu, Buginyanya, and Tororo stations. For SOND, Sen's lope analysis showed that the rate of change for these stations is 5.9, 4.9, and 68.7 mm/decade at Namalu, Buginyanya, and Tororo stations, respectively.

The annual and seasonal rainfall revealed that there is a high spatial variation of rainfall within the region as some stations reported an amount about thrice the other stations within the regions, and others showed statistically significant trends compared to the others. The high spatial variability of rainfall in the region has been reported [17,37,41]. This high spatial variability, therefore, calls for location-specific approaches in managing the impacts of rainfall and climate events in the region.

4.4. Onset and Cessation of Rainfall for Lake Kyoga Basin

Table 3 shows the summary statistics for onset, cessation date, and seasonal length for 5 major rainfall stations in the Lake Kyoga Basin. For Soroti station, the analysis results showed that over the recent years 1981–2017, the mean start of rains, or season onset, is 15 March of the year, the mean cessation date is 27 June, and the mean season's length is approximately 3.5 months. The earliest start of the rains could be as early as 29 February. The latest possible date for the start of the rains is as late as 15 April.

Table 3. Summary of onset, cessation dates, and seasonal length for different rainfall stations in the Lake Kyoga Basin 1981–2017. CV is the coefficient of variation of the different seasonal characteristics.

		MAM			SOND		
Station	**Statistics**	**Onset (Dates)**	**Cessation (Dates)**	**Seasonal Length Months**	**Onset (Date)**	**Cessation (Dates)**	**Seasonal Length Days**
Soroti	Mean	15 March	27 June	3.5	21 July	15 November	3.7
	Minimum	29 February	30 May	2.0	1 July	1 November	1.8
	Maximum	15 April	29 September	6.7	23 October	31 December	5.3
	CV	11%	11%	33%	11%	5%	5%
Namulonge	Mean	30 March	22 June	2.7	21 August	24 November	3.1
	Minimum	3 March	1 June	1.0	1 August	1 November	1.6
	Maximum	14 May	10 August	4.6	31 October	26 December	4.4
	CV	22%	9%	30%	9%	6%	22%
Tororo	Mean	19 March	7 July	3.6	26 August	7 December	3.3
	Minimum	1 March	1 June	2.2	1 August	17 November	1.5
	Maximum	27 April	15 October	6.2	7 October	31 December	4.7
	CV	19%	16%	27%	8%	5%	23%
Buginyanya	Mean	16 March	13 July	6.5	4 September	24 November	2.7
	Minimum	29 February	29 June	6.0	19 August	20 November	3.1
	Maximum	26 April	29 November	11.1	4 November	24 December	3.3
	CV	21%	16%	23%	7%	3%	20%
Lira	Mean	29 March	6 August	2.9	14 August	27 November	3.4
	Minimum	2 March	3 June	2.0	1 August	1 November	3.0
	Maximum	17 May	14 December	4.5	9-Oct	30 December	3.6
	CV	19%	31%	1%	7%	5%	1%

Similarly, at Namulonge station, results revealed that 19 March is the mean date for the onset of seasonal rainfall, with 22 June as the mean cessation date. It was revealed that the earliest possible date is 3 March, while the latest onset of the first rainfall period could be as late as 14 May. In regard to the cessation date, the mean cessation date is 7 July, while the mean seasonal length is 3.3 months.

For Tororo station, results revealed that the mean onset of the rainy season is on 19 March, and the mean cessation date is 7 July, while the mean seasonal length is about 3.6 months. It was also found that the first season can start as early as 1 March and end by 1 June. Additionally, the second season presented a mean onset date of 26 August and a cessation date of 7 December, with about 3.3 months as the mean seasonal length. Conversely, the second season revealed 1 Aug as the earliest onset date and 17 November as the earliest cessation date; this also indicated 1.5 months as the shortest seasonal length that could be experienced. The second rainfall season could also start on 7 October and cease as late as 31 December, presenting the longest seasonal length of 4.7 months.

For the Lira station, the mean onset and cessation of the first rainy seasons are revealed as 29 March and 6 August, respectively, with the mean seasonal length being approximately 2.9 months. Similarly, the mean onset and cessation dates for the second rainy season are approximated to be 14 August and 27 November, with a mean seasonal length of 3.4 months revealed for this station. At Lira station, the first rainy season of MAM could start as early as 2 March and end as early as 3 June, showing the shortest season of approximately 2 months. Moreover, the second rainfall season could also start (onset) by 1 August and end by 1 November, with the shortest seasonal length of 3 months. For the second season, the latest onset and cessation dates are 9 October and 14 December, respectively. This also shows the longest seasonal length, 4.5 months. In addition to these, the rainfall station showed 9 October and 30 December as the latest onset and cessation of the second rainy season, respectively. The longest seasonal length in this rainfall zone is approximately 3.6 months.

Finally, at Buginyanya station, results revealed that 13 March is the mean date for the onset of seasonal rainfall, with 13 July as the mean cessation date. It was revealed that the earliest possible date is 29 February, while the latest onset of the first rainfall period could be as late as 26 April. In regard to the cessation date, the mean cessation date is 13 July, while the mean seasonal length is 3.3 months. For the second season, the mean onset date is 4 September, and the cessation date is 24 November, with a seasonal length of 2.7 months. The earliest possible start of the rains is 19 August, and the cessation date is 20 November, with a seasonal length of 3.1 months. The latest possible start of the second season is 4 November, and the cessation date is 24 December, with a seasonal length of 3.3 months.

4.5. Temporal Variation in Annual and Seasonal Rainfall in Lake Kyoga Basin

Figure 4 shows the temporal variation in the annual rainfall over the Lake Kyoga Basin during 1981–2017. Results indicate a decline in the annual rainfall during the first period of the study, 1981–1985, for most stations, including Kiige, Namulonge, Buginyanya, Serere, Lira, and Namalu; this coincides with the reported drought episodes of 1983–1985 over EA which caused severe impacts on socio-economic activities in the region [40].

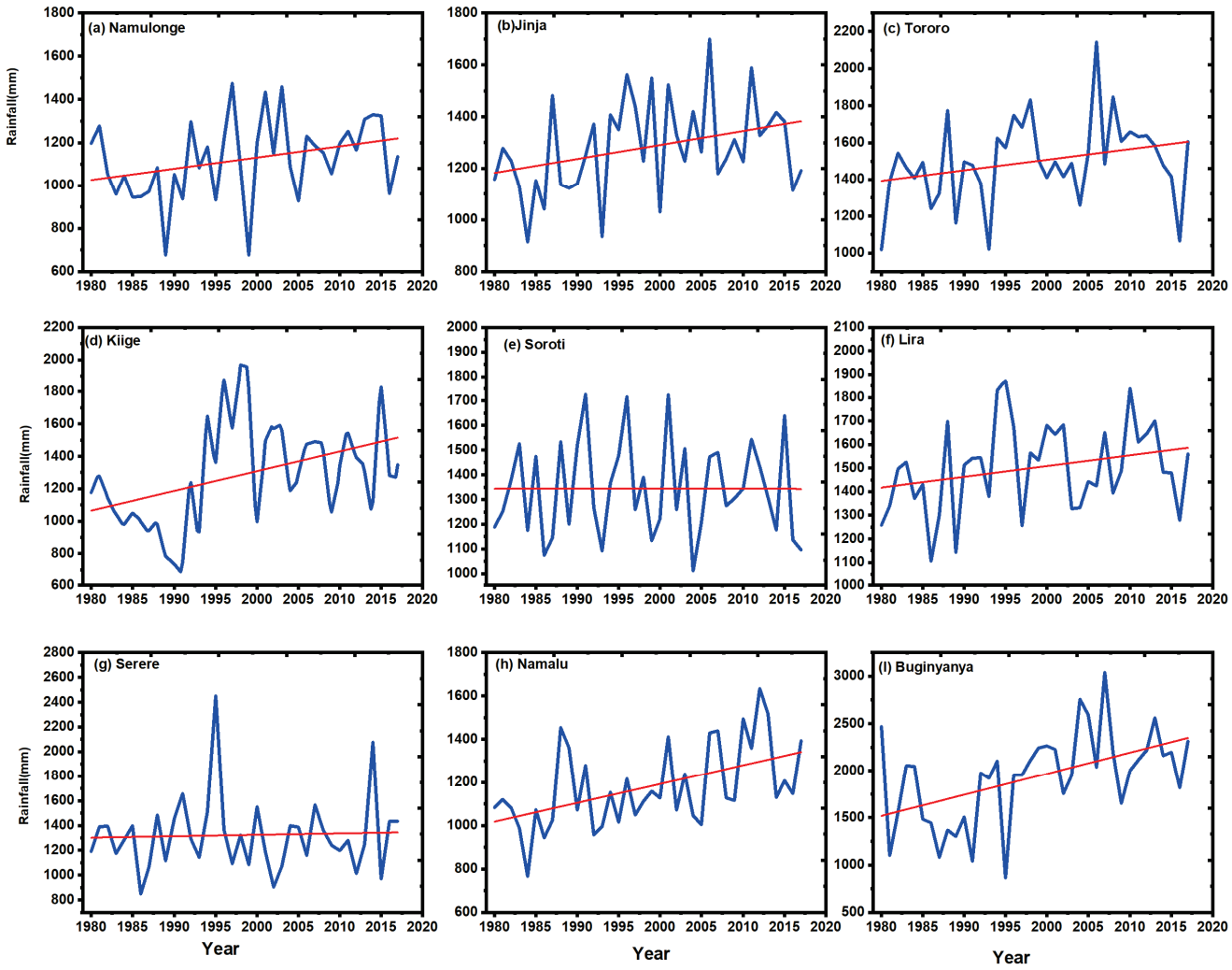

Figure 4. Temporal variation in total annual rainfall for selected stations during 1983–2017. The blue lines in the graphs shows the variation of the annual rainfall over the years, while red lines indicate the simple regression lines showing increasing trends for upward lines and decreasing trends for downward lines. Significance of the trends are tested using MK test and results indicated in Table 2.

The mean annual rainfall in the Lake Kyoga Basin gradually increased from 1985 to 2005 except for the two adjacent stations, Soroti (e) and Serere (g), which indicated a declining trend over the same period. Conversely, after 2005, most rainfall stations in the Lake Kyoga Basin revealed a drop in annual precipitation. The declining rainfall in Uganda was reported in a recent analysis [42].

Contrarily, parts of the Lake Kyoga Basin experienced a lot of rainfall over the years, which caused mudslides on several occasions, such as in 2015, 2018, and 2019, to the extent of causing catastrophic loss of human lives and destruction of property and infrastructure [20].

4.6. Number of Wet/Dry Days During MAM and SOND Rainfall Seasons

The Lake Kyoga Basin received an average of 30–70 wet days during MAM rainfall seasons over most parts of the region, with a few areas receiving less than 20 wet days during MAM (Figure 5a,b). The average number of dry days from two gridded satellite datasets, CHIRPS 2.0 and TAMSAT v3.1, are provided in Figure 5c,d. The highest number of dry days (80) occurred in the northeastern part of the Lake Kyoga Basin, while the lowest number of dry days were experienced in the southern part of the basin, bordering the Lake

Victoria region, which usually receives the highest rainfall amount in Uganda. As observed from Figure 5, the number of dry days during MAM rainfall seasons outstripped their corresponding wet days during the same rainfall seasons.

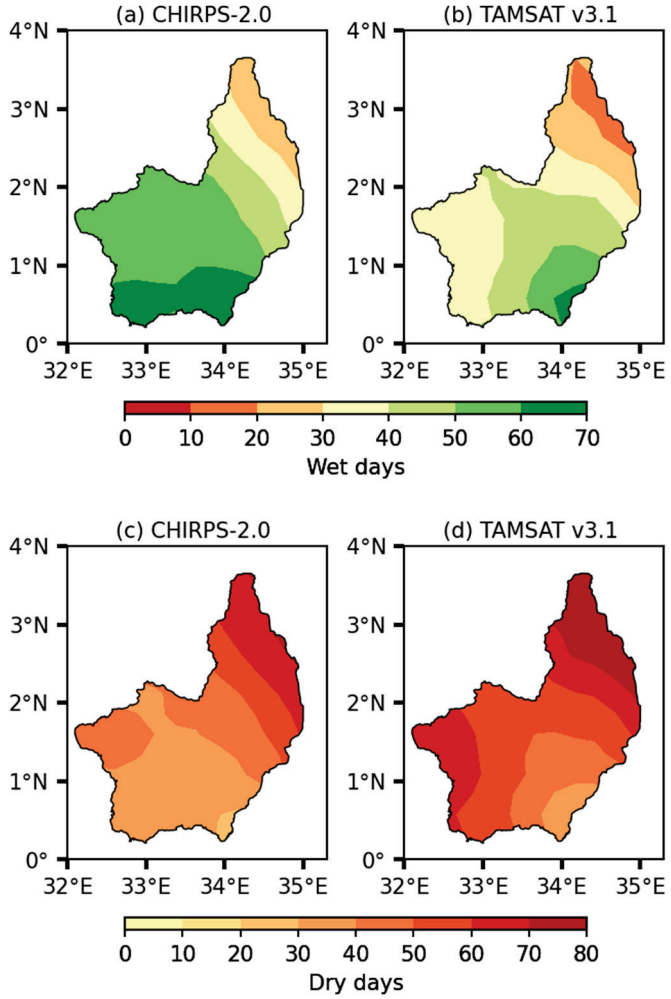

Figure 5. Comparison of wet/dry days during the MAM season using two gridded satellite datasets, CHIRPS-2.0 and TAMSAT v3.1, for the historical period 1983–2017.

For the second rainfall season, during SOND, a similar pattern and range for the number of wet and dry days are observed (Figure 6). For instance, the southern and western parts of the Lake Kyoga Basin experienced more wet days compared to the northeastern part of the basin. In this case, the number of wet days ranged from 40 to 70 days. For the northeastern parts of the Lake Kyoga Basin, the number of wet days ranged from 20 to 50 days (Figure 6a,b).

Concerning the dry days, the southern and western parts of the Lake Kyoga Basin experienced few wet days compared to the northeastern part of the basin, which ranged from 20 to 40 days mainly (Figure 6c). In both reanalysis datasets, the northeastern part of the Lake Kyoga Basin revealed the highest number of dry days, ranging from 50 to 80 days.

Northeastern Uganda is part of Uganda (known as the Karamoja region) and receives the lowest number of wet days, which is translated to the lowest amount of rainfall received in Uganda. The region is typically semi-arid in nature and usually experiences harsh weather conditions with high temperatures and poor rainfall distribution associated with very short rainy periods, which causes flash floods [37,41,43]. Poor rainfall distribution in the northeastern region frequently results in droughts, crop failures, death of livestock, famine, loss of livelihood, and even human death [43].

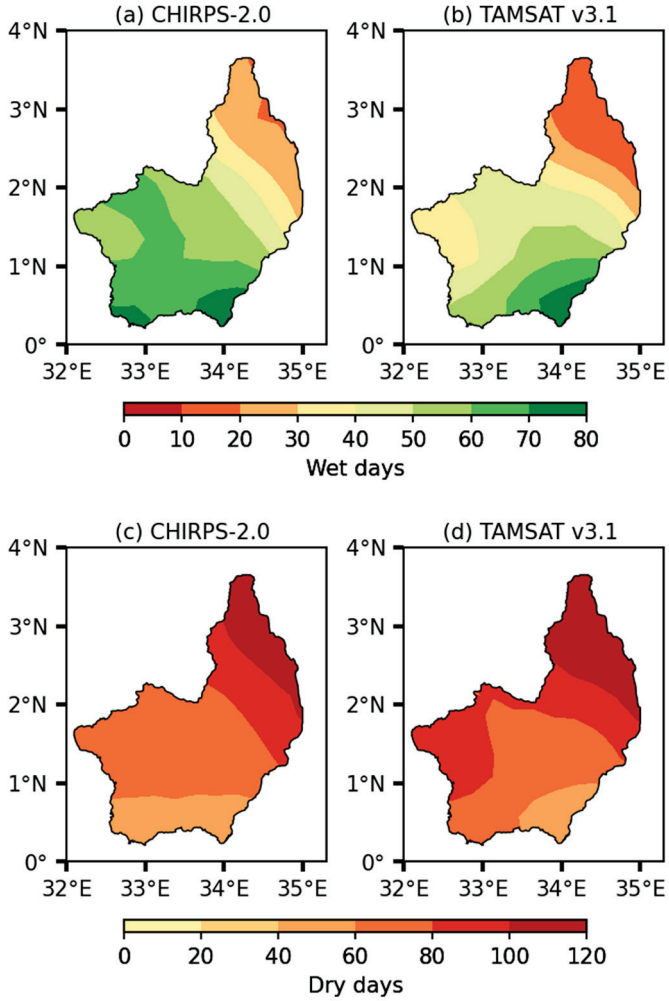

Figure 6. Comparison of wet/dry days during the SOND season using two gridded satellite datasets, CHIRPS-2.0 and TAMSAT v3.1, for the historical period 1983–2017.

4.7. Cumulative Departure Index (CDI) over Lake Kyoga Basin

Figure 7a–g shows a graphical representation of the seasonal CDI for selected stations in the Lake Kyoga Basin over the period 1981–2017. The variability of seasonal rainfall is shown by an upward and downward movement of the CDI graphs, which correspond to surplus and deficit rainfall, respectively.

For Namulonge station (Figure 6a), the "long rains" (MAM) season is observed to show below-average rainfall for most of the years during the period 1983–2017, with only 3 years showing positive rainfall, while SOND showed either near normal rainfall or below average. The years that have anomalously high MAM seasonal rainfall include 1982, 1997–1998, and 2016. The years that showed anomalously low MAM rainfall at this station include 1996, 2000, and 2007–2008. Meanwhile, analysis of SOND seasonal rainfall revealed anomalously high and low rainfall in 1995 and 1982–1983, 1986, 1989, and 2016, respectively.

At Tororo station, the variability in seasonal rainfall is also evidenced as the CDI graphs presented both downward and upward movement in both seasons (Figure 6b), but both seasons recorded near normal long-term mean rainfall. The CDI curve for MAM indicates extremely high rainfall in 2013, 2012, and 2006 in the last 10 years and 1990–1991 in the previous decade. Contrarily, 2004 and 2016 are two years that present below-average rainfall for MAM seasons. There is no clear pattern for the SOND rainfall season as both downward and upward trends are observed randomly, showing high variability in

seasonal rainfall. The SOND season revealed that the highest upward trends in rainfall were recorded in 1997, 2006, and 2014, while 1986, 1990, and 2010 showed highly marked downward movement of the cumulative departure index.

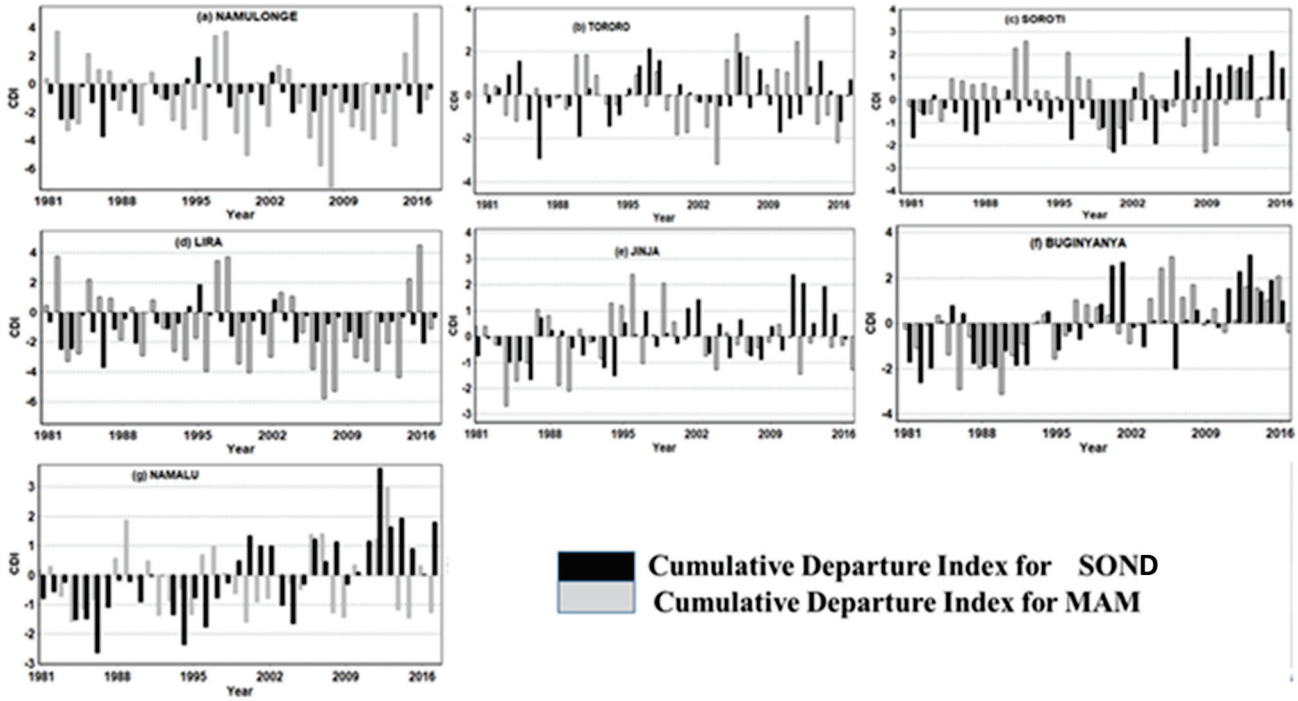

Figure 7. (**a**–**g**) Graphical representation of the time series of seasonal cumulative departure index (CDI) for selected stations in the Lake Kyoga Basin. The light grey color bar chart represents MAM and the black color chart shows SOND.

As in the first two stations above, the seasonal variability in rainfall at Soroti station (Figure 7c) is visibly clear, as the MAM season records below-normal rainfall in the first 2 years. An improvement in MAM rainfall is attained during the period 1985–1998, as indicated by the upward movement of CDI graphs. This is subsequently followed by a reduction in MAM rainfall in the next 4 years, as the CDI graphs move into the negative phase from 1999 to 2002. From 2003 to 2017, 5 years showed positive CDI values and upward trends in rainfall, while the remaining years indicate below-normal rainfall. The station showed extremely low rainfall during MAM in 1999 and over 2009–2010, while extremely high rainfall was experienced in 1991–1992 and 1996. The results revealed negative CDI graphs for SOND in 22 years during the period 1981–2005 and only 3 years of positive CDI graphs. Toward the last decade (2006–2017), SOND seasonal rainfall expressed improvement, as all the years registered positive CDI values and an upward movement of CDI graphs.

At Lira station (Figure 7d), both the MAM and SOND seasons are observed to show below-average rainfall for most of the years; however, a few years recorded extremely high rainfall (above average) during the MAM rainy season, including 1982, 1997–1998, 2015–2016, and extremely below-average rainfall during 1983–1984, 1999–2000, 2007–2008, 2010, 2012, and 2014. The worst-case scenario is seen during SOND, where only 3 years show above-average rainfall, namely the years 1994–1995 and 2002. Extremely dry conditions and below-normal rainfall are observed in all years, most notably in 1982–1983,1986, 1989, 2004–2006, 2009–2010, and 2015.

Further, Jinja station (Figure 7e) showed clear seasonal variability in rainfall from 1981 to 1993; most years displayed below-average rainfall in both the MAM and SOND seasonal rainfall except in a few cases, such as in 1987–1988 and previously in 1982–1983

with above-average seasonal rainfall. From 1995 to 2002, MAM received two years of extremely high rainfall (1996 and 1999), as SOND recorded above-average rainfall in six years. Similarly, the years 2003–2011 showed below-normal rainfall in both seasons except on a few occasions, such as in 2003 and 2006. The last 6 years (2011–2017) showed more upward movement in SOND seasonal and downward movement in MAM rainfall. The MAM season received substantially high rainfall during 1995–1997 and 2000, and a drastic reduction in MAM seasonal rainfall in 1985–1986, 1990–1991, 2005, and 2013. The CDI bars showed a negative trend in rainfall in the second season of SOND from 1981–1987 and 1991–1995. From 1996 onward, SOND rainfall indicated a positive trend punctuated with years of reduced rainfall, most predominantly in 2006 and 2008–2009.

Buginyanya station (Figure 7f), in the montane region, shows the downward movement of MAM seasonal rainfall from 1981 to 1996, with the exception of 1984 and 1994 with near-normal rainfall. There is no difference in the observed trends for SOND seasonal rainfall at Buginyanya station, as most years (1981–1999) show decreased rainfall (below-average rainfall) except on a few occasions in 1985–1987 and 1994–1995. Proceeding from 2000–2002, a positive trend indicated by upward bars in rainfall is recorded, followed by below-average rainfall over the period 2003–2004, which is followed by near-normal rainfall from 2005 to 2011. CDI graphs showed that the last 6 years registered the wettest years for SOND rainfall, including 2001–2002 and 2013–2014, while 1982–1984,1988–1993, and 2007 were shown to be the driest years in terms of SOND rainfall for this period of analysis.

At Namalu station (Figure 7g), the years 1983–1987, 1992–1995, 1999–2005, 2008–2009, 2014–2015, and 2017 were significantly dry (below average) in terms of MAM seasonal rainfall. The dry MAM seasons were punctuated with occasionally wet seasons (above-average rainfall), such as during the periods 2006–2007, 1996–1999, and 2012–2013. The second season (SOND) showed below-average rainfall over the period 1981–1998 and above-average rainfall in the following 4 years (1999–2002), followed by a further 3 years of below-average rainfall (2003–2005). Over the last 12 years (2006–2017), SOND received improved rainfall performance, with the only drop in 2009. Extremely high and low rainfall during SOND was experienced in 2012 and 1986, respectively.

4.8. RAI over Lake Kyoga Basin for 1981–2017

The results of the annual rainfall anomaly index (RAI) are presented in Figure 8. The results show that annual rainfall varied a lot in the long-term mean, as different stations revealed different ranges of RAI values throughout the analyzed years. For example, Namulonge station recorded an extreme range of -5.4 to 6.3 in 1983 and 1997, respectively. For the case of Tororo station, the two extreme range values of -5.2 to 7.5 were reported in more recent years, 2001 and 2004. The range at Soroti is from -3.9 to 5.6, which occurred in the earlier years of 1984 and 1988. Meanwhile, Serere station recorded a range of -4.8 to 6.7 in 2012 and 2000, respectively. The negative indices represent dry years, and the positive indices show wet or rainy years with varying intensities in each case.

For the first 20 years (1981–2000), 12 cases of extremely dry conditions were revealed within the Lake Kyoga Basin. In such circumstances, Soroti station reported 3 cases of extremely dry years in 1982, 1984, and 1989, while Namulonge station also reported 3 cases in 1983, 1993, and 2000. Meanwhile, the remaining stations showed one case of an extremely dry year. RAI values indicate that 1981 and 1999 were the wettest years when all the stations reported extremely wet conditions (positive RAI). Moreover, during the period (2000–2017), 34 cases of extremely dry years were experienced in 9 locations examined in the Lake Kyoga Basin. The distribution of extremely dry conditions was uniform at some stations. For example, Soroti, Serere, and Buginyanya stations each recorded 5 years of extremely dry

conditions, while Jinja registered 4 years of extremely dry years. The remaining stations recorded at least 3 years of extremely dry years.

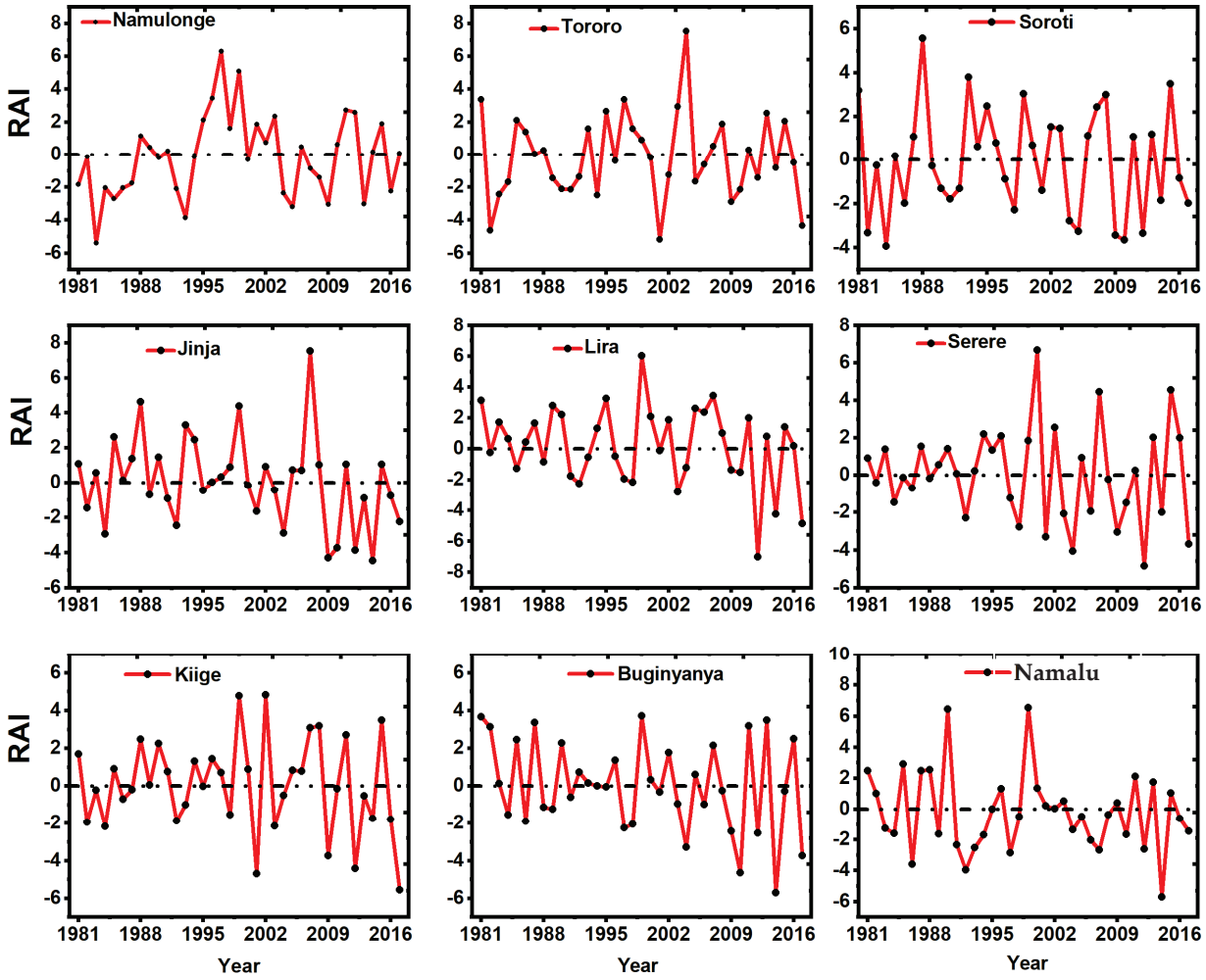

Figure 8. The annual rainfall anomaly index (RAI) for selected stations in the Lake Kyoga Basin in Uganda.

5. Discussion

Results from the cumulative departure index show several years of below-average rainfall, showing drying or drought tendencies over the region during the first rainy period of March–May (MAM). The March–May long rains are critical for the East Africa region and have been quite poor in recent years [24]. The decline in MAM rainfall in the EA region has been prominently analyzed and discussed [44]. The last 10 years of the study showed rainfall increasing in both the MAM and SOND seasons, contributing to an increase in annual rainfall over most stations in the basin. However, the increase in rainfall over the basin is punctuated with extreme or severe drought years, as witnessed in results in 2009–2010, 2014, 2016, and 2017, further indicating a drought condition in the region. Ongoma et al. [8] also showed a positive trend in March–April–May (MAM) and October–November–December (OND) seasonal rainfall over the East Africa region. The months of November–December have seen an increase, probably reflecting increased November rainfall in East Africa [45].

These results showed high positive RAI values for Namulonge station in the same region in the years 1989,1997, and 2001, indicating that they were extremely wet, which is in agreement with recent studies that analyzed rainfall variability for the Lake Victoria

Basin adjacent to the Lake Kyoga Basin [45] and found that the years 1989, 1997, and 2001 had anomalously high total annual rainfall in the region. The most notable extremely wet years are 1981 for most stations except Namulonge station and 1999, 2011, and 2015 for most stations. However, using rainfall data for 1949–2009, ref. [46] found that rainfall at the Namulonge station decreased.

The main controlling mechanism of these extremely high rainfall events has been linked to the reversal of dipole in atmospheric circulation and Indian Ocean sea surface temperatures [47]. The rains are moderated by weather phenomena such as the El Niño Southern Oscillation (ENSO) [38] and the Indian Ocean Dipole (IOD) [48]. The El Niño Southern Oscillation (ENSO) phenomena are strongly associated with the inter-annual variability of rainfall in this region [38]. This agrees with our present study, as years with El Niño events such as 1981, 1997–1998, 2006–2007, and 2015 were recorded as wet years.

The result showed high spatial variability, as stations indicate different results when similar weather phenomena occur. For example, in 1996 and 2015, most stations showed extremely high rainfall, but a few stations still showed extremely dry conditions over the same period. Such differences in weather conditions are closely related to the contribution of the local circulation systems resulting from land surface heterogeneity induced by biophysical factors such as vegetation, large open water bodies, and topography [49,50]. Drought conditions exhibited in some years in most stations severely affect agricultural, water, economic, and health sectors and human death has been reported in the Lake Kyoga Basin [43].

In the East African tropical climate, rainfall remains one of the most important drivers of many socio-economic activities like agriculture and electricity generation [51], but variability in rainfall imposes greater risks to such socio-economic sectors. Extreme drought and famine occurred in other parts of Africa at the beginning of 2006, spreading to the East African region, especially the northern part of Uganda, Kenya, and Somalia, more severe than those of 1984, 1999, and 2000 in the East African region [44,46].

Globally, an estimated eleven million people have died of drought-related causes, while two billion people have been affected by drought since 1900 [52]. The frequencies and intensity of drought are predicted to increase [2], which confirms the results that the current years (2001–2017) had the highest frequencies and more intense droughts than the period 1981–2000.

Generally, 2010 was extremely dry for Soroti, Jinja, and Buginyanya and severely dry for most stations, including Tororo and Namalu, possibly caused by the failure of the "short rains" of 2010 linked to the La Nina condition. This was followed by a further decline in the "long rains" in MAM in 2011 in EA [53]. The year 2011 was one of the wettest years in the Lake Kyoga Basin, as most of the RAI values were greater than 0.3. The results also showed that in the period 1997–1998, some stations, such as Namulonge, Tororo, Jinja, and Kiige, had positive RAI, representing extremely wet years. This could be associated with the strong El Niño episode of that year, which is referred to as the "climate event" of the century [54].

Similarly, the extreme El Niño events in 1982/1983 could have boosted the rainfall of other stations in the region; however, extremely dry conditions were recorded in stations such as Namulonge, Tororo, and Soroti. This also shows the variability of rainfall in the region occurring within short distances [55]. The recent wet year (2015) is possibly another effect of El Niño events experienced in the region. This increases the chances of most locations recording extremely wet conditions [56], but this is usually followed by the opposite phase, the La Nina event, which is usually dry and delivers less rainfall in some areas [57], consistent with the results of 2016 in this study. However, this is not exclusively

true, as some patches of dry conditions persisted at some stations within the basin in the same year (2016).

According to these results, the region registered five incidences of extremely dry years and seven cases of severely dry years at different stations. The results agree with seven drought cases reported between 1991 and 2000 [58]. The Greater Horn of Africa has been affected by drought almost every year for the past two decades, and the most severe drought occurred in 2009 and 2011 in Kenya [51], which is true to the test results for RAI in 2009.

6. Conclusions

This study analyzed the rainfall data for the Lake Kyoga Basin using the CDI and RAI. The results show a declining trend in March–May (MAM) rainfall, indicating drying or drought tendencies over the region. However, the last decade of the study period showed an increase in rainfall in both MAM and October–December (SOND) seasons. The study also identified extreme wet and dry years, with El Niño events contributing to the wet years. The results highlight the high spatial variability in rainfall in the region, with local circulation systems playing a significant role. The study's findings have important implications for agricultural, water, economic, and health sectors in the region, which are vulnerable to rainfall variability and droughts. Overall, this study contributes to the understanding of rainfall variability in the Lake Kyoga Basin and highlights the need for effective climate risk management strategies to mitigate the impacts of droughts and floods in the region.

The study's findings highlight the need for effective climate risk management strategies to mitigate the impacts of droughts and floods in the Lake Kyoga Basin, which can be achieved through the development of early warning systems, climate-resilient agriculture practices, and water harvesting and storage infrastructure. Finally, the study's findings emphasize the importance of understanding rainfall variability and its impacts on socio-economic sectors. To improve climate monitoring and prediction capabilities, investing in climate observation networks, enhancing climate modeling and forecasting capabilities, and promoting climate information dissemination and applications are essential. This will enable decision-makers to make informed decisions and develop effective adaptation strategies.

Author Contributions: Conceptualization, M.A.O. and H.B.; methodology, M.A.O.; software, M.A.O. and H.B.; validation, M.A.O.; formal analysis, M.A.O. and H.B.; investigation, M.O; resources, M.A.O. and H.B.; data curation, M.A.O. and H.B.; writing—original draft preparation, M.A.O.; writing—review and editing, M.A.O.; visualization, M.A.O. and H.B.; supervision, M.O; project administration, M.A.O.; funding acquisition, M.A.O. and H.B.; All authors have read and agreed to the published version of the manuscript.

Funding: This research received no external funding.

Data Availability Statement: Data are available upon request.

Conflicts of Interest: Author Moses A. Ojara was employed by the company Green Life Research Initiative Uganda Limited. The remaining authors declare that the research was conducted in the absence of any commercial or financial relationships that could be construed as a potential conflict of interest.

References

1. Min, S.; Zhang, X.; Zwiers, F.W.; Hegerl, G.C. Human Contribution to More-Intense Precipitation Extremes. *Nature* **2011**, *470*, 378–381. [CrossRef] [PubMed]
2. IPCC. *Managing the Risks of Extreme Events and Disasters to Advance Climate Change Adaptation*; IPCC: Geneva, Switzerland, 2012.

3. IPCC. *Climate Change 2014: Synthesis Report*; Pachauri, R.K., Ed.; IPCC: Geneva, Switzerland, 2014.
4. Adhikari, U.; Nejadhashemi, A.P.; Woznicki, S.A. Climate Change and Eastern Africa: A Review of Impact on Major Crops. *Food Energy Secur.* **2015**, *4*, 110–132. [CrossRef]
5. Almazroui, M.; Saeed, F.; Saeed, S.; Islam, M.N.; Ismail, M. Projected Change in Temperature and Precipitation Over Africa from CMIP6. *Earth Syst. Environ.* **2020**, *4*, 455–475. [CrossRef]
6. Nuwagira, U.; Yasin, I. Review of the Past, Current, and the Future Trend of the Climate Change and Its Impact in Uganda. *East Afr. J. Environ. Nat. Resour.* **2022**, *5*, 115–126. [CrossRef]
7. Lobell, D.B.; Burke, M.B.; Tebaldi, C.; Mastrandrea, M.D.; Falcon, W.P.; Naylor, R.L. Prioritizing Climate Change Adaptation Needs for Food Security in 2030. *Science* **2008**, *319*, 607–610.
8. Ongoma, V.; Chen, H.; Omony, G.W. Variability of Extreme Weather Events over the Equatorial East Africa, a Case Study of Rainfall in Kenya and Uganda. *Theor. Appl. Climatol.* **2018**, *131*, 295–308. [CrossRef]
9. Government of Uganda; UNFPA. *The State of Uganda Population Report 2009: Addressing the Effects of Climate Change on Migration*; United Nations Population Fund: New York, NY, USA, 2009.
10. MacLeod, D.; Caminade, C. The Moderate Impact of the 2015 El Niño over East Africa and Its Representation in Seasonal Reforecasts. *J. Clim.* **2019**, *32*, 7989–8001. [CrossRef]
11. Palmer, P.I.; Wainwright, C.M.; Dong, B.; Maidment, R.I.; Wheeler, K.G.; Gedney, N.; Hickman, J.E.; Madani, N.; Folwell, S.S.; Abdo, G.; et al. Drivers and Impacts of Eastern African Rainfall Variability. *Nat. Rev. Earth Environ.* **2023**, *4*, 254–270. [CrossRef]
12. Thornton, P.K.; Owiyo, T.; Jones, P.G.; Owiyo, T.; Kruska, R.L.; Herrero, M.; Orindi, V.; Bhadwal, S.; Kristjanson, P.; Notenbaert, A.; et al. Climate Change and Poverty in Africa: Mapping Hotspots of Vulnerability. *Afr. J. Agric. Resour. Econ.* **2008**, *2*, 24–44. [CrossRef]
13. Shikuku, K.M.; Winowiecki, L.; Twyman, J.; Eitzinger, A.; Perez, J.G.; Mwongera, C.; Läderach, P. Climate Risk Management Smallholder Farmers' Attitudes and Determinants of Adaptation to Climate Risks in East Africa. *Clim. Risk Manag.* **2017**, *16*, 234–245. [CrossRef]
14. Schlenker, W.; Lobell, D.B. Robust Negative Impacts of Climate Change. *Environ. Res. Lett.* **2010**, *5*, 014010. [CrossRef]
15. Pachauri, R.K.; Reisinger, A. *Climate Change 2007: Synthesis Report. Contribution of Working Groups I, II and III to the Fourth Assessment Report of the Intergovernmental Panel on Climate Change*; IPCC: Geneva, Switzerland, 2007.
16. African Union. *State of Africa's Population 2017: Keeping Rights of Girls, Adolescents and Young Women at the Centre of Africa's Demographic Dividend*; African Union: Ababa, Ethiopia, 2017.
17. Onyutha, C.; Acayo, G.; Nyende, J. Analyses of Precipitation and Evapotranspiration Changes across the Lake Kyoga Basin in East Africa. *Water* **2020**, *12*, 1134. [CrossRef]
18. Mubialiwo, A.; Chelangat, C.; Onyutha, C. Changes in Precipitation and Evapotranspiration over Lokok and Lokere Catchments in Uganda. *Bull. Atmos. Sci. Technol.* **2021**, *2*, 2. [CrossRef]
19. Atube, F.; Malinga, G.M.; Nyeko, M.; Okello, D.M.; Mugonola, B.; Omony, G.W.; Uma, I.O. Farmers' Perceptions of Climate Change, Long-Term Variability and Trends in Rainfall in Apac District, Northern Uganda. *CABI Agric. Biosci.* **2022**, *4*, 1–16. [CrossRef]
20. Obubu, J.P.; Mengistou, S.; Fetahi, T.; Alamirew, T.; Odong, R.; Ekwacu, S. Recent Climate Change in the Lake Kyoga Basin, Uganda: An Analysis Using Short-Term and Long-Term Data with Standardized Precipitation and Anomaly Indexes. *Climate* **2021**, *9*, 179. [CrossRef]
21. Onyutha, C. Trends and Variability of Temperature and Evaporation over the African Continent: Relationships with Precipitation. *Atmosfera* **2021**, *34*, 267–287.
22. Filahi, S.; Tanarhte, M.; Mouhir, L.; El Morhit, M.; Tramblay, Y. Trends in Indices of Daily Temperature and Precipitations Extremes in Morocco. Theor. *Appl. Climatol.* **2016**, *124*, 959–972. [CrossRef]
23. Funk, C.; Peterson, P.; Landsfeld, M.; Pedreros, D.; Verdin, J.; Shukla, S.; Husak, G.; Rowland, J.; Harrison, L.; Hoell, A.; et al. The Climate Hazards Infrared Precipitation with Stations—A New Environmental Record for Monitoring Extremes. *Sci. Data* **2015**, *2*, 1–21. [CrossRef]
24. Wainwright, C.M.; Marsham, J.H.; Keane, R.J.; Rowell, D.P.; Finney, D.L.; Black, E.; Allan, R.P. 'Eastern African Paradox' Rainfall Decline Due to Shorter Not Less Intense Long Rains. *Npj Clim. Atmos. Sci.* **2019**, *2*, 1–9. [CrossRef]
25. Maidment, R.I.; Grimes, D.; Black, E.; Tarnavsky, E.; Young, M.; Greatrex, H.; Allan, R.P.; Stein, T.; Nkonde, E.; Senkunda, S.; et al. Data Descriptor: A New, Long-Term Daily Satellite-Based Rainfall Dataset for Operational Monitoring in Africa. *Sci. Data* **2017**, *4*, 170063. [CrossRef]
26. Taylor, K.E. Taylor Diagram Primer. 2005. Available online: https://pcmdi.llnl.gov/staff/taylor/CV/Taylor_diagram_primer.pdf (accessed on 20 January 2025).

27. Mann, H.B. Non-Parametric Test Against Trend. *Econometrica* **1945**, *13*, 245–259.
28. Kendall, M.G. *Appendix: Mann-Kendall Trend Tests*; Oxford University Press: Oxford, UK, 1975; p. 202.
29. Ayugi, B.O.; Tan, G. Recent Trends of Surface Air Temperatures over Kenya from 1971 to 2010. *Meteorol. Atmos. Phys.* **2019**, *131*, 1401–1413. [CrossRef]
30. Theil, H. A Rank-Invariant Method of Linear and Polynomial Regression Analysis. In *Henri Theil's Contributions to Economics and Econometrics*; Springer: Dordrecht, The Netherlands, 1950; pp. 345–381. [CrossRef]
31. Sen, P.K. Estimates of the Regression Coefficient Based on Kendall's Tau. *Am. Stat. Assoc.* **1968**, *63*, 1379–1389. [CrossRef]
32. Mumo, L.; Yu, J.; Ayugi, B. Evaluation of Spatiotemporal Variability of Rainfall over Kenya from 1979 to 2017. *J. Atmos. Sol. Terr. Phys.* **2019**, *194*, 105097. [CrossRef]
33. Caloiero, T.; Coscarelli, R. Analysis of the Characteristics of Dry and Wet Spells in a Mediterranean Region. *Environ. Process.* **2020**, *7*, 691–701.
34. Kendon, E.J.; Stratton, R.A.; Tucker, S.; Marsham, J.H.; Berthou, S.; Rowell, D.P.; Senior, C.A. Enhanced Future Changes in Wet and Dry Extremes over Africa at Convection-Permitting Scale. *Nat. Commun.* **2019**, *10*, 1794. [CrossRef]
35. Tilahun, K. Analysis of Rainfall Climate and Evapo-Transpiration in Arid and Semi-Arid Regions of Ethiopia Using Data over the Last Half a Century. *J. Arid Environ.* **2006**, *64*, 474–487. [CrossRef]
36. Hänsel, S.; Schucknecht, A.; Matschullat, J. The Modified Rainfall Anomaly Index (MRAI)—Is This an Alternative to the Standardised Precipitation Index (SPI) in Evaluating Future Extreme Precipitation Characteristics? *Theor. Appl. Climatol.* **2015**, *123*, 827–844. [CrossRef]
37. Kansiime, M.K.; Wambugu, S.K.; Shisanya, C.A. Perceived and Actual Rainfall Trends and Variability in Eastern Uganda: Implications for Community Preparedness and Response. *J. Nat. Sci. Res.* **2013**, *3*, 179–195.
38. Indeje, M.; Semazzi, F.H.M.; Ogallo, L.J. ENSO Signals in East African Rainfall Seasons. *Int. J. Climatol.* **2000**, *46*, 19–46. [CrossRef]
39. Brown, E.; Sutcliffe, J.V.; Brown, E.; John, V. The Water Balance of Lake Kyoga, Uganda the Water Balance of Lake Kyoga, Uganda. *Hydrol. Sci. J.* **2013**, *58*, 341–353. [CrossRef]
40. Ogwang, B.; Nimusiima, A.; Tindamanyire, T.; Serwanga, M.; Ayesiga, G.; Ojara, M.; Ssebabi, F.; Gugwa, G.; Nsubuga, Y.; Atim, R.; et al. Characteristics and Changes in SON Rainfall Over. *J. Environ. Agric. Sci.* **2016**, *8*, 45–53.
41. Mubiru, D.N.; Komutunga, E.; Agona, A.; Apok, A.; Ngara, T. Characterising Agrometeorological Climate Risks and Uncertainties: Crop Production in Uganda. *S. Afr. J. Sci.* **2012**, *108*, 108–118. [CrossRef]
42. Nsubuga, F.W.; Rautenbach, H. Climate Change and Variability: A Review of What Is Known and Ought to Be Known For. *Int. J. Clim. Change Strateg. Manag.* **2018**, *10*, 752–771. [CrossRef]
43. NAPA. *Climate Change: Uganda National Adaptation Programmes of Action (NAPA)*; Ministry of Water and Environment (MWE): Kampala, Uganda, 2007.
44. Rowell, D.P.; Booth, B.B.; Nicholson, S.E.; Good, P. Reconciling Past and Future Rainfall Trends over East Africa. *J. Clim.* **2015**, *28*, 9768–9788. [CrossRef]
45. Clive, A.S. The Changing Climate of Africa Part I: Introduction and Eastern Africa. In *African Ecology—Benchmarks and Historical Perspectives*; Springer: Berlin/Heidelberg, Germany, 2012; pp. 57–140. ISBN 9783642228711.
46. Kizza, M.; Rodhe, A.; Xu, C.-Y.; Ntale, H.K.; Halldin, S. Temporal Rainfall Variability in the Lake Victoria Basin in East Africa during the Twentieth Century. *Theor. Appl. Climatol.* **2009**, *98*, 119–135. [CrossRef]
47. Nsubuga, F.W.N.; Olwoch, J.M.; Rautenbach, C.J.D.W. Climatic Trends at Namulonge in Uganda: 1947–2009. *J. Geogr. Geol.* **2011**, *3*, 119–131. [CrossRef]
48. Saji, N.H.; Vinayachandran, P.N. A Dipole Mode in the Tropical Indian Ocean. *Nature* **1999**, *401*, 360–363.
49. Behera, S.K.; Luo, J.J.; Masson, S.; Delecluse, P.; Gualdi, S.; Navarra, A.; Yamagata, T. Paramount Impact of the Indian Ocean Dipole on the East African Short Rains: A CGCM Study. *J. Clim.* **2005**, *18*, 4514–4530. [CrossRef]
50. Ogwang, B.A.; Chen, H.; Li, X.; Gao, C. The Influence of Topography on East African October to December Climate: Sensitivity Experiments with RegCM4. *Adv. Meteorol.* **2014**, *2014*, 14. [CrossRef]
51. Ayugi, B.; Tan, G.; Rouyun, N.; Zeyao, D.; Ojara, M.; Mumo, L.; Babaousmail, H.; Ongoma, V. Evaluation of Meteorological Drought and Flood Scenarios over Kenya, East Africa. *Water* **2020**, *11*, 307. [CrossRef]
52. Ghaleb, F.; Mario, M.; Sandra, A. Regional Landsat-Based Drought Monitoring from 1982 to 2014. *Climate* **2015**, *3*, 563–577. [CrossRef]
53. Lyon, B.; Dewitt, D.G. A Recent and Abrupt Decline in the East African Long Rains. *Geophys. Res. Lett.* **2012**, *39*, 1–5. [CrossRef]
54. Cai, W.; Borlace, S.; Lengaigne, M.; Van Rensch, P.; Collins, M. Increasing Frequency of Extreme El Niño Events Due to Greenhouse Warming. *Nat. Clim. Change* **2014**, *4*, 111–116. [CrossRef]
55. Nicholson, S.E. Climate and Climatic Variability of Rainfall over Eastern Africa. *Rev. Geophys.* **2017**, *55*, 590–635. [CrossRef]
56. ACF. *2015/16 El Nino Event Global Report*; ACF: London, UK, 2015.

57. Ntale, H.K.; Gan, T.Y. East African Rainfall Anomaly Patterns in Association with El Niño/Southern Oscillation. *J. Clim.* **2004**, *9*, 257–268. [CrossRef]
58. UNISDR. *Progress and Challenges in Disaster Risk Reduction: A Contribution Towards the Development of Policy Indicators for the Post-2015 Framework for Disaster Risk Reduction*; ISDR: Geneva, Switzerland, 2014.

water

MDPI

Article

Characteristics of Runoff Changes during the Freeze–Thaw Period and the Response to Environmental Changes in a High-Latitude Water Tower

Moran Xu [1,2,†], Yongming Chen [3,*,†], Dongmei Liu [3], Peng Qi [2,*], Yingna Sun [1], Licheng Guo [4] and Guangxin Zhang [2]

[1] Institute of Water Conservancy and Electric Power, Heilongjiang University, Harbin 150080, China; xumoran@iga.ac.cn (M.X.); sunyingna@iga.ac.cn (Y.S.)
[2] Key Laboratory of Wetland Ecology and Environment, Northeast Institute of Geography and Agroecology, Chinese Academy of Sciences, Changchun 130102, China; zhgx@iga.ac.cn
[3] Jilin Institute of Hydraulic Research, Changchun 130500, China; liudongmei@iga.ac.cn
[4] College of Software, Jilin University, Changchun 130021, China; guolc2002@163.com
* Correspondence: chenym2477@163.com (Y.C.); qipeng@iga.ac.cn (P.Q.)
† These authors contributed equally to this work.

Abstract: Runoff in high-latitude water towers is crucial for ecological and human water demands during freeze–thaw periods but is highly sensitive to climate change and human activities. This study focuses on Changbai Mountain, the source of the Songhua, Tumen, and Yalu rivers, analyzing runoff variation and its environmental responses using the modified Mann–Kendall method and the water–energy balance equation. The results show significant non-stationarity in runoff trends, with an increasing trend in the Yalu River basin ($p < 0.05$), a decreasing trend in the Tumen River basin ($p < 0.05$), and complex trends in the Songhua River basin. Additionally, the relationship between runoff and driving factors during freeze–thaw periods was quantized. When the snowfall, potential evapotranspiration (E0), and subsurface changes increased by 1%, the snowmelt runoff changes were 1.58~1.96%, −0.58~−1.96%, and −0.86~−1.11% in the Yalu River basin; 2.16~2.35%, −1.04~−1.35%, and −1.56~−1.95% in the Tumen River basin; and 1.44~2.41%, −0.44~−1.41%, and −0.72~−1.62% in the Songhua River basin. The increased snowfall was the most prominent reason for the increase in snowmelt runoff during spring. The results of this study will benefit ecosystem conservation and the stability of downstream water supply in this high-latitude water tower.

Keywords: snowmelt runoff; water tower; climate change; human activities

1. Introduction

Runoff produced during the freeze–thaw period plays an important role in maintaining downstream production, livelihoods, and spring agricultural irrigation in high-latitude water towers [1,2]. At the same time, runoff during the freeze–thaw period can be significantly altered by climate change and human activities, increasing the uncertainty of sustainable water supply for downstream environments [3–5]. Owing to spatial and temporal heterogeneity, this new runoff requires further study [6].

The spatial and temporal evolution of runoff during the freeze–thaw period has received increasing attention globally, for example, in the western United States [2,7,8], Canada [9,10], the Czech Republic [11], the Mediterranean [6], and the Qinghai–Tibet Plateau in China [5,12]. Snowmelt runoff trends are often complex. Musselman et al. [2] analyzed the long-term changes in snowmelt runoff in North America and found that 34% of monitoring stations showed an increasing trend at ($p < 0.05$), with three times as many monitoring stations exhibiting a decreasing trend ($p < 0.05$). In this article, p reflects the significance of the results: $p < 0.05$ indicates that the results are statistically significant and that the change did not occur by chance, while $p > 0.05$ indicates that the results are not

statistically significant and that the change may have occurred randomly. Typically, runoff during the freeze–thaw period is influenced by climate change, with the uncertainty of snowfall increasing and snowmelt occurring earlier in the spring [13,14]. Li et al. [8] indicated that snowmelt's contribution to runoff in the western United States will be reduced by one-third before 2100 under RCP 8.5. RCP 8.5 represents the climate projections for the High Emissions Scenario, which assumes a significant increase in global GHG concentrations by 2100, leading to a large increase in temperature. Snowmelt runoff is also influenced by changes in the subsurface, even more so than climate change [15]. Nevertheless, more extensive quantitative evaluations of the contribution of climate change and underlying surface changes to snowmelt runoff are required. Some studies have used models to quantify the contribution of snowmelt to runoff [5,16,17]. However, constructing these models requires a large amount of basic observational data, specifically in mountainous areas, where data are difficult to obtain [18]. In recent years, the Budyko-based analysis method has gained popularity for quantifying environmental contributions owing to its simplicity and effectiveness [19–22]. This method has been predominantly applied to assess the effects of climate change and human activities on annual runoff changes, with limited application to analyzing snowmelt runoff contributions.

Changbai Mountain is the source of the Songhua River (SR), Tumen River (TR), and Yalu River (YR), providing a stable supply of abundant freshwater resources to the downstream region. In addition, the YR and TR are important borders between the three countries of China, North Korea, and Russia [23,24]. With a freeze–thaw period of up to eight months a year, snowmelt runoff is a vital factor in maintaining the health of Changbai Mountain's ecosystem and provides a sustainable water supply for downstream production and living. Thus, previous studies have quantified the response characteristics of annual runoff to changing environments in tributaries of the Changbai Mountain region [25,26]. However, our knowledge is still limited regarding the characteristics of runoff changes during the freeze–thaw period and its response to climate and subsurface changes in this region.

This study investigates the variations and trends in runoff during the freeze–thaw period and responses to anthropogenic drivers and climatic change in a specific high-latitude water tower. Firstly, the non-stationary change in runoff during the freeze–thaw period on Changbai Mountain was analyzed (from October to May of the next year). Secondly, the relationship between runoff and driving factors during freeze–thaw periods was quantized. Finally, the contributions of these drivers to changes in spring runoff were identified. This study reveals the changing laws of water resources in high-latitude water towers in the context of climate change and human activities. This not only provides a scientific basis for water resource management in the Changbai Mountain region but also provides a reference for hydrological studies and management strategies in similar regions, contributing to sustainable water resource management on a global scale.

2. Materials and Methods

2.1. Study Site Description

Changbai Mountain is located in northeast Asia (39.8–45.4° N and 123.5–131.3° E), as shown in Figure 1. The total area is approximately 17.16×10^4 km^2. Changbai Mountain is also an important ecological function area in eastern Eurasia, with a significant variation characteristic for vegetation along its altitude.

The altitude of Changbai Mountain ranges from −8 m to 2738 m, showing a significant altitude gradient. Owing to the high altitude, the annual average temperature in this area is between −7 and 3 °C, the annual average snowfall is 200~400 mm, and the freeze–thaw period is up to 8 months (from October to May of the following year) [27].

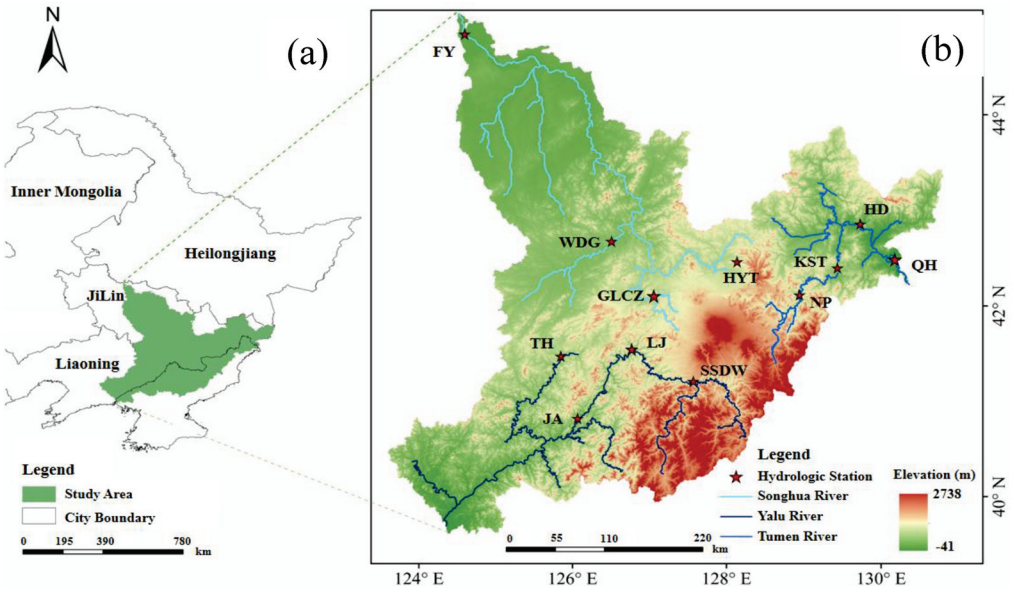

Figure 1. Study site location. (**a**) Location of Changbai Mountain region in China. (**b**) DEM, three rivers, and hydrological stations.

2.2. Data

Meteorological data from 48 hydrological stations (1984–2019) on Changbai Mountain were obtained from the China Meteorological Data Service Centre (http://data.cma.cn/). The variables include snowfall and potential evapotranspiration (E_0). Daily hydrological data from 1960 to 2020 were provided by the Hydrological Bureau for 12 stations (runoff data from the Hedong Hydrological Station on the TR are missing for 2011–2020), as shown in Table 1).

Table 1. Hydrological stations in the river-source region in the Changbai Mountain region.

ID	Hydrological Stations	Shorthand Form	Basins
1	Shisandaowan	SSDW	YR
2	Linjiang	LJ	
3	Tonghua	TH	
4	Jian	JA	
5	Nanping	NP	TR
6	Kaishantun	KST	
7	Hedong	HD	
8	Quanhe	QH	
9	Gaolichengzi	GLCZ	SR
10	Hanyangtun	HYT	
11	Wudaogou	WDG	
12	Fuyu	FY	

2.3. Method

2.3.1. Modified Mann–Kendall Method

The modified Mann–Kendall test analyzed the changing trend in runoff during freeze–thaw periods. The process for this method is described in detail by Yue et al. [28].

2.3.2. Water–Energy Balance Equation

The climate elasticity of runoff is defined as "the change degree of runoff in a watershed caused by the change of climate factors". Here, the basin substrate change is mainly due to human activities, such as land use change and frozen soil. Under certain climatic and

substratum conditions, the long-term hydroclimatic characteristics of the basin obey the principle of water and energy balance [19]. The expressions are as follows:

$$E = \frac{PE_0}{(P^n + E_0^n)^{\frac{1}{n}}} \tag{1}$$

where E is the average actual evapotranspiration; P is the average snowfall; E_0 is the average potential evapotranspiration; and n characterizes the subsurface of the basin (the subsurface parameter), including topography, soil, vegetation, etc.

P, E_0, and n are mutually independent variables in the aforementioned equation.

The variation in runoff (R) can be expressed in a fully differentiated form as follows:

$$dR = \frac{\partial f}{\partial P}dP + \frac{\partial f}{\partial E_0}dE_0 + \frac{\partial f}{\partial n}dn \tag{2}$$

The snowfall elasticity coefficient is the degree of change in the runoff volume from a watershed due to a unit change in snowfall. Similarly, the potential evapotranspiration elasticity coefficient of runoff and the subsurface elasticity coefficient of runoff can be defined: $\varepsilon_P = \frac{\frac{dR}{R}}{\frac{dP}{P}}$ is the elasticity coefficient of snowfall, $\varepsilon_{E_0} = \frac{\frac{dR}{R}}{\frac{dE_0}{E_0}}$ is the elasticity coefficient of E_0, and $\varepsilon_n = \frac{\frac{dR}{R}}{\frac{dn}{n}}$ is the elasticity coefficient of subsurface change. Based on the definition of these elasticity coefficients, the change in runoff can be expressed in the following fully differential form.

By dividing Equation (1) by the average runoff depth R, we obtain

$$\frac{dR}{R} = \varepsilon_P \frac{dP}{P} + \varepsilon_{E_0} \frac{dE_0}{E_0} + \varepsilon_n \frac{dn}{n} \tag{3}$$

Let $\phi = \frac{E_0}{P}$. The formulas are then expressed as follows:

$$\varepsilon_P = \frac{(1+\phi^n)^{\frac{1}{n+1}} - \phi^{n+1}}{(1+\phi^n)\left[(1+\phi^n)^{\frac{1}{n}} - \phi\right]} \tag{4}$$

$$\varepsilon_{E_0} = \frac{1}{(1+\phi^n)\left[1 - \left(1+\phi^{-n}\right)^{\frac{1}{n}}\right]} \tag{5}$$

$$\varepsilon_n = \frac{\ln(1+\phi^n) + \phi^n \ln\left(1+\phi^{-n}\right)}{n\left[(1+\phi^n) - (1+\phi^n)^{\frac{1}{n+1}}\right]} \tag{6}$$

According to Equations (4)–(6), the three runoff elasticity coefficients reflect the multi-year average hydroclimatic characteristics of the basin.

The study period can be divided into two subperiods according to the abrupt change points. To more comprehensively understand the key drivers of runoff changes during the freeze–thaw period, we employed a change point analysis to identify significant shifts in the runoff time series. Applying this method enabled us to precisely pinpoint the turning points at which different influencing factors impacted runoff, allowing for more accurate quantification of their contributions to runoff over different periods. The multi-year average runoff depths for period 1 and period 2 are denoted as R^1 and R^2, respectively. The change in runoff depth during the freeze–thaw period from period 1 to period 2 can be expressed as the difference between two factors, symbolized as ΔR_{2-1}.

$$\Delta R_{2-1} = R^2 - R^1 \tag{7}$$

The change in runoff depth (ΔR_{c-l}) arises from changes in the meteorological elements and subsurface and can be expressed in terms of the change in runoff as

$$\Delta R_{c-1} = \Delta R_c - \Delta R_l \quad (8)$$

where ΔR_c is the runoff change affected by climate change and ΔR_l is the runoff change affected by the change in subsurface. The effects of meteorological element changes can be further refined into two parts: runoff affected by snowfall changes (ΔR_P) and runoff affected by E_0 changes (ΔR_{E_0}).

Based on the ε_P, ε_{E_0}, and ε_n values, the runoff changes affected by changes in snowfall, E_0, and the subsurface can be estimated as follows:

$$\Delta R_P = \varepsilon_P \frac{R}{P}\Delta P, \Delta R_{E_0} = \varepsilon_{E_0} \frac{R}{E_0}\Delta E_0, \Delta R_l = \varepsilon_{E_0} \frac{R}{n}\Delta n \quad (9)$$

where A and B are the differences between the multi-year average snowfall and E_0 for the two time periods. n_1 and n_2 represent the basin subsurface conditions for period 1 and period 2, respectively.

3. Results

3.1. Runoff Variation Characteristics during Freeze–Thaw Periods

At SSDW station located in the source area of the YR, a significant decreasing trend occurred in runoff in October, November, December, and April. All months showed the largest increase after 2000. By contrast, runoff increased in March and fluctuated in January, February, and May; however, there was no clear trend (Figure 2a). LJ station, situated in the middle reaches of the YR, exhibited decreasing runoff trends from October to April, with the most notable increases in November through April after 2000. May's runoff also fluctuated without a significant trend (Figure 2b). TH station in the Hun River showed a continuously increasing trend throughout the freeze–thaw period (Figure 2c). JA station, located in the lower reaches of the YR, experienced a significant decrease in runoff from October to December and May after 2013, with a decreasing trend followed by an increase from January to March (Figure 2d).

At SSDW station, runoff showed non-significant changes in October, April, and May ($p > 0.05$) but significant increasing trends from November to March ($p < 0.01$). LJ station experienced increasing runoff across all months, with significant increases from November to April ($p < 0.05$). At JA station, runoff increased in October, January, March, April, and May, though these changes were not significant ($p > 0.05$). Decreasing trends were observed in November, December, and February, with December showing a significant decrease ($p < 0.05$). Specific trend results can be found in Table 2.

NP station, located in the source area of the TR, exhibited a significant decreasing runoff trend during the freeze–thaw period, with the most notable decrease in January. After 2000, runoff in April and May showed an increasing trend (Figure 3a). KST station in the middle reaches of the TR showed no significant changes in October, November, or May and a decreasing and then increasing trend from December to April. (Figure 3b). At HD station, located in the middle and lower parts of the TR, runoff remained stable in October, November, and December and then decreased before increasing from January to April, with a significant rise in May (Figure 3c). QH station, in the lower reaches, had no significant trends in October, November, or December, with runoff showing a general decreasing and then increasing trend in other months (Figure 3d).

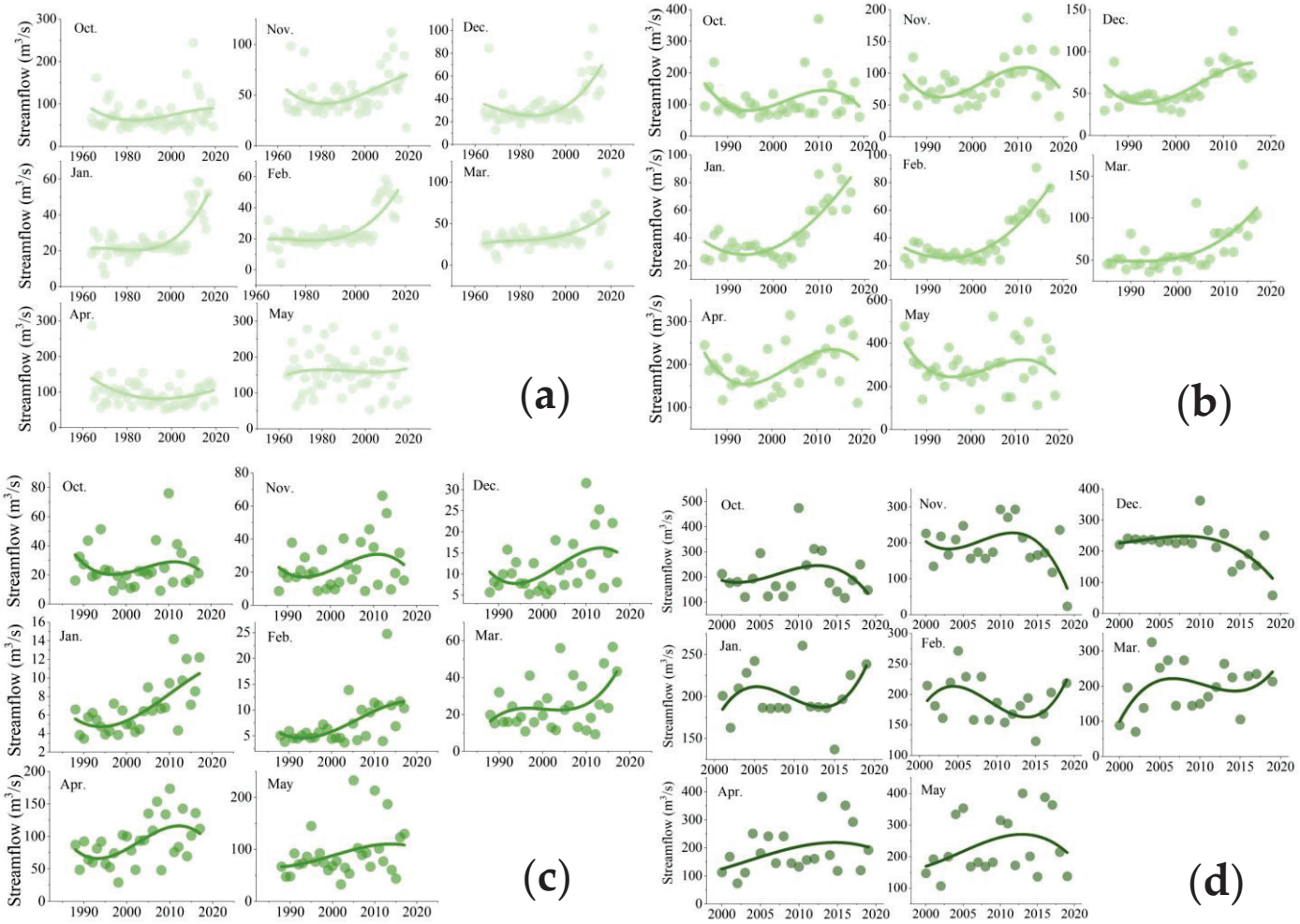

Figure 2. Variation characteristics of runoff during freeze–thaw periods in the YR basin: (**a**) SSDW; (**b**) LJ; (**c**) TH; (**d**) JA. Different colored scatter points are used to distinguish different stations. The fitted curves use polynomial regression to capture the nonlinear trends in the data.

Table 2. Detection of runoff variation trends during the freeze–thaw period in the YR.

Stations	Parameters	October	November	December	January	February	March	April	May
SSDW	Mean (m^3/s)	73.66	51.09	35.75	26.22	25.37	35.61	95.57	161.54
	Z Value	0.79	3.60	4.05	4.26	3.75	4.23	−1.04	0.45
	Slope	0.13	0.44	0.38	0.27	0.26	0.43	−0.26	0.22
	Sig.		**	**	**	**	**		
LJ	Mean (m^3/s)	115.29	86.03	58.08	43.45	38.73	63.60	196.10	293.63
	Z Value	0.11	2.40	3.32	3.64	3.64	3.86	2.22	0.03
	Slope	0.14	1.07	1.32	1.34	1.16	1.38	2.68	0.08
	Sig.		*	**	**	**	**	*	
TH	Mean (m^3/s)	25.25	23.95	11.83	6.70	7.40	25.14	91.12	91.86
	Z Value	0.04	1.07	2.14	3.78	2.89	1.46	2.62	3.78
	Slope	0.02	0.32	0.25	0.18	0.22	0.38	2.00	0.18
	Sig.			*	**				**
JA	Mean (m^3/s)	205.88	190.76	218.47	200.90	188.30	193.47	187.85	233.55
	Z Value	0.03	−0.68	−1.98	0.30	−0.95	1.14	1.33	1.01
	Slope	0.02	−1.23	−2.63	0.15	−2.25	5.56	4.01	3.04
	Sig.			*					

Note: ** is $p < 0.01$, * is $p < 0.05$.

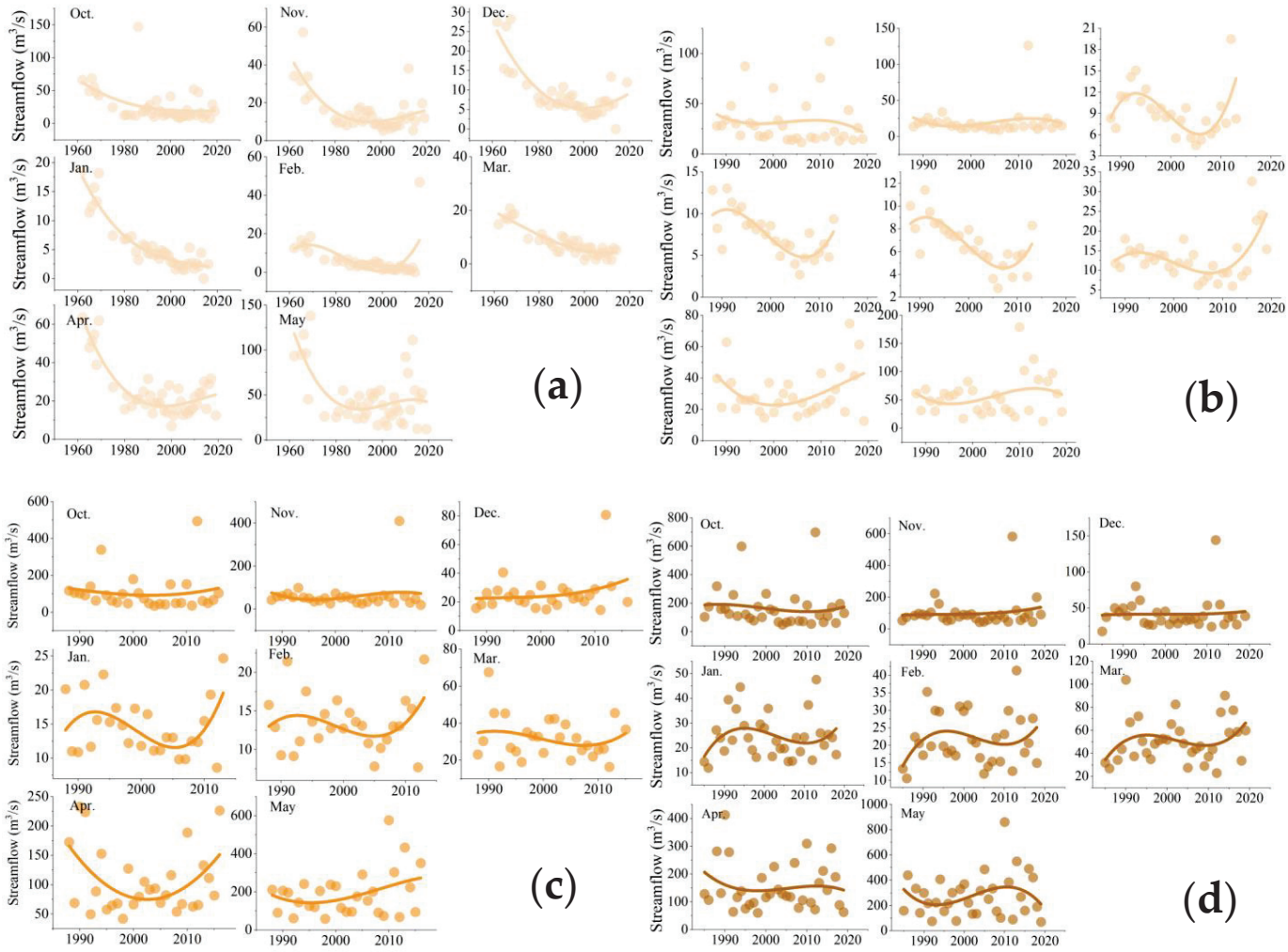

Figure 3. Runoff variation characteristics during freeze–thaw periods in the TR basin: (**a**) NP; (**b**) KST; (**c**) HD; (**d**) QH. Different colored scatter points are used to distinguish different stations. The fitted curves use polynomial regression to capture the nonlinear trends in the data.

During the freeze–thaw period, NP station exhibited a significantly decreasing runoff trend for all months except May ($p < 0.01$). KST station showed a decreasing trend from October to March, with significant decreases in January and February ($p < 0.01$). Runoff in April and May increased, though not significantly ($p > 0.05$). At HD station, runoff trends varied by month but were not significant. QH station showed an increasing trend in October, November, and December and a decreasing trend from February to May, though none of these trends were significant (Table 3).

GLCZ station, located on the Toudaosonghua River at the headwater of the SR, showed a decreasing runoff trend in October. Before 2000, there was no obvious trend from November to March, but after 2000, runoff increased significantly, with a slight upward trend in May (Figure 4a). HYT station, on the Erdaosonghua River in the SR source area, experienced significant decreases in runoff from October to February, with an increasing trend in March after 2000 (Figure 4b). April and May showed no significant trends. WDG station, on the Huifa River, displayed a decreasing trend followed by an increasing trend from October to May (Figure 4c). FY station, in the lower reaches of the SR, had consistent monthly trends during the freeze–thaw period, with no significant changes (Figure 4d).

Table 3. Runoff variation trends during freeze–thaw period in the TR.

Stations	Parameters	October	November	December	January	February	March	April	May
NP	Mean (m^3/s)	27.57	15.10	8.71	5.57	5.09	7.79	24.67	48.99
	Z Value	−3.02	−3.31	−4.62	−6.24	−6.29	−5.44	−2.73	−1.14
	Slope	−0.51	−0.30	−0.25	−0.23	−0.22	−0.31	−0.41	−0.41
	Sig.	**	**	**	**	**	**	**	
KST	Mean (m^3/s)	31.45	19.80	9.27	7.54	6.71	13.14	30.32	56.74
	Z Value	−1.86	−0.99	−1.94	−3.61	−4.06	−0.70	0.21	0.34
	Slope	−0.33	−0.12	−0.15	−0.28	−0.22	−0.09	0.06	0.21
	Sig.				**	**			
HD	Mean (m^3/s)	109.55	64.79	25.62	14.57	13.37	31.57	100.90	184.67
	Z Value	−1.68	−0.57	1.01	−0.79	−0.13	−0.93	−0.57	0.40
	Slope	−1.94	−0.30	0.24	−0.14	−0.01	−0.28	−0.50	1.34
	Sig.								
QH	Mean (m^3/s)	164.62	100.31	41.47	24.58	21.74	51.16	155.85	281.40
	Z Value	−1.66	−0.60	−0.93	0.05	0.05	0.76	0.29	0.98
	Slope	−2.02	−0.29	−0.19	0.00	0.01	0.34	0.41	2.25
	Sig.								

Note: ** is $p < 0.01$.

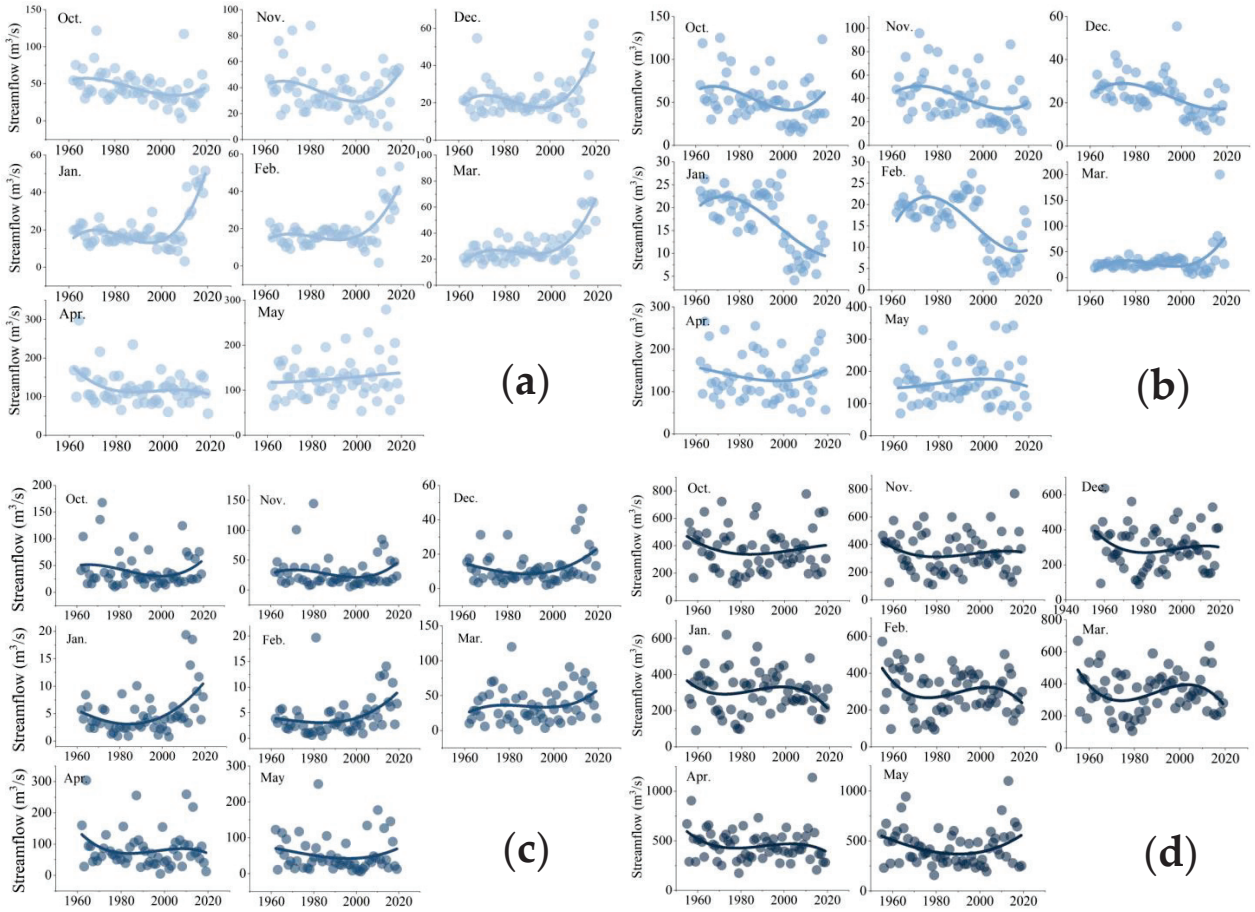

Figure 4. Runoff variation characteristics during freeze–thaw periods in the YR basin: (**a**) GLCZ; (**b**) HYT; (**c**) WDG; (**d**) FY. Different colored scatter points are used to distinguish different stations. The fitted curves use polynomial regression to capture the nonlinear trends in the data.

At GLCZ station, significant trends were observed in October, February, and March. October saw a significant decrease ($p < 0.01$), while February and March showed significant

increases ($p < 0.05$ and $p < 0.01$, respectively). Trends in other months were not significant. At HYT station, significant decreases were recorded from October to February ($p < 0.05$), with no significant changes in March, April, or May. WDG station experienced significant increases in January and February ($p < 0.05$ and $p < 0.01$, respectively), while other months showed no significant trends. FY station exhibited a decreasing trend with no significant changes ($p > 0.05$) (Table 4).

Table 4. Runoff variation trends during freeze–thaw period in the SR.

Stations	Parameters	October	November	December	January	February	March	April	May
GLCZ	Mean (m^3/s)	45.15	37.78	23.58	20.98	19.15	30.47	122.03	126.37
	Z Value	−3.46	−0.60	1.76	0.70	2.25	3.96	−1.23	0.63
	Slope	−0.49	−0.09	0.11	0.05	0.15	0.32	−0.38	0.25
	Sig.	**				*	**		
HYT	Mean (m^3/s)	54.28	40.72	23.55	17.31	16.03	31.74	136.12	165.35
	Z Value	−2.39	−3.05	−3.90	−4.50	−3.70	1.03	−0.32	0.14
	Slope	−0.47	−0.41	−0.26	−0.26	−0.23	0.10	−0.18	0.06
	Sig.	*	**	**	**	**			
WDG	Mean (m^3/s)	41.04	28.81	12.08	4.96	4.33	36.70	82.95	52.41
	Z Value	−0.45	−0.10	1.21	2.25	2.74	1.52	−0.89	−0.87
	Slope	−0.05	−0.01	0.06	0.05	0.06	0.30	−0.35	−0.25
	Sig.				*	**			
FY	Mean (m^3/s)	372.83	340.87	300.04	307.36	302.75	351.39	459.61	434.34
	Z Value	−0.66	−0.57	−0.52	−1.10	−0.78	−0.13	−1.42	−0.87
	Slope	−0.74	−0.68	−0.48	−0.75	−0.76	−0.14	−1.42	−0.89
	Sig.								

Note: ** is $p < 0.01$; * is $p < 0.05$.

3.2. Relationship between Runoff and Driving Factors during Freeze–Thaw Periods

There is a significant difference in snowmelt runoff between seasonally frozen soil areas and non-frozen soil areas. The precipitation in winter occurs in the form of snowfall and accumulates in the region. It is only affected by evaporation and will not immediately form runoff. As the temperature rises in the spring, snowmelt and snowmelt runoff form in the basin. Thus, the spring snowmelt runoff is mainly influenced by a combination of snowfall and evaporation during the freeze–thaw period under the condition that the subsurface remains unchanged.

Snowfall in different areas of the YR ranged from 206.57 mm to 275.37 mm; E_0 ranged from 313.97 mm to 329.54 mm; spring runoff ranged from 68.82 mm to 114.03 mm; the drought index ranged from 1.18 to 1.60; the runoff coefficient ranged from 0.29 to 0.41; and the subsurface parameter (n) ranged from 1.58 to 1.96. When the snowfall increased by 1%, the snowmelt runoff increased by 1.58~1.96%. When the E_0 increased by 1%, the snowmelt runoff decreased by 0.58~1.96%. When the lower bedding surface parameter increased by 1%, the snowmelt runoff decreased by 0.86~1.11%. The elasticity coefficient of each station showed that runoff at LJ station was more sensitive to climate and subsurface change; see Table 5.

Snowfall in different areas of the TR ranged from 155.74 mm to 180.17 mm; E_0 ranged from 341.79 mm to 364.40 mm; spring runoff ranged from 68.82 mm to 114.03 mm; the drought index ranged from 1.92 to 2.34; the runoff coefficient ranged from 0.14 to 0.22; and n ranged from 1.39 to 1.65. Compared with the YR, the TR basin had less snowfall during the freeze–thaw period, greater E_0, more significant drought, and smaller runoff coefficients. When snowfall increased by 1%, snowmelt runoff increased by 2.16~2.35%. When E_0 increased by 1%, snowmelt runoff decreased by 1.04~1.35%. When n increased by 1%, snowmelt runoff decreased by 1.56~1.95%. The elasticity coefficients of each station show that the snowmelt runoff at KST station was the most sensitive to climate and subsurface.

The sensitivity of snowmelt runoff to climate and subsurface changes was more prominent in the TR basin than in the YR; see Table 5.

Table 5. Climate and subsurface elasticity coefficients of snowmelt runoff from key sections on Changbai Mountain.

Basins	Stations	Area (km^2)	Snowfall (mm)	E_0 (mm)	Snowmelt Runoff (mm)	E_0/P	R/P	n	ε_P	ε_{E0}	ε_n
YR	SSDW	9104	206.57	329.54	82.54	1.60	0.40	0.97	1.58	−0.58	−1.04
	LJ	20,687	235.47	313.97	68.82	1.33	0.29	1.46	1.96	−0.96	−1.11
	TH	4731	275.37	325.61	114.03	1.18	0.41	1.13	1.64	−0.64	−0.86
	JA	24,359	258.66	320.03	65.75	1.78	0.25	1.78	2.19	−1.19	−1.11
TR	NP	6745	155.74	364.40	25.57	2.34	0.16	1.44	2.16	−1.16	−1.90
	KST	11,062	165.74	354.66	23.48	2.14	0.14	1.65	2.35	−1.35	−1.95
	HD	25,970	173.62	341.79	32.35	1.97	0.19	1.50	2.16	−1.16	−1.69
	QH	31,800	180.17	345.16	39.10	1.92	0.22	1.39	2.04	−1.04	−1.56
SR	GLCZ	4728	297.15	329.54	154.41	1.11	0.52	0.88	1.44	−0.44	−0.72
	HYT	8532	220.80	313.97	103.74	1.42	0.47	0.87	1.48	−0.48	−0.88
	WDG	12,391	204.24	337.43	34.28	1.65	0.17	1.83	2.41	−1.41	−1.62
	FY	71,783	167.49	359.83	45.24	2.15	0.27	1.12	1.80	−0.80	−1.47

Snowfall in different areas of the SR ranged from 167.49 mm to 297.15 mm; E_0 ranged from 313.97 mm to 359.83 mm; spring runoff ranged from 34.28 mm to 154.41 mm; the drought index ranged from 1.11 to 2.15; the runoff coefficient ranged from 0.17 to 0.52; and n ranged from 0.87 to 1.83. The climatic and subsurface parameters of each section of the SR varied significantly. The drought index at FY station was the largest at 2.15. The runoff coefficient at GLCZ station was the largest at 0.52. The runoff coefficient at WDG station was the smallest at 0.17. When snowfall increased by 1%, snowmelt runoff increased by 1.44~2.41%. When E_0 increased by 1%, snowmelt runoff decreased by 0.44~1.41%. When n increased by 1%, snowmelt runoff decreased by 0.72~1.62%. The elasticity coefficient of each station showed that the snowmelt runoff at WDG station was the most sensitive to climate and subsurface change; see Table 5.

3.3. Contribution of Driving Factors to Runoff during Freeze–Thaw Periods

According to the m-k mutation test, the abrupt change in spring snowmelt runoff in the three major basins of Changbai Mountain occurred after 2000. Compared with the pre-mutation period, all stations except for HYT exhibited an increasing trend; see Table 6.

After the abrupt change, the increase in snowmelt runoff in the YR was between 9.60 and 45.69 mm; the increase in snowfall was between 8.84 and 46.84 mm; the evaporation change was −2.6~12.21 mm; and the subsurface change was −0.03~−0.16 mm. The change in snowmelt runoff was mainly affected by climate and subsurface changes. After the abrupt change, the snowmelt runoff increased by 16.02 mm at SSDW station; the increase in snowfall led to a 5.6 mm increase in snowmelt runoff; and the increase in E_0 led to a 1.2 mm decrease in snowmelt runoff. The subsurface change led to a 10.8 mm increase in snowmelt runoff. The contributions of snowfall, E_0, and subsurface change to runoff change were 31.8%, 6.9%, and 61.3%, respectively. The increase in runoff at LJ station was 9.60 mm; the increase in snowfall led to a 10.6 mm increase in snowmelt runoff; the increase in E_0 led to a 2.6 mm decrease in snowmelt runoff; and the subsurface change led to a 1.6 mm increase in snowmelt runoff. The contributions of snowfall, E_0, and subsurface change to the change in runoff were 72.0%, 17.4%, and 10.6%, respectively. The largest increase in runoff volume was 45.69 mm at TH station. The increase in snowfall led to a 31.8 mm increase in snowmelt runoff; the decrease in E_0 led to a 0.6 mm increase in snowmelt runoff; and the subsurface change led to a 13.7 mm increase in snowmelt runoff. The contributions of snowfall, change in E_0, and subsurface to the change in runoff were 69.0%, 1.3%, and 29.8%, respectively.

Table 6. Contribution of climate and subsurface changes to snowmelt runoff. A represents after; B represents before.

Basins	Stations	Area (km^2)	Abrupt Year	Snowfall (mm)		E_0 (mm)		Snowmelt Runoff (mm)		ΔR_P (mm)	ΔR_{E0} (mm)	ΔR_n (mm)	ρ_P (%)	ρ_{E0} (%)	ρ_n (%)
				B	A	B	A	B	A						
YR	SSDW	9104	2012	204.7	213.5	327.6	335.9	79.4	95.4	5.6	−1.2	10.8	31.8	6.9	61.3
	LJ	20,687	2009	230.4	248.9	310.4	322.6	65.0	74.6	10.6	−2.6	1.6	72.0	17.4	10.6
	TH	4731	2002	253.1	300.0	326.9	324.3	91.2	136.9	31.8	0.6	13.7	69.0	1.3	29.8
	JA	24,359	2006	250.0	264.2	311.4	345.8	60.6	68.5	7.9	−8.4	7.9	32.7	34.8	32.5
TR	NP	6745	2012	148.3	187.6	366.9	354.9	23.9	32.0	13.9	1.0	−7.4	62.5	4.4	33.2
	KST	11,062	2013	159.5	198.4	352.4	365.1	22.3	28.8	13.0	−1.1	−5.5	66.2	5.8	28.0
	HD	25,970	2009	162.3	205.1	344.9	341.2	28.6	43.7	17.3	0.4	−3.2	82.9	2.0	15.1
	QH	31,800	2004	162.0	203.7	348.3	343.9	36.3	42.7	18.5	0.5	−12.7	58.2	1.6	40.2
SR	GLCZ	4728	2004	267.8	338.1	331.0	333.6	146.2	165.3	52.7	−0.5	−33.5	60.7	0.6	38.7
	HYT	8532	2001	201.0	240.3	314.8	340.0	105.9	101.7	27.3	−4.0	−26.6	47.2	6.9	45.9
	WDG	12,391	2004	189.1	225.3	338.1	336.6	27.3	43.1	14.6	0.2	0.9	92.8	1.4	5.8
	FY	71,783	2004	150.7	196.0	360.3	356.5	42.9	46.7	22.1	0.4	−19.4	52.8	0.9	46.3

After the abrupt change, the increase in snowmelt runoff in TR was between 6.39 and 15.15 mm; snowfall increased by 38.97~42.85 mm; the E_0 change was −3.70~12.66 mm; and the subsurface change was 0.09~0.22. After the abrupt change, the increase in runoff at NP station was 8.09 mm. The snowfall, E_0, and subsurface changes contributed 62.5%, 4.4%, and 33.2% to the runoff change, respectively. The snowmelt runoff at KST station increased by 6.52 mm; the increase in snowfall led to a 13.0 mm increase in snowmelt runoff; the decrease in E_0 led to a 1.1 mm decrease in snowmelt runoff; and the change in subsurface led to a 5.5 mm decrease in snowmelt runoff. The contributions of snowfall, E_0, and subsurface change to the change in runoff were 66.2%, 5.8%, and 28.0%, respectively. At HD station, snowmelt runoff increased by 15.15 mm, snowfall increased by 17.3 mm, E_0 decreased by 0.4 mm, and subsurface changes decreased by 3.2 mm; the contributions of snowfall, E_0, and subsurface changes to the change in snowmelt runoff were 82.9%, 2.0%, and 15.1%, respectively. The snowmelt runoff increased by 6.39 mm at QH station, the increase in snowfall led to an 18.5 mm increase in snowmelt runoff, the decrease in E_0 led to a 0.5 mm increase in snowmelt runoff, and the change in subsurface led to a 12.7 mm decrease in snowmelt runoff; see Table 6.

After the abrupt change, the change in snowmelt runoff at SR station was between −4.27 and 19.08 mm; snowfall increased by 36.13~70.33 mm; the E_0 change was −3.74~25.16 mm; and the lower bedding surface change was −0.03~0.33. After the abrupt change, the runoff at GLCZ station increased by 19.08 mm. The increase in snowfall led to a 52.7 mm increase in snowmelt runoff. The increase in E_0 led to a 0.5 mm decrease in snowmelt runoff. The subsurface change led to a 33.5 mm decrease in snowmelt runoff. The contributions of snowfall, E_0, and subsurface to the change in runoff were 60.7%, 0.6%, and 38.7%, respectively. At HYT station, the runoff decreased by 4.27 mm; the increase in snowfall led to a 27.3 mm increase in snowmelt runoff; the increase in E_0 led to a 4.0 mm decrease in snowmelt runoff; and the subsurface change led to a 26.6 mm decrease in snowmelt runoff. The contributions of snowfall, E_0, and subsurface to the change in runoff were 47.2%, 6.9%, and 45.9%, respectively. The runoff at WDG station increased by 15.86 mm; the increase in snowfall led to a 14.6 mm increase in snowmelt runoff; the increase in E_0 led to a 0.2 mm increase in snowmelt runoff; and the subsurface change led to a 0.9 mm increase in snowmelt runoff. The contributions of snowfall, E_0, and subsurface to the change in runoff were 92.8%, 1.4%, and 5.8%, respectively. The runoff at FY station increased by 3.83 mm; the increase in snowfall led to a 22.1 mm increase in snowmelt runoff; the increase in E_0 led to a 0.4 mm increase in snowmelt runoff; and the subsurface change led to a 19.4

mm decrease in snowmelt runoff. The contributions of snowfall, E_0, and subsurface to the change in runoff were 52.8%, 0.9%, and 46.3%, respectively.

4. Discussion

4.1. The Impact of Climate Change on Runoff during Freeze–Thaw Periods

This study assessed the impact of climate change on runoff during the freeze–thaw period in the Changbai Mountain region. Runoff regime shifts occurred at all three basins after 2000. Apart from HYT station, runoff during the freeze–thaw period increased across all stations (Table 4), primarily driven by increased snowfall during this period. Previous studies have indicated a significant increase in snowfall over the past 60 years on Changbai Mountain [29]. This increase has led to higher spring temperatures and greater snowmelt, indirectly contributing to the increased runoff. Although changes in runoff during the freeze–thaw period on Changbai Mountain have received little attention in past research and lack comparable results, numerous studies have demonstrated the significant contribution of snowmelt to mountain runoff. Our previous study used isotopic methods in the Changbai Mountain source area, showing that spring snowmelt contributes an average of 42.6% to runoff, supporting the validity of our findings [30]. Jenicek and Ledvinka [11] used a bucket-type watershed model to study 59 mountain watersheds in the Czech Republic. Their results indicated that 17–42% (an average of 26%) of total runoff comes from snowmelt. Additionally, snowmelt contributes approximately 23–26% to runoff in the headwaters of the Yellow River [31]. In our findings, SSDW station in the TR basin is unique, with groundwater being the primary factor influencing runoff during the freeze–thaw period. This is mainly because SSDW station is located at the headwaters of Changbai Mountain, and as shown in Figure 1, it is the highest-elevation hydrological station. Groundwater and surface water significantly interact at this station [32], where groundwater replenishment diminishes the contribution of snowmelt to surface runoff. Evaporation has the least impact on runoff during the freeze–thaw period in the Changbai Mountain region, and this phenomenon can be explained by three factors. First, temperatures are generally low during the freeze–thaw period. Although spring temperatures rise during the snowmelt season, they remain relatively low, resulting in slower evaporation rates [33]. Second, most of the soil remains frozen during this period, further inhibiting evaporation. Finally, runoff during the freeze–thaw period is primarily derived from snowmelt and groundwater recharge, both of which more significantly influence runoff, reducing the impact of evaporation.

4.2. The Impact of Subsurface Change on Runoff during Freeze–Thaw Periods

The impact of groundwater changes on runoff during the freeze–thaw period demonstrates significant differences across the three basins. In the YR basin, groundwater changes significantly increased runoff during the freeze–thaw period, whereas runoff in the TR and SR basins decreased, except at WDG station. Zhang et al. [25] found that human activities had a greater impact on annual runoff at WDG station than climate change. However, this study reveals that human activities account for only 5.8% of the impact on WDG station, with a related significant increase in winter snowfall [29]. This indicates that the drivers of freeze–thaw period runoff significantly differ from those in other seasons and warrant further investigation [34]. Furthermore, the impact of land use changes on runoff also varies. The primary land use type in the Changbai Mountain area is forest (Figure 5), with forest coverage ratios of 80.4% in the YR basin, 82.6% in the TR basin, and 49.0% in the SR basin. Since 2000, following the implementation of China's Natural Forest Protection Project, the dry land area has decreased, and forest areas have increased in the YR basin. By contrast, land use changes in the TR and SR basins have shown complex trends. Specifically, the SR basin has a significantly higher proportion of dry land than the other basins, which is related to agricultural activities. The dry land expansion notably impacts the hydrological cycle during the freeze–thaw period. In addition, changes in permafrost are another important factor affecting runoff during the freeze–thaw period. Our study indicates that

permafrost degradation in the YR basin has significantly increased spring runoff [27,35]. Although land use changes, such as increased forest area, may slightly reduce runoff, the impact of permafrost degradation during the freeze–thaw period is more pronounced. In summary, the variability in freeze–thaw period runoff is influenced by multiple factors, including groundwater changes, land use changes, and permafrost degradation, which interact in complex ways across different basins. Permafrost degradation in high-altitude areas may significantly increase runoff, while low-altitude areas are more affected by land use changes and groundwater variations. Future research should pay closer attention to the coupling effects between permafrost degradation and land use changes to better predict and manage water resources under extreme climate conditions. This will contribute to developing more scientifically based water resource management strategies and addressing the challenges posed by climate change.

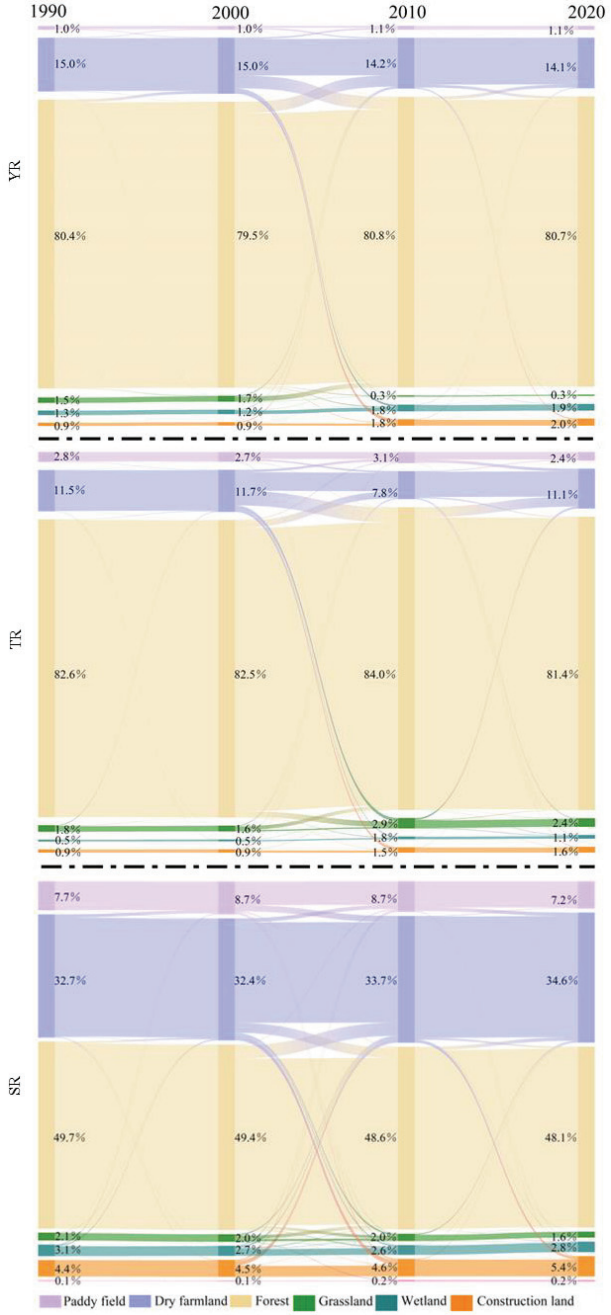

Figure 5. Changes in land use/land cover in the Changbai Mountain area.

5. Conclusions

This study identified the runoff change trends during the freeze–thaw period and its response to a changing environment in a high-latitude water tower. Based on these findings, the following conclusions can be drawn: (1) Runoff during the freeze–thaw period in the Changbai Mountain area was significantly non-stationary. The runoff trends in each month in the three basins were not completely consistent. The runoff in most months showed an increasing trend in the YR basin ($p < 0.05$), a decreasing trend in the TR basin ($p < 0.05$), and a more complex and inconsistent trend in the SR basin. (2) The spring runoff in the YR was 68.82 mm~114.03 mm when the snowfall, E_0, and subsurface changes increased by 1%, and the snowmelt runoff changes were 1.58~1.96%, −0.58~−1.96%, and −0.86~−1.11%, respectively. The spring runoff in the TR was 23.48 mm~39.10 mm when the snowfall, E_0, and subsurface changes increased by 1%, and the snowmelt runoff changes were 2.16~2.35%, −1.04~−1.35%, and −1.56~−1.95%, respectively. The spring runoff in the SR was 34.28 ~154.41 mm when the snowfall, E_0, and subsurface changes increased by 1%, and the snowmelt runoff changes were 1.44~2.41%, −0.44~−1.41%, and −0.72~−1.62%, respectively. (3) After the abrupt change, the increase in snowmelt runoff in YR ranged from 9.60 mm to 45.69 mm; the increase in snowmelt runoff in TR ranged from 6.39 mm to 15.15 mm; and the change in snowmelt runoff in the SR ranged from −4.27 mm to 19.08 mm. The increase in snowfall was the most prominent reason for the increase in snowmelt runoff in the spring, with a contribution of between 31.8% and 72.0% in the YR basin, 62.5% and 82.9% in the TR basin, and 47.2% and 92.8% in the SR basin. This study quantitatively analyzed the driving factors of runoff during the freeze–thaw period, providing managers with a strategic basis for coping with climate change and providing researchers with new methods and data support for studying hydrological processes in high-latitude regions, promoting in-depth explorations in related fields.

Author Contributions: Conceptualization, M.X. and P.Q.; methodology, D.L.; software, G.Z.; validation, M.X., P.Q. and Y.S.; formal analysis, L.G.; investigation, Y.C.; resources, P.Q.; data curation, D.L.; writing—original draft preparation, M.X.; writing—review and editing, M.X.; visualization, P.Q. All authors have read and agreed to the published version of the manuscript.

Funding: This research was funded by the National Natural Science Foundation of China; the grant numbers are 42371037 and 42001032.

Data Availability Statement: The data adopted in the study are included in the article; further inquiries can be directed to the corresponding author.

Conflicts of Interest: The authors declare no conflicts of interest.

References

1. Qin, Y.; Abatzoglou, J.T.; Siebert, S.; Huning, L.S.; AghaKouchak, A.; Mankin, J.S.; Hong, C.; Tong, D.; Davis, S.J.; Mueller, N.D. Agricultural risks from changing snowmelt. *Nat. Clim. Chang.* **2020**, *10*, 459–465. [CrossRef]
2. Musselman, K.N.; Addor, N.; Vano, J.A.; Molotch, N.P. Winter melt trends portend widespread declines in snow water resources. *Nat. Clim. Chang.* **2021**, *11*, 418–424. [CrossRef] [PubMed]
3. Jeelani, G.; Feddema, J.J.; van der Veen, C.J.; Stearns, L. Role of snow and glacier melt in controlling river hydrology in Liddar watershed (western Himalaya) under current and future climate. *Water Resour. Res.* **2012**, *48*, 1–16. [CrossRef]
4. Musselman, K.N.; Clark, M.P.; Liu, C.; Ikeda, K.; Rasmussen, R. Slower snowmelt in a warmer world. *Nat. Clim. Chang.* **2017**, *7*, 214–219. [CrossRef]
5. Kraaijenbrink, P.D.; Stigter, E.E.; Yao, T.; Immerzeel, W.W. Climate change decisive for Asia's snow meltwater supply. *Nat. Clim. Chang.* **2021**, *11*, 591–597. [CrossRef]
6. Fayad, A.; Gascoin, S.; Faour, G.; López-Moreno, J.I.; Drapeau, L.; Le Page, M.; Escadafal, R. Snow hydrology in Mediterranean mountain regions: A review. *J. Hydrol.* **2017**, *551*, 374–396. [CrossRef]
7. Vano, J.A.; Scott, M.J.; Voisin, N.; Stöckle, C.O.; Hamlet, A.F.; Mickelson, K.E.B.; McGuire Elsner, M.; Lettenmaier, D.P. Climate change impacts on water management and irrigated agriculture in the Yakima River Basin, Washington, USA. *Clim. Chang.* **2010**, *102*, 287–317. [CrossRef]
8. Li, D.; Wrzesien, M.L.; Durand, M.; Adam, J.; Lettenmaier, D.P. How much runoff originates as snow in the western United States, and how will that change in the future? *Geophys. Res. Lett.* **2017**, *44*, 6163–6172. [CrossRef]

9. Woo, M.K.; Thorne, R. Snowmelt contribution to discharge from a large mountainous catchment in subarctic Canada. *Hydrol. Process.* **2006**, *20*, 2129–2139. [CrossRef]
10. Zaremehrjardy, M.; Victor, J.; Park, S.; Smerdon, B.; Alessi, D.S.; Faramarzi, M. Assessment of snowmelt and groundwater-surface water dynamics in mountains, foothills, and plains regions in northern latitudes. *J. Hydrol.* **2022**, *606*, 127449. [CrossRef]
11. Jenicek, M.; Ledvinka, O. Importance of snowmelt contribution to seasonal runoff and summer low flows in Czechia. *Hydrol. Earth Syst. Sci.* **2020**, *24*, 3475–3491. [CrossRef]
12. Qi, W.; Feng, L.; Kuang, X.; Zheng, C.; Liu, J.; Chen, D.; Tian, Y.; Yao, Y. Divergent and Changing Importance of Glaciers and Snow as Natural Water Reservoirs in the Eastern and Southern Tibetan Plateau. *J. Geophys. Res. Atmos.* **2022**, *127*, e2021JD035888. [CrossRef]
13. Barnett, T.P.; Adam, J.C.; Lettenmaier, D.P. Potential impacts of a warming climate on water availability in snow-dominated regions. *Nature* **2005**, *438*, 303–309. [CrossRef] [PubMed]
14. Morán-Tejeda, E.; Lorenzo-Lacruz, J.; López-Moreno, J.I.; Rahman, K.; Beniston, M. Streamflow timing of mountain rivers in Spain: Recent changes and future projections. *J. Hydrol.* **2014**, *517*, 1114–1127. [CrossRef]
15. Arheimer, B.; Donnelly, C.; Lindstrom, G. Regulation of snow-fed rivers affects flow regimes more than climate change. *Nat. Commun.* **2017**, *8*, 62–71. [CrossRef]
16. Liu, W.; Wang, L.; Sun, F.; Li, Z.; Wang, H.; Liu, J.; Yang, T.; Zhou, J.; Qi, J. Snow Hydrology in the Upper Yellow River Basin Under Climate Change: A Land Surface Modeling Perspective. *Water Resour. Res.* **2018**, *123*, 676–691. [CrossRef]
17. Romshoo, S.A.; Marazi, A. Impact of climate change on snow precipitation and streamflow in the Upper Indus Basin ending twenty-first century. *Clim. Chang.* **2022**, *170*, 6. [CrossRef]
18. Liu, Z.; Cuo, L.; Sun, N. Tracking snowmelt during hydrological surface processes using a distributed hydrological model in a mesoscale basin on the Tibetan Plateau. *J. Hydrol.* **2023**, *616*, 128796. [CrossRef]
19. Yang, H.; Yang, D.; Lei, Z.; Sun, F. New analytical derivation of the mean annual water-energy balance equation. *Water Resour. Res.* **2008**, *44*, W03410. [CrossRef]
20. Roderick, M.L.; Farquhar, G.D. A simple framework for relating variations in runoff to variations in climatic conditions and catchment properties. *Water Resour. Res.* **2011**, *47*, W00G07. [CrossRef]
21. Tang, Y.; Wang, D.B. Evaluating the role of watershed properties in long-term water balance through a Budyko equation based on two-stage partitioning of precipitation. *Water Resour. Res.* **2017**, *53*, 4142–4157. [CrossRef]
22. Sharma, P.; Mondal, A. Probabilistic Budyko-based Separation of Climate and Catchment Effects on Streamflow. *J. Hydrol.* **2022**, *608*, 127665. [CrossRef]
23. Yu, E.; Qi, L.; Dai, L.; Yu, D.; Zhao, F.; Zhou, L.; Zhou, W.; Zhu, Q.; Mao, C.; Wu, G. Correlation analysis of elements in the mountains-rivers-forests-farmlands-lakes-grasslands life community: Using Changbai mountains as an example. *Acta Ecol. Sin.* **2019**, *39*, 8837–8845.
24. Qi, P.; Huang, X.R.; Xu, Y.J.; Li, F.; Wu, Y.; Chang, Z.; Li, H.; Zhang, W.; Jiang, M.; Zhang, G.; et al. Divergent trends of water bodies and their driving factors in a high-latitude water tower, Changbai Mountain. *J. Hydrol.* **2021**, *603*, 127094. [CrossRef]
25. Zhang, A.; Zhang, C.; Fu, G.; Wang, B.; Bao, Z.; Zheng, H. Assessments of Impacts of Climate Change and Human Activities on Runoff with SWAT for the Huifa River Basin, Northeast China. *Water Resour. Manag.* **2012**, *26*, 2199–2217. [CrossRef]
26. Xin, Z.; Li, Y.; Zhang, L.; Ding, W.; Ye, L.; Wu, J.; Zhang, C. Quantifying the relative contribution of climate and human impacts on seasonal streamflow. *J. Hydrol.* **2019**, *574*, 936–945. [CrossRef]
27. Chang, Z.; Qi, P.; Zhang, G.; Sun, Y.; Tang, X.; Jiang, M.; Sun, J.; Li, Z. Latitudinal characteristics of frozen soil degradation and their response to climate change in a high-latitude water tower. *Catena* **2022**, *214*, 106272. [CrossRef]
28. Yue, S.; Wang, C.Y. Applicability of prewhitening to eliminate the influence of serial correlation on the Mann-Kendall test. *Water Resour. Res.* **2002**, *38*, 1–7. [CrossRef]
29. Chen, Y.; Chang, Z.; Xu, S.; Qi, P.; Tang, X.; Song, Y.; Liu, D. Altitudinal Gradient Characteristics of Spatial and Temporal Variations of Snowpack in the Changbai Mountain and Their Response to Climate Change. *Water* **2021**, *13*, 3580. [CrossRef]
30. Feng, M.; Zhang, W.; Zhang, S.; Sun, Z.; Li, Y.; Huang, Y.; Wang, W.; Qi, P.; Zou, Y.; Jiang, M. The role of snowmelt discharge to runoff of an alpine watershed: Evidence from water stable isotopes. *J. Hydrol.* **2022**, *604*, 127209. [CrossRef]
31. Zhang, T.; Li, D.; Lu, X. Response of runoff components to climate change in the source-region of the Yellow River on the Tibetan plateau. *Hydrol. Process.* **2022**, *36*, e14633. [CrossRef]
32. Hu, Y.; Sun, Z.; Ma, R. Springs Emerging along the Elevation Gradient Indicate Intensive Groundwater-Surface Water Exchange in an Alpine Headwater Catchment, Northwestern China. *J. Earth Sci.* **2023**, *34*, 181–193. [CrossRef]
33. Linacre, E.T. A simple formula for estimating evaporation rates in various climates, using temperature data alone. *Agric. Meteorol.* **1977**, *18*, 409–424. [CrossRef]
34. Li, Z.; Huang, S.; Liu, D.; Leng, G.; Zhou, S.; Huang, Q. Assessing the effects of climate change and human activities on runoff variations from a seasonal perspective. *Stoch. Environ. Res. Risk Assess.* **2020**, *34*, 575–592. [CrossRef]
35. Sun, A.; Yu, Z.; Zhou, J.; Acharya, K.; Ju, Q.; Xing, R.; Huang, D.; Wen, L. Quantified hydrological responses to permafrost degradation in the headwaters of the Yellow River (HWYR) in High Asia. *Sci. Total Environ.* **2020**, *712*, 135632. [CrossRef]

water

MDPI

Article

Multiscale Factors Driving Extreme Flooding in China's Pearl River Basin During the 2022 Dragon Boat Precipitation Season

Jiawen Zheng [1], Naigeng Wu [2], Pengfei Ren [2,*], Wenjian Deng [3] and Dong Zhang [2]

[1] Guangzhou Meteorological Observatory, Guangzhou 511430, China; karmanzheng@163.com
[2] Guangdong Meteorological Observatory, Guangzhou 510641, China
[3] Guangzhou Institute of Tropical and Marine Meteorology, China Meteorological Administration, Guangzhou 510641, China
* Correspondence: renpf@gd121.cn

Abstract: This study delves into the once-in-a-century extreme precipitation events in the northern region of the Pearl River Basin during the 2022 Dragon Boat Festival period. Through a comprehensive analysis spanning various temporal scales, from synoptic-scale systems to subseasonal oscillations, including the rare triple-peaked La Niña phenomenon, we illuminate the intricate interactions among these factors and their impact on extreme precipitation events. Specifically, we present a conceptual model of multiscale interaction systems contributing to extreme precipitation in the BeiJiang Basin. Our findings reveal that, during the 2022 Dragon Boat Festival period, precipitation in the BeiJiang Basin exhibited characteristics across multiple time scales, with the synoptic-scale environment proving highly conducive. Systems such as the South Asian High, Western Pacific Subtropical High, and South China Sea summer monsoon were identified as the direct influencing factors of precipitation. Importantly, our study highlight the pivotal role of subseasonal oscillation propagation stagnation in extreme precipitation in the BeiJiang Basin, with synoptic-scale systems playing a contributing role. We emphasize the indirect influence of ENSO signals, regulating not only monsoons but also the propagation of subseasonal oscillations. The interplay of these factors across different temporal scales significantly impacts flood hazards. Overall, our study significantly enhances the understanding of mechanisms driving extreme precipitation events in the Pearl River Basin, with profound implications for water resource management and disaster prevention.

Keywords: dragon-boat precipitation; pearl river basin; extreme flood; multiscale factors; cause analysis

1. Introduction

"Dragon-Boat Precipitation (DBP)" refers to intense rainfall occurring in southern China during the Dragon Boat Festival period, typically from late May to mid-June (21 May–21 June). It is associated with the South China Sea (SCS) summer monsoon, convective precipitation, and frontal precipitation from the convergence of cold and warm air masses [1]. The Beijiang River Basin (BJB), one of the three major rivers of the Pearl River Basin (PRB, shown in Figure 1), mainly flows through Guangdong Province before merging with Xijiang River to form the Pearl River Delta and finally emptying into the SCS. With a total length of approximately 470 km and a basin area of 42,930 km^2, the BJB is the second largest river in the PRB and one of the most important rivers in Guangdong Province. The basin experiences a humid subtropical climate, with a long-term mean annual precipitation

of approximately 1700 mm and a mean annual potential evapotranspiration (PET) exceeding 1200 mm. These climatic conditions, combined with the region's complex topography, make the BJB highly susceptible to extreme rainfall and flooding events. In 2022, the PRB experienced multiple episodes of heavy rainfall, leading to widespread flooding. The BJB, a major sub-basin of the PRB, witnessed two significant flood events, which were officially designated as the first and second floods of the year. These floods occurred at 11:00 on 14 June and 12:00 on 19 June, respectively, marking the most severe flooding in the region since 1915 [2]. These statistics highlight the importance of accurate precipitation forecasting for river basins, especially in regions like the PRB where extreme rainfall events have significant socio-economic impacts.

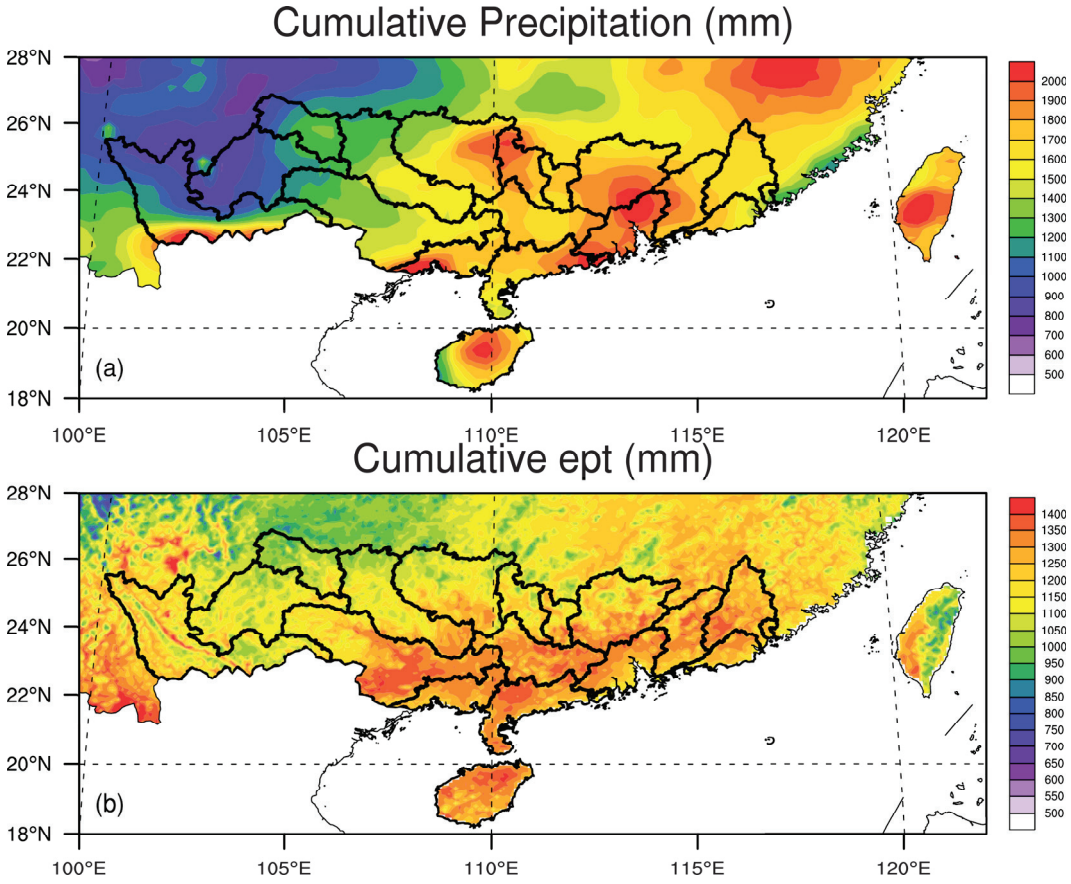

Figure 1. (**a**) Location of the Pearl River Basin within China, with shaded areas representing the multi-year mean annual precipitation (1998–2022, units: mm). (**b**) Same as (**a**) but for the multi-year mean annual evapotranspiration (1991–2020, units: mm).

Heavy rainfall results from the interactions among various systems operating at multiple temporal scales. Particularly, extreme or persistent heavy rainfall occurs when systems at different scales (planetary, synoptic, mesoscale, and small-scale) interact significantly. Among these multiscale systems, while planetary-scale systems (3000–8000 km) do not directly cause heavy rainfall, they play a crucial role in events lasting over two days by influencing the movement of synoptic-scale systems, thereby indirectly affecting heavy rainfall. For instance, pre-flood precipitation in southern China exhibits distinct subseasonal variability [3–6], with periods of increased and decreased rainfall occurring on time scales of 10–20 days and 30–60 days. The low-frequency characteristics of precipitation are primarily driven by low-frequency variations in atmospheric circulation. A key modulator of rainfall anomalies in southern China, particularly extreme rainfall events [7,8], is the Madden–Julian Oscillation (MJO) [9,10]. The MJO is a large-scale tropical phenomenon characterized

by eastward-propagating anomalies in rainfall and circulation, with typical timescale of 30–60 days. Originating over the Indian Ocean, it propagates eastward across the Maritime Continent and into the Pacific Ocean, exerting a global influence on weather patterns. During specific phases, the MJO enhances convective activity and moisture transport via teleconnection waves, leading to increased rainfall in regions such as southern China. This oscillatory behavior makes the MJO a crucial predictor of subseasonal weather variability, especially in monsoon regions. The eastward propagation of MJO convection, from the western Indian Ocean to the western Pacific, is commonly monitored using the real-time multivariate MJO (RMM) index [11], which divides MJO activity into eight phases. Phases 2–3 and 6–7 are particularly significant, representing "wet" and "dry" phases, respectively, that strongly influence pre-flood precipitation in southern China. Recent research has also highlighted the significant impact of prolonged stagnation of the MJO in specific phases on persistent heavy rainfall in certain regions. For example, Roxy et al. [12] attributed strong Southeast Asian rainfall in 2011 to the long-term stagnation of the MJO in phases 5–7. Chinese scholars have also indicated that the prolonged stagnation of MJO convection in the Indian Ocean region (phases 1–2) was a key factor in the occurrence of super-heavy rainfall events in the Yangtze River Basin in 2020 [13,14].

At seasonal and longer time scales, the El Niño-Southern Oscillation (ENSO) is the strongest signal of the tropical Pacific Ocean–atmosphere interaction on interannual scales and is a crucial influencing factor on East Asian climate [15]. ENSO is a natural climate phenomenon characterized by periodic fluctuations in sea surface temperatures (SSTs) and atmospheric pressure in the tropical Pacific Ocean. It consists of two main phases: El Niño, associated with warmer-than-average SSTs in the central and eastern Pacific, and La Niña, associated with cooler-than-average SSTs in the same region. These phases alter global atmospheric circulation patterns, leading to significant impacts on weather and climate worldwide. China, located in eastern Asia, is profoundly influenced by the East Asian monsoon. The timing and intensity of the onset of the South China Sea (SCS) summer monsoon are modulated by ENSO [16–19], thereby regulating the intensity and frequency of rainfall, including extreme rainfall events [20], in southern China. For example, during El Niño years, the SCS summer monsoon tends to be weaker and delayed, often resulting in reduced rainfall. Conversely, during La Niña years, the monsoon is typically stronger and earlier, leading to increased rainfall and a higher likelihood of extreme precipitation events.

Given that multiscale factors may modulate precipitation in South China, analyzing only the synoptic-scale systems responsible for flood-triggering heavy rainfall is insufficient to fully explain this extreme event. Previous studies on the causes of extreme rainfall in 2022 have mostly focused on the synoptic scale [1,21–24] or individual influencing systems with longer timescales [7,8,13,20,25], with fewer studies revealing the causes from the perspective of multiscale influencing factors. This paper focuses on why the BJB experienced a once-in-a-century flood-triggering heavy rainfall event in 2022 [2]. The aim is to reveal the causes of flood-triggering precipitation in the BJB during the DBP period in 2022 from the perspective of multiscale influencing systems and their interactions. While our study aims to provide a comprehensive understanding of the multiscale factors contributing to the 2022 DBP event in the BJB, it is important to acknowledge some research limitations. Firstly, while we focus on the key multiscale systems and their interactions, the complexity of the atmospheric system means that other factors may also play a role, which may not be fully captured in this study. Secondly, data availability and resolution constraints may limit the depth and precision of our analysis, particularly at smaller scales. Despite these limitations, this paper will provide valuable insights into the multiscale mechanisms that contributed to the once-in-a-century flood-triggering heavy rainfall event in the BJB region in 2022.

The remaining sections of this paper are structured as follows: Section 2 presents the data and methods utilized. Section 3 discusses the multiscale characteristics of the flood-triggering heavy rainfall in the BJB during the 2022 Dragon Boat Festival. Following that, Section 4 reveals the influences of multiscale factors on the extreme DBP events. Finally, Section 5 offers a summary and discussion.

2. Data and Methods

This study explores the relationship between heavy precipitation events in the BJB and various multiscale factors by utilizing multiple data sources. Specifically, we utilized precipitation data from the Global Precipitation Measurement (GPM) and Tropical Rainfall Measuring Mission (TRMM) satellites [26,27], as well as precipitation data from national and regional meteorological stations collected and compiled by the China Meteorological Administration's (CMA) National Meteorological Information Center. Since the TRMM satellite concluded its mission in April 2015, with the GPM satellite succeeding its tasks, we merged the precipitation data from both satellites into a single-gridded precipitation dataset. It is noteworthy that we validated the satellite precipitation data using station-based precipitation data, and the results remained consistent regardless of the precipitation product chosen, indicating independence from the choice of precipitation product. Furthermore, we employed circulation and humidity fields from European Centre for Medium-Range Weather Forecasts (ECMWF) Reanalysis 5th Generation (ERA5) data [28], as well as outgoing longwave radiation (OLR) data [29] and sea surface temperature (SST) data [30] from the National Oceanic and Atmospheric Administration (NOAA).

To monitor the activity of tropical intraseasonal signals, we adopted the Boreal Summer Intraseasonal Oscillation (BSISO) index [31]. The BSISO index is a widely used metric to track the evolution of large-scale tropical convection and circulation patterns during the boreal summer (May–October). It captures two main modes of variability: BSISO1, which operate on a 30–60 day timescale, and BSISO2, which operates on a 10–30 day timescale. These modes are characterized by the northward and eastward propagation of rainfall and wind anomalies, influencing monsoon activity and extreme weather events in regions such as South Asia and East Asia. By dividing BSISO activity into eight phases, the index provides a framework for understanding the spatial and temporal evolution of intraseasonal variability, making it a valuable tool for studying subseasonal climate phenomena (see Table 1).

In Figure 2, we employ the precipitation anomaly percentage to describe the deviation of precipitation from a reference period or long-term average (for example, the temporal coverage for precipitation data are from 1998 to 2002, while for ERA5 data, it is from 1991 to 2020). The formula for calculating the anomaly percentage is as follows:

$$AP = \frac{Anom}{LTM} \times 100\% \quad (1)$$

where AP represents the anomaly percentage, anomaly represents the anomaly value, and LTM represents the climatological mean.

When conducting significance tests for correlation coefficients, this study employs the t-test formula (as shown in Equation (2)) at a 95% confidence level with $(n - 2)$ degrees of freedom (where n is the sample size) to compute the critical value of the correlation coefficient. If the absolute value of the calculated correlation coefficient exceeds the critical value, it is considered to pass the significance test. The t-test was chosen because it is robust and widely used for comparing two groups under the assumption of normally distributed data, and a 95% confidence level ($p < 0.05$) was selected to ensure the balance between Type I and Type II errors, consistent with common practices in climate studies. Sensitivity

tests were conducted using 90% and 99% confidence levels to ensure the robustness of our findings.

$$t = r\sqrt{\frac{n-2}{1-r^2}} \tag{2}$$

Table 1. Summary of datasets used in this study.

Dataset	Variables	Spatial Resolution	Temporal Resolution	Temporal Coverage	Source	Notes
GPM	Precipitation	0.1° × 0.1°	Daily	2014–2022	National Aeronautics and Space Administration (NASA)/ Japan Aerospace Exploration Agency (JASA)	Merged with TRMM data; validated against station observations
TRMM	Precipitation	0.25° × 0.25°	Daily	1998–2015	NASA/JAXA	Mission ended in April 2015; data merged with GPM
ERA5	Geopotential, UV winds, temperature, specific humidity	0.25° × 0.25°	Hourly	1979–2022	ECMWF	Used for synoptic and subseasonal analysis
CMA Stations	Precipitation	Stations	Daily	2005–2022	CMA	Used for validation of satellite precipitation data
NOAA OLR	Outgoing longwave radiation	2.5° × 2.5°	Daily	1974–2022	NOAA	Used to monitor tropical convection
NOAA SST	Sea surface temperature	0.25° × 0.25°	Monthly	1981–2022	NOAA	Used for interannual-scale analysis (e.g., ENSO)
China Ept	Evapotranspiration	0.01° × 0.01°	Monthly	1991–2020	National Tibetan Plateau Data Center in China	
BSISO Index	BSISO1, BSISO2	N/A	Daily	1981–2022	Lee et al. [31]	Used to monitor tropical intraseasonal signals

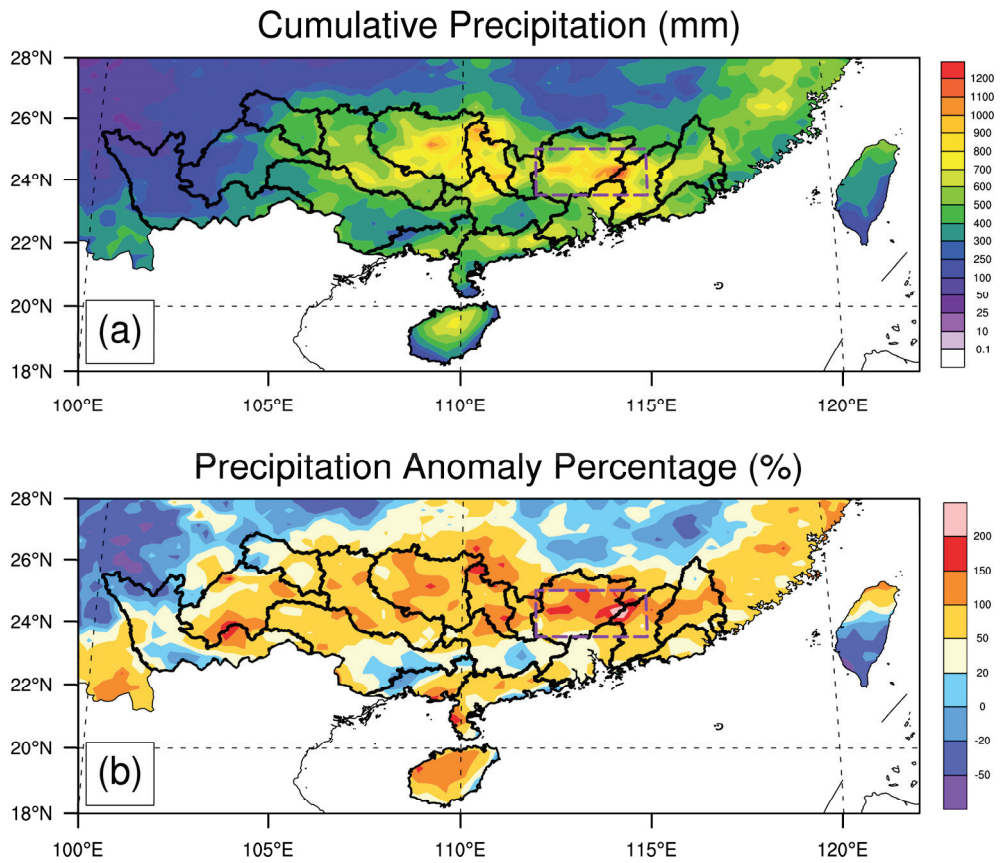

Figure 2. (**a**) Accumulated precipitation (units: mm) and (**b**) precipitation anomaly percentage (units: %) from 21 May to 21 June 2022. The boxed area in the figure corresponds to the latitude and longitude range of 23.5–25° N and 112–115° E, representing the Beijiang River Basin (The same geographical range is used for boxed areas in subsequent figures).

3. The Multiscale Nature of Flood-Inducing Rainfall in the BJB

The precipitation during this event exhibited a typical pattern of more rainfall in the north and less in the south (see Figure 2). Specifically, the BJB became the epicenter of this precipitation event, with an accumulated rainfall of 1200 mm and a precipitation anomaly percentage of 200%. The immense cumulative precipitation during this event far exceeded the long-term average, leading to a once-in-a-century flood in the BJB.

We selected the region between 23.5–25° N and 112–115° E as the primary precipitation zone in the BJB. During the 32-day period of DBP in 2022, as shown in Figure 3a, precipitation exceeded historical climatological norms on 18 days. From 12 June to 21 June, daily cumulative precipitation exceeded the historical average by an average of 39 mm (range: 9–72 mm), with consecutive days of precipitation surpassing double the historical average after 16 June. A *t*-test confirmed that the daily precipitation during this period was significantly higher than the historical average ($p < 0.01$). This period represented the peak of precipitation during the 2022 DBP, significantly increasing the flood control pressures in the area.

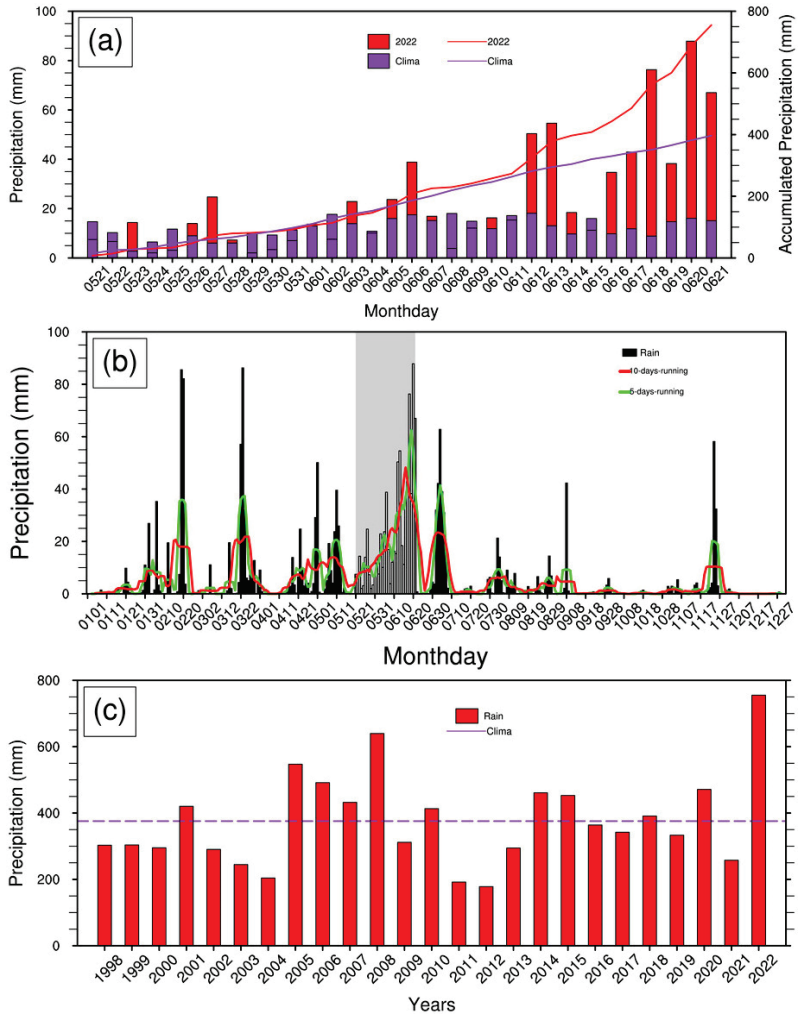

Figure 3. Temporal evolution of precipitation during the Dragon Boat Festival period in the Beijiang River Basin (BJB). (**a**) Daily precipitation during the DBP period (21 May–21 June) in the BJB. The red line and bars represent the year 2022, while the purple line and bars indicate the climatological mean (1991–2020). (**b**) Daily precipitation for the year 2022, displayed as a bar chart with green and red lines representing 5-day and 10-day moving averages, respectively. (**c**) Cumulative precipitation during the DBP period for selected years, displayed as a bar chart with a purple line indicating the climatological mean.

During the 2022 DBP, the precipitation in the BJB exhibited significant multiscale characteristics. From a synoptic-scale perspective (Figure 3b), the maximum daily rainfall in the BJB during the DBP was comparable to that of February and March of the same year, indicating that individual daily rainfall events were not extreme. However, it was precisely at the subseasonal scale that we observed a notable peak in precipitation. The moving average results (illustrated by the green line for 5-day average and red line for 10-day averages) clearly highlighted the pronounced subseasonal scale characteristics of basin precipitation. Remarkably, subseasonal scale precipitation in the BJB peaked during the 2022 DBP. This emphasizes the crucial role likely played by subseasonal scale signals in the extreme precipitation event of 2022. Taking a broader temporal perspective, comparing the precipitation levels during DBP across different years (Figure 3c), the annual precipitation in the BJB during the 2022 DBP period peaked, surpassing that of 2008, a year previously regarded as experiencing the strongest DBP in the history of Guangdong Province [21]. However, in 2008, the DBP precipitation was more concentrated in the coastal cities and counties of South China.

In brief, the precipitation during the 2022 DBP period exhibited a distinct north–south gradient and historical extremity, serving as the primary cause of the flood-triggering heavy rainfall in the BJB. The precipitation in the BJB during this period displayed multiscale characteristics. From a synoptic-scale perspective, the basin-average precipitation did not show historical extremity. The occurrence of flood-triggering precipitation in the BJB in 2022 can be attributed to the prolonged duration and significant accumulation of rainfall during the DBP period, resulting in the historical extremity of precipitation on subseasonal and even climatic time scales. Therefore, comprehensively discussing the extremity of the 2022 DBP in the BJB necessitates the consideration of multiscale factors and the modulation effect of the entire climatic environment.

4. Impact of Multiscale Temporal Factors on Extreme Precipitation

The multiscale characteristics of heavy precipitation in the pre-flood season of the BJB in 2022 imply that key influencing factors may involve multiple temporal scales. Understanding these multiscale influencing factors and their interactions is crucial for effectively preventing and mitigating catastrophic flood-triggering heavy rainfall events. In the following, we will discuss the favorable conditions for this flood-triggering heavy rainfall event from the perspectives of synoptic-scale systems, subseasonal scale signals, and interannual scale background, focusing particularly on how the historical extremity of this precipitation event was formed.

4.1. Favorable Synoptic Environments

The synoptic-scale systems play a direct and crucial role in precipitation, revealing not only the distribution, movement, and vertical motion of atmospheric moisture but also determining the location, intensity, and duration of precipitation. Therefore, the timely and accurate analysis and understanding of synoptic-scale patterns are essential for precipitation prediction and the mitigation of associated risks, such as flooding. Figure 4 illustrates the linear correlation of circulation patterns with precipitation in the BJB during the 2022 DBP period. A broad anticyclonic circulation is observed in the lower levels over the SCS, with Southern China situated to its north, promoting the onshore southwest monsoon flow. The upper-level divergence field closely aligns with the precipitation area in the BJB, providing crucial clues for predicting precipitation regions. In the region controlled by the anticyclonic circulation (10–20° N), significant subsidence airflow is evident. Correspondingly, influenced by the convergence circulation of the southwest monsoon, significant upward motion is observed in the BJB. In summary, the combination of a lower-level

anticyclonic circulation, enhanced southwest monsoon, upper-level divergence field, and the interplay between subsidence and upward airflows collectively constitutes a synoptic system configuration favorable for precipitation in the BJB region.

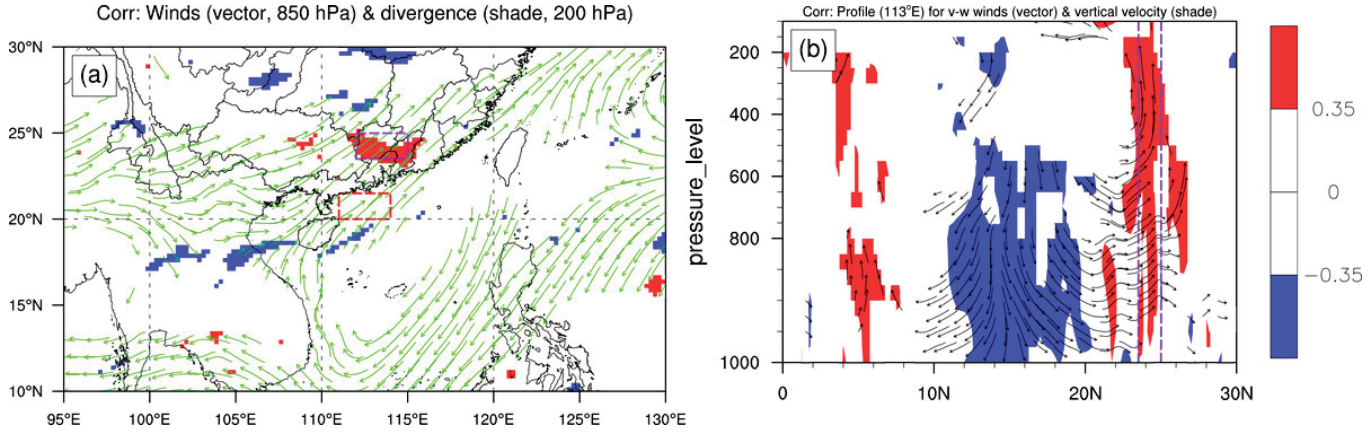

Figure 4. Correlation analysis between the average precipitation in the Beijiang River Basin (BJB) during the 2022 Dragon Boat Festival period and atmospheric circulation patterns. (**a**) Correlation coefficients between BJB precipitation and the 850 hPa wind field (vectors) and 200 hPa divergence field (shading). (**b**) Correlation coefficients between BJB precipitation and the meridional-vertical (v-ω) wind field along 113° E (vectors) and vertical velocity (ω) field (shading). Only results passing the 95% confidence level are displayed.

To clarify the backgrounds that contributed to the aforementioned circulation patterns, Figure 5 further elucidates the favorable environmental conditions prevalent during the post-June 12 period of the DBP, focusing on aspects such as dynamic fields (Figure 5a,b), water vapor distribution (Figure 5c), and geographical context (Figure 5d). As previously noted, the extreme event associated with the 2022 DBP predominantly unfolded after 12 June. Following this date, persistent heavy rainfall led to flood-inducing downpours in the BJB.

Dynamic fields like the South Asia High (SAH) and Western Pacific Subtropical High (WPSH) played pivotal roles in shaping these background field. The SAH, a high-pressure system in the upper troposphere, is typically centered over the Tibetan Plateau during summer. Meanwhile, the WPSH, a semi-permanent high-pressure system in the lower troposphere, influences moisture transport and precipitation patterns. The SAH was located over the Tibetan Plateau, with its core positioned over the northern Indian subcontinent or nearby regions, placing the BJB under the northwesterly flow along the northeastern edge of the SAH, precisely within the outflow divergence zone of this high-pressure system (Figure 5a). This location facilitates the upper-level divergence, thereby enhancing the atmospheric pumping action and favoring upward motion (Figure 5d). Meanwhile, the WPSH was located over the eastern SCS, and combined with shortwave trough fluctuations over the Tibetan Plateau region, further intensified the convergence of air masses with contrasting temperature and humidity from the north and south over Guangdong (Figure 6e).

It is worth noting that the specific position of the WPSH is crucial for determining the precipitation zones, as rainfall typically occurs on the northern side of the WPSH. When the WPSH's main body extends northward, encompassing the entirety of South China, it results in prolonged periods of sunny, scorching, and arid weather. However, the WPSH maintained a generally southern position, situated over the eastern South China Sea and the western Pacific. This alignment allows WPSH's southeastern easterly flow to merge smoothly with the southwesterly monsoon from the SCS. As depicted in Figure 5c, a high

humidity zone is observed on the northern side of the WPSH, coupled with regions of high wind speeds associated with low-level jets. This combination results in the BJB being a zone of high water vapor flux, creating favorable moisture conditions conducive to precipitation.

Many studies have shown that low-level jets play a critical role in heavy rainfall during the pre-summer rainy season in South China [22,23]. During this event, the low-level jet also played a crucial role. Even the average low-level wind speed for the event reached the jet stream threshold of 12 m/s. On the mornings of June 18 and 19, maximum wind speeds of over 20 m/s and 16 m/s were recorded in Guangxi and Guangdong, respectively. The core of the jet extended from the northern SCS to inland Guangdong, with the precipitation area located in the jet's exit region, consistent with the classical relationship between jets and heavy precipitation.

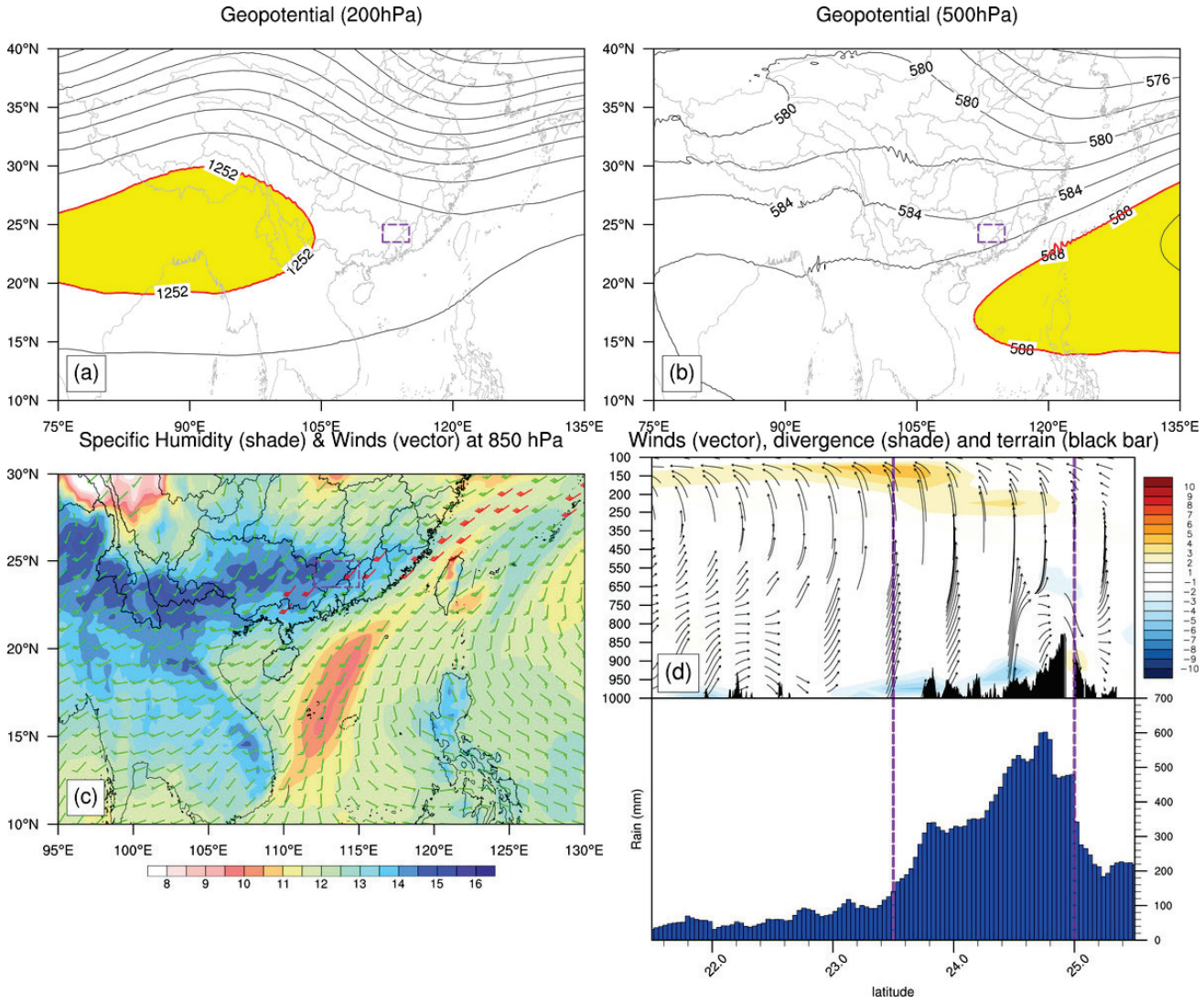

Figure 5. Atmospheric circulation and moisture conditions during the extreme precipitation event in the Beijiang River Basin (BJB) from 12 to 21 June 2022. (**a**) Average 200 hPa geopotential height. (**b**) Average 500 hPa geopotential height. (**c**) Average 850 hPa specific humidity (shading, units: g/kg) and wind field (vectors, units: m/s; Wind speeds exceeding 12 m/s are highlighted in red). (**d**) Meridional-vertical cross-section along 113° E, showing the v-ω wind field (vector: v in m/s, ω in 10^{-2} Pa/s) and horizontal divergence (shading, units: 10^{-6} s^{-1}), with cumulative rainfall distribution (units: mm) overlaid. The purple line represents the BJB, and the black bars indicate topography.

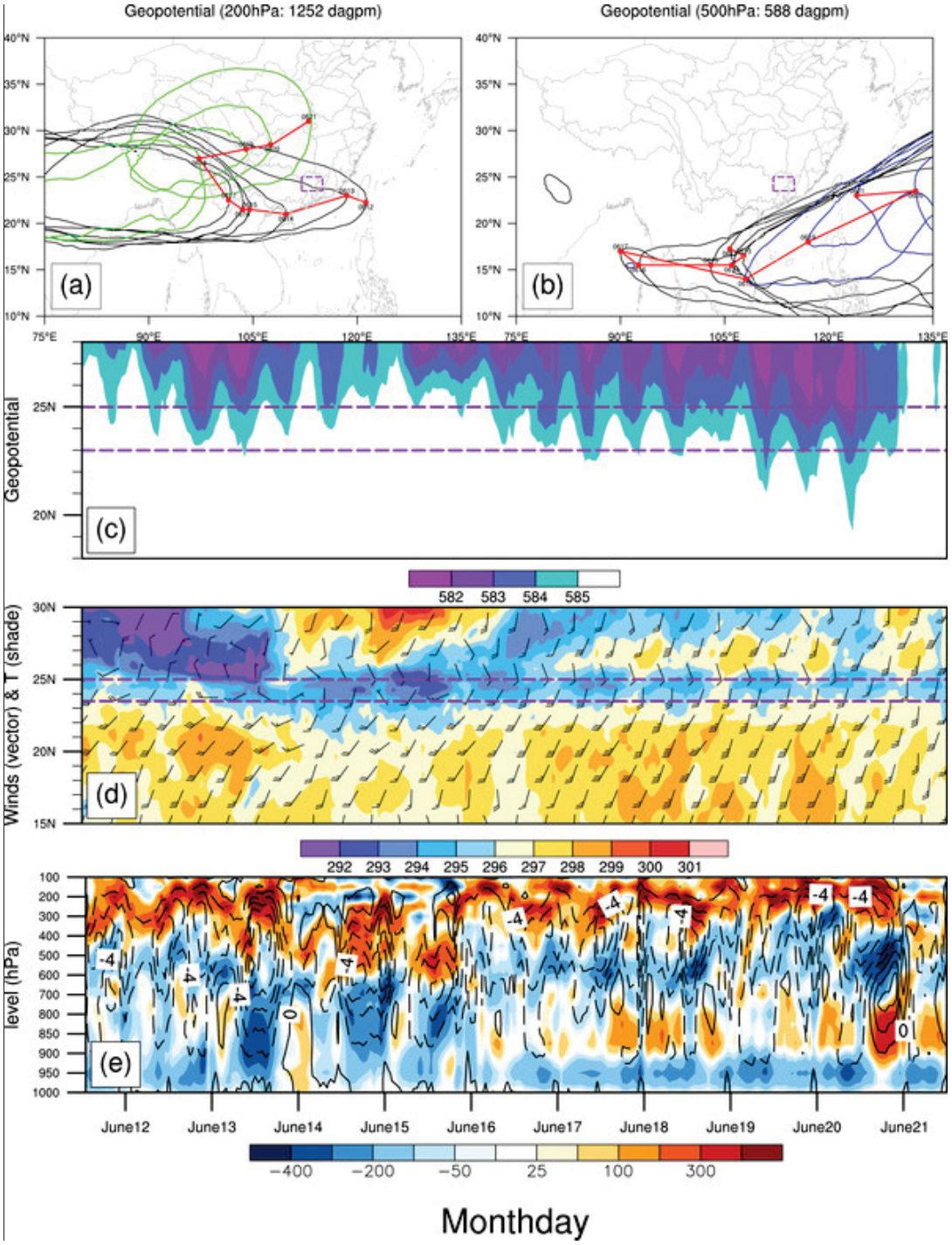

Figure 6. Temporal evolution of atmospheric circulation and thermodynamic conditions during the extreme precipitation event in the Beijiang River Basin (BJB) from 12 June to 21st, 2022. (**a**) Characteristics of the 200 hPa geopotential height 1252-dagpm line, with red dots indicating the eastern ridge point of the South Asian High (SAH). (**b**) Characteristics of the 500 hPa geopotential height 588-dagpm line, with red dots indicating the western ridge point of the Western Pacific Subtropical High (WPSH). Numbers within the line segments represent dates, and red lines connect the ridge points, black contours represent pre-17 June conditions; colored contours denote post-18 June evolution. (**c**) Latitude–time distribution of the 500 hPa geopotential height field along 113° E. (**d**) Latitude–time distribution of the 925 hPa horizontal wind (vectors, units: m/s) and temperature (shading, units: K) along 113°E, with the purple line indicating the latitudinal range of the BJB. (**e**) Level–time distribution of the divergence field (shading, units: 10^{-7} s^{-1}) and vertical velocity (contours, units: 10^{-1} Pa/s) averaged over the BJB region.

The terrain of the Nanling Mountains plays a crucial role in enhancing moisture convergence, which subsequently increases the precipitation intensity. As moist air moves inland, it encounters the windward slopes of the Nanling Mountains (Figure 5d). The interaction of this moist, low-level airflow with the mountain slopes creates an orographic effect, causing the horizontal convergence of the airflow as it slows and accumulates at the base of the mountains. This process forces the moist air to ascend, intensifying vertical motion. Additionally, the combination of low-level convergence and upper-level divergence over the mountainous region further supports uplift (Figure 5d), leading to strong convection and increased rainfall intensity on the windward slopes. This topographic influence is thus a key factor in amplifying precipitation during heavy rainfall events in the region.

Seasonal mean patterns provide a broader perspective on the occurrence of precipitation in the BJB region. However, to gain a deeper understanding of how synoptic disturbances impact precipitation in this area, we now delve into the daily evolution of key synoptic systems. These changes in atmospheric pressure systems can significantly influence the pathways and strength of monsoonal airflow, thereby affecting the spatiotemporal distribution of precipitation. Monitoring and studying the SAH and the WPSH is of great importance for predicting precipitation in South China. To achieve the real-time monitoring of the activity characteristics of these key synoptic systems, the scientific community calculates indices that reflect information on system intensity and position, tracking changes in these indices over time [32]. In operational weather forecasting, meteorologists typically observe the characteristic contours in the 200 hPa and 500 hPa geopotential height fields. Specifically, the 1252-dagpm line represents the SAH, while the 588-dagpm line represents the WPSH. This approach has proven to be both simple and effective, gaining popularity among forecasters [33].

Figure 6a,b illustrates the daily evolution of these two characteristic lines. From 12 June to 17 June, the core of the SAH moved westward. However, after 18 June, the SAH's center began to shift northward from the northern part of the Indian subcontinent, gradually entering the Tibetan Plateau region. Overall, from 12 June to 21 June, the SAH's core underwent a transition from the northern part of the Indian subcontinent to over the plateau. During this stage, the configuration of atmospheric systems kept the upper atmosphere over the BJB in a state of persistent divergence (Figure 6e, shading area), leading to continuous heavy precipitation. Previous studies have indicated that, when the SAH's core is positioned over the Tibetan Plateau, it usually signifies the end of the pre-flood season in South China [34]. This finding is consistent with the gradual cessation of precipitation in the BJB after 21 June.

The activity of the WPSH from 12 June to 21 June can be distinctly divided into two stages ([20], also shown in Figure 6b). During the first phase, spanning from 12 June to 15 June, the WPSH underwent a notable westward extension. This extension facilitated the convergence of cold air from the north with warm, moist air from the south over South China (Figure 6d), thereby creating meteorological conditions favorable for frontal shear rainstorms. In the second stage, from 17 June to 21, the WPSH began to retreat eastward. Despite this retreat, the plateau shortwaves intensified and shifted southward (Figure 6c), leading to an increase in low-level wind speeds due to the enhanced pressure gradient between the trough and the WPSH (Figure 6d). This enhancement further facilitated the transport of moisture by the SCS monsoon, directing the convergence of low-level moisture over the BJB region (shaded area in Figure 6e). The combination of low-level convergence with upper-level divergence created a suction effect, resulting in strong upward motion in the middle troposphere (contours in Figure 6e). These conditions collectively contributed to a favorable synoptic pattern conducive to precipitation in the BJB area.

It is noteworthy that, whether in the earlier westward extension stage or the later eastward retreat stage, the overall position of the WPSH ridge remained south of 20° N. This positioning provided a continuous favorable environment for precipitation over the BJB region. After 21 June, as the WPSH covered the entire South China region, precipitation in the BJB tended to cease, marking the end of the precipitation events in this area and also signaling the cessation of the DBP period.

In brief, the occurrence of flood-triggering heavy rainfall in the BJB in 2022 was facilitated by favorable synoptic-scale, with the position of SAH and WPSH, and the intensity of the SCS monsoon being a crucial systems leading to sustained precipitation. Notably, the relatively southern position of the WPSH and the consistently strong intensity of the monsoon were the primary reasons for the sustained heavy precipitation in the BJB. However, historical extreme precipitation should not be solely viewed from the perspective of synoptic scales. For example, the 2008 Dragon Boat Festival extreme rainfall also occurred under favorable synoptic conditions, yet the spatial distribution of heavy rainfall differed significantly from that in 2022 [21]. A comparison of the 2022 and 2008 events reveals distinct differences in the intensity and position of the WPSH: in 2022, the WPSH was positioned anomalously south and west compared to climatology, while in 2008, it was positioned north and east. This raises critical questions: What factors maintained the relatively southern position of the WPSH in 2022? Did signals on longer time scales also play significant roles? These questions may require explanations from abnormal signals on longer time scales, as large-scale signals typically constrain their smaller-scale systems. Additionally, the 2008 event occurred under La Niña conditions, which are known to enhance the intensity of the SCS monsoon [21]. Similarly, the 2022 extreme rainfall may have been influenced by interannual-scale signals, which also modulate subseasonal-scale phenomena. Therefore, the subsequent sections of this paper will focus on the pivotal role of factors beyond synoptic scales in the extreme precipitation events in the BJB in 2022.

4.2. Influence of Subseasonal-Scale Signal Stagnation

While synoptic-scale systems directly influence short-term precipitation patterns, subseasonal oscillations modulate the persistence and intensity of rainfall over longer periods (>10 days). In the subseasonal time scale, a significant source of predictability comes from intraseasonal oscillations (ISOs), particularly the eastward propagation of the MJO on planetary scales [6,7]. Studies have shown that tropical ISOs exhibit significant variations across different seasons [35–37], with MJO typically more active during winter in the Northern Hemisphere and the BSISO exhibiting more complexity, including pronounced northward propagation features besides eastward propagation across the Indian and western Pacific monsoon regions [31,38]. The BSISO signal is considered one of the key factors influencing rainfall and flooding in the Asian monsoon region [39–44]. Although the precipitation in the BJB during the 2022 DBP period exhibits clear low-frequency characteristics in multi-day sliding averages, it remains unclear whether such features correspond to low-frequency signals in tropical regions. Figure 7 illustrates the correlation distribution of subseasonal-scale precipitation in the BJB with the 925hPa wind field and OLR. The regions extending from South Asia through the southern SCS to the western equatorial Pacific exhibit convective suppression, while the southern China region (including the BJB) exhibits a convective active area. An anomalous anticyclone exists between these two convective activity areas. Although this circulation anomaly is similar to the synoptic-scale-related results (Figure 4), the subsidence in the synoptic scale background mainly occurs in the southern SCS, whereas the subseasonal-scale convective suppression is primarily concentrated on the southern side of the SCS anomalous anticyclone near the equator. These results indicate that with the extension of time scales, the corresponding circulation

anomalies also expand in spatial scale, consistent with the principle of spatiotemporal equivalence, thereby emphasizing the significant role of tropical intraseasonal oscillations in extreme heavy rainfall processes during the DBP period.

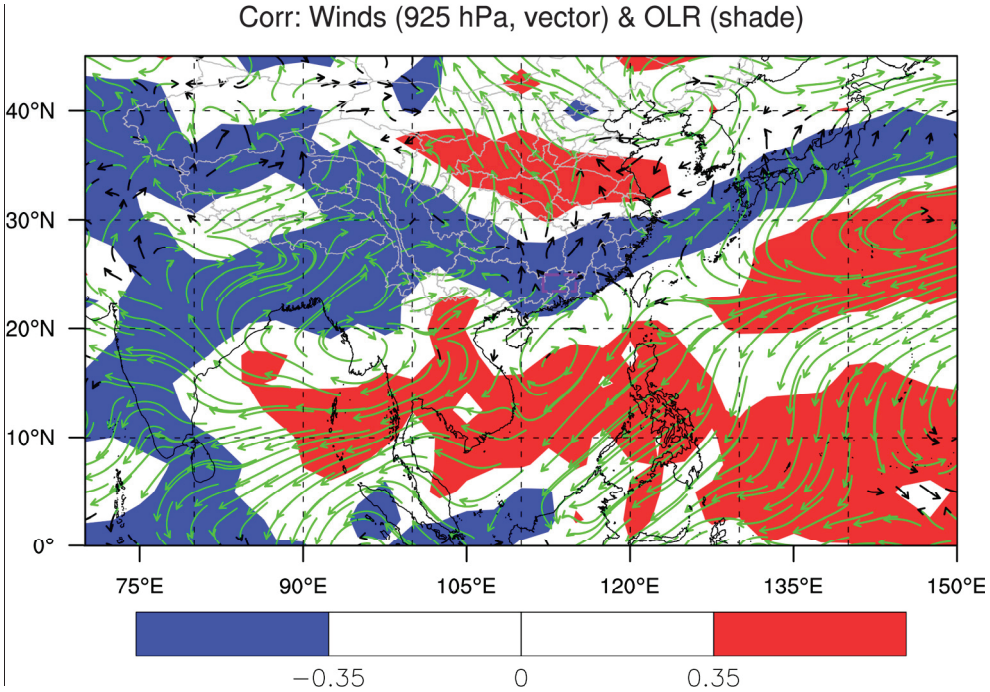

Figure 7. Correlation analysis between subseasonal precipitation anomalies in the Beijiang River Basin (BJB) during the 2022 Dragon Boat Festival period and anomalies of the 925 hPa wind field and outgoing longwave radiation (OLR). The subseasonal anomalies represent 10–90-day filtered signals. Colored regions indicate areas where the correlation coefficients are significant at the 95% confidence level.

In June to July 2020, record-breaking floods struck the Meiyu Belt in China, Japan, and Korea, which were attributed to the unusually persistent (lasting 59 days) and quasi-stationary MJO activity over the Indian Ocean during the same period [12]. To investigate whether intraseasonal-scale signals also played a crucial role during the extreme DBP period in 2022, this study employed the BSISO index [31] to monitor its activity, as it is more representative in influencing precipitation in the summer monsoon regions of Asia. Figure 8 illustrates the monitoring of the BSISO index during the 2022 DBP period. Unlike the classic intraseasonal oscillations, both BSISO1 (representing 30–60-day oscillations) and BSISO2 (representing 10–30-day oscillations) exhibited anomalous propagation stagnation during the 2022 DBP period (spanning 32 days). Specifically, the BSISO1 index monitoring showed that quasi-30–60-day oscillations were in the phase 1 for 17 days, which significantly exceeded the climatological state (~5 days per phase). The BSISO2 index monitoring revealed that quasi-10–30-day oscillations were in the phase 5 for 23 days, also well above the historical climatological average (~5 days per phase).

The aforementioned phase anomalies indicate that the propagation of low-frequency oscillation signals ceased during the 2022 DBP period, a phenomenon that is also extreme historically (see Figure 9). Compared to historical counterparts, the duration of Phase 1 for BSISO1 and Phase 5 for BSISO2 during the 2022 DBP period reached historical extremes, indicating that the anomalous behavior of subseasonal-scale signals during this period was exceptionally rare in history. Furthermore, the linear trend (green line) and polynomial fit trend (purple line) analyses reveal a notable upward trend in the frequency of these specific phase changes in ISO. The phase anomaly changes in BSISO1 align with the findings of

Sasikumar et al. [45], which also indicate an accelerated regeneration speed of the MJO in the western Indian Ocean, increased residence time in the western hemisphere and western Indian Ocean, but reduced time in the eastern Indian Ocean and eastern Pacific. This anomaly is attributed to the local feedback of the MJO on the Indian Ocean and the emergence of a La Niña-like mode in Pacific SST.

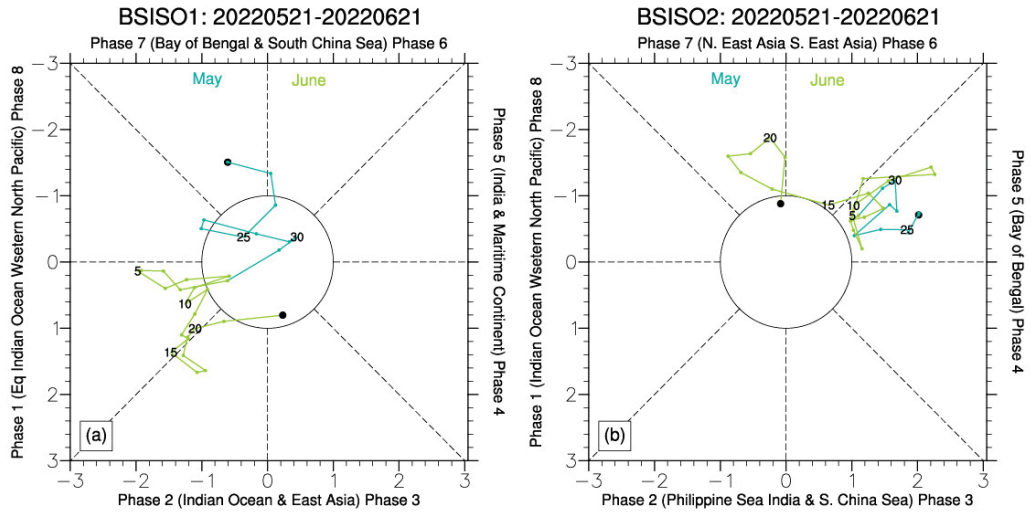

Figure 8. Daily evolution of the Boreal Summer Intraseasonal Oscillation (BSISO) indices during the 2022 Dragon Boat Festival period (21 May–21 June). (**a**) BSISO1 index (30–60-day timescale) and (**b**) BSISO2 index (10–30-day timescale).

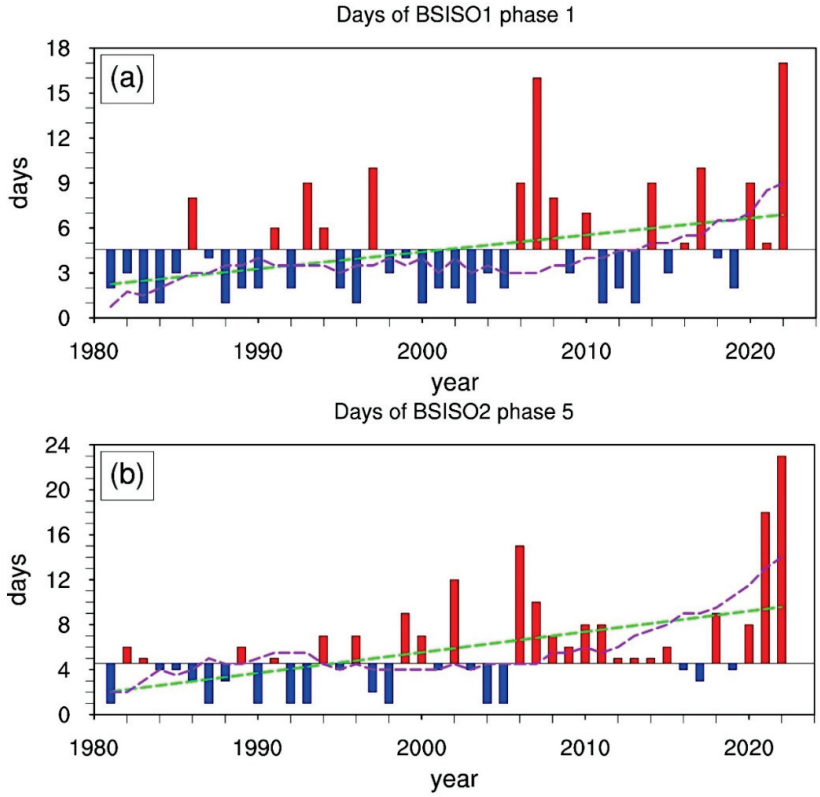

Figure 9. Annual statistics of the duration of (**a**) Phase 1 for BSISO1 and (**b**) Phase 5 for BSISO2 during the Dragon Boat Festival period (21 May–21 June). Blue (red) bars indicate years with durations below (above) the historical climatology (1991–2020). The green line represents a linear regression trend, while the purple line depicts a third-degree polynomial fit using the least squares method.

To investigate the potential mechanisms underlying the unusual ISO events and their modulation of extreme precipitation in the BJB, we composited anomaly maps of OLR and low-level wind fields within the ISO frequency range in Figure 10. Convection anomalies associated with Phase 1 of BSISO1 appear over the equatorial Indian Ocean, accompanied by anomalous anticyclonic circulation and suppressed convection prevailing over the Western North Pacific (WNP). This enhances the intensity of the SCS summer monsoon, facilitating the transport of abundant warm and moist airflow from the tropical Indian Ocean–Pacific region to East Asia. In the South China region, the convergence of anomalous southwesterly flows leads to exceptionally active convective activity. It is noteworthy that the composited results in Figure 10a closely resemble those in Figure 7, once again highlighting the crucial modulating role of this phase anomaly of BSISO1 on precipitation in the BJB at the subseasonal time scale. Circulation anomalies associated with Phase 5 of BSISO2 manifest as anomalous anticyclonic circulation from the east of the Philippines to the western Pacific region. While this circulation anomaly may not linearly modulate precipitation in the BJB (as shown in Figure 7), the enhanced SCS summer monsoon and convective activity in the SCS region, coupled with the upslope terrain of the Nanling Mountains, still contributes to an amplifying effect on precipitation in the BJB.

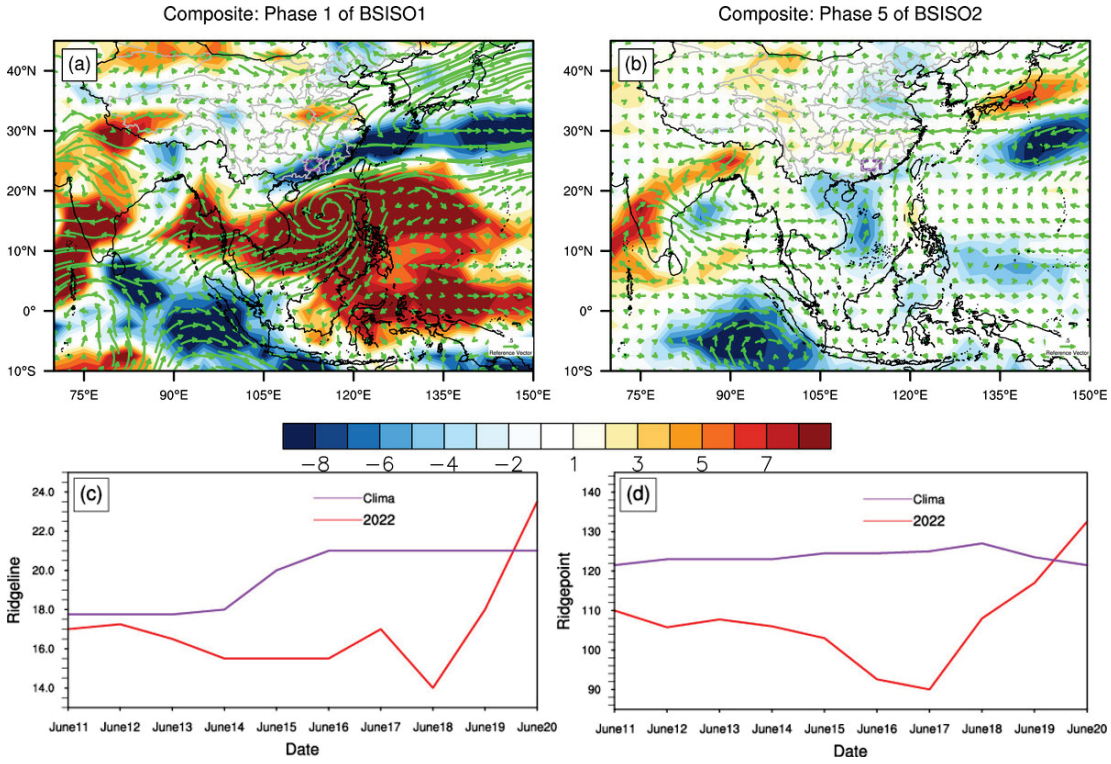

Figure 10. (**a**,**b**) The composited outgoing longwave radiation (OLR) anomalies (shading: W/m^2) and 925 hPa wind anomalies (green vectors: m/s) associated with (**a**) Phase 1 of BSISO1 and (**b**) Phase 5 of BSISO2 during the 2022 Dragon Boat Festival period. (**c**,**d**) Evolution of the indices of the Western Pacific Subtropical High (WPSH; purple line: climatological mean, red line: 2022) for (**c**) the ridgeline index and (**d**) the ridgepoint index.

The stagnation in the propagation of the BSISO may also indirectly impact precipitation by modulating the activities of the WPSH. Huang et al. [46] observed that the cumulative influence of convection within the tropical WNP ISO plays a crucial role in regulating the meridional displacement of the WPSH. Specifically, their findings revealed that active WNP ISO activities can stimulate a poleward-propagating Rossby wave train, promoting a northward shift of the WPSH. To illustrate the positional changes of the WPSH during the DBP period in 2022, we adopted the western boundary point (hereinafter referred to

as ridgepoint) and ridge line index (hereinafter referred to as ridgeline) defined by Liu et al. [47]. During the DBP period in 2022, the WPSH ridgeline was abnormally positioned farther south, and its ridgepoint unusually farther west (relative to the climatic state, as illustrated in Figure 10c,d), thereby creating conducive conditions for precipitation in the South China. Notably, the anomalous positioning of the WPSH in 2022 could be attributed to the suppression resulting from the cumulative influence of tropical WNP ISO convection, which coincided with the opposite phase of the ISO described in Huang et al. [46]. In that study, BSISO1 persisted for an extended period during phases 6–8, corresponding to an active convective state in the WNP. Conversely, during the 2022 DBP period, BSISO1's phase 1 persisted for a longer duration, corresponding to a convective suppression state in the WNP. The rapid northward shift and eastward retreat of the WPSH after the prolonged stagnation of the ISO ended (e.g., the transition of BSISO1 from phase 1 to phases 2–3 and BSISO2 from phase 5 to phases 6–7, after the 17th) may suggest a coupling between these two cross-timescale signals. Of course, this hypothesis warrants further exploration to confirm the existence of this regulatory mechanism and to investigate the potential impacts of BSISO2's prolonged maintenance in phase 5.

In brief, during the 2022 DBP period, the active days of BSISO1 in phase 1 (17 days) and BSISO2 in phase 5 (23 days) were more than three times and four times the climatological average (5 days), respectively. This prolonged subseasonal oscillation favored the intensified SCS summer monsoon, potentially causing the WPSH to be abnormally positioned farther south and west, compared to climatology, providing continuous tropical moisture supply for prolonged rainfall in the BJB.

Notably, the abnormal propagation of BSISO observed during the 2022 DBP period was not seen in 2008, representing a key difference between the two events. This suggests that subseasonal-scale signals may play a critical role in modulating synoptic-scale systems, such as the WPSH and SCS monsoon, thereby influencing the spatial and temporal characteristics of extreme precipitation. The stagnation of BSISO propagation during this period may have been further modulated by interannual-scale anomalies. Specifically, the cooler-than-average SSTs in the central-eastern Pacific during the triple-peak La Niña event likely enhanced western Pacific convection and strengthened the Walker circulation, creating favorable conditions for BSISO phase stagnation. This interannual modulation of subseasonal variability underscores the complex interactions across temporal scales, which played a critical role in the 2022 extreme precipitation event. Therefore, the subsequent sections of this paper will focus on the pivotal role of interannual-scale anomalies in modulating BSISO propagation and their indirect effects on extreme precipitation in the BJB.

4.3. Indirect Effects of Rare Tri-Peak La Niña Phenomenon

On an even larger scale, interannual phenomena such as La Niña set the background conditions for BSISO activity. Is there a connection between the extreme heavy rainfall event in the BJB in 2022 and tropical anomalous interannual signals? According to the latest data released by the NOAA in April 2023, SST in the central and eastern equatorial Pacific have remained below average since the winter of 2020 (see Figure 11). The current La Niña event began in September 2020, strengthened again in September after weakening in May 2021, and persisted until January 2023 when the La Niña event ended. The occurrence of consecutive La Niña events over three consecutive winters is extremely rare, marking the first occurrence of a "triple peak" La Niña phenomenon in this century.

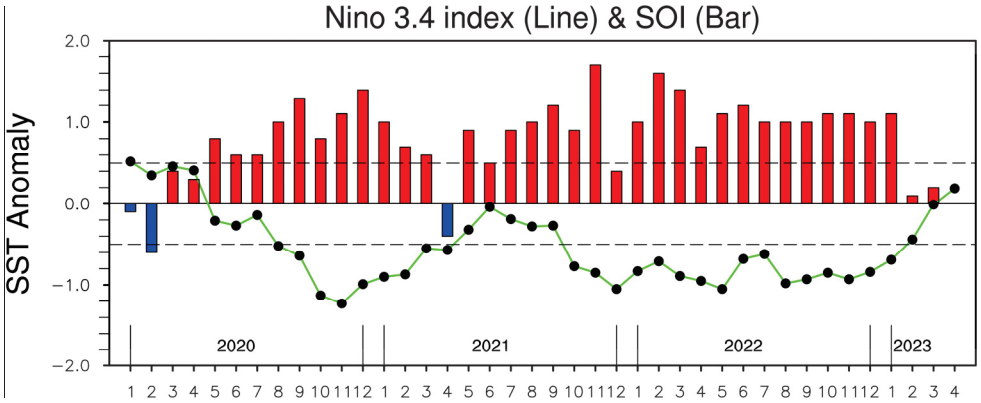

Figure 11. Monthly evolution of the Niño 3.4 index and the Southern Oscillation Index (SOI) from January 2020 to April 2023. The Niño 3.4 index (line, units: °C) represents sea surface temperature (SST) anomalies in the central equatorial Pacific, while the Southern Oscillation Index (SOI, bars) reflects the atmospheric pressure difference between Tahiti and Darwin.

Interestingly, we did not find a significant concurrent correlation between La Niña-like SST anomalies and the interannual-scale anomalies in precipitation over the BJB (Figure omitted). Instead, significant SST signals were found in the Northeast Pacific and maritime continental regions, consistent with the findings of Liu et al. [21], who attributed the extreme precipitation event in 2022 to historical warm anomalies in the Northeast Pacific and maritime continental regions. While such results indicate no direct link between the extreme DBP in 2022 and the rare tri-peaked La Niña phenomenon, this does not rule out the possibility of indirect effects of the interannual-scale anomaly signals. Firstly, the warm SST anomalies in the Northeast Pacific and maritime continental regions are closely related to the ENSO phenomenon. Secondly, anomalous ENSO signals can indirectly affect the timing and intensity of the onset of the SCS summer monsoon, thereby influencing the heavy rainfall in southern China [19]. Generally, in the year following a La Niña event, the onset of the summer monsoon tends to be early. According to statistics, the onset of the SCS summer monsoon in 2022 (12 May) was earlier than the average onset time (the fourth pentad of May). After the monsoon onset, the warm and humid conditions in southern China significantly improved, leading to an increase in heavy rainfall events. Additionally, under the forcing of La Niña background SST, the enhancement of anticyclonic circulation in the Northwest Pacific region favors interannual-scale southerly wind anomalies in the SCS region (Figure 12), increasing the intensity of the SCS summer monsoon, thereby contributing to the extreme precipitation during the 2022 DBP period.

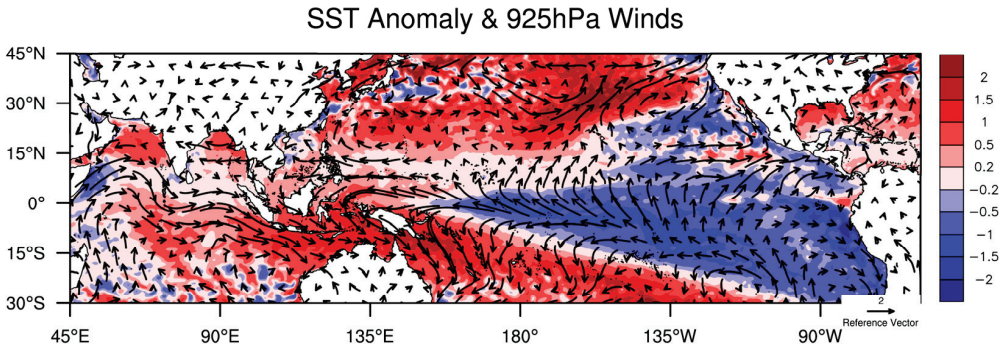

Figure 12. Anomalies in sea surface temperature (SST) and 925 hPa wind field during the 2022 Dragon Boat Festival period (21 May–21 June). Shading represents SST anomalies (units: °C), while vectors indicate 925 hPa wind anomalies (units: m/s).

From a perspective of multiscale interactions, abnormal ENSO signals may indirectly influence the extreme DBP in 2022 by modulating the anomalies in subseasonal-scale signals. For instance, Pohl and Matthews [48] found that the lifespan of the MJO is significantly shortened (extended) under warm (cold) conditions in the eastern Pacific. Wei and Ren [49] systematically investigated the influence of different ENSO types on the propagation speed of the MJO. Their results showed that, during El Niño, the MJO propagates rapidly and symmetrically from the Indian Ocean to the equatorial western Pacific, whereas during La Niña, the MJO moves slowly eastward and often takes a detour around the southern maritime continent. Wang et al. [50] classified MJO events into four categories using a clustering analysis method, including "non-propagating", "jumping", "slow-propagating", and "fast propagating" MJO events. Through the composite analysis of the SST anomalies in the background fields of each type of MJO event, they found that "non-propagating" MJO events correspond to significant La Niña-like SST anomalies, providing further evidence that La Niña background SST conditions are unfavorable for the eastward propagation of the MJO.

During the 2022 DBP period, the number of days with BSISO1 in the phase 1 and BSISO2 in the phase 5 reached historical extremes (Figure 9), which may also be related to the rare three-peak La Niña phenomenon. To reveal this possibility, Figure 13 calculates the correlation coefficients between the summer (May to August) occurrences of BSISO1 in the phase 1 and BSISO2 in the phase 5 and the interannual SST. The figure shows that La Niña-like SST positively contributes to the summer occurrences of BSISO1 in phase 1 and BSISO2 in phase 5. In other words, the rare three-peak La Niña phenomenon impedes the propagation of intraseasonal oscillations, indirectly leading to sustained heavy rainfall during the DBP period in 2022.

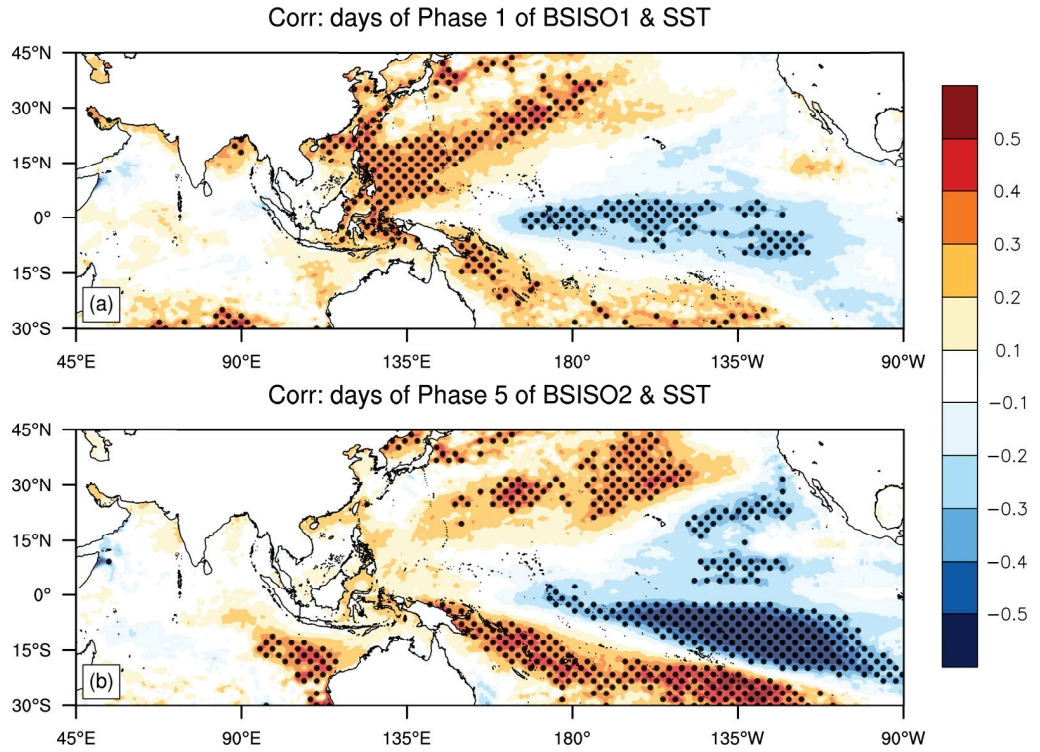

Figure 13. Annual correlation coefficients between the number of days with (**a**) BSISO1 in Phase 1 and (**b**) BSISO2 in Phase 5 during May to August (1981–2022) and concurrent sea surface temperature (SST). Points in the figure indicate correlations that are significant at the 95% confidence level.

5. Conclusions and Discussion

This study aims to investigate the causes of extreme precipitation events in the PRB during the DBP period of 2022. We conducted a comprehensive analysis spanning multiple time scales, from synoptic-scale systems to subseasonal oscillations, and even the rare triple-peaked La Niña phenomenon of this century. We constructed a conceptual framework summarizing the contributions of multiscale interactions to the extreme precipitation process, revealing the complex relationships among these factors and their impacts on extreme precipitation events in the study area (Figure 14).

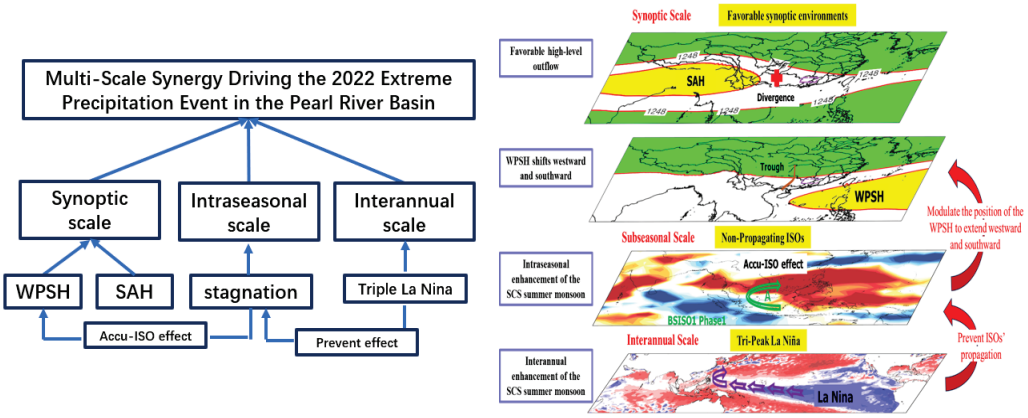

Figure 14. Conceptual framework illustrating multiscale interactions contributing to extreme precipitation events in the Pearl River Basin (PRB) during the 2022 Dragon Boat Festival period. This figure summarizes the synergistic effects of interannual (e.g., triple-peak La Niña), subseasonal (e.g., BSISO phase stagnation), and synoptic-scale (e.g., SAH, WPSH, SCS monsoon) systems on the extreme rainfall event.

The extreme precipitation during the 2022 Dragon Boat Festival Period in the Pearl River Basin represents a paradigm case of multiscale synergy—an aspect underexplored in prior studies focusing on single-scale drivers [20,21]. At the synoptic scale, systems such as SAH, the WPSH, and the SCS monsoon are the direct influencing factors leading to precipitation. The SAH transitioned from the Indian subcontinent towards the Tibetan Plateau, providing favorable conditions for upper-level outflow in the BJB. The dominance of the WPSH in the eastern SCS region facilitated the opening of a low-level moisture transport corridor. Meanwhile, the strong summer monsoon in the SCS transported moisture to the northern regions of South China. This, coupled with the unique terrain of the Nanling Mountains, led to the intense convergence and uplift of moist air on the windward slopes. At the subseasonal scale, our analysis revealed a connection between this sustained heavy rainfall and anomalous behavior in subseasonal oscillations, specifically, the duration of BSISO1 in phase 1 and BSISO2 in phase 5 far exceeded climatological averages. This extended duration in the specific phases of ISO, by exciting Rossby–Kelvin wave trains [51], enhanced the intensity of the SCS summer monsoon and moisture transport at subseasonal scales. Additionally, the Accu-ISO signals can indirectly affect the precipitation by modulating the activity of synoptic-scale systems [46]. At the interannual scale, the emergence of the triple-peak La Niña phenomenon was found to advance the timing and intensify the eruption of the SCS summer monsoon, thereby augmenting the extremity of rainfall at the interannual scale in 2022. Additionally, a La Niña-type SST distribution was identified as impeding the propagation of ISOs, leading to specific phase anomalies and consequently regulating the persistence of heavy rainfall.

Our study advances the field through two novel contributions:

(1) First identification of the combined impacts from a rare triple-peaked La Niña, stalled BSISO phases, and synoptic–system interactions on South China rainfall extremes;

(2) A new conceptual framework (Figure 14) quantifying cross-scale feedbacks between interannual (ENSO), subseasonal (ISO), and synoptic systems.

These findings redefine operational extreme weather forecasting by emphasizing cross-scale precursors, which have significant implications for both research and practical applications in water resource management:

(1) Early warning potential: The co-occurrence of third-year La Niña and BSISO phase 1/5 persistence (detectable 4–6 weeks pre-event) could serve as a novel predictor for South China rainstorms;
(2) Methodological innovation potential: The paradigm shift calls for revisiting attribution methodologies in climate science and developing scale-integrated prediction systems.

While rooted in a regional case study, this work illuminates the universal principles of multiscale climate interactions. The framework developed here—highlighting the synergistic coupling of synoptic (e.g., SAH-WPSH dipole), subseasonal (BSISO stagnation), and interannual (triple-peak La Niña) systems—provides a transferable toolkit for analyzing flood extremes in other global basins (e.g., the Amazon, Ganges–Brahmaputra, and Mekong River basins). Although the impacts of specific weather or climate systems may vary across regions due to geographic differences, the role of multiscale interactions in driving extreme precipitation is universally applicable. This framework not only advances our understanding of compound meteorological hazards but also offers practical insights for improving flood risk assessments and early warning systems under evolving climate conditions.

However, the complex interaction mechanisms between these multiscale factors remain an area of ongoing exploration. Two critical frontiers warrant further investigation: How do synoptic-scale systems (e.g., SAH, WPSH) respond to versus drive subseasonal anomalies such as BSISO stagnation? Resolving this causality requires advanced diagnostic tools (e.g., vorticity budget analysis) to quantify the bidirectional feedback between scales.

While existing studies confirm climate models' ability to simulate ENSO's modulation of monsoon systems [18] and the combined impacts of central Pacific SST anomalies with BSISO signals on regional extremes [24,52], a pivotal challenge lies in assessing whether current-generation models (e.g., CESM2, EC-Earth3) can replicate cross-temporal scale synergies. Systematic sensitivity experiments—such as spectral nudging to isolate BSISO-scale perturbations or prescribed SST experiments to evaluate La Niña–ISO teleconnections—could rigorously test model fidelity in capturing these interactions while guiding physics parameterization improvements. Addressing these questions will refine our understanding of multiscale climate dynamics and improve the spatial adaptability of early warning systems.

Author Contributions: Conceptualization, P.R.; Methodology, N.W.; Formal analysis, J.Z.; Resources, W.D.; Data curation, W.D.; Writing—original draft, J.Z.; Writing—review & editing, P.R.; Supervision, N.W. and D.Z.; Funding acquisition, D.Z. All authors have read and agreed to the published version of the manuscript.

Funding: This work was supported by the Guangdong Provincial Meteorological Bureau's Leader Disclosing and Taking Charge Project (GRMCGS202101); the Guangdong Meteorological Joint Fund (2024A1515510013); the CMA Leader Disclosing and Taking Charge Project (CMAJBGS202217); Special Fundings for Youth Innovation Teams from CMA (CMA2023QN05, CMA2024QN01); the Science and Technology Research Project of Guangdong Meteorological Bureau (GRMC2023Q18); and the National Natural Science Foundation of China (42075087).

Data Availability Statement: Data is contained within the article.

Conflicts of Interest: The authors declare no conflicts of interest.

References

1. Lin, L.X.; Wu, N.G.; Huang, Z.; Cai, A.A. Causality analysis of the infrequent Dragon-Boat Precipitation in Guangdong Province in 2008. *Meteor. Mon.* **2009**, *35*, 43–50. (In Chinese)
2. Yao, W.G. Successful flood defense in the Pearl River Basin in 2022 with multiple measures. *China Water Resour.* **2022**, 1–4.
3. Tang, T.Y.; Wu, C.S.; Wang, A.Y.; Hao, I.P.; Luo, H.B. An observational study of intraseasonal variations over Guangdong province China during the rainy season of 1999. *J. Trop. Meteor.* **2007**, *23*, 683–689. (In Chinese)
4. Ji, Z.P.; Hu, L.T.; Gu, D.J.; Wu, N.G.; Liang, J. The quasi-biweekly oscillation of flood-causing tropical rain in Xijiang River region and its atmospheric circulation models. *J. Trop. Meteor.* **2011**, *27*, 775–784. (In Chinese)
5. Cao, X.; Ren, X.J.; Yang, X.Q.; Fang, J.B. The quasi-biweekly oscillation characteristics of persistent severe rain and its general circulation anomaly over southeast China from May to August. *Acta Meteor. Sin.* **2012**, *70*, 766–778. (In Chinese)
6. Hong, W.; Ren, X.J. Persistent heavy rainfall over South China during May–August: Subseasonal anomalies of circulation and sea surface temperature. *J. Meteor. Res. Appl.* **2014**, *27*, 769–787. [CrossRef]
7. Zhang, L.; Wang, B.; Zeng, Q. Impact of the Madden–Julian Oscillation on Summer Rainfall in Southeast China. *J. Clim.* **2009**, *22*, 201–216.
8. Ren, H.L.; Ren, P. Impact of Madden–Julian Oscillation upon Winter Extreme Rainfall in Southern China: Observations and Predictability in CFSv2. *Atmosphere* **2017**, *8*, 192. [CrossRef]
9. Madden, R.A.; Julian, P.R. Detection of a 40–50 Day Oscillation in the Zonal Wind in the Tropical Pacific. *J. Atmos. Sci.* **1971**, *28*, 702–708. [CrossRef]
10. Madden, R.A.; Julian, P.R. Description of Global-Scale Circulation Cells in the Tropics with a 40–50 Day Period. *J. Atmos. Sci.* **1972**, *29*, 1109–1123.
11. Wheeler, M.C.; Hendon, H.H. An all-season real-time multivariate MJO index: Development of an index for monitoring and prediction. *Mon. Weather Rev.* **2004**, *132*, 1917–1932. [CrossRef]
12. Roxy, M.K.; Dasgupta, P.; McPhaden, M.J.; Suematsu, T.; Zhang, C.; Kim, D. Twofold expansion of the Indo-Pacific warm pool warps the MJO life cycle. *Nature* **2019**, *575*, 647–651. [CrossRef]
13. Zhang, W.J.; Huang, Z.C.; Jiang, F.; Stuecker, M.F.; Chen, G.; Jin, F. Exceptionally persistent Madden-Julian Oscillation activity contributes to the extreme 2020 East Asian summer monsoon rainfall. *Geophys. Res. Lett.* **2021**, *48*, e2020GL091588.
14. Wang, Y.; Ren, H.L.; Wei, Y.; Jin, F.; Ren, P.; Gao, L.; Wu, J. MJO phase swings modulate the recurring latitudinal shifts of the 2020 extreme summer-monsoon rainfall around Yangtse. *J. Geophys. Res. Atmos.* **2022**, *6*, 127.
15. Biabanaki, M.; Eslamian, S.S.; Koupai, J.A.; Cañón, J.; Boni, G.; Gheysari, M. A principal components/singular spectrum analysis approach to ENSO and PDO influences on rainfall in western Iran. *J. Hydrol. Res.* **2014**, *45*, 250–262.
16. Huang, R.H.; Wu, Y.F. The influence of ENSO on the summer climate change in China and its mechanism. *Adv. Atmos. Sci.* **1989**, *6*, 21–32.
17. Zhang, R.H.; Sumi, A.; Kimoto, M. Impact of El Niño on the East Asian monsoon: A diagnostic study of the '86/87 and '91/92 events. *J. Meteor. Soc. Jpn.* **1996**, *74*, 49–62.
18. Tao, S.Y.; Zhang, Q.Y. Response of the Asian winter and summer monsoon to ENSO events. *Chin. J. Atmos. Sci.* **1998**, *22*, 399–407. (In Chinese)
19. Wang, B.; Wu, R.G.; Fu, X.H. Pacific-East Asian teleconnection: How does ENSO affect East Asian climate? *J. Clim.* **2000**, *13*, 1517–1536.
20. Liu, M.H.; Ren, H.L.; Zhang, W.J.; Ren, P.F. Influence of super El Nino events on the frequency of spring and summer extreme precipitation over eastern China. *Acta Meteor. Sin.* **2018**, *76*, 539–553. (In Chinese)
21. Deng, W.J.; Ren, P.F.; Zhang, D.; Sun, Y.; Wu, N.-G. An Extreme Monsoonal Heavy Rainfall Event over Inland South China in June 2022: A Synoptic Causes Analysis. *J. Trop. Meteor.* **2023**, *29*, 16–25.
22. Wang, T.; Hu, Y.M.; Pan, W.J. Climate causation analysis of the strongest Dragon-Boat precipitation in Guangdong province in 2008. *Guangdong Meteor.* **2008**, *30*, 5–7. (In Chinese)
23. Du, Y.; Chen, G. Heavy rainfall associated with double low-level jets over Southern China. Part II: Convection initiation. *Mon. Weather Rev.* **2019**, *147*, 543–565. [CrossRef]
24. Liu, X.; Luo, Y.; Huang, L.; Zhang, D.; Guan, Z. Roles of double low-level jets in the generation of coexisting inland and coastal heavy rainfall over south China during the pre-summer rainy season. *J. Geophys. Res. Atmos.* **2020**, *125*, e2020JD032890. [CrossRef]
25. Liu, B.; Zhu, C.; Xu, K.; Ma, S.; Lu, M.; Han, X.; Hua, L. Record-breaking pre-flood rainfall over South China in 2022: Role of historic warming over the Northeast Pacific and Maritime Continent. *Clim. Dyn.* **2023**, *61*, 3147–3163. [CrossRef]
26. Kummerow, C.; Barnes, W.; Kozu, T.; Shiue, J.; Simpson, J. The Tropical Rainfall Measuring Mission (TRMM) Sensor Package. *J. Atmos. Ocean.* **1998**, *15*, 809–817. [CrossRef]
27. Hou, A.Y.; Kakar, R.K.; Neeck, S.; Azarbarzin, A.A.; Kummerow, C.D.; Kojima, M.; Oki, R.; Nakamura, K.; Iguchi, T. The Global Precipitation Measurement Mission. *Bull. Am. Meteorol. Soc.* **2014**, *95*, 701–722. [CrossRef]

28. Hersbach, H.; Bell, B.; Berrisford, P.; Hirahara, S.; Horányi, A.; Muñoz-Sabater, J.; Nicolas, J.; Peubey, C.; Radu, R.; Schepers, D.; et al. The ERA5 global reanalysis. *Q. J. R. Meteorol. Soc.* **2020**, *146*, 1999–2049. [CrossRef]
29. Liebmann, B.; Smith, C.A. Description of a Complete (Interpolated) Outgoing Longwave Radiation Dataset. *Bull. Am. Meteorol. Soc.* **1996**, *77*, 1275–1277.
30. Reynolds, R.W.; Rayner, N.A.; Smith, T.M.; Stokes, D.C.; Wang, W. An Improved In Situ and Satellite SST Analysis for Climate. *J. Clim.* **2002**, *15*, 1609–1625. [CrossRef]
31. Lee, J.Y.; Wang, B.; Wheeler, M.C.; Fu, X.; Waliser, D.E.; Kang, I.-S. Real-time multivariate indices for the boreal summer intraseasonal oscillation over the Asian summer monsoon region. *Clim. Dyn.* **2013**, *40*, 493–509.
32. Liu, B.; Zhu, C.; Yuan, Y. Two interannual dominant modes of the South Asian High in May and their linkage to the tropical SST anomalies. *Clim. Dyn.* **2017**, *49*, 2705–2720.
33. Chen, Y.; Zhai, P. Mechanisms for concurrent low-latitude circulation anomalies responsible for persistent extreme precipitation in the Yangtze River Valley. *Clim. Dyn.* **2016**, *47*, 989–1006.
34. Sun, Z.; Zhou, H.; Peng, L.; Ni, D. Relationships between different types of South Asian high and atmospheric circulation in the Northern Hemisphere in July. *Trans. Atmos. Sci.* **2016**, *39*, 577–588. (In Chinese)
35. Wang, B.; Rui, H. Synoptic climatology of transient tropical intraseasonal convection anomalies: 1975–1985. Meteor. *Atmos. Phys.* **1990**, *44*, 43–61. [CrossRef]
36. Madden, R.A.; Julian, P.R. Observations of the 40–50-Day Tropical Oscillation—A Review. *Mon. Weather Rev.* **1994**, *122*, 814–837. [CrossRef]
37. Zhang, C.D.; Dong, M. Seasonality in the Madden-Julian Oscillation. *J. Clim.* **2004**, *17*, 3169–3180. [CrossRef]
38. Jiang, X.; Li, T.; Wang, B. Structures and mechanisms of the northward propagating boreal summer intraseasonal oscillation. *J. Clim.* **2004**, *17*, 1022–1039.
39. Zhu, C.W.; Nakazawa, T.; Li, J.P.; Chen, L. The 30–60 day intraseasonal oscillation over the western North Pacific Ocean and its impacts on summer flooding in China during 1998. *Geophys. Res. Lett.* **2003**, *30*, 1952.
40. Mao, J.; Wu, G. Intraseasonal variations of the Yangtze rainfall and its related atmospheric circulation features during the 1991 summer. *Clim. Dyn.* **2006**, *27*, 815–830. [CrossRef]
41. Yang, J.; Wang, B.; Bao, Q. Biweekly and 21–30-day variations of the subtropical summer monsoon rainfall over the lower reach of the Yangtze River basin. *J. Clim.* **2010**, *23*, 1146–1159. [CrossRef]
42. Chen, J.; Wen, Z.; Wu, R.; Chen, Z.; Zhao, P. Influences of northward propagating 25–90-day and quasi-biweekly oscillations on eastern China summer rainfall. *Clim. Dyn.* **2015**, *45*, 105–124. [CrossRef]
43. Hsu, P.C.; Lee, J.Y.; Ha, K.J. Influence of boreal summer intraseasonal oscillation on rainfall extremes in southern China. *Int. J. Climatol.* **2016**, *36*, 1403–1412. [CrossRef]
44. Lee, S.; Moon, J.; Wang, B.; Kim, H.-J. Subseasonal Prediction of Extreme Precipitation over Asia: Boreal Summer Intraseasonal Oscillation Perspective. *J. Clim.* **2017**, *30*, 2849–2865. [CrossRef]
45. Sasikumar, K.; Nath, D.; Wang, X.; Chen, W.; Yang, S. Recent enhancement and prolonged occurrence of MJO over the Indian Ocean and their impact on Indian summer monsoon rainfall. *Clim. Dyn.* **2022**, *59*, 2585–2598. [CrossRef]
46. Huang, Z.; Zhang, W.; Geng, X.; Hsu, P.-C. Accumulated Effect of Intra-Seasonal Oscillation Convections over the Tropical Western North Pacific on the Meridional Location of Western Pacific Subtropical High. *Front. Earth Sci.* **2020**, *8*, 579442. [CrossRef]
47. Liu, Y.; Li, W.; Ai, W.; Li, Q. Reconstruction and Application of the Monthly Western Pacific Subtropical High Indices. *J. Appl. Meteorol. Sci.* **2012**, *23*, 414–423. (In Chinese)
48. Pohl, B.; Matthews, A.J. Observed changes in the lifetime and amplitude of the Madden-Julian Oscillation associated with interannual ENSO sea surface temperature anomalies. *J. Clim.* **2007**, *20*, 2659–2674. [CrossRef]
49. Wei, Y.; Ren, H. Modulation of ENSO on Fast and Slow MJO Modes during Boreal Winter. *J. Clim.* **2019**, *32*, 7483–7506. [CrossRef]
50. Wang, B.; Chen, G.; Liu, F. Diversity of the Madden-Julian Oscillation. *Sci. Adv.* **2019**, *5*, eaax0220. [CrossRef]
51. Ambrizzi, T.; Hoskins, B.J.; Hsu, H.-H. Rossby wave propagation and teleconnection patterns in the austral winter. *J. Atmos. Sci.* **1995**, *52*, 3661–3672. [CrossRef]
52. Ren, P.; Ren, L.; Fu, X.; Wu, J.; Du, L. Impact of Boreal Summer Intraseasonal Oscillation on Rainfall Extremes in Southeastern China and its Predictability in CFSv2. *J. Geophys. Res. Atmos.* **2018**, *123*, 4423–4442. [CrossRef]

water

MDPI

Article

Intercomparison of Runoff and River Discharge Reanalysis Datasets at the Upper Jinsha River, an Alpine River on the Eastern Edge of the Tibetan Plateau

Shuanglong Chen [1,†], Heng Yang [2,†] and Hui Zheng [3,*]

[1] Baihetan Hydropower Plant, China Three Gorges Corporation, Liangshan 615421, China; chen_shuanglong@ctg.com.cn
[2] Science and Technology Research Institute, China Three Gorges Corporation, Beijing 100038, China; yang_heng2@ctg.com.cn
[3] Institute of Atmospheric Physics, Chinese Academy of Sciences, Beijing 100029, China
* Correspondence: hzheng_iap@outlook.com
† These authors contributed equally to this work and should be considered co-first authors.

Abstract: This study assesses the effectiveness and limitations of publicly accessible runoff and river discharge reanalysis datasets through an intercomparison in the Upper Jinsha River, an alpine region with substantial hydropower potential on the eastern edge of the Tibetan Plateau. The examined datasets are the European Centre for Medium-Range Weather Forecast Reanalysis version 5 (ERA5-Land), the Global Flood Awareness System (GloFAS), the Global Reach-Level Flood Reanalysis (GRFR), and the China Natural Runoff Dataset (CNRD). These datasets are created using various meteorological forcing, runoff generation models, river routing models, and calibration methods. To determine the causes of discrepancies, additional simulations were carried out. One simulation, driven by meteorological forcing similar to that of ERA5-Land and GloFAS but utilizing the uncalibrated NoahMP land surface model at a higher spatial resolution, was included to evaluate the effects of meteorological inputs, spatial resolution, and calibration on runoff estimation. Runoff from all datasets was rerouted on a high-resolution river network derived from the 3-arcsecond Multi-Error-Removed Improved-Terrain Hydrography (MERIT-Hydro) dataset, allowing for a comparison between vector- and grid-based river routing models for discharge estimates. The intercomparison is grounded in observations from three gauging stations—Zhimenda, Gangtuo, and Benzilan—at monthly, daily, and hourly scales. The results suggest that model calibration has a more significant influence on runoff and discharge estimates than meteorological data. Calibrated datasets, such as GloFAS and GRFR, perform better than others, despite variations in the forcing data. The runoff characteristics-based calibration method used in GRFR exhibits superior performance at Zhimenda and Benzilan. However, at Gangtuo, GRFR's performance is unsatisfactory, highlighting the limitation of the machine learning-based method in regions with rugged terrain and limited observations. Vector-based river routing models demonstrate advantages over grid-based models. GloFAS, which uses a grid-based routing model, encounters difficulties in simultaneously producing accurate runoff and discharge estimates. The intercomparison shows that GRFR's river routing is sub-optimally configured. However, when GRFR's runoff rerouted, the performance of discharge improves substantially, attaining a Kling–Gupta efficiency of approximately 0.9. These findings offer valuable insights for the further development of reanalysis datasets in this region.

Keywords: runoff; river discharge; model intercomparison; Upper Jinsha River

1. Introduction

The rapid growth of global- and continental-scale runoff and discharge reanalysis datasets marks a significant advancement in hydrological research. Datasets such as the European Centre for Medium-Range Weather Forecasts (ECMWF) Reanalysis version 5 (ERA5) [1], ERA5-Land [2], the Global Flood Awareness System (GloFAS) [3,4], and the Global Reach-Level Flood Reanalysis (GRFR) [5,6] provide continuous, spatially comprehensive runoff and river discharge estimates. Additionally, regional datasets like the National Water Model (NWM) of the United States [7], the European Flood Early Warning Systems [8], and the China Natural Runoff Dataset (CNRD) [9,10] provide runoff and discharge estimates tailored to specific regions. These datasets have greatly improved our understanding of river systems [11,12] and their interactions with other components of the Earth system [13]. Furthermore, they have been instrumental in supporting decision-making processes, particularly in the area of water resources utilization and flood protection [7,14].

Reanalysis datasets are generated through a complex chain of methodologies that include meteorological forcing data, land surface models or hydrological models, river routing models, river network delineations, and calibrations. The diversity among these components can significantly influence the estimation of runoff and river discharge. Studies have demonstrated that meteorological forcing data can differ remarkably [15,16]. The use of different meteorological forcing data [17,18], in combination with varying model structure [19], spatial resolutions [20–22], parameterizations [23,24], and parameters [25] of land surface models or hydrological models, can lead to disparate estimates of runoff [26,27]. Furthermore, these differences in runoff estimation can be further amplified by the methods employed in river routing [28–30].

The diversity in estimation methodologies necessitates careful intercomparison before using reanalysis datasets. In the past decades, a variety of intercomparison studies have been conducted with different objectives. Land surface model comparisons such as the Project for Intercomparison of Land-surface Parameterization Schemes [31] and the Land Surface, Snow and Soil Moisture Model Intercomparison Project [32], conducted with the same meteorological forcing data, greatly help to reveal the weakness of the participant models and the interactions of land surface processes. The Distributed Model Intercomparison Project [33,34] compared distributed models with lumped models. This project revealed the superiority of distributed routing models in reproducing flood peaks and reported the importance of calibration on distributed rainfall-runoff models. Beck et al. [27] compared ten hydrological models at the global scale. Their results further confirm that proper parameter calibration is vital for accurate runoff estimation. The Continental Hydrological Intercomparison Project [35] compared two high-resolution, physics-based models at the continental scale. The intercomparison promotes high-resolution modeling to enhance topographic processing and to improve topographic representation over complex topography. There are also intercomparisons with regional focuses. The Great Lakes Runoff Intercomparison Project [29] and the Nelson Model Intercomparison Project under the Integrated Modelling Program of Canada initiative [30] are two examples. These intercomparison studies aim to select the best-performing estimation methodologies for the region and guide further improvements of operations.

The Upper Jinsha River, the source of the Changjiang River, is notable for its steep gradient and high hydroelectric potential. The river is located on the eastern edge of the Tibetan Plateau. Thirteen hydroelectric facilities have been built or planned along its main stem, collectively possessing an installed capacity of approximately 14.6 gigawatts. The river originates from the Tibetan Plateau. The source area of the river consists of a major part of the Sanjiangyuan National Nature Reserve, the highest and largest nature reserve in China yet. The operations of hydroelectric facilities and natural reserves require accurate estimation of water resources. However, the scarcity of in situ hydrometeorological observations in the region is a notable challenge. In this context, reanalysis datasets of runoff and discharge emerge as an indispensable data source for the area. Simultaneously, the Upper Jinsha River's intricate topography, high-alpine environmental conditions, and the pressing need for accurate runoff and river discharge estimations render it an exemplary testing ground for these reanalysis datasets.

This study intercompares runoff and river discharge reanalysis data obtained from ERA5-Land, GloFAS, GRFR, and CNRD for the Upper Jinsha River as a pilot analysis. The primary objective is to assess the effectiveness and limitations of the methodologies employed in these reanalyses, providing insights to guide future improvements in runoff and discharge estimation.

2. Materials and Methods

Figure 1 illustrates the terrain and river network of the upper Jinsha River. The study area encompasses the region upstream of the Benzilan gauging station. The elevation ranges from approximately 6600 m at its highest point to 2000 m at its lowest. The river network was extracted from the Multi-Error-Removed Improved-Terrain Hydrography (MERIT-Hydro) dataset [36,37]. MERIT-Hydro is a globally recognized dataset providing hydrologically conditioned elevation, flow direction, and flow accumulation area data, with a spatial resolution of 3 arcseconds. The river network was extracted using a flow accumulation area threshold of 25 km^2, resulting in 5787 river reaches.

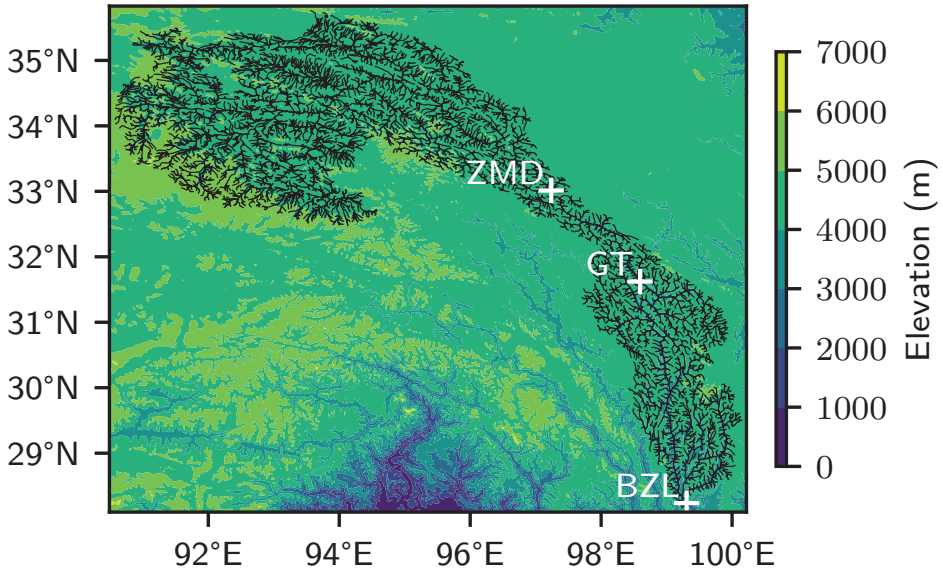

Figure 1. Study domain and river network of the source region of the upper Jinsha River. White crosses mark the gauging stations: ZMD, Zhimenda; GT, Gangtuo; BZL, Benzilan.

2.1. Reanalysis Datasets

Table 1 presents an overview of the datasets employed in this study. ERA5-Land [2] is an enhanced global dataset, an improvement over ERA5 [1]. This dataset features a significant improvement in spatial resolution, increasing from ERA5's 31 km to 0.1° globally. A variety of land surface variables, including runoff, are simulated using the Carbon Hydrology-Tiled ECMWF Scheme for Surface Exchanges over Land (CHTESSEL) model [38,39], operating at an hourly temporal resolution.

Table 1. The datasets used in this study.

Dataset	Time Period	Temporal Resolution	Runoff Resolution	River Routing	References
Publically available datasets					
ERA5-Land	1950–Present	Hourly	0.10°	N/A	Muñoz-Sabater et al. [2]
GloFAS v4.0	1979–Present	Daily	0.10°	LISFLOOD	Harrigan et al. [4]
GRFR v1.0	1980–2019	3-hourly	0.05°	RAPID	Yang et al. [5]
CNRD v1.0	1961–2018	Monthly	0.25°	N/A	Miao et al. [10]
Datasets produced in this study					
ERA5-Land/NoahMP	2009–2016	Hourly	0.01°	MC	This study

The GloFAS historical reanalysis version 4.0 [3,4] is another dataset produced by the European Centre for Medium-Range Weather Forecasts (ECMWF), with a focus on hydrological variables. GloFAS shares the same spatial resolution of 0.1° as ERA5-Land. It is driven by ERA5 meteorological data, which is highly similar to ERA5-Land. The primary distinctions between GloFAS and ERA5-Land lie in the hydrological model employed, the temporal resolution, and the output variables. GloFAS utilizes the LISFLOOD model [40] at a daily time step. Unlike ERA5-Land, the parameters of LISFLOOD are calibrated against daily river discharge observations using an evolutionary algorithm [41]. LISFLOOD simulates both runoff and river discharge, whereas ERA5-Land provides only runoff estimates.

The GRFR dataset [5] is a comprehensive global dataset providing runoff and river discharge data at a 3-hourly temporal resolution. The runoff is simulated using the Variable Infiltration Capacity (VIC) model [42] at a spatial resolution of 0.05°, which is driven by precipitation data from the Multi-Source Weighted-Ensemble Precipitation (MSWEP) dataset [43] and other meteorological variables from ERA5. The VIC model's parameters are calibrated [44] at each 0.05° grid cell against a machine learning-derived runoff characteristics dataset produced by Beck et al. [45]. The bias in the VIC-simulated runoff is further corrected using the same runoff characteristics dataset, following the methodology of Lin et al. [6]. The calibrated and bias-corrected runoff data are then utilized to drive the Routing Application for Parallel computatIon of Discharge (RAPID) river routing model [46] for simulating river discharge. The parameters of RAPID are estimated using a statistical relationship that correlates discharge with river width, water depth, channel slope, and celerity [6]. The river network employed in the routing process is also derived from the MERIT Hydro dataset [47].

The China Natural Runoff Dataset (CNRD) [9,10] comprises runoff data at a 0.25° spatial resolution. This dataset is simulated using the VIC model, driven by the China Meteorological Forcing Dataset [48]. The parameters of the VIC model were calibrated against river discharge observations from approximately 200 catchments across China and then extrapolated to ungauged river basins using the multiscale regionalization method [49].

As presented in Table 1, a new dataset was generated in this study for comparative purposes. This dataset was driven by ERA5-Land meteorological data and simulated via a distinct land surface model and river routing model. Given that the new dataset shares a similar meteorological forcing dataset with GloFAS and ERA5-Land, this comparison can effectively isolate the impacts of model selection, spatial resolution, and calibration on runoff and discharge estimations. The model employed in this study emulates the National Water Model (NWM). The Noah with Multi - Parameterization (NoahMP) land surface model [50] was utilized, operating at a spatial resolution of 0.01° from 2008 to 2016. The static parameters for NoahMP are derived from the Weather Research and Forecasting geographic static data (https://www2.mmm.ucar.edu/wrf/users/download/get_sources_wps_geog.html, accessed on 10 November 2024). The initial condition for 2008 is sourced from ERA5-Land. The first year is allocated for model spin-up, with the simulated runoff from 2009 to 2016 used for analysis. NoahMP offers a variety of parameterization schemes for land surface processes, and we adopted the same schemes as those used in the NWM of the United States [7]. The runoff is routed using the variable-parameter Muskingum–Cunge (MC) method on the river network depicted in Figure 1 to estimate river discharge. The routing algorithm mirrors that of the NWM, assuming a trapezoidal channel cross-section. Channel cross-section geometry and roughness parameters are sourced from the default parameter lookup table of the NWM [51] and the Strahler stream order for each river reach within the network. In theory, the MC routing method would outperform the kinematic wave routing method used in GloFAS by also additionally considering diffusive wave dynamics, while the Muskingum routing method used in GRFR would be the least performing among the three. It is important to note that this comparison is theoretical, and actual performance can vary significantly with model implementation and parameter settings.

2.2. River Discharge Observations

We utilized river discharge observations from three gauging stations along the mainstream of the upper Jinsha River: Zhimenda (ZMD), Gangtuo (GT), and Benzilan (BZL), covering the period from 2009 to 2016. Zhimenda serves as the demarcation point between the source region of the Changjiang River and the Upper Jinsha River. All the planned hydroelectric power stations are located on the river segment stretching between Zhimenda and Benzilan. The inclusion of Gangtuo provides additional data coverage along the river's mainstream. By choosing these stations, the performance of reanalysis datasets in a region of high hydropower potential and complex hydrological processes can be assessed. The selection of this timeframe is justified by the minimal presence of hydroelectric facilities, which ensures that the river discharge data are largely unaffected by human interventions.

The dataset from Zhimenda is compiled at a daily resolution. The dataset comprises 1477 records, with 49% of the days missing between 2009 and 2016. In contrast, Gangtuo and Benzilan provide data at an hourly resolution, aaccumulating 52,246 h and 69,011 h, respectively. The respective missing data rates for these stations are 25% for Gangtuo and 1.6% for Benzilan. Given the nature of our analysis, we have chosen not to impute the missing values, opting instead to focus solely on the complete data records. This choice was made with the aim of maximizing the utilization of available observations in this region where data are scarce. Additionally, by avoiding the use of gap-filling methods, we sought to minimize the potential biases that could be introduced, especially given that the proportion of missing data is substantial.

To our knowledge, the daily river discharge observations at Zhimenda have been used to calibrate GloFAS and GRFR, while the observations at Gangtuo and Benzilan have not been incorporated into the datasets analyzed in this study.

2.3. Evaluation Methods

As shown in Table 1, the datasets vary in spatial and temporal resolution. River discharge estimates are not available in every dataset examined. To address these inconsistencies, we remapped the runoff onto a common 0.01° grid and refined both daily and monthly values to hourly values, as depicted in Figure 2. The spatial remapping was conducted using a first-order conservative method. For temporal refinement, we used the fraction of hourly ERA5-Land runoff to the accumulated runoff within a day or a month to redistribute the daily or monthly values. Subsequently, the runoff from all datasets was routed using the same Muskingum–Cunge (MC) method, as previously described, to estimate river discharge. For GloFAS and GRFR, which provide river discharge estimates, we also refined the 3-hourly or daily values to hourly values using the same refinement method as the runoff.

The river discharge estimates derived from the Muskingum–Cunge method, as well as the temporally refined river discharge data from GRFR and GloFAS, are then compared with the observations at the gauging stations. This evaluation is conducted across three temporal scales—monthly, daily, and hourly—to comprehensively assess the accuracy and consistency of the estimates with the actual observations.

The structure and parameters of the river routing model significantly influence the river discharge estimates. To isolate the impact of river routing on these estimates, we not only compared the model-derived river discharge with observations at gauging stations but also aggregated the runoff above these stations for a more direct comparison. This aggregation helps to isolate the effects of routing by focusing on the input runoff rather than the routing process itself. The aggregated runoff is calculated by summing the runoff within the upstream area of each gauging station. The delineation of the upstream area was based on the flow direction data from the MERIT-Hydro dataset.

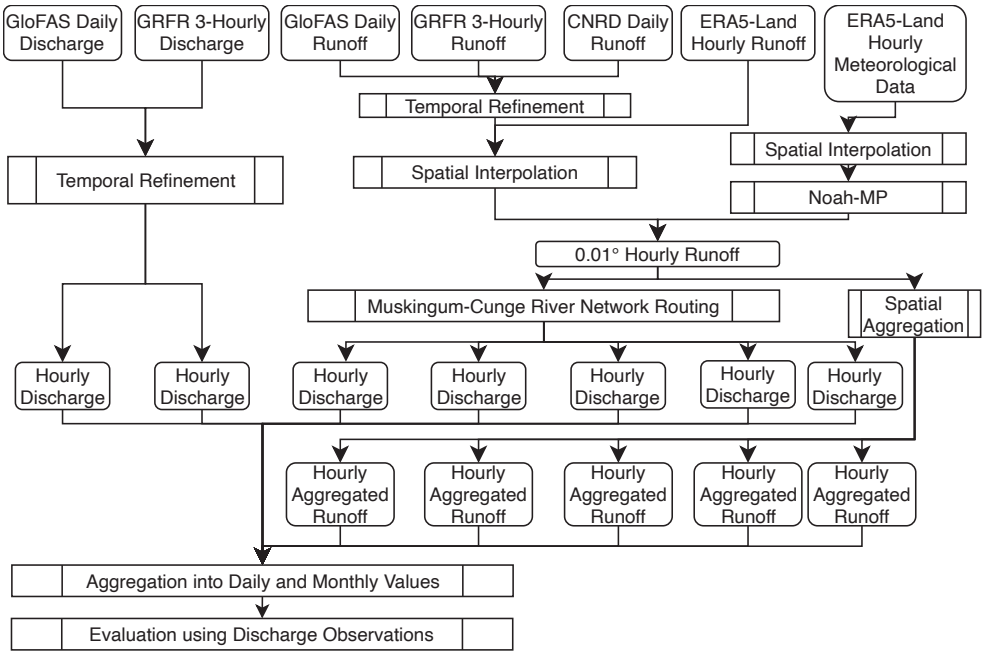

Figure 2. Workflow of this study.

2.4. Evaluation Metrics

We employed the Kling–Gupta efficiency (KGE) [52] to assess the performance of the reanalysis datasets. The KGE shares similarities with the commonly used mean squared

error (MSE) and Nash–Sutcliffe efficiency (NSE). It incorporates the correlation coefficient, the ratio of the standard deviations, and the ratio of the mean values of both the observed and simulated data. Unlike MSE or NSE, in the KGE, these three components are combined in an independent manner. This enables a straightforward separation of their relative contributions to the overall metric. The KGE is formulated as follows:

$$\mathrm{KGE} = 1 - \sqrt{G_1^2 + G_2^2 + G_3^2}, \tag{1}$$

$$G_1 = r - 1, \tag{2}$$

$$G_2 = \frac{\sigma_s}{\sigma_o} - 1, \tag{3}$$

$$G_3 = \frac{\mu_s}{\mu_o} - 1, \tag{4}$$

where r is the correlation coefficient, σ_s and σ_o are the standard deviations of the simulated and observed data, respectively, and μ_s and μ_o are the mean values of the simulated and observed data, respectively. The KGE ranges from $-\infty$ to 1, with a value of 1 indicating a perfect match between the simulated and observed data. A KGE value significantly less than 1 indicates a poor match.

The relative contribution of the three terms in the KGE can be calculated using the following formula [52]:

$$g_i = \frac{G_i^2}{G_1^2 + G_2^2 + G_3^2}, \quad \text{for } i = 1, 2, 3, \tag{5}$$

where g_1, g_2, and g_3 are the relative contributions of correlation coefficient, variability, and bias, respectively. A higher value indicates a greater contribution of the corresponding term to the deviation of the KGE from 1.

3. Results and Discussion

3.1. Runoff

Figure 3 geographically compares the runoff estimates within the Benzilan catchment. The five datasets fall into three categories: ERA5-Land and ERA5-Land/NoahMP; GloFAS and GRFR; and CNRD. The first group utilizes uncalibrated land surface models, the second group employs extensively calibrated hydrological models, and the third group features a hydrological model with parameters that are regionalized rather than individually calibrated. Notably, ERA5-Land, ERA5-Land/NoahMP, and GloFAS exhibit significant differences despite similar meteorological forcing data. On the other hand, GloFAS and GRFR, which are driven by different meteorological forcing data, show close spatial patterns. This comparison indicates that the calibration of land surface models or hydrological models has a profound impact on runoff estimation, more than the meteorological data.

Figure 4 intercompares the monthly variations and annual cycle of the aggregated runoff above Zhimenda, Gangtuo, and Benzilan. Since the river flow travel time is typically smaller than a month [53], it is generally safe to neglect the impact of river routing at the monthly time scale. Both ERA5 and CNRD overestimate the runoff at all examined stations, but the reasons for this overestimation differ. The overestimation in ERA5 is consistent with previous studies, which attribute it to overestimated precipitation in high-altitude regions [54–57]. In contrast, the overestimation of CNRD is primarily observed in the upstream area of Zhimenda. Given that CMFD, the meteorological data that drive CNRD, has shown closeness to in situ precipitation observations in this region [57], the

overestimation of the CNRD runoff is likely due to less constrained hydrological model parameters. CNRD uses parameters calibrated at gauged basins and extrapolates these parameters to ungauged basins using multiscale regionalization functions [9,10]. The scarcity of river discharge gauges on the Tibetan Plateau means that this extrapolation can lead to bias.

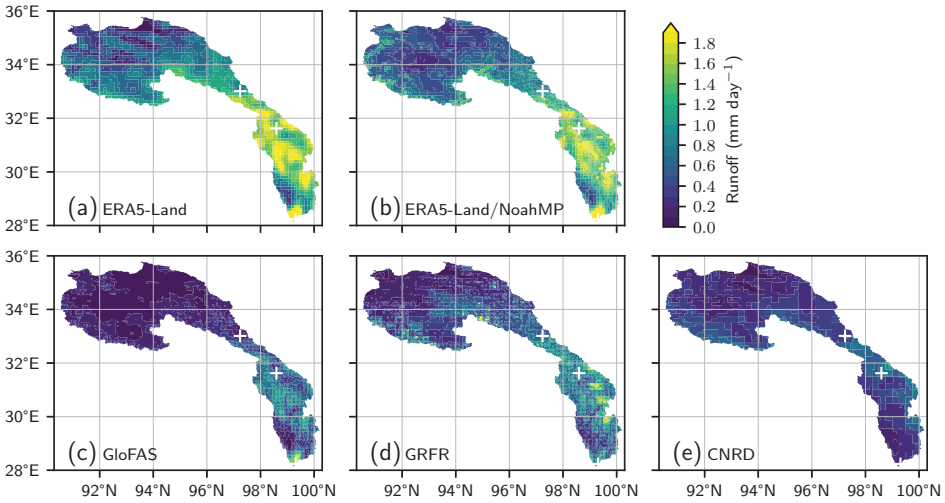

Figure 3. Intercomparison of the spatial distribution of multiyear averaged runoff from 2009 to 2016. White crosses denote the gauging stations.

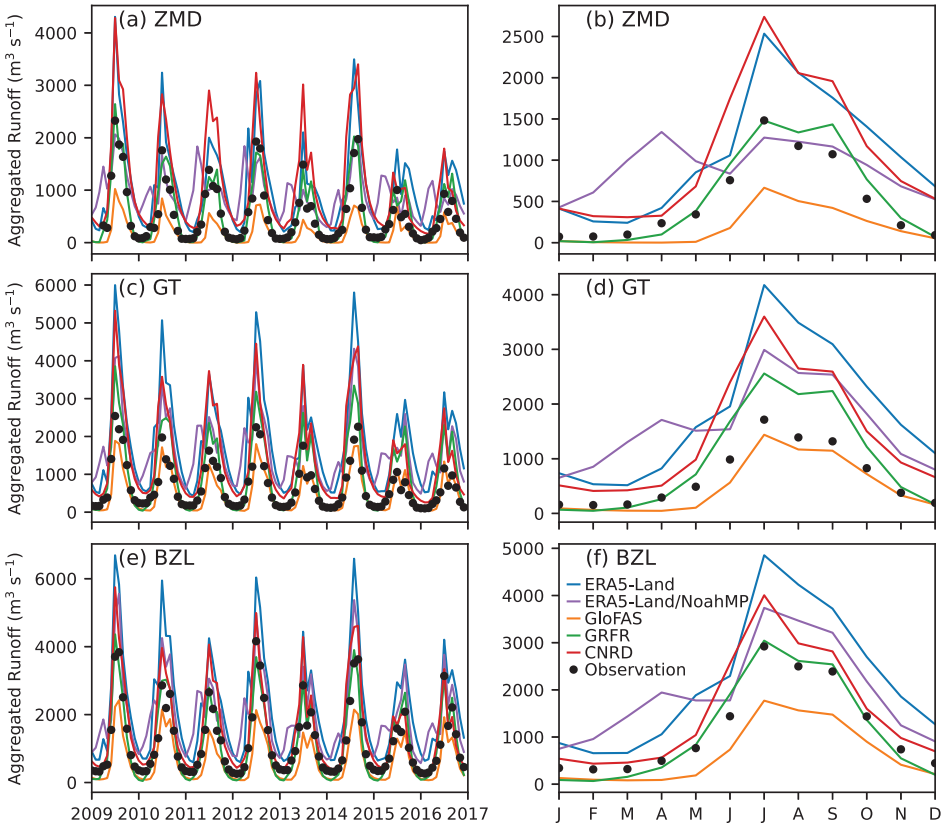

Figure 4. Intercomparison of the aggregated runoff at the gauging stations: (**a**) monthly aggregated runoff at Zhimenda; (**b**) annual cycle of the aggregated runoff at Zhimenda; (**c**) monthly aggregated runoff at Gangtuo; (**d**) annual cycle of the aggregated runoff at Gangtuo; (**e**) monthly aggregated runoff at Benzilan; and (**f**) annual cycle of the aggregated runoff at Benzilan.

The runoff from ERA5-Land/NoahMP exhibits two peaks, particularly in the high-altitude regions above Zhimenda. In contrast, ERA5-Land, which utilizes the same meteorological data, shows an insignificant rise in runoff during spring. The discrepancy between ERA5-Land/NoahMP and ERA5-Land is likely due to differences in the spatial resolution of the land surface model. The higher resolution of ERA5-Land/NoahMP allows for a better capture of the vertical gradient of the land surface temperature. The combination of overestimated precipitation in the ERA5-Land meteorological data and increased snowmelt in low-altitude model grids [21] results in an artificial spring runoff peak not observed in the actual data.

The two calibrated datasets, GloFAS and GRFR, exhibit distinct behaviors. This difference is even evident at Zhimenda, where observations are publicly available through the Global Runoff Data Centre and have been utilized in both datasets. The distinct calibration approaches of the two datasets likely account for this difference. GloFAS is calibrated against river discharge observations [41], while its runoff is not directly calibrated. Since river discharge can be calculated by multiplying the catchment area by runoff, different estimates of the catchment area will lead to different runoff values after the calibration of river discharge. In contrast, GRFR's runoff is directly calibrated against a machine learning-derived runoff characteristics dataset [44]. The results suggest that the calibration method employed by GRFR is highly effective, yielding the best-performing runoff among the examined datasets.

Figure 5 presents the performance of the aggregated runoff in comparison with discharge observations at the monthly time scale. ERA5-Land consistently underperforms across all stations and time scales, corresponding to the overestimation shown in Figure 4. CNRD also performs poorly in high-altitude areas above Gangtuo due to overestimation, but its performance improves at Benzilan. The performance of CNRD slightly outperforms the high-resolution ERA5-Land/NoahMP. Among the examined datasets, the two calibrated datasets, GloFAS and GRFR, perform the best at almost every station examined, highlighting the importance of calibration for land surface models or hydrological models. Notably, GRFR's performance is exceptionally good, with a KGE above 0.8 at Zhimenda and Benzilan. GRFR's high performance underscores the effectiveness of the characteristics-based calibration method. Meanwhile, GRFR shows subpar performance at Gangtuo. This underperformance can be attributed to the underestimation of both the variability and the long-term mean, as detailed in Section 3.2. Since both variability and the long-term mean are the characteristics to which GRFR is calibrated, the poor performance of GRFR at Gangtuo implies that the machine learning-derived runoff characteristics dataset does not accurately represent the runoff characteristics at Gangtuo. This is likely because the terrain at Gangtuo is steep, and the observations from this location were not incorporated into the training dataset.

3.2. Streamflow

Figure 6 compares the monthly discharge estimations with observations. The patterns generally follow the runoff pattern shown in Figure 4. The overestimation observed in ERA5-Land and CNRD closely mirrors their runoff overestimation. The artificial spring peak, which is also present in the ERA5-Land/NoahMP discharge, aligns with the runoff pattern.

It is interesting to note that the GloFAS and GRFR discharge behave differently from the runoff. Our rerouted GloFAS runoff (GloFAS-MC in Figure 6) can reproduce the underestimated patterns observed for the runoff (Figure 4), confirming that GloFAS underestimates runoff. However, the underestimation of runoff is no longer presented in the

river discharge. GloFAS closely reproduced the observed river discharge (Figure 6). The contradiction between the runoff underestimation and the unbiased discharge estimation suggests that the spatial resolution of GloFAS's routing grid plays a role. GloFAS is routed on a $\frac{1}{10}^\circ$ grid cell basis, whereas the river basins delineated in this study (as shown in Figure 1) are based on $\frac{1}{1200}^\circ$ grids. The resolution of GloFAS may be too coarse to accurately delineate the river basins. However, this error is mitigated in the discharge due to the calibration, and the impact is transferred to errors in the runoff.

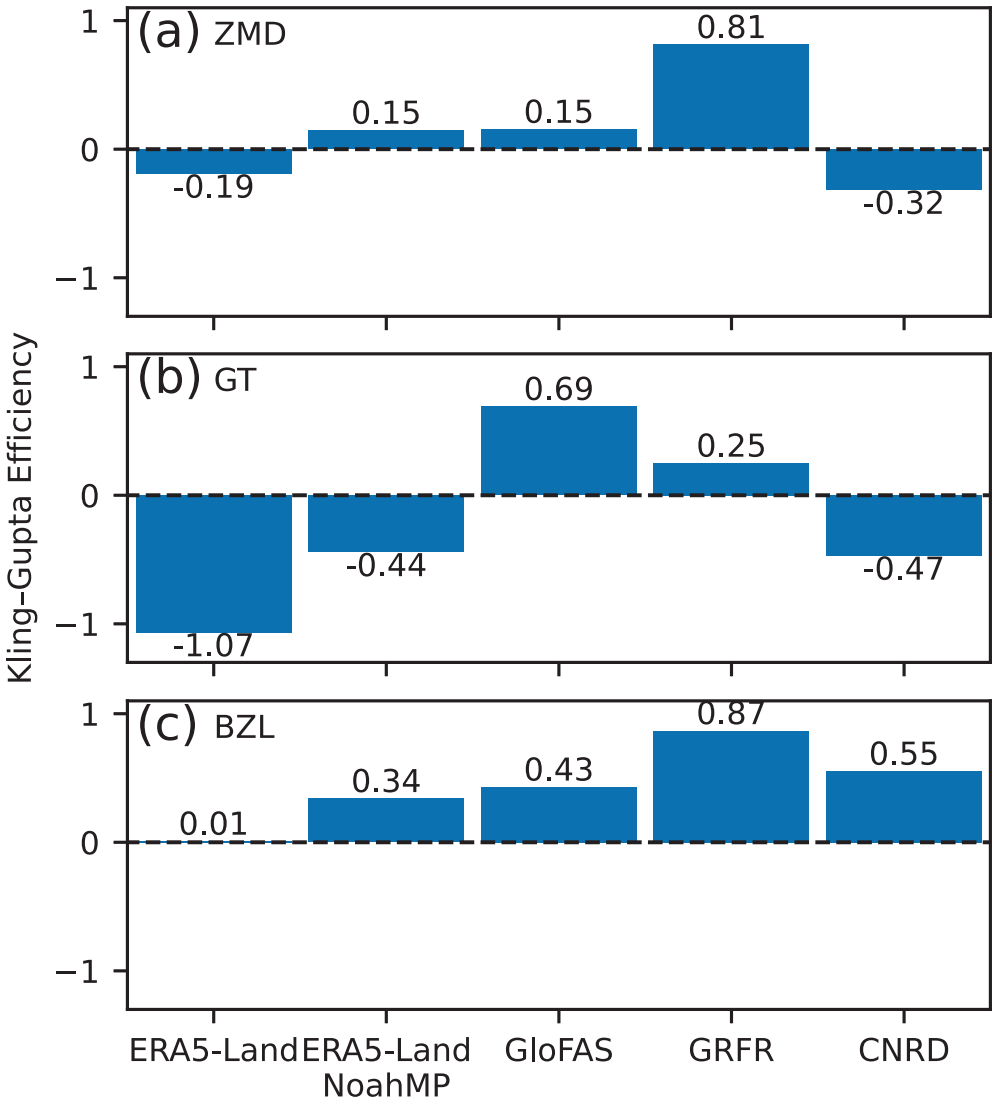

Figure 5. Kling–Gupta efficiency of the monthly aggregated runoff: (**a**) the measures at Zhimenda; (**b**) the measures at Gangtuo; and (**c**) the measures at Benzilan.

Despite the high skill of GRFR's runoff demonstrated in Figure 4, the skill of GRFR's discharge is unexpectedly unsatisfactory. GRFR remarkably overestimates discharge at all gauging stations. The overestimation is also reported in the literature [58,59]. We argue that neither the dynamics nor the parameters of the river routing model should have such significant impacts on monthly discharge, and that the unexpected overestimation in GRFR is likely attributable to some inadequate configurations of the river routing model. Our rerouted discharge (GRFR-MC) using the GRFR runoff and the Muskingum–Cunge routing method can closely reproduce the observed discharge patterns. This confirms that the overestimation in GRFR is not due to the runoff but rather the routing process.

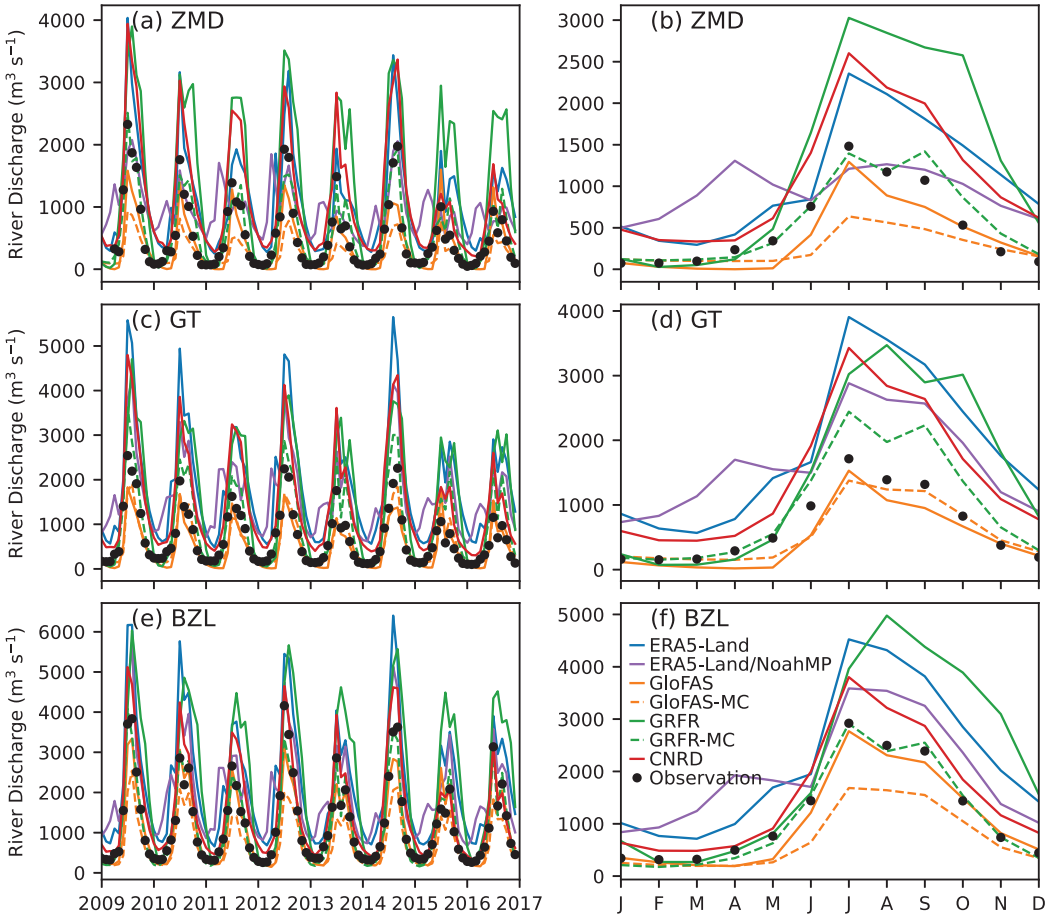

Figure 6. Same as Figure 4, but for river discharge.

Figure 7 presents the river discharge estimates compared with both daily and hourly observations. The aggregated runoff is also displayed for comparison. The difference between aggregated runoff and river discharge highlights the impact of river routing. The comparison shows that river routing has a marginal impact in low flow conditions and at the monthly time scale. The impact increases with flow rate and on shorter time scales. Significant impacts of river routing are found on the hourly high flow estimations at all gauging stations. This finding suggests the indispensable role of river routing in flood forecasting.

The differences among the examined river discharge estimates are mainly exhibited in high flow conditions. However, these differences do not vary significantly with the time scale of the estimates (i.e., daily or hourly). The GRFR river discharge estimation suspiciously indicates a high probability of discharge at approximately 4000 $m^3 s^{-1}$ at all the examined stations, whereas such a high probability is not found in the other estimates including GRFR-MC. This suspicious pattern is another strong indicator of inadequate configurations within GRFR's routing process. The GloFAS estimate can reproduce the observed discharge probability patterns well. Our rerouted river discharge using the GloFAS runoff and the Muskingum–Cunge method deviates from the observed pattern of discharge probability. The discrepancy arises from the calibration of river discharge, which compensates for imprecise river basin area estimation.

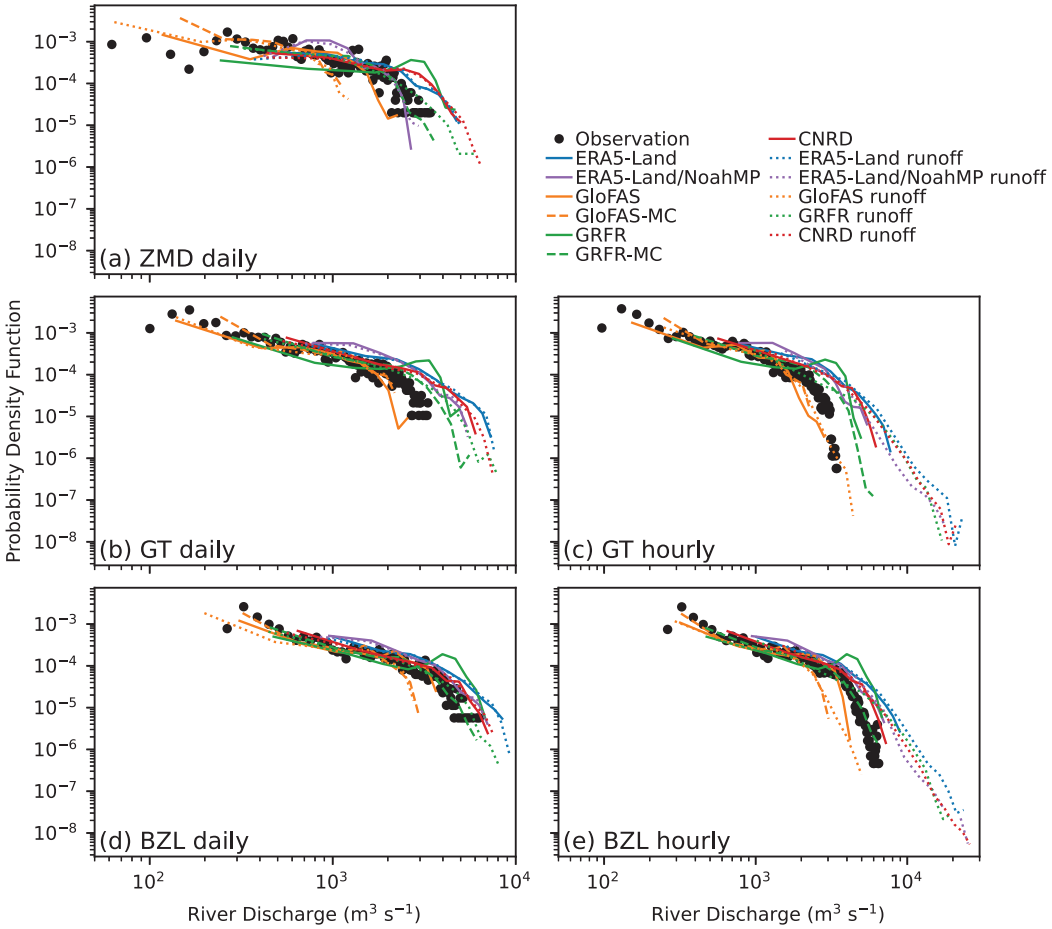

Figure 7. Intercomparison of the probability distribution of river discharge and aggregated runoff at the river gauging stations: (**a**) daily estimates at Zhimenda; (**b**) daily estimates at Gangtuo; (**c**) hourly estimates at Gangtuo; (**d**) daily estimates at Benzilan; and (**e**) hourly estimates at Benzilan. Dotted lines denote the aggregated runoff. Solid lines denote the river discharge estimates provided by the examined datasets. Dashed lines denote the river discharge estimates using the runoff and the Muskingum–Cunge routing method. Zhimenda is not shown in the hourly estimates due to the lack of hourly observations.

Figure 8 illustrates the skill scores for the estimation of river discharge across monthly, daily, and hourly temporal scales. At the monthly scale, the river discharge estimation's skill closely mirrors that of the runoff, as depicted in Figure 5. The coincidence hints that the primary determinant of river discharge variability within the study area is the runoff estimation, rather than the river routing process. An exception to this pattern is observed with GloFAS, where the divergence in discharge skill scores from those of runoff is likely due to the coarse and imprecise river routing grid employed, as previously discussed.

Among the examined dataset, GloFAS, GloFAS-MC, and GRFR-MC perform the best at all gauging stations and across all time scales. Proper calibration of the land surface model and the hydrological model is essential for accurate river discharge estimation. As revealed in Figure 9, the primary reasons for the poor performance of the examined datasets, except for GRFR-MC, are errors in reproducing the observed mean and variability of river discharge. GRFR-MC can effectively reproduce the observed mean and variability of river discharge. The KGE of GRFR-MC's hourly discharge can reach a high score of approximately 0.9 at Benzilan, which again confirms the effectiveness of the characteristics-based calibration method. The relatively lower performance of GRFR at Gangtuo implies

that the machine learning-based calibration method employed by GRFR needs to incorporate more local observations to enhance its applicability in specific regions. At all three gauging stations, the deviation of the KGE from 1 for GRFR-MC is mainly attributed to the correlation coefficient, which can be further improved through the calibration of the river routing parameters. The exceptionally high skill of GRFR-MC again confirms the effectiveness of the characteristics-based calibration method.

It is worth noting that the KGE (Figure 8) and the relative contribution within the KGE (Figure 9) are consistent for both hourly and daily estimates. This consistency suggests that calibration at the daily time scale could potentially be applied to the hourly time scale. However, the relative contributions of the correlation coefficient, variability, and bias differ between the monthly, daily, and hourly time scales, as illustrated in Figure 9. At the monthly scale, the datasets under examination mainly exhibit differences in the variability and bias of river discharge estimations. The correlation coefficient plays a relatively minor role, indicating that all the examined datasets are capable of reasonably capturing the timing of the peak discharge, as evidenced by Figure 6. In contrast, at the daily and hourly scales, the correlation coefficient emerges as a crucial factor. This suggests that the examined datasets face challenges in accurately reproducing the observed timing of floods.

The KGE of river discharge is also consistent between daily and monthly estimates for most datasets, with the exception of the high-resolution ERA5-Land/NoahMP estimation (Figure 8). The increase in KGE from the monthly to daily time scale indicates that a more accurate representation of the spatial distribution of runoff and river routing could improve the temporal variations in river discharge estimates, aligning with the concept of the time of concentration [60]. However, these findings are based on a limited number of gauging stations and limited time periods. Further studies are needed to validate these preliminary observations.

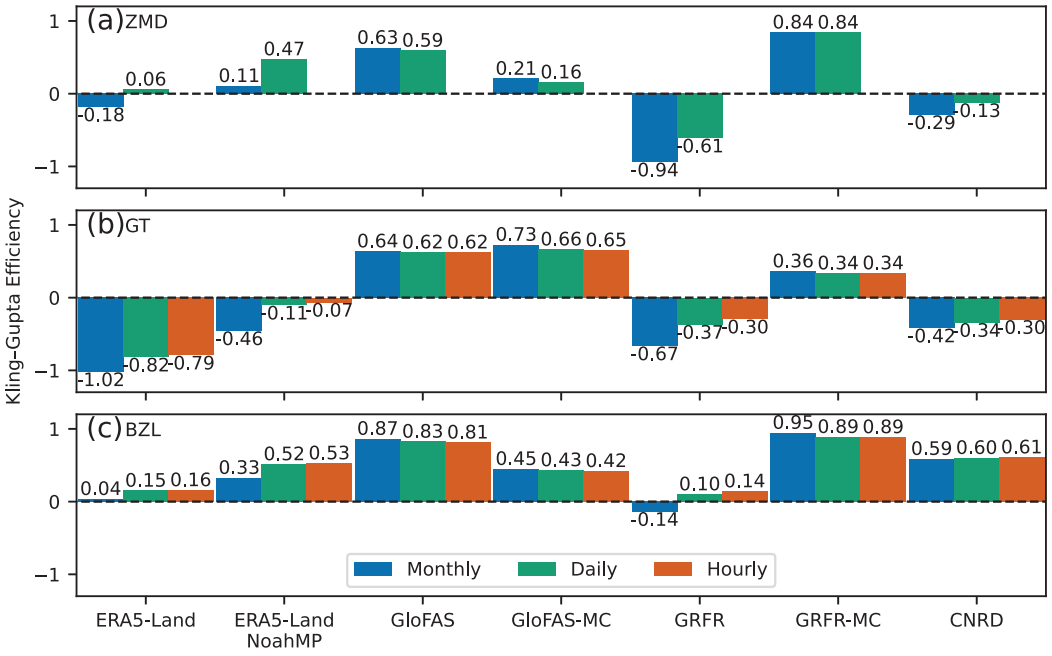

Figure 8. Kling–Gupta efficiency of the river discharge estimation: (**a**) the measures at the Zhimenda station; (**b**) the measures at the Gangtuo station; and (**c**) the measures at the Benzilan station.

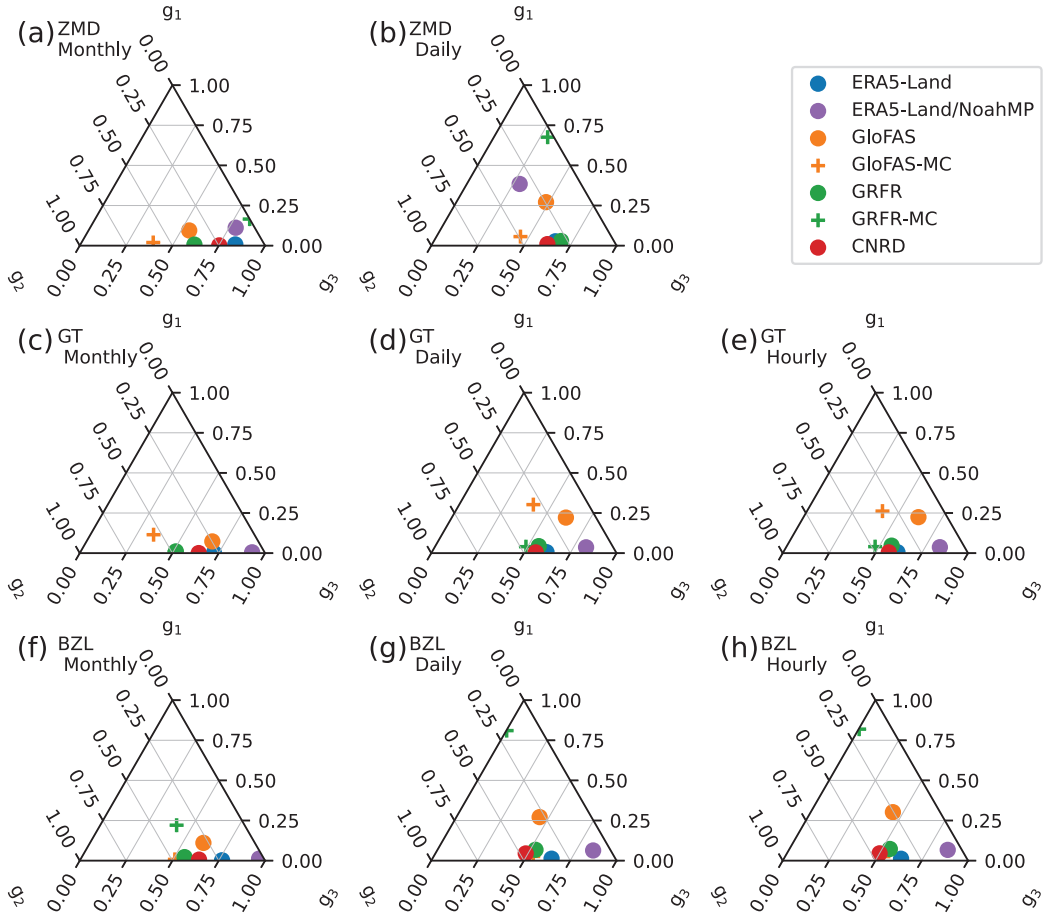

Figure 9. Ternary plot showing the relative contribution of the correlation coefficient (g_1), variability (g_2), and bias (g_3) to the deviation of the Kling–Gupta efficiency of simulated river discharge from one. The three rows of the plot represent the estimation at Zhimenda, Gangtuo, and Benzilan, respectively. The three columns of the plot represent the results of the monthly, daily, and hourly estimates, respectively.

4. Conclusions

This study presents a pilot intercomparison of several publicly available large-domain reanalysis datasets of runoff and river discharge in the Upper Jinsha River basin. The datasets under scrutiny include ERA5-Land, GloFAS, GRFR, and CNRD. To enhance the understanding of the effects of calibration, spatial resolution, and meteorological forcing on runoff estimation, a high-resolution runoff simulation has been incorporated into the comparison. The runoff from the examined datasets is rerouted on a high-resolution river network delineated from the 3-arcsecond MERIT-Hydro dataset. This rerouting aids in identifying the impacts of different river routing models and river network delineations on river discharge estimation. The estimated runoff and river discharge are compared with observations at three gauging stations—Zhimenda, Gangtuo, and Benzilan—spanning monthly, daily, and hourly time scales. The principal findings of this study are as follows:

- Among ERA5-Land, GloFAS, GRFR, and CNRD, GloFAS performs the best in river discharge estimation. The superior performance is attributed to the extensive calibration of model parameters rather than the quality of meteorological forcing. The other datasets, driven by similar meteorological forcing but using uncalibrated models—including ERA5-Land and a high-resolution simulation conducted in this study—did not perform on a par with GloFAS.

- Despite its high skill in river discharge estimation, GloFAS's runoff estimation is subpar. This discrepancy is attributable to the coarse resolution of GloFAS's routing grid. A 0.1° grid cell resolution is insufficient to accurately delineate the catchment area in the study region. Since river discharge is calculated by multiplying runoff by the catchment area, errors in catchment area estimation propagate to runoff estimates during the calibration of river discharge.
- GRFR demonstrates the best performance in runoff estimation at two out of the three stations examined. The high performance of GRFR runoff is attributed to its runoff characteristics-based calibration method. However, this machine learning-based method is more sensitive to the training dataset used than the traditional method employed by GloFAS. At Gangtuo, the station with steep terrain where observations are not included in the training dataset, GRFR's performance is subpar.
- GRFR's river discharge estimation is unexpectedly poor. GRFR substantially overestimates river discharge, a finding consistent with previous studies. Our study confirms that the overestimation is due to inadequate settings in river routing. By rerouting the discharge using GRFR runoff and the Muskingum–Cunge routing method, we closely reproduce the observed discharge patterns, achieving the best skill among all the examined datasets.

Given the scarcity of in situ observations in the Upper Jinsha River, reanalysis datasets are indispensable for these regions. The findings of this study have implications for both the utilization of existing reanalysis datasets and the future development of new ones. For users of reanalysis datasets, the datasets investigated in this study exhibit notable variances in the estimation of runoff and river discharge. Generally, GloFAS is found to be relatively more reliable for estimating river discharge, while GRFR shows more promise for runoff estimation. For users with prior modeling experience, rerouting the runoff data from GRFR can be beneficial.

For those involved in developing reanalysis datasets, calibrating land surface and hydrological models is a critical step in obtaining accurate runoff and river discharge estimates. The calibration process should be carefully designed to incorporate as many relevant observations as possible within the target region to better capture distinct runoff characteristics, especially for machine learning-based methods. In terms of river routing methods, the vector-based approach demonstrates advantages over the grid-based method. The vector-based method better represents the detailed geometry of the river network and accurately defines the catchment area, both of which are essential for achieving reliable runoff and river discharge estimations.

Author Contributions: Conceptualization, H.Z.; methodology, H.Z.; software, H.Z.; validation, S.C. and H.Y.; formal analysis, S.C. and H.Y.; investigation, S.C. and H.Y.; resources, S.C., H.Y. and H.Z.; data curation, S.C. and H.Y.; writing—original draft preparation, S.C. and H.Y.; writing—review and editing, S.C., H.Y., and H.Z.; visualization, S.C. and H.Y.; supervision, H.Z.; project administration, H.Z.; funding acquisition, H.Z. All authors have read and agreed to the published version of the manuscript.

Funding: This study is funded by China Three Gorges Corporation (contract Z5323020043) and the Natural Science Foundation of China (grants 42075165 and 42275178).

Data Availability Statement: The MERIT-Hydro dataset was obtained from https://hydro.iis.u-tokyo.ac.jp/~yamadai/MERIT_Hydro/ (accessed on 10 November 2024). The ERA5-Land dataset was obtained from https://cds.climate.copernicus.eu/datasets/reanalysis-era5-land (accessed on 10 November 2024). The GloFAS v4.0 dataset was obtained from https://ewds.climate.copernicus.eu/datasets/cems-glofas-historical (accessed on 10 November 2024). The GRFR v1.0 dataset was

obtained from https://www.reachhydro.org/home/records/grfr (accessed on 10 November 2024). The COMIDs used to extract the river discharge from GRFR are 43037713 for Zhimenda, 43046824 for Gangtuo, and 43066085 for Benzilan, respectively. The CNRD v1.0 dataset was obtained from https://doi.org/10.11888/Atmos.tpdc.272864 (accessed on 10 November 2024). The river discharge observations were obtained from the China Three Gorges Corporation; however, the authors do not have permission to share the data. The delineated river network, the aggregated runoff and simulated river discharge at the gauging stations, along with the scripts for figure generation used throughout this paper, can be found at the GitHub repository https://github.com/hzheng88/paper-2025-upperjsj-streamflow-intercomp (accessed on 3 February 2025).

Acknowledgments: The authors acknowledge the technical support provided by the National Large Scientific Infrastructure "Earth System Numerical Simulation Facility" (https://cstr.cn/31134.02.EL, accessed on 10 November 2024).

Conflicts of Interest: Authors Shuanglong Chen and Heng Yang were employed by the China Three Gorges Corporation. The remaining author declares that the research was conducted in the absence of any commercial or financial relationships that could be construed as a potential conflict of interest.

References

1. Hersbach, H.; Bell, B.; Berrisford, P.; Hirahara, S.; Horányi, A.; Muñoz-Sabater, J.; Nicolas, J.; Peubey, C.; Radu, R.; Schepers, D.; et al. The ERA5 global reanalysis. *Q. J. R. Meteorol. Soc.* **2020**, *146*, 1999–2049. [CrossRef]
2. Muñoz-Sabater, J.; Dutra, E.; Agustí-Panareda, A.; Albergel, C.; Arduini, G.; Balsamo, G.; Boussetta, S.; Choulga, M.; Harrigan, S.; Hersbach, H.; et al. ERA5-Land: A state-of-the-art global reanalysis dataset for land applications. *Earth Syst. Sci. Data* **2021**, *13*, 4349–4383. [CrossRef]
3. Alfieri, L.; Lorini, V.; Hirpa, F.A.; Harrigan, S.; Zsoter, E.; Prudhomme, C.; Salamon, P. A global streamflow reanalysis for 1980–2018. *J. Hydrol. X* **2020**, *6*, 100049. [CrossRef]
4. Harrigan, S.; Zsoter, E.; Alfieri, L.; Prudhomme, C.; Salamon, P.; Wetterhall, F.; Barnard, C.; Cloke, H.; Pappenberger, F. GloFAS-ERA5 operational global river discharge reanalysis 1979–present. *Earth Syst. Sci. Data* **2020**, *12*, 2043–2060. [CrossRef]
5. Yang, Y.; Pan, M.; Lin, P.; Beck, H.E.; Zeng, Z.; Yamazaki, D.; David, C.H.; Lu, H.; Yang, K.; Hong, Y.; et al. Global reach-level 3-hourly river flood reanalysis (1980–2019). *Bull. Am. Meteorol. Soc.* **2021**, *102*, E2086–E2105. [CrossRef]
6. Lin, P.; Pan, M.; Beck, H.E.; Yang, Y.; Yamazaki, D.; Frasson, R.; David, C.H.; Durand, M.; Pavelsky, T.M.; Allen, G.H.; et al. Global reconstruction of naturalized river flows at 2.94 million reaches. *Water Resour. Res.* **2019**, *55*, 6499–6516. [CrossRef]
7. Cosgrove, B.; Gochis, D.; Flowers, T.; Dugger, A.; Ogden, F.; Graziano, T.; Clark, E.; Cabell, R.; Casiday, N.; Cui, Z.; et al. NOAA's National Water Model: Advancing operational hydrology through continental-scale modeling. *J. Am. Water Resour. Assoc.* **2024**, *60*, 247–272. [CrossRef]
8. Najafi, H.; Shrestha, P.K.; Rakovec, O.; Apel, H.; Vorogushyn, S.; Kumar, R.; Thober, S.; Merz, B.; Samaniego, L. High-resolution impact-based early warning system for riverine flooding. *Nat. Commun.* **2024**, *15*, 3726. [CrossRef]
9. Gou, J.; Miao, C.; Samaniego, L.; Xiao, M.; Wu, J.; Guo, X. CNRD v1.0: A high-quality natural runoff dataset for hydrological and climate studies in china. *Bull. Am. Meteorol. Soc.* **2021**, *102*, E929–E947. [CrossRef]
10. Miao, C.; Gou, J.; Fu, B.; Tang, Q.; Duan, Q.; Chen, Z.; Lei, H.; Chen, J.; Guo, J.; Borthwick, A.G.L.; et al. High-quality reconstruction of China's natural streamflow. *Sci. Bull.* **2022**, *67*, 547–556. [CrossRef]
11. Feng, D.; Gleason, C.J.; Lin, P.; Yang, X.; Pan, M.; Ishitsuka, Y. Recent changes to Arctic river discharge. *Nat. Commun.* **2021**, *12*, 6917. [CrossRef] [PubMed]
12. Collins, E.L.; David, C.H.; Riggs, R.; Allen, G.H.; Pavelsky, T.M.; Lin, P.; Pan, M.; Yamazaki, D.; Meentemeyer, R.K.; Sanchez, G.M. Global patterns in river water storage dependent on residence time. *Nat. Geosci.* **2024**, *17*, 433–439. [CrossRef]
13. Liu, M.; Raymond, P.A.; Lauerwald, R.; Zhang, Q.; Trapp-Müller, G.; Davis, K.L.; Moosdorf, N.; Xiao, C.; Middelburg, J.J.; Bouwman, A.F.; et al. Global riverine land-to-ocean carbon export constrained by observations and multi-model assessment. *Nat. Geosci.* **2024**, *17*, 896–904. [CrossRef]
14. Coughlan de Perez, E.; van den Hurk, B.; van Aalst, M.K.; Amuron, I.; Bamanya, D.; Hauser, T.; Jongma, B.; Lopez, A.; Mason, S.; Mendler de Suarez, J.; et al. Action-based flood forecasting for triggering humanitarian action. *Hydrol. Earth Syst. Sci.* **2016**, *20*, 3549–3560. [CrossRef]
15. Sun, Q.; Miao, C.; Duan, Q.; Ashouri, H.; Sorooshian, S.; Hsu, K.L. A review of global precipitation data sets: Data sources, estimation, and intercomparisons. *Rev. Geophys.* **2018**, *56*, 79–107. [CrossRef]

16. Henn, B.; Newman, A.J.; Livneh, B.; Daly, C.; Lundquist, J.D. An assessment of differences in gridded precipitation datasets in complex terrain. *J. Hydrol.* **2018**, *556*, 1205–1219. [CrossRef]
17. Renard, B.; Kavetski, D.; Kuczera, G.; Thyer, M.; Franks, S.W. Understanding predictive uncertainty in hydrologic modeling: The challenge of identifying input and structural errors. *Water Resour. Res.* **2010**, *46*, W05521. [CrossRef]
18. Bai, F.; Wei, Z.; Wei, N.; Lu, X.; Yuan, H.; Zhang, S.; Liu, S.; Zhang, Y.; Li, X.; Dai, Y. Global assessment of atmospheric forcing uncertainties in the Common Land Model 2024 simulations. *J. Geophys. Res. Atmos.* **2024**, *129*, e2024JD041520. [CrossRef]
19. Butts, M.B.; Payne, J.T.; Kristensen, M.; Madsen, H. An evaluation of the impact of model structure on hydrological modelling uncertainty for streamflow simulation. *J. Hydrol.* **2004**, *298*, 242–266. [CrossRef]
20. Haddeland, I.; Matheussen, B.V.; Lettenmaier, D.P. Influence of spatial resolution on simulated streamflow in a macroscale hydrologic model. *Water Resour. Res.* **2002**, *38*, 29-1–29-10. [CrossRef]
21. Barnhart, T.B.; Putman, A.L.; Heldmyer, A.J.; Rey, D.M.; Hammond, J.C.; Driscoll, J.M.; Sexstone, G.A. Evaluating distributed snow model resolution and meteorology parameterizations against streamflow observations: Finer is not always better. *Water Resour. Res.* **2024**, *60*, e2023WR035982. [CrossRef]
22. Li, L.; Bisht, G.; Leung, L.R. Spatial heterogeneity effects on land surface modeling of water and energy partitioning. *Geosci. Model Dev.* **2022**, *15*, 5489–5510. [CrossRef]
23. Zheng, H.; Yang, Z.L.; Lin, P.; Wei, J.; Wu, W.Y.; Li, L.; Zhao, L.; Wang, S. On the sensitivity of the precipitation partitioning into evapotranspiration and runoff in land surface parameterizations. *Water Resour. Res.* **2019**, *55*, 95–111. [CrossRef]
24. Zheng, H.; Fei, W.; Yang, Z.L.; Wei, J.; Zhao, L.; Li, L.; Wang, S. An ensemble of 48 physically perturbed model estimates of the 1/8° terrestrial water budget over the conterminous United States, 1980–2015. *Earth Syst. Sci. Data* **2023**, *15*, 2755–2780. [CrossRef]
25. Li, J.; Chen, F.; Lu, X.; Gong, W.; Zhang, G.; Gan, Y. Quantifying contributions of uncertainties in physical parameterization schemes and model parameters to overall errors in noah-mp dynamic vegetation modeling. *J. Adv. Model. Earth Syst.* **2020**, *12*, e2019MS001914. [CrossRef]
26. Saxe, S.; Farmer, W.; Driscoll, J.; Hogue, T.S. Implications of model selection: A comparison of publicly available, conterminous US-extent hydrologic component estimates. *Hydrol. Earth Syst. Sci.* **2021**, *25*, 1529–1568. [CrossRef]
27. Beck, H.E.; van Dijk, A.I.J.M.; de Roo, A.; Dutra, E.; Fink, G.; Orth, R.; Schellekens, J. Global evaluation of runoff from 10 state-of-the-art hydrological models. *Hydrol. Earth Syst. Sci.* **2017**, *21*, 2881–2903. [CrossRef]
28. Fry, L.M.; Gronewold, A.D.; Fortin, V.; Buan, S.; Clites, A.H.; Luukkonen, C.; Holtschlag, D.; Diamond, L.; Hunter, T.; Seglenieks, F.; et al. The Great Lakes Runoff Intercomparison Project Phase 1: Lake Michigan (GRIP-M). *J. Hydrol.* **2014**, *519*, 3448–3465. [CrossRef]
29. Mai, J.; Shen, H.; Tolson, B.A.; Gaborit, E.; Arsenault, R.; Craig, J.R.; Fortin, V.; Fry, L.M.; Gauch, M.; Klotz, D.; et al. The Great Lakes Runoff Intercomparison Project Phase 4: the Great Lakes (GRIP-GL). *Hydrol. Earth Syst. Sci.* **2022**, *26*, 3537–3572. [CrossRef]
30. Ahmed, M.I.; Stadnyk, T.; Pietroniro, A.; Awoye, H.; Bajracharya, A.; Mai, J.; Tolson, B.A.; Shen, H.; Craig, J.R.; Gervais, M.; et al. Learning from hydrological models' challenges: A case study from the Nelson basin model intercomparison project. *J. Hydrol.* **2023**, *623*, 129820. [CrossRef]
31. Henderson-Sellers, A.; Yang, Z.L.; Dickinson, R.E. The Project for Intercomparison of Land-surface Parameterization Schemes. *Bull. Am. Meteorol. Soc.* **1993**, *74*, 1335–1349. [CrossRef]
32. van den Hurk, B.; Kim, H.; Krinner, G.; Seneviratne, S.I.; Derksen, C.; Oki, T.; Douville, H.; Colin, J.; Ducharne, A.; Cheruy, F.; et al. LS3MIP (v1.0) contribution to CMIP6: The Land Surface, Snow and Soil moisture Model Intercomparison Project – aims, setup and expected outcome. *Geosci. Model Dev.* **2016**, *9*, 2809–2832. [CrossRef]
33. Reed, S.; Koren, V.; Smith, M.; Zhang, Z.; Moreda, F.; Seo, D.J.; DMIP Participants. Overall Distributed Model Intercomparison Project results. *J. Hydrol.* **2004**, *298*, 27–60. [CrossRef]
34. Smith, M.B.; Seo, D.J.; Koren, V.I.; Reed, S.M.; Zhang, Z.; Duan, Q.; Moreda, F.; Cong, S. The Distributed Model Intercomparison Project (DMIP): motivation and experiment design. *J. Hydrol.* **2004**, *298*, 4–26. [CrossRef]
35. Tijerina, D.; Condon, L.; FitzGerald, K.; Dugger, A.; O'Neill, M.M.; Sampson, K.; Gochis, D.; Maxwell, R. Continental hydrologic intercomparison project, phase 1: A large-scale hydrologic model comparison over the continental united states. *Water Resour. Res.* **2021**, *57*, e2020WR028931. [CrossRef]
36. Yamazaki, D.; Ikeshima, D.; Sosa, J.; Bates, P.D.; Allen, G.H.; Pavelsky, T.M. MERIT Hydro: A high-resolution global hydrography map based on latest topography dataset. *Water Resour. Res.* **2019**, *55*, 5053–5073. [CrossRef]
37. Yamazaki, D.; Ikeshima, D.; Tawatari, R.; Yamaguchi, T.; O'Loughlin, F.; Neal, J.C.; Sampson, C.C.; Kanae, S.; Bates, P.D. A high-accuracy map of global terrain elevations. *Geophys. Res. Lett.* **2017**, *44*, 5844–5853. [CrossRef]
38. Boussetta, S.; Balsamo, G.; Arduini, G.; Dutra, E.; McNorton, J.; Choulga, M.; Agustí-Panareda, A.; Beljaars, A.; Wedi, N.; Munõz-Sabater, J.; et al. ECLand: The ECMWF land surface modelling system. *Atmosphere* **2021**, *12*, 723. [CrossRef]

39. Balsamo, G.; Beljaars, A.; Scipal, K.; Viterbo, P.; van den Hurk, B.; Hirschi, M.; Betts, A.K. A revised hydrology for the ECMWF model: Verification from field site to terrestrial water storage and impact in the Integrated Forecast System. *J. Hydrometeorol.* **2009**, *10*, 623–643. [CrossRef]
40. Knijff, J.M.V.D.; Younis, J.; Roo, A.P.J.D. LISFLOOD: A GIS-based distributed model for river basin scale water balance and flood simulation. *Int. J. Geogr. Inf. Sci.* **2010**, *24*, 189–212. [CrossRef]
41. Hirpa, F.A.; Salamon, P.; Beck, H.E.; Lorini, V.; Alfieri, L.; Zsoter, E.; Dadson, S.J. Calibration of the Global Flood Awareness System (GloFAS) using daily streamflow data. *J. Hydrol.* **2018**, *566*, 595–606. [CrossRef] [PubMed]
42. Liang, X.; Lettenmaier, D.P.; Wood, E.F.; Burges, S.J. A simple hydrologically based model of land surface water and energy fluxes for general circulation models. *J. Geophys. Res. Atmos.* **1994**, *99*, 14415–14428. [CrossRef]
43. Beck, H.E.; Wood, E.F.; Pan, M.; Fisher, C.K.; Miralles, D.G.; van Dijk, A.I.J.M.; McVicar, T.R.; Adler, R.F. MSWEP V2 global 3-hourly 0.1° precipitation: Methodology and quantitative assessment. *Bull. Am. Meteorol. Soc.* **2019**, *100*, 473–500. [CrossRef]
44. Yang, Y.; Pan, M.; Beck, H.E.; Fisher, C.K.; Beighley, R.E.; Kao, S.C.; Hong, Y.; Wood, E.F. In quest of calibration density and consistency in hydrologic modeling: Distributed parameter calibration against streamflow characteristics. *Water Resour. Res.* **2019**, *55*, 7784–7803. [CrossRef]
45. Beck, H.E.; de Roo, A.; van Dijk, A.I.J.M. Global maps of streamflow characteristics based on observations from several thousand catchments. *J. Hydrometeorol.* **2015**, *16*, 1478–1501. [CrossRef]
46. David, C.H.; Maidment, D.R.; Niu, G.Y.; Yang, Z.L.; Habets, F.; Eijkhout, V. River network routing on the NHDPlus dataset. *J. Hydrometeorol.* **2011**, *12*, 913–934. [CrossRef]
47. Lin, P.; Pan, M.; Wood, E.F.; Yamazaki, D.; Allen, G.H. A new vector-based global river network dataset accounting for variable drainage density. *Sci. Data* **2021**, *8*, 28. [CrossRef]
48. He, J.; Yang, K.; Tang, W.; Lu, H.; Qin, J.; Chen, Y.; Li, X. The first high-resolution meteorological forcing dataset for land process studies over China. *Sci. Data* **2020**, *7*, 25. [CrossRef]
49. Samaniego, L.; Bárdossy, A.; Kumar, R. Streamflow prediction in ungauged catchments using copula-based dissimilarity measures. *Water Resour. Res.* **2010**, *46*, W02506. [CrossRef]
50. Niu, G.Y.; Yang, Z.L.; Mitchell, K.E.; Chen, F.; Ek, M.B.; Barlage, M.; Kumar, A.; Manning, K.; Niyogi, D.; Rosero, E.; et al. The community Noah land surface model with multiparameterization options (Noah-MP): 1. Model description and evaluation with local-scale measurements. *J. Geophys. Res. Atmos.* **2011**, *116*, D12109. [CrossRef]
51. Read, L.K.; Yates, D.N.; McCreight, J.M.; Rafieeinasab, A.; Sampson, K.; Gochis, D.J. Development and evaluation of the channel routing model and parameters within the National Water Model. *JAWRA J. Am. Water Resour. Assoc.* **2023**, *59*, 1051–1066. [CrossRef]
52. Gupta, H.V.; Kling, H.; Yilmaz, K.K.; Martinez, G.F. Decomposition of the mean squared error and NSE performance criteria: Implications for improving hydrological modelling. *J. Hydrol.* **2009**, *377*, 80–91. [CrossRef]
53. Allen, G.H.; David, C.H.; Andreadis, K.M.; Hossain, F.; Famiglietti, J.S. Global estimates of river flow wave travel times and implications for low-latency satellite data. *Geophys. Res. Lett.* **2018**, *45*, 7551–7560. [CrossRef]
54. Bian, Q.; Xu, Z.; Zhao, L.; Zhang, Y.F.; Zheng, H.; Shi, C.; Zhang, S.; Xie, C.; Yang, Z.L. Evaluation and intercomparison of multiple snow water equivalent products over the Tibetan Plateau. *J. Hydrometeorol.* **2019**, *20*, 2043–2055. [CrossRef]
55. Bian, Q.; Xu, Z.; Zheng, H.; Li, K.; Liang, J.; Fei, W.; Shi, C.; Zhang, S.; Yang, Z.L. Multiscale changes in snow over the Tibetan Plateau during 1980–2018 represented by reanalysis data sets and satellite observations. *J. Geophys. Res. Atmos.* **2020**, *125*, e2019JD031914. [CrossRef]
56. Sun, H.; Su, F.; Yao, T.; He, Z.; Tang, G.; Huang, J.; Zheng, B.; Meng, F.; Ou, T.; Chen, D. General overestimation of ERA5 precipitation in flow simulations for High Mountain Asia basins. *Environ. Res. Commun.* **2021**, *3*, 121003. [CrossRef]
57. Wang, X.; Zhou, J.; Ma, J.; Luo, P.; Fu, X.; Feng, X.; Zhang, X.; Jia, Z.; Wang, X.; Huang, X. Evaluation and comparison of reanalysis data for runoff simulation in the data-scarce watersheds of alpine regions. *Remote Sens.* **2024**, *16*, 751. [CrossRef]
58. Tu, T.; Wang, J.; Zhao, G.; Zhao, T.; Dong, X. Scaling from global to regional river flow with global hydrological models: Choice matters. *J. Hydrol.* **2024**, *633*, 130960. [CrossRef]
59. Cui, H.; Huang, C. Accuracy evaluation of multiple runoff products: A case study of the middle reaches of the Yellow River. *Water* **2025**, *17*, 461. [CrossRef]
60. Beven, K.J. A history of the concept of time of concentration. *Hydrol. Earth Syst. Sci.* **2020**, *24*, 2655–2670. [CrossRef]

water

MDPI

Article

Streamflow Prediction with Time-Lag-Informed Random Forest and Its Performance Compared to SWAT in Diverse Catchments

Desalew Meseret Moges [1], Holger Virro [1], Alexander Kmoch [1], Raj Cibin [2], Rohith A. N. Rohith [3], Alberto Martínez-Salvador [4], Carmelo Conesa-García [5] and Evelyn Uuemaa [1,*]

[1] Department of Geography, Institute of Ecology and Earth Sciences, University of Tartu, Vanemuise 46, 51003 Tartu, Estonia; desalew.moges@ut.ee (D.M.M.); holger.virro@ut.ee (H.V.); alexander.kmoch@ut.ee (A.K.)
[2] Department of Civil and Environmental Engineering, The Pennsylvania State University, University Park, PA 16802, USA; czr58@psu.edu
[3] Department of Agricultural and Biological Engineering, The Pennsylvania State University, University Park, PA 16802, USA; rfa5378@psu.edu
[4] Research Group on Erosion and Desertification in Mediterranean Environments, University of Murcia, Campus de La Merced, 30001 Murcia, Spain; aa.martinezsalvador@um.es
[5] Department of Geography, University of Murcia, Campus de La Merced, 30001 Murcia, Spain; cconesa@um.es
* Correspondence: evelyn.uuemaa@ut.ee

Abstract: This study introduces a time-lag-informed Random Forest (RF) framework for streamflow time-series prediction across diverse catchments and compares its results against SWAT predictions. We found strong evidence of RF's better performance by adding historical flows and time-lags for meteorological values over using only actual meteorological values. On a daily scale, RF demonstrated robust performance (Nash–Sutcliffe efficiency [*NSE*] > 0.5), whereas SWAT generally yielded unsatisfactory results (*NSE* < 0.5) and tended to overestimate daily streamflow by up to 27% (*PBIAS*). However, SWAT provided better monthly predictions, particularly in catchments with irregular flow patterns. Although both models faced challenges in predicting peak flows in snow-influenced catchments, RF outperformed SWAT in an arid catchment. RF also exhibited a notable advantage over SWAT in terms of computational efficiency. Overall, RF is a good choice for daily predictions with limited data, whereas SWAT is preferable for monthly predictions and understanding hydrological processes in depth.

Keywords: hydrological modeling; machine learning; process-based models; green AI; computational efficiency

1. Introduction

Accurate and timely streamflow estimation in watersheds and water resource systems is essential for efficient and effective water resource management [1–3]. However, the quickly changing nature of the flow, shaped by ecohydrological and climate changes coupled with human activities, poses a considerable challenge for flow prediction [2–4]. To mitigate this problem, several hydrological models, ranging from simple empirical models to sophisticated process-based models, have been developed and extensively employed to effectively simulate a wide range of hydrological processes, including streamflow [5–10]. The Soil and Water Assessment Tool (SWAT) is a widely utilized process-based eco-hydrological model that integrates hydrological processes based on the water-balance principle [11]. Several studies have demonstrated the reliability of SWAT for accurately depicting spatial information and efficiently modeling diverse hydrological processes across a range of watershed scales [7,9,12,13].

Despite its widespread adoption, SWAT has faced criticism for its demanding data requirements, which make hydrological modeling computationally expensive and challenging [10,14–16]. The inherent complexity of its process-based approach also poses

difficulties for users with limited hydrologic expertise [2]. In addition, its heavy reliance on detailed soil and land use information presents a significant challenge, particularly in regions with limited data availability [14,17]. The calibration of multiple parameters in SWAT is a complex process, and introduces uncertainties in the model's outcomes [15] and the potential for misleading conclusions due to equifinality, in which different parameter sets yield similar results [18]. SWAT also has limitations in representing groundwater systems accurately, as it lacks the ability to account for geological information and neglects inter-basin groundwater flows [18,19]. Furthermore, its shortcomings extend to an inability to capture non-linear flows [15] and to model hydrological processes in mid- and high-latitude regions and arid areas [20]. However, using physics-based models such as SWAT continues to be a crucial method for comprehending the fundamental physical mechanisms that govern hydrological fluctuations.

In recent years, the use of machine learning (ML) techniques including the Random Forest (RF) model [21–25], support-vector regression [21,26,27], and deep learning such as artificial neural network [28,29], long-short-term-memory (LSTM) neural networks [30,31], and extreme gradient-boosting neural networks [32–34], have gained significant attention among hydrologists as alternatives to traditional process-based models [15,35]. ML methods are capable of capturing non-linear processes numerically with no knowledge of the underlying physical processes involved [1,36–39]. Moreover, ML models can identify relationships between input and output variables, which lead to inherent errors in streamflow estimates [2,35]. Despite the potentially time-consuming training phases, ML predictions are faster than process-based models [35]. In addition, ML models pre-trained on data from diverse basins can be fine-tuned for specific basins through transfer learning.

Previous studies have mainly shown that LSTM models perform very well in flow prediction [30,31,37–40]. LSTM models can also store and regulate information over time [41,42], making these models particularly suitable for simulating the memory effects of different hydrological variables with short-term and long-term dependencies. However, LSTM, as a deep learning method, is computationally quite expensive and produces results that are not easily explainable. This is problematic because, in modeling natural processes, explainability is essential so that model users can understand the outputs and validate them against physical processes.

Among regression-based models, RF has gained popularity in flow prediction due to its advantages in terms of visualization and interpretation of the model structure, as well as its computational efficiency [43–47]. Shortridge et al. [46] showed that RF can also outperform artificial neural networks but pointed out that model predictions have too-high uncertainty under extreme weather conditions. Tongal and Booij [47] observed good performance of RF in predicting streamflow for four rivers in the United States. Similarly, Fernández-Delgado et al. [48] compared 179 learning models from 17 families using 121 classification datasets, and found that RF performed best in terms of its error magnitude.

Despite its notable strengths, RF lacks the inherent capability to consider ordered sequences or the time-dependent structure of data, which poses challenges in time-series forecasting [49,50]. Unlike other ML or deep learning models, such as LSTM, which capture long-term dependencies and complex patterns in hydrological time series [37,51], RF has a limited ability to capture temporal dependencies.

Our study aimed to overcome these limitations of RF by incorporating covariates that explicitly account for temporal dependencies into the RF model. We introduced time lags, rolling aggregates, and calendar-based variables like day and month of the year, which allow the model to capture relevant temporal patterns and seasonal variations in the data. These modifications aimed to improve the predictive power of RF in time-series-based streamflow forecasting by simulating the temporal awareness inherent in models such as LSTM. In addition, we aimed to compare the performance of RF with SWAT more rigorously. Previous comparisons have mainly centered around aspects like forecasting sediment yield and soil erosion [15,52,53], evaluating aquatic ecosystems [54], and assessing the impact

of climate change on stream ecology [55]. This highlights the need for a comparison that specifically addresses streamflow prediction. Moreover, previous studies that compared SWAT and RF models for streamflow prediction were often restricted to catchments with similar climates and topographic conditions, and typically focused on daily or monthly time scales. Therefore, the second aim of this study was to compare the predictive capabilities of RF and SWAT in simulating streamflow on daily and monthly time steps across four catchments with very different climatic and topographic conditions.

Specifically, our study answered the following research questions: (1) How can RF's limitations in handling time-series data be addressed? (2) How well does the time-lag-adjusted RF perform compared to the process-based model SWAT among different catchments? (3) Which model is more computationally efficient? The last research question is particularly relevant in light of efforts to reduce the carbon footprint of AI to achieve "green AI" [56,57].

2. Study Areas

We used four study catchments with different sizes, land use, topography, and climatic conditions as our study areas: Argos (Spain), Porijõgi (Estonia), Rib (Ethiopia), and Bald Eagle (USA) (Figure 1).

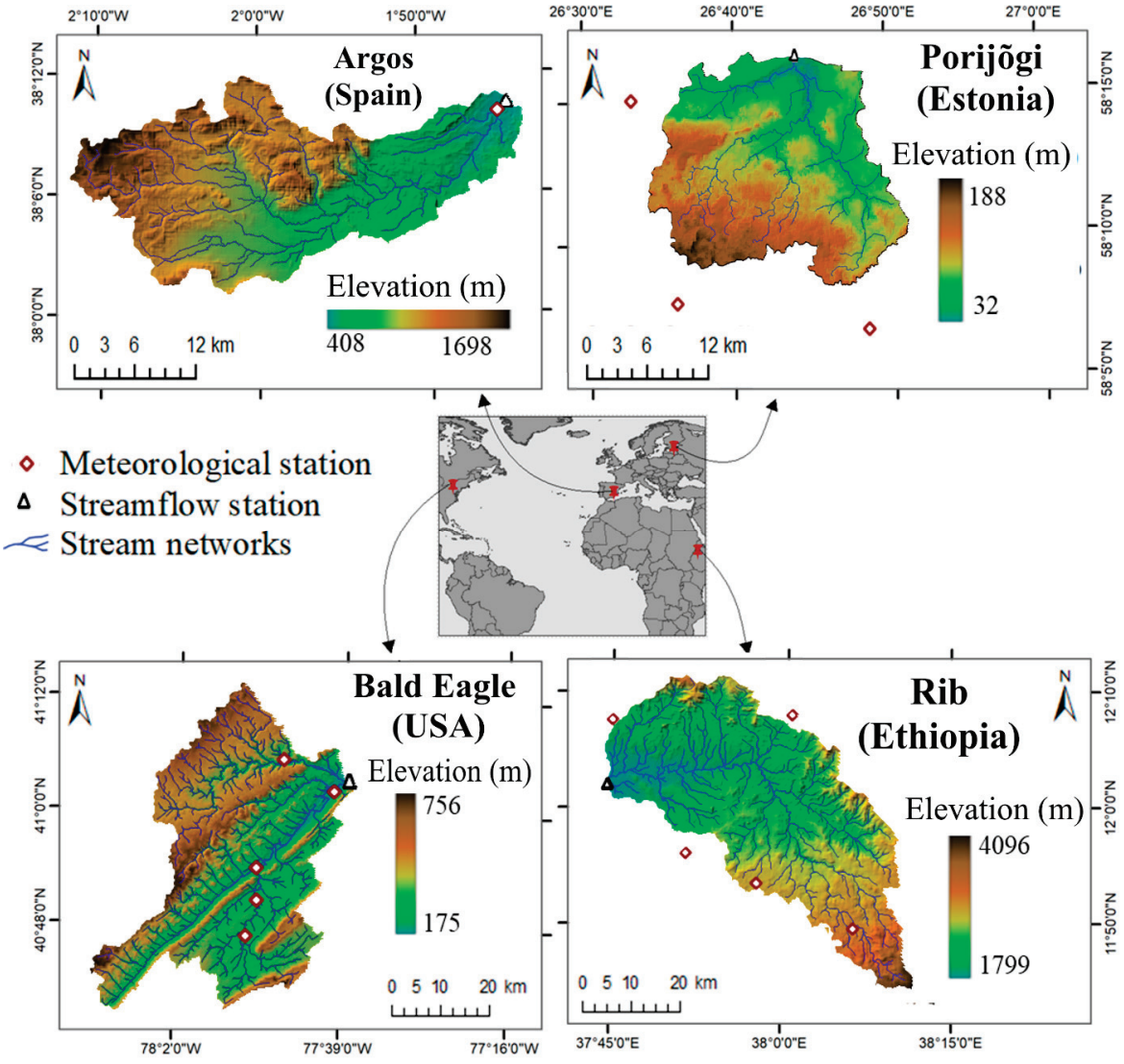

Figure 1. Locations of the study areas.

The Argos catchment, covering an area of 448 km^2, is situated in southeastern Spain at elevations ranging from 408 to 1698 m above sea level (m a.s.l.). The catchment primarily comprises calcic Xerosols, although a range of soil types can be found [58]. The catchment is characterized by a semi-arid climate with mean annual precipitation between 345 and 440 mm, and an average monthly temperature that typically ranges from 11 to 16 °C [58].

The Porijõgi catchment, situated in southern Estonia, spans an area of 235 km^2 at elevations ranging from 32 to 188 m a.s.l. Agriculture and forests account for 45 and 49% of the total area, respectively [59]. The predominant upland soils are podzoluvisols, planosols, and podzols with loamy sand or fine sandy loam texture and a surface soil organic matter content of 1.6 to 1.9% (Kmoch et al., 2021). The mean annual precipitation and temperature are 678 mm and 6.4 °C, respectively [60].

The Rib catchment, spanning 1293 km^2, is situated in the northwestern Ethiopian highlands, with an elevation range of 1799 to 4096 m a.s.l. The dominant land use is cropland, accounting for more than 85% of the area [61]. The catchment contains various soil types, including Luvisols, Vertisols, Leptosols, and Regosols, which cover more than 80% of the land [62]. The mean annual precipitation and temperature are 1502 mm and 15.6 °C, respectively [63].

The Bald Eagle–Spring Creek catchment (1446 km^2) lies in Pennsylvania State, USA, spanning Center and Clinton counties. Its elevation ranges between 175 and 756 m a.s.l, and the physiographic province comprises valley, ridge, and Appalachian plateau topography. To simplify the modeling, we restricted the catchment boundary to the sub-basin, including the streamflow gauge location farthest downstream. Loam and fine loam soils are predominant, and the catchment experiences an average annual precipitation of around 1000 mm and a mean annual temperature of approximately 10 °C [64].

3. Materials and Methods

3.1. RF Model

RF is a supervised ensemble-learning algorithm that consists of many regression trees that together form the "forest" [65]. RF uses a set of observed input training data to predict the mean of the decision-tree ensemble for new input data [45]. The model minimizes over-fitting and statistical uncertainty by using the bootstrap aggregation (bagging) technique to build many decision trees by randomly sampling the observed dataset with replacement [47,66]. As a result, the trees have low bias and high variance, which leads to a more robust overall model after averaging the predictions of the individual regression trees [67,68].

We developed six RF models for each watershed (three for daily and three for monthly flow prediction) using different combinations of predictors. The predictor variables (features) we utilized were derived from datasets containing daily precipitation, streamflow, maximum temperature, and minimum temperature (Table 1). Unlike deep learning methods such as LSTM, RF generally has no internal concept to model or to explain ordered data sequences, such as time steps. One way to model temporal dependencies in time series, such as the sequence of streamflow days and weeks before a focal time, is to create these explicitly as individual covariates. Here, we employed various time lags, rolling aggregates of previous observations, and numeric representations of the day or month of the year alongside the actual measurement value at each time step to let RF learn the time sequences and improve its predictive capabilities. In the context of our RF model, a time lag refers to using past measurements of predictor variables (precipitation, temperature, and streamflow) from previous days or months to predict future streamflow. Rolling aggregates refer to using summary statistics (mean, maximum, and minimum) of variables over a certain period of time (e.g., 7 days or 3 months) as additional predictors. Day and month of the year represent the calendar time at which a particular measurement was recorded.

For daily prediction, we focused on time lags of 1 to 7 days, with a 1-day lead time, following Rasouli et al.'s [69] recommendation that shorter lead times are more effective for local observation-based predictors. For monthly prediction, we extended the time

lag window to 12 months with a 1-month lead time to capture longer-term patterns and dependencies (Figure 2). We also used rolling aggregates as predictor variables, encompassing the previous 7 to 28 days with a 7-day gap for daily steps, and 3 to 12 months with a 3-month gap for monthly steps. Consequently, we created different feature sets (predictor combinations), which resulted in three daily models (DM1, DM2, and DM3) and three monthly models (MM1, MM2, and MM3). Streamflow was not used as a predictor in DM1 and MM1. The precipitation and temperature were excluded from DM2 and MM2. Finally, DM3 and MM3 used all predictors from DM1 and MM1, respectively, while also including the streamflow measurement for the corresponding day or month. We allocated the observed streamflow data into two datasets: 50% for model development (training) and 50% for model evaluation (testing). The number of trees used to train each of the RF models was set to 100. The RF models were built using the Scikit-learn Python package version 1.5.2 [70].

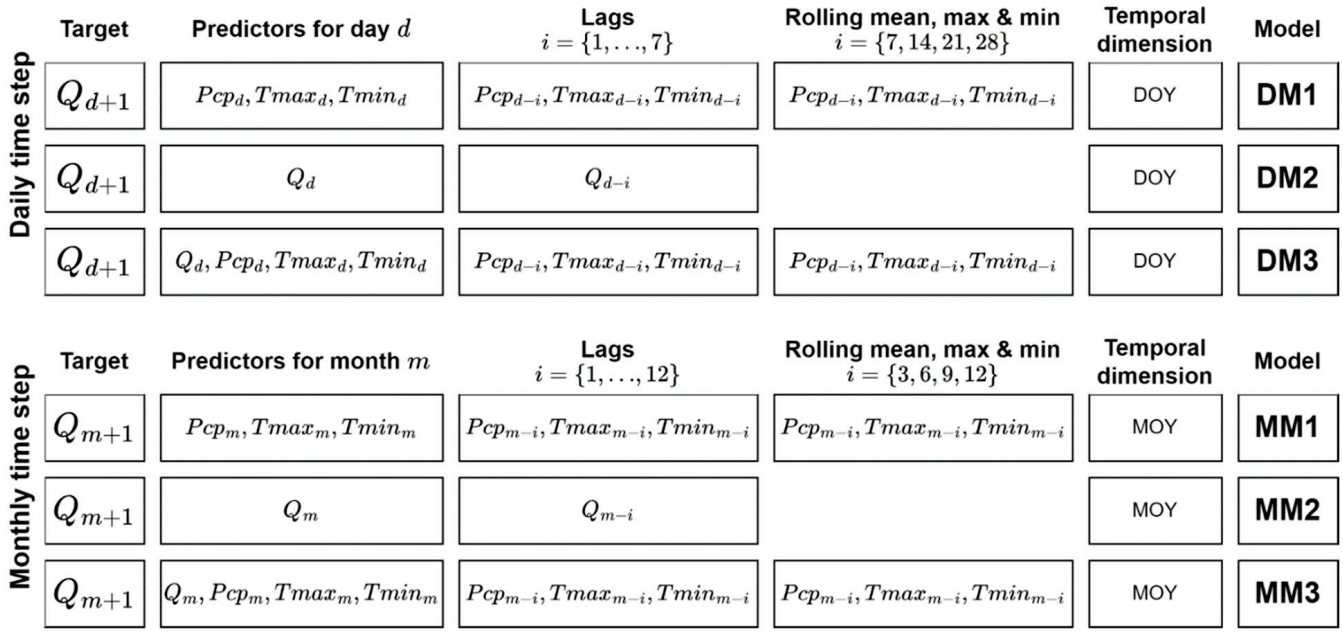

Figure 2. Overview of the three daily and three monthly Random Forest models with different feature sets. Abbreviations: *DM1*, *DM2*, and *DM3*, RF models at a daily time step; *DOY*, numeric day of the year; *i*, lag days or months; *MM1*, *MM2*, and *MM3*, Random Forest models at a monthly time step; *MOY*, numeric month of the year; Pcp_d, average precipitation on day *d*; Pcp_m, average precipitation in month *m*; Q_d, average streamflow on day *d*; Q_{d+1}, streamflow prediction for the next day; Q_m, average streamflow in month *m*; Q_{m+1}, streamflow prediction for the next month; $Tmax_d$ and $Tmin_d$, maximum and minimum air temperature on day *d*; $Tmax_m$ and $Tmin_m$, maximum and minimum air temperature in month *m*.

3.2. SWAT Model

SWAT is a hydrological model that operates at different time steps and regulates the hydrological processes in a catchment to quantify their rate of change [11]. The model uses a water-balance equation that includes factors such as precipitation, surface runoff, percolation, evapotranspiration, lateral flow, and baseflow [71]. The model requires input data such as a digital elevation model (DEM), soil, land use, and hydro-climatic data. We used the same global land use, soil, and DEM data sources for all catchments (Table 1). These environmental factors greatly influence SWAT's performance by affecting hydrological processes such as evapotranspiration, runoff, infiltration, and nutrient dynamics, which in turn enhance its simulation accuracy across different conditions (refer to [72] for detailed insights on their impact and spatial variability within the studied watershed). We obtained the daily hydro-meteorological data records (streamflow, precipitation, maximum

temperature, and minimum temperature; Figure S1) from the hydro-meteorological service centers of the studied countries. We used the QSWAT3 interface [73] with QGIS 3.16 to build one model for each catchment. We simulated the models at daily and monthly time steps and calibrated and validated the models using the SUFI-2 method in the SWAT-CUP software version 5.1.3 [74]. Hereafter, we will use the terms "training" and "testing" to refer to the calibration and validation phases of SWAT to maintain consistency with the RF model nomenclature. For all catchments, we utilized the same period of 14 years, with the initial 2 years designated for model warmup and the remaining years evenly divided between training and testing phases (Tables S1 and S2).

Table 1. Summary of the data used in this study. Abbreviations: DEM, digital elevation model; ESA, European Space Agency.

Dataset	Description	Sources
Elevation data	AW3D30 DEM at 30 m spatial resolution, released in 2022	JAXA [75]
Landcover map	ESA land cover data for 2020 at 10 m spatial resolution	Zanaga et al. [76]
Soil map	Harmonized World Soil Database v1.2 for 2008 at 1 km spatial resolution	Fischer et al. [77]
Hydro-meteorological data	Daily streamflow, precipitation, maximum temperature, and minimum temperature	Hydro-meteorological service centers of the studied countries

3.3. Model Evaluation Metrics

We assessed the predictive capacity of the models using three metrics: the Nash–Sutcliffe efficiency coefficient (*NSE*) [78], normalized root-mean-squared errors (*NRMSE*), and percentage of bias (*PBIAS*) [79] (Table 2). *NSE* measures the agreement between observed and predicted values, with a perfect fit indicated by a value of 1 and a value exceeding 0.5 considered acceptable [80]. *NRMSE* offers a standardized measure of accuracy by normalizing the error and accounting for data variability. We selected *NRMSE* over *RMSE* to facilitate comparisons across different catchments (i.e., catchments with varying ranges of parameter values). *PBIAS* quantifies the average tendency of simulated data to deviate from observed data, and expresses the extent of over- or underestimation as a percentage [81].

Table 2. Statistical metrics used for performance evaluation of the Soil and Water Assessment Tool (SWAT) and Random Forest (RF) models. O and P refer to the observed and predicted (simulated) streamflow, respectively; $\bar{O}$ refers to the mean observed streamflow, and n is the number of observations. Abbreviations: *NRMSE*, normalized root-mean-squared error; *NSE*, Nash–Sutcliffe efficiency; *PBIAS*, percentage of bias.

Metric	Equations	Range	Performance Rating [a]			
			Very Good	Good	Satisfactory	Unsatisfactory
NSE	$\frac{\sum_{i=1}^{n}(O_i-P_i)^2}{\sum_{i=1}^{n}(P_i-\overline{O})^2}$	$-\infty$ to 1.0	$0.75 < NSE < 1.00$	$0.65 < NSE < 0.75$	$0.50 < NSE < 0.65$	$NSE < 0.50$
PBIAS	$\left(\frac{\sum_{i=1}^{n}(P_i-O_i)}{\sum_{i=1}^{n}O_i}\right) \times 100$	$-\infty$ to ∞	$PBIAS < \pm 10$	$\pm 10 < PBIAS < \pm 15$	$\pm 15 < PBIAS < \pm 25$	$PBIAS > \pm 25$
NRMSE	$100 \times \frac{1}{\overline{O}}\sqrt{\frac{1}{n}\sum_{i=1}^{n}(O_i-P_i)^2}$	0 to 1				

Note: [a] Adapted from Moriasi et al. [80] for the monthly time step.

The results were visualized using boxplots, Taylor diagrams, and hydrographs. The Taylor diagram [82] provides a visual representation that effectively illustrates the proximity between predicted values and observed data based on key metrics such as Pearson's correlation coefficient, centered root-mean-squared errors (*CRMSE*), and standard deviations. Figure 3 illustrates the workflow we applied to compare and evaluate the performance of

the SWAT and RF models. In addition, the most important predictors for the RF models were detected using the SHapley Additive exPlanations (SHAP) explainable AI method [83]. SHAP values indicate how much (i.e., m^3 s^{-1}) and in which direction (i.e., increase or decrease in streamflow) each predictor contributes to the model's prediction, with more important predictors accounting for more variance in the predictions.

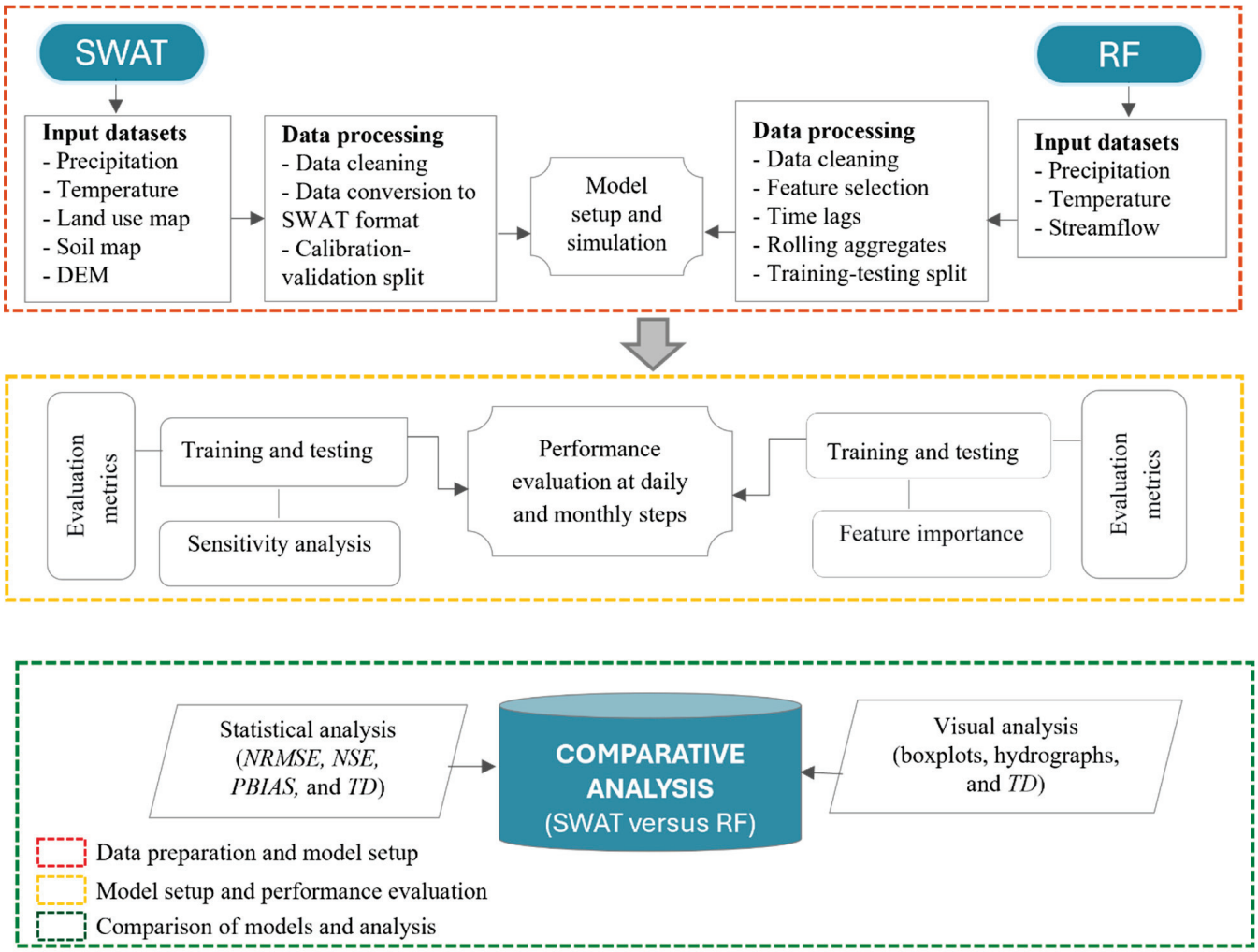

Figure 3. Workflow used to compare the performance of SWAT and RF models. Abbreviations: DEM, digital elevation model; *NRMSE*, normalized root-mean-square error; *NSE*, Nash–Sutcliffe efficiency coefficient; *PBIAS*, percentage of bias; RF, Random Forest; SWAT, Soil and Water Assessment Tool; TD, Taylor diagram.

4. Results

4.1. Performance of RF

There were differences in RF performance between catchments. Of the three daily RF models, DM2 and DM3 generally achieved satisfactory performance on a daily time step ($NSE > 0.5$), except for the Argos catchment ($NSE < 0.25$; Figure 4A). However, when streamflow was excluded as a predictor (model DM1), the model failed to accurately predict daily flows in all catchments ($NSE < 0$), except for Rib ($NSE = 0.81$). For monthly predictions, all RF models exhibited poor performance during the testing period ($NSE < 0.4$) in all catchments, except for Rib ($NSE > 0.75$) (Figure 4B). All RF models generally performed well in the Rib catchment at both temporal steps. For Argos, all monthly RF models outperformed the daily models. Overall, when the streamflow is considered as a predictor (MM2 and MM3), RF exhibited better performance on a daily step than on a monthly step in most cases. Flow (Q) consistently emerged as the main predictor in all catchments for

daily predictions (DM3 model; Figure S2) and, in most cases, for monthly predictions (MM3 model; Figure S3), highlighting its strong influence on the model's predictions.

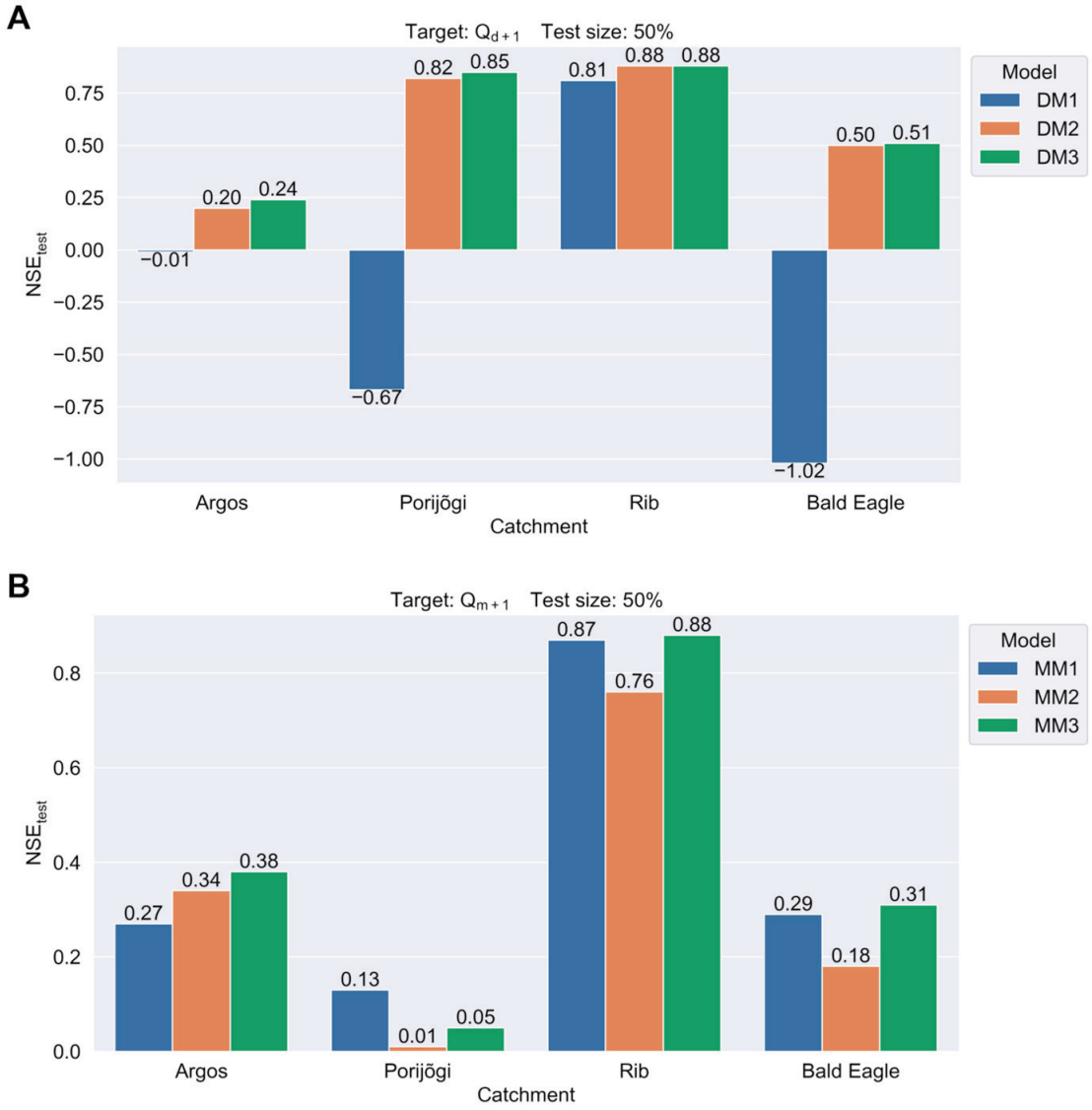

Figure 4. Nash–Sutcliffe efficiency (*NSE*) for the (**A**) daily and (**B**) monthly streamflow predictions (during the testing period) for the Random Forest models.

4.2. Performance of SWAT

The global sensitivity analysis for streamflow calibrations with SWAT revealed that among the sensitive parameters identified, the Curve Number (r_CN2) exhibited the highest statistically significant sensitivity across all catchments (Table 3). In addition, the parameters associated with groundwater (v_GWQMN, v_ALPHA_BF, v_RCHRG_DP), soil properties (r_SOL_BD), and slope steepness (v_HRU_SLP) exhibited a statistically significant sensitivity in most catchments. In the Rib catchment, a substantial reduction (36%) in the fitted value of r_CN2 was observed, but there was an increase in the value of v_HRU_SLP (0.42 m/m). The forested catchments (Porijõgi and Bald Eagle) had a higher soil evaporation compensation factor (v_ESCO) than the other catchments. Furthermore, in the Argos and Rib catchments, the fitted values of v_GW_DELAY were much higher than the values in the other catchment and indicated a significant time delay (>400 days) between the water leaving the soil profile and it entering the shallow aquifer.

Table 3. Sensitivity analysis results for parameters that were commonly sensitive across all catchments during the training period on a monthly time step. Parameters (r = relative change to the initial value (i.e., multiplication of the existing value by [1 + given value]), v = replacement of the actual value by a given value: CN2, Soil Conservation Service (SCS) runoff curve number; SOL_BD, moist soil bulk density (g/cm^3); GW_DELAY, groundwater delay (days); RCHRG_DP, recharge to the deep aquifer; GWQMN, depth of water for return flow (mm); GW_REVAP, groundwater "revap" coefficient; ALPHA_BF, baseflow alpha factor for the recession constant (days); HRU_SLP, average slope steepness (m/m); ESCO, soil evaporation compensation factor; CH_N2, Manning coefficient for main channel; CH_K1, effective hydraulic conductivity in tributary channel alluvium (mm/h). *, significant at $p < 0.05$.

Parameter	Argos		Porijõgi		Rib		Bald Eagle	
	Rank	Fitted Value	Rank	Fitted Value	Rank	Fitted Value	Rank	Fitted Value
r_CN2	1 *	0.01	1 *	0.04	1 *	−0.36	1 *	−0.12
r_SOL_BD	11	−0.03	2 *	−0.02	2 *	−0.10	10 *	−0.03
v_GW_DELAY	2 *	476	4	287	8	417	4 *	137
v_RCHRG_DP	3 *	0.15	7 *	0.44	7 *	−0.78	3 *	0.40
v_GWQMN	5 *	2686	3 *	3086	4 *	2539	2 *	2268
v_GW_REVAP	6 *	−0.03	5	0.24	5 *	0.18	6 *	0.22
v_ALPHA_BF	9	0.51	6	0.88	6	−0.34	5	0.58
v_HRU_SLP	7 *	0.15	11	0.00	3 *	0.42	7 *	0.27
v_ESCO	8 *	0.10	8 *	0.52	11	0.13	11	0.45
v_CH_N2	10	0.13	10 *	0.33	9 *	0.14	9	0.01
v_CH_K2	4	144	9 *	164	10 *	63.7	8	208

During the testing period, the performance of SWAT for daily predictions was generally unsatisfactory (*NSE* < 0.5), except in the Rib catchment (*NSE* = 0.86) (Table 4). Most catchments (except Argos) also experienced overestimation of the daily streamflow prediction (positive *PBIAS* values) and significant discrepancies between predicted and measured values, resulting in larger prediction errors (*NRMSE* > 5%). However, SWAT generally exhibited good performance for monthly predictions. Based on the criteria of Moriasi et al. (2007), the model achieved satisfactory or better performance (*NSE* > 0.5) in most cases, except for Argos and Bald Eagle during the testing period (*NSE* < 0.5) (Table 5). However, the Argos and Porijõgi catchments exhibited significant prediction errors on the monthly time step, particularly during testing (*NRMSE* > 18%, except for Rib). SWAT showed a general tendency to underestimate peak flows and overestimate base flows across all catchments on both daily and monthly steps.

Table 4. Statistical summary of daily streamflow prediction performance across catchments using the Soil and Water Assessment Tool (SWAT) model and the Random Forest (RF) DM3 model. Abbreviations: *NRMSE*, normalized root-mean-square error; *NSE*, Nash–Sutcliffe efficiency; *PBIAS*, percentage of bias.

Catchment	Metric	SWAT		RF	
		Training	Testing	Training	Testing
Argos	*NSE*	0.18	0.10	0.90	0.24
	NRMSE	4.42	4.76	1.46	4.94
	PBIAS	−7.6	−4.7	0.2	−2.7
Porijõgi	*NSE*	0.72	0.44	0.99	0.85
	NRMSE	5.36	6.66	0.95	2.07
	PBIAS	22.6	3.18	−0.1	1.9
Rib	*NSE*	0.78	0.86	0.98	0.88
	NRMSE	11.04	8.07	2.38	6.17
	PBIAS	12.1	2.02	0.6	4.5
Bald Eagle	*NSE*	0.55	0.33	0.93	0.51
	NRMSE	2.68	8.98	0.99	2.32
	PBIAS	15.2	27.4	−4.9	−2.5

Table 5. Statistical summary of monthly streamflow prediction performance across catchments using the Soil and Water Assessment Tool (SWAT) model and Random Forest (RF) MM3 model. Abbreviations: *NRMSE*, normalized root-mean-square error; *NSE*, Nash–Sutcliffe efficiency.

Catchment	Metric	SWAT		RF	
		Training	Testing	Training	Testing
Argos	*NSE*	0.51	0.26	0.93	0.38
	NRMSE	18.15	21.14	5.0	16.25
Porijõgi	*NSE*	0.82	0.51	0.9	0.05
	NRMSE	7.65	18.2	5.75	9.89
Rib	*NSE*	0.88	0.95	0.97	0.88
	NRMSE	9.54	6.37	4.5	8.88
Bald Eagle	*NSE*	0.58	0.34	0.88	0.31
	NRMSE	14.49	18.11	6.89	16.74

4.3. Comparing the Performance of RF and SWAT

To compare RF with SWAT, we focused on the daily DM3 model and the monthly MM3 model, which included all predictors and were the best-performing RF models. For daily predictions, RF outperformed SWAT, with higher correlation coefficients and lower *CRMSE* values between the observed and modeled values across all catchments in both the training and testing periods (Figure 5). SWAT's predictions on a daily time step generally displayed lower correlations and larger deviations from the observed data, indicating a greater difference between actual and predicted flows. Moreover, daily RF generally demonstrated strong performance based on the other statistical metrics ($NSE > 0.5$, $NRMSE < 7\%$, $PBIAS \leq \pm 5$; Table 4). In most cases, SWAT tended to overestimate the daily streamflow, especially for Bald Eagle during testing ($PBIAS = 27.4\%$) and Porijõgi during training ($PBIAS = 22.6\%$). Conversely, RF provided more reasonable predictions, with only slight over- or underestimation in a few cases. This trend was further supported by visual analysis of the hydrographs (Figure 6), where the RF model demonstrated better performance in capturing both peak- and base-flow levels.

For the monthly predictions, SWAT outperformed RF, particularly in catchments with irregular flow regimes (Figure 7). The SWAT and RF models both achieved satisfactory or better performance during training in all catchments ($NSE > 0.5$). However, RF struggled to maintain acceptable performance during testing, especially for Porijõgi ($NSE = 0.05$; Table 5). The monthly predictions showed higher *NRMSE* values than the daily predictions across all catchments except Rib. However, the monthly prediction for Rib exhibited the lowest *NRMSE* values compared to the monthly and daily predictions in other catchments. For Argos (the arid catchment), RF generally outperformed SWAT in terms of all metrics and in the visual analysis for both temporal steps.

4.4. Computational Efficiency

We evaluated the computational efficiency of SWAT and RF by measuring the total time required to complete a simulation. On a single-core Windows computer with a 3.60 GHz processor and 64 GB of RAM, the average time needed for a single simulation in SWAT ranged between 78 s (on a monthly time step) to 90 s (on a daily time step). Achieving satisfactory *NSE* values in SWAT demanded a considerable amount of time: 10 to 14 iterations, each requiring 1500 to 2000 simulations. The time needed for SWAT simulations, therefore, ranged from approximately 72 h for Porijõgi on a monthly time step to approximately 241 h for Bald Eagle on a daily time step (Figure S4A). In contrast, the RF models exhibited remarkable computational efficiency compared to SWAT. With a maximum training time of less than 12 s for the daily time step (Figure S4B), testing RF on both daily and monthly time steps required less than 12 s. It is essential to highlight that our comparison primarily focused on the training and testing phases of the models; nevertheless, developing a fully functional SWAT model demanded considerable overall time.

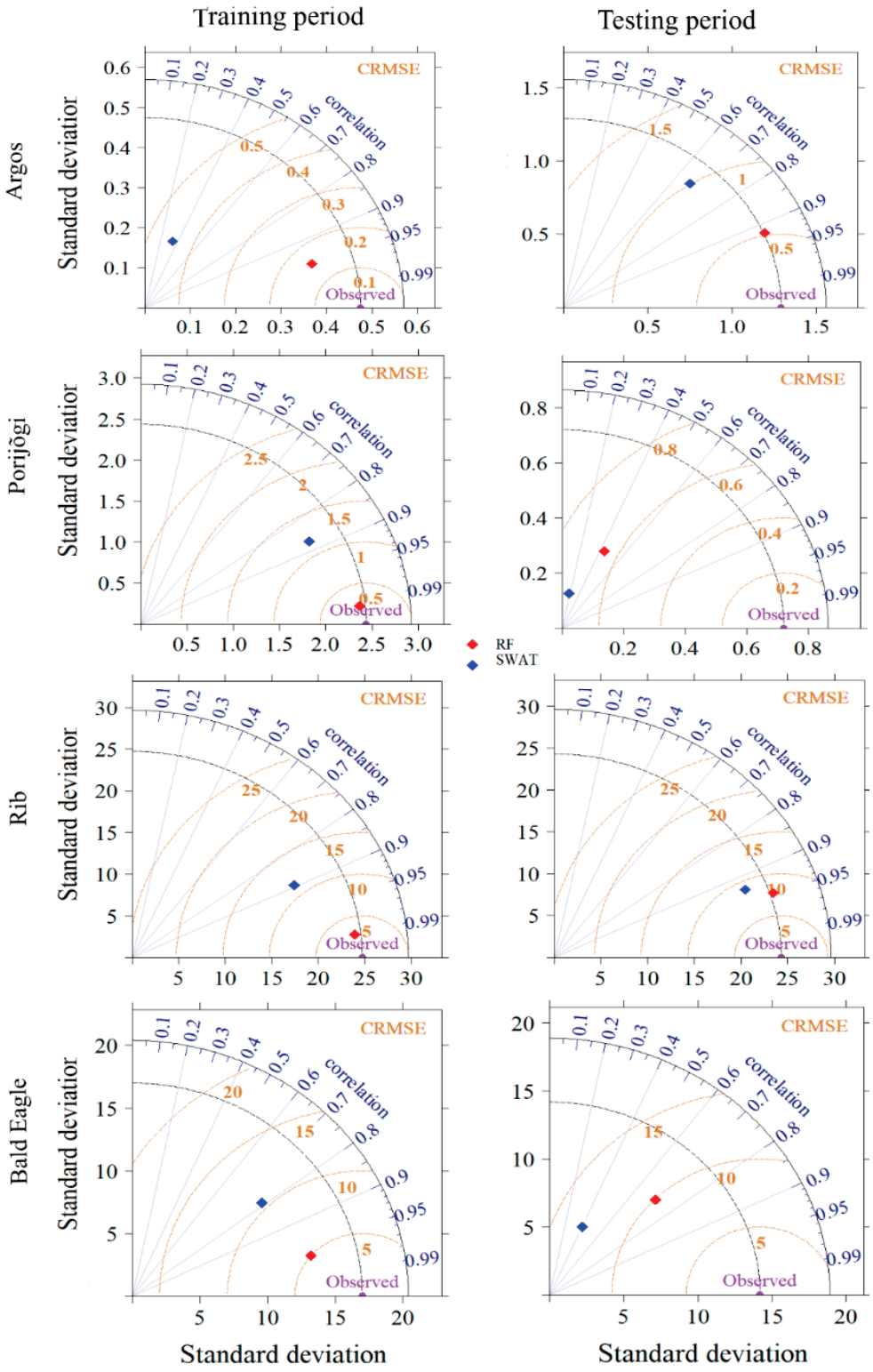

Figure 5. Taylor diagrams for comparison of the observed daily streamflow and the predictions by the Random Forest (RF) DM3 model and the Soil and Water Assessment Tool (SWAT) model across catchments. The "observed" data points (purple) are the reference values for evaluating the model predictions. The black dashed line corresponds to the standard deviation of the observed data. The golden contour lines indicate the values of the centered root-mean-squared errors (*CRMSE*). Perfect alignment between the observed and predicted values at the "observed" data point suggests a strong correlation, with no error (zero *CRMSE*) and similar variability (a similar standard deviation).

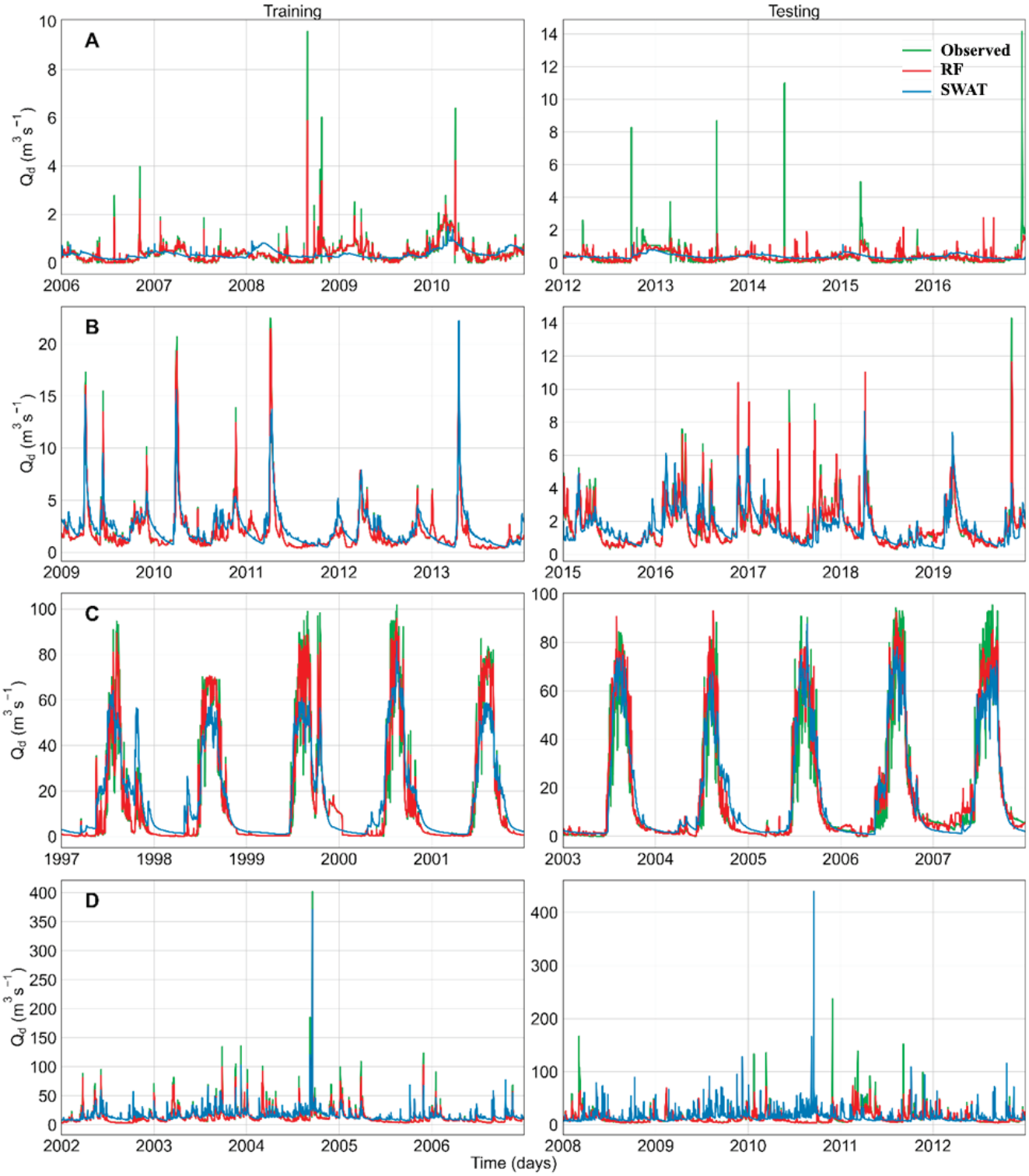

Figure 6. Hydrographs for comparison of the observed daily streamflow to the predictions of the Random Forest (RF) DM3 model and the Soil and Water Assessment Tool (SWAT) model for the (**A**) Argos, (**B**) Porijõgi, (**C**) Rib, and (**D**) Bald Eaglecatchments.

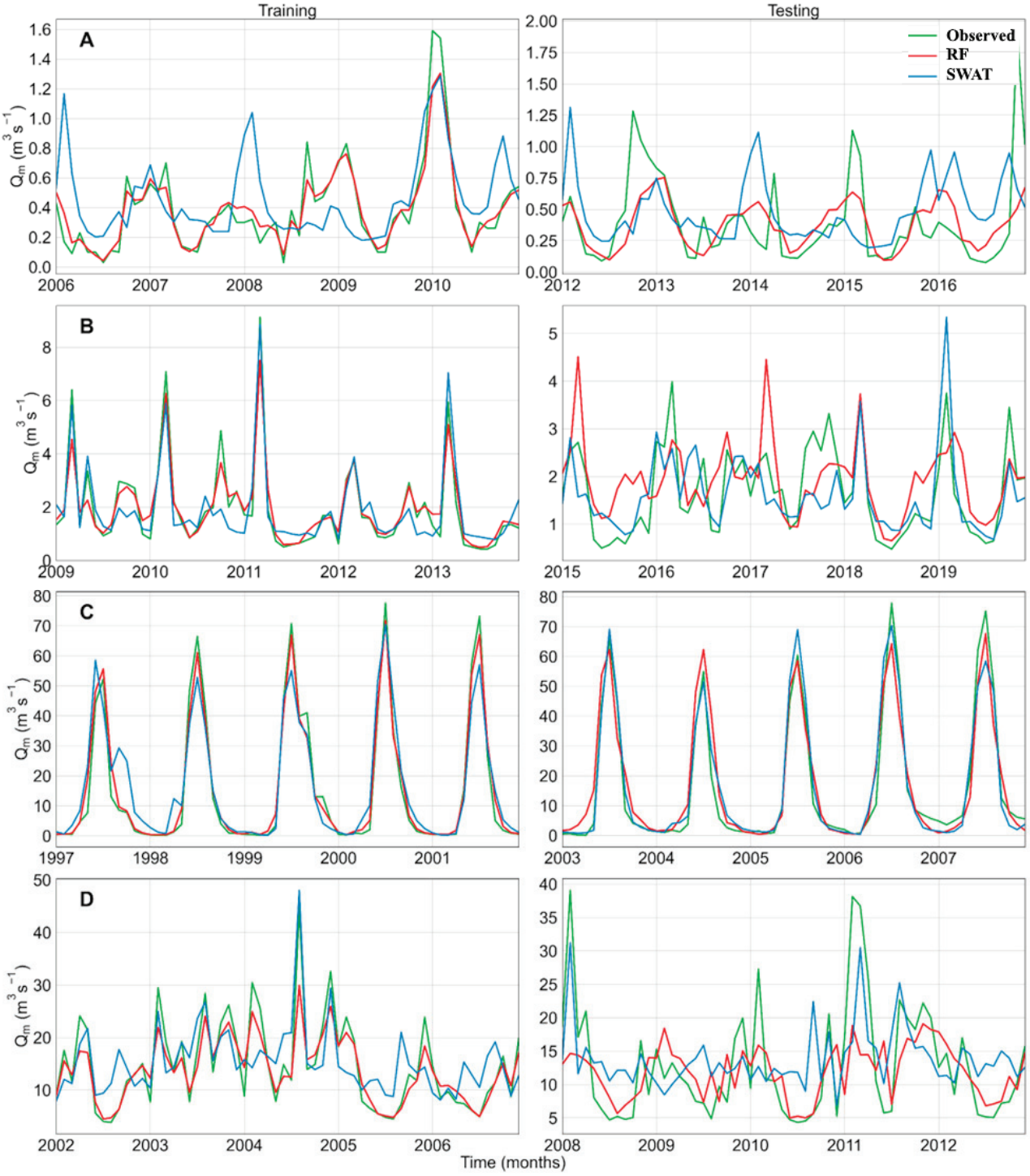

Figure 7. Hydrographs for comparison of the observed monthly streamflow and the predictions by the Random Forest (RF) MM3 model and the Soil and Water Assessment Tool (SWAT) model in the (**A**) Argos, (**B**) Porijõgi, (**C**) Rib, and (**D**) Bald Eagle catchments.

5. Discussion

5.1. Temporal Considerations and Feature Engineering for RF Models

Our investigation of the performance of RF revealed significant differences that depended on the combination of predictors employed. Sole reliance on precipitation and temperature proved insufficient for precise streamflow predictions, which is likely to be attributable to the existence of non-linear relationships and a weak correlation between

meteorological variables and streamflow [47]. However, we observed a notable improvement in prediction accuracy when incorporating historical flow values as inputs. This improvement can be ascribed to the influence of prior observations, which facilitate and improve utilization of historical patterns and permit more effective management of temporal dependencies [15,45,47,84]. Moreover, our results suggest that RF models that incorporate time-lag information as inputs performed better than models without lag information. This could be associated with the complex and lagged relationship between streamflow and meteorological variables [47,85], which is influenced by factors such as variable soil types, land cover and use types, and geological characteristics [85,86]. As a result, integrating the lagged information into predictions supports a more thorough comprehension of the temporal dynamics of streamflow and a more accurate representation of the interplay between meteorological factors and streamflow processes.

The selection of optimal time lags as predictors significantly influence the accuracy of streamflow predictions [28,47,87]. Conversely, including inefficient or redundant lags may lead to the development of poor or overly complex models [28]. Our analysis indicates that time lags ranging from 1 to 7 days for daily predictions and 1 to 3 months for monthly predictions result in satisfactory model performance. This suggests that shorter time lags effectively capture relevant patterns and dependencies in the data, which agrees with previous findings that historical data with longer intervals, significantly exceeding 60 days, do not yield notable improvements [85,88]. However, it is essential to note that the ideal lag periods for hydrological variables may differ among sub-basins of a catchment [85].

5.2. Comparison of RF and SWAT

RF outperformed SWAT in daily predictions, whereas SWAT was more accurate for monthly predictions, particularly in catchments with irregular flow patterns. This observation agrees with Jimeno-Sáez et al.'s [15] findings, and highlights the better performance of ML models, including RF, over SWAT for daily hydrological predictions. RF has exhibited robust performance, even at shorter temporal scales such as hourly scales, as has been indicated in multiple studies [89,90]. This suggests that ML can effectively capture the characteristics of complex hydrological systems [8,15,91]. RF's ensemble learning, which incorporates multiple decision trees, enhances its ability to recognize patterns under extreme flow conditions, thereby improving its accuracy in capturing both peak events and baseflow dynamics, which is critical for flood forecasting and water resource management [45,92]. Akbarian et al. [93] and Ferreira et al. [94] also confirmed RF's better performance in high-flow basins. RF's feature importance analysis based on SHAP values also aids in identifying key variables that influence streamflow, thereby contributing to a better understanding of hydrological processes than with process-based models [91].

SWAT encountered challenges in accurately predicting daily streamflow, particularly in capturing peak and base flows, whereas RF exhibited better performance for these characteristics. The more dispersed the data points, the worse the SWAT model's performance [15,95]. This might be associated with the fact that SWAT was initially designed for long-term analyses and is more suitable for monthly or longer time scales [11], thereby providing weaker capability at handling event-based simulations, such as flash floods and peak flows [96]. The uncertainties introduced by daily data, including measurement errors and missing values, pose challenges to SWAT's reliability in model calibration. Additionally, simulating hydrological processes on a daily time step demands complex parameterization and calibration, which further complicates SWAT's performance in such scenarios. However, SWAT demonstrated better performance on a monthly time step than its own daily predictions and the monthly predictions of RF. This aligns with other findings that highlight the enhanced efficacy of SWAT at lower temporal resolutions, such as an annual time step [91]. Monthly data, which are more reliable and have fewer gaps, improves the model's performance by reducing uncertainties associated with measurement errors. In addition, our findings indicated that SWAT demonstrated a more robust capability in catchments with irregular flow patterns, which results from SWAT's ability to incorporate

hydrological processes explicitly, monitor the catchment's water budget, and effectively represent dynamic changes within the system [11]. Given its ability to operate without direct input from observed streamflow data, SWAT remains a valuable model, particularly in basins with limited streamflow data [15].

Hydrological modeling in arid and semi-arid regions poses a formidable challenge that can be attributed to water scarcity, irregular precipitation, and complex hydrological interactions [97,98]. In the arid (Argos) catchment that we studied, the SWAT and RF models both exhibited poorer performance than in wetter catchments, with RF consistently outperforming SWAT across metrics and temporal steps. Argos's hydrogeological complexity, influenced by ground and surface water flows, presents challenges for effective modeling [58]; RF's advantage lies in managing non-linear relationships and adapting to spatial and temporal variability, which is especially beneficial for predicting streamflow in conditions with extended droughts or with flash floods. With only one hydro-meteorological station, Argos highlights the challenge of limited climate data, a situation in which RF excels compared to the data-intensive SWAT [99].

Hydrological models also face challenges in catchments influenced by snow, resulting in variable performance [45,98]. Both SWAT and RF showed diminished performance in predicting peak flows in the snow-influenced Porijõgi and Bald Eagle catchments. Winter precipitation as snow introduces complexities in hydrological processes, particularly the intricate freeze–thaw dynamics, which affect soil moisture, groundwater, and overall model predictions [100]. RF's inability to directly account for snow retention adds to its challenges in capturing snow-related hydrological processes [45]. SWAT's poor performance in snow-dominated catchments can be attributed to difficulties in modeling snow dynamics, insufficient parameterization, and constraints in capturing spatial and temporal variations. Improving parameter tuning, representing snow-related processes, and enhancing data quality may enhance model accuracy in snow-dominated catchments.

RF greatly outperforms SWAT in computational efficiency during both training and testing. Creating a fully functional SWAT model demands substantial time due to the intricate workflow, including data preparation, model setup, and the training and testing processes [101]. SWAT's computational intensity increases notably with larger scales and high-resolution data, and this is amplified by iterative procedures [102]. In contrast, RF's streamlined model structure results in efficiency across feature selection, engineering, training, and testing. Overall, our findings show that with significantly less modeling effort and resources, RF still performs better than SWAT in daily streamflow prediction. Nonetheless, for monthly predictions, especially in catchments with irregular flow patterns, SWAT may be a preferred option. SWAT considers numerous parameters in its flow simulation, making it the preferred choice for studies that analyze the influence of diverse parameters on flow simulation and conduct more in-depth investigations of hydrological processes. Researchers should carefully consider the specific demands and objectives of their hydrological modeling task to review the potential trade-offs between the two models.

Accurate hydrological modeling often relies on in situ gauges, but limited distribution of such gauges in the studied catchments hinders overall model performance. Although our RF model focused on 1-day streamflow forecasting, exploring extended lag times would be helpful for strategic water resource management [1]. Separating streamflow components into peak and base flows can enhance ML models [47], though our study did not explore this aspect. Likewise, separating streamflow for dry and wet periods and then combining the optimal results into an overall simulation series can notably enhance SWAT's performance, especially in catchments with seasonal variations [103]. Moreover, RF might perform better at a sub-daily time step, but we did not examine this possibility due to the unavailability of data for such a timeframe.

Incorporating the RF and SWAT models into water resource management and flood warning systems could offer significant potential for enhancing environmental protection and scientific research. RF is particularly advantageous due to its flexibility and rapid setup, especially in data-scarce situations, making it suitable for quick assessments and flood

predictions. Together, these models can optimize water allocation and conservation strategies while improving flood preparedness and response, ultimately helping to safeguard communities and ecosystems against climate variability and change. Furthermore, their integration can facilitate advanced scientific research by providing reliable data-driven insights into hydrological processes and environmental dynamics.

6. Conclusions

In this study, we incorporated time lags into RF models to make them more efficient in predicting flow time-series and compared the performance of time-lag-adjusted RF with process-based SWAT models to predict streamflow across diverse catchments. We showed that incorporating time lags for predictor values improved RF's ability to predict time series, and the performance of SWAT and RF differed among catchments due to catchment-specific characteristics that affected model efficacy. To address the limitations associated with ensemble learning methods such as RF in time-series predictions, we introduced time lag values for the predictors as model inputs. This greatly improved RF's accuracy and applicability in flow prediction, which confirms our first hypothesis. RF outperformed SWAT for daily predictions, whereas SWAT showed greater accuracy for monthly predictions, albeit with a much greater computational effort. SWAT also performed better in catchments with irregular flow patterns, which can likely be attributed to its explicit integration of hydrological processes, water budget monitoring, and effective representation of dynamic system changes. SWAT is also preferable in basins with limited streamflow data since it does not require observed streamflow as a direct input. Our findings also revealed the limited efficacy of both SWAT and RF in predicting peak flows in snow-influenced catchments. However, RF demonstrated better adaptability to the arid catchment, which showcases its ability to handle spatial and temporal variability under dry environmental conditions. In terms of computational efficiency, RF greatly outperformed SWAT, requiring less data and time, especially for daily streamflow prediction. The ensemble learning approach used by RF contributed to its effectiveness under extreme flow conditions, making it a valuable tool for real-time flood forecasting with reduced computational demands. This creates another advantage for RF: it adapts more easily to changes in conditions such as climate change, since the model can be retrained and revalidated more quickly than a SWAT model. SWAT and RF generally differed in prediction accuracy and computational efficiency across catchments and time steps, which confirms our second hypothesis. Our results contribute valuable insights into the strengths and weaknesses of both models, emphasizing their suitability in different contexts and shedding light on their performance across diverse catchments.

Supplementary Materials: The following supporting information can be downloaded at: https://www.mdpi.com/article/10.3390/w16192805/s1, Table S1. The lengths of the warmup, training, and testing periods (year–month–day) for the daily SWAT and RF models, Table S2. The lengths of the warmup, training, and testing periods (year–month–day) for the monthly SWAT and RF models. Figure S1. Daily streamflow (Qd), precipitation (Pcpd), maximum temperature (Tmax,d), and minimum temperature (Tmin,d) observations in the (A) Argos, (B) Porijõgi, (C) Rib, and (D) Bald Eagle catchments during the corresponding study periods. Figure S2. SHapley Additive exPlanation (SHAP) values for the most important (top 10) features for the Random Forest (RF) DM3 model (with a daily time step) for the four catchments. Figure S3. SHapley Additive exPlanation (SHAP) values for the most important (top 10) features for the Random Forest (RF) MM3 model with a monthly time step for the four catchments. Figure S4. Total time required to train and test (A) the Soil and Water Assessment Tool (SWAT) model at both time steps and (B) the Random Forest (RF) model at a daily time step. Qd+1 represents daily flow the day after the focal date. For the SWAT model, the process considered 14 parameters and 10 to 14 iterations, each containing 1500 to 2000 runs.

Author Contributions: D.M.M.: Conceptualization, data curation, formal analysis, methodology, software, validation, visualization, writing—original draft, writing—review and editing. H.V.: Conceptualization, formal analysis, methodology, software, validation, visualization, writing—original draft, writing—review and editing. A.K.: Conceptualization, methodology, funding acquisition,

writing—review and editing. R.C.: Conceptualization, data curation, writing—review and editing. R.A.N.R.: Data curation, writing—review and editing. A.M.-S.: Data curation, writing—review and editing. C.C.-G.: Data curation, writing—review and editing. E.U.: Conceptualization, investigation, methodology, supervision, resources, project administration, writing—review and editing, funding acquisition. All authors have read and agreed to the published version of the manuscript.

Funding: This work was funded by the Estonian Research Agency (grant number PRG1764, PSG841), Estonian Ministry of Education and Research, Centre of Excellence for Sustainable Land Use (TK232) and by the European Union (ERC, WaterSmartLand, 101125476). However, the views and opinions expressed are those of the author(s) only and do not necessarily reflect those of the European Union or the European Research Council Executive Agency. Neither the European Union nor the granting authority can be held responsible for them.

Data Availability Statement: The datasets utilized in this study are available on Zenodo at https://zenodo.org/doi/10.5281/zenodo.11066218, and the source code for flow modeling with RF is available in a public GitLab repository at https://github.com/LandscapeGeoinformatics/flow_swat_ml_paper (accessed on 29 September 2024).

Conflicts of Interest: The authors declare that they have no known competing financial interests or personal relationships that could have appeared to influence the work reported in this paper.

References

1. Cheng, M.; Fang, F.; Kinouchi, T.; Navon, I.M.; Pain, C.C. Long Lead-Time Daily and Monthly Streamflow Forecasting Using Machine Learning Methods. *J. Hydrol.* **2020**, *590*, 125376. [CrossRef]
2. Fathian, F.; Mehdizadeh, S.; Kozekalani Sales, A.; Safari, M.J.S. Hybrid Models to Improve the Monthly River Flow Prediction: Integrating Artificial Intelligence and Non-Linear Time Series Models. *J. Hydrol.* **2019**, *575*, 1200–1213. [CrossRef]
3. Lian, X.; Hu, X.; Bian, J.; Shi, L.; Lin, L.; Cui, Y. Enhancing Streamflow Estimation by Integrating a Data-Driven Evapotranspiration Submodel into Process-Based Hydrological Models. *J. Hydrol.* **2023**, *621*, 129603. [CrossRef]
4. Zhang, X.; Liu, P.; Cheng, L.; Xie, K.; Han, D.; Zhou, L. The Temporal Variations in Runoff-Generation Parameters of the Xinanjiang Model Due to Human Activities: A Case Study in the Upper Yangtze River Basin, China. *J. Hydrol. Reg. Stud.* **2021**, *37*, 100910. [CrossRef]
5. Devia, G.K.; Ganasri, B.P.; Dwarakish, G.S. A Review on Hydrological Models. *Aquat. Procedia* **2015**, *4*, 1001–1007. [CrossRef]
6. Parra, V.; Fuentes-Aguilera, P.; Muñoz, E. Identifying Advantages and Drawbacks of Two Hydrological Models Based on a Sensitivity Analysis: A Study in Two Chilean Watersheds. *Hydrol. Sci. J.* **2018**, *63*, 1831–1843. [CrossRef]
7. Rahman, K.; Shang, S.; Shahid, M.; Wen, Y. Hydrological Evaluation of Merged Satellite Precipitation Datasets for Streamflow Simulation Using SWAT: A Case Study of Potohar Plateau, Pakistan. *J. Hydrol.* **2020**, *587*, 125040. [CrossRef]
8. Rahman, K.U.; Pham, Q.B.; Jadoon, K.Z.; Shahid, M.; Kushwaha, D.P.; Duan, Z.; Mohammadi, B.; Khedher, K.M.; Anh, D.T. Comparison of Machine Learning and Process-Based SWAT Model in Simulating Streamflow in the Upper Indus Basin. *Appl. Water Sci.* **2022**, *12*, 178. [CrossRef]
9. Singh, A.; Imtiyaz, M.; Isaac, R.K.; Denis, D.M. Comparison of Soil and Water Assessment Tool (SWAT) and Multilayer Perceptron (MLP) Artificial Neural Network for Predicting Sediment Yield in the Nagwa Agricultural Watershed in Jharkhand, India. *Agric. Water Manag.* **2012**, *104*, 113–120. [CrossRef]
10. Zakizadeh, H.; Ahmadi, H.; Zehtabian, G.; Moeini, A.; Moghaddamnia, A. A Novel Study of SWAT and ANN Models for Runoff Simulation with Application on Dataset of Metrological Stations. *Phys. Chem. Earth Parts A/B/C* **2020**, *120*, 102899. [CrossRef]
11. Arnold, J.G.; Srinivasan, R.; Muttiah, R.S.; Williams, J.R. Large Area Hydrologic Modeling and Assessment Part I: Model Development. *J. Am. Water Resour. Assoc.* **1998**, *34*, 73–89. [CrossRef]
12. Abbaspour, K.C.; Rouholahnejad, E.; Vaghefi, S.; Srinivasan, R.; Yang, H.; Kløve, B. A Continental-Scale Hydrology and Water Quality Model for Europe: Calibration and Uncertainty of a High-Resolution Large-Scale SWAT Model. *J. Hydrol.* **2015**, *524*, 733–752. [CrossRef]
13. Aloui, S.; Mazzoni, A.; Elomri, A.; Aouissi, J.; Boufekane, A.; Zghibi, A. A Review of Soil and Water Assessment Tool (SWAT) Studies of Mediterranean Catchments: Applications, Feasibility, and Future Directions. *J. Environ. Manag.* **2023**, *326*, 116799. [CrossRef]
14. Akoko, G.; Le, T.H.; Gomi, T.; Kato, T. A Review of SWAT Model Application in Africa. *Water* **2021**, *13*, 1313. [CrossRef]
15. Jimeno-Sáez, P.; Martínez-España, R.; Casalí, J.; Pérez-Sánchez, J.; Senent-Aparicio, J. A Comparison of Performance of SWAT and Machine Learning Models for Predicting Sediment Load in a Forested Basin, Northern Spain. *Catena* **2021**, *212*, 105953. [CrossRef]
16. Pradhan, P.; Tingsanchali, T.; Shrestha, S. Evaluation of Soil and Water Assessment Tool and Artificial Neural Network Models for Hydrologic Simulation in Different Climatic Regions of Asia. *Sci. Total Environ.* **2020**, *701*, 134308. [CrossRef]
17. Panagopoulos, Y.; Makropoulos, C.; Baltas, E.; Mimikou, M. SWAT Parameterization for the Identification of Critical Diffuse Pollution Source Areas under Data Limitations. *Ecol. Model.* **2011**, *222*, 3500–3512. [CrossRef]

18. Sánchez-Gómez, A.; Martínez-Pérez, S.; Pérez-Chavero, F.M.; Molina-Navarro, E. Optimization of a SWAT Model by Incorporating Geological Information through Calibration Strategies. *Optim. Eng.* **2022**, *23*, 2203–2233. [CrossRef]
19. Senent-Aparicio, J.; Alcalá, F.J.; Liu, S.; Jimeno-Sáez, P. Coupling SWAT Model and CMB Method for Modeling of High-Permeability Bedrock Basins Receiving Interbasin Groundwater Flow. *Water* **2020**, *12*, 657. [CrossRef]
20. Cai, Y.; Zhang, F.; Shi, J.; Carl Johnson, V.; Ahmed, Z.; Wang, J.; Wang, W. Enhancing SWAT Model with Modified Method to Improve Eco-Hydrological Simulation in Arid Region. *J. Clean. Prod.* **2023**, *403*, 136891. [CrossRef]
21. Abbasi, M.; Farokhnia, A.; Bahreinimotlagh, M.; Roozbahani, R. A Hybrid of Random Forest and Deep Auto-Encoder with Support Vector Regression Methods for Accuracy Improvement and Uncertainty Reduction of Long-Term Streamflow Prediction. *J. Hydrol.* **2021**, *597*, 125717. [CrossRef]
22. Li, X.; Sha, J.; Wang, Z.-L. Comparison of Daily Streamflow Forecasts Using Extreme Learning Machines and the Random Forest Method. *Hydrol. Sci. J.* **2019**, *64*, 1857–1866. [CrossRef]
23. Peng, F.; Wen, J.; Zhang, Y.; Jin, J. Monthly Streamflow Prediction Based on Random Forest Algorithm and Phase Space Reconstruction Theory. *J. Phys. Conf. Ser.* **2020**, *1637*, 012091. [CrossRef]
24. Pham, L.T.; Luo, L.; Finley, A. Evaluation of Random Forests for Short-Term Daily Streamflow Forecasting in Rainfall- and Snowmelt-Driven Watersheds. *Hydrol. Earth Syst. Sci.* **2021**, *25*, 2997–3015. [CrossRef]
25. Shen, Y.; Ruijsch, J.; Lu, M.; Sutanudjaja, E.H.; Karssenberg, D. Random Forests-Based Error-Correction of Streamflow from a Large-Scale Hydrological Model: Using Model State Variables to Estimate Error Terms. *Comput. Geosci.* **2022**, *159*, 105019. [CrossRef]
26. Fadhillah, M.F.; Lee, S.; Lee, C.-W.; Park, Y.-C. Application of Support Vector Regression and Metaheuristic Optimization Algorithms for Groundwater Potential Mapping in Gangneung-Si, South Korea. *Remote Sens.* **2021**, *13*, 1196. [CrossRef]
27. Liu, J.; Xu, L.; Chen, N. A Spatiotemporal Deep Learning Model ST-LSTM-SA for Hourly Rainfall Forecasting Using Radar Echo Images. *J. Hydrol.* **2022**, *609*, 127748. [CrossRef]
28. Danandeh, A.; Ghadimi, S.; Marttila, H.; Torabi Haghighi, A. A New Evolutionary Time Series Model for Streamflow Forecasting in Boreal Lake-River Systems. *Theor. Appl. Clim.* **2022**, *148*, 255–268. [CrossRef]
29. Wei, Y.; Hashim, H.; Chong, K.L.; Huang, Y.F.; Ahmed, A.N.; El-Shafie, A. Investigation of Meta-Heuristics Algorithms in ANN Streamflow Forecasting. *KSCE J. Civ. Eng.* **2023**, *27*, 2297–2312. [CrossRef]
30. Dehghani, A.; Moazam, H.M.Z.H.; Mortazavizadeh, F.; Ranjbar, V.; Mirzaei, M.; Mortezavi, S.; Ng, J.L.; Dehghani, A. Comparative Evaluation of LSTM, CNN, and ConvLSTM for Hourly Short-Term Streamflow Forecasting Using Deep Learning Approaches. *Ecol. Inform.* **2023**, *75*, 102119. [CrossRef]
31. Sabzipour, B.; Arsenault, R.; Troin, M.; Martel, J.-L.; Brissette, F.; Brunet, F.; Mai, J. Comparing a Long Short-Term Memory (LSTM) Neural Network with a Physically-Based Hydrological Model for Streamflow Forecasting over a Canadian Catchment. *J. Hydrol.* **2023**, *627*, 130380. [CrossRef]
32. Ni, L.; Wang, D.; Wu, J.; Wang, Y.; Tao, Y.; Zhang, J.; Liu, J. Streamflow Forecasting Using Extreme Gradient Boosting Model Coupled with Gaussian Mixture Model. *J. Hydrol.* **2020**, *586*, 124901. [CrossRef]
33. Sahour, H.; Gholami, V.; Torkaman, J.; Vazifedan, M.; Saeedi, S. Random Forest and Extreme Gradient Boosting Algorithms for Streamflow Modeling Using Vessel Features and Tree-Rings. *Environ. Earth Sci.* **2021**, *80*, 747. [CrossRef]
34. Yu, X.; Wang, Y.; Wu, L.; Chen, G.; Wang, L.; Qin, H. Comparison of Support Vector Regression and Extreme Gradient Boosting for Decomposition-Based Data-Driven 10-Day Streamflow Forecasting. *J. Hydrol.* **2020**, *582*, 124293. [CrossRef]
35. Gurbuz, F.; Mudireddy, A.; Mantilla, R.; Xiao, S. Using a Physics-Based Hydrological Model and Storm Transposition to Investigate Machine-Learning Algorithms for Streamflow Prediction. *J. Hydrol.* **2024**, *628*, 130504. [CrossRef]
36. Boo, K.B.W.; El-Shafie, A.; Othman, F.; Khan, M.M.H.; Birima, A.H.; Ahmed, A.N. Groundwater Level Forecasting with Machine Learning Models: A Review. *Water Res.* **2024**, *252*, 121249. [CrossRef]
37. Liang, W.; Chen, Y.; Fang, G.; Kaldybayev, A. Machine Learning Method Is an Alternative for the Hydrological Model in an Alpine Catchment in the Tianshan Region, Central Asia. *J. Hydrol. Reg. Stud.* **2023**, *49*, 101492. [CrossRef]
38. Deng, C.; Yin, X.; Zou, J.; Wang, M.; Hou, Y. Assessment of the Impact of Climate Change on Streamflow of Ganjiang River Catchment via LSTM-Based Models. *J. Hydrol. Reg. Stud.* **2024**, *52*, 101716. [CrossRef]
39. Ghimire, S.; Yaseen, Z.M.; Farooque, A.A.; Deo, R.C.; Zhang, J.; Tao, X. Streamflow Prediction Using an Integrated Methodology Based on Convolutional Neural Network and Long Short-Term Memory Networks. *Sci. Rep.* **2021**, *11*, 17497. [CrossRef]
40. Majeske, N.; Zhang, X.; Sabaj, M.; Gong, L.; Zhu, C.; Azad, A. Inductive Predictions of Hydrologic Events Using a Long Short-Term Memory Network and the Soil and Water Assessment Tool. *Environ. Model. Softw.* **2022**, *152*, 105400. [CrossRef]
41. Gauch, M.; Kratzert, F.; Klotz, D.; Nearing, G.; Lin, J.; Hochreiter, S. Rainfall–Runoff Prediction at Multiple Timescales with a Single Long Short-Term Memory Network. *Hydrol. Earth Syst. Sci.* **2021**, *25*, 2045–2062. [CrossRef]
42. Yang, M.; Yang, Q.; Shao, J.; Wang, G.; Zhang, W. A New Few-Shot Learning Model for Runoff Prediction: Demonstration in Two Data Scarce Regions. *Environ. Model. Softw.* **2023**, *162*, 105659. [CrossRef]
43. Belgiu, M.; Drăguţ, L. Random Forest in Remote Sensing: A Review of Applications and Future Directions. *ISPRS J. Photogramm. Remote Sens.* **2016**, *114*, 24–31. [CrossRef]
44. Li, J.; Wang, Z.; Lai, C.; Zhang, Z. Tree-Ring-Width Based Streamflow Reconstruction Based on the Random Forest Algorithm for the Source Region of the Yangtze River, China. *Catena* **2019**, *183*, 104216. [CrossRef]

45. Schoppa, L.; Disse, M.; Bachmair, S. Evaluating the Performance of Random Forest for Large-Scale Flood Discharge Simulation. *J. Hydrol.* **2020**, *590*, 125531. [CrossRef]
46. Shortridge, J.E.; Guikema, S.D.; Zaitchik, B.F. Machine Learning Methods for Empirical Streamflow Simulation: A Comparison of Model Accuracy, Interpretability, and Uncertainty in Seasonal Watersheds. *Hydrol. Earth Syst. Sci.* **2016**, *20*, 2611–2628. [CrossRef]
47. Tongal, H.; Booij, M.J. Simulation and Forecasting of Streamflows Using Machine Learning Models Coupled with Base Flow Separation. *J. Hydrol.* **2018**, *564*, 266–282. [CrossRef]
48. Fernandez-Delgado, M.; Cernadas, E.; Barro, S.; Amorim, D. Do We Need Hundreds of Classifiers to Solve Real World Classification Problems? *J. Mach. Learn. Res.* **2014**, *15*, 3133–3181.
49. Goehry, B.; Yan, H.; Goude, Y.; Massart, P.; Poggi, J.-M. Random Forests for Time Series 2021. *REVSTAT-Stat. J.* **2023**, *21*, 283–302.
50. Qiu, X.; Zhang, L.; Nagaratnam Suganthan, P.; Amaratunga, G.A.J. Oblique Random Forest Ensemble via Least Square Estimation for Time Series Forecasting. *Inf. Sci.* **2017**, *420*, 249–262. [CrossRef]
51. Hauswirth, S.M.; Bierkens, M.F.P.; Beijk, V.; Wanders, N. The Potential of Data Driven Approaches for Quantifying Hydrological Extremes. *Adv. Water Resour.* **2021**, *155*, 104017. [CrossRef]
52. Ghosh, A.; Maiti, R. Application of SWAT, Random Forest and Artificial Neural Network Models for Sediment Yield Estimation and Prediction of Gully Erosion Susceptible Zones: Study on Mayurakshi River Basin of Eastern India. *Geocarto Int.* **2022**, *37*, 9663–9687. [CrossRef]
53. Khosravi, K.; Golkarian, A.; Booij, M.J.; Barzegar, R.; Sun, W.; Yaseen, Z.M.; Mosavi, A. Improving Daily Stochastic Streamflow Prediction: Comparison of Novel Hybrid Data-Mining Algorithms. *Hydrol. Sci. J.* **2021**, *66*, 1457–1474. [CrossRef]
54. Woo, S.Y.; Jung, C.G.; Lee, J.W.; Kim, S.J. Evaluation of Watershed Scale Aquatic Ecosystem Health by SWAT Modeling and Random Forest Technique. *Sustainability* **2019**, *11*, 3397. [CrossRef]
55. Woo, S.Y.; Jung, C.G.; Kim, J.U.; Kim, S.J. Assessment of climate change impact on Aquatic ecology Health Indices in Han River basin using SWAT and random forest. *J. Korea Water Resour. Assoc.* **2018**, *51*, 863–874.
56. Dhar, P. The Carbon Impact of Artificial Intelligence. *Nat. Mach. Intell.* **2020**, *2*, 423–425. [CrossRef]
57. Verdecchia, R.; Sallou, J.; Cruz, L. A Systematic Review of Green AI 2023. *Data Min. Knowl. Discov.* **2023**, *13*, e1507. [CrossRef]
58. Martínez-Salvador, A.; Conesa-García, C. Suitability of the SWAT Model for Simulating Water Discharge and Sediment Load in a Karst Watershed of the Semiarid Mediterranean Basin. *Water Resour. Manag.* **2020**, *34*, 785–802. [CrossRef]
59. Mander, Ü.; Kull, A.; Kuusemets, V.; Tamm, T. Nutrient Runoff Dynamics in a Rural Catchment: Influence of Land-Use Changes, Climatic Fluctuations and Ecotechnological Measures. *Ecol. Eng.* **2000**, *14*, 405–417. [CrossRef]
60. Moges, D.M.; Kmoch, A.; Uuemaa, E. Application of Satellite and Reanalysis Precipitation Products for Hydrological Modeling in the Data-Scarce Porijõgi Catchment, Estonia. *J. Hydrol. Reg. Stud.* **2022**, *41*, 101070. [CrossRef]
61. Moges, D.M.; Bhat, H.G. An Insight into Land Use and Land Cover Changes and Their Impacts in Rib Watershed, North-Western Highland Ethiopia. *Land. Degrad. Dev.* **2018**, *29*, 3317–3330. [CrossRef]
62. Moges, D.M.; Kmoch, A.; Bhat, H.G.; Uuemaa, E. Future Soil Loss in Highland Ethiopia under Changing Climate and Land Use. *Reg. Environ. Chang.* **2020**, *20*, 32. [CrossRef]
63. Moges, D.M.; Bhat, H. Integration of Geospatial Technologies with RUSLE for Analysis of Land Use/Cover Change Impact on Soil Erosion: Case Study in Rib Watershed, North-Western Highland Ethiopia. *Environ. Earth Sci.* **2017**, *76*, 765. [CrossRef]
64. Jayaprathiga, M.; Cibin, R.; Sudheer, K.P. Reliability of Hydrology and Water Quality Simulations Using Global Scale Datasets. *J. Am. Water Resour. Assoc.* **2022**, *58*, 453–470. [CrossRef]
65. Breiman, L. Random Forests. *Mach. Learn.* **2001**, *45*, 5–32. [CrossRef]
66. Ferreira, L.B.; da Cunha, F.F.; de Oliveira, R.A.; Fernandes Filho, E.I. Estimation of Reference Evapotranspiration in Brazil with Limited Meteorological Data Using ANN and SVM–A New Approach. *J. Hydrol.* **2019**, *572*, 556–570. [CrossRef]
67. Li, J.; Heap, A.D.; Potter, A.; Daniell, J.J. Application of Machine Learning Methods to Spatial Interpolation of Environmental Variables. *Environ. Model. Softw.* **2011**, *26*, 1647–1659. [CrossRef]
68. Tyralis, H.; Papacharalampous, G.; Langousis, A. A Brief Review of Random Forests for Water Scientists and Practitioners and Their Recent History in Water Resources. *Water* **2019**, *11*, 910. [CrossRef]
69. Rasouli, K.; Hsieh, W.W.; Cannon, A.J. Daily Streamflow Forecasting by Machine Learning Methods with Weather and Climate Inputs. *J. Hydrol.* **2012**, *414*, 284–293. [CrossRef]
70. Pedregosa, F.; Varoquaux, G.; Gramfort, A.; Michel, V.; Thirion, B.; Grisel, O.; Blondel, M.; Prettenhofer, P.; Weiss, R.; Dubourg, V.; et al. Scikit-Learn: Machine Learning in Python. *J. Mach. Learn. Res.* **2011**, *12*, 2825–2830.
71. Neitsch, S.L.; Arnold, J.G.; Kiniry, J.R.; Williams, J.R. *Soil and Water Assessment Tool Theoretical Documentation Version 2009*; Texas Water Resources Institute: College Station, TX, USA, 2011.
72. Moges, D.M.; Virro, H.; Kmoch, A.; Cibin, R.; Rohith, A.N.; Martínez-Salvador, A.; Conesa-García, C.; Uuemaa, E. How Does the Choice of DEMs Affect Catchment Hydrological Modeling? *Sci. Total Environ.* **2023**, *892*, 164627. [CrossRef]
73. Dile, Y.T.; Daggupati, P.; George, C.; Srinivasan, R.; Arnold, J. Introducing a New Open Source GIS User Interface for the SWAT Model. *Environ. Model. Softw.* **2016**, *85*, 129–138. [CrossRef]
74. Abbaspour, K.C.; van Genuchten, M.T.; Schulin, R.; Schläppi, E. A Sequential Uncertainty Domain Inverse Procedure for Estimating Subsurface Flow and Transport Parameters. *Water Resour. Res.* **1997**, *33*, 1879–1892. [CrossRef]

75. JAXA ALOS Global Digital Surface Model (DSM). ALOS World 3D-30m (AW3D30) Version 3.1: Product Description; Earth Obs. Res. Cent. Japan Aerosp. Explor. Agency (JAXA EORC). Available online: https://www.eorc.jaxa.jp/ALOS/ (accessed on 29 March 2022).
76. Zanaga, D.; Van De Kerchove, R.; De Keersmaecker, W.; Souverijns, N.; Brockmann, C.; Quast, R.; Wevers, J.; Grosu, A.; Paccini, A.; Vergnaud, S.; et al. ESA WorldCover 10 m 2020 V100 2021. Available online: https://worldcover2020.esa.int/download (accessed on 21 March 2022).
77. Fischer, G.; Nachtergaele, V.F.; Prieler, S.; van Velthuizen, H.T.; Verelst, L.; Wiberg, D. *Global Agro-Ecological Zones Assessment for Agriculture (GAEZ 2008)*; IIASA Laxenburg Austria FAO: Rome, Italy, 2008.
78. Nash, J.E.; Sutcliffe, J.V. River Flow Forecasting through Conceptual Models Part I—A Discussion of Principles. *J. Hydrol.* **1970**, *10*, 282–290. [CrossRef]
79. Gupta, H.V.; Sorooshian, S.; Yapo, P.O. Status of Automatic Calibration for Hydrologic Models: Comparison with Multilevel Expert Calibration. *J. Hydrol. Eng.* **1999**, *4*, 135–143. [CrossRef]
80. Moriasi, D.N.; Arnold, J.G.; Van Liew, M.W.; Bingner, R.L.; Harmel, R.D.; Veith, T.L. Model Evaluation Guidelines for Systematic Quantification of Accuracy in Watershed Simulations. *Trans. ASABE* **2007**, *50*, 885–900. [CrossRef]
81. Moriasi, D.N.; Gitau, M.W.; Pai, N.; Daggupati, P. Hydrologic and Water Quality Models: Performance Measures and Evaluation Criteria. *Trans. ASABE* **2015**, *58*, 1763–1785. [CrossRef]
82. Taylor, K.E. Summarizing Multiple Aspects of Model Performance in a Single Diagram. *J. Geophys. Res.* **2001**, *106*, 7183–7192. [CrossRef]
83. Lundberg, S.M.; Erion, G.; Chen, H.; DeGrave, A.; Prutkin, J.M.; Nair, B.; Katz, R.; Himmelfarb, J.; Bansal, N.; Lee, S.-I. From Local Explanations to Global Understanding with Explainable AI for Trees. *Nat. Mach. Intell.* **2020**, *2*, 56–67. [CrossRef]
84. Hussain, D.; Khan, A.A. Machine Learning Techniques for Monthly River Flow Forecasting of Hunza River, Pakistan. *Earth Sci. Inf.* **2020**, *13*, 939–949. [CrossRef]
85. Ma, K.; He, D.; Liu, S.; Ji, X.; Li, Y.; Jiang, H. Novel Time-Lag Informed Deep Learning Framework for Enhanced Streamflow Prediction and Flood Early Warning in Large-Scale Catchments. *J. Hydrol.* **2024**, *631*, 130841. [CrossRef]
86. Kalu, I.; Ndehedehe, C.E.; Ferreira, V.G.; Kennard, M.J. Machine Learning Assessment of Hydrological Model Performance under Localized Water Storage Changes through Downscaling. *J. Hydrol.* **2024**, *628*, 130597. [CrossRef]
87. Garg, V.; Sambare, R.S.; Thakur, P.K.; Dhote, P.R.; Nikam, B.R.; Aggarwal, S.P. Improving Stream Flow Estimation by Incorporating Time Delay Approach in Soft Computing Models. *ISH J. Hydraul. Eng.* **2022**, *28*, 57–68. [CrossRef]
88. Feng, D.; Fang, K.; Shen, C. Enhancing Streamflow Forecast and Extracting Insights Using Long-Short Term Memory Networks With Data Integration at Continental Scales. *Water Resour. Res.* **2020**, *56*, e2019WR026793. [CrossRef]
89. Besaw, L.E.; Rizzo, D.M.; Bierman, P.R.; Hackett, W.R. Advances in Ungauged Streamflow Prediction Using Artificial Neural Networks. *J. Hydrol.* **2010**, *386*, 27–37. [CrossRef]
90. Saadi, M.; Oudin, L.; Ribstein, P. Random Forest Ability in Regionalizing Hourly Hydrological Model Parameters. *Water* **2019**, *11*, 1540. [CrossRef]
91. Islam, K.I.; Elias, E.; Carroll, K.C.; Brown, C. Exploring Random Forest Machine Learning and Remote Sensing Data for Streamflow Prediction: An Alternative Approach to a Process-Based Hydrologic Modeling in a Snowmelt-Driven Watershed. *Remote Sens.* **2023**, *15*, 3999. [CrossRef]
92. Papacharalampous, G.A.; Tyralis, H. Evaluation of Random Forests and Prophet for Daily Streamflow Forecasting. *Adv. Geosci.* **2018**, *45*, 201–208. [CrossRef]
93. Akbarian, M.; Saghafian, B.; Golian, S. Monthly Streamflow Forecasting by Machine Learning Methods Using Dynamic Weather Prediction Model Outputs over Iran. *J. Hydrol.* **2023**, *620*, 129480. [CrossRef]
94. Ferreira, R.G.; da Silva, D.D.; Elesbon, A.A.A.; Fernandes-Filho, E.I.; Veloso, G.V.; de Souza Fraga, M.; Ferreira, L.B. Machine Learning Models for Streamflow Regionalization in a Tropical Watershed. *J. Environ. Manag.* **2021**, *280*, 111713. [CrossRef]
95. Choukri, F.; Raclot, D.; Naimi, M.; Chikhaoui, M.; Nunes, J.P.; Huard, F.; Hérivaux, C.; Sabir, M.; Pépin, Y. Distinct and Combined Impacts of Climate and Land Use Scenarios on Water Availability and Sediment Loads for a Water Supply Reservoir in Northern Morocco. *Int. Soil. Water Conserv. Res.* **2020**, *8*, 141–153. [CrossRef]
96. Ahmadi, M.; Moeini, A.; Ahmadi, H.; Motamedvaziri, B.; Zehtabiyan, G.R. Comparison of the Performance of SWAT, IHACRES and Artificial Neural Networks Models in Rainfall-Runoff Simulation (Case Study: Kan Watershed, Iran). *Phys. Chem. Earth Parts A/B/C* **2019**, *111*, 65–77. [CrossRef]
97. Samimi, M.; Mirchi, A.; Moriasi, D.; Ahn, S.; Alian, S.; Taghvaeian, S.; Sheng, Z. Modeling Arid/Semi-Arid Irrigated Agricultural Watersheds with SWAT: Applications, Challenges, and Solution Strategies. *J. Hydrol.* **2020**, *590*, 125418. [CrossRef]
98. Wing, O.E.J.; Bates, P.D.; Sampson, C.C.; Smith, A.M.; Johnson, K.A.; Erickson, T.A. Validation of a 30 m Resolution Flood Hazard Model of the Conterminous United States. *Water Resour. Res.* **2017**, *53*, 7968–7986. [CrossRef]
99. Ruiz-AÍvarez, M.; Gomariz-Castillo, F.; Alonso-Sarría, F. Evapotranspiration Response to Climate Change in Semi-Arid Areas: Using Random Forest as Multi-Model Ensemble Method. *Water* **2021**, *13*, 222. [CrossRef]
100. Sharifinejad, A.; Hassanzadeh, E. Evaluating Climate Change Effects on a Snow-Dominant Watershed: A Multi-Model Hydrological Investigation. *Water* **2023**, *15*, 3281. [CrossRef]
101. Yen, H.; Ahmadi, M.; White, M.J.; Wang, X.; Arnold, J.G. C-SWAT: The Soil and Water Assessment Tool with Consolidated Input Files in Alleviating Computational Burden of Recursive Simulations. *Comput. Geosci.* **2014**, *72*, 221–232. [CrossRef]

102. Ahmadi, M.; Ascough, J.C.; DeJonge, K.C.; Arabi, M. Multisite-Multivariable Sensitivity Analysis of Distributed Watershed Models: Enhancing the Perceptions from Computationally Frugal Methods. *Ecol. Model.* **2014**, *279*, 54–67. [CrossRef]
103. Zhang, D.; Chen, X.; Yao, H.; Lin, B. Improved Calibration Scheme of SWAT by Separating Wet and Dry Seasons. *Ecol. Model.* **2015**, *301*, 54–61. [CrossRef]

water

MDPI

Article

Intelligent Methods for Estimating the Flood Susceptibility in the Danube Delta, Romania

Romulus Costache [1], Anca Crăciun [1,*], Nicu Ciobotaru [1] and Alina Bărbulescu [2,*]

[1] Danube Delta National Institute for Research and Development, 165 Babadag Street, 820112 Tulcea, Romania; romuluscostache2000@yahoo.com (R.C.); ciobotarunicu@gmail.com (N.C.)
[2] Department of Civil Engineering, Transilvania University of Brasov, 5, Turnului Street, 500152 Brasov, Romania
* Correspondence: anca.craciun@ddni.ro (A.C.); alina.barbulescu@unitbv.ro (A.B.)

Abstract: Floods, along with other natural and anthropogenic disasters, profoundly disrupt both society and the environment. Populations residing in deltaic regions worldwide are particularly vulnerable to these threats. A prime example is the Danube Delta (DD), located in the Romanian sector of the Black Sea. This research paper aims to identify areas within the DD that are highly or very highly susceptible to flooding. To accomplish this, we employed a combination of multicriteria decision-making (AHP) and artificial intelligence (AI) techniques, including deep learning neural networks (DLNNs), support vector machines (SVMs), and multilayer perceptron (MLP). The input data comprised previously flooded regions alongside eight geographical factors. All models identified high or very high flood potential of over 65% of the studied area. The models' performance was assessed using receiver operating characteristic (ROC) analysis, demonstrating excellent outcomes evaluated by the area under the curve (AUC) exceeding 0.908. This study is significant as it lays the groundwork for implementing measures against flood impacts in the DD.

Keywords: AHP; flood potential index; machine learning; MLP; SVM

1. Introduction

Floods lead to significant socioeconomic losses and environmental damage worldwide. Reducing flood risk and managing water resources in the face of global environmental changes presents a major challenge for contemporary society [1]. Floods are complex phenomena that can create varying levels of damage depending on the geographical conditions of the affected areas. Given the increasing frequency and severity of floods, accurately identifying flood risk areas is essential [2].

Every year, numerous regions face natural disasters linked to water in excess. Floods, in particular, rank as the most destructive among natural hazards, impacting nearly 200 million people worldwide annually [3,4]. During recent decades, there has been an important recorded increase in the frequency of these disasters [5,6], mostly attributed to the global climate change. This trend is expected to continue, resulting in more damages from floods [7]. In Europe, Romania ranks third after Italy and France in terms of the financial impact and casualties caused by these phenomena [8].

According to the European Directive on Floods 2007/60/EC [9], all actions aimed at reducing the adverse impacts of floods need to be grounded in the prior identification of areas most vulnerable to these natural hazards [10]. Assessing flood susceptibility in a region is also a critical non-structural measure for effective flood risk management. National hydrological forecasting centers issue flood forecasts and warnings by evaluating predicted precipitation and the area's susceptibility to flooding. To maximize the effectiveness of flood mitigation efforts, accurate assessment of flood potential in a given region is crucial.

In general, worldwide, floodplains and deltas are very sensitive to increased flows and river levels that can easily generate floods [11,12]. Flood susceptibility indices and

hydrodynamic modeling are very prevalent in the studies aimed to estimate areas affected by river flooding. It should be noted that river deltas are extremely vulnerable to environmental changes and natural disasters [13]. Therefore, it is crucial to examine the natural hazards that may impact the ecological systems of coastal environment and deltaic areas, with a particular focus on identifying areas susceptible to these phenomena.

In recent years, numerous models for estimating susceptibility to flooding have been proposed by the specialized scientific literature and have also been applied, including for deltaic areas [14–16]. Traditional hydrological techniques, like data-driven analysis and also rainfall-runoff models, cannot comprehensively analyze rivers and floodplains. Significant advancements in flood modeling and prediction have been achieved through the use of geographic information systems (GIS) and remote sensing [17]. Along with the increase in the number of papers dealing with this theme, there has also been a significant diversification of models applied to evaluate the flood hazard. From a qualitative point of view, in the specialized literature, flood hazard is expressed through the susceptibility or potential for the occurrence of these phenomena [10,18]. The first category of widely used methods for determining areas susceptible to flooding is multicriteria decisional analysis. This category includes the AHP, analytical network process, TOPSIS, and VIKOR methods [19,20]. Fuzzy systems have also been applied to identify the zones most prone to floods [21].

Both decisional multicriteria analysis and fuzzy systems are methods that rely on expert opinions, which introduce a certain degree of subjectivity [22]. In contrast, there are algorithms that do not rely on expert intervention; instead, their application is based solely on the available data [23]. Bivariate statistics, such as frequency ratios, evidence weights, the entropy index, and statistical indices, fall into this category. Additionally, various techniques from the field of artificial intelligence have been adapted for calculating flood susceptibility, including ANN and the ANFIS [24,25]. Another group of methods that relies exclusively on available data belongs to ML (a subfield of AI), which includes SVM, random forests (RFs), classification and regression trees, rotation forests, and naïve Bayes [26]. All of these models utilize datasets that contain the locations of past flood events along with a variable number of predictors [27]. The ability to evaluate a model's precision and verify the results is a significant benefit of using these methods to evaluate susceptibility to floods.

In Romania, most studies investigated water quality [28–30], a few articles utilized AI or hybrid methods for flood evaluation of some rivers [31–35], and only a limited number of studies [36,37] were dedicated to hydrological modeling for small zones in the DD biosphere reserve, which is the subject of this study. Therefore, the main goal of our article is determining the flood hazard in the DD biosphere reserve through AI methods. The study will highlight aspects that were not investigated until now, which will also contribute to a better understanding of the flooding mechanism and serve as a background for policymakers for insight into the measures that can be taken for flood prevention and the mitigation of their effects.

2. Data Series and Methodology

2.1. The Study Zone

The analyzed region is the DD (Figure 1), which was formed in the last 5200 years between the Bugeacului Plain and the Dobrogea Plateau. A morphological analysis classifies the DD as a developing alluvial plain, with reduced hypsometry. The maximum elevation range of 64 m is related to the region of the Letea fluvial sea dike and Tulcea Branch. The DD is formed by the deposition of sediments carried by the Danube River, creating a complex network of channels, lakes, islands, marshes, and reed beds. It constantly shifts, with new islands and channels forming, while older ones may disappear or become more saline over time.

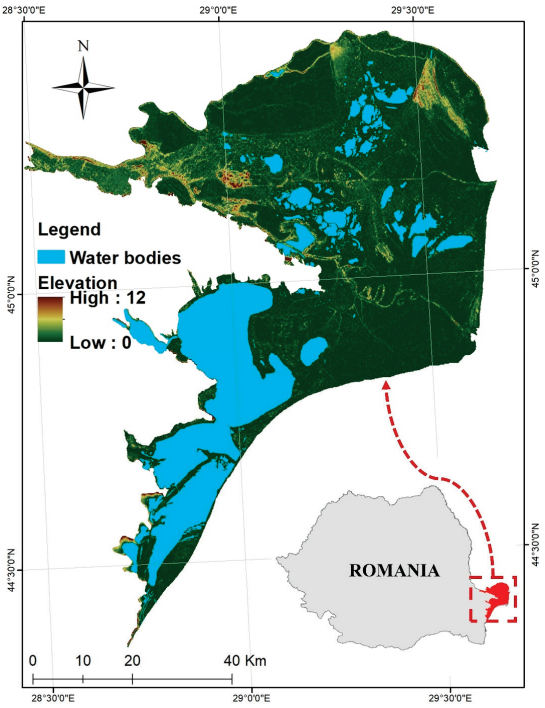

Figure 1. Map of the research zone.

The DD faces significant flood hazards due to its low-lying geography, the seasonal variability of the Danube River, and climate change. The delta's ecosystem stability is threatened by sea-level depth rise, temperature rising, and shifts in rainfall patterns. Its biodiversity is also at significant risk from increasingly frequent extreme meteorological phenomena like drought and floods.

2.2. Data Series

2.2.1. Inventory of Flooded Areas

In our pursuit of applying AI methods to understand the influence of geographical factors on flood occurrence, we identified the zones previously subjected to floods. We divided this dataset into training areas (70% of the total) and validation areas (30%). To ensure the highest degree of objectivity of the results, we randomly selected other dry areas within the DD, with a total area equal to those affected by floods. These were also split into training and validation zones (70–30%). Given that the flood susceptibility detection is a binary process, the first dataset used in the AI models, signifying the presence of flood phenomena, was coded with 1, while the second dataset, signifying the absence of flood phenomena, was coded with 0. The presence/absence of flood-affected areas will constitute the dependent variable within the AI models for flood-susceptible zones.

2.2.2. Flood Conditioning Factors

Identifying areas susceptible to flooding requires consideration of eight key factors that significantly influence flood occurrence: relief slope, altitude, distance from watercourses, land use, vertical distance from rivers, distance from water bodies, lithology, and soil hydrological group. The relief slope, elevation, and vertical distance from rivers are morphometric factors derived from the digital terrain model (DTM).

The study area's DTM was extracted utilizing the SRTM database. The other five factors were obtained by extracting or processing existing vector databases. Specifically, the distances to rivers and water bodies were calculated using the recorded hydrographic network of rivers and lakes. Additionally, the land use dataset was obtained from the Corine Land Cover 2018, while lithological information was sourced from the Geological Map of Romania in digital format at 1:200,000 scale. The spatial distribution of the soil

hydrological group in the DD was also represented using the Digital Soil Map of Romania at 1:200,000 scale. Below is a brief description of all eight geographic factors that were used in this research.

The slope of the relief can influence the flooding susceptibility in a given area. Slope angle refers to the steepness or gradient of the land surface and decisively influences surface runoff during a flood event [38]. Here, the slope categories are as follows: 0–1°, 1.1–2°, 2.1–3°, 3.1–4°, and >4° (Figure 2a).

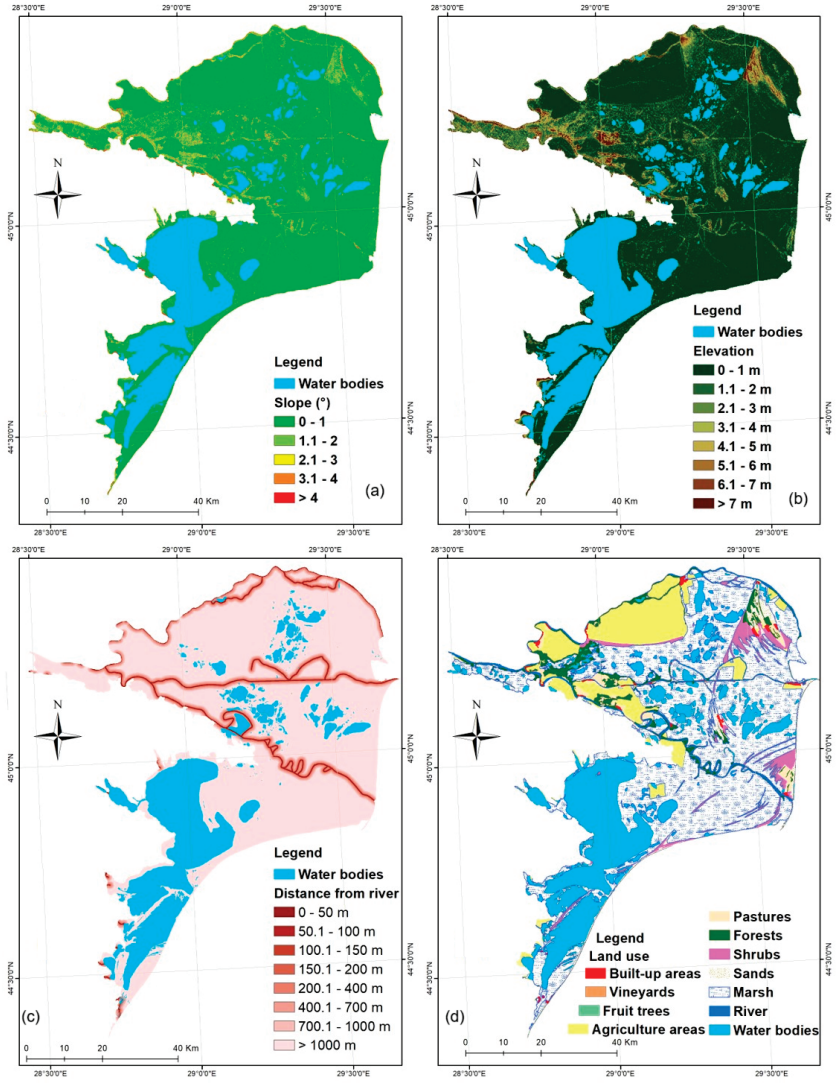

Figure 2. Factors conditioning the flooding (**a**) slope, (**b**) altitude, (**c**) distance to rivers, and (**d**) land use.

Elevation significantly impacts flood susceptibility. Zones having low altitudes are more exposed to flood genesis because of proximity to water bodies or their tendency to collect water during heavy rains [39]. In this study, eight classes were established for elevation: 0–1 m, 1–2 m, 2–3 m, 3–4 m, 4–5 m, 5–6 m, 6–7 m, and >7 m (Figure 2b).

Distance to rivers greatly influences flood susceptibility, with regions near rivers or within low-lying floodplains facing a higher risk [40]. Even distant low-lying zones can collect water during heavy rains, making them prone to flooding. Specific distance classes have been established to assess this factor: [0, 50), [50, 100), [100, 150), [150, 200), [200, 400), [400,700), [700, 1000), and above 100 m (Figure 2c).

Land use in deltaic regions can significantly impact flood susceptibility. The presence of impervious surfaces (roads and buildings) can increase the amount of runoff on the ground surface and contribute to flooding genesis [41]. According to the Corine Land

Cover database, 10 classes could be found in the DD (Figure 2d). Areas of the DD occupied by swamps that are not ecologically designed as floodwater retention areas can be highly flood-prone.

The vertical distance to the river affects flood susceptibility, and higher elevations above the drainage channel are less prone to flooding. However, areas in narrow valleys or steep slopes may still face risks due to rapid water drainage. In the DD, the altitude above the channel was categorized into the following specific groups: [0, 1), [1, 2), [2, 3), [3, 4), [4, 5), [5, 6), [6, 7), and greater than 7 m (Figure 3a).

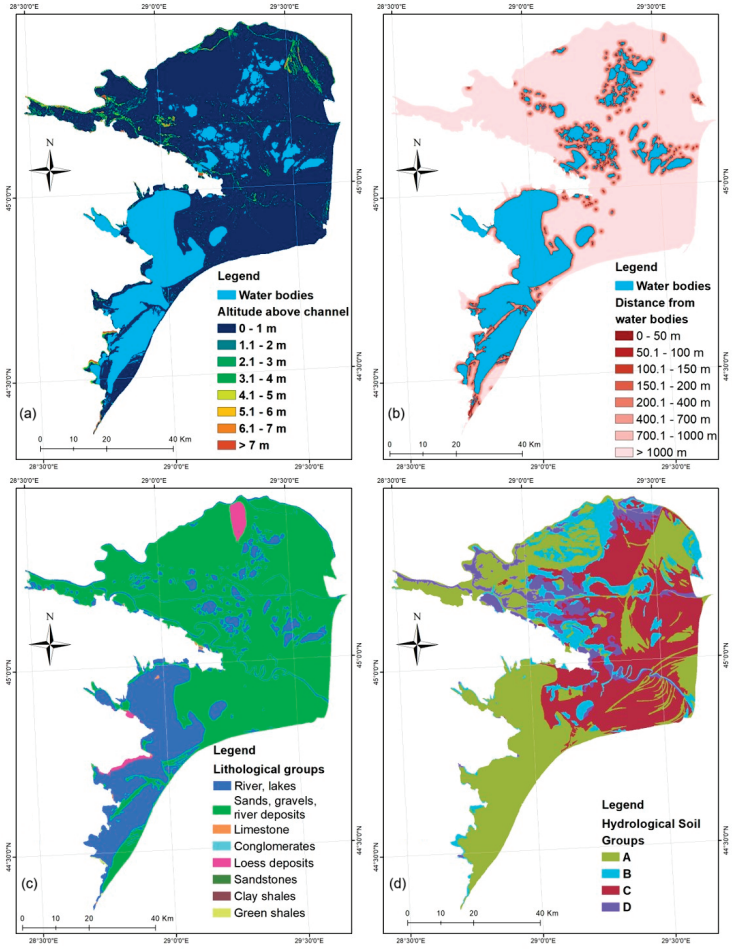

Figure 3. Factors conditioning the flood (**a**) vertical distance to rivers, (**b**) distance to water bodies, (**c**) lithology, and (**d**) hydrological soil group.

In the DD, water bodies cover vast areas, and any rise in their water levels poses a significant threat to surrounding regions. The distance to these water bodies was calculated using the Euclidean distance method. Eight distance classes (in meters) were established to define the proximity to water bodies: [0, 50), [50, 100), [100, 150), [150, 200), [200, 400), [400, 700), [700, 1000), and greater than 1000 m (Figure 3b).

Lithology influences flood susceptibility as different rock types vary in permeability. Impermeable rocks, like clay, increase surface runoff, raising flood risk, while permeable rocks, like sand or gravel, promote water infiltration, reducing risk [24]. Six lithological categories were identified in the DD (Figure 3c).

Soil type also impacts the rate of water infiltration, sometimes favoring the accumulation of water at the surface of the soil. For this study, the digital Romanian soil map at a 1:200,000 scale was used as a data source. As shown in Figure 3d, all four hydrological groups are represented in the DD.

The classification of the following factors was based on expert judgment, which considered the study area's characteristics: slope, altitude, distance from water bodies, distance from rivers, and vertical distance to the river network. Land use, lithological groups, and hydrological soil groups were classified according to their categories.

2.3. Methodology

2.3.1. Information Gain (IG)

IG measures the reduction in uncertainty (entropy) of a target variable Y when a feature X is known. Here, Y is the location of flooded areas, while each conditioning factor represents X. Features with higher IG are considered more informative and are often selected for building predictive models.

IG was used to test each factor's predictive ability regarding rapid water runoff on slopes. This method reduces uncertainties by eliminating factors with a low predictive capacity.

The quality of a discrete attribute is defined as the expected decrease in impurity when the attribute value is known. Information gain is determined as the difference between the entropy of a class and the entropy of the same class conditioned by the attribute [42]. It should be noted that the IG results do not have general applicability, being influenced by the characteristics of the zone and the location of the dependent variable.

The IG values were determined in WEKA 3.9.2 software.

2.3.2. Analytical Hierarchy Process (AHP)

Given the importance of establishing weights as objectively as possible for the classes of factors that influence the potential for flood formation, the AHP method was used in the present study. This algorithm [43] allows for solving and analyzing a problem flexibly and easily. A key feature of this approach is the active involvement of specialists throughout the entire methodological process. AHP is commonly used in research aiming to assess susceptibility to natural risk phenomena [44]. The core of the methodology lies in breaking down complex problems into a hierarchical structure, placing at the top the main goal, with criteria and sub-criteria following at lower levels. At the bottom, the alternative decisions are situated.

Five main stages can be distinguished when using AHP to determine the coefficients of the factor classes within the study area:

(i) Divide the problem into several parts, then set the objectives.
(ii) Determine the criteria and alternatives.
(iii) Create a comparison matrix, X, for the pairs of factors that influence flood production, and the pairs composed of their respective categories or classes. X is built taking into account the expert judgment regarding the impact of each factor category/class on flooding potential. If one class/category is more significant than another, its relative value will range from 1 to 9 and be assigned horizontally. Conversely, when a class/category is less important, the values assigned horizontally will vary between 1/9 and 1/2.
(iv) Compute the relative weights of the factors category/class using the eigenvalue technique.
(v) Calculate the consistency ratio (CR) matrix, which shows the pairwise comparisons' quality. CR is obtained using Equation (2), which involves first calculating the consistency index (CI) from Equation (1):

$$CI = \frac{\lambda_{max} - n}{n - 1} \quad (1)$$

where λ_{max} is the highest eigenvalue and n is the number of factors conditioning the potential for flash floods, respectively.

$$CR = CI/RI \quad (2)$$

The number of categories/classes of the factors, and *RI* depend on the number of factors included in the comparison matrix (Table 1).

Table 1. *RI* [43].

n	3	4	5	6	7	8	9	10	11	12	13	14	15
RI	0.58	0.90	1.12	1.24	1.32	1.41	1.45	1.49	1.51	1.53	1.56	1.57	1.59

A qualitatively performing comparison matrix is indicated by a $CR < 0.1$.

All mathematical operations were performed in Microsoft Excel 2016 software, while maps and primary data related to geographic factors were obtained in ArcGIS 10.5.

The values of the AHP coefficients formed the input data in the AI algorithm to calculate the flood susceptibility within the DD.

2.3.3. DLNN

Deep learning (DL) belongs to of machine learning (ML) category, which utilizes AI networks to learn from large datasets. It relies on layers of neural networks, which are heavily inspired by brain functions. Training these networks with extensive data adjusts the configuration of neurons within the system. Once trained, a DL model can process new data. These models analyze information from various data sources in real-time, without human intervention.

Compared to basic ANNs, DLNNs feature a structure with multiple hidden layers composed of neurons. Whereas a simple neural network may have one or two hidden layers, a DLNN may have a high number of layers. Increasing this number and the nodes can improve the performance, but an increased number of parameters and computational resources are also required. DL processes and classifies information, each layer receiving the raw data as input [45,46].

In this study, the DLNN model was applied to estimate flood susceptibility. The flood conditioning factors served as input data in the input layer, while the dataset indicating the presence or absence of flooded areas was used as output data in the output layer. A sigmoid function, $E(Y = 1/x)$, was employed to classify pixels as either flooded or non-flooded. The output layer consisted of a single neuron for each class i, providing an approximation of $E(Y = i/x)$. The sum of all estimated values equaled 1. For this study, the *softmax* function was used for the final classification:

$$softmax(a_i) = \frac{\exp(a_i)}{\sum_k \exp(a_i)} \quad (3)$$

where a_i is a layer of the *softmax* function.

A neural network with multiple hidden layers (h) can be expressed utilizing the following mathematical relations:

$$a^{(h)}(x) = b^{(h)} + W^{(h)} p^{(h-1)}(x), \quad (4)$$

$$p^{(h)}(x) = \varnothing(a^{(h)}(x)) \quad (5)$$

where $\varnothing$ is the activation function, and for $h = 1, \ldots, H$ (hidden layers).

The TensorFlow2.0 platform and Keras in Python 3.13.1 were used to run the DLNN model.

2.3.4. Support Vector Machine

SVM is a robust, supervised mathematical ML algorithm widely used in training dataset classification. It is primarily a binary classification technique that identifies an optimal hyperplane in an n-dimensional space based on the training data. This hyper-

plane is then used to classify new datasets, effectively dividing the training data into two distinct classes.

To classify multidimensional data, SVM employs "kernels" that enable the construction of multidimensional hyperplanes. A hyperplane acts as a boundary that separates data points, serving as a decision boundary between the two classes. When there are two input variables, the hyperplane is represented as a straight line; if there are more than two inputs, it becomes a plane in higher dimensions.

Support vectors are the data points that play a crucial role in optimizing the hyperplane. These vectors are positioned closest to the hyperplane and represent the most challenging cases to classify. The location of the decision hyperplane is directly influenced by the SVs. If these SVs are removed, the position of the hyperplane will change as a result [47]. The inputs and outputs of an SVM are similar to those of a neural network. Constructing an optimized hyperplane in a linearly separable problem is done using Kernels functions.

2.3.5. Multilayer Perceptron (MLP)

An MLP [48] is an ANN formed by multiple layers of neurons, among which is an input and output layer and one or many hidden layers. Hidden layers are formed of interconnected neurons and have the role of processing the input data. All neurons from a hidden layer receive information from all neurons from the previous layer. Each input value is multiplied by a certain weight, influencing the output. A bias is also associated with each neuron. During the training phase, the biases and weights are learned, and the output of each neuron in a hidden or output layer is obtained by computing the weighted sum of the inputs plus the bias. Training the network is done by a backpropagation algorithm aiming to minimize the root mean square error (RMSE). RMSE values close to 0 highlight the models' good performance.

2.3.6. ROC Curve for Results Validation

The ROC curve is built in orthogonal coordinates, where the *X*-axis contains the specificity and the *Y*-axis the sensitivity. It is used to measure the efficiency of a model. The larger the AUC, the better the model. The following reference intervals are considered for AUC: [0.9, 1]—the model is excellent, [0.8, 0.9)—very good, [0.7, 0.8)—good, [0.6, 0.7)—fair; values under 0.6 lead to the model's rejection [49].

The workflow for the present research is shown in Figure 4.

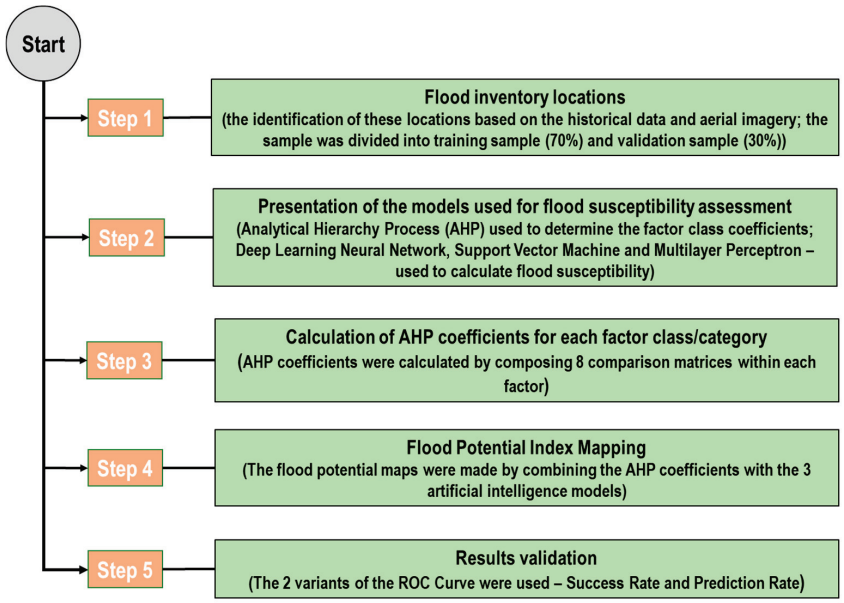

Figure 4. Workflow diagram.

3. Results

3.1. Information Gain Results

After applying the IG, it was found that the slope of the relief had the highest predictability for flood events, with an indicator value of 0.67. The vertical distance from nearby rivers was identified as the second most significant factor, with a value of 0.53. The hierarchy of the remaining factors is as follows: Altitude (0.41), Land use (0.36), Distance from rivers (0.29), Lithology (0.27), Distance from water bodies (0.22), and Hydrological soil groups (0.15) (Figure 5). Overall, the results from this method indicate that all eight geographic factors analyzed have some capacity to influence flooding events. Therefore, all eight variables will be considered for further analysis.

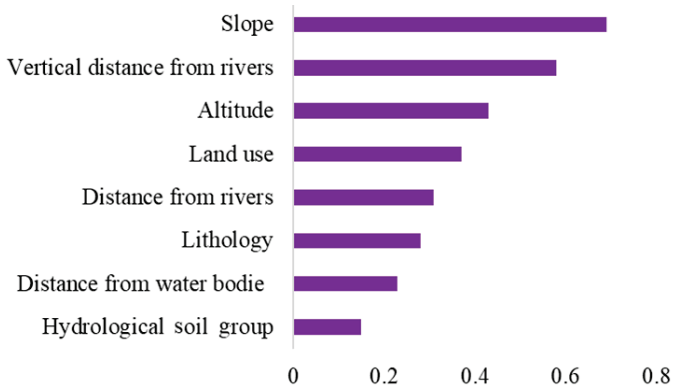

Figure 5. IG values.

3.2. Analytical Hierarchy Process Results

Table 2 contains all the possible combinations made between the classes/categories of geographical factors that condition the occurrence of floods. Each factor or class/category was compared to the others by assigning a dominant relative value, based on insights from the specialized literature [50]. The corresponding weights are provided in Table 2.

Table 2. AHP matrices used for factor weighting and factor classes/categories.

Factors/Classes Categories	**Pair-Wise Comparison**								**AHP**
Class/Categories	**[1]**	**[2]**	**[3]**	**[4]**	**[5]**	**[6]**	**[7]**	**[8]**	**Weights**
Slope (°)									
[1] 0–1	1	4	6	7	9				0.546
[2] 1–2	1/4	1	3	4	6				0.229
[3] 2–3	1/6	1/3	1	2	4				0.113
[4] 3–4	1/7	1/4	1/2	1	3				0.075
[5] >4	1/9	1/6	1/4	1/3	1				0.037
Altitude (m)									
[1] 0–1	1	2	3	4	5	6	7	8	0.327
[2] 1–2	1/2	1	2	3	4	5	6	7	0.227
[3] 2–3	1/3	1/2	1	2	3	4	5	6	0.157
[4] 3–4	1/4	1/3	1/2	1	2	3	4	5	0.108
[5] 4–5	1/5	1/4	1/3	1/2	1	2	3	4	0.073
[6] 4–6	1/6	1/5	1/4	1/3	1/2	1	2	3	0.050
[7] 6–7	1/7	1/6	1/5	1/4	1/3	1/2	1	2	0.034
[8] >7	1/8	1/7	1/6	1/5	1/4	1/3	1/2	1	0.024

Table 2. *Cont.*

Factors/Classes Categories	**Pair-Wise Comparison**								**AHP**
Class/Categories	**[1]**	**[2]**	**[3]**	**[4]**	**[5]**	**[6]**	**[7]**	**[8]**	**Weights**
Distance from river (m)									
[1] 0–50	1	2	3	4	5	6	7	9	0.323
[2] 50–100	1/2	1	2	3	4	5	6	7	0.221
[3] 100–150	1/3	1/2	1	2	3	4	5	6	0.152
[4] 150–200	1/4	1/3	1/2	1	2	3	4	5	0.104
[5] 200–400	1/5	1/4	1/3	1/2	1	3	3	3	0.073
[6] 400–700	1/6	1/5	1/4	1/3	1/3	1	4	6	0.063
[7] 700–1000	1/7	1/6	1/5	1/4	1/3	1/4	1	6	0.043
[8] >1000	1/9	1/7	1/6	1/5	1/3	1/6	1/6	1	0.021
Land use									
[1] Forests, sands	1	1/3	1/5	1/7	1/9				0.035
[2] Vineyards, fruit trees, shrubs	3	1	1/3	1/5	1/7				0.069
[3] Agriculture areas	5	3	1	1/3	1/5				0.136
[4] Pastures	7	5	3	1	1/2				0.286
[5] Built-up areas, marsh, river, water bodies	9	7	5	2	1				0.474
Altitude above channel (m)									
[1] 0–1	1	2	3	4	5	6	7	8	0.327
[2] 1–2	1/2	1	2	3	4	5	6	7	0.227
[3] 2–3	1/3	1/2	1	2	3	4	5	6	0.157
[4] 3–4	1/4	1/3	1/2	1	2	3	4	5	0.108
[5] 4–5	1/5	1/4	1/3	1/2	1	2	3	4	0.073
[6] 4–6	1/6	1/5	1/4	1/3	1/2	1	2	3	0.050
[7] 6–7	1/7	1/6	1/5	1/4	1/3	1/2	1	2	0.034
[8] >7	1/8	1/7	1/6	1/5	1/4	1/3	1/2	1	0.024
Distance from water bodies (m)									
[1] 0–50	1	2	3	4	5	6	8	9	0.324
[2] 50–100	1/2	1	2	3	4	5	7	8	0.225
[3] 100–150	1/3	1/2	1	2	3	4	6	7	0.156
[4] 150–200	1/4	1/3	1/2	1	2	4	5	6	0.113
[5] 200–400	1/5	1/4	1/3	1/2	1	2	3	4	0.069
[6] 400–700	1/6	1/5	1/4	1/4	1/2	1	2	6	0.053
[7] 700–1000	1/8	1/7	1/6	1/5	1/3	1/2	1	6	0.040
[8] >1000	1/9	1/8	1/7	1/6	1/4	1/6	1/6	1	0.019
Lithology									
[1] Sands, gravels, river deposits	1	1/2	1/4	1/6	1/9				0.043
[2] Loess deposits	2	1	1/2	1/3	1/4				0.090
[3] Limestone, conglomerates	4	2	1	1/2	1/5				0.142
[4] Clay shale, green shale	6	3	2	1	1/2				0.256
[5] Sandstone	9	4	5	2	1				0.469
Hydrological soil groups									
[1] A	1	3/4	1/2	1/5					0.108
[2] B	4/3	1	3/4	1/3					0.157
[3] C	2	4/3	1	1/3					0.201
[4] D	5	3	3	1					0.534

It can be seen that the highest AHP coefficient is assigned to slopes between 0° and 1°, which is equal to 0.546. A high value of this type of coefficient, of 0.534, was also obtained by soil hydrological group D. This factor class was followed by swamps within the land use mode, with a value of 0.474, and by the lithological category represented by sandstones, with a value of 0.469. Also, areas located far from watercourses below 50 m (0.362) and altitudes below 1 m (0.327) are considered categories of factors with high values of AHP coefficients.

CR values were involved in the quality assessment of matrices comparison procedure (Table 3). The *CR* values for all eight comparison matrices are below 0.1, indicating a high-quality analysis. Additionally, the table includes the values for the other parameters discussed in the theoretical section of the AHP model. These AHP coefficient values were

then used as input data in the AI models to identify the final flood-prone areas within the DD.

Table 3. Properties of AHP pair-wise comparison matrices.

Factors	No. of Factors/Classes	λ_{max}	*CI*	*RI*	*CR*
All factors	8	8.067	0.010	1.41	0.007
Slope	5	5.223	0.056	1.12	0.050
Elevation	8	8.048	0.007	1.41	0.005
Distance from river	8	8.351	0.050	1.41	0.036
Land use	5	5.223	0.056	1.12	0.050
Altitude above channel	8	8.048	0.007	1.41	0.005
Distance from water bodies	8	8.351	0.050	1.41	0.036
Lithology	5	5.223	0.056	1.12	0.050
Hydrological soil groups	4	4.011	0.004	0.90	0.004

3.3. DLNN Results

To train the DLNN model, a maximum of 100 epochs were set. For the training set, the minimum value of the loss parameter, equal to 0.0746, was reached after 99 epochs. The same situation was recorded for the validation set. In this regard, there were several parameters used: ReLU activation function, uniform kernel initialization function, a dropout rate of 0.1, a lot dimension of 100, a validation rate of 0.3, eight input neurons, a maximum of 100 hidden neurons, three hidden layers, and two output neurons. The architecture of DLNN, containing the input, hidden, and output layers, is represented in Figure 6.

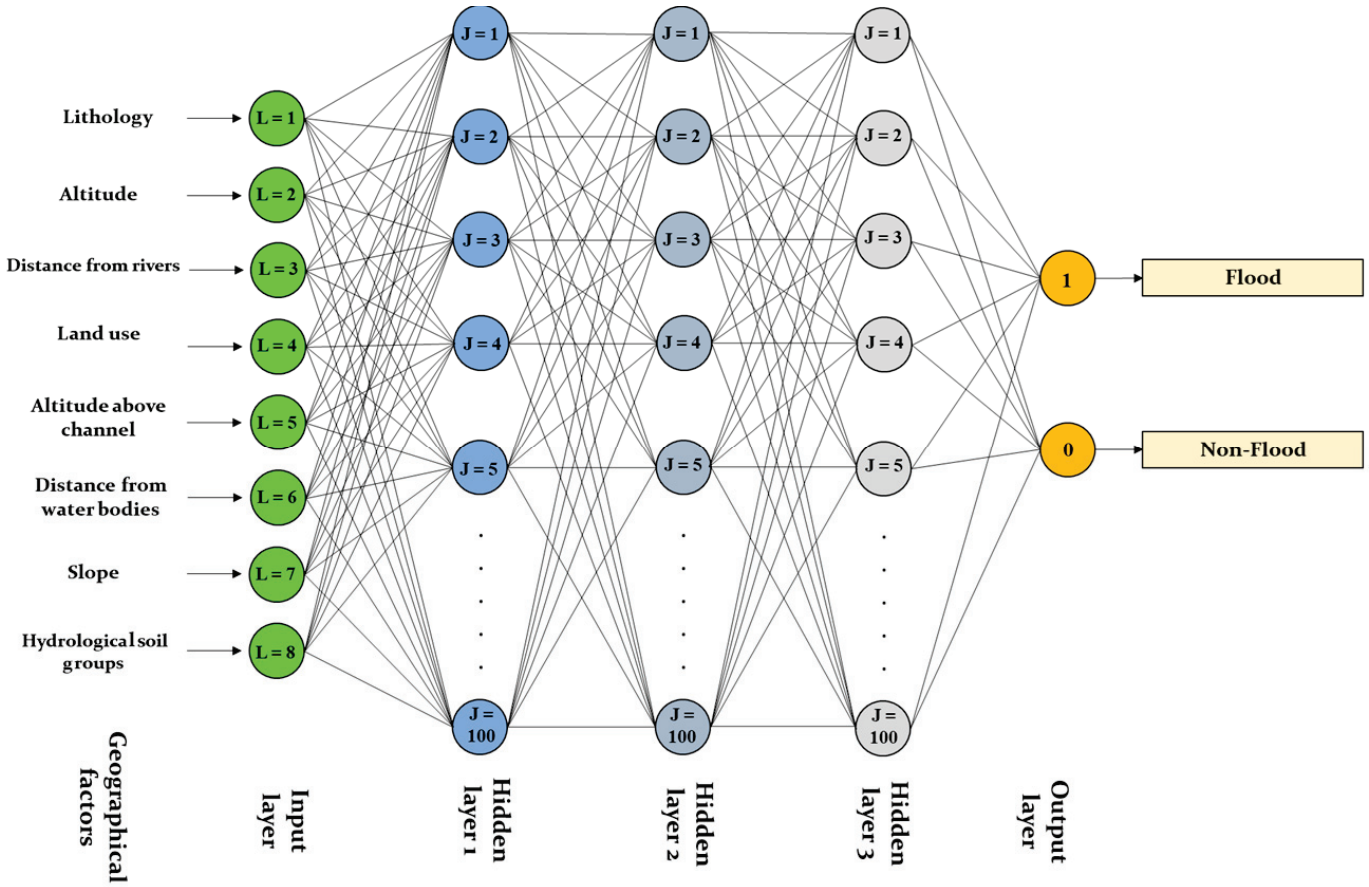

Figure 6. Architecture of the DLNN model used to determine flood susceptibility.

After training the model, the weights of each geographic factor used in this step were determined. Thus, the relief slope got the highest weight (0.241), followed by elevation (0.212), distance to rivers (0.173), land use (0.148), vertical distance to rivers (0.102), distance

to water bodies (0.069), lithology (0.029), and soil hydrologic group (0.026) (Figure 7). Utilizing cartographic algebra, these weights were multiplied by the AHP coefficients, after which the products resulting from the multiplication were added. Thus, the spatialized values of the susceptibility to floods, represented by the FPI, resulted (Figure 8a).

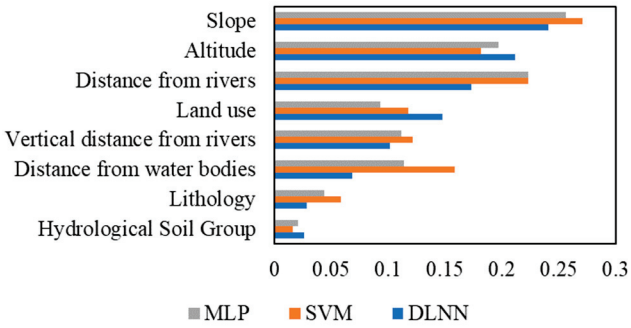

Figure 7. The weight of the geographic factors in the AI models.

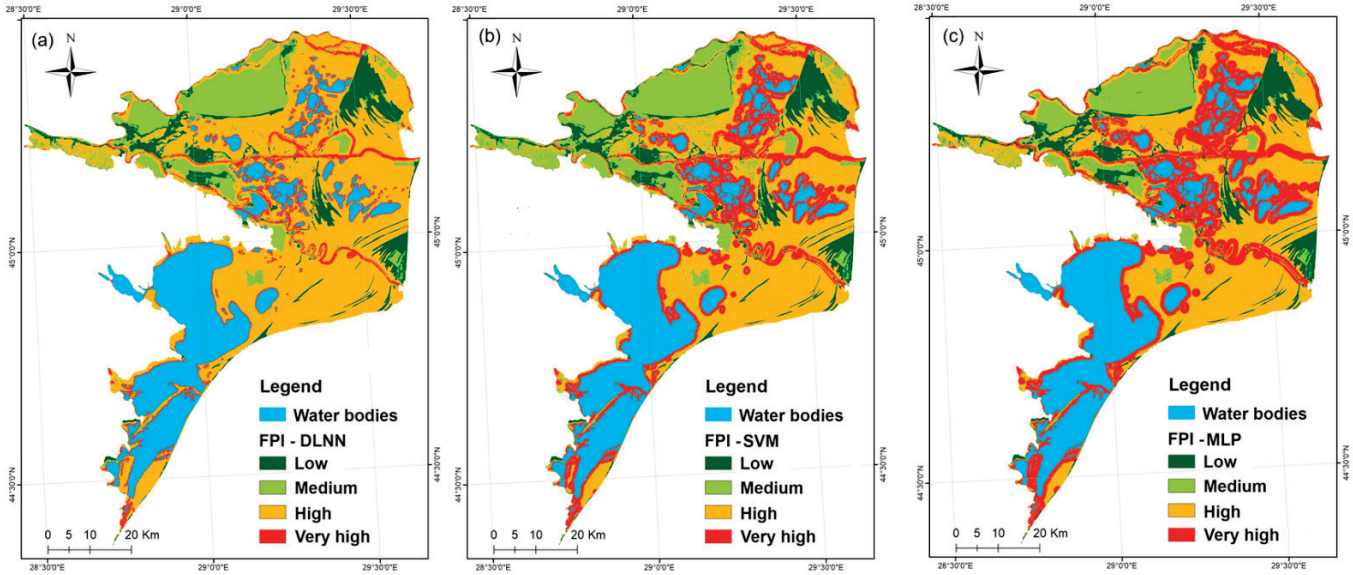

Figure 8. FPI (**a**) DLNN, (**b**) SVM, and (**c**) MLP.

The FPI-DLNN values were grouped into four classes using the natural breaks method. The first class refers to the reduced flood susceptibility values within the DD, which covers the higher areas, represented mainly by beams. The share of this class is 15% of the total study area (Figure 9). Next, the average flood susceptibility class is mainly distributed in the northern area of the DD. Overall, a percentage of 20% of the territory subject to research is moderately prone to flooding.

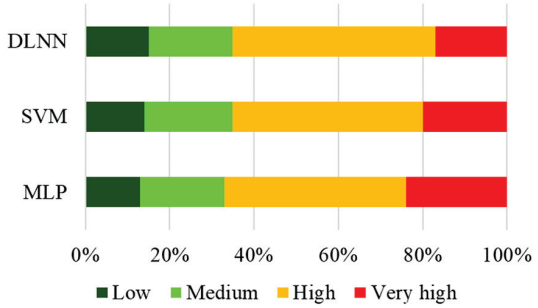

Figure 9. Weight of FPI classes calculated through ML methods.

The highest surface is occupied by areas with a high flood potential, which extend to about 48% of the study area. The areas characterized by a very high susceptibility to flooding are mainly located along the main watercourses in the study area. They extend over approximately 17% of the total territory occupied by the DD.

3.4. SVM Model Results

As with DLNN, the AHP values for each geographic factor class and category were used as input data within the SVM model. The accuracy of the results provided by SVM depends on the correct selection of the kernel function and the estimation of two parameters, C and γ, through the cross-validation procedure. The value of the parameter C was estimated at 2.1, and the value of γ was equal to 0.2. This pair of values shows a very well-optimized SVM model [51]. Once the training procedure was completed, the weights associated with the geographical factors could also be determined. Again, the slope of the relief obtained the highest importance (0.271), followed by the distance from rivers (0.223), altitude (0.182), distance from water bodies (0.159), vertical distance from rivers (0.122), land use (0.118), lithology (0.059), and soil hydrologic group (0.016). Like in the DLNN case, the spatialization of the FPI values was also achieved (Figure 8b) through cartographic algebra.

To compare the model's results, the values were again grouped into four classes using the natural breaks method. The lowest share, equal to 14%, can be attributed to areas where the susceptibility to flooding has a low value. Beams occupy the areas with higher altitudes than the surrounding regions. The average FPI extends mainly in the study area's northern half and occupies 21% of the total. A high susceptibility to flooding characterizes the equivalent of 45% of the DD, while the very high potential areas, represented on the map in red, have a weight of 20%.

3.5. MLP Model Results

To apply MLP, an architecture with eight neurons in the input layer, a maximum of 100 hidden neurons, and two neurons in the output layer (representing the presence or absence of flooding) was used (Figure 10). After the training process, RMSE reached its minimum value of 0.014 (Figure 11a) for 43 hidden neurons. The estimated pseudo-likelihood parameter indicates the accuracy of the classification process. A significant presence of values below 0.2 (for true positives) or above 0.8 (for false positives) in both flood and non-flood locations (areas where no floods occurred) indicates good classification accuracy. As shown in Figure 11b, these two classifications (floods and non-floods) are prominently present within the specified intervals, suggesting that the classification operation performed using the MLP model is highly accurate.

After training the MLP model, we derived the weights of the geographic factors used to assess flood susceptibility in the DD.

The factor with the highest weight was slope, at 0.256, followed by distance from rivers at 0.223, altitude at 0.197, distance from water bodies at 0.114, vertical distance from rivers at 0.112, land use at 0.093, lithology at 0.044, and soil hydrologic group at 0.021. Using the weights of these eight geographic factors in cartographic algebra, we calculated the flood potential index (FPI) through the MLP model. The final results were categorized into four value classes using the natural breaks method, as illustrated in Figure 8.

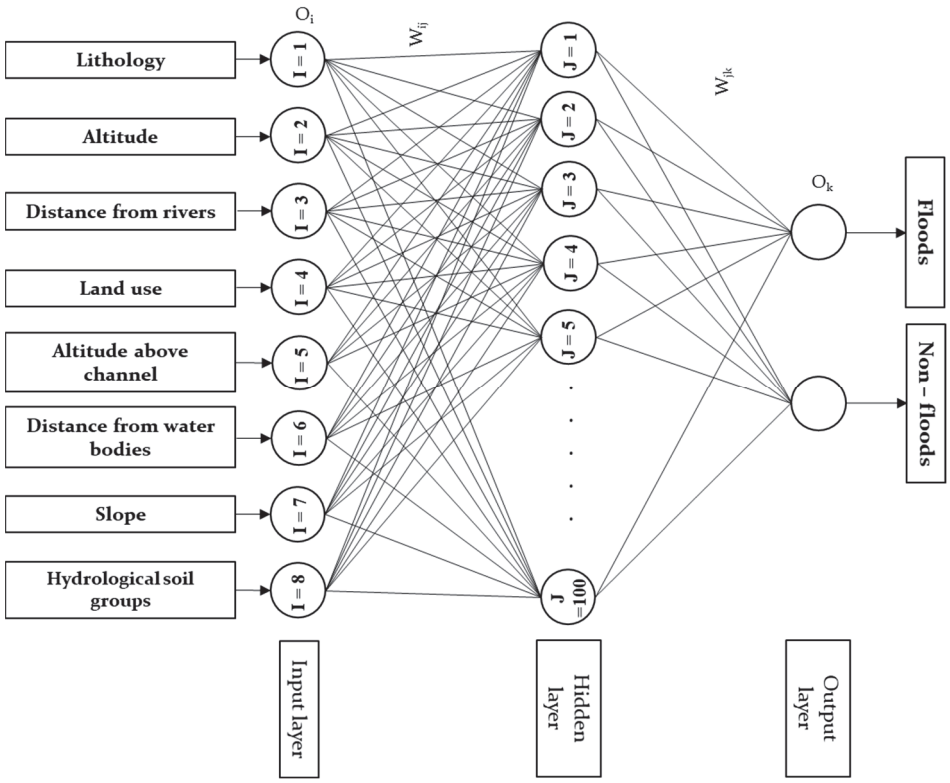

Figure 10. Architecture of the MLP model used to determine flood susceptibility.

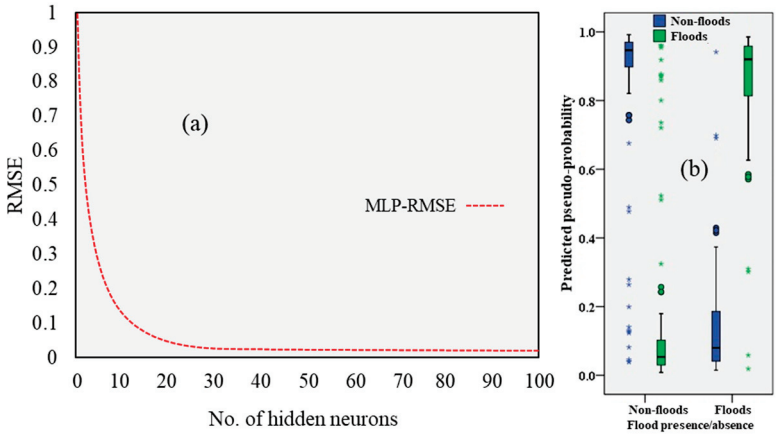

Figure 11. (**a**) Evolution of RMSE with respect to the number of hidden neurons and (**b**) estimated pseudo-likelihood for MLP.

3.6. Results Validation Using ROC Curve

The ROC curve was constructed for two variants: the success rate and the prediction rate, using SPSS 21 software. The success rate was calculated using the training sample and indicates how effectively the AI model classified the results. As shown in Figure 12a, the model with the highest performance was the DLNN, with an AUC of 0.963. The SVM followed it with an AUC of 0.954, and the MLP with an AUC of 0.939. All models performed well, as their AUC values were greater than 0.8.

The prediction rate was also determined using the test set. SVM provided the best results with an AUC of 0.942, followed by the DLNN with an AUC of 0.924 and the MLP with an AUC of 0.908 (Figure 12b). All models achieved an AUC value greater than 0.8 in the prediction rate analysis.

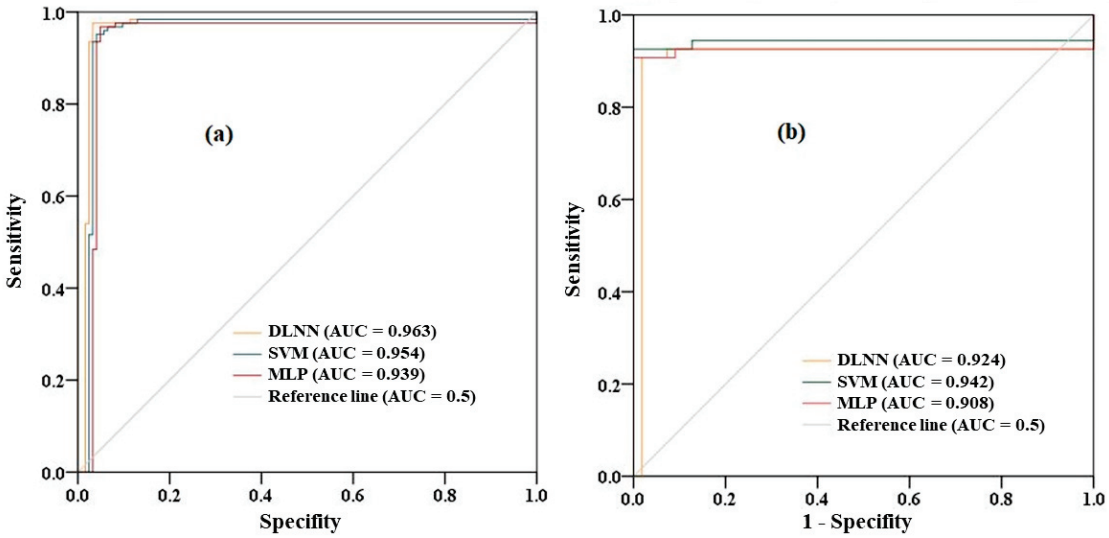

Figure 12. ROC curve (**a**) success rate and (**b**) prediction rate.

4. Discussion

The present workflow and the methodology proposed in this study represent a faster alternative to determine the flood hazard than hydraulic modeling. One of the study area's most famous flood risk assessment projects is the Danube FloodRisk Project, led by the Ministry of Environment from Romania and directly supervised by the International Commission for the Protection of the Danube River (ICPDR). Within this project, flood maps were generated through hydraulic modeling (a quantitative approach) for different river discharges determined based on statistical analysis (return periods: 30 years, 100 years, and 1000 years). Also, three classes of hazards were established according to the flood depth. Meanwhile, in the case of the current study, a qualitative approach was adopted to determine the susceptibility to floods, resulting from the overlap of several factors that influence the formation of this hydrological hazard. Unlike the project mentioned above, in this article, four classes were used to spatialize the severity of the hazard. Although the approaches differ, the results offered by them are, to a certain extent, similar. Thus, the highest flood hazard values are located along the main elements of the hydrographic network (the Danube arms and canals), and the lowest occur in the highest areas related to the banks. Flooding maps of the DD were also made within Cycle 1 of implementing the provisions of the Flood Directive 2007/60/EC of the European Commission. In this case, hydraulic modeling methods were also used to estimate the hazard's spatial variability. The results are very close to those of the Danube Flood Risk Project.

5. Conclusions

In this article, a DLNN, SVM, and MLP were used to qualitatively determine the hazard (susceptibility) to flooding within the Danube Delta based on information regarding the presence or absence of flood phenomena at the study area's level and data regarding the spatial values of eight geographic factors. All models revealed that the relief slope has the most significant influence on the flood phenomenon. Information gain was employed to test the predictive capacity of each geographic factor in flood genesis. Once this capacity was confirmed, the AHP coefficients that fed into the models were determined. A key aspect was validating the results using the ROC curve method, which confirmed that all models had an accuracy of over 90%.

Applying the entire workflow to determine the flood hazard qualitatively allowed the following output to be obtained:

- A GIS database with the training and validation samples comprising flood-affected areas in the DD reserve and an equal number of pixels with non-flood-affected areas.

- A GIS database with the eight geographical factors that influence the occurrence of floods within the study zone.
- An Excel tabular template with the AHP method that can also be applied to other study areas.
- A GIS database with the three susceptibility indices to flooding within the DD. According to the results provided by the three indices, approximately 65–70% of the DD's surface has a high or very high risk of flooding.

Moreover, the approach also represents the study's novelty in using techniques—ML algorithms combined with multicriteria decision-making analysis—that have not been used until now to evaluate the susceptibility to flooding in the DD. This research is also important because the DD represents one of the natural regions of Europe, having been declared a biosphere reserve and included in the UNESCO World Heritage List. The authorities can focus on finding the most environmentally friendly flood mitigation measures based on it.

The present research results are closely related to both facades of flood sustainability: sustainable management of floods and long-term flood resilience. The sustainable management of floods refers to strategies and practices harmonizing flood mitigation efforts with ecological conservation. Examples include maintaining the natural functioning of floodplains, implementing green infrastructure, and cultivating flood-resistant crops in agricultural areas. Meanwhile, long-term flood resilience emphasizes enabling societies and environments to recover from floods while sustaining essential functions, including planning for sustainable development in flood-prone regions and building resilient infrastructure.

Author Contributions: Conceptualization, R.C., A.C., N.C., and A.B.; methodology, R.C., A.C., N.C., and A.B.; software, R.C., A.C., and N.C.; validation, R.C.; formal analysis, R.C., N.C., and A.B.; investigation, R.C.; resources, R.C., A.C., and N.C.; data curation, R.C.; writing—original draft preparation, R.C., A.C., and N.C.; writing—review and editing, R.C., N.C., and A.B.; visualization, R.C., N.C., and A.B.; supervision, R.C.; project administration, R.C.; funding acquisition, R.C. and A.B. All authors have read and agreed to the published version of the manuscript.

Funding: This research was funded by the Ministry of Research, Innovation, and Digitization within the framework of Nucleus Program "DD 2030" PN 23 13, 2023–2026—Nucleus Project: "Research on the contribution of ecological restoration activities in the management of environmental risks caused by global climate change in the DD Biosphere Reserve—PN 23 13 02 01".

Data Availability Statement: The datasets generated during and/or analyzed during the current study are available from the corresponding author on reasonable request.

Conflicts of Interest: The authors declare no conflicts of interest.

References

1. Zhao, J.; Zhang, Q.; Xu, L.; Sun, S.; Wang, G.; Singh, V.P.; Wu, W. Flood-susceptible areas within the Yellow River Basin, China: Climate changes or socioeconomic behaviors. *J. Hydrol. Reg. Stud.* **2024**, *55*, 101900. [CrossRef]
2. Amiri, A.; Soltani, K.; Ebtehaj, I.; Bonakdari, H. A novel machine learning tool for current and future flood susceptibility mapping by integrating remote sensing and geographic information systems. *J. Hydrol.* **2024**, *632*, 130936. [CrossRef]
3. Acquaotta, F.; Faccini, F.; Fratianni, S.; Paliaga, G.; Sacchini, A.; Vilímek, V. Increased flash flooding in Genoa Metropolitan Area: A combination of climate changes and soil consumption? *Meteorol. Atmos. Phys.* **2019**, *131*, 1099–1110. [CrossRef]
4. Khosravi, K.; Shahabi, H.; Pham, B.T.; Adamowski, J.; Shirzadi, A.; Pradhan, B.; Dou, J.; Ly, H.-B.; Gróf, G.; Ho, H.L. A comparative assessment of flood susceptibility modeling using Multi-Criteria Decision-Making Analysis and Machine Learning Methods. *J. Hydrol.* **2019**, *573*, 311–323. [CrossRef]
5. Arnell, N.W.; Gosling, S.N. The impacts of climate change on river flood risk at the global scale. *Clim. Chang.* **2016**, *134*, 387–401. [CrossRef]
6. Swain, K.C.; Singha, C.; Nayak, L. Flood susceptibility mapping through the GIS-AHP technique using the cloud. *ISPRS Int. J. Geo Inf.* **2020**, *9*, 720. [CrossRef]
7. Bubeck, P.; Botzen, W.J.; Aerts, J.C. A review of risk perceptions and other factors that influence flood mitigation behavior. *Risk Anal.* **2012**, *32*, 1481–1495. [CrossRef]
8. Vinke-de Kruijf, J.; Kuks, S.M.; Augustijn, D.C. Governance in support of integrated flood risk management? The case of Romania. *Environ. Develop.* **2015**, *16*, 104–118. [CrossRef]

9. European Directive on Floods 2007/60/EC. Available online: https://www.legislation.gov.uk/eudr/2007/60 (accessed on 24 October 2024).
10. Arora, A.; Arabameri, A.; Pandey, M.; Siddiqui, M.A.; Shukla, U.; Bui, D.T.; Mishra, V.N.; Bhardwaj, A. Optimization of state-of-the-art fuzzy-metaheuristic ANFIS-based machine learning models for flood susceptibility prediction mapping in the Middle Ganga Plain, India. *Sci. Total Environ.* **2021**, *750*, 141565. [CrossRef]
11. Vogel, A.; Seeger, K.; Brill, D.; Brückner, H.; Kyaw, A.; Myint, Z.N.; Kraas, F. Towards Integrated Flood Management: Vulnerability and Flood Risk in the Ayeyarwady Delta of Myanmar. *Int. J. Disaster Risk Reduct.* **2024**, *114*, 104723. [CrossRef]
12. Guven, D.S.; Yenigun, K.; Isinkaralar, O.; Isinkaralar, K. Modeling flood hazard impacts using GIS-based HEC-RAS technique towards climate risk in Şanlıurfa, Türkiye. *Nat. Hazards* **2024**, 1–19. [CrossRef]
13. Zhu, K.; Lai, C.; Wang, Z.; Zeng, Z.; Mao, Z.; Chen, X. A novel framework for feature simplification and selection in flood susceptibility assessment based on machine learning. *J. Hydrol. Reg. Stud.* **2024**, *52*, 101739. [CrossRef]
14. Dottori, F.; Szewczyk, W.; Ciscar, J.-C.; Zhao, F.; Alfieri, L.; Hirabayashi, Y.; Bianchi, A.; Mongelli, I.; Frieler, K.; Betts, R.; et al. Increased human and economic losses from river flooding with anthropogenic warming. *Nat. Clim. Chang.* **2018**, *8*, 781–786. [CrossRef]
15. Pradhan, B. Remote sensing and GIS-based landslide hazard analysis and cross-validation using multivariate logistic regression model on three test areas in Malaysia. *Adv. Space Resear.* **2010**, *45*, 1244–1256. [CrossRef]
16. Anand, A.K.; Pradhan, S.P. Evaluation of bivariate statistical and hybrid models for the preparation of flood hazard susceptibility maps in the Brahmani River Basin, India. *Environ. Earth Sci.* **2023**, *82*, 389. [CrossRef]
17. Wang, W.; Sang, G.; Zhao, Q.; Liu, Y.; Shao, G.; Lu, L.; Xu, M. Prediction of flash flood peak discharge in hilly areas with ungauged basins based on machine learning. *Hydrol. Resear.* **2024**, *55*, 801–814. [CrossRef]
18. Abdulrazzak, M.; Elfeki, A.; Kamis, A.; Kassab, M.; Alamri, N.; Chaabani, A.; Noor, K. Flash flood risk assessment in urban arid environment: Case study of Taibah and Islamic universities' campuses, Medina, Kingdom of Saudi Arabia. *Geomat. Nat. Hazards Risk* **2019**, *10*, 780–796. [CrossRef]
19. Rafiei-Sardooi, E.; Azareh, A.; Choubin, B.; Mosavi, A.H.; Clague, J.J. Evaluating urban flood risk using hybrid method of TOPSIS and machine learning. *Int. J. Disaster Risk Reduct.* **2021**, *66*, 102614. [CrossRef]
20. Dutta, P.; Deka, S. A novel approach to flood risk assessment: Synergizing with geospatial based MCDM-AHP model, multi-collinearity, and sensitivity analysis in the Lower Brahmaputra Floodplain, Assam. *J. Clean. Prod.* **2024**, *467*, 142985. [CrossRef]
21. Ahmadlou, M.; Karimi, M.; Alizadeh, S.; Shirzadi, A.; Parvinnejhad, D.; Shahabi, H.; Panahi, M. Flood susceptibility assessment using integration of adaptive network-based fuzzy inference system (ANFIS) and biogeography-based optimization (BBO) and BAT algorithms (BA). *Geocarto Int.* **2019**, *34*, 1252–1272. [CrossRef]
22. Termeh, S.V.R.; Kornejady, A.; Pourghasemi, H.R.; Keesstra, S. Flood susceptibility mapping using novel ensembles of adaptive neuro fuzzy inference system and metaheuristic algorithms. *Sci. Total Environ.* **2018**, *615*, 438–451. [CrossRef] [PubMed]
23. Wang, Y.; Hong, H.; Chen, W.; Li, S.; Panahi, M.; Khosravi, K.; Shirzadi, A.; Shahabi, H.; Panahi, S.; Costache, R. Flood susceptibility mapping in Dingnan County (China) using adaptive neuro-fuzzy inference system with biogeography based optimization and imperialistic competitive algorithm. *J. Environ. Manag.* **2019**, *247*, 712–729. [CrossRef] [PubMed]
24. Bui, D.T.; Tsangaratos, P.; Ngo, P.-T.T.; Pham, T.D.; Pham, B.T. Flash flood susceptibility modeling using an optimized fuzzy rule based feature selection technique and tree based ensemble methods. *Sci. Total Environ.* **2019**, *668*, 1038–1054. [CrossRef]
25. Pham, B.T.; Shirzadi, A.; Bui, D.T.; Prakash, I.; Dholakia, M. A hybrid machine learning ensemble approach based on a radial basis function neural network and rotation forest for landslide susceptibility modeling: A case study in the Himalayan area, India. *Int. J. Sediment Res.* **2018**, *33*, 157–170. [CrossRef]
26. Shafizadeh-Moghadam, H.; Valavi, R.; Shahabi, H.; Chapi, K.; Shirzadi, A. Novel forecasting approaches using combination of machine learning and statistical models for flood susceptibility mapping. *J. Environ. Manag.* **2018**, *217*, 1–11. [CrossRef]
27. Janizadeh, S.; Kim, D.; Jun, C.; Bateni, S.M.; Pandey, M.; Mishra, V.N. Impact of climate change on future flood susceptibility projections under shared socioeconomic pathway scenarios in South Asia using artificial intelligence algorithms. *J. Environ. Manag.* **2024**, *366*, 121764. [CrossRef]
28. Tăban, C.I.; Sandu, A.; Oancea, S.; Stoia, M. Gross Alpha/Beta Radioactivity of Drinking Water and Relationships with Quality Parameters of Water from Alba County, Romania. *Rom. J. Phys.* **2024**, *69*, 806.
29. Chirosca, G.; Mihailov, M.A.; Tomescu-Chivu, M.I.; Chirosca, A.V. Enhanced Machine Learning Model for Meteo-Oceanographic Time-Series Prediction. *Rom. J. Phys.* **2022**, *67*, 815.
30. Nichita, C.; Voinea, S. Removal of the pharmaceutical pollutants from water using natural filter materials-experimental lab. *Rom. Rep. Phys.* **2024**, *76*, 706. [CrossRef]
31. Costache, R.; Bărbulescu, A.; Pham, Q.B. Integrated Framework for Detecting the Areas Prone to Flooding Generated by Flash-Floods in Small River Catchments. *Water* **2021**, *13*, 758. [CrossRef]
32. Costache, R.; Țîncu, R.; Elkhrachy, I.; Pham, Q.B.; Popa, M.C.; Diaconu, D.C.; Avand, M.; Costache, I.; Arabameri, A.; Bui, D.T. New neural fuzzy-based machine learning ensemble for enhancing the prediction accuracy of flood susceptibility mapping. *Hydrol. Sci. J.* **2020**, *65*, 2816–2837. [CrossRef]
33. Costache, R.; Pham, Q.B.; Avand, M.; Linh, N.T.T.; Vojtek, M.; Vojteková, J.; Lee, S.; Khoi, D.N.; Nhi, P.T.T.; Dung, T.D. Novel hybrid models between bivariate statistics, artificial neural networks and boosting algorithms for flood susceptibility assessment. *J. Environ. Manag.* **2020**, *265*, 110485. [CrossRef] [PubMed]

34. Popescu, N.C.; Bărbulescu, A. On the flash flood susceptibility and accessibility in the Vărbilău catchment (Romania). *Rom. J. Phys.* **2022**, *67*, 811.
35. Popescu, C.; Bărbulescu, A. Flood Hazard Evaluation using a Flood Potential Index. *Water* **2023**, *15*, 3533. [CrossRef]
36. Stancu, M.V.; Chevereșan, M.I.; Sârbu, D.; Maizel, A.; Soare, R.; Bărbulescu, A.; Dumitriu, C.S. Influence of marine currents, waves and shipping traffic on Sulina channel fairway at the mouth of Black Sea. *Water* **2024**, *16*, 2779. [CrossRef]
37. Crăciun, A.; Costache, R.; Bărbulescu, A.; Chandra Pal, S.; Costache, I.; Dumitriu, C.S. Modern techniques for flood susceptibility estimation across the Deltaic Region (DD) from the Black Sea's Romanian Sector. *J. Mar. Sci. Eng.* **2022**, *10*, 1149. [CrossRef]
38. Carey, S.K.; Woo, M. Slope runoff processes and flow generation in a subarctic, subalpine catchment. *J. Hydrol.* **2001**, *253*, 110–129. [CrossRef]
39. Bakuła, K.; StĘpnik, M.; Kurczyński, Z. Influence of elevation data source on 2D hydraulic modelling. *Acta Geophys.* **2016**, *64*, 1176–1192. [CrossRef]
40. Allahbakhshian-Farsani, P.; Vafakhah, M.; Khosravi-Farsani, H.; Hertig, E. Regional flood frequency analysis through some machine learning models in semi-arid regions. *Water Resour. Manag.* **2020**, *34*, 2887–2909. [CrossRef]
41. Biswas, M.; Banerji, S.; Mitra, D. Land-use–land-cover change detection and application of Markov model: A case study of Eastern part of Kolkata. *Environ. Dev. Sustain.* **2020**, *22*, 4341–4360. [CrossRef]
42. Kononenko, I.; Kukar, M. *Machine Learning and Data Mining*; Woodhead Publishing: Swaston, UK, 2007; pp. 153–180.
43. Saaty, T.L. Decision making with the analytic hierarchy process. *Int. J. Serv. Sci.* **2008**, *1*, 83–98. [CrossRef]
44. Hasanuzzaman, M.; Adhikary, P.P.; Bera, B.; Shit, P.K. Flood vulnerability assessment using AHP and frequency ratio techniques. In *Spatial Modelling of Flood Risk and Flood Hazards: Societal Implications*; Pradhan, B., Shit, P.K., Bhunia, G.S., Adhikary, P.P., Pourghasemi, H.R., Eds.; Springer International Publishing: Cham, Switzerland, 2022; pp. 91–104.
45. Sejnowski, T.J. *The Deep Learning Revolution*; The MIT Press: Cambridge, MA, USA, 2018.
46. Chan, K.Y.; Abu-Salih, B.; Qaddoura, R.; Al-Zoubi, A.M.; Palade, V.; Pham, D.-S.; Del Ser, J.; Muhammad, K. Deep neural networks in the cloud: Review, applications, challenges and research directions. *Neurocomputing* **2023**, *545*, 126327. [CrossRef]
47. Smola, A.J.; Schölkopf, B. A tutorial on support vector regression. *Stat. Comput.* **2004**, *14*, 199–222. [CrossRef]
48. Park, Y.-S.; Lek, S. Chapter 7—Artificial neural networks: Multilayer Perceptron for Ecological Modeling. In *Developments in Environmental Modelling*; Jørgensen, S.E., Ed.; Elsevier: Amsterdam, The Netherlands, 2016; Volume 28, pp. 123–140.
49. Matsuki, Y.; Nakamura, K.; Watanabe, H.; Aoki, T.; Nakata, H.; Katsuragawa, S.; Doi, K. Usefulness of an artificial neural network for differentiating benign from malignant pulmonary nodules on high-resolution CT: Evaluation with receiver operating characteristic analysis. *Am. J. Roentgenol.* **2002**, *178*, 657–663. [CrossRef]
50. Ali, S.A.; Parvin, F.; Pham, Q.B.; Vojtek, M.; Vojteková, J.; Costache, R.; Linh, N.T.T.; Nguyen, H.Q.; Ahmad, A.; Ghorbani, M.A. GIS-based comparative assessment of flood susceptibility mapping using hybrid multi-criteria decision-making approach, naïve Bayes tree, bivariate statistics and logistic regression: A case of Topľa basin, Slovakia. *Ecol. Indic.* **2020**, *117*, 106620. [CrossRef]
51. Tehrany, M.S.; Pradhan, B.; Jebur, M.N. Flood susceptibility analysis and its verification using a novel ensemble support vector machine and frequency ratio method. *Stoch. Environ. Res. Risk Assess.* **2015**, *29*, 1149–1165. [CrossRef]

water

MDPI

Article

Influence of Marine Currents, Waves, and Shipping Traffic on Sulina Channel Fairway at the Mouth of the Black Sea

Mihai Valentin Stancu [1], Maria Ilinca Cheveresan [2,*], Daniela Sârbu [1], Adrian Maizel [3], Romeo Soare [4], Alina Bărbulescu [5,*] and Cristian Ștefan Dumitriu [6,*]

[1] DHI SW Project, 22 Nicolae G. Caramfil Street, 014143 Bucharest, Romania; mvs@dhigroup.com (M.V.S.); dasa@dhigroup.com (D.S.)
[2] Department of Hydrotechnics, Technical University of Civil Engineering of Bucharest, 122-124 Lacul Tei Bd., 020396 Bucharest, Romania
[3] Lower Danube Administration, 32 Portului Street 3, 800025 Galati, Romania; adrian.maizel@afdj.ro
[4] Lower Danube Administration, 4 Stefan cel Mare Street, 080388 Giurgiu, Romania; romeo.soare@afdj.ro
[5] Department of Civil Engineering, Transilvania University of Brasov, 5, Turnului Street, 500152 Brasov, Romania
[6] Department of Mechanical Engineering and Robotics in Constructions, Technical University of Civil Engineering of Bucharest, 59 Calea Plevnei, 010223 Bucharest, Romania
* Correspondence: maria.cheveresan@utcb.ro (M.I.C.); alina.barbulescu@unitbv.ro (A.B.); cristian.dumitriu@utcb.ro (C.Ș.D.)

Abstract: This study comprehensively explores the intricate hydrodynamic and geomorphological processes that affect the Sulina Channel and bar area. It employs advanced hydrodynamic, wave, and sediment transport models to simulate the influence of marine currents, waves, and shipping traffic on sediment transport and deposition patterns, providing valuable insights for maintaining navigable conditions in the Sulina Channel. It is shown that sediment deposition is highly dynamic, particularly in the Sulina bar area, where rapid sediment recolonization occurs within one to two months after dredging. The simulation indicates that vessels with drafts of 11.5 m cause notable erosion. In comparison, drafts of 7 m have a minimal impact on sediment transport, emphasizing the importance of managing vessel drafts to mitigate sediment disturbances. This research highlights and quantifies the siltation phenomenon from the Black Sea to the mouth of the Sulina Channel, effectively addressing the challenges posed by natural and anthropogenic factors to ensure the Channel's sustainability and operational efficiency.

Keywords: hydrodynamic modeling; sediment transport; marine currents; wave impact; vessel traffic

1. Introduction

Sediment transport in rivers and interaction between two different flow regimens (river–sea, for example) is an important study field due to the navigation safety and economic impact. In his article about sediment depositions in the British seas, Lebour [1] indicates that this subject is not new. However, the involved processes are highly dynamic and require modern solutions to assess and propose improvements. According to [2], the first theoretical attempt to calculate the sediment transport under waves and currents was carried out by Bijker [3] in 1967. Since then, multiple improvements to the approaches and methodologies have been proposed, the most recent involving the use of numerical models to solve hydraulic and sediment transport equations [2,4–7]. Due to the dynamic exchange involved, as the interaction between river flow, waves, and currents, sediment transport is a complicated problem from a computational viewpoint [8,9]. Vessel sediment resuspension has been studied in various contexts, such as the effects of the waves produced by the recreational boat passage [10,11] and the propeller impact on the riverbed sediment stability [12–14]. Research in various locations has tackled the impact of vessel traffic on potential sediment resuspension. The results have indicated that the sediment characteristics, the

hydrodynamic changes produced by the vessel, and the vessel characteristics significantly influence this process.

Spoolder [15] investigated the return flow velocity produced by the propeller and performed a sensitivity analysis of the vessel velocity, width, and keel clearance. The results indicate that decreasing the values of the first two parameters and the rate of power efficiency will decrease the sediment transport. Other research [16,17] analyzed the impact of the wake waves on sediment resuspension, given the additional stress they exert on the protection infrastructure (such as dykes or jetties).

In Romania, the main studies in this research field concern the Sulina Channel, one of the Danube River's branches. Budileanu [18] studied the Sulina bar's evolution, discussing the hydrological conditions, the sediment transport, and the human intervention in the area. Over time, a steady evolution of the bar has been observed, starting from 1876, when observations were made about the Sulina mouth area and sediment depositions.

Mateescu et al. [19] described the processes occurring at the Danube River mouth on the Sulina Channel, pointing out that the interaction between waves and currents produced by the freshwater discharge leads to longitudinal and riparian currents, with visible effects in short periods. Boșneagu et al. [20] analyzed the flow conditions using numerical modeling software and applied computational fluid dynamics theory. They addressed the flow transfer between the Danube and the Black Sea, at the mouth and longitudinally, along the jetties.

Bondar [21] made significant strides in modeling the sediment transport interactions around the Sulina mouth, showing the longitudinal evolution of the sediment deposition and erosion processes. Constantinescu et al. [22] analyzed the potential negative impacts of fluvial or coastal hazards and dike breaching on Sulina City. The two jetties constructed along the Sulina Channel impact the morphological conditions, splitting the area into two zones, north and south of the jetties. The most impacted zone is the northern one, where the jetties block sediment transport, leading to rapid sedimentation and the closing of the Musura Bay [23,24]. A sediment spit continues almost perpendicular to the two jetties. Răileanu et al. [25] and Ivan et al. [26] have focused on the effects of the wind and waves over the jetties and Sulina mouth area, highlighting the impact on the navigation conditions under heavy conditions.

We developed comprehensive hydrodynamic, wave, and sediment transport models to understand the impact of increasing the navigation depths on the Sulina bar, the hydromorphology, and the hydrodynamics of the Sulina Channel. They are designed to accurately simulate the complex hydrodynamic and geomorphological processes in the Sulina Channel and bar area. Our approach includes an analysis of marine currents, waves, and shipping traffic and their collective influence on the Sulina Channel fairway at the mouth of the Black Sea. We studied two predefined scenarios based on a representative vessel (predefined draught and characteristics) to determine the vessels' impact on sediment transport.

This research has significant practical implications. It provides crucial insights into the environmental processes influencing navigation, including wave action, sediment deposition, and erosion. The results of our research ensure the background for the safe and efficient passage of vessels with varying draughts, thereby enhancing the overall navigability of the Sulina bar.

2. Materials and Methods

2.1. Study Area

The Danube splits into three branches before it flows into the Black Sea. The Sulina branch is the middle navigable channel, with a length of approximately 60 km. The Sulina bar (Figure 1) is located at the mouth of the Sulina Channel and the Black Sea.

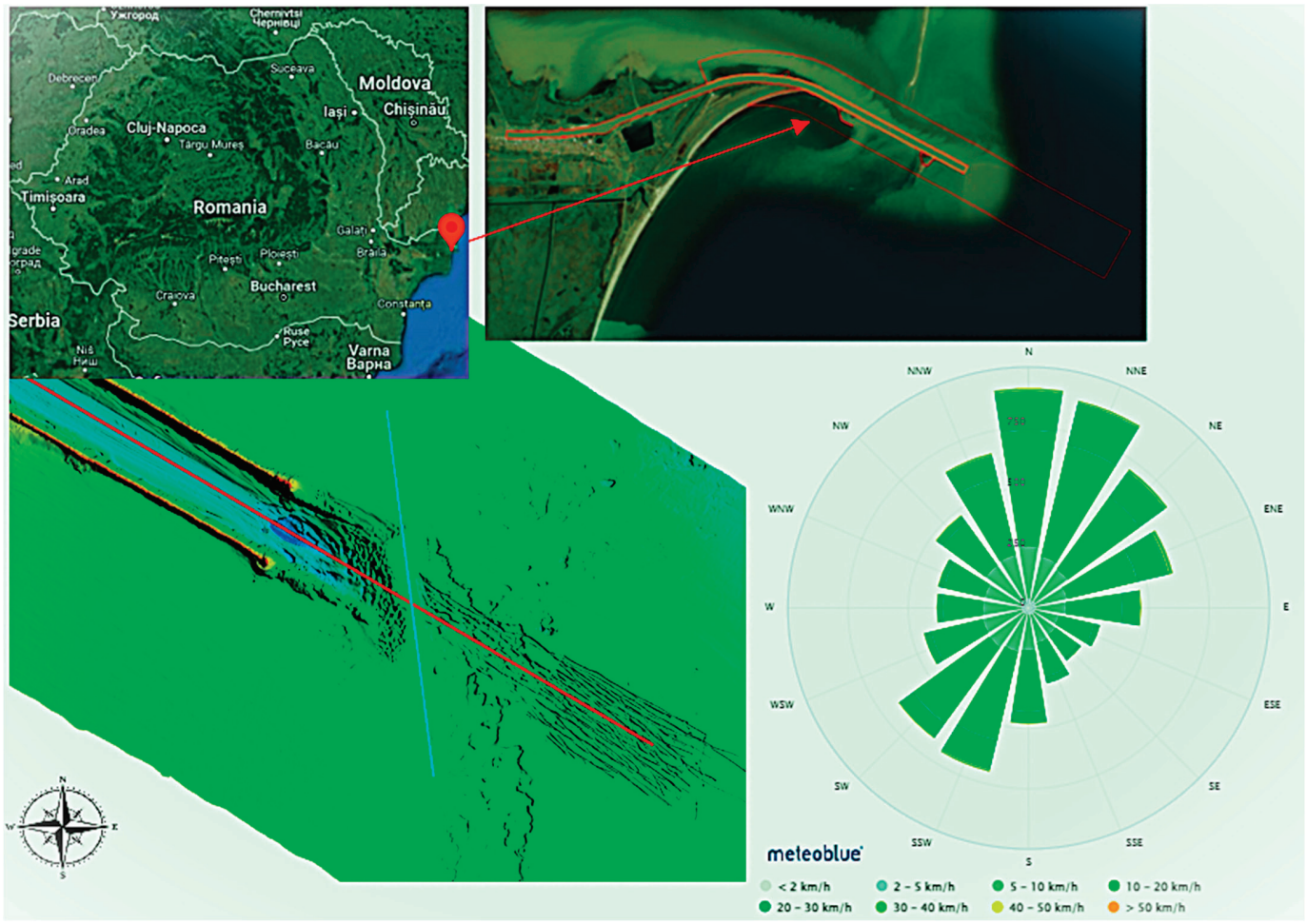

Figure 1. A map of Romania (top left), the study area (top right), a bathymetric picture of a channel section (bottom left), and the wind rose (bottom right).

It represents a diked canal that allows smooth navigation from the Danube River branch into the sea. The dominant wave direction, from north-east, leads to the transport of the sediment southward, influencing coastal features. The jetties extend several kilometers from the original coastline, with shallow waters north of the breakwaters. A spit, formed by breaking waves, is growing southward due to longshore transport from the northeast. This growth may be stopped by water flowing between the spit and the northern jetty, potentially carrying sediment from the spit to the bar in front of the Channel's mouth.

The climate in the area is continental with oceanic influences. The annual precipitation varies in the interval of 109–487 mm, with an average of about 260 mm and a coefficient of variation of about 30. In summer, the temperature is lower than in other zones of the Dobrogea Region to which the study belongs. The winters are cold due to the influence of the atmospheric masses that come from Russia [27–33].

As previous studies [18–26] have shown, the Sulina bar area is significantly influenced by the transport of fine alluvial material along the Sulina Channel and by wind-induced currents and waves in the Black Sea. These processes result in a prominent accumulation zone for alluvial material near the mouth and submersible dams in the sea.

2.2. Data Series

This study utilized a comprehensive series of input data. This included a Digital Terrain Model (DTM) with a 1 × 1 m resolution derived from multibeam bathymetric measurements covering the entire riverbed and supplemented by topographic measurements

of the defense dams. In the areas where these DTM sources were incomplete, DTMs from free sources were also incorporated.

Historical topo-bathymetric data consisted of raster files detailing the dynamics of the Sulina Channel bed and its mouth area in the Black Sea over nine years from 2014 to 2022. From 2014 to 2017, data were available only for the mouth area of the Sulina branch, with at least one measurement campaign per year. For 2018 and 2022, the minor riverbed was completely covered within the initially defined study area.

Hydrological data, such as flow rates and levels, were obtained from specific observations and measurements conducted within the project across 54 profiles. These data were used as boundary conditions and calibration information for the models. Additionally, data on the particle size distribution of riverbed sediments and solid flows were gathered from these profiles.

Information on the parental material within the riverbed perimeter and details of the riverbed substrate were collected through specific observations and measurements. This information was analyzed and processed to generate files for use in the models. A wave data string for the period 24 September 2020–29 July 2022, was recorded by a beacon, although the wave monitoring sensor was not operational for the entire period. Consequently, wave height data were available only for 24 September 2020–19 September 2021.

Data on marine currents from 1 February 2021 to 10 January 2023, were sourced from Copernicus. Wind data covering December 2008–January 2023 included the monthly frequency of wind directions and information on wind direction and speed in the Sulina branch area. Information was also gathered on a representative vessel.

Meteorological data recorded at the Sulina meteorological station from 1 January 2013 to 31 December 2022 were also used in this study. These data included multiannual monthly wind roses, average wind speed by direction, wind frequency by direction, wind frequency at different speed thresholds, maximum wind speed and its corresponding direction, and maximum gust wind speed.

Additional studies, documents, and scientific papers were also reviewed, including technical documentation on the existing port trestles for berthing sea and river vessels along the left bank of the Sulina Channel in the Commercial Port and vessel traffic data on the Sulina Channel from 2001 to 2022. Data from other sources, such as satellite imagery from Google Earth/Google Maps, and previous technical works and research studies conducted in the area or equivalent locations, were also consulted.

2.3. Methodology—Generalities

This study aims to assess the navigation conditions in the Sulina bar by developing and utilizing a series of advanced numerical models that that replicate the complex hydraulic and siltation phenomena.

Using the MIKE 21 FM software developed by the Danish Hydraulic Institute, the study examines the wave patterns in the Black Sea and sediment transport along the Sulina bar and coast and within the Sulina Canal, as well as the impact of vessel transit on sediment dynamics. The models provide insights into the environmental processes influencing navigation, including wave action, sediment deposition, and erosion, to ensure the safe and efficient passage of vessels with varying draughts.

In the subsequent sections, we outline the methodology, discuss the integration of various data sources, and highlight the significant findings that enhance navigation depths while mitigating potential adverse effects on the surrounding marine and coastal environments. Figure 2 shows the chart flow of the analysis.

- *Large-scale wave model in the Black Sea area and Sulina Bar and small-scale wave model*

A wave model was developed to estimate the general wave conditions impacting the infrastructure at the Sulina bar and surroundings. Due to the complexity of the processes in the Sulina Channel discharge area and the limited detailed data on the local wave regimen, it was necessary to extend the model to cover a larger area of the Black Sea. This

broad model provides boundary conditions for a more focused wave model around the Sulina mouth.

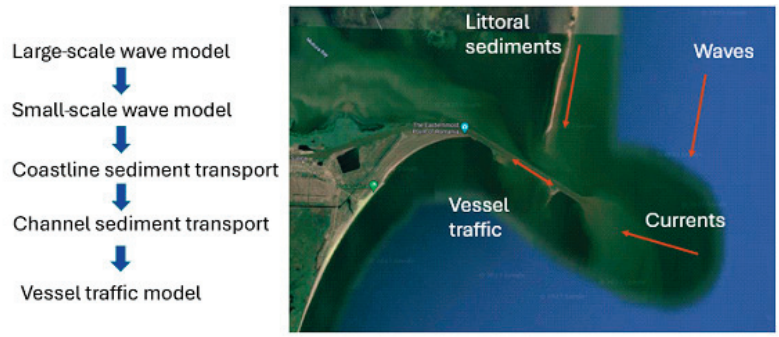

Figure 2. The flowchart of the study.

The domain of the large-scale hydrodynamic model encompasses a significant portion of the Black Sea around the Sulina Channel, extending approximately 15 km from the Sulina branch into the Black Sea (Figure 3).

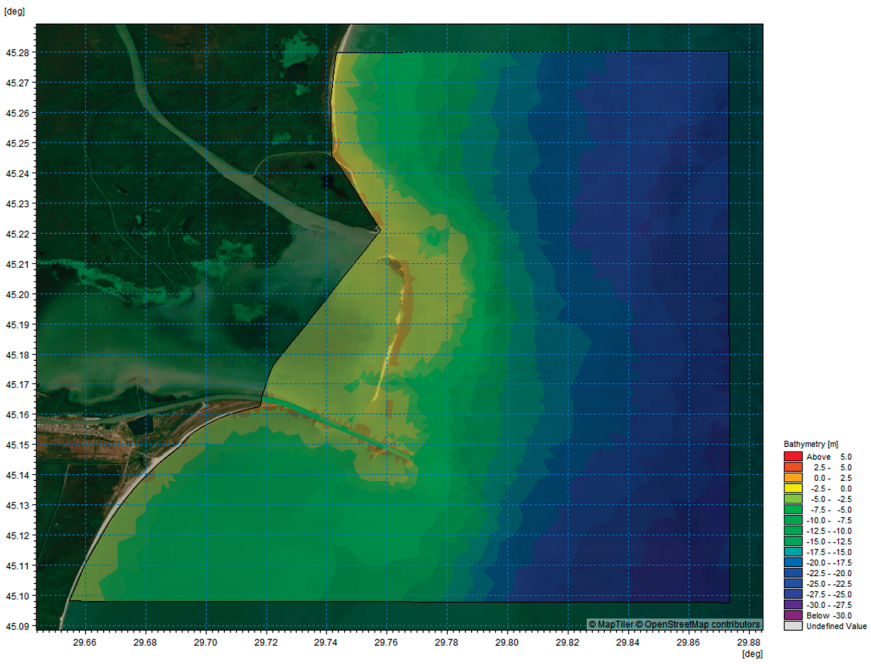

Figure 3. The large-scale domain.

This domain was chosen to capture the interactions between large-scale wave and current patterns in the Black Sea and their influence on sediment transport and navigational conditions within the Sulina Channel. The model grid was generated using the MIKE 21 Flexible Mesh Spectral Wave (SW) model, ensuring a wide enough area to provide reliable boundary conditions for smaller-scale models focusing on the Sulina mouth and bar area.

The large-scale model was validated by comparing simulated wave height and period data against available wave measurements from offshore monitoring stations and satellite-derived wave data. The validation process covered both long-term simulations and extreme wave events. For wave heights, data from a beacon (available from September 2020 to September 2021) were utilized to calibrate the model, while for marine current data, we relied on the Copernicus Marine Service, which provided a reliable set of boundary conditions. Additionally, hindcast simulations of key historical storm events were compared to recorded observations, showing strong alignment between modeled and observed wave

heights, current velocities, and directions, thus confirming the robustness of the large-scale model in representing offshore wave dynamics.

- *Coastline sediment transport model*

The Sulina Channel and bar area are influenced by various processes, particularly in the transition zone from river to marine environments. This zone experiences more pronounced sedimentation, primarily due to fine materials carried by the Danube and deposited at the bar due to current influences and density differences, as well as sands deposited by marine currents. The sediment transport model was designed to estimate the sediment intake along the shore, helping to determine the time required for recolonization after dredging activities.

- *Channel sediment transport model*

Like the coastal sediment transport model, a detailed model of fine sediment flow and transport within the Sulina Channel was created. This model simulates the transport, erosion, and deposition of fine sediments, particularly at the discharge area into the sea, where depths decrease from an average of -11 m to about -7 m. The model aids in estimating the quantities of sediments moving from the Channel to the mouth, ensuring timely dredging to maintain the minimum depth required for vessels with draughts of 11 or 11.5 m. Additionally, by monitoring sediment transport dynamics, the model assists in planning field interventions to maintain the continuous fairway.

- *Vessel traffic model*

To ensure navigable conditions for vessels with draughts higher than currently practiced, a model was developed to assess the impact of vessel transit on sediment resuspension and redeposition within the Channel and bar. This model integrates the hydrodynamic and fine sediment transport models, incorporating data on vessel routes, speeds, draughts, propulsion coefficients, and travel direction (upstream or downstream). This comprehensive approach allows for an accurate assessment of how vessel transit affects sediment dynamics, aiding in maintaining navigable depths.

It is important to note that the study took into account the currents from both the river and the marine sides when developing hydrodynamic and sediment transport models. The freshwater discharge from the Danube River interacts with the marine currents of the Black Sea, creating a complex hydrodynamic environment.

The model incorporated the river discharge from the Sulina branch as an upstream boundary condition based on the average value measured during the bathymetry survey. The MIKE 21 FM hydrodynamic module simulated the downstream flow of the Danube into the Black Sea, considering variations in discharge rates. The study particularly analyzed the impact of the river discharge on sediment transport and siltation in the Sulina bar, identifying areas of high sediment deposition in the transition zone between the river and the sea.

For marine currents, we used boundary conditions from the Copernicus Marine Service database, covering the period from February 2021 to January 2023. These currents were introduced at the seaward boundaries of the model to simulate large-scale water movement in the Black Sea. We paid particular attention to the interaction between these marine currents and wave action in the Sulina mouth area. The combined effect of longshore currents driven primarily by northeast winds and marine currents was crucial for accurately representing sediment transport along the coast and in the channel. Additionally, we evaluated the impact of wave-driven currents on the stability of protective jetties and the navigation fairway through sensitivity analysis.

3. Case Study

3.1. Large-Scale Wave Model in the Black Sea Area and Sulina Bar and Small-Scale Wave Model

To characterize the wave climate at the river mouth with respect to extreme waves, a two-step approach was employed:

a. A wave simulation model for the Black Sea was used to determine the local offshore wave climate.
b. A local wave model was developed to (i) propagate extreme wave conditions towards the river mouth and (ii) determine the local wave conditions necessary for calculating littoral sediment transport.

Note that the effect of currents (both offshore and riverine current) is disregarded in the analysis presented in 3.1.

3.1.1. Offshore Wave Climate Characterization

The wave model developed for the Black Sea, specifically for the area adjacent to the Sulina Channel and bar, was simulated over 10 years. The purpose was to identify a representative year to be used in simulating the impact of waves on flow conditions in the Sulina bar area (local wave model) and to extract information on the external forces acting on the existing dike infrastructure of the Sulina Channel into the Black Sea for further use in other potential stability analyses.

To investigate the wave conditions near the Sulina Channel mouth, a directional extreme value analysis (EVA) of significant wave heights and associated return periods was performed at point P1, located in the Black Sea, near the Sulina Channel (Figure 4). The EVA utilized wave data from the spectral wave model (Metocean Data) developed by DHI for the Black Sea, covering the period from 31 December 1979 to 31 December 2020.

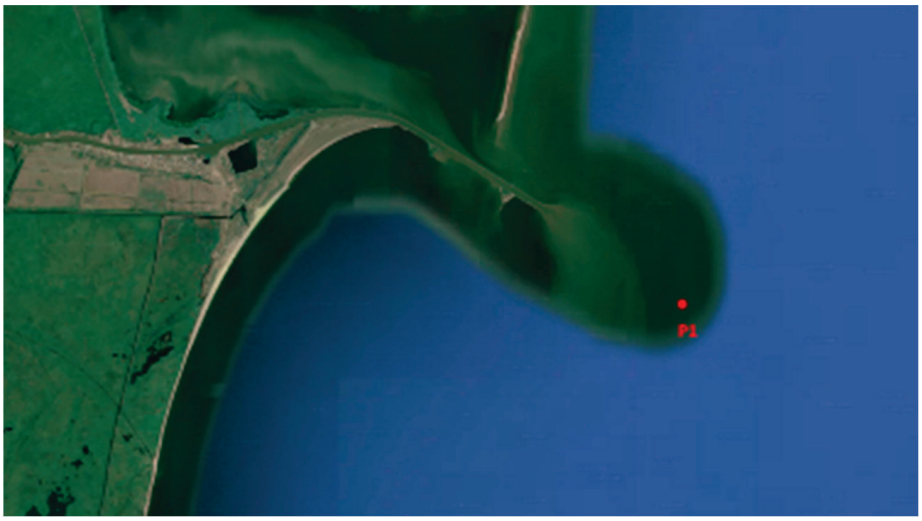

Figure 4. The position of the point (P1) where the wave analysis was developed.

The wave rose at P1 (Figure 5(left)) is a significant source of information, providing insights into significant wave heights (H_{m0}) and mean wave directions (MWD). It is accompanied by the current rose, presented in Figure 5(right)) which gives indications about the current directions and intensity.

The main wave direction is between 0° N and 180° N, with the highest waves predominantly from 60° N–120° N sector. The information provided by the wave rose is presented in Table 1. Figure 6 shows the wave heights (H_{m0}) for the relevant MWDs from 0°N to 180°N in 30° intervals and for the ominidirectional directions. Among the various distribution functions tested, the two-parameter Weibull distribution (fitted using the least squares methods and a threshold value corresponding to the average annual peak ($\lambda = 1$)) provided the best model for wave height data over the 41 years for which wave information is available.

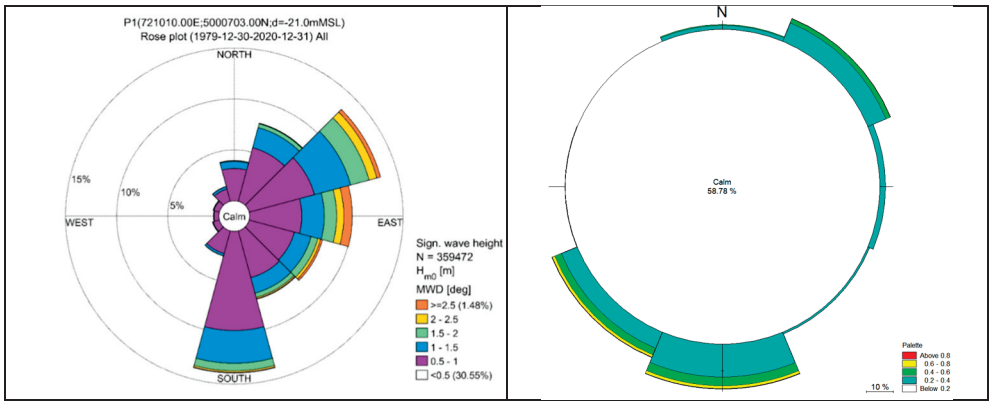

Figure 5. The wave rose at P1, showing the significant waves' height and the mean wave direction (**left**) and the current rose at P1 (**right**).

Table 1. Mean wave direction and frequency of occurrence.

MWD	Frequency of Occurrence (%)	MWD	Frequency of Occurrence (%)
[Interval°]	H_{m0}	[Interval°]	H_{m0}
[315–345]	2.89	[135–165]	9.81
[285–315]	1.55	[105–135]	10.23
[255–285]	1.40	[75–105]	13.54
[225–255]	1.95	[45–75]	17.47
[195–225]	5.36	[15–45]	10.99
[165–195]	18.62	[−15–15]	6.19

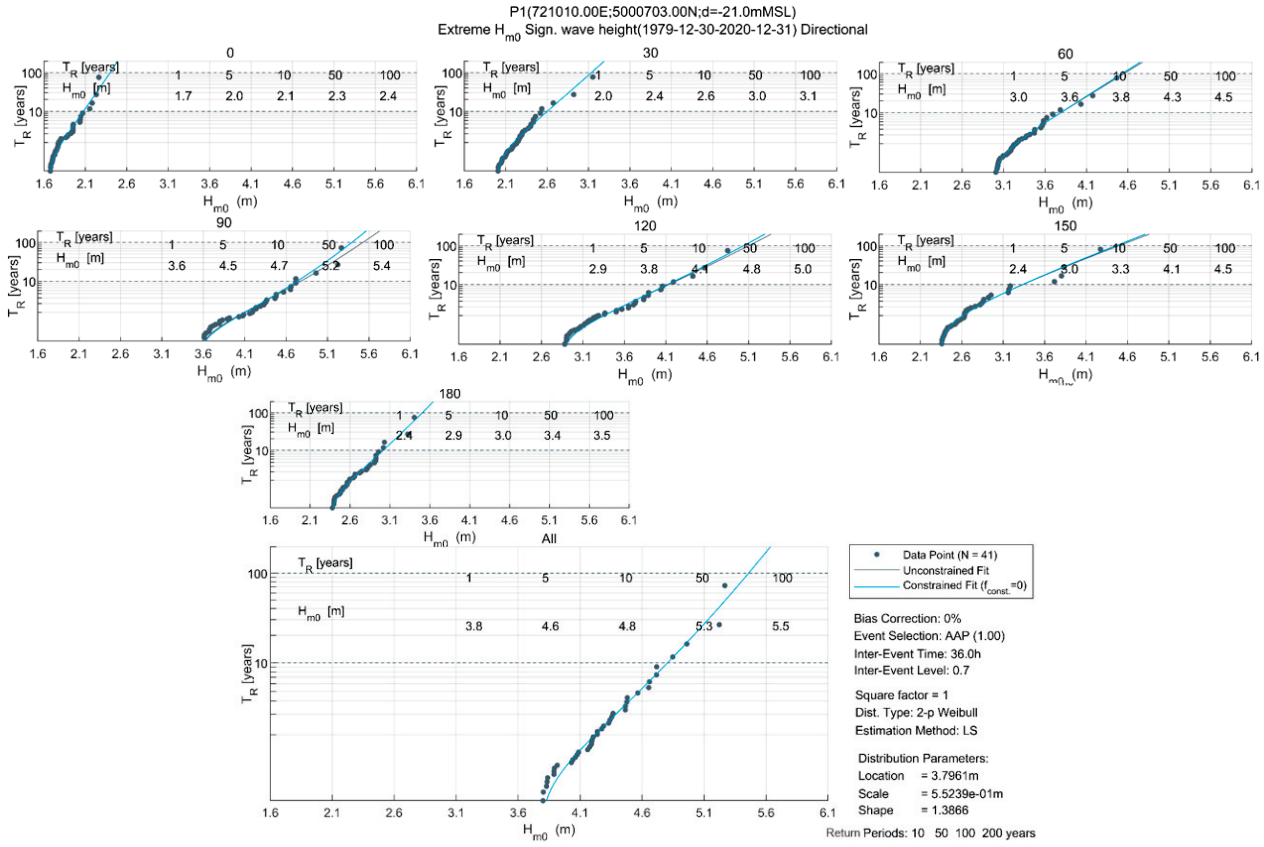

Figure 6. The distribution of H_{m0} for directional 30° and omnidirectional ranges at P1.

The directional and omnidirectional extreme values of wave heights for return periods (TR) of 1, 5, 10, 50, and 100 years are detailed in Table 2.

Table 2. Extreme wave heights (H_{m0}) for 30° intervals and directions for return periods of 1, 5, 10, 50, and 100 years at P1.

MWD	H_{m0} [m]				
[Interval °]	TR = 1	TR = 5	TR = 10	TR = 50	TR = 100
[165–195]	2.4	2.9	3.0	3.4	3.5
[135–165]	2.4	3.0	3.3	4.1	4.5
[105–135]	2.9	3.8	4.1	4.8	5.0
[75–105]	3.6	4.5	4.7	5.2	5.4
[45–75]	3.0	3.6	3.8	4.3	4.5
[15–45]	2.0	2.4	2.6	3.0	3.1
[−15–15]	1.7	2.0	2.1	2.3	2.4
Omni	3.8	4.6	4.8	5.3	5.5

The peak wave periods (T_p) associated with extreme waves are derived from the graph shown in Figure 7, highlighting the functional relationship between H_{m0} and T_p for all waves (omnidirectional). The matching coefficients are given in Table 3. These values were used as boundary conditions for spectral wave simulations propagating waves from offshore to the Channel mouth.

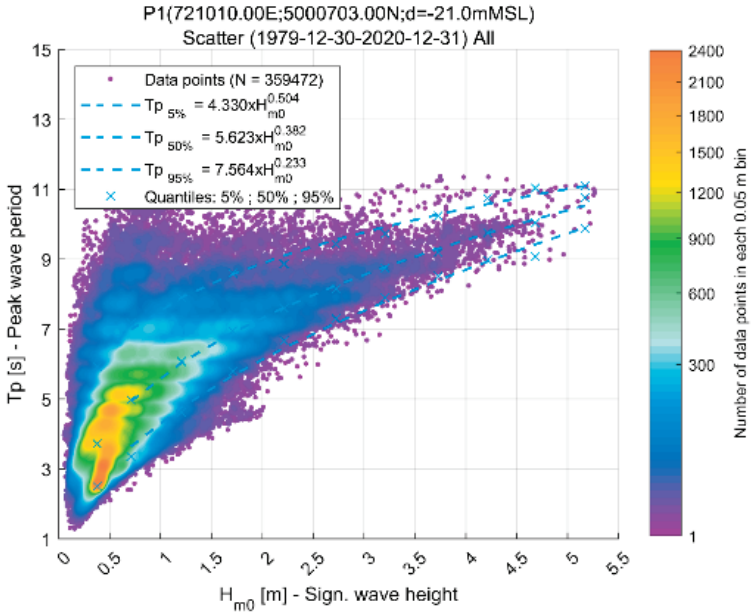

Figure 7. The significant wave height (H_{m0}) and peak wave period (T_p) at P1.

Table 3. Matching coefficients (T_p = a H_{m0} b) at P1.

Percentage [%]	5		50		95	
Matching coefficient	a	b	a	b	a	b
T_p	4.330	0.504	5.623	0.382	7.564	0.233

To simulate the extreme wave conditions in the Sulina Canal area, a local wave model was developed using Mike 21 Flexible Mesh Spectral (Danish Hydraulic Institute).

The full spectral formulation is based on the wave action conservation equation, presented in [34,35], where the direction–frequency wave action spectrum serves as the dependent variable.

3.1.2. Local Wave Climate Characterization

Specific wave events were simulated using a local wave model to provide extreme wave conditions in the Sulina Channel area for stability analysis. Additionally, a 10-year simulation of spectral waves (from 1 January 2011 to 31 December 2020) was conducted to establish a database to assist in calculating littoral sediment transport processes.

The model is based on the topographic and bathymetric data provided within the project, as well as data from open sources, as detailed in the input data chapter. The computational mesh consists of 7043 elements, with the smallest element area being approximately 3600 m^2 and the largest 550,000 m^2.

For specific wave events, H_{m0}, T_p, and MWD were determined based on the statistical analyses described in previous sections. For the 10-year simulation, data were extracted from the spectral wave model developed for the Black Sea.

3.1.3. Loads Acting on Protection Dikes

To accurately compute the loads on the protective dikes, it was necessary to simulate local wave conditions using the above described 2D model for a series of selected events (local wave climate characterization). The wave heights were extracted from the simulation results and subsequently applied in the stability computations. The wave model was simulated over an extended period to identify representative wave conditions in the bar area that could affect the dikes. Detailed information regarding the current structure of the dike, including its design and verification criteria, was not available. Therefore, the analysis was conducted based on the relevant literature and expertise.

Due to the uncertainty regarding the probability associated with the design and verification standards of the protective works and the size of the rocks used during construction, it was reasonable to use, for calculations, events with a 1% return period. The wave heights were extracted from the simulation results. The boundary conditions were used in the dikes stability analysis by comparing design values for unit weights for the dike rocks with known weights. In the calculations, a series of dike sections on the northern structure (SN) and the southern structure (SS) of the Sulina Channel were considered, as shown in Figure 8.

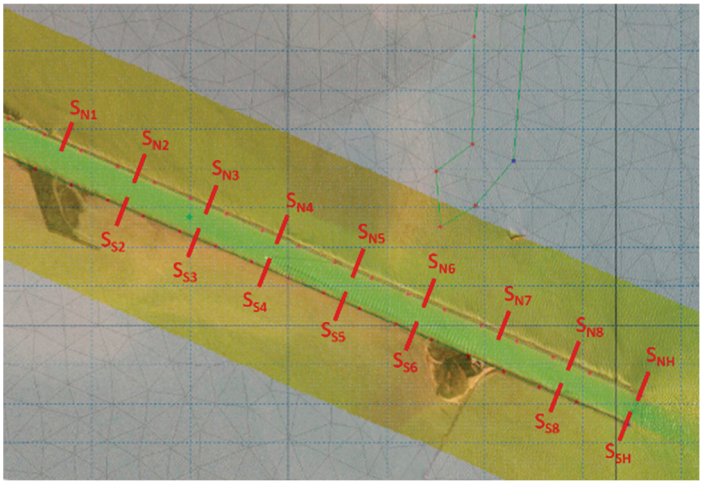

Figure 8. Sections selected for calculating loads on north and south dikes.

Sections were selected at the beginning of the dikes into the sea and upstream, ensuring that a variety of wave heights and cross-sectional characteristics were captured. The two sections at the sea entrance (dike heads) are designated as S_{NH} (north) and S_{SH} (south). The analysis of the dike sections utilized the available LIDAR data, which included the most recent and detailed measurements from the project's survey campaign (2023) providing crucial information on the actual dikes' dimensions and slopes. The S_{S1} to S_{S6} sections (located on the southern dike) have recorded water levels lower than the terrain elevation

and, therefore, were not considered in the calculation of wind-generated wave loads on the southern side.

The Hudson equations [36,37] were used to estimate the minimum unit weight required for the dike's surface layer, assuming minimal damage due to wave action for different dike sections. The overtopping height and overflow across the dike were calculated according to Eurotop [38]. The physical or geometric parameters related to the waves characteristics that were included in the calculations are:

- H [m]—Wave height, which is the height of the wave from crest to trough,
- T [s]—Wave period, which represents the time it takes for two consecutive wave crests to pass a fixed point,
- Direction (°)—Wave direction, which is the angle of wave propagation relative to true north,
- β [°]*—A parameter related to the wave incidence angle relative to the dike structure,
- L [m]—Wavelength, which is the distance between two consecutive wave crests.
- h/L [-]—Ratio of water depth (h) to wavelength (L)
- H/h [-]—Ratio of wave height (H) to water depth (h).

Wave breaking was considered for horizontal beds with H/h = 0.78 and for sloped beds with H/h = 0.55.

The required weight for tetrapod elements was also calculated to provide context for the necessary weights to withstand wave loads for a 100-year return period.

3.2. Coastline Sediment Transport Model

The sediment transport models along the coast and within the Sulina Channel and bar area were employed to estimate the dynamics of sediment deposition. This model includes solid discharges from the channel, influenced by currents and waves, and marine sediments deposited in the bar area due to changes in the flow regime.

A one-dimensional model (LITDRIFT), developed by DHI, was used to investigate the temporal and spatial variation of sediment transport along the northern coast of the Sulina Channel. It focuses on littoral evolution and excludes the two-dimensional processes already addressed by other models. LITDRIFT is an integrated modeling system that simulates non-cohesive sediment transport along quasi-stationary coastal lines using an "n-line" approach, combining a robust deterministic sediment transport model with the ability to simulate a wide range of wave and current scenarios, employing methods such as the integrated momentum approach [39], the Engelund and Fredsoe model [40] for bedload transport, and the vertical diffusion equation for suspended sediments [41] to evaluate coastal currents and sediment transport for applications like coastal works impact assessment and beach development optimization.

The inputs in the model are the wave climate, coastal profile data, sediment characteristics, and water levels.

The LITDRIFT calculations were based on a 10-year wave climate simulation (2011–2020). Three profiles were used to model the coastal zone between the Chilia branch and the Sulina Channel. The results were presented as net and gross transport capacities along these profiles and their distribution along the coastline.

3.2.1. The Wave Climate

The wave climate is the primary factor driving sediment movement. Wave data were extracted from the hydraulic model, which provided time series of transformed waves (height, period, and direction) at the seaward ends of the profiles. These locations (Figure 9), with water depths of approximately −8 m relative to mean sea level (MSL), were chosen to avoid the wave breaking and closure zones, ensuring the model captured a full range of conditions. Predominant wave directions were identified as NE-E.

Figure 9. The locations of the coastal profiles (red lines) and the associated wave climates represented as wave roses. Satellite image from Google Earth Pro, dated 11 July 2017.

3.2.2. Coastal Profiles

For the given wave conditions, the shape of coastal profiles determines the wave breaking zone and its magnitude. The profiles were derived from bathymetric data with an 80 × 100 m resolution, primarily based on GEBCO Gridded Bathymetric Datasets, and refined with higher-resolution local data. It is noted that the resolution may not fully capture the beach slope and sand dune (Figure 10). Beach slopes were manually adjusted using satellite imagery to reflect field conditions accurately. The profiles extended perpendicularly from the shore to a depth of −8 m MSL.

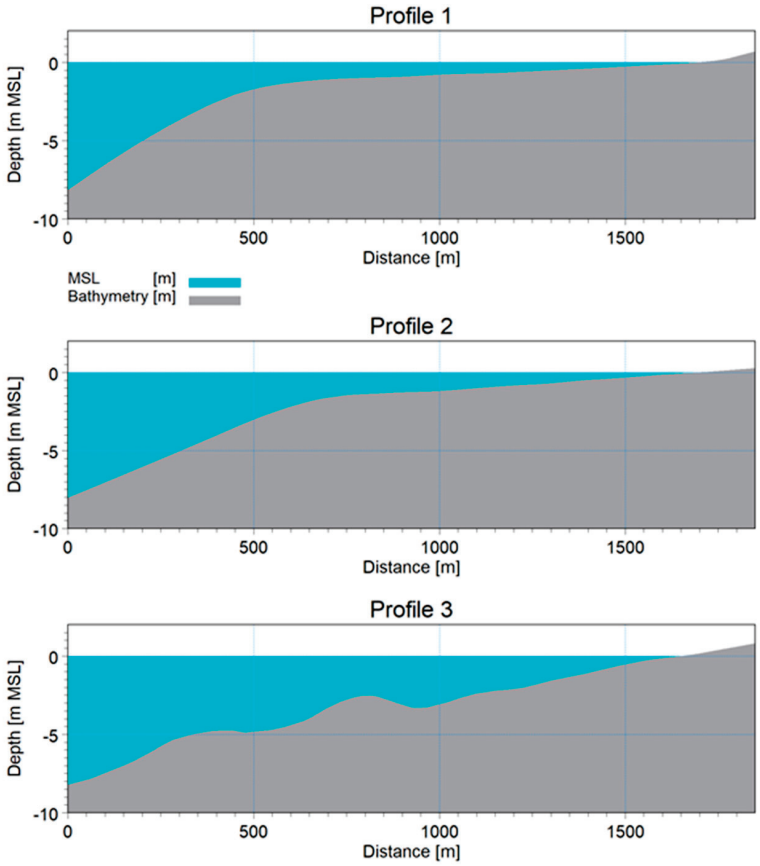

Figure 10. Cross-sectional profiles extracted along the sand dune north of the Sulina Channel.

3.2.3. Water Level

The variation in water levels within the study area is minimal, and the tidal range is negligible. Therefore, a constant mean sea level was assumed for the simulations, as the wave-induced variations were deemed more significant.

3.2.4. Sediment Characteristics

The model incorporated two median particle sizes (d50) of 0.15 mm and 0.2 mm, with associated settling velocities of 0.0183 m/s and 0.0267 m/s. A roughness coefficient of 0.0037 m and 0.005 m was applied to account for coastal changes in the simulations.

3.3. Channel Sediment Transport

To simulate water flow and sediment transport in the downstream sector of the Sulina branch, we developed a two-dimensional model that operated continuously on a distance of 11 km from Sulina to the discharge point into the Black Sea. The model used is Mike 21 Flexible Mesh of Danish Hydraulic Institute from Denmark with Mud Transport (MT) module. The hydrodynamic system is based on the Navier–Stokes equations, encompassing the mass continuity equation, the momentum continuity equation, and variations in temperature, salinity, and density, as well as incorporating a turbulence model, while computational equations underlying the MT module are based on those described in [42]. For enhanced accuracy and model stability, the calculation range was extended approximately 19 km northward, encompassing the Musura Gulf, and around 19 km eastward and 24 km southward into the Black Sea.

The study area (Figure 3) was defined after the analysis of topo-bathymetric data, superimposed on maps and orthophotos. This zone, covering 1077 km^2, includes all relevant features: the minor bed of the Sulina branch, defense dams, the locality, and the extension into the Black Sea.

Based on the analyzed and vectorized data, a bathymetry file specific to MIKE 21 FM software was created by constructing a network of finite elements (mesh) (Figure 11), with various dimensions tailored to each area of interest:

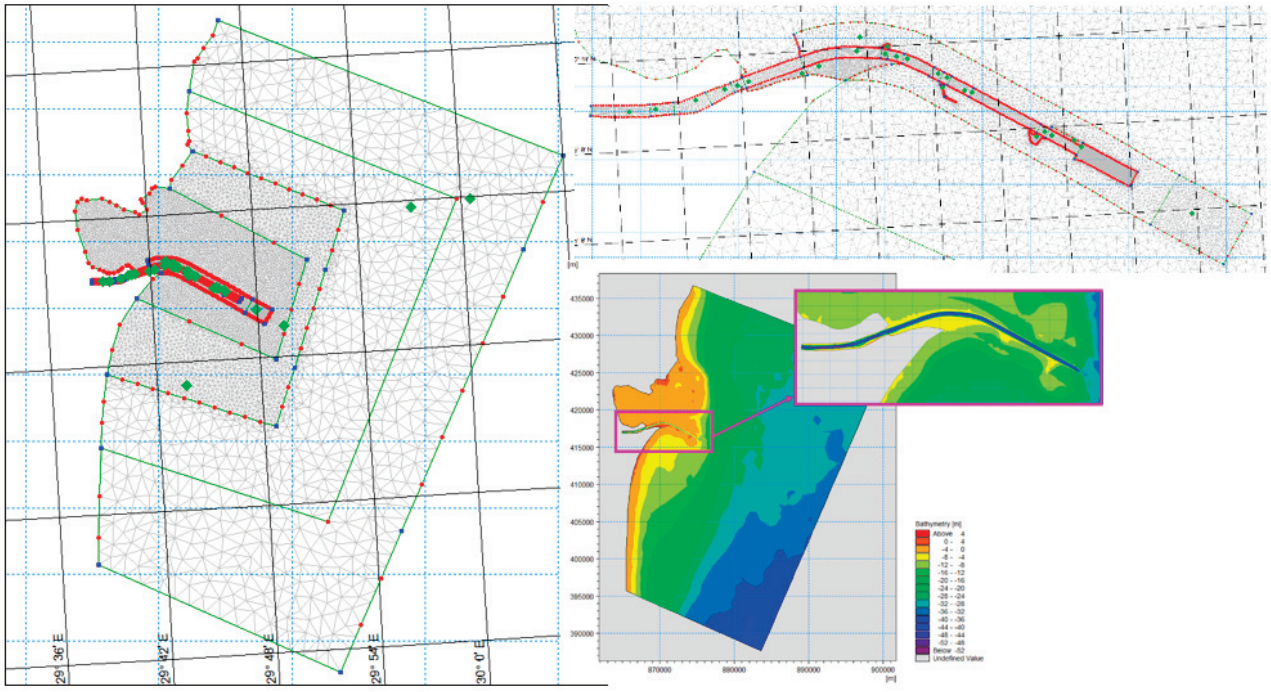

Figure 11. The finite elements mesh (left and top right); Bathymetry file used in hydrodynamic model (right down).

- In the minor riverbed, quadrilateral elements were used with sizes varying from 90 × 30 m to 90 × 10 m along the Channel. Locally, triangular elements with a maximum size of 50 m^2 were utilized in the upstream area. For the Danube River–Sulina Branch mouth area, a triangular mesh with elements sized at 55 m^2 was employed.
- For the rest of the domain, triangular elements were generated with surfaces ranging from 500 m^2 to 75,000 m^2, and the element size progressively increased from the land towards the Black Sea coast.

To find an optimal solution, it was essential to determine the appropriate number of finite elements that would accurately describe the areas of interest while avoiding stability and convergence issues and optimize the computational time. Based on the requirement for precision and taking into account previous experience, a finite element network consisting of 37,925 elements was established. Figure 12 displays the mesh details, allowing for an observation of the elements' density.

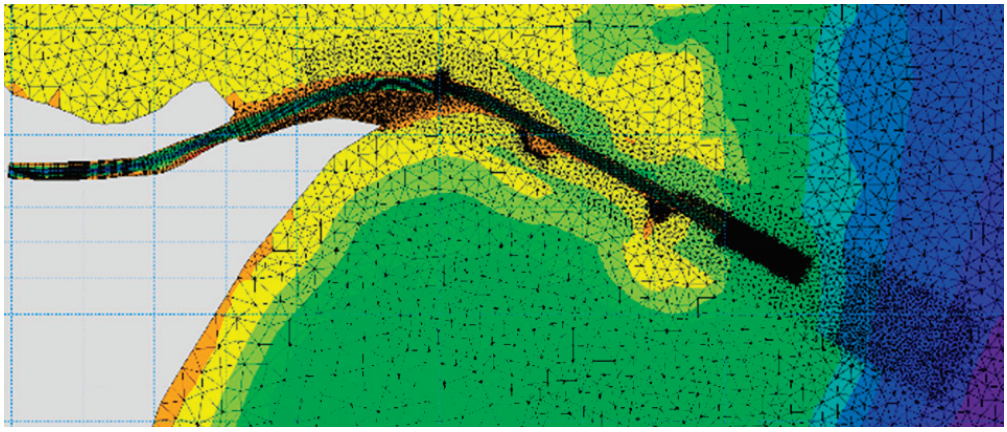

Figure 12. Detail of the network of finite elements (mesh).

The two-dimensional hydrodynamic model integrated the information below:

- Turbulent viscosity;
- The Manning Roughness Coefficient [43], *n*, crucial for the hydrodynamics of a watercourse, which was determined based on the following information:
    - o The type and size of materials composing the bed and banks of the riverbed;
    - o The shape of the riverbed.

To assess the vegetation and land use in the major riverbed, the roughness coefficients were selected according to recommendations from specialized literature [44]. This selection was further refined through analysis of available aerial photography charts. Using the available land use data, the CLC (Corine Land Cover 2018) file was processed and improved, assigning values to each type of use:

- The values assigned to *n* were between 0.023 and 0.027 in the minor bed of the Sulina Channel;
- The Manning coefficient was set to 0.014 in the Black Sea area;
- The Manning coefficient ranged from 0.050 to 0.085 in the major riverbed.

Based on experience from previous studies and sensitivity analyses, an average wind speed of 5 m/s and a direction of 55 degrees were used. Hydrological data (flow and levels) from project measurement campaigns were also included, with an upstream flow value of 1410 m^3/s and variable boundary level conditions for the northern and southern areas, the beach, and the Black Sea.

The model integrates two-dimensional sediment transport processes, addressing sedimentary flow and morphology changes through erosion or accumulation. Measurements were processed to determine particle size distribution and bed stratification, enabling precise simulation of sediment resuspension dynamics.

The Engelund & Hansen model [45] was selected for sand transport, with the following sediment properties: porosity—0.4, relative density—2.65, and particle diameter based on field data, including a grain size of 0.15/0.2 mm for the Black Sea area. Roughness coefficients from the hydrodynamic model were applied.

For mud transport, cohesive material transport was calculated based on flow conditions, with additional data for three layers of parental material and erosion and density parameters set according to field sampling information. Wave regime data, with average values for height (1.0 m), period (3 s), and direction (55 degrees), were also incorporated.

Several fairway depth scenarios (8–12 m) were analyzed to simulate sediment transport. The "Fairway −12 m" scenario was used as a baseline, representing an extreme but informative hypothesis. The model was validated by comparing hydrodynamic results with field measurements, showing accurate reproduction of flow phenomena.

3.4. Vessel Traffic Model

The model was further developed to analyze the dynamics of the fairway under the influence of currents, waves, and naval traffic by incorporating elements that account for the location and direction of ship movement, such as route, draught, propeller diameter, speed, propulsion coefficient, and propeller RPM. It also considers the tangential forces produced by the ship propellers, comparing them with the threshold force needed to resuspend sediments, which helps in identifying areas of erosion and deposition.

4. Results and Discussion

4.1. Results of the Large-Scale Wave Model in the Black Sea Area and Sulina Bar and Small-Scale Wave Model

The MIKE 21 SW non-stationary simulation was conducted over 10 years from 1 January 2011 to 31 December 2020. For example, the maximum values of wave heights can be seen in Figure 13.

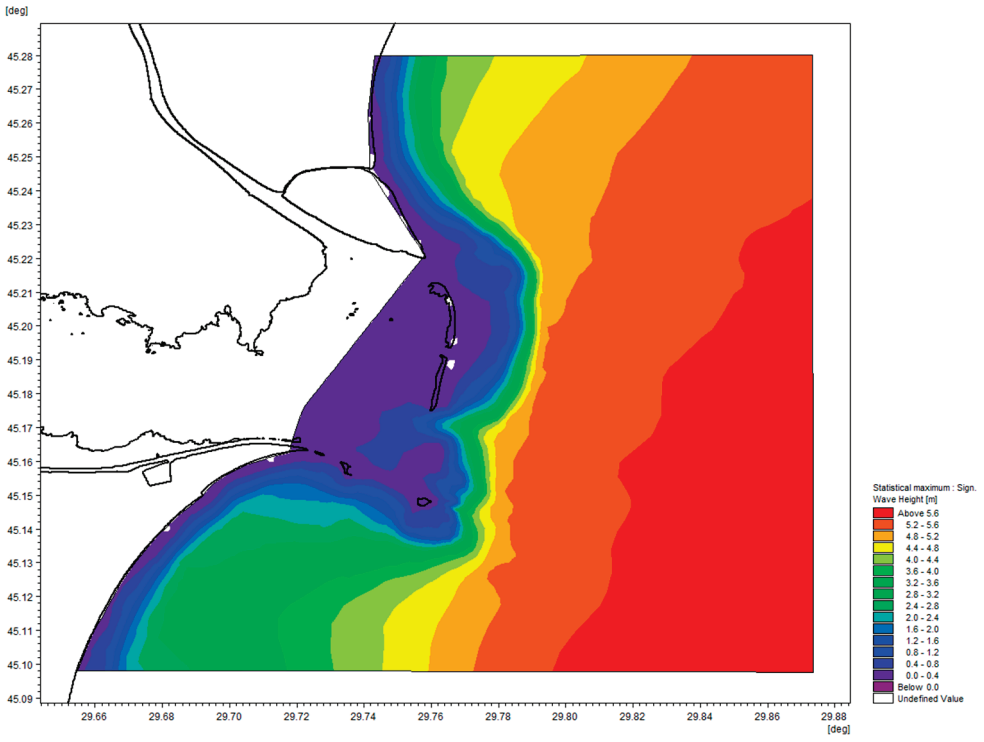

Figure 13. The maximum value of the significant wave height (H_{m0}) for a 10-year simulation.

The maximum wave heights for a 100-year return period were determined using the results from the MIKE 21 SW model. Table 4 presents the wave characteristics at the selected sections.

Table 4. Wave properties at the selected sections.

Section	H [m]	T [s]	Direction [°]	β * [°]	L [m]	h/L	H/h	Wave Breaking
S_{NH}	3.2	10.3	124	0	54.23	0.0756	0.780	Yes
S_{SH}	3	10.3	96	0	53.61	0.0746	0.750	Yes
S_{N8}	1.3	9.9	77	54	44.88	0.0668	0.433	No
S_{S8}	1.24	9	146	57	30.13	0.0531	0.775	Yes
S_{N7}	1.14	9.9	81	58	37.91	0.0554	0.543	No
S_{N6}	1.03	9.9	87	64	47.34	0.0710	0.307	No
S_{N5}	0.58	10.3	80	57	53.61	0.0746	0.145	No
S_{N4}	0.19	9.9	22.5	0.5	44.17	0.0657	0.066	No
S_{N3}	0.21	9.9	41	18	40.41	0.0594	0.088	No
S_{N2}	0.19	10.6	48	25	38.24	0.0484	0.103	No
S_{N1}	0.24	10.6	36	13	34.08	0.0428	0.164	No

The computed values for the minimum unit weight required for the surface layer, overtopping height, and overflow across the dike are presented in Table 5, where K_D is a stability coefficient, W is the weight, and Q is the overflow over the crest.

Table 5. Estimated minimum weight of rocks along with overtopping height (Ru2%) and the overflow over the crest (Q).

Section	Natural Rock		Tetrapods		$R_{u2\%}$ [m]	Rc [m]	Q [m^3/s.m]
	K_D	W [Tone]	K_D	W [Tone]			
S_{NH}	1.1	24.61	4.5	6.02	2.37	4.7	0.03
S_{SH}	1.1	14.96	4	4.12	2.25	5	0.00
S_{N8}	2.4	1.21	-	-	2.34	3	0.00
S_{S8}	1.2	2.02	-	-	2.27	3	0.00
S_{N7}	1.2	1.77	-	-	2.33	2.6	0.00
S_{N6}	2.4	<1	-	-	2.28	2.8	0.00
S_{N5}	2.4	<1	-	-	2.37	2.5	0.00
S_{N4}	2.4	<1	-	-	1.61	2.6	0.00
S_{N3}	2.4	<1	-	-	1.06	2.5	0.00
S_{N2}	2.4	<1	-	-	1.00	2.45	0.00
S_{N1}	2.4	<1	-	-	1.07	2.5	0.00

The unit weights of the surface layer components are reasonable along most of the dike length, matching the known values of the stones forming the dike structure. For the sections at the heads, these weights reach high values, justified by greater depths and stronger wave impacts on these sections, which are the most exposed to the wave climate. Given that the dike's entire structure and the constituent rocks' weight are only partially known, it is impossible to conclude definitively on the stability of the protective structure's elements. However, the dikes' stability was assessed by considering them as a cohesive mass influenced by hydrostatic and hydrodynamic pressures from wave action. The computation shows that the overtopping height $R_{u2\%}$ is lower than the freeboard for all sections, and the overflow over the crest (Q) is negligible.

4.2. Results of the Coastline Sediment Transport Model

A modeling scenario was implemented to analyze sediment transport dynamics between the Chilia Branch and the Sulina Channel, corresponding to a median particle diameter of 0.15 m. The 10-year time series of littoral sediment transport, illustrated in Figure 14, focuses on Profile 2 for 0.15 mm.

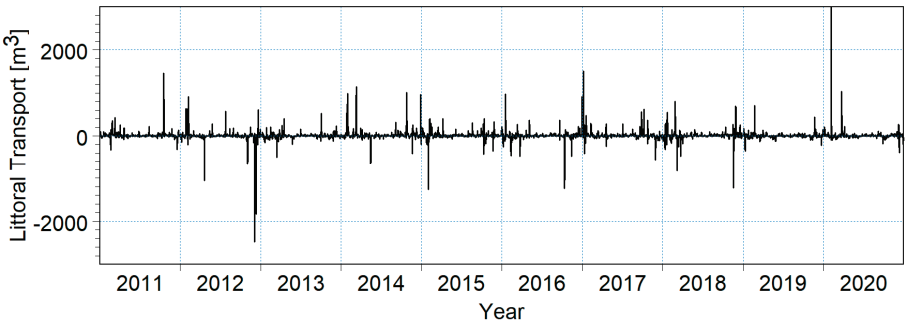

Figure 14. Time series of estimated littoral transport (m^3) over 10-years for Profile 2, with a beach orientation of 94° and a sand particle size of 0.15 mm. Negative values indicate transport towards the north, whereas positive values indicate transport towards the south.

These time series highlight seasonal and interannual variations in sediment transport, most occurring during winter. Notably, negative values indicate sediment transport from south to north, while positive values indicate transport from north towards the Sulina Channel and bar. Similar sediment transport trends are observed in Profiles 1 and 3.

The distribution of modeled sediment transport along the cross-sectional profiles is presented in Figure 15. The charts display the bathymetric elevation (relative to mean sea level) on the left *Y*-axis and transport rates on the right *Y*-axis, including annual net and gross transport rates from north to south and from south to north.

Remember that Net Transport is defined as the difference between the transport in both directions. In contrast, Gross Transport refers to the sum of transport in both directions, considering movement from the Sulina Channel towards Chilia and vice versa.

The resulting distribution indicates that sediment transport is mainly concentrated along the slope of the beach and sand dune (as observed in Profile 3) and around the beach where waves break, generating littoral currents and, consequently, sediment transport.

For sediments with a median diameter (D50) of 0.15 mm, the net transport capacities (the difference between transport capacities in both directions, N-S and S-N) across the three modeled profiles range from approximately 40,000 m^3/year to 70,000 m^3/year. The predominant direction of transport for all three profiles is from north to south towards the Sulina Channel. The annual gross transport capacities range from 150,000 m^3/year to 230,000 m^3/year.

Considering the limitations in data availability, net sediment transport along the coast north of the Sulina Channel is estimated to range between 30,000 m^3/year and 70,000 m^3/year towards the river mouth. Consequently, an intensive deposition process is expected in the river mouth area. However, sedimentation and annual sediment transport are likely to increase due to additional sediment input from the Danube, which also deposits in the Sulina bar area.

Figure 16 shows the results of the sediment transport model along the coast. The measurement unit is 1000 m^3/year. The net transport (left number) and gross transport (right number) are shown in yellow, along with the transport direction. The profile orientation relative to the beach is shown in green.

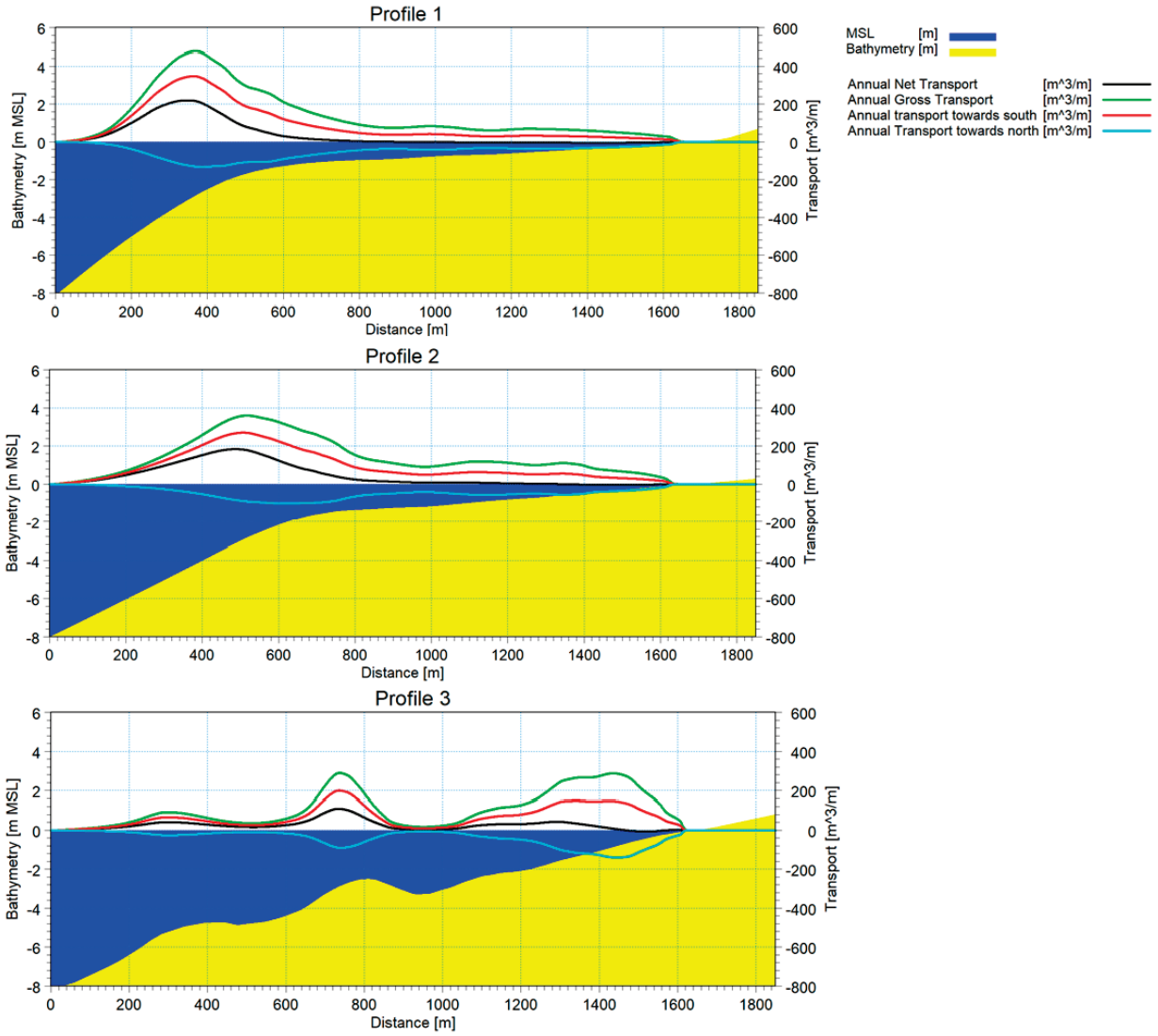

Figure 15. The distribution of littoral transport across three profiles for sediment sizes with a median diameter (D50) of 0.15 mm.

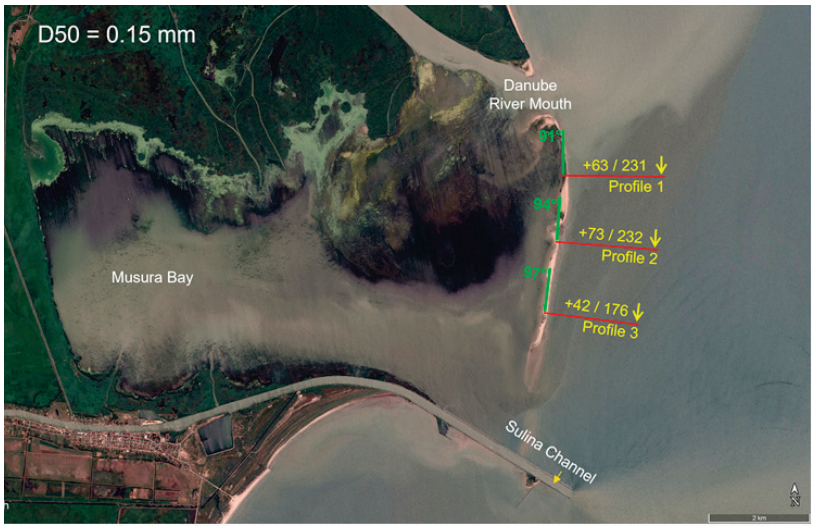

Figure 16. Forecasted littoral transport capacities for 0.15 mm sediments.

4.3. Results of the Channel Sediment Transport Model

The results show sediment deposition in the Sulina Channel's discharge area into the Black Sea. A representative image shows bed elevation changes from −12.0 m to about −7.3 m. The sediment deposition dynamics were analyzed in various scenarios, with estimates for required maintenance volumes. Figure 17 shows, in the longitudinal profile through the bar, the differences between the results obtained from the modeling (green line), the topo-bathymetric data obtained in the project campaign (blue line), and the processed file in which the fairway level has been established as −12 m (red line).

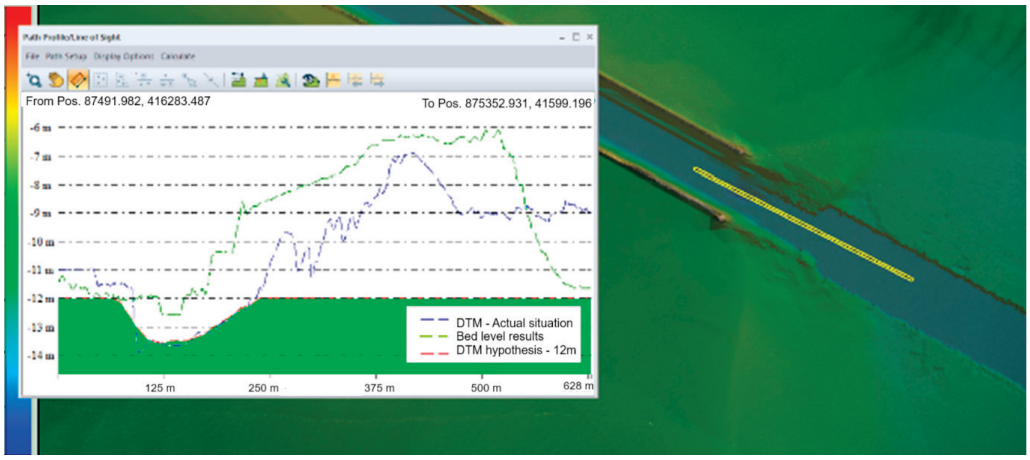

Figure 17. Comparison between modeling result and DTM in the current situation—longitudinal profile.

All available historical data have been used for a proper comparison with the results from the coupled hydrodynamic-sediment transport model. The historical data were acquired during various monitoring surveys done in 2018, 2022, and 2022 by the Lower Danube Administration specialists. The comparison has pointed out a dynamic phenomenon of sediment deposition in the river channel around the river mouth area. The deposition is slightly uneven, both transversally and longitudinally, but happens continuously.

Figure 18 depicts the comparison between the simulated deposition (green line) and the measured deposition bar.

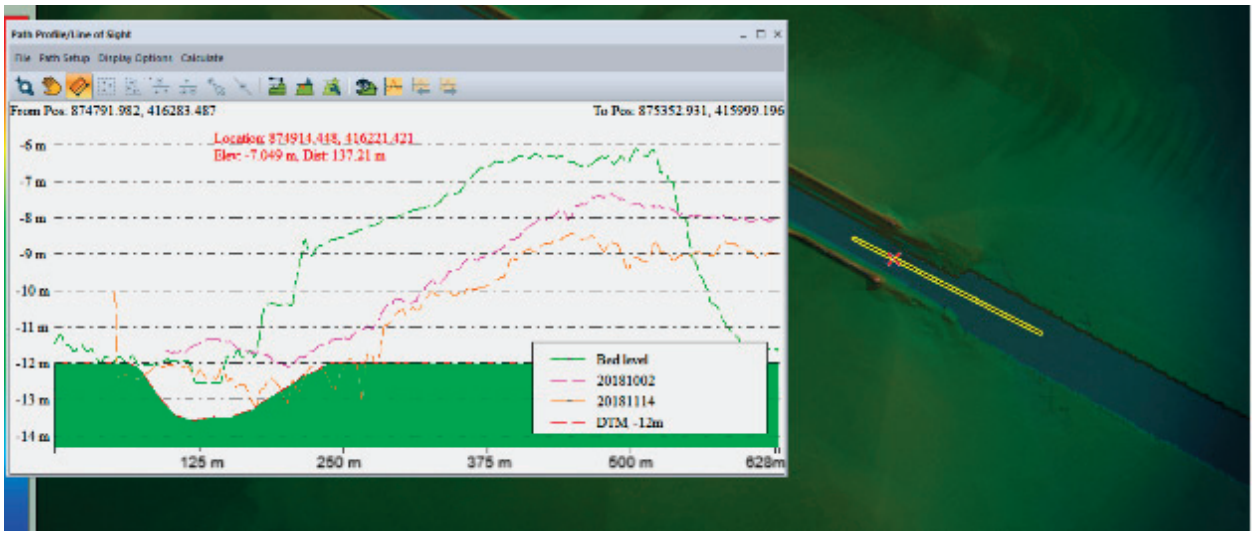

Figure 18. Comparison between the simulated scenario and historical measurements.

4.4. Results of Vessel Traffic Model

Simulations conducted over a week, with approximately 150 vessels of 11.5 m draught moving at 2.5 m/s, revealed that ships cause additional erosion along their routes, particularly in the upper layer of less consolidated clay. This erosion process stabilizes after 3–5 passages, with the more consolidated second layer experiencing less erosion. Scenarios involving tugboat-assisted vessels showed similar trends, with slightly higher erosion at the fairway's edges.

The model results indicate that a vessel with a draught of 11.5 m transiting the new navigable channel generates additional erosion due to the currents produced by the propellers. The results show that this additional erosion generally occurs within a 30–50 cm range, with only a few areas where these values are exceeded (Figure 19).

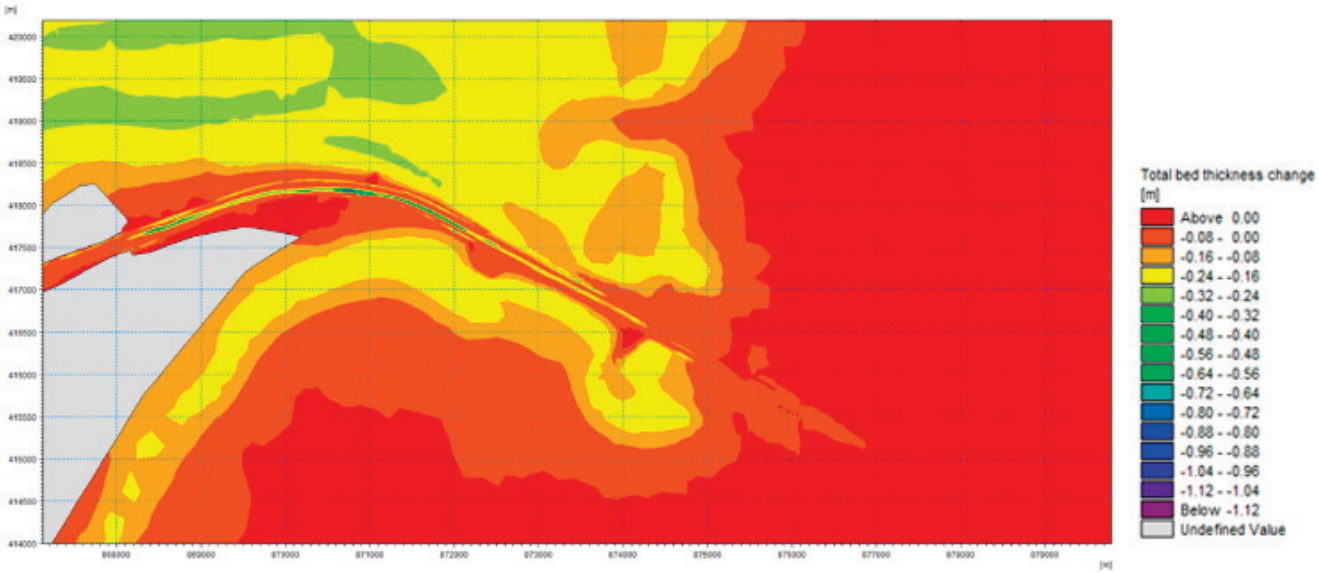

Figure 19. Riverbed erosion due to propellers.

For ships with a draught of 7 m, propeller effect on sediment transport is minimal.

It is crucial to note that the erosion caused by vessels is primarily concentrated along the ships' route. This means that vessels do not impact the dikes if they adhere to the defined channel route. Therefore, it is of utmost importance that ships remain as close as possible to the channel's center, thereby avoiding additional tangential stress on the dike bottoms.

4.5. Discussion

Regarding the sediments recolonization, the results show that the Sulina Channel mouth area is highly dynamic. The particles resedimentation occurs quite rapidly, with the water depth varying from −12 m to the stability depth of around −7 m in one to two months. Figure 20 presents the riverbed evolution in time in a representative area of the bar. Remark that about 800 h after dredging, the depth to the riverbed is above −7 m.

This recolonization happens mainly in places with a sudden transition between the Danube's fluvial flow regime and the Black Sea's marine current regime because sand particles from the Black Sea are deposited rapidly. The obtained results match the observations regarding the deposition area and deposited quantity and the development of a sand dune from north to south directly through the Sulina bar.

The dikes' stability analysis has shown that the longitudinal dike along the Sulina canal is stable and not influenced by external conditions in terms of the lateral pressure applied by the hydrodynamic wave forces and potential erosion or rock displacement caused by waves overtopping.

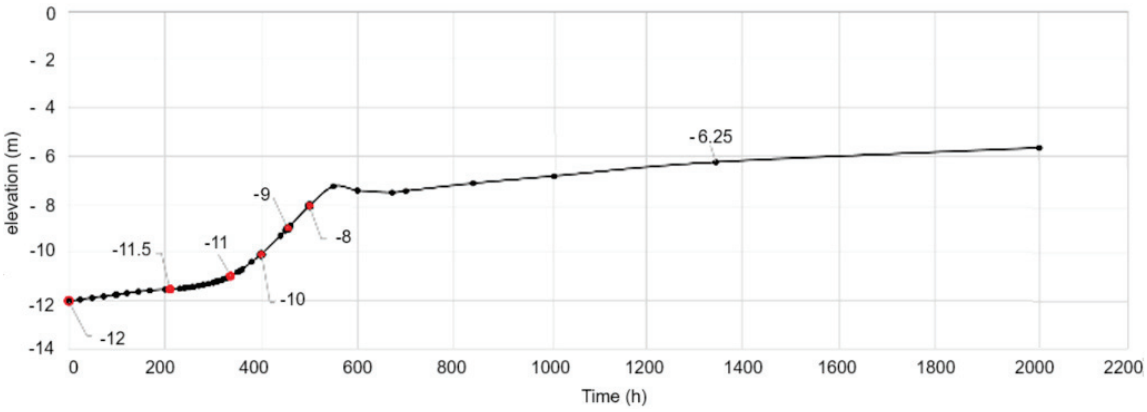

Figure 20. Evolution of the seabed level in the Sulina Channel's mouth area.

In this study, an additional scenario considered the vessel propulsion, where the vessel would not be self-propelled but rather assisted by tugboats, which would have much smaller draughts than the cargo vessel. The same route and travel speed have been proposed as for the self-propelled vessel. This scenario was mainly simulated to assess if the tugboats would induce any scouring in the protection dikes. The simulation results showed that the tugboats would not have a scouring impact on the dikes' bottom, thus not threatening the dike stability. Also, considering the smaller draught values, the tugboat propellers are not powerful enough to cause any significant material resuspension.

The study brings significant insight into the integrated dynamics of various forcings (waves, currents, winds, river discharge, mud transport, sediment transport, and vessel traffic) that act on the Sulina Channel's mouth area and bar.

The novelty of the study is represented by:

- Proposing various models for assessing the individual and combined effects of the processes that impact the navigability in the Sulina Channel;
- Designing a vessel traffic model to evaluate the impact of the increased vessel traffic (that takes into account the increase in vessel sizes) on the sediment resuspension;
- Evaluating the potential sediments' redeposition in the Sulina bar area;
- Evaluating the dredging period to maintain the navigability on the canal. This is especially important during wintertime when the bar could suffer significant re-sedimentation due to storms and increased sediment transport.

5. Conclusions

The study brings significant insight into the complex dynamics occurring in the Sulina Channel mouth area accounting for the combined effects of natural forces and anthropogenic activities. Its novelty consists of presenting an integrated approach that aims to obtain the necessary input to fully assess the area in terms of interactions between waves, currents, river flows, and sediment transport and the impact of vessels' navigation on sediment resuspension in the Sulina Channel.

Through advanced hydrodynamic, wave, and sediment transport models, the following key conclusions have been drawn.

- The transition zone between the Danube River and the Black Sea experiences significant sedimentation, primarily due to the fine materials carried by river discharge and sand deposited by marine currents. This finding is crucial for planning regular maintenance dredging and the associated costs for maintaining the navigability in the Channel.
- The vessels' transit contributes to additional erosion along predefined routes, with propeller-induced currents causing significant sediment resuspension. Erosion stabilizes after multiple vessel passages, primarily affecting the less consolidated upper sediment layers.

- The developed wave model successfully estimated the wave conditions impacting the Sulina Channel and its infrastructure, providing essential data for understanding the coastal sediment transport processes.
- Extreme wave height analyses revealed significant wave directions predominantly between 60° N and 120° N. Therefore, it is necessary to consider these directions in future coastal management plans.
- Stability analyses of the dikes along the Sulina Channel demonstrate that the existing structures can withstand extreme hydrodynamic forces, with calculated wave-induced pressures confirming the dikes' resilience. Longitudinal dikes were stable against both lateral hydrodynamic pressures and potential erosion or rock displacement caused by wave overtopping, ensuring the continued protection of the Sulina Channel.

The findings underscore the importance of an integrated approach in managing navigable waterways, ensuring operational efficiency and environmental sustainability.

To enhance the accuracy of future studies, it is recommended that more detailed field measurements be acquired, particularly regarding wave and current conditions in the Black Sea. Further investigations should include the impact of wake waves on dike erosion processes and sensitivity analyses of different vessel characteristics to refine the understanding of their effects on sediment transport.

Overall, this study presents significant insights into the complex dynamics at the Sulina Channel mouth, offering valuable information that could significantly shape the future of the sustainable management and maintenance of this critical navigational route.

Author Contributions: Conceptualization, M.I.C. and M.V.S.; methodology, M.I.C. and M.V.S.; software, M.V.S. and D.S.; validation, M.I.C., A.B. and C.Ș.D.; formal analysis, R.S., A.B. and C.Ș.D.; investigation A.M. and R.S.; resources, M.V.S.; data curation, A.M. and R.S.; writing—original draft preparation, M.I.C. and A.B.; writing—review and editing, A.B. and C.Ș.D.; visualization, D.S.; supervision, A.B.; project administration, M.I.C. All authors have read and agreed to the published version of the manuscript.

Funding: This research received no external funding.

Data Availability Statement: Data will be available on request from the authors.

Conflicts of Interest: The authors declare no conflicts of interest.

References

1. Lebour, G. 1. On the deposits now forming in British seas. *Proc. Geolog. Assoc.* **1875**, *4*, 158–164. Available online: https://eurekamag.com/research/080/857/080857833.php (accessed on 19 July 2024). [CrossRef]
2. Sediment Transport under Waves and Currents. 1985. Available online: https://eprints.hrwallingford.com/66/1/SR22.pdf (accessed on 19 July 2024).
3. Bijker, E.W. *Some Considerations about Scales for Coastal Models with Moveable Beds*; Delft Hydraulics Laboratory Publisher: Delft, The Netherlands, 1967; Volume 50, Available online: https://repository.tudelft.nl/record/uuid:cdf2f061-3fe6-4361-a0e7-636fc69c9eca (accessed on 8 August 2024).
4. Slingerland, R.L. Numerical models and simulation of sediment transport and deposition. In *Sedimentology. Encyclopedia of Earth Science*; Finkl, C.H., Ed.; Springer: Berlin/Heidelberg, Germany, 1978; pp. 775–783.
5. Duan, J.G.; Yu, C.; Ding, Y. Numerical Simulation of Sediment Transport in Unsteady Open Channel Flow. *Water* **2023**, *15*, 2576. [CrossRef]
6. Zerihun, Y.T. Numerical Modeling of Sediment Transport and Bed Evolution in Nonuniform Open-Channel Flows. *Arch. Hydro-Eng. Environ. Mech.* **2024**, *71*, 1–27. [CrossRef]
7. Shmakova, M. Sediment Transport in River Flows: New Approaches and Formulas. In *Modeling of Sediment Transport*; Pasquali, D., Ed.; IntechOpen: London, UK, 2022; Available online: https://www.intechopen.com/chapters/81410 (accessed on 9 August 2024).
8. Popescu, C.; Bărbulescu, A. On the Flash Flood Susceptibility and Accessibility in the Vărbilău Catchment (Romania). *Rom. J. Phys.* **2022**, *67*, 811.
9. Crăciun, A.; Costache, R.; Bărbulescu, A.; Pal, S.C.; Costache, I.; Dumitriu, C.Ș. Modern Techniques for Flood Susceptibility Estimation across the Deltaic Region (Danube Delta) from the Black Sea's Romanian Sector. *J. Mar. Sci. Eng.* **2022**, *10*, 1149. [CrossRef]

10. Parchure, T.M.; Davis, J.E.; McAdory, R.T. Modeling fine sediment resuspension due to vessel passage. *Proc. Mar. Sci.* **2007**, *8*, 449–464.
11. Chakraborty, M.; Sriram, V.; Murali, K. Investigation of ship-induced hydrodynamics and sediment resuspension in a restricted water-way. *Appl. Ocean Resear.* **2024**, *142*, 103831. [CrossRef]
12. Stoschek, O.; Precht, E.; Larsen, O.; Jain, M.; Yde, L.; Ohle, N.; Strotmann, T. Sediment Resuspension and Seabed Scour Induced by Ship-Propeller Wash. Available online: https://www.dhigroup.com/upload/publications/coastsea/Stoschek_2014.pdf (accessed on 8 July 2024).
13. Guarnieri, A.; Saremi, S.; Pedroncini, A.; Jensen, J.H.; Torretta, S.; Vaccari, M.; Vincenzi, C. Effects of marine traffic on sediment erosion and accumulation in ports: A new model-based methodology. *Ocean Sci.* **2021**, *17*, 411–430. [CrossRef]
14. Srše, J.; Perkovič, M.; Grm, A. Sediment Resuspension Distribution Modelling Using a Ship Handling Simulation along with the MIKE 3 Application. *J. Mar. Sci. Eng.* **2023**, *11*, 1619. [CrossRef]
15. Spoolder, B. Influence of Inland Shipping on Sediment Transport in the Waal River. Master's Thesis, University of Twente, Enschede, The Netherlands, 2023. Available online: https://essay.utwente.nl/97135/ (accessed on 19 July 2024).
16. Ji, S.C.; Ouahsine, A.; Smaoui, H.; Sergent, P.; Jing, G.Q. Impacts of ship movement on the sediment transport in shipping channel. *J. Hydrodyn. Ser. B* **2014**, *26*, 706–714. [CrossRef]
17. McConchie, J.A.; Toleman, I.E.J. Boat wakes as a cause of riverbank erosion: A case study from the Waikato River. *J. Hydrol.* **2003**, *42*, 163–179.
18. Budileanu, M. Evolution of Sulina Mouth Bar (Danube River) Evolution of Sulina Mouth Bar (Danube River). Available online: https://www.researchgate.net/publication/309427460_Evolution_of_Sulina_mouth_bar_Danube_river (accessed on 23 July 2024).
19. Mateescu, R.; Ivan, A.; Omer, I.; Butunoiu, D.; Niculescu, D. Aspects of the coastal hydro-geomorphological processes at the Danube river mouths. *Ann. Univ. Dunarea De Jos Galati Fascicle II Math. Phys. Theor. Mech.* **2013**, *2*, 316–322.
20. Boșneagu, R.; Scurtu, I.C.; Popov, P.; Mateescu, R.; Dumitrache, L.; Mihailov, M.E. Hydraulics numerical simulations using computational fluid dynamics (CFD) method for the mouth of Sulina channel. *J. Environ. Prot. Ecol.* **2019**, *20*, 2059–2067.
21. Bondar, C. On a mathematical model of simulating the hydraulic process of bars' formation at the Danube River mouths. *Sci. Ann. "Danube Delta" Instit.* **2018**, *23*, 3–12. Available online: https://www.ddniscientificannals.ro/images//23_01.pdf (accessed on 12 August 2024).
22. Constantinescu, A.C.; Pindic, P.; Bănescu, A.; Anore, C. Flooding Hazard and Risk Maps for Localities along Sulina and Sf. Gheorghe branches. *Sci. Ann. Danube Delta Instit.* **2019**, *24*, 233–242.
23. Stănică, A.; Dan, S.; Ungureanu, V.G. Coastal changes at the Sulina mouth of the Danube River as a result of human activities. *Mar. Pollut. Bull.* **2007**, *55*, 555–663. [CrossRef] [PubMed]
24. Dumitrache, L.; Popov, P. The Port of Sulina. Eastern European Seagate—Past and Present. Available online: https://tulcealibrary.ro/wp-content/uploads/2020/09/The-Port-of-Sulina-Past-and-Present-Dumitrache-L.-Popov-P..pdf (accessed on 8 August 2024).
25. Răileanu, A.B.; Rusu, L.; Marcu, A.; Rusu, E. The Expected Dynamics for the Extreme Wind and Wave Conditions at the Mouths of the Danube River in Connection with the Navigation Hazards. *Inventions* **2024**, *9*, 41. [CrossRef]
26. Ivan, A.S.; Gasparotti, C.; Rusu, E. Influence of the interactions between waves and currents on the navigation at the entrance of the Danube Delta. *J. Environ. Prot. Ecol.* **2012**, *13*, 1673–1682.
27. Bărbulescu, A.; Dumitriu, C.S.; Dragomir, F. Detecting Aberrant Values and Their Influence on the Time Series Forecast. In Proceedings of the 2021 International Conference on Electrical, Computer, Communications and Mechatronics Engineering (ICECCME), Mauritius, Mauritius, 7–8 October 2021. [CrossRef]
28. Bărbulescu, A.; Dumitriu, C.S.; Maftei, C. On the Probable Maximum Precipitation Method. *Rom. J. Phys.* **2022**, *67*, 801.
29. Bărbulescu, A.; Maftei, C.E. Evaluating the Probable Maximum Precipitation. Case study from the Dobrogea region, Romania. *Rom. Rep. Phys.* **2023**, *75*, 704. [CrossRef]
30. Chirosca, G.; Mihailov, M.E.; Tomescu-Chivu, M.I.; Chirosca, A.V. Enhanced Machine Learning Model For Meteo-Oceanographic Time-Series Prediction. *Rom. J. Phys.* **2022**, *67*, 815.
31. Lungu, M. *Climatic Risk Phenomena in Dobrogea*; Editura Universitara: Bucharest, Romania, 2010. (In Romanian)
32. Lungu, M. *Dobrogea Climate Resources*; Editura Universitara: Bucharest, Romania, 2010. (In Romanian)
33. Nitu, O.A.; Ivan, E.S.; Nitu, D.S. Climate change and its impact on water consumption in the main agricultural crops of the Romanian Plain and Dobrogea. *Sci. Papers. Ser. A Agron.* **2023**, *66*, 474–478.
34. Komen, G.J.; Cavaleri, L.; Donelan, M.; Hasselmann, K.; Hasselmann, S.; Janssen, P.A.E.M. *Dynamics and Modelling of Ocean Waves*; Cambridge University Press: Cambridge, UK, 1994.
35. Young, I.R. *Wind Generated Ocean Waves*; Elsevier: Amsterdam, The Netherlands, 1999; Volume 2.
36. Coastal Engineering Manual Part VI: Design of Coastal Project Elements, US Army Corps of Engineers. 2002. Available online: https://www.publications.usace.army.mil/Portals/76/Publications/EngineerManuals/EM_1110-2-1100_Part-06.pdf (accessed on 10 July 2024).
37. Shore Protection Manual, Part II, USACE, US Army Corps of Engineers. 1984. Available online: https://www.academia.edu/37917948/SHORE_PROTECTION_MANUAL (accessed on 10 July 2024).

38. EurOtop. Manual on Wave Overtopping of Sea Defence and Related Structures. Available online: http://www.overtopping-manual.com/ (accessed on 10 July 2024).
39. Fredsoe, J. Turbulent Boundary Layer in Wave-current Motion. *J. Hydraul. Eng.* **1984**, *100*, 1103. [CrossRef]
40. Engelund, F.; Fredsoe, J. A sediment Transport Model for Straight Alluvial Channels. *Nord. Hydrol.* **1976**, *7*, 293–306. [CrossRef]
41. Fredsoe, J.; Anderse, O.A.; Silberg, S. Distribution of Suspended Sediment in Large Waves. *J. Waterw. Port C Div.* **1985**, *111*, 1041. [CrossRef]
42. Mehta, A.J.; Hayter, E.J.; Parker, W.R.; Krone, R.B.; Teeter, A.M. Cohesive Sediment Transport. I: Process Description. *J. Hydraul. Eng.* **1989**, *115*, 1076. [CrossRef]
43. Manning, R. On the flow of water in open channels and pipes. *chez Trans. Inst. Civ. Eng. Irel.* **1891**, *20*, 161–207.
44. Manning's n (Roughness Coefficient) for HEC-RAS 2D Modeling. 2021. Available online: https://rashms.com/blog/mannings-n-roughness-coefficient-for-hec-ras-2d-modeling/ (accessed on 25 July 2024).
45. Engelund, F.; Hansen, E. *A Monograph on Sediment Transport in Alluvial Stream*; Teknisk Forlag: Copenhagen, Denmark, 1967.

water

MDPI

Article

The Necessity of Updating IDF Curves for the Sharjah Emirate, UAE: A Comparative Analysis of 2020 IDF Values in Light of Recent Urban Flooding (April 2024)

Khalid B. Almheiri [1,*], Rabee Rustum [1], Grant Wright [2] and Adebayo J. Adeloye [2]

[1] Dubai Campus, Heriot-Watt University, Dubai Knowledge Park, Dubai P.O. Box 38103, United Arab Emirates; r.rustum@hw.ac.uk
[2] School of Energy, Geoscience, Infrastructure and Society (EGIS), Heriot-Watt University, Edinburgh EH14 4AS, UK; g.b.wright@hw.ac.uk (G.W.); a.j.adeloye@hw.ac.uk (A.J.A.)
* Correspondence: kba3@hw.ac.uk

Abstract: In the arid Arabian Peninsula, particularly within the United Arab Emirates (UAE), the perception of rainfall has shifted from a natural blessing to a significant challenge for infrastructure and community resilience. The unprecedented storm on 17 April 2024, exposed critical vulnerabilities in the UAE's urban infrastructure and flood management practices, revealing substantial gaps in handling accumulated precipitation. This study addresses the necessity of updating the Intensity–Duration–Frequency (IDF) curves for the Sharjah Emirate by utilizing recent precipitation data from 2021 to April 2024, alongside previously published 2020 data. By recalibrating the IDF curves based on data from three meteorological stations, this study reveals a substantial increase in rainfall intensities across all durations and return periods. Rainfall intensities increased by an average of 36.76% in Sharjah, 26.52% in Al Dhaid, and 17.55% in Mleiha. These increases indicate a trend towards more severe and frequent rainfall events, emphasizing the urgent need to revise hydrological models and infrastructure designs to enhance flood resilience. This study contributes valuable insights for policymakers, urban planners, and disaster management authorities in the UAE and similar regions worldwide.

Keywords: intensity–duration–frequency (IDF) curves; update; urban floods; rainfall; Sharjah City; the UAE

1. Introduction

In the arid region of the Arabian Peninsula, particularly within the UAE, the long-anticipated arrival of rain has shifted from being a natural blessing to becoming a formidable and hazardous event. What was once a welcomed event has become intertwined with urban floods, steadily intensifying in both amount and depth, thereby posing a growing threat to the community and the surrounding environments. The rainfall occurrences on 17 April 2024, in the UAE highlighted significant vulnerabilities in the nation's infrastructure and community readiness. According to the Emirates News Agency, WAM, this event exceeded any previously recorded rainfall since data collection began in 1949 [1]. Substantial shortcomings were revealed in the drainage systems' capacity to manage storm runoff effectively. Extensive urban regions experienced unprecedented flooding, surpassing previous records and lasting expectations. Instances of complete ground-floor submersion of residential properties were observed across various regions of the country, as depicted in Figure 1a,b. Major and local road blockages remained for several days, as evidenced in Figure 2a,b. Vehicles submerged entirely were a ubiquitous sight, illustrated in Figure 3a,b. Moreover, without exception, all wadis reverted to their original courses, some of which had not been seen for decades. Notably, a significant wadi, originating from the eastern mountains between the UAE and Oman and terminating at the Gulf in Umm Al Quwain

city in the north, caused substantial damage to roads and water tunnels inadequately equipped to manage its actual capacity and variability, as illustrated in Figure 4a,b.

(**a**) (**b**)

Figure 1. (**a**,**b**) The submersion of ground floors in residential properties.

(**a**) (**b**)

Figure 2. (**a**,**b**) The submergence of major roads due to rainwater.

(**a**) (**b**)

Figure 3. (**a**,**b**) Vehicles partially and fully submerged.

Consequently, nationwide schools became inaccessible, prompting a transition to online education for over four days across all cities, with an extension to six days for schools in flood-affected areas. Similarly, government departments implemented a shift to online work arrangements for all employees nationwide, spanning four days from the onset of the rainstorm. Regrettably, official reports have confirmed the loss of a life resulting from a sink accident in Wadi Isfni, located within the southern regions of Ras

Al Khaimah [2]. This was a time of significant impact, as detailed in this paper. The briefly documented findings above can serve as valuable references for future research and exploration, addressing the tangible and complex contexts of this topic.

(**a**) (**b**)

Figure 4. (**a**,**b**) Two roads impacted by the destructive wadi.

Considering the vast and unprecedented impacts of the April 2024 urban floods on the UAE and the surrounding region compels us, as researchers and specialists in this field, to take a stance on the distressing circumstances that revealed vulnerabilities in the mechanical operations of drainage infrastructure and underscored the significance of the findings and recommendations derived from valuable research conducted over the past decade. A previous study by Almheiri et al. (2021) analyzed the influence of cloud-seeding operations on IDF curve values and proposed two significant recommendations to mitigate potential urban flood impacts in the region [3]. These recommendations encompassed a re-evaluation of the comprehensive functionality of urban stormwater drainage systems as essential components of city development and the regular updating of IDF data to accommodate evolving climatic conditions. Furthermore, the study emphasized the importance of assessing the broader ramifications of these changes, particularly on the efficacy and functionality of storm drainage networks within the urban environment.

In the UAE, the precision and reliability of hydrological assessments are critically constrained by the limited historical meteorological data, especially concerning IDF curves [3]. These curves are crucial for analyzing how rainfall intensity varies with its duration and frequency, providing essential data for accurately predicting extreme weather events and designing systems that can effectively manage and mitigate flood risks. The scarcity of comprehensive, long-term rainfall data has hindered the accurate formulation of these assessments. This limitation has become particularly evident through the recurrent failures of hydrological infrastructure to adequately manage and respond to rainfall events over the past decade [4]. This underscores the urgent need for updated and more accurate IDF curves to enhance infrastructure resilience and improve flood management practices in the face of changing weather patterns.

The situation is further complicated by the impacts of climate change, which introduce significant variability in rainfall intensity, frequency, and overall weather patterns. The increasing unpredictability of climatic conditions necessitates regular updates to IDF curves to ensure they reflect these evolving climatic shifts accurately [5]. Existing IDF curves are increasingly inadequate as shifts in hydro-climate variables, such as rainfall and temperature, no longer align with current conditions or account for recent trends in urban development [6]. As climate patterns become more erratic and extreme weather events become more frequent, the necessity for revising these curves is more pressing than ever.

Furthermore, urban expansion profoundly affects hydrological dynamics, necessitating updates to IDF curves to accurately represent changes in land use [7]. As cities grow and land use patterns shift, the hydrological response of regions evolves, requiring precise adjustments to IDF curves. Incorporating the latest meteorological data into these curves is

crucial for advancing flood risk management, supporting strategic urban planning, and enhancing preparedness for extreme weather events. Accurate IDF curves are essential for effectively addressing the rapidly changing environmental conditions in the UAE. By ensuring that infrastructure and flood management strategies are based on the most up-to-date information, cities can develop resilient and cutting-edge systems capable of confronting the challenges posed by both climate change and accelerated urbanization.

This study is set to advance the understanding of evolving weather patterns and their implications for urban floods and aims to update the IDF curve values for the Sharjah Emirate, utilizing the latest precipitation data from 2021 to April 2024. By integrating these recent datasets with existing historical records that span from 1992 to 2020, the IDF curves will be recalibrated and compared with previous values across three distinct meteorological stations. This comprehensive approach enables the refinement of flood risk assessments and enhances infrastructure planning, ensuring that current and future urban development is supported by the most accurate and up-to-date hydrological data.

2. Methodology

2.1. Description of the Study Area

Sharjah, situated within the UAE, is recognized as the third-largest emirate in the country, encompassing a total land area of 2600 square kilometers. Geographically, it is positioned approximately between 25.2° N to 25.4° N and 55.4° E to 55.6° E. Sharjah serves as a pivotal urban hub, bordered by Ajman and Al Um Al Quwain to the north, Fujairah and Ras Al Khaimah to the east and southeast, Dubai to the south, and the Arabian Gulf to the west (refer to Figure 5). The emirate comprises three distinct regions: Sharjah City in the west, the central region, and the mountainous eastern region. This paper will focus on Sharjah City and the central region, following the approach of the 2021 baseline study [3].

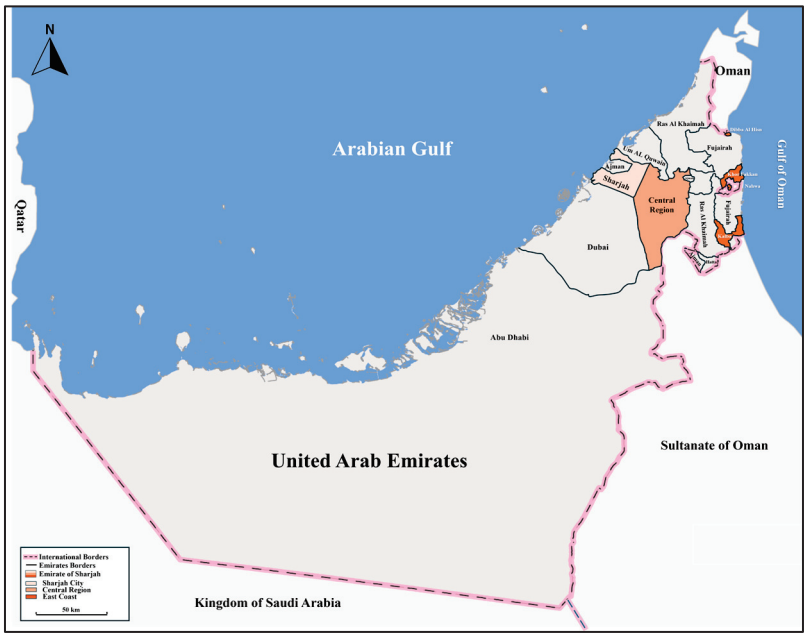

Figure 5. Map of the UAE showing the location of the Sharjah Emirate and its three regions [8].

2.2. Data Collection

The previous study [3] utilized rainfall data from three meteorological stations within the Sharjah Emirate, as detailed in Table 1 [9–13].

Table 1. Meteorological station coordinates and rainfall observation dates.

Station Name	Altitude (M amsl)	Coordinates		Original Records Duration	Extended Records Duration "Previous Paper"	Newly Added Records Duration
		Longitude	Latitude			
Sharjah Airport	34	55° 31 02 E	25° 19 43 N	16 September 2014–31 May 2020	1 January 1992–31 May 2020	1 June 2020–17 April 2024
Al Dhaid	111	55° 49 01 E	25° 14 13 N	1 March 2010–31 May 2020		
Mleiha	186	55° 53 17 E	25° 07 50 N	1 January 2003–31 May 2020		

These stations, located in Sharjah City, Al Dhaid, and Mleiha, as shown in Figure 6, were strategically chosen to capture diverse geographical perspectives, ensuring unbiased results concerning IDF curve values and comprehensively depicting trends. As indicated in Table 1, the initially acquired hourly records for each station were limited to the years 2014 in Sharjah, 2010 in Al Dhaid, and 2003 in Mleiha. However, data from the nearby Dubai Airport spanning from 1992 were employed to address gaps in the dataset. The multivariate self-organizing map (SOM) artificial neural network was employed to interpolate missing data for the Sharjah stations. Detailed information on the application of a self-organizing map for data infilling can be found in references [9–13]. As of 17 April 2024, these records have been updated to facilitate comparative analysis following recent flooding events in the UAE.

Figure 6. Map of the Sharjah Emirate showing the locations of the meteorological stations used in this study [8].

This study employs a rigorous methodology to update the IDF curve values for three meteorological stations in Sharjah, utilizing the latest rainfall data from the past three years and four months alongside historical records. The updated IDF values will be compared to the 2020 values for each station independently. This methodology aims to achieve three primary objectives: first, to build upon the approach established in the previous study; second, to minimize bias by analyzing data from three distinct meteorological stations situated in different geographical locations; and third, to assess changes in IDF curve values, whether increases or decreases.

The Gumbel Distribution is employed to characterize extreme rainfall events at these stations. Additionally, statistical analyses are conducted using historical rainfall data to determine the 24 h annual maximum and mean annual rainfall figures. These results are fundamental for generating updated IDF curves and enabling a comparative statistical assessment against previous data. The findings will be disseminated for the benefit of researchers and other stakeholders.

The entire process is implemented using the HyFran-Plus Version 2.1 frequency analysis software tool [14]. This comprehensive approach underscores the necessity of regularly updating IDF curves to effectively address the evolving hydrological conditions and support robust flood risk management and infrastructure planning at both local and regional levels.

2.3. Frequency Analysis

To analyze the frequency of extreme rainfall events, we use the Weibull formula (1) to calculate the probability P of exceeding each ranked annual maximum rainfall:

$$\mathrm{P} = \frac{Rank - a + b}{(n+1) - 2a + b}\,, \tag{1}$$

where a and b are set to zero, and n is the number of years. The return period T, the average interval in years between storms of a given magnitude, is then determined by Equation (2):

$$\mathrm{T} = \frac{1}{P}\,, \tag{2}$$

Using historical rainfall data, we rank maximum daily rainfall depths and calculate the probability of exceedance and corresponding return periods. The HyFran-Plus Version 2.1 software [14] is employed for this frequency analysis, using Weibull and Gumbel distributions to fit the data, specifically focusing on a 100-year return period for the estimations in this study.

The maximum daily rainfall depth for any given return period was calculated based on the best-fitting distribution. Following the World Meteorological Organization (WMO) 2009 guidelines [15], daily rainfall amounts are adjusted by a factor of 1.13 to correct for observational biases.

For different return periods, the rainfall intensities over various durations (e.g., 10 min, 20 min, 30 min, 60 min, 120 min) were computed using depth–duration ratios derived from Frederick and Bell (1969) [16]. The depth–duration ratio is given by Equation (3):

$$\frac{PT^t}{PT^{60}} = 0.54t^{0.25} - 0.50 \;\; if \;\; 5 \le t \le 120\,, \tag{3}$$

where PT^t is the rainfall depth at duration t, and PT^{60} is the maximum 60 min rainfall depth.

Finally, the IDF curves were developed by plotting the computed IDF values, providing critical insights into the intensity and frequency of rainfall events. These steps are instrumental in evaluating historical rainfall data and predicting future trends, ensuring robust planning and management of water resources [3].

2.4. Statistical Analysis of IDF Curve Fitting

Updating IDF curve values requires a thorough statistical analysis to ensure precision and reliability. This process involves fitting rainfall data to appropriate probability distributions to derive accurate IDF curves for the Sharjah Emirate.

The Gumbel Distribution is employed to model extreme rainfall events due to its proven effectiveness in capturing such extremes. The IDF curves are generated by analyzing annual maximum rainfall data from three meteorological stations across the Sharjah Emirate, as detailed in Section 2.2. The data used include rainfall records from January 1992 to April 2024. The analysis is conducted using the HyFran-Plus Version 2.1 frequency

analysis software [14], which facilitates the statistical fitting of data to both Weibull and Gumbel distributions.

The process begins with ranking the annual maximum daily rainfall depths to compute the probability of exceedance. This probability is crucial for determining the return period, which represents the average time interval between rainfall events of a given magnitude. The analysis then calculates the return period and associated rainfall intensities for various durations, ranging from 10 to 120 min. These data are essential for updating the IDF curves, which illustrate variations in rainfall intensity across different durations and return periods.

To ensure the robustness of the IDF curves, depth–duration ratios are calculated. These ratios account for variations in rainfall duration and ensure that the IDF curves accurately reflect realistic rainfall patterns. The ratios are derived from established guidelines and used to refine the IDF values.

A significant advancement in this study is the use of the multivariate self-organizing map (SOM) neural network, which was employed in our previous paper, as referenced in Section 2.2. This approach has provided an extended and reliable set of historical rainfall records for Sharjah City, synthesizing an additional 21 years of hourly rainfall data for the three meteorological stations. This improvement enhances the efficacy and reliability of future design studies in the study area, as discussed by Almheiri et al. (2021) [3]. By effectively addressing the issue of incomplete and missing data in historical meteorological records, the SOM neural network offers effective solutions for infilling these records, significantly improving the comprehensiveness of the dataset.

Overall, the rigorous statistical fitting and analysis ensure that the updated IDF curves for the Sharjah Emirate are based on the most recent and comprehensive rainfall data, accurately reflecting current hydrological conditions. This approach provides valuable insights into rainfall frequency and intensity, supporting effective flood risk management and infrastructure planning.

3. Results and Discussion

The IDF curves are essential for understanding rainfall characteristics and estimating frequency and intensity. Recent high rainfall in the Sharjah Emirate has raised concerns about the adequacy of existing IDF values to reflect changing precipitation patterns. Updated IDF curves for the Sharjah Airport, Al Dhaid, and Mleiha stations were compared with 2021 values. The revised figures show a significant rise, likely due to long-term climate oscillations rather than cloud seeding. This finding aligns with Modabbermm-Azizi et al. [17], who observed similar variability in Iran. Recent rainfall records in the UAE have surpassed all previous levels since data collection began in 1949.

The comprehensive rainfall dataset spanning from 1992 to 2020, which was collected and analyzed previously [3], is summarized in Table 2. Table 3 documents the corresponding records up to 30 April 2024, providing an up-to-date depiction of rainfall patterns. These updated records have not only contributed to establishing a robust climatological database but have also served as inputs for calculating the updated IDF curve values for the Sharjah Emirate, as discussed in Section 3.1.

Significantly, the NEW IDF values, updated with additional rainfall data from January 2021 to April 2024, have exceeded all previous OLD IDF values, which are based on rainfall records from January 1992 to 2020, as compared in Table 4. These findings underscore the significance of recording and updating meteorological data, particularly in a country like the UAE, where past records are relatively limited and a comprehensive understanding of rainfall intensity fluctuations is still developing.

Table 2. Maximum daily rainfall depths (mm) across three stations (1992–2020).

Year	Sharjah	Al Dhaid	Mleiha
1992	11.4	8.3	5.1
1993	2.4	0	0
1994	2.4	15	61.3
1995	32.8	53.5	156.7
1996	16	26.6	121.1
1997	13	24.6	92.4
1998	14.3	24.3	43.5
1999	4.8	30.1	88.6
2000	10.1	26.8	71.7
2001	2.4	15.7	47.8
2002	5.9	14.2	44.3
2003	10.1	11	23.8
2004	7.6	5.8	9.8
2005	17.4	6.1	12.2
2006	7.4	37.3	18.2
2007	0.4	2.6	24
2008	61	41	50.4
2009	26.9	11.7	18.6
2010	24.3	36.8	22.2
2011	11.7	17	17.8
2012	5.5	30.2	62.6
2013	10.3	26.6	29.6
2014	6.5	14	34.8
2015	37.4	5.5	13.6
2016	13.5	140.8	461
2017	10.9	17.2	146.8
2018	78.2	7.2	25
2019	39.8	10.6	28.8
2020	53.9	41.2	64.3
Mean	18.6	24.2	61.9

Table 3. Maximum daily rainfall depths (mm) across three stations (2020–30 April 2024).

Year	Sharjah	Al Dhaid	Mleiha
2021	13.2	12.7	17.7
2022	32.2	33.3	39.8
2023	44	62	55
2024	123.8	153.2	163.4
Mean	53.3	65.3	69.0

Table 4. Comparison of NEW [1] 2024 IDF curve values with OLD [2] 2020 data.

Return Period	City		IDF Curve Values over Different Durations (mm/h)				
			10 min	20 min	30 min	60 min	120 min
2	Sharjah	OLD	25.09	17.50	13.88	9.11	5.85
		NEW	34.96	24.38	19.34	12.70	8.15
	Al Dhaid	OLD	31.92	22.26	17.66	11.59	7.44
		NEW	44.24	30.85	24.47	16.07	10.31
	Mleiha	OLD	73.10	50.98	40.44	26.55	17.04
		NEW	92.66	64.62	51.25	33.65	21.60

Table 4. *Cont.*

Return Period	City		IDF Curve Values over Different Durations (mm/h)				
			10 min	**20 min**	**30 min**	**60 min**	**120 min**
3	Sharjah	OLD	39.32	27.42	21.75	14.28	9.16
		NEW	55.46	38.68	30.68	20.14	12.93
	Al Dhaid	OLD	51.19	35.70	28.32	18.59	11.93
		NEW	70.69	49.30	39.10	25.67	16.48
	Mleiha	OLD	127.13	88.65	70.32	46.17	29.63
		NEW	158.69	110.66	87.78	57.63	36.98
5	Sharjah	OLD	55.42	38.65	30.66	20.13	12.92
		NEW	78.30	54.60	43.31	28.43	18.25
	Al Dhaid	OLD	73.48	51.24	40.65	26.68	17.13
		NEW	100.15	69.84	55.40	36.37	23.34
	Mleiha	OLD	190.78	133.05	105.53	69.28	44.46
		NEW	232.23	161.95	128.46	84.34	54.12
10	Sharjah	OLD	77.70	54.19	42.98	28.22	18.11
		NEW	106.99	74.61	59.18	38.85	24.94
	Al Dhaid	OLD	104.84	73.11	57.99	38.07	24.43
		NEW	113.17	78.92	62.60	41.10	26.38
	Mleiha	OLD	285.23	198.91	157.77	103.58	66.48
		NEW	324.64	226.39	179.57	117.89	75.66
20	Sharjah	OLD	99.80	69.60	55.20	36.24	23.26
		NEW	134.51	93.81	74.40	48.85	31.35
	Al Dhaid	OLD	136.19	94.98	75.33	49.46	31.74
		NEW	172.68	120.42	95.52	62.71	40.25
	Mleiha	OLD	379.68	264.78	210.02	137.88	88.49
		NEW	413.28	288.21	228.60	150.08	96.32
50	Sharjah	OLD	128.82	89.84	71.26	46.78	30.02
		NEW	170.14	118.65	94.11	61.79	39.65
	Al Dhaid	OLD	177.56	123.83	98.22	64.48	41.38
		NEW	218.64	152.47	95.52	79.40	50.96
	Mleiha	OLD	508.13	354.35	281.07	184.53	118.43
		NEW	528.01	368.22	292.07	191.75	123.06
100	Sharjah	OLD	150.73	105.11	83.37	54.74	35.13
		NEW	196.83	137.27	108.88	71.48	45.87
	Al Dhaid	OLD	209.67	146.22	115.98	76.14	48.87
		NEW	253.08	176.49	139.99	91.91	58.98
	Mleiha	OLD	606.35	422.85	335.40	220.20	141.32
		NEW	613.99	428.18	339.62	222.97	143.10

Note(s): [1] NEW: IDF values updated with additional rainfall data from January 2021 to April 2024. [2] OLD: IDF values from 2020, based on January 1992 to 2020 rainfall records.

3.1. Analysis of Updated IDF Curve Values in Sharjah City, Al Dhaid, and Mleiha

Table 4 provides a detailed overview of IDF curve values for various durations (10, 20, 30, 60, and 120 min) and return periods (2, 3, 5, 10, 20, 50, and 100 years) for three distinct locations: Sharjah City, Al Dhaid, and Mleiha. The data are divided into two categories: OLD and NEW, as mentioned in Section 3 above. This division enables a comparative analysis to evaluate the impact of recent high rainfall records on IDF curves and to provide insights into potential changes in precipitation patterns due to extreme weather. It is important to note that each station is studied independently and compared within the old and new datasets rather than comparing values across different stations. The following

subsections will illustrate the statistical comparison of OLD and NEW IDF curve values for each station under study.

3.1.1. Sharjah City

A comparison of IDF curve values between OLD and NEW records for Sharjah City reveals a significant increase in rainfall intensities across all durations and return periods. This trend is particularly pronounced for shorter durations (10 and 20 min) and lower return periods (2 and 3 years). For example, for a 2-year return period, the 10 min duration increased from 25.09 mm/h to 34.96 mm/h, representing a 39.3% rise, while the 60 min duration increased from 9.11 mm/h to 12.70 mm/h, showing a 39.4% rise. These changes are illustrated in Figure 7a.

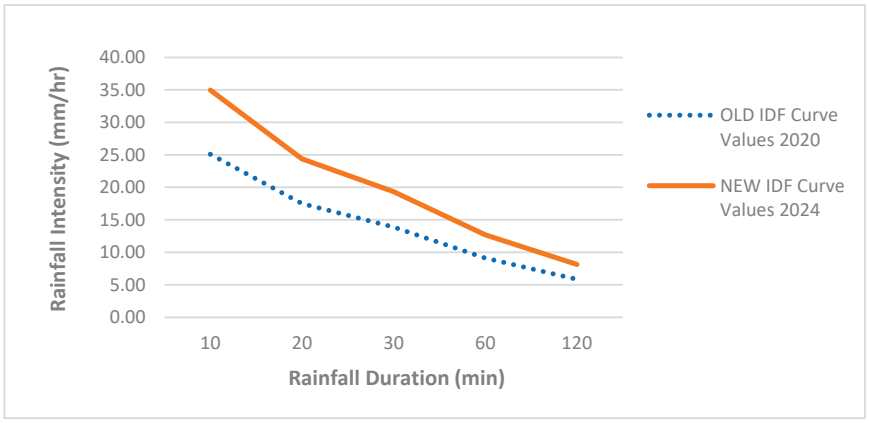

(**a**)

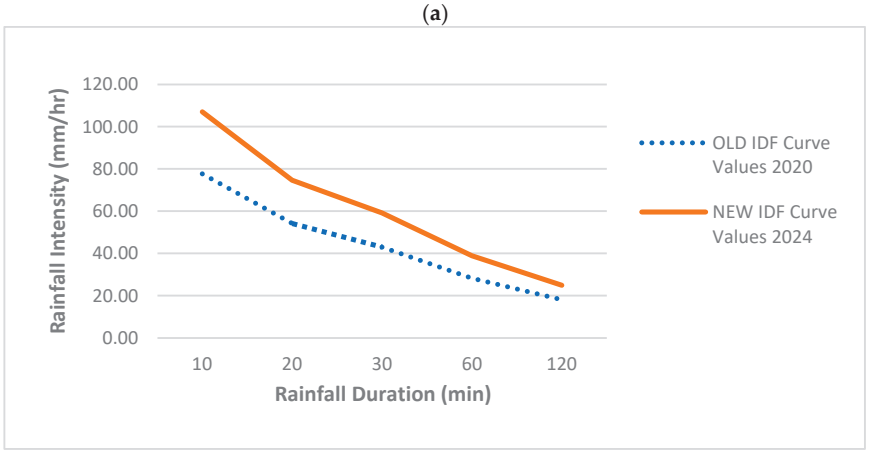

(**b**)

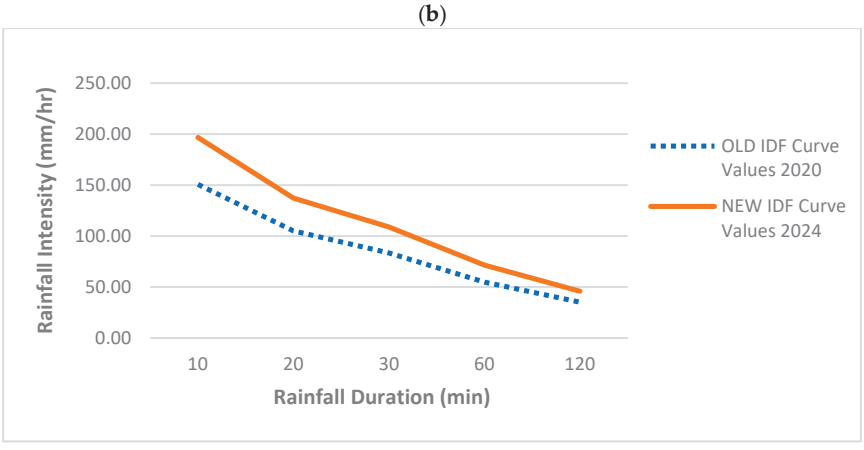

(**c**)

Figure 7. *Cont.*

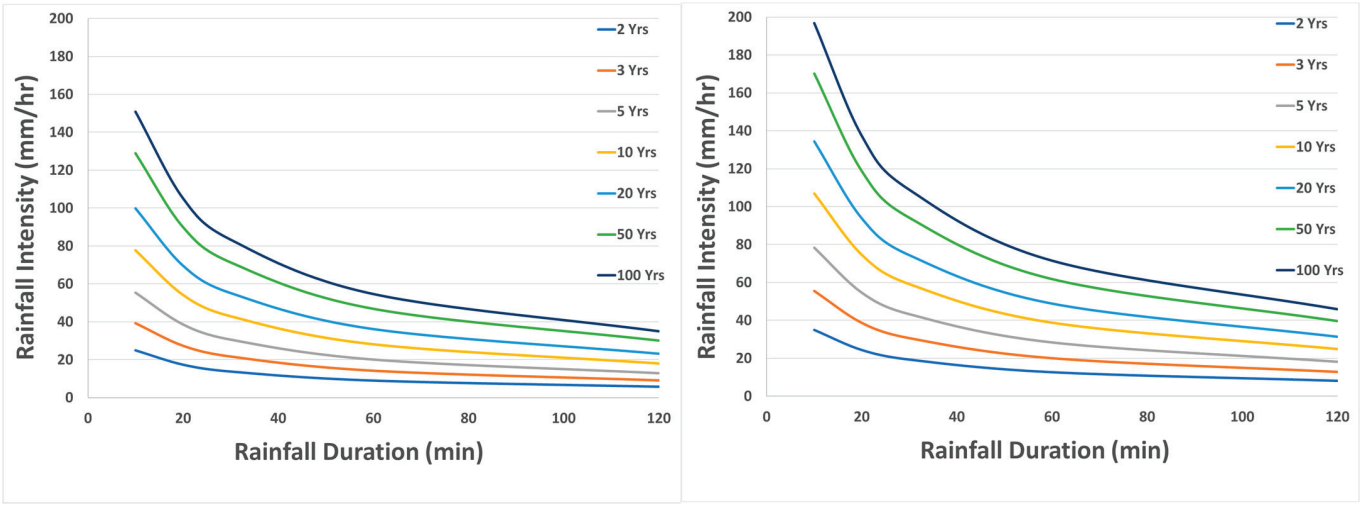

(**d**) (**e**)

Figure 7. (**a**) The increase in IDF curve values for a 2-year return period in Sharjah City. (**b**) The increase in IDF curve values for a 10-year return period in Sharjah City. (**c**) The increase in IDF curve values for a 100-year return period in Sharjah City. (**d**,**e**) OLD and NEW IDF curve values for Sharjah City, respectively.

Figure 7a presents the increase in IDF curve values for a 2-year return period in Sharjah City. A clear upward shift in the intensity–duration curve is observed, indicating a notable increase in rainfall intensity. This suggests that Sharjah City is experiencing more intense rainfall events even for shorter durations, and this trend needs to be considered in urban planning and flood management.

Figure 7b demonstrates the increase in IDF curve values for a 10-year return period. Similar to Figure 7a, a clear upward shift in the curve is seen, indicating an increase in rainfall intensity. For example, the 30 min duration for a 10-year return period increased from 42.98 mm/h to 59.18 mm/h, reflecting a 37.7% rise. This suggests that the trend of increased rainfall intensity is not limited to shorter return periods but also applies to longer return periods.

Figure 7c shows the increase in IDF curve values for a 100-year return period. Again, a consistent upward shift in the curve is noted, suggesting a continued trend of increasing rainfall intensity even for the longest return period considered. For the 30 min duration, the intensity rose from 83.37 mm/h to 108.88 mm/h, representing a 30.6% increase.

These trends suggest that Sharjah City is experiencing increasingly intense rainfall events, highlighting evolving climate patterns in the region. An overall comparison of the OLD and NEW IDF curve values reveals significant increases in rainfall intensities across various return periods, indicating a shift towards more severe rainfall. This shift is depicted in Figure 7d for the OLD values and Figure 7e for the NEW values.

Figure 7e displays the updated IDF curves, highlighting a consistent and notable increase in rainfall intensities across various return periods and durations. This pattern clearly indicates a rising frequency and intensity of rainfall events over time, underscoring a growing vulnerability of Sharjah City's infrastructure and systems to more severe rainfall. The observed changes emphasize the urgent need for enhanced adaptation and resilience strategies to effectively mitigate the potential impacts of these more intense events. A thorough understanding of these trends is essential for effective future planning and risk management.

3.1.2. Al Dhaid

A comparison of IDF curve values between OLD and NEW values for Al Dhaid reveals a significant increase in rainfall intensities across all durations and return periods. Similar to the analysis conducted for Sharjah City, this trend is particularly pronounced for shorter

durations (10 and 20 min) and lower return periods (2 and 3 years). For example, for a 2-year return period, the 10 min duration increased from 31.92 mm/h to 44.24 mm/h, reflecting a 38.6% rise, while the 60 min duration rose from 11.59 mm/h to 16.07 mm/h, a 38.7% increase. These changes are illustrated in Figure 8a.

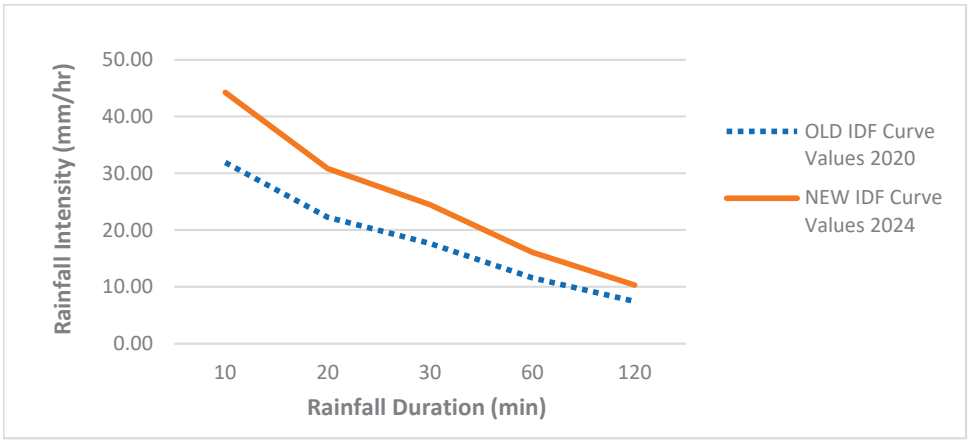

(**a**)

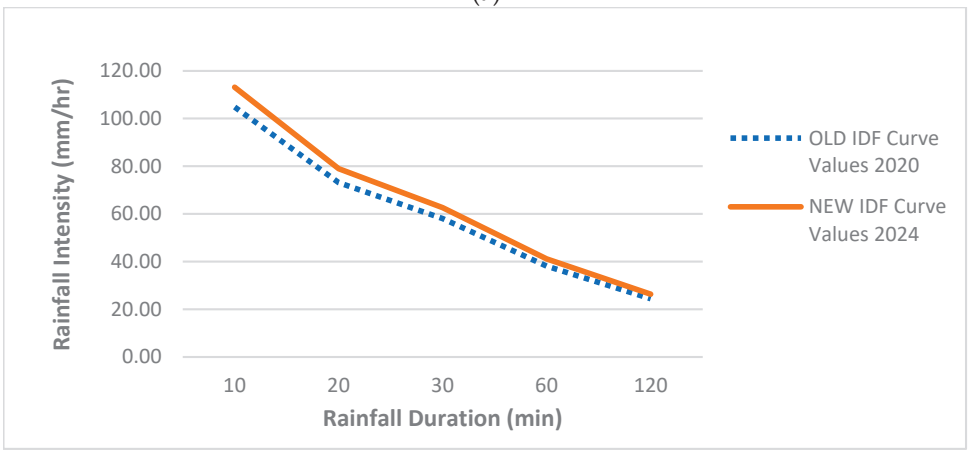

(**b**)

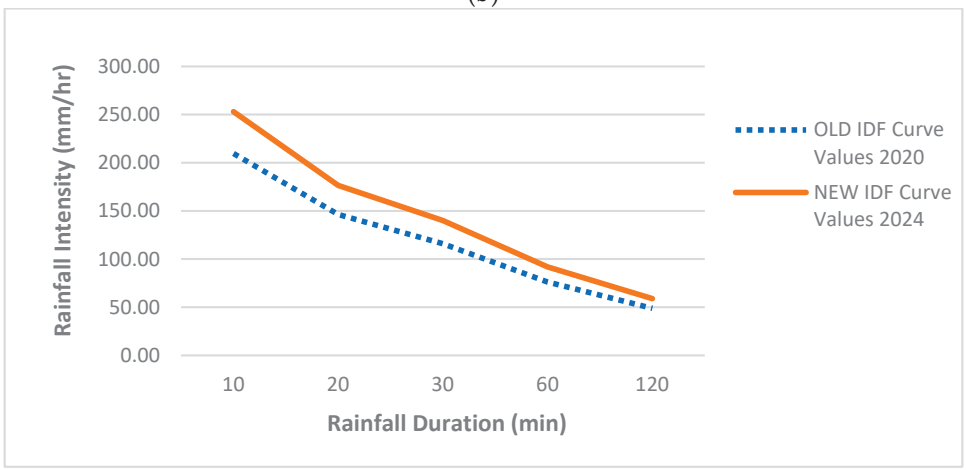

(**c**)

Figure 8. *Cont.*

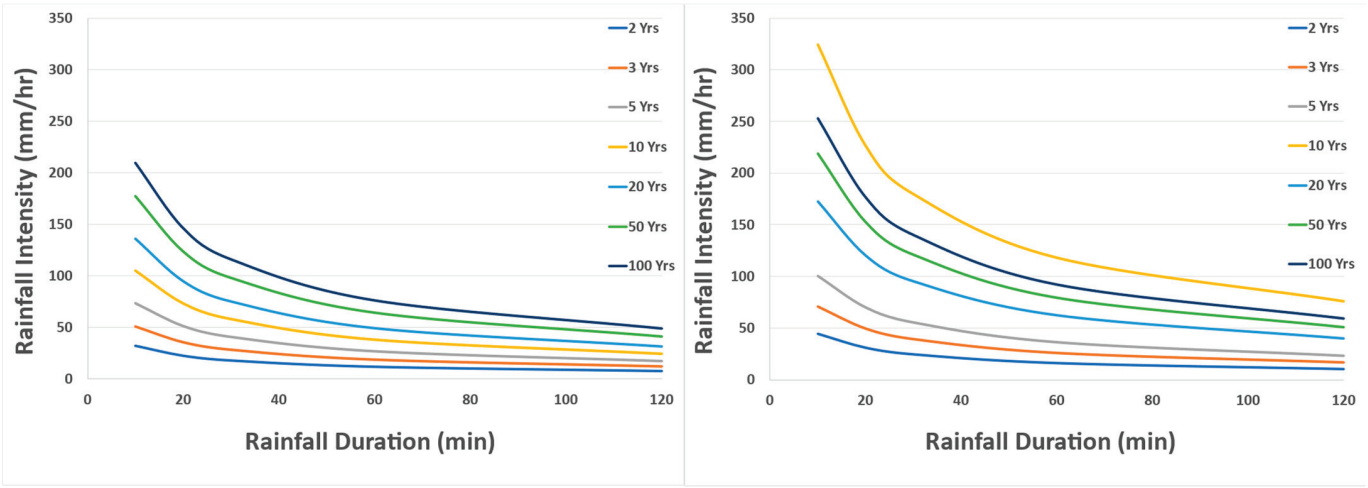

Figure 8. (**a**) The increase in IDF curve values for a 2-year return period in Al Dhaid. (**b**) The increase in IDF curve values for a 10-year return period in Al Dhaid. (**c**) The increase in IDF curve values for a 100-year return period in Al Dhaid. (**d**,**e**) OLD and NEW IDF curve values for Al Dhaid, respectively.

The trend of increased rainfall intensity is not limited to shorter return periods, as evident in Figure 8b,c. These figures illustrate that rainfall intensity has increased for both 10-year and 100-year return periods, demonstrating a consistent upward shift in the IDF curve values. This suggests a sustained trend of increasing rainfall intensity across all return periods. For example, the rainfall intensity for a 10-year return period with a 30 min duration increased from 57.99 mm/h to 62.60 mm/h (a 7.9% rise), as shown in Figure 8b. This increase is even more pronounced for a 100-year return period with a 30 min duration, where the rainfall intensity surged from 115.98 mm/h to 139.99 mm/h (a 20.7% increase), as illustrated in Figure 8c.

Figure 8d,e provide a visual comparison of the OLD and NEW IDF curves for Al Dhaid, clearly illustrating the increase in rainfall intensity across various durations and return periods. This consistent upward trend in the curves underscores the shift towards more intense rainfall events.

Figure 8e specifically presents updated IDF curves for Al Dhaid, confirming the trend of increasing rainfall intensity observed across the study area. These curves reveal a significant increase in rainfall intensity across a range of durations and return periods, particularly for shorter durations and lower return periods. This suggests a potential shift towards more frequent and intense rainfall events.

Comparing these findings to the results observed in Sharjah City, the pattern of increasing rainfall intensity across various durations and return periods appears to be a consistent trend across the entire study area, indicating a possible broader shift in rainfall patterns affecting the region.

3.1.3. Mleiha

A comparison of IDF curve values between OLD and NEW records for Mleiha reveals a significant increase in rainfall intensities across all durations and return periods. However, the percentage increase is relatively lower than in the other two stations, likely due to Mleiha's initially higher rainfall records. Figure 9a presents the increase in IDF curve values for a 2-year return period. A clear upward shift in the intensity–duration curve is observed, indicating a notable increase in rainfall intensity. For example, the 10 min duration increased from 73.10 mm/h to 92.66 mm/h, representing a 26.7% rise, while the 60 min duration increased from 26.55 mm/h to 33.65 mm/h, showing a 26.7% rise. This suggests that Mleiha is experiencing more intense rainfall events even for shorter durations, and this trend needs to be considered in urban planning and flood management.

Figure 9b illustrates the increase in IDF curve values for a 10-year return period. Similar to Figure 9a, a clear upward shift in the curve is observed, indicating a continued increase in rainfall intensity. For instance, the 30 min duration for a 10-year return period increased from 157.77 mm/h to 179.57 mm/h, representing a 13.8% rise. Figure 9c further reinforces this trend, showcasing the increase in IDF curve values for a 100-year return period. Even for this longest return period, the curve displays a consistent upward shift, demonstrating that the trend of increased rainfall intensity is not limited to shorter return periods but extends to longer ones as well. While the increase for the 30 min duration is less pronounced at 1.3% (from 335.40 mm/h to 339.62 mm/h), it reinforces the overall pattern of rising intensity.

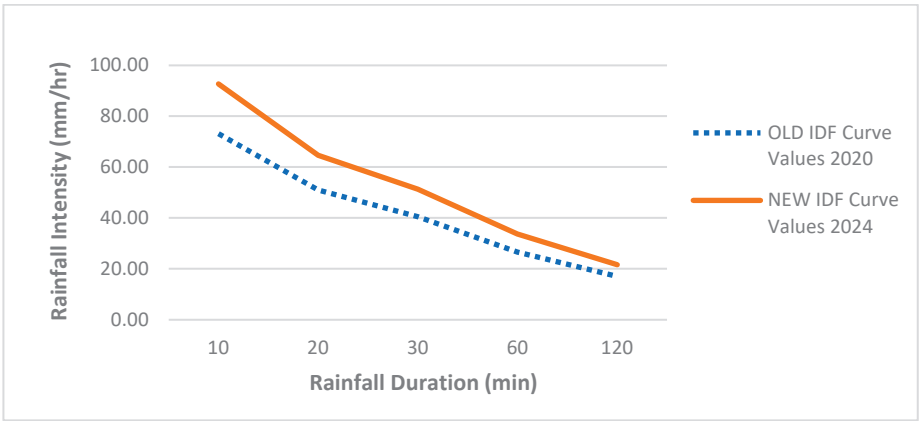

(**a**)

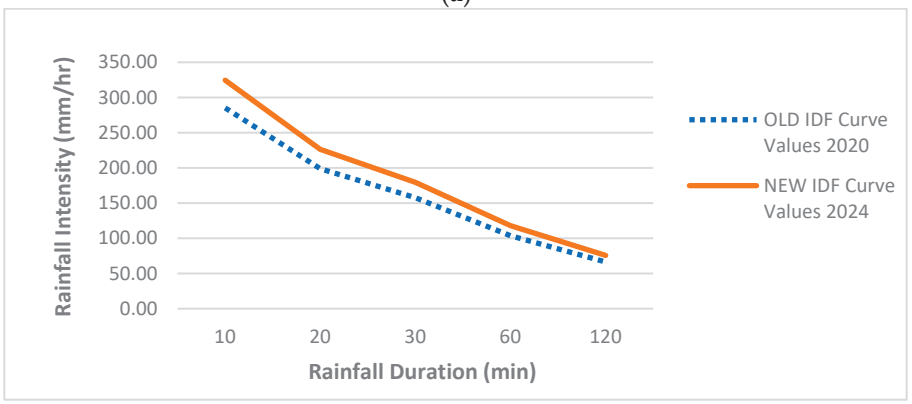

(**b**)

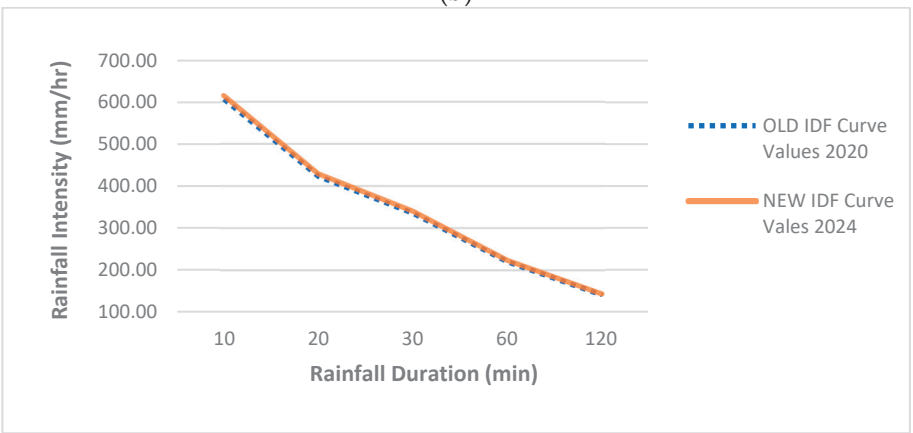

(**c**)

Figure 9. *Cont.*

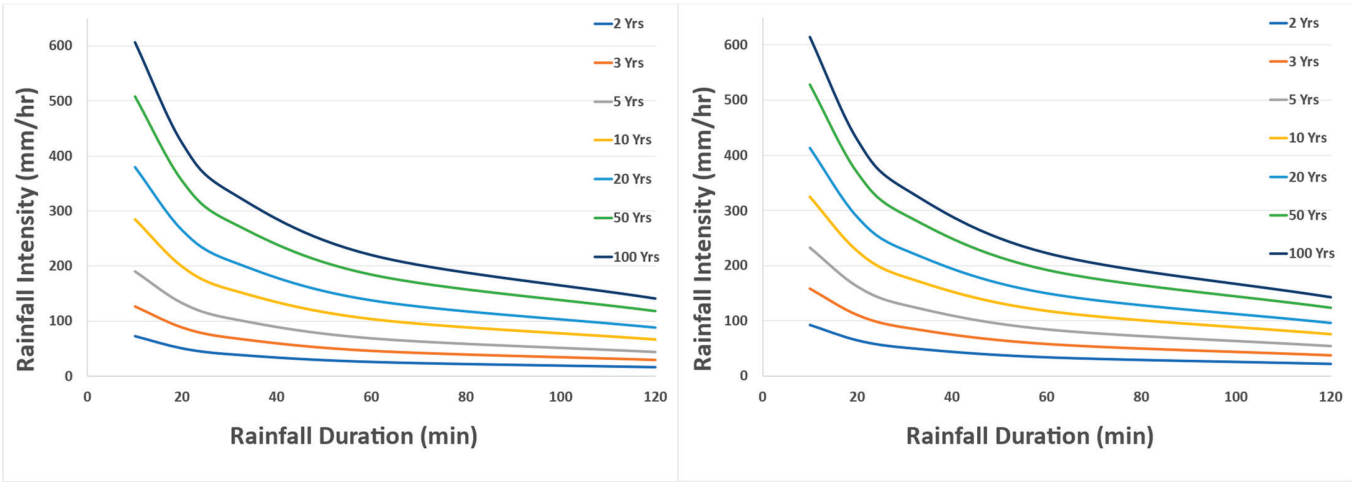

(**d**) (**e**)

Figure 9. (**a**) The increase in IDF curve values for a 2-year return period in Mleiha. (**b**) The increase in IDF curve values for a 10-year return period in Mleiha. (**c**) The increase in IDF curve values for a 100-year return period in Mleiha. (**d**,**e**) OLD and NEW IDF curve values for Mleiha, respectively.

An analysis of IDF curves for Mleiha reveals a clear trend towards more intense rainfall events, evident across all return periods. This upward trend in rainfall intensity is visually illustrated in Figure 9d,e, which compare the OLD and NEW IDF curves for the area. These figures clearly demonstrate the increasing intensity across a range of durations and return periods.

While the trend towards more intense rainfall events in Mleiha is less pronounced than the significant increases observed in Sharjah City and Al Dhaid, an analysis of IDF curves for Mleiha does reveal a clear upward trend in rainfall intensity across all return periods. This trend, though less dramatic than in the other two cities, is nonetheless notable, indicating a shift towards more frequent and intense rainfall events. This is reflected in the updated IDF curves for Mleiha, which show a clear increase in intensity across a range of durations and return periods.

3.2. Comparative Insights on Rainfall Variability in the Region: A Focus on the Sharjah Emirate

Understanding the changing patterns of rainfall is critical for effective water management and infrastructure planning in arid regions. This section delves into the intricacies of rainfall variability in the region by comparing findings from this study, which focuses on the recent intensification of rainfall in the Sharjah Emirate, with two studies examining longer-term rainfall patterns in neighboring Qatar. This comparative analysis reveals both commonalities and distinct perspectives, highlighting the complexities of rainfall variability in this region and the importance of considering both short-term and long-term trends when developing solutions for a changing climate.

The current study analyzed recent rainfall data from 2021 to April 2024, integrated with historical records spanning from 1992 to 2020. This research revealed a notable increase in rainfall intensities, with average increases of 36.76% in Sharjah, 26.52% in Al Dhaid, and 17.55% in Mleiha across various durations and return periods. These findings indicate a concerning trend towards more intense and frequent rainfall events, highlighting the urgent need for updates in hydrological models and infrastructure designs to bolster flood resilience.

In contrast, Mamoon and Rahman [18] examined rainfall patterns in Qatar over a longer timeframe, specifically from 1962 to 2010. Their research identified mixed trends across different monitoring stations. While some areas in the northern and eastern regions showed increasing rainfall, others, particularly in the southern and western regions, ex-

perienced declines or persistent dry conditions. This spatial variability underscores the importance of localized assessments for effective water resource management.

Furthermore, Mamoon and Rahman [19], in a second study, focused on determining the best-fit probability distributions for rainfall frequency analysis, covering the years from 1972 to 2010. They concluded that the Generalized Extreme Value (GEV) distribution was most suitable for the majority of monitoring stations. They emphasized the necessity of utilizing extended datasets to achieve accurate rainfall quantile estimates, especially for higher return periods. This reinforces the critical need for ongoing data collection to enhance the predictability and management of extreme weather events in arid regions.

This Sharjah Emirate study stands out for its focus on the rapid and urgent rise in rainfall intensity over a relatively shorter timeframe. This rapid change, potentially driven by climate change influences, highlights the immediate need for adaptation in infrastructure and hydrological models. However, the studies from Qatar provide a broader perspective, demonstrating both increases and decreases in rainfall across various regions over a longer timescale. This broader temporal variability may mask underlying long-term climate trends when viewed collectively.

While this Sharjah study emphasizes immediate adaptations in local infrastructure to address rapid shifts in weather patterns, the Qatar studies advocate for a nuanced understanding of rainfall variability that considers spatial differences and long-term trends. Taken together, these studies underscore the critical necessity of updating IDF curves regionally to accurately reflect changing precipitation patterns.

Ultimately, this comparative analysis emphasizes the urgency and complexity involved in understanding rainfall variability in arid regions. While the increasing intensity of rainfall in the Sharjah Emirate necessitates prompt action, the insights derived from Qatar's extensive studies provide valuable guidance on considering spatial differences and the importance of robust statistical methods for long-term planning. By incorporating these diverse perspectives, it is possible to develop more effective strategies for water resource management and infrastructure planning in the face of an evolving climate.

3.3. Impact of Climate Change on Rainfall Patterns in the Region

Recent results in Sharjah City, Al Dhaid, and Mleiha (UAE) have identified a concerning trend: an increase in rainfall intensity across various durations and return periods. This trend suggests that more intense and frequent rainfall events are becoming likely, driven by natural climate variability and anthropogenic climate change. The findings emphasize the urgent need for a comprehensive understanding of how climate change is reshaping rainfall patterns in the region.

These trends observed in the UAE are echoed in neighboring countries. In Qatar, studies indicate similar shifts towards unpredictable and intense rainfall, underscoring that these changes are indicative of broader climatic trends across the Arabian Peninsula and highlight shared vulnerabilities to climate impacts [20].

Research in Oman also emphasizes the effects of climate change on rainfall patterns. Studies have shown that rainfall intensities vary significantly across regions, with mountainous areas experiencing higher rainfall than coastal or desert regions. This indicates the importance of considering topographical influences in rainfall assessments [21]. Additionally, in Iran, Modabbermm-Azizi et al. [17] provide further context, illustrating notable variability in precipitation patterns largely driven by long-term climatic oscillations. While cloud seeding has impacted rainfall patterns in the UAE, recent drastic shifts indicate a more significant influence of climate change.

The implications of these findings are substantial for the countries in the region. Increasing rainfall intensity raises the risk of urban flooding, potentially overwhelming drainage systems and jeopardizing infrastructure, transportation networks, and public safety. Additionally, changes in the timing and frequency of rainfall complicate water resource management, increasing the risk of drought during dry spells and threatening agricultural productivity and water supplies.

These challenges necessitate updated IDF curves to reflect evolving climatic realities. Regular updates are essential for accurate flood risk assessments and for designing resilient infrastructure. It is recommended that updates occur at least every five years, supported by systematic rainfall data monitoring and advanced analytical techniques.

By prioritizing the update of IDF curves and understanding localized findings, cities in the region can enhance their resilience to the challenges of climate change. The insights from these studies provide a crucial foundation for strategic adaptation and planning in an era marked by increased climatic variability.

3.4. Implications and Recommendations

The analysis of rainfall data from January 2021 to April 2024, encompassing recent storm events, has revealed a significant increase in IDF curve values across Sharjah City, Al Dhaid, and Mleiha. This increase is evident across all durations and return periods, with particularly notable rises observed in shorter durations and lower return periods. For instance, Sharjah City has experienced a 39.3% increase in rainfall intensity for a 10 min duration at a 2-year return period. Similar trends are present in Al Dhaid and Mleiha, demonstrating a consistent pattern throughout the study area.

These findings emphasize the critical necessity to update IDF curves on both national and regional levels. The observed increase in rainfall intensity indicates more frequent and severe precipitation events, highlighting the need for revised hydrological models and updated infrastructure designs. Incorporating the revised IDF values is crucial for improving urban drainage systems, flood management strategies, and overall infrastructure resilience. This update will ensure better alignment with current and future precipitation patterns, thereby supporting sustainable development amid rising climatic variability.

This research significantly advances the field by integrating recent data to refine the assessment of rainfall intensity and frequency in arid regions, addressing a critical gap in understanding precipitation variability. By identifying substantial increases in IDF values and their implications for infrastructure and flood management, this study provides valuable insights into the impact of recent climatic changes on IDF curves. The detailed findings offer a comprehensive perspective for policymakers, urban planners, and researchers and present a methodology for updating IDF values with recent data and comparing them with historical records. This approach not only serves as a model for similar studies in arid climates but also significantly advances local flood risk management. The insights gained are applicable to other arid regions facing similar climatic challenges, highlighting the importance of developing effective adaptation strategies and improving infrastructure planning in the face of a changing climate.

4. Conclusions

The April 2024 rainfall events in the UAE have exposed critical vulnerabilities in the country's infrastructure and urban planning strategies. Despite advances in meteorological monitoring and predictive capabilities, the unprecedented intensity and duration of the rainfall revealed significant deficiencies in managing and mitigating urban flooding. The extensive submersion of residential properties, persistent road blockages, and the reactivation of long-dormant wadis highlight the urgent need for a thorough reassessment of current flood management practices.

This study, utilizing recent rainfall data, updated the IDF curves for the Sharjah Emirate, revealing a marked increase in rainfall intensities across all durations and return periods. Specifically, Sharjah showed an average increase of 36.76%, Al Dhaid experienced a 26.52% rise, and Mleiha had a 17.55% increase. These increases reflect a trend towards more severe and frequent rainfall events, influenced by both natural climatic changes and human activities such as cloud seeding.

The updated IDF values underscore the necessity for immediate revisions to the UAE's IDF curves used in urban drainage system designs. Accurate and up-to-date IDF curves are essential for developing infrastructure that can withstand both current

and future extreme weather events. However, addressing these challenges goes beyond updating IDF curves. It requires a comprehensive evaluation of urban planning practices, hydrological infrastructure, flood preparedness, crisis management strategies, and global climatic coordination. Additionally, integrating advanced forecasting methodologies is crucial.

In conclusion, while updating IDF curves is critical, it must be part of a broader strategy that includes enhanced data collection, improved hydrological modeling, and a coordinated approach to flood management. Implementing these measures will strengthen the resilience of UAE cities, better protect communities and infrastructure, and ensure preparedness for future extreme weather challenges.

Author Contributions: Conceptualization, R.R. and K.B.A.; methodology, R.R. and K.B.A.; software, K.B.A.; validation, R.R.; formal analysis, K.B.A.; investigation, K.B.A.; resources, K.B.A.; data curation, K.B.A.; writing—original draft, K.B.A.; writing—review and editing, R.R., G.W. and A.J.A.; visualization, R.R.; supervision, R.R., G.W. and A.J.A. All authors have read and agreed to the published version of the manuscript.

Funding: This research received no external funding.

Data Availability Statement: Data could be requested from the first author.

Acknowledgments: We sincerely thank the National Center of Meteorology in the UAE for their prompt response and ongoing support in providing updated meteorological records for the stations utilized in this study. We are particularly grateful to HE Abdullah Al Mandous, Director of the Center, and his dedicated team for their outstanding support in all meteorological and research-related matters. Additionally, we would like to express our gratitude to Eng. Anwaar Alshimmari, Executive Director of the Geospatial Governance Sector at the Federal Geographic Information Center in the UAE, for consistently providing valuable data on the tangible impact of the flooding discussed in this study.

Conflicts of Interest: The authors declare no conflicts of interest.

References

1. Emirates News Agency-WAM. UAE Witnesses Largest Rainfall in 75 Years. 2024. Available online: https://wam.ae/en/article/13vbuq9-uae-witness-largest-rainfall-over-past-years (accessed on 25 May 2024).
2. Ali, A. Emirati Man Drown after Car Is Swept into Wadi in Ras Al Khaimah. *Gulf News*. 17 April 2024. Available online: https://gn24.ae/111172dc41b09000 (accessed on 26 May 2024).
3. Almheiri, K.B.; Rustum, R.; Wright, G.; Adeloye, A.J. Study of impact of cloud-seeding on intensity-duration-frequency (IDF) curves of Sharjah city, the United Arab Emirates. *Water* **2021**, *13*, 3363. [CrossRef]
4. Almheiri, K.B.; Rustum, R.; Wright, G.; Adeloye, A.J. A Review of Hydrological Studies in the United Arab Emirates. *Water* **2023**, *15*, 1850. [CrossRef]
5. Aldosari, D.; Almedeij, J.; Alsumaiei, A.A. Update of intensity–duration–frequency curves for Kuwait due to extreme flash floods. *Environ. Ecol. Stat.* **2020**, *27*, 491–507. [CrossRef]
6. Chowdhury, R.; Mohamed, M.M.A.; Murad, A. Variability of Extreme Hydro-Climate Parameters in the North-Eastern Region of United Arab Emirates. *Procedia Eng.* **2016**, *154*, 639–644. [CrossRef]
7. Shanableh, A.; Al-Ruzouq, R.; Siddique, M.; Merabtene, T.; Yilmaz, A.; Imteaz, M. Impact of urban expansion on potential flooding, storage and water harvesting in the city of Sharjah, United Arab Emirates. *MATEC Web Conf.* **2017**, *120*, 09007. [CrossRef]
8. Department of Town Planning and Survey Sharjah the UAE 2024. GIS Maps. *UAE Map Modified By Author*, Provided in-person on 8 August 2024.
9. Rustum, R.; Adeloye, A.; Simala, A. Kohonen Self-Organising Map (KSOM) Extracted Features for Enhancing MLP-ANN Prediction Models of BOD_5. In Proceedings of the Symposium HS2005 at IUGG2007, Perugia, Italy, 2–13 July 2007; IAHS Publication, Volume 314; IAHS: Oxfordshire, UK, 2007.
10. Adeloye, A.J.; Adeloye, A.J.; Rustum, R. *KSOM Clustering as a Possible Cure for the Wicked Water Problem of Inadequate Data for Water Resources Planning Sustaining Himalayan Water Resources in a Changing Climate (SusHi-Wat) View Project Water Management View Project KSOM Clustering as a Possible Cure for the Wicked Water Problem of Inadequate Data for Water Resources Planning Introduction: The Key Wicked Water Problem*; IAHS Publication, Volume 338; IAHS: Oxfordshire, UK, 2010. Available online: https://www.researchgate.net/publication/287188128 (accessed on 10 June 2024).
11. Mwale, F.D.; Adeloye, A.J.; Rustum, R. Infilling of missing rainfall and streamflow data in the Shire River basin, Malawi—A self organizing map approach. *Phys. Chem. Earth* **2012**, *50–52*, 34–43. [CrossRef]

12. Adeloye, A.J.; Rustum, R. Self-organising map rainfall-runoff multivariate modelling for runoff reconstruction in inadequately gauged basins. *Hydrol. Res.* **2012**, *43*, 603–617. [CrossRef]
13. Mwale, F.D.; Adeloye, A.J.; Rustum, R. Application of self-organising maps and multi-layer perceptron-artificial neural networks for streamflow and water level forecasting in data-poor catchments: The case of the Lower Shire floodplain, Malawi. *Hydrol. Res.* **2014**, *45*, 838–854. [CrossRef]
14. Eldouni, S.E.; Bobée, B. Hydrological Frequency Analysis Using HYFRAN-PLUS (Version-V2.1). Published Online 2015. Available online: https://wrpllc.com/books/HyfranPlus/hyfranplusdescrip.html (accessed on 26 May 2024).
15. World Meteorological Organization (Ed.) Guide to Hydrological Practices Volume II Management of Water Resources and Application of Hydrological Practices. 2009. Available online: www.wmo.int (accessed on 8 June 2024).
16. Frederick, B.; Bell, C. Generalized rainfall-duration-frequency relationships. *Proc. Am. Soc. Civ. Eng.* **1969**, *95*, 311–328.
17. Modabber-Azizi, S.; Salarijazi, M.; Ghorbani, K. A novel approach to recognize the long-term spatial-temporal pattern of dry and wet years over Iran. *Phys. Chem. Earth* **2023**, *131*, 103426. [CrossRef]
18. Mamoon, A.A.; Rahman, A. Rainfall in Qatar: Is it changing? *Nat. Hazards* **2017**, *85*, 453–470. [CrossRef]
19. Mamoon, A.A.; Rahman, A. Selection of the best fit probability distribution in rainfall frequency analysis for Qatar. *Nat. Hazards* **2017**, *86*, 281–296. [CrossRef]
20. Mamoon, A.A.; Rahman, A. Uncertainty analysis in design rainfall estimation due to limited data length: A case study in Qatar. In *Extreme Hydrology and Climate Variability: Monitoring, Modelling, Adaptation and Mitigation*; Elsevier: Amsterdam, The Netherlands, 2019; pp. 37–45. [CrossRef]
21. Chitrakar, P.; Sana, A.; Hamood Nasser Almalki, S. Regional distribution of intensity–duration–frequency (IDF) relationships in Sultanate of Oman. *J. King Saud Univ. Sci.* **2023**, *35*, 102804. [CrossRef]

water

MDPI

Article

Making Different Decisions: Demonstrating the Influence of Climate Model Uncertainty on Adaptation Pathways

Jessica Dimond [1,2], William Roose [3] and Lindsay Beevers [1,*]

[1] Institute for Infrastructure and Environment (IIE), School of Engineering, University of Edinburgh, Edinburgh EH8 9YL, UK; dimond.jess11@gmail.com
[2] Ramboll UK, 80 George Street Edinburgh, Scotland EH2 3BU, UK
[3] Faculté des Sciences et Ingénierie, Sorbonne Université, 75005 Paris, France; william.roose.1@etu.sorbonne-universite.fr
* Correspondence: l.beevers@ed.ac.uk; Tel.: +44-1316507209

Abstract: The total global economic cost of flood damages between 1990 and 2024 exceeds £790 billion, with over half of these losses attributed to flood damages occurring in the last decade alone. Recent severe flood events have prompted a shift in flood risk management towards probabilistic approaches, leading to the notion that flood risk management is a continuous process of adaptive management. While substantial research has been dedicated towards characterising and quantifying climate model uncertainty, less focus has been directed towards the propagation of this uncertainty into hydraulically modelled systems and adaptive decision making. Recently, the concept of adaptation pathways has gained growing interest as a decision-focused, analytical tool to assess climate adaptation scenarios under uncertainty. This research develops an approach to quantify climate model uncertainty across multiple plausible adaptation scenarios and examines its influence on adaptation pathways using the case study area of Inverurie, Scotland. Uncertainty is quantified using stratified sampling and captured across scenarios, resulting in the identification and development of adaptation pathways within the context of specified flood risk management objectives and identified adaptation tipping points. The findings underscore the critical importance of embracing uncertainty in adaptation pathways to support robust, informed decision making.

Keywords: flood risk; uncertainty; probabilistic; climate change; climate model; adaptation; pathways; flood damages

1. Introduction

The total global economic cost of flood damages between 1990 and 2024 is estimated to exceed £790 billion, with £455 billion (58%) incurred over the last decade [1]. In the United Kingdom (UK), Expected Annual Damage (EAD) attributed to flooding is projected to rise significantly by the 2080s, increasing by 50% under a 2 °C warming scenario, 150% under a 4 °C warming scenario and 500% under a "worst-case" warming scenario [2]. Fluvial flooding is the most significant contributor, accounting for approximately 40% of total projected EAD [2]. However, high spatial and temporal climate variability and differences in local exposure and vulnerability introduce uncertainty in regional flood damage estimates [3,4].

Historically, uncertainty in flood risk management has been treated implicitly, relying largely on deterministic flood models [5–7]. In the UK, climate model uncertainty is accounted for through the application of climate change allowances (or uplift factors) on

deterministic flood models across different return periods and regions based largely on historical observations [8]. Two-dimensional hydraulic models remain the most widely used tools for simulating flood dynamics with reasonable accuracy at an acceptable computational cost [8–10]. While deterministic modelling may be justified when physically realistic models and inputs are used, it often requires complex setups and may still suffer from spurious precision [9].

Recent severe flood events have catalysed a shift, driven largely by the research community, toward probabilistic approaches to flood risk management [4,6,11]. The increasing recognition of climate change uncertainty underscores the need to explicitly account for the spatial and temporal variability of flood risk [5,6]. This perspective frames flood risk management as a dynamic, adaptive process, presenting significant challenges in quantifying uncertainty—an inherently complex process [6].

Advancements in computational power, numerical modelling techniques, and high-resolution spatial data have improved the ability to perform uncertainty quantification in flood modelling [12,13]. Several approaches can be used to quantify climate model uncertainty within a hydrological system, the most common of which is the Monte Carlo (MC) approach [4]. However, the computational demand required to perform Full Monte Carlo (FMC) simulations is significant due to the large sample size required to achieve convergence. Other more computationally efficient methods for quantifying climate model uncertainty exist, perhaps the most straightforward of which are stratified sampling approaches such as Latin Hypercube Sampling (LHS) [5].

The mainstream adoption of probabilistic approaches towards flood risk management has largely been policy-driven, for example, by the 2007 European Directive on the Assessment and Management of Flood Risks [14]. While substantial research has focused on characterising climate model uncertainty, less attention has been given to its propagation through hydrological systems [15] and its influence on adaptation decisions [16].

The concept of adaptation pathways has gained growing interest as a decision-focused, analytical tool to assess climate adaptation scenarios under uncertain conditions [16–18]. Adaptation pathways are defined as a sequence of adaptation actions that can achieve pre-defined objectives under uncertain future conditions [19]. It provides a framework to facilitate decision making under uncertainty by mapping sequential yet flexible decisions, thereby removing inherent path dependency [20]. Adaptation pathways ultimately provide decision makers a way to recognise the inter-temporal complexities and uncertainties associated with climate change and a mechanism to manage uncertainty at chosen spatial and temporal scales [21].

Transient adaptation scenarios describe alternative, hypothetical futures based on coherent and consistent assumptions about the past, present and future and are a valuable tool for decision makers to assess the robustness of potential actions under uncertain futures [21]. A key component of assessing adaptation pathways is the clear and explicit identification of adaptation tipping points (ATPs)—the point (or points) at which a system change, initiated by an external force, requires an alternative action (or set of actions) to provide an adequate level of risk management [21–23].

Downscaled regional climate models play an indispensable role in robust pathway derivation and tipping point identification [21]; however, for adaptation pathways to be robust, climate model uncertainty ought to be explicitly quantified and captured. Despite the growing emphasis on adaptation pathways in flood risk management, no known research has quantified climate model uncertainty within this context. This study aims to address this gap by exploring the research question:

"Can uncertainty quantification be integrated into adaptation pathway development and, if so, how does it influence adaptation decisions?"

While this research focuses on the case study area of Inverurie, Scotland, the approach presented is applicable to other regions and river catchments, provided comparable datasets are available. A key component of this research question is exploring how uncertainty quantification influences adaptation decision making. In the context of risk management, decision makers are inclined to favour actions that maximise value and minimise probability; however, where future states are uncertain, there are several rational decisions and actions that could achieve the defined risk management objectives [6]. Therefore, robust decision making trades optimal performance over a single future for adequate performance over a range of plausible futures, echoing the Keynesian view that it is better to be approximately right rather than precisely wrong [9].

2. Materials and Methods

2.1. Case Study

Figure 1 presents the case study area of Inverurie used within this research. Inverurie is located in Aberdeenshire, Scotland, approximately 16 miles north-west of Aberdeen. The Aberdeen to Inverness railway and A96 road passing through Inverurie make the town a strategic growth area for the North East of Scotland. The river Don is the primary source of flood risk to Inverurie, and the majority of the land use within the Don catchment is rural, comprising predominantly pastoral and arable land and woodlands [24]. River flows for the river Don are recorded at the Haughton gauging station [25], located approximately 1.5 km due west of the A96 [26].

Figure 1. Case study area of Inverurie, Scotland (Source: Open Street Map).

Inverurie has a long history of fluvial flooding dating back to 1768, with the most notable flood events occurring in November 2002 and January 2016 [26]. The 2002 floods resulted in the highest water level ever recorded, resulting in significant flooding to multiple properties. Across two significant events in January 2016, following Storm Frank, over 80 properties were reported damaged in Inverurie, necessitating evacuation efforts and closure of a number of key transport routes [27]. Given its distinct vulnerability to

flooding and long history of severe flood events, Inverurie provides a useful case study for this research.

2.2. Methodology

Figure 2 illustrates the overall research methodology. Observed river flows were extracted from the National River Flow Archive (NRFA) database [25] for the baseline period (1990–2020), and projected flows were extracted from the Earth System Grid Federation (ESGF) across the baseline, near future and far future time horizons (1990–2100). Extreme value (EV) analysis was undertaken on the observed flows, while flow projections were transformed onto the relevant river catchment and bias-corrected to the observed flows across the baseline period (1990–2020), producing the projected flow distributions.

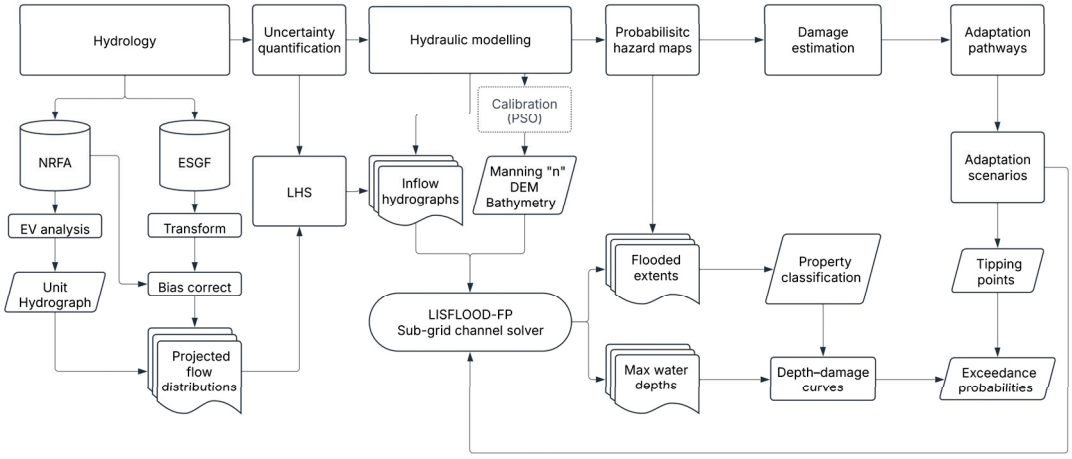

Figure 2. Research method.

Latin Hypercube Sampling (LHS) was used to quantify climate model uncertainty within the projected flow distributions and transformed into inflow hydrographs, producing upper boundary conditions for the hydraulic model. For the probabilistic approach, each of the inflow hydrographs (n = 100) across the time horizons were used within the LISFLOOD-FP hydraulic model. For the deterministic approach, a single upper boundary condition was used, i.e., the inflow hydrograph for the January 2016 flood event. The hydraulic model's Manning "n" parameter was calibrated using Particle Swarm Optimization (PSO) techniques, the details of which are reported in [4]. This was done using historical flood data recorded from the November 2002 event, where the Manning "n" friction coefficients were fine-tuned across three parameters. PSO allows for iterative improvements in the fit between the observed and modelled results, until the fitting error is minimised. The fitting statistic (FSTAT), the critical success index determined for each grid cell, was calculated for flood extents, and stage errors (SE) were calculated from the SEPA gauged levels recorded at the Haughton gauge. These were calculated to be 0.77 (FSTAT) and 0.11 (SE) [4].

Flooded extents and maximum water depths were extracted from the model outputs across each of the model runs and were converted into damage estimates based on the maximum water depths recorded for each of the affected properties within Inverurie. The total estimated damage for the deterministic (January 2016) event was calculated. The probabilistic damage estimates and associated probabilities were integrated across all model runs to output a single damage estimate. If the integrated probabilistic damage estimate was found to be greater than the deterministic damage estimate, the adaptation tipping point (ATP) was said to have been reached. However, the probabilistic approach

recognises the role that uncertainty plays within adaptation decision making and thus refers rather to the probability at which the ATP is exceeded.

Adaptation scenarios were defined on the basis of plausible local and regional actions [27]. The scenarios were represented in the hydraulic model through variations in the input parameters, for example, changes to the Digital Elevation Model (DEM), river bathymetry, friction coefficients or inflow hydrographs. This was done across the relevant time horizon within which these actions could realistically be implemented, and uncertainty was quantified using the approach described above. The adaptation scenarios were also appraised on the basis of reaching or not reaching the defined ATP, making direct reference to their exceedance probabilities. Each exceedance probability was mapped on the adaptation pathways to facilitate comparison between plausible future scenarios under uncertainty.

NRFA: National River Flow Archive; ESGF: Earth System Grid Federation; EV: extreme value; LHS: Latin Hypercube Sampling; PSO: Particle Swarm Optimization; DEM: Digital Elevation Model.

2.2.1. Hydrology: Boundary Conditions

Daily observed flows for the River Don were extracted from the National River Flow Archive (NRFA) [25], and extreme value (EV) analysis was undertaken to identify annual maximum (AMAX) river flows across the baseline period (1990–2020). Maximum Likelihood Estimation (MLE) was used to fit a generalized extreme value (GEV) statistical distribution to produce a flood frequency curve (Appendix A.1), from which the 95% confidence intervals (CIs) were calculated using parametric bootstrapping, ensuring reproducibility. The range of peak flows for the 1:100-year return period was then determined from the flood frequency curve.

The GEV distribution, G(F), is a three-parameter distribution [28] typically used in the UK to estimate extreme river flows at high return periods [29,30] in accordance with the Flood Estimation Handbook (FEH) [31]:

$$G(F) = \xi + \frac{\mu}{k}\left\{1 - (-\ln F)^k\right\} \ (k \neq 0) \quad (1)$$

where ξ is the location parameter, μ is the scale parameter, k is the shape parameter and F is the probability of non-exceedance for a defined return period (T) where F = 1–(1/T).

Daily surface runoff ("mrro") projections for the RCP8.5 scenario were extracted from the ESGF database for the time periods: 1990–2020 (baseline), 2030–2060 (near future) and 2070–2100 (far future) [32]. EURO-CORDEX is a multi-model ensemble (MME) covering the European (EUR-11) domain [33]. Incomplete datasets were screened out to ensure consistency, resulting in a total of 28 regional climate model (RCM)-global climate model (GCM) combinations [Appendix A.2]. The resolution of the EURO-CORDEX MME was 0.11° (≈12.5 km), and daily surface runoff projections were mapped onto polar rotated co-ordinates in EURO-CORDEX, assuming even distribution across cells. Therefore, the models were transformed onto the Don River catchment and projected onto the British National Grid Coordinates Reference System (CRS) as shown in Figure 3 and described by Equation (2):

$$Q_{cat} = l_g^2/\rho \ \times \sum_{i=1}^{Ng} A_i \times mrro_i \quad (2)$$

where Q_{cat} is the flow rate at the catchment scale, Ng is the total number of grid cells the cover the catchment area (14), l_g is the grid cell length (≈12.5 km), ρis water density (≈1000 kg/m^3), A_i is the fraction of the i-th grid cell and $mrro_i$ is the surface runoff of the i-th grid cell. This follows the methodology detailed within [33].

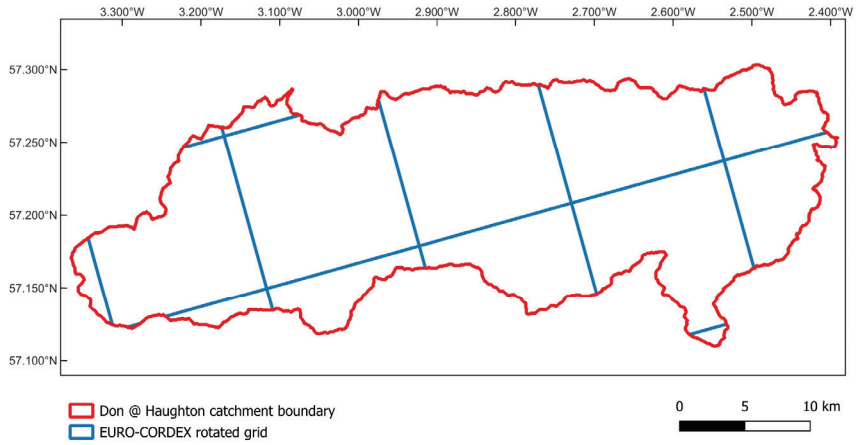

Figure 3. Transformation of projected flows on the catchment boundary.

Bias correction was performed on each of the 28 RCM-GCM combinations through aggregation and percentile mapping of the projected flows (1990–2100) onto the observed baseline (1990–2020) data extracted for the Haughton gauge from the NRFA. This process applies Percentile Delta Mapping (PDM) to both the observed and projected baseline data by adjusting the projected cumulative density function (CDF) using percentile delta changes between observed and projected flow rates across the baseline period (1990–2020) for each of the 28 ensemble members. This method was chosen over the mean difference or quantile methods as it best captures distributional distances across the range of flows [34]. This process is computationally efficient as it negates the need for catchment-scale modelling [33].

The maximum upper limit and minimum lower limit projected flow rates (m^3/s) across the 28 model ensembles for each of the time horizons are summarised in Table A3, Appendix A.3. The range (minimum and maximum values across all 28 ensembles) for each time horizon were extracted, ensuring that all unscreened projections are reflected in the uncertainty quantification process.

2.2.2. Uncertainty Quantification

Latin Hypercube Sampling (LHS), a stratified sampling technique, was used to sample flows across the ensemble ranges. Fewer samples are needed with LHS to obtain convergence whilst maintaining uniformity within the parameter space, when compared with Full Monte Carlo (FMC) methods [4]. In order to construct a normalised hydrograph shape for the upper boundary conditions in the hydraulic model, the January 2016 hydrograph was extracted from the SEPA Online API [35]. The sampled maximum flows were then scaled to produce (n = 100) inflow hydrographs across each of the time horizons.

2.2.3. Hydraulic Model

LISFLOOD-FP, a reduced physics, two-dimensional (2D) model developed to efficiently simulate floodplain inundation, was used for hydraulic (floodplain) modelling [36–39]. Its reduced physics formulation assists with handling complex topographies over large scales and dynamically simulates the propagation of flood waves across a fluvial floodplain to determine water depths in each grid cell [40].

The 2D model simulates propagation of flood waves along channels and across floodplains by assuming the advection component of the momentum equation is negligible and applying improvements to account for instabilities at large surface friction values [40]:

$$q_{t+\Delta t} = \frac{q_t - gh_t\,\Delta t\,\frac{\partial(h_t+z)}{\partial x}}{\left(1 + gh_t\,\Delta t\,n^2 q_t / h_t^{10/3}\right)} \quad (3)$$

where q is the flow per unit width (m^2/s), h is the flow depth (m), z is the bed elevation (m), g is the acceleration due to gravity (m/s^2), n is Manning's friction coefficient ($s/m^{1/3}$), t is the time at the current timestep and t + Δt is time at the next timestep (seconds). This flux equation is predicated on the selection of a suitable timestep to ensure that the model stability is maintained for most floodplain flow situations:

$$\Delta t_{max} = \alpha\,\frac{\Delta x}{\sqrt{gh_t}} \quad (4)$$

where α is a dimensionless coefficient [0.2–0.7] necessary to produce a stable simulation for floodplain flows and Δx horizontal is the cell dimension in the x-direction.

The LISFLOOD-FP base model was created using the acceleration solver for floodplain flow, a computationally efficient finite difference solver represented at a sub-grid resolution [36–39]. The basic component of the model is the Digital Elevation Model (DEM) created using light detection and ranging (LiDAR) data made available by SEPA [4]. The Manning "n" input raster was created using land cover maps [24] and calibrated through Particle Swarm Optimization (PSO) [4].

To define the boundary conditions, the sampled upstream inflow hydrographs, produced through LHS, were divided by the model resolution (10 m) to generate point-source mass fluxes per unit width (q (m^2/s)). The upstream inflows were defined as time-varying, while the downstream boundary condition was modelled as a normal-depth, free boundary to reduce backwater effects, typically experienced when using observed downstream water levels [13]. The boundary condition for the River Urie inflows were modelled as a fixed boundary assuming a constant flow of 10 m^3/s, reduced to a point-source fixed mass flux per unit width, q = 1 m^2/s. The constant flow assumption of the River Urie was used to isolate the uncertainty related to the River Don and negates the need to undertake joint probability analysis prior to uncertainty quantification. N = 100 models were run for each of the defined time horizons, the outputs from which were converted into probabilistic flooded extents and flood depth hazard maps.

2.2.4. Damage Estimation

Damage curves are a common method to estimate economic loss to properties as a direct function of water depth [41–43]. Uncaptured uncertainty in flood hazard analyses, and consequently damage estimates, can lead to poor investment decisions and result in over and under preparedness to respond to future flood hazards. Therefore, uncertainty within the flood hazard analyses was captured in the damage estimations by accounting for the range of water depths and therefore the range of estimated damages experienced by the 1:100-year event.

Property data was extracted from the Scottish Property Database (SPD) within Scotland's Land Information Service (ScotLIS) [44] and overlayed onto OS Map data in QGIS. The property thresholds were calculated by overlaying the DEM onto the property database, and the properties were classified as per the definitions within the Multi-Coloured Manual (MCM) [45] as presented in Figure 4. Damage curves (as a function of water depth)

were derived from the MCM following the UK industry standard approach to economic damage estimation.

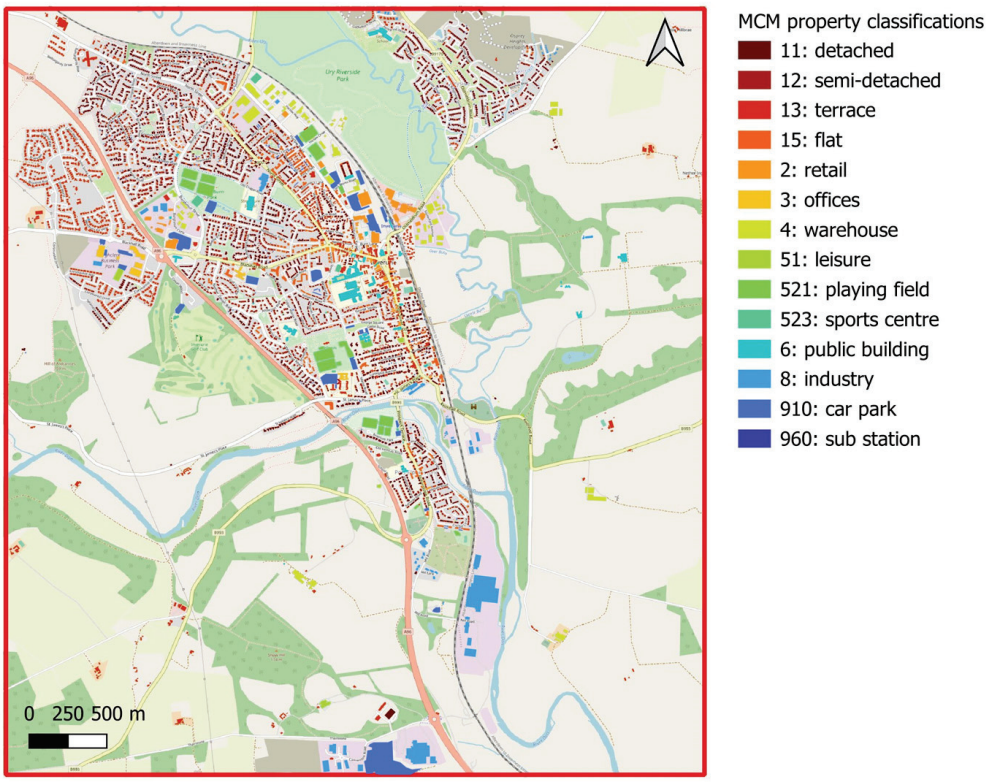

Figure 4. Property classification according to the MCM [45].

The empirical probability distribution of damages across each time horizon and adaptation scenario were produced, and the probabilities of exceeding the defined adaptation tipping point (ATP) were determined, thereby providing the probabilistic solution across time horizons and scenarios. The objective of flood risk management is explicitly defined by the Local North East Flood Risk Management Plan [27] as "reducing flood risk" or "avoiding an overall increase in risk" relative to the baseline year (2016), where risk is defined as economic losses quantified in terms of total estimated damages (£) incurred in any given year. In contrast, the deterministic solution under risk-based decision making, in any given year, is defined by:

$$\int_0^{\infty} D(x_t) f(x_t)\, dx_t \quad (5)$$

where $D(x_t)$ is the polynomial damage curves (from the MCM based on the property classification) as a function of temporally variable water depths (x_t) for the affected properties and $f(x_t)$ is the fitted continuous probability distribution [6].

The deterministic solutions was computed across all time horizons and scenarios to enable direct comparison with the probabilistic solutions. The application of Equation (5) is predicated on the ability to (i) estimate the time-dependent probability distribution functions f(x) of flooded water depths, (ii) relate water depths to probabilities of flooding where damage may occur and (iii) calculate the damage that is caused by floods of a given magnitude. It also assumes that the flooded system is not significantly sensitive to sub-annual temporal dimensions (such as seasonal variations), and this method ultimately collapses the climate model uncertainty captured through LHS, resulting in a deterministic solution.

The probability functions $f(x_t)$ of the water depth distributions were defined, and several goodness-of-fit statistics and criteria were calculated for each scenario across a range of affected grid cells. It was found that 2-parameter Weibull distributions, using the MLE method, fit the water depth distributions most accurately. A 2-parameter Weibull distribution is a continuous probability distribution defined by its shape (k) and scale (λ) as defined by [46]:

$$f(x) = \begin{cases} \frac{k}{\lambda}\left(\frac{x}{\lambda}\right)^{k-1} e^{-\left(\frac{x}{\lambda}\right)^{k}}, & x \geq 0 \\ 0, & x < 0 \end{cases} \quad (6)$$

The damage within each cell was then summed across the study area to calculate total estimated damages (£) across time horizons and scenarios.

2.2.5. Adaptation Scenarios

A summary of all adaptation scenarios is presented in Table 1, within which the relevant time horizons and adaptation actions are identified. A table of all input parameter modifications and descriptions is enclosed within Appendix B.

Table 1. Summary of adaptation scenarios, time horizons and actions.

Scenario	Time Horizon	Adaptation Actions
No adaptation	Baseline Near future Far future	None
Do minimum	Near future	Direct defences Old canal restoration
Storage	Near future Far future	Increase floodplain storage
Woodlands	Near future Far future	Riparian woodland creation along the riverbanks
Land-use management	Far future	Whole-catchment woodland creation

The "No adaptation" scenario represents the future scenario whereby no adaptation actions are implemented. The "Do minimum" scenario represents actions such as the implementation of property-level protection and raised thresholds. This also includes direct flood defences such as 1.5 m flood walls around affected properties. In addition, restoration of the old canal, to provide an additional channel for the flow of water during high-flow conditions, was identified as a relatively cost-effective action and would involve removal of two weirs.

The "storage" scenario represents actions that increase the river and floodplain storage through modifications to the bathymetry of the river channel, setting back of embankments and changes to the floodplain topography. The "woodlands" scenario represents riparian woodland planting. In the near future, it was assumed that the trees will not be fully grown, and therefore a reduced surface friction was used.

A whole-catchment approach, the "land-use management" scenario, represents the implementation of long-term upper catchment land-use management practices to capture surface runoff and increase upstream infiltration, thereby decreasing downstream flows and increasing the time to peak discharge in the far future. A study undertaking catchment-scale modelling of the Tarland catchment found that for a winter 1:100-year event and 15 h storm duration, 100% coniferous afforestation would reduce peak flows by 18% and delay the time to peak by 1 hour [47]. The Tarland catchment is comparable to the Don

in terms of location, area, Standard Average Annual Rainfall (SAAR), Base Flow Index (BFI) and standard percentage runoff (SPR). Whole catchment land use change is highly unlikely and the Land Capability for Forestry map [48] indicates that only 19.5% of the Don catchment is classified as having "good" or "moderate" suitability for riparian forestry. This scenario was represented in the hydraulic models as modified inflow hydrographs following resampling using LHS.

These adaptation scenarios were represented within the hydraulic model by modifying the appropriate input parameters, as described in Table A3, Appendix B. The "Do minimum" model included increased Manning coefficients at affected property locations and thresholds across the raster grid cells within to represent property level protection. Grid cell elevations within the DEM were increased by 0.3–1.5 m to account for raised thresholds and impermeable barriers. Canal restoration included incorporating the 1D channel in the flood model and modifications to the DEM and bathymetry (bank, width and bed) input parameters.

The "Storage" model included modifications to the river channel elevations within the DEM and bathymetry parameters by widening the river channel, setting-back the riverbanks and deepening the riverbed depths in locations where increased floodplain storage was viable. These modifications were also undertaken for the "Woodlands" scenario, where riparian woodland planting is represented in the hydraulic model, but included modifications to the Manning coefficients, which represent changes in the surface friction as a result of the increased vegetation.

The "Land-use management" scenario was represented by modifications to the inflow hydrographs through including a decrease in peak flows and a 1-hour delay to peaks across all sampled hydrographs.

3. Results

3.1. Hydrology

Annual maximum (AMAX) discharges (Q) (m^3/s) for the baseline period (1991–2020) were extracted for the Don at the Haughton gauge, revealing a maximum peak discharge, Q_{peak}, of 396.3 m^3/s that occurred in January 2016, and the upper and lower limits for the 1:100-year return period were found to be 184.4 m^3/s and 733.6 m^3/s, respectively.

Figure 5 presents the violin plots for the downscaled and bias-corrected EURO-CORDEX projections, revealing how the distributions of flow rates (m^3/s) and associated uncertainties are projected to change over time. Table 2 summarises the transformed and bias-corrected ranges of flow rates used, i.e., the maximum upper limit and minimum lower limit flow rates across the 28 unscreened ensembles, enclosed within Appendix A.3.

Table 2. Minimum lower limit and maximum upper limit flow rates (m^3/s) across time horizons.

Time Horizon	Lower Limit (m^3/s)	Upper Limit (m^3/s)
Baseline	124.0	777.8
Near future	126.2	928.9
Far future	109.8	1075.9

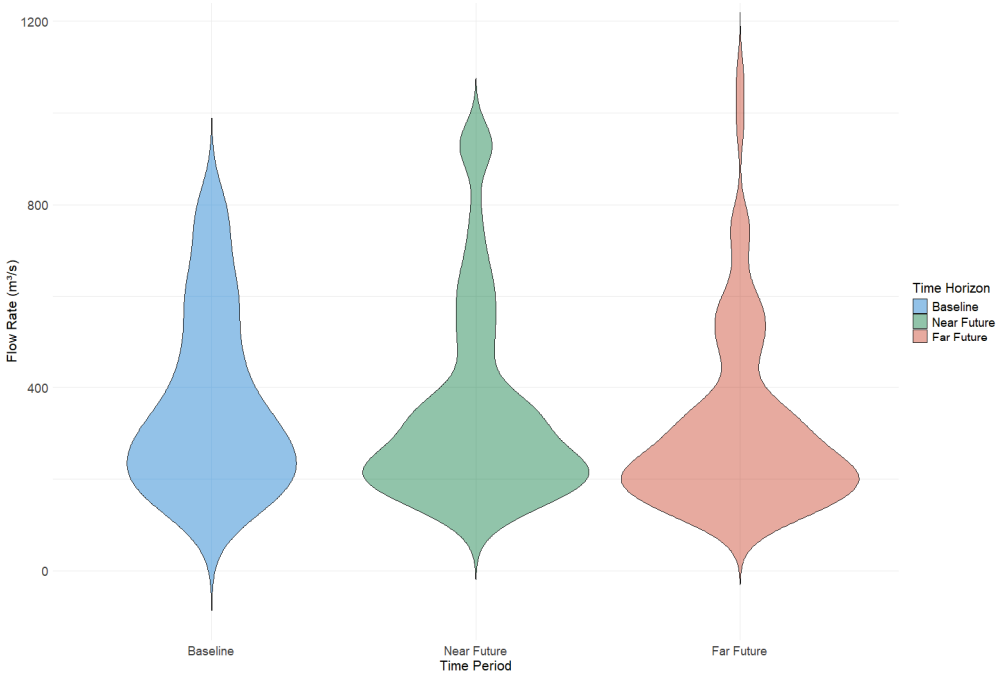

Figure 5. Violin plot showing the projected flow distributions across time horizons for the 1:100-year return period.

3.2. Probabilistic Hazard Maps

Figure 6 presents the deterministic and probabilistic flood hazard maps (flood extents and maximum water depths) for the 1:100-year return period, revealing the spatial and temporal distributions of flood risk across the case study region and across time horizons. While mapping probabilistic flood extents has been demonstrated by several authors, probabilistic representation of flood depths is less common, and Figure 6 presents the range of flood depths in the deterministic solution as well as the probability of maximum flood depths categorised within four continuous ranges, i.e., <0.3 m, 0.3–1 m, 1–2 m and >2 m, computed across each of the time horizons.

The deterministic maps (Figure 6a) show a single flood extent and maximum water depth output for the January 2016 event. In contrast, the probabilistic maps (baseline (Figure 6b), near future (Figure 6c) and far future (Figure 6d)) capture uncertainty within the flood extents and depths. Probabilistic flood extents (top row) demonstrate increasing spatial coverage of inundation over time, with the far future scenario showing the greatest extent and highest likelihood of flooding across the floodplain. Probabilistic flood depths (bottom row) also reveal a clear intensification of flood hazard over time, with deeper floodwaters (>2 m) becoming increasingly probable, especially along river-adjacent and low-lying areas.

These results highlight the growing exposure of Inverurie to more severe and widespread fluvial flooding under future climate scenarios. Moreover, they illustrate the additional insight gained through probabilistic modelling, particularly in capturing spatial distributions of flood risk and identifying areas where the likelihood of extreme flood depths significantly increases across time horizons.

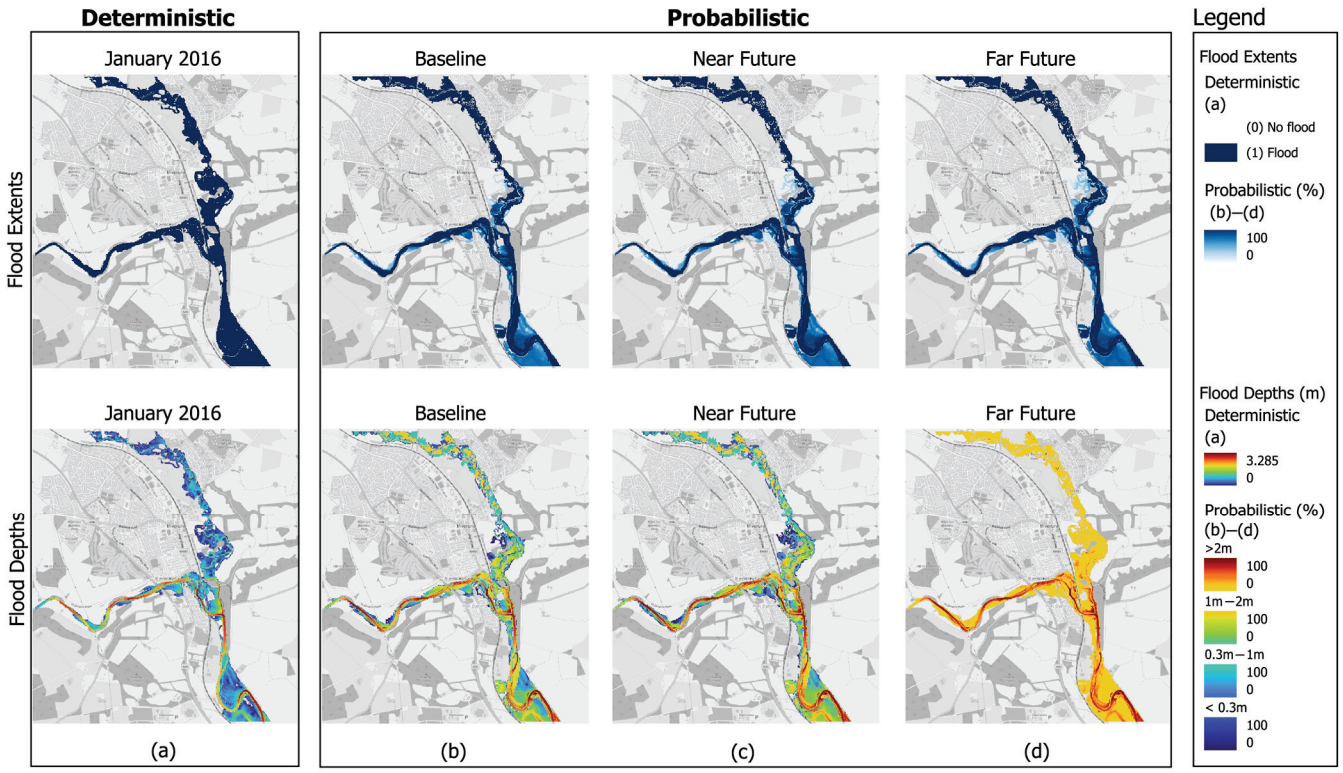

Figure 6. Deterministic flood extents and depths (**a**) and probabilistic flood extents and depths across the baseline (**b**), near future (**c**) and far future (**d**).

3.3. Damage Estimation

Using the property classification method prescribed by the MCM and applying the polynomial expressions for a long duration storm event assuming no early warning, flood damages (£) as a function of maximum flood depths (m) were calculated for the January 2016 event and across time horizons and adaptation scenarios. The January 2016 event is defined explicitly as the adaptation tipping point (ATP) against which future risks (damages) are compared. The total estimated damage of the January 2016 event was calculated to be £147,933.66. The performance of the base (January 2016) hydraulic model was evaluated by comparing simulated flood extents and depths with observed data from the January 2016 event. In terms of damages, the model demonstrated a strong performance, achieving an agreement of 0.88 between observed flood damages attributed to fluvial flooding and the modelled base-year results [27]. To compute the deterministic solutions across time horizons and scenarios, the product of damages within each grid cell were fitted to suitable probability distributions (Equation (6)) integrated across distributions (Equation (5)) and summed across all affected grid cells within the case study area.

Figure 7 presents the spatial distribution of theoretical flood damages (£) across various adaptation scenarios and future time horizons. Theoretical damages were computed by integrating depth–damage curves, derived from the MCM property classification, with appropriately fitted probability distributions (Equation (5)), resulting in deterministic estimates of total damages. Figure 7 presents the spatial distribution of damages across the case study area using a graduated red scale, where higher intensities represent greater estimated damages.

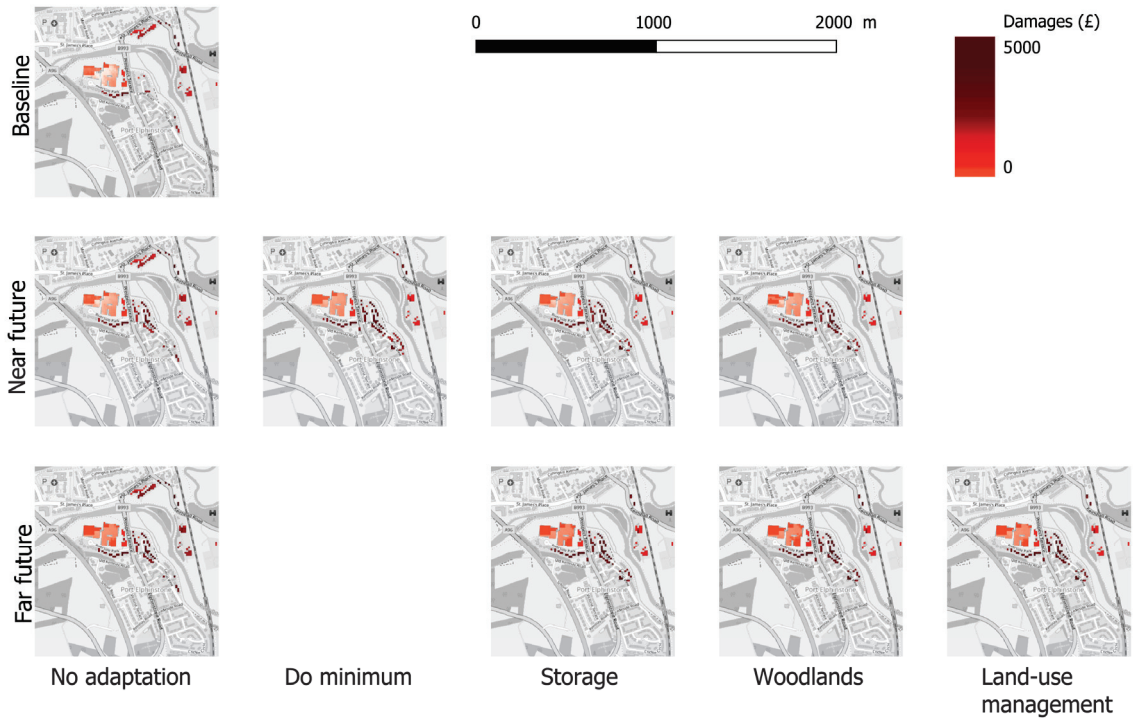

Figure 7. Spatial distribution of theoretical total estimated damage (£) across scenarios and time horizons.

While spatial patterns of damage remain broadly consistent across all scenarios, with the most affected areas appearing repeatedly, there are subtle yet important differences in both the extent and intensity of fluvial flooding. These variations, although not visually discernible at the 10 m resolution, are reflected in the total damage estimates provided in Table 3.

Table 3. Total damages (£) across the case study area for each scenario and time horizon.

Scenario	Time Horizon	Total Damage (£)
January 2016	ATP	147,933.66
No adaptation	Baseline	175,576.20
	Near future	273,502.31
	Far future	316,786.38
Do minimum	Near future	261,469.62
Storage	Near future	224,552.60
	Far future	260,089.96
Woodlands	Near future	224,740.00
	Far future	260,307.02
Land-use management	Far future	233,057.62

Table 3 summarises total theoretical damages for each scenario and time horizon. The results indicate that, under the deterministic solution, none of the adaptation strategies achieve a reduction in total damages relative to the ATP, i.e., the January 2016 event. This is reflected in adaptation pathways as binary termination points (see Section 3.4 and Figure 8); however, the "no adaptation" scenario yields the highest total damages in both the near and far future, revealing the potential benefit of adaptive interventions.

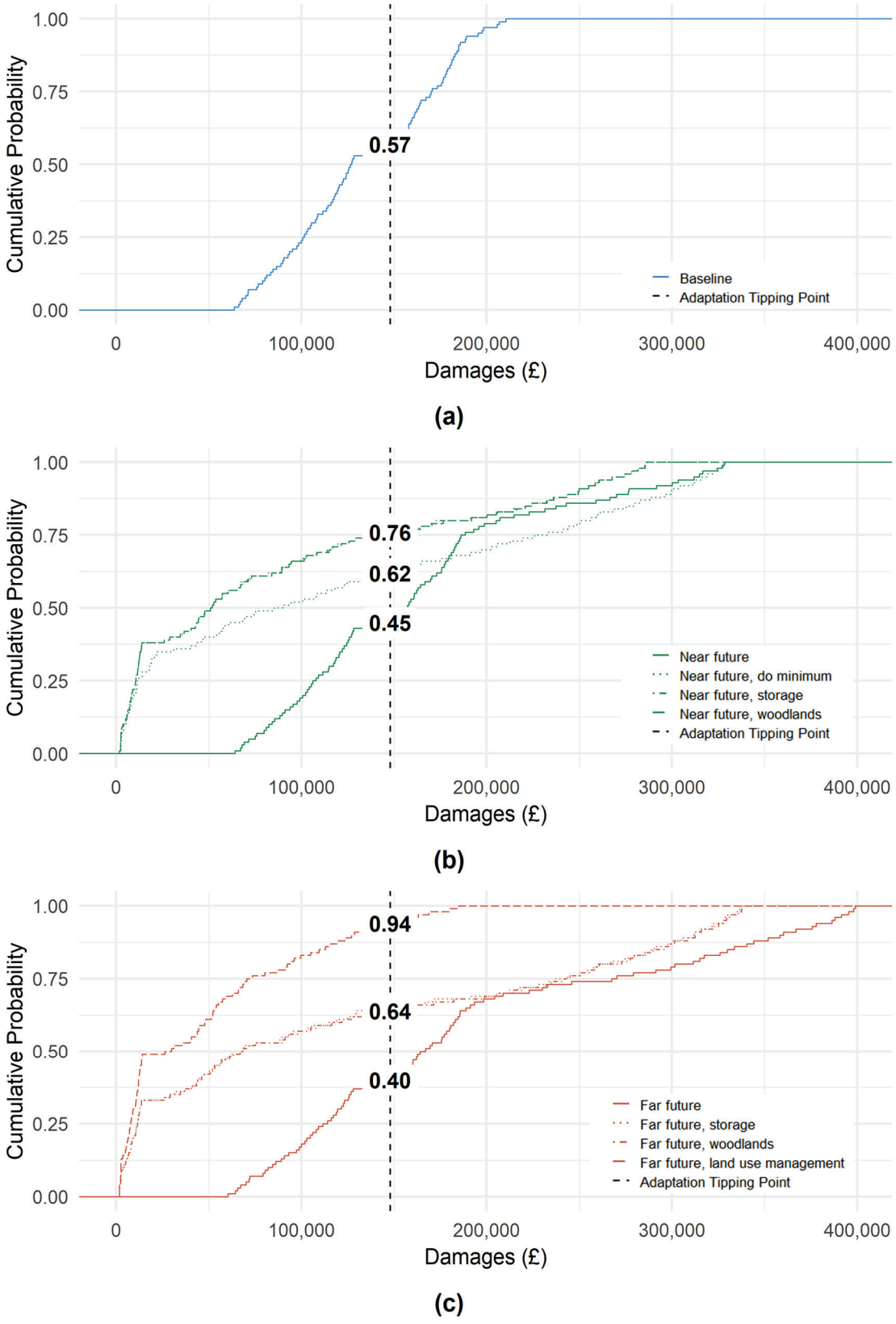

Figure 8. Empirical cumulative probability distribution of damages (£) for the baseline (**a**), near future (**b**) and far future (**c**).

Although the adaptation scenarios offer some mitigation of future flood damages, particularly in the near future, the deterministic solutions do not capture the relative probabilities of exceeding the ATP. Therefore, while useful for understanding cumulative

potential damages of fluvial flooding, the results ought to be presented within a probabilistic framework to fully evaluate adaptation performance.

3.4. Adaptation Pathways

The probabilistic solutions were plotted as empirical cumulative density functions (CDFs), highlighting the probability of each adaptation scenario reaching the defined ATP, as shown in Figure 8. The explicit definition of the ATP is the January 2016 total flood damages (£), calculated at £147,933.66. Figure 8 also presents numerical values on the CDF curves at the ATP thresholds, which represent the non-exceedance probabilities for each scenario, i.e., the probabilities that damages will remain below the ATP.

This facilitates the development of adaptation pathways across time horizons and allows for a direct comparison of exceedance probabilities within the probabilistic solution, as presented in Figure 9, and identification of binary termination points within the deterministic solution. The probabilistic solution prescribes a probability of exceedance on the basis of:

$$\overline{F}(x) = EP(x) = P(X > x) = 1 - F(x) \quad (7)$$

where $F(x) = P(X \leq x)$ is the CDF (or non-exceedance probability), x = ATP (£) and $(\overline{F}(x))$ is the exceedance probability. Ultimately, this demonstrates the method through which climate model uncertainty can be quantified within the development of adaptation pathways, i.e., through calculation of the ATP exceedance probabilities (EP(x)). The tipping points are defined as the points where flood damages exceed the ATP, and the numbers indicated on the curves reflect the likelihood of remaining below this critical threshold. This enables direct comparison of probabilistic performance between scenarios across time horizons.

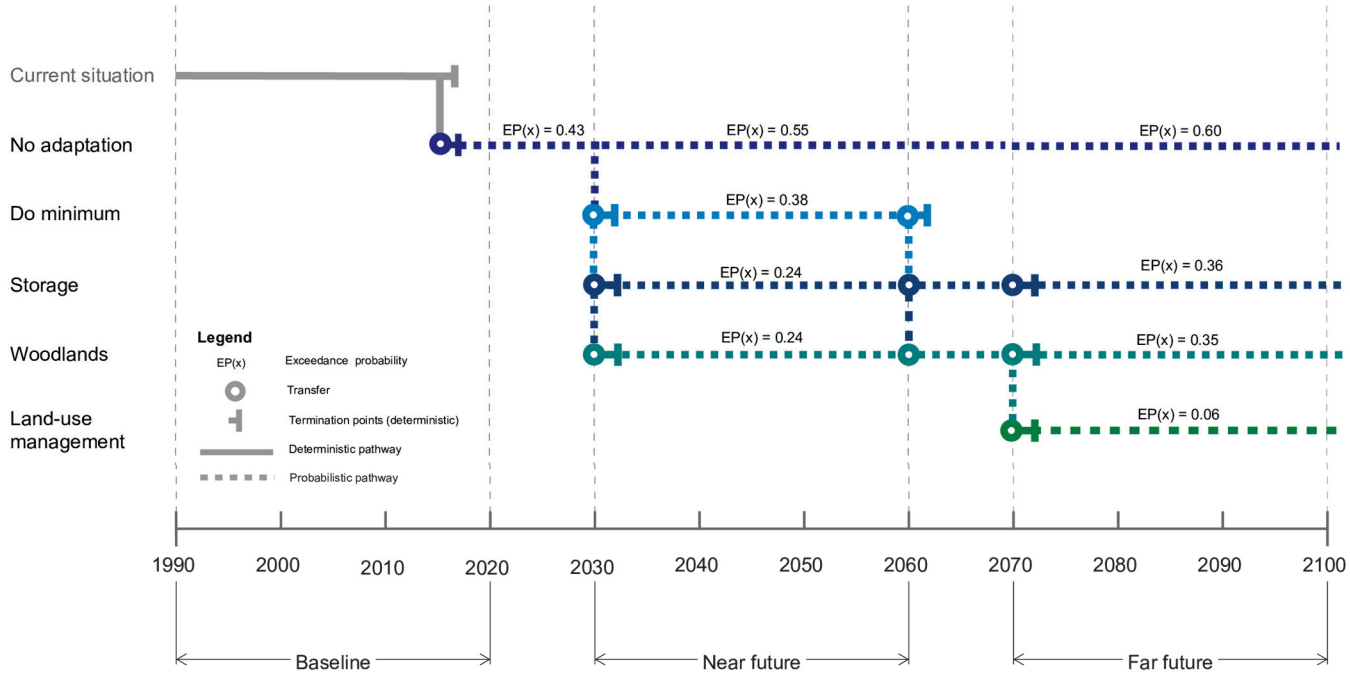

Figure 9. Adaption pathways identifying deterministic termination points (deterministic), adaptation tipping point exceedance probabilities (probabilistic).

Figure 9 presents the adaptation pathways, identifying multiple combinations of sequences of actions that can be taken across the baseline, near future and far future. The EP(x) values represent a probabilistic performance threshold, i.e., how well each strategy performs in reducing flood risk (in terms of exceedance probabilities). The termination

points represent points in time where the deterministic solution, i.e., the integral of the product of damages and probabilities across time horizons, exceeds the base year level of risk (in damages (£)). The pathways depict how adaptation actions can be implemented in sequence, with transfer points indicating when a switch to another action is, or may be, needed. In this way, the pathways allow for flexibility and transitions between actions, removing inherent path dependency and identifying pathways that maintain an acceptable level of risk.

4. Discussion

4.1. Hydrology

An assessment of the future climate hydrology for the River Don reveals a distribution of flow rates for the 1:100-year return period event across time horizons. The violin plots reveal a baseline distribution across RCMs concentrated around lower values (200–400 m^3/s), with larger spread in the lower range, tapering towards higher flow rates. The near future distribution has a slightly broader spread with a secondary peak identified (800–900 m^3/s), suggesting an increase in extreme flows and indicating larger uncertainty compared to the baseline. The far future projections have the widest distribution, with an extended tail reaching higher extreme flow rates, thereby shifting the central tendency upwards. This reveals that climate model uncertainty and extreme maximum flows increase as the time horizon increases. RCP8.5 has the largest model distribution and therefore captures the largest uncertainty, generally increasing across time horizons, suggesting that flood risk becomes increasingly more uncertain in the future under an RCP8.5 scenario.

4.2. Probabilistic Hazard Maps

The projected flow distributions are reflected in the probabilistic hazard maps, whereby flood extents and depths increase as time horizons increase for the 1:100-year event. The far future scenario has the largest flood extents, indicating that climate-induced increases in fluvial flows contribute to a greater flood-prone area. In addition, uncertainty, captured through the probability of flooding to each affected grid cell, is greater for all scenarios when compared to the deterministic solution and also depicts an increasing trend across time horizons. The far future scenario shows the highest climate model uncertainty, concurring with the results of the hydrological analysis.

The deterministic flood depths show significant flooding along the river channel and adjacent floodplains, generally in agreement with observations recorded following the January 2016 storm event. The probabilistic flood depths show an increase in magnitude and extent over time, with the baseline depicting lower flood depths concentrated near the river channel, while the near future reveals an increase in flood depths and higher water depths (>2 m) within low-lying areas, and the far future reveals more widespread and deeper flooding across large areas, with water depths exceeding 2 m.

The probabilistic hazard maps suggest that flood risk is projected to increase over time, both in extent and depth, with increasing climate model uncertainty and therefore increased risk as time horizons increase. The probabilistic projections provide a more robust assessment of flood risk across time horizons, indicating a range of possible flood outcomes through the capturing of uncertainty, thereby assisting decision making through identification of the likelihood of flooding in conjunction with magnitude. This could improve prioritisation of adaptation actions and supports a more flexible and adaptive approach to flood risk management, accounting for a range of future conditions.

4.3. Damage Estimation

An evaluation of the spatial distribution of flood damages, presented in Figure 7, indicates that the majority of damage is concentrated between the A96 and the railway line, primarily upstream of the confluence of the Rivers Don and Urie. This area includes a mix of land uses: open fields, a sports club, a wastewater treatment facility, and a number of residential and commercial properties.

Across all time horizons, total estimated damages increase significantly, particularly under the "no adaptation" scenario. Table 3 quantifies total damages, demonstrating that while none of the tested adaptation strategies fully mitigate damages to levels observed during the January 2016 event (ATP), all scenarios offer some degree of reduction compared to the "no adaptation" pathway. This trend is particularly evident in the near future, where strategies such as implementing riparian floodplain storage and woodland planting yield notable reductions in expected damages.

The damage estimation process involved the integration of depth–damage curves, derived from the Multi-Coloured Manual (MCM) property classifications, and the relevant fitted probability distributions for each scenario. While this deterministic approach provides valuable insights into potential spatial and temporal flood damage patterns, it has notable limitations. The fitted probability distributions do not account for the full range of variability and uncertainty across time horizons and scenarios. This restricts the ability of the analysis to evaluate the likelihood of exceeding the ATP and underrepresents the probabilistic nature of future flood risks.

Furthermore, the use of MCM depth–damage curves introduce variability in estimated damages based on property type and classification. This means that even when properties experience similar water depths, the resulting damages can differ substantially due to differences in structural vulnerability, use and asset value, introducing an additional layer of complexity, especially when interpreting spatial distribution of flooding across a heterogeneous area.

While the deterministic framework enables a comparative evaluation of adaptation performance and highlights key at-risk areas, the probabilistic approach, whereby uncertainty is captured in the solution, allows for a more robust comparison of adaptation scenario performances based on event likelihood and probabilities of exceeding the defined ATP.

4.4. Adaptation Pathways

Figures 8 and 9 illustrate how combining adaptation pathway mapping with empirical cumulative distribution functions (CDFs) and identification of exceedance probabilities (EP(x)) enables a more dynamic and risk-informed decision-making framework.

Figure 8 presents empirical cumulative distribution functions (CDFs) for the baseline, near future and far future time horizons, showing the probability distributions of flood damages under various adaptation scenarios. The use of a defined adaptation tipping points (ATP) enables direct comparison between scenarios. The exceedance probability at the ATP reflects the likelihood that damages will exceed the defined threshold. The ATP was determined based on total damages during the January 2016 flood event, providing a context-specific threshold for unacceptable risk. The numbers indicated on the CDF curves represent the cumulative probabilities of non-exceedance at the ATP, allowing for a clear interpretation of how likely each scenario is to stay below this risk threshold. For instance, in the far future, a "no adaptation" approach leads to a 60% probability of exceeding the ATP (40% cumulative probability of non-exceedance), while the introduction of "land-use management" reduces this risk to just 6% (94% cumulative probability of non-exceedance). This quantification of exceedance probabilities (EP(x)) under each scenario enables decision

makers to assess the relative effectiveness of interventions, not just in deterministic terms but across a full range of possible outcomes.

Figure 9 presents a suite of probabilistic adaptation pathways, each quantified using exceedance probabilities (EP(x)) of reaching the defined adaptation tipping point (ATP). Unlike deterministic models that simply identify binary thresholds, this approach assigns a probability of exceedance to each strategy at different points in time. For instance, the "no adaptation" pathway depicting increasing EP(x) values over time highlights growing exposure to flood risk. In contrast, strategies such as "storage" and "woodlands" reduce EP(x) significantly in the near future (24%), while "land-use management" emerges as the most robust long-term solution, achieving an EP(x) of just 6% by 2070. This quantification enables a meaningful comparison between adaptation scenarios across time horizons.

In contrast, the deterministic solution, which integrates all potential damages and their associated probabilities over time, results in fixed termination points that indicate no single adaptation action, nor sequence of actions, in the near or far future can permanently prevent exceedance of the ATP, thereby falling short of fully mitigating long-term flood risk. This illustrates the difference between probabilistic and deterministic approaches: while deterministic results indicate when risk thresholds are crossed, probabilistic methods provide insight into how probable this is to occur across different scenarios and periods, underscoring the importance of probabilistic approaches to flood risk management.

Together, Figures 8 and 9 demonstrate that embedding climate model uncertainty into adaptation pathways enables more informed, risk-based decision making. Rather than relying on deterministic decision making, different actions can be assessed based on their probabilistic performance across a range of future conditions while preserving flexibility to adapt over time. The probabilistic solution enables identification of plausible future pathways that maintain an acceptable level of risk while allowing flexibility and robustness in decision making under uncertainty.

Finally, these results indicate that adaptation pathways are influenced by the decision context within which the ATPs are defined. Therefore, careful consideration of the selection of appropriate ATPs is recommended to ensure that decisions are made in an informed and consistent manner so as to ensure that the adaptation objectives can be quantified. Climate change under the RCP8.5 climate scenario demonstrates challenges to achieving an overall avoidance of risk in the future when implementing a deterministic approach to decision making; however, through a probabilistic approach, adaptation actions can be suitably appraised through their ability to reduce the exceedance probabilities.

4.5. Further Work

Given the inherent complexity and uncertainty related to the climate models, modelling using alternative climate projections would further validate this methodology. A range of emission scenarios (including RCP2.6 and 4.5) could be considered [49], the outputs from which could be compared with the RCP8.5 scenario. In addition, checking for overfitting for the bias correction of the projections to the observed data is recommended, the results of which could be compared across several bias correction methods.

This research has only considered a 1:100-year return period; however, a range of return periods could be considered (e.g., 1:10, 1:30, 1:200, 1:1000). This would increase the spread of the distributions and therefore uncertainty of the water depths and damages, and the theoretical risk function could be used to integrate across multiple return periods to give a wider spread of data across various magnitudes. In addition, the damage functions could include damage to agricultural land, woodlands, roads, railways, and other critical infrastructure.

The number of samples taken across projected peak flow distributions could be increased from n = 100 to n = 10,000 to ensure a wider and more accurate spread. This would result in a significant increase in model runs and would be computationally more onerous. However, alternative methods of uncertainty quantification, such as Multi-Level Monte Carlo (MLMC) methods [4] or the building of emulators, could be used [30]. In addition, the hydraulic models could be run at a higher resolution (5 m × 5 m) to improve the accuracy of outputs.

Future research could analyse several alternative adaptation actions that integrate engineered solutions and natural flood management (NFM), for which economic appraisals using Cost–Benefit Analysis (CBA) or real options analysis (ROA) could be undertaken. Since the climate projections indicate potential low-flow conditions in the far future, future work could assess the robustness of adaptation options across both high and low flows.

Finally, the success of adaptation depends largely on the vulnerabilities and capabilities of the local community to respond to flood hazards [50]. Therefore, engaging with and understanding the needs of the local community and involving them in the decision-making process is integral to achieving transformational adaptation. A "bottom-up" approach could be compared with the "top-down" approach presented in this research and should include community and stakeholder engagement and elucidation, quantitative or qualitative assessments of vulnerability and assessment of multi-benefits and unquantifiable (or intangible) benefits of flood risk management, not only from an economic perspective but also from environmental and social anthropogenic perspectives.

4.6. Assumptions and Limitations

To isolate the uncertainty attributed to the climate models, other drivers (e.g., population growth) have not been included in the hydraulic models. In addition, non-fluvial hydrological processes such as evaporation, transpiration and groundwater flows have not been hydraulically modelled; however, these are not routinely included in hydraulic simulations of floodplain inundation. Isolation of climate model uncertainty in the hydraulic models allowed for consideration of a theoretical system whereby other sources of uncertainty are appropriately managed and are assumed to be negligible relative to climate model uncertainty [5].

An identified limitation of uncertainty quantification is the computational burden of running a sufficiently large sample of model realisations [11]. This research has used n = 100 iterations to quantify uncertainty using a stratified approach. Full Monto Carlo simulations are often considered to be the "gold standard" approach; however, this requires a larger sample size (e.g., n = 10,000) to ensure the full input distribution uncertainty is captured.

Damage estimation was undertaken in accordance with the MCM [45], accounting for direct damages, measured in terms of 2019–2020 prices. This makes the relative damages across the scenarios directly comparable. However, damage estimation only considered impacts to residential and non-residential properties and did not account for damage to agricultural land and transportation infrastructure, for which there is limited empirical data to derive damage curves. Similarly, indirect damages or damages to natural assets and the environment were not included. In reality, flood damages depend not only on inundation extent and water depth but also velocity, duration of inundation, sediment concentration as well as the communication of flood warnings. However, this paper excludes such factors as there are limited data available.

Real options theory builds upon financial options theory, whereby investment decisions are appraised in terms of net present costs and benefits by applying an appropriate discount factor. It is an alternative approach to cost–benefit analyses (CBA), explicitly accounting for uncertainty for robust decision making [51]. This calculates the (net present)

costs of adaptation actions (including capital, operation, maintenance, replacement and decommissioning costs) [52] and often uses "damages avoided" for the basis of the quantification of benefits [53]. Additionally, the comparison of economic value of risk proposes a simplified approach to informing flood management decisions; however, this fails to consider other more complex decision criteria, such as costs to human life, environmental costs, safety, public health and social impacts of floods, the quantification of which would be subject to unquantifiable uncertainties [6].

5. Conclusions

This research has demonstrated that probabilistic approaches to flood risk management can be used to inform adaptation pathways, and that in doing so, different decisions may be taken. It presents a methodology to quantify and capture climate model uncertainty in adaptation pathways for multiple plausible adaptation scenarios across three 30-year time horizons (baseline, near future and far future). Uncertainty is quantified using Latin Hypercube Sampling and captured across hydraulic models, resulting in the identification of adaptation actions and subsequent pathways within the context of a specified flood risk management objective.

The impact of the quantified climate model uncertainty on adaptation pathways is demonstrated through the quantification of exceedance probabilities relative to defined adaptation tipping points across a range of adaptation scenarios and time horizons. This research has identified how climate model uncertainty can be captured in adaptation pathways and subsequently be used to inform decisions on the selection of an appropriate pathway that minimises the probabilities of exceedance. It discusses potential considerations that influence the chosen adaptation pathway in the context of uncertainty.

The results indicate that adaptation pathways are influenced by the type of function fitted to the maximum flood water depth distributions in the deterministic solution and discusses how the decision context may influence the identification of adaptation tipping points. Ultimately, by quantifying climate model uncertainty in adaptation pathways, this study enables more robust, adaptive decision making over multiple time horizons. This research concludes that uncertainty could be embraced in flood risk decision making, particularly to inform adaptation pathways. By quantifying climate model uncertainty in adaptation pathways, decisions can be made about adaptation actions across a range of time horizons, which are different to those made under deterministic modelling. These decisions could support inclusive, "bottom-up" planning decisions in a risk-informed manner.

Author Contributions: Conceptualisation, J.D., W.R. and L.B.; methodology, J.D. and L.B.; software, J.D. and W.R.; validation, J.D. and W.R.; formal analysis, J.D. and W.R.; investigation, J.D. and W.R.; resources, J.D., W.R. and L.B.; data curation, J.D. and W.R.; writing—original draft preparation, J.D.; writing—review and editing, L.B.; visualisation, J.D.; supervision, L.B.; project administration, L.B. All authors have read and agreed to the published version of the manuscript.

Funding: This work was supported by EPSRC EP/X041093/1.

Data Availability Statement: The original data presented in the study are openly available in Zenodo at https://doi.org/10.5281/zenodo.15195618.

Acknowledgments: River flow data and the catchment shapefiles were extracted from the UK National River Flow Archive (NRFA) (National River Flow Archive), flow projections were extracted from the Earth System Grid Federation (ESGF) search portal (CEDA ESGF Search Portal | ESGF-CEDA | ESGF-CoG), the 15-min time series data were extracted from Scottish Environment Protection Agency's (SEPA) online API (SEPA Time series data service (API) | Scottish Environment Protection Agency | SEPA), property data were extracted from Scotland's Land Information Service (ScotLIS)

(ScotLIS—Registers of Scotland) and LISFLOOD-FP were downloaded from SEAMLESS-WAVE (LISFLOOD-FP8.0 | SEAMLESS-WAVE).

Conflicts of Interest: The authors declare no conflicts of interest.

Abbreviations

The following abbreviations are used in this manuscript:

AMAX	Annual maximum
ATP	Adaptation tipping point
BFI	Base Flow Index
CBA	Cost–benefit analyses
CDF	Cumulative density function
CI	Confidence interval
CMIP	Coupled Model Intercomparison Project
CORDEX	Coordinated Regional Climate Downscaling EXperiment
CRS	Coordinates Reference System
DEM	Digital Elevation Model
EV	Extreme value
ESGF	Earth System Grid Federation
FEH	Flood Estimation Handbook
FMC	Full Monte Carlo
GCM	General Circulation Model
GEV	Generalised extreme value
GHG	Greenhouse gas
HOST	Hydrology of Soil Types
LHS	Latin Hypercube Sampling
MC	Monte Carlo
MCM	Multi-Coloured Manual
MLE	Maximum Likelihood Estimation
NRFA	National River Flow Archive
NFM	Natural flood management
PDF	Probability density function
PFM	Probabilistic flood map
RCM	Regional climate model
RCP	Representative Concentration Pathway
ROA	Real options analysis
SAAR	Average annual rainfall in the standard period (1961–1990)
ScotLIS	Scotland Land Information Service
SPD	Scottish Property Database
SPR	Standard percentage runoff
SEPA	Scottish Environmental Protection Agency
TFRCD	Task Force for Regional Climate Downscaling
UKCEH	UK Centre for Ecology & Hydrology
WCRP	World Climate Research Programme

Appendix A

Appendix A.1

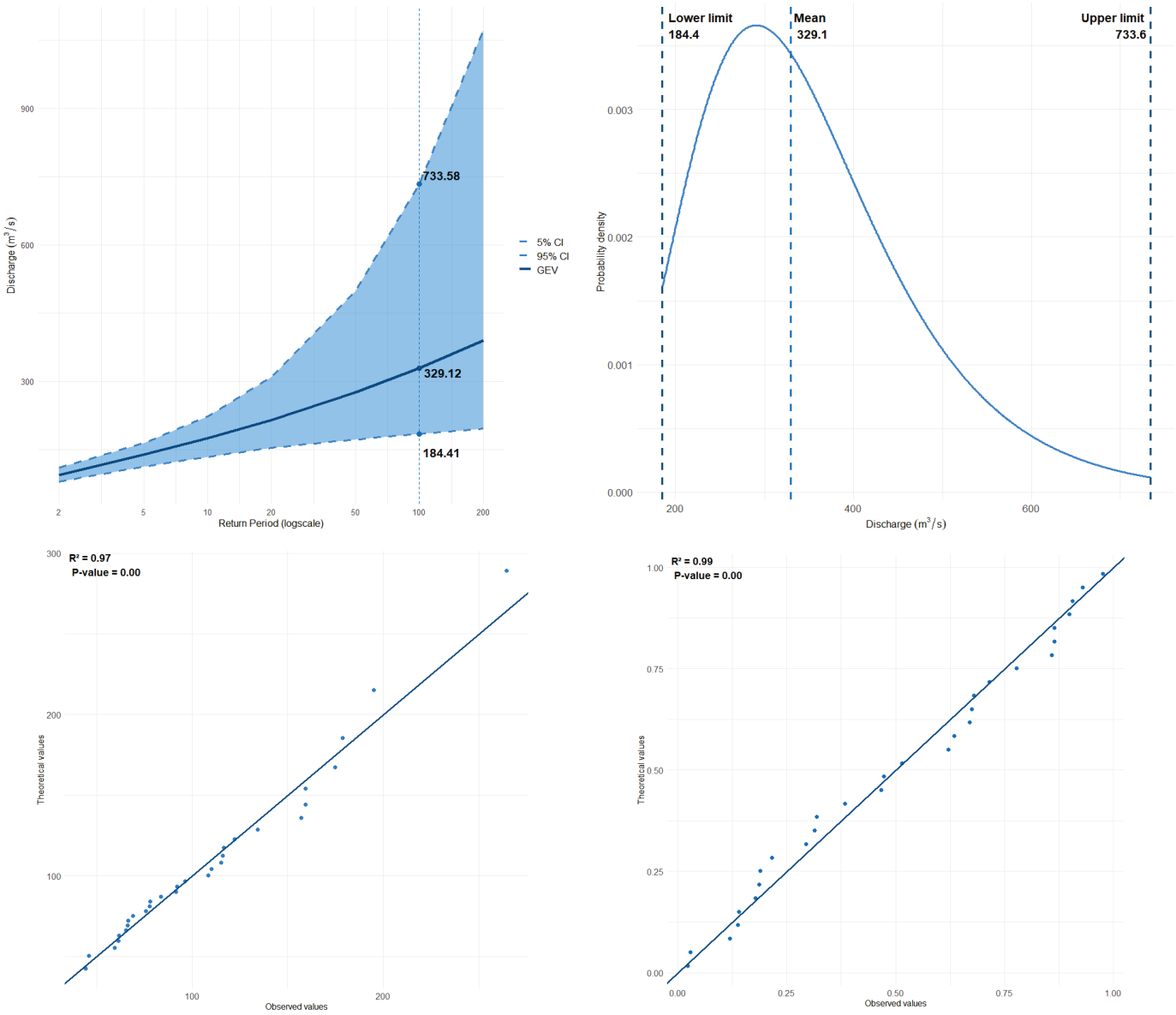

Figure A1. Extreme value analysis.

Appendix A.2

Table A1. EURO-CORDEX GCM-RCM combinations.

Driving Model (GCM)	Institution	RCM
ICHEC-EC-EARTH	CLM (Climate-Limited Area Modelling) data	CCLM4-8-17_1
		CCLM4-8-17_3
		CCLM4-8-17_4
		CCLM4-8-17_5
	KNMI (Koninklijk Nederlands Metrologisch Institute)	RACMO22E_2
		RACMO22E_3

Table A1. *Cont.*

Driving Model (GCM)	Institution	RCM
		RACMO22E_4
		RACMO22E_5
		RACMO22E_6
	CLM (Climate-Limited Area Modelling)	COSMO-crCLIM-v1-1_1
		COSMO-crCLIM-v1-1_2
		COSMO-crCLIM-v1-1_3
		COSMO-crCLIM-v1-1_4
	MOHC (Met Office Hadley Centre)	HadREM3-GA7-05_1
		HadREM3-GA7-05_3
		HadREM3-GA7-05_4
	DMI (Danmarks Meterologiske Institut)	HIRHAM5_1
		HIRHAM5_2
		HIRHAM5_3
		HIRHAM5_5
		HIRHAM5_6
MPI-ESM1-M	MPI-M (Max Planck Institute for Meteorology)	REMO2009
NCC-NorESM1-M	GERICS (Climate Service Center Germany)	REMO2015_2
		REMO2015_3
		REMO2015_4
		REMO2015_5
		REMO2015_6
		REMO2015_7

Appendix A.3

Table A2. Minimum lower limit and maximum upper limit flow rates (m^3/s) across each climate model for each time horizon.

Climate Model	Baseline		Near Future		Far Future	
	Min. Lower (m^3/s)	Max. Upper (m^3/s)	Min. Lower (m^3/s)	Max. Upper (m^3/s)	Min. Lower (m^3/s)	Max. Upper (m^3/s)
CCLM4-8-17_1	192.9	378.2	172.9	397.8	121.0	209.9
CCLM4-8-17_3	175.1	407.9	149.1	502.9	131.4	574.4
CCLM4-8-17_4	186.5	471.7	158.1	366.0	139.4	290.3
CCLM4-8-17_5	173.6	582.9	160.8	233.8	109.8	170.2
RACMO22E_2	212.9	563.7	219.6	928.9	137.6	652.0
RACMO22E_3	225.2	601.6	211.2	317.2	167.5	718.0
RACMO22E_4	170.3	621.1	135.4	228.6	119.9	355.7
RACMO22E_5 RACMO22E_6	222.8	754.3	190.9	617.3	123.0	455.9
COSMO-crCLIM-v1-1_1	184.1	490.2	172.0	263.2	181.7	368.5
COSMO-crCLIM-v1-1_2	161.5	526.8	185.4	554.9	216.9	754.8
COSMO-crCLIM-v1-1_3	193.6	688.9	192.2	614.8	194.1	365.2
COSMO-crCLIM-v1-1_4	200.1	474.1	216.7	733.4	198.8	491.9
HadREM3-GA7-05_1	213.4	444.4	218.7	380.5	229.5	338.5
HadREM3-GA7-05_3	156.2	422.6	153.1	279.1	185.9	767.2

Table A2. *Cont.*

Climate Model	Baseline		Near Future		Far Future	
	Min. Lower (m^3/s)	Max. Upper (m^3/s)	Min. Lower (m^3/s)	Max. Upper (m^3/s)	Min. Lower (m^3/s)	Max. Upper (m^3/s)
HadREM3-GA7-05_4	187.2	665.9	211.2	544.9	187.1	243.6
HIRHAM5_1	197.4	427.3	205.7	325.5	209.9	396.5
HIRHAM5_2	125.5	765.5	128.1	619.5	226.8	1075.9
HIRHAM5_3	135.6	763.2	133.7	356.1	135.9	489.8
HIRHAM5_5	163.5	771.6	243.1	928.9	123.7	251.6
HIRHAM5_6	134.3	762.4	129.7	928.9	135.8	556.8
REMO2009	124.0	647.8	169.6	795.9	172.5	595.6
REMO2015_2	198.4	593.9	222.5	664.7	219.3	489.3
REMO2015_3	199.9	656.9	196.7	343.6	209.4	573.8
REMO2015_4	183.6	575.0	210.0	928.9	167.0	198.2
REMO2015_5	195.8	595.8	235.1	464.3	240.4	542.5
REMO2015_6	219.0	777.8	210.5	583.9	208.4	561.7
REMO2015_7	197.7	550.9	245.6	928.9	207.5	501.8
Min lower limit	**124.0**		**128.1**		**109.8**	
Max. upper limit		**777.8**		**928.9**		**1075.9**

Appendix B

Table A3. Adaptation scenarios, actions, modified parameters and description of modifications.

Scenario	Time Horizon	Adaptation Actions	Modified Parameters	Description
No adaptation	Baseline Near future Far future	None	None	None
Do minimum	Near future	Direct defences	DEM, Manning "n"	Levels raised by 1.5 m at location of proposed walls to the WWTP and commercial properties Residential property thresholds raised by 0.3 m N = 1 for impermeable barriers
		Old canal restoration	DEM, bed, width, bank, Manning "n"	Includes the old canal channel N = 0.05
Storage	Near future Far future	Increase floodplain storage	DEM, bed, width, bank, Manning "n"	Uniformly reduced elevations relative to the river channel elevations Setting back and reprofiling of embankments N = 0.05
Woodlands	Near future Far future	Riparian woodland creation along the riverbanks	DEM, bed, width, bank, Manning "n"	As above N = 0.06 (near future); n = 0.1 (far future)
Land-use management	Far future	Whole-catchment woodland creation	Upstream inflows	Reduced peak flow by 3.5% Delay to peak flow by 1 h

Table A4. Theoretical (deterministic) damages (£) across adaptation scenarios.

Scenario	Time Horizon	Total Estimated Damage (£)	Exceeds ATP?
ATP	January 2016	147,933.66	
No adaptation	Baseline	175,576.20	Y
	Near future	273,502.31	Y
	Far future	228,929.28	Y
Do minimum	Near future	261,469.62	Y
Storage	Near future	224,552.60	Y
	Far future	153,918.23	Y
Woodlands	Near future	224,740.00	Y
	Far future	163,360.93	Y
Land-use management	Far future	159,968.55	Y

References

1. Ritchie, H.; Rosado, P. Global Damage Costs from Natural Disasters. Natural Disasters. Available online: https://ourworldindata.org/grapher/damage-costs-from-natural-disasters (accessed on 2 August 2024).
2. Sayers, P.B.; Horritt, M.S.; Penning-Rowsell, E.; Mckenzie, A. Climate Change Risk Assessment 2017: Projections of Future Flood Risk in the UK. 2015. Available online: www.sayersandpartners.co.uk (accessed on 18 January 2025).
3. Caretta, M.A.; Mukherji, A.; Arfanuzzaman, M.; Betts, R.A.; Gelfan, A.; Hirabayashi, Y.; Lissner, T.K.; Liu, J.; Gunn, E.L.; Morgan, R.; et al. Water. In *Climate Change 2022: Impacts, Adaptation and Vulnerability*; Contribution of Working Group II to the Sixth Assessment Report of the Intergovernmental Panel on Climate Change; Cambridge University Press: Cambridge, UK; New York, NY, USA, 2022; pp. 551–712. [CrossRef]
4. Aitken, G.; Beevers, L.; Christie, M.A. Multi-Level Monte Carlo Models for Flood Inundation Uncertainty Quantification. *Water Resour. Res.* **2022**, *58*, e2022WR032599. [CrossRef]
5. Beevers, L.; Collet, L.; Aitken, G.; Maravat, C.; Visser, A. The influence of climate model uncertainty on fluvial flood hazard estimation. *Nat. Hazards* **2020**, *104*, 2489–2510. [CrossRef]
6. Hall, J.; Solomatine, D. A framework for uncertainty analysis in flood risk management decisions. *Int. J. River Basin Manag.* **2008**, *6*, 85–98. [CrossRef]
7. Di Baldassarre, G.; Montanari, A. Hydrology and Earth System Sciences Uncertainty in River Discharge Observations: A Quantitative Analysis. 2009. Available online: www.hydrol-earth-syst-sci.net/13/913/2009/ (accessed on 15 July 2024).
8. Collet, L.; Beevers, L.; Stewart, M.D. Decision-Making and Flood Risk Uncertainty: Statistical Data Set Analysis for Flood Risk Assessment. *Water Resour. Res.* **2018**, *54*, 7291–7308. [CrossRef]
9. Di Baldassarre, G.; Schumann, G.; Bates, P.D.; Freer, J.E.; Beven, K.J. Cartographie de zone inondable: Un examen critique d'approches déterministe et probabiliste. *Hydrol. Sci. J.* **2010**, *55*, 364–376. [CrossRef]
10. Horritt, M.S.; Di Baldassarre, G.; Bates, P.D.; Brath, A. Comparing the performance of a 2-D finite element and a 2-D finite volume model of floodplain inundation using airborne SAR imagery. *Hydrol. Process.* **2007**, *21*, 2745–2759. [CrossRef]
11. Teng, J.; Jakeman, A.J.; Vaze, J.; Croke, B.F.W.; Dutta, D.; Kim, S. *Flood Inundation Modelling: A Review of Methods, Recent Advances and Uncertainty Analysis*; Elsevier Ltd.: Amsterdam, The Netherlands, 2017. [CrossRef]
12. Collet, L.; Beevers, L.; Prudhomme, C. Assessing the impact of climate change and extreme value uncertainty to extreme flows across Great Britain. *Water* **2017**, *9*, 103. [CrossRef]
13. Horritt, M.S. A methodology for the validation of uncertain flood inundation models. *J. Hydrol.* **2006**, *326*, 153–165. [CrossRef]
14. European Parliament and Council. Directive 2007/60/EC on the Assessment and Management of Flood Risk. 2007. Available online: https://eur-lex.europa.eu/legal-content/EN/TXT/?uri=CELEX:32007L0060 (accessed on 2 June 2024).
15. Clark, M.P.; Wilby, R.L.; Gutmann, E.D.; Vano, J.A.; Gangopadhyay, S.; Wood, A.W.; Fowler, H.J.; Prudhomme, C.; Arnold, J.R.; Brekke, L.D. *Characterizing Uncertainty of the Hydrologic Impacts of Climate Change*; Springer: Berlin, Germany, 2016. [CrossRef]
16. Sparkes, E.; Totin, E.; Werners, S.E.; Wise, R.M.; Butler, J.R.A.; Vincent, K. Adaptation pathways to inform policy and practice in the context of development. *Env. Sci. Policy* **2023**, *140*, 279–285. [CrossRef]
17. Werners, S.E.; Wise, R.M.; Butler, J.R.A.; Totin, E.; Vincent, K. *Adaptation Pathways: A Review of Approaches and a Learning Framework*; Elsevier Ltd.: Amsterdam, The Netherlands, 2021. [CrossRef]
18. Haasnoot, M.; Middelkoop, H.; Offermans, A.; van Beek, E.; van Deursen, W.P.A. Exploring pathways for sustainable water management in river deltas in a changing environment. *Clim. Change* **2012**, *115*, 795–819. [CrossRef]
19. Haasnoot, M.; Kwakkel, J.H.; Walker, W.E.; Maat, J.T. Dynamic adaptive policy pathways: A method for crafting robust decisions for a deeply uncertain world. *Glob. Environ. Change* **2013**, *23*, 485–498. [CrossRef]

20. Lin, B.B.; Capon, T.; Langston, A.; Taylor, B.; Wise, R.; Williams, R.; Lazarow, N. Adaptation Pathways in Coastal Case Studies: Lessons Learned and Future Directions. *Coast. Manag.* **2017**, *45*, 384–405. [CrossRef]
21. Haasnoot, M.; Schellekens, J.; Beersma, J.J.; Middelkoop, H.; Kwadijk, J.C.J. Transient scenarios for robust climate change adaptation illustrated for water management in the Netherlands. *Environ. Res. Lett.* **2015**, *10*, 105008. [CrossRef]
22. Haasnoot, M.; Lawrence, J.; Magnan, A. *Pathways to Coastal Retreat*; American Association for the Advancement of Science: Washington, DC, USA, 2021. [CrossRef]
23. Kwadijk, J.C.J.; Haasnoot, M.; Mulder, J.P.M.; Hoogvliet, M.M.C.; Jeuken, A.B.M.; van der Krogt, R.A.A.; van Oostrom, N.G.C.; Schelfhout, H.A.; van Velzen, E.H.; van Waveren, H.; et al. Using adaptation tipping points to prepare for climate change and sea level rise: A case study in the Netherlands. *Wiley Interdiscip. Rev. Clim. Change* **2010**, *1*, 729–740. [CrossRef]
24. Marston, C.; Rowland, C.S.; O'Neil, A.W.; Morton, R.D. *Land Cover Map 2021 (land Parcels, GB)*; UKCEH: Wallingford, UK, 2022.
25. UKCEH. NRFA Peak Flow Data for Station 11002. Available online: https://nrfa.ceh.ac.uk/data/station/peakflow/1100 (accessed on 2 July 2024).
26. JBA. Inverurie (Port Elphinstone and Kintore) FPS Study Information Review Report. 2019. Available online: http://www.inverurieflоodstudy.com/media/reports/InformationReview.pdf (accessed on 18 July 2024).
27. Aberdeenshire Council. North East Local Plan District-Local Flood Risk Management Plan 2016–2022. 2016. Available online: https://www.aberdeenshire.gov.uk/media/17163/north-east-local-flood-risk-management-plan-2016-2022.pdf (accessed on 10 July 2024).
28. Morrison, J.E.; Smith, J.A. Stochastic modeling of flood peaks using the generalized extreme value distribution. *Water Resour. Res.* **2002**, *38*, 41-1–41-12. [CrossRef]
29. Ellis, C.; Visser-Quinn, A.; Aitken, G.; Beevers, L. Quantifying uncertainty in the modelling process; future extreme flood event projections across the UK. *Geosciences* **2021**, *11*, 33. [CrossRef]
30. Aitken, G.; Beevers, L.; Christie, M.A. Advanced Uncertainty Quantification for Flood Inundation Modelling. *Water* **2024**, *16*, 1309. [CrossRef]
31. Robson, A.; Reed, D. *Flood Estimation Handbook: 3. Statistical Procedures for Flood Frequency Estimation*; Institute of Hydrology: Wallingford, UK, 1999.
32. CEDA. ESGF Interface for CORDEX Data. Available online: https://esgf-ui.ceda.ac.uk/cog/search/cordex-ceda/ (accessed on 15 June 2024).
33. Aitken, G.; Visser-Quinn, A.; Beevers, L. EURO-CORDEX: A Multi-Model Ensemble Fit for Assessing Future Hydrological Change? *Front. Water* **2022**, *4*, 804146. [CrossRef]
34. Zhu, L.; Kang, W.; Li, W.; Luo, J.J.; Zhu, Y. The optimal bias correction for daily extreme precipitation indices over the Yangtze-Huaihe River Basin, insight from BCC-CSM1.1-m. *Atmos. Res.* **2022**, *271*, 106101. [CrossRef]
35. SEPA. SEPA Timeseries API. Available online: https://timeseriesdoc.sepa.org.uk/api-documentation/ (accessed on 5 July 2024).
36. Neal, J.; Schumann, G.; Bates, P. A subgrid channel model for simulating river hydraulics and floodplain inundation over large and data sparse areas. *Water Resour. Res.* **2012**, *48*, W11506. [CrossRef]
37. Bates, P.D.; Horritt, M.S.; Fewtrell, T.J. A simple inertial formulation of the shallow water equations for efficient two-dimensional flood inundation modelling. *J. Hydrol.* **2010**, *387*, 33–45. [CrossRef]
38. Neal, J.; Keef, C.; Bates, P.; Beven, K.; Leedal, D. Probabilistic flood risk mapping including spatial dependence. *Hydrol. Process.* **2013**, *27*, 1349–1363. [CrossRef]
39. Bates, P.D.; De Roo, A.P.J. A Simple Raster-Based Model for Flood Inundation Simulation. 2000. Available online: www.elsevier.com/locate/jhydrol (accessed on 8 July 2024).
40. Hunter, N.M.; Bates, P.D.; Horritt, M.S.; Wilson, M.D. Improved simulation of flood flows using storage cell models. *Proc. Inst. Civ. Eng.-Water Manag.* **2006**, *159*, 9–18. [CrossRef]
41. Paprotny, D.; Kreibich, H.; Morales-Nápoles, O.; Wagenaar, D.; Castellarin, A.; Carisi, F.; Bertin, X.; Merz, B.; Schröter, K. A probabilistic approach to estimating residential losses from different flood types. *Nat. Hazards* **2021**, *105*, 2569–2601. [CrossRef]
42. McGrath, H.; El Ezz, A.A.; Nastev, M. Probabilistic depth–damage curves for assessment of flood-induced building losses. *Nat. Hazards* **2019**, *97*, 1–14. [CrossRef]
43. Merz, B.; Kreibich, H.; Thieken, A.; Schmidtke, R. Estimation uncertainty of direct monetary flood damage to buildings. *Nat. Hazards Earth Syst. Sci.* **2004**, *4*, 153–163. [CrossRef]
44. Registers of Scotland. ScotLIS Map Search. 2024. Available online: https://scotlis.ros.gov.uk/map-search (accessed on 15 July 2024).
45. Penning-Rowsell, E.; Priest, S.; Parker, D.; Morris, J.; Tunstall, S.; Viavattene, C.; Chatterton, J.; Owen, D. *Flood and Coastal Erosion Risk Management: A Manual for Economic Appraisal*, 1st ed.; Routledge: Abingdon-on-Thames, UK, 2013. [CrossRef]
46. Lai, C.; Murthy, D.; Xie, M. *Handbook of Engineering Statistics*; Springer: London, UK, 2006. [CrossRef]
47. Iacob, O.; Brown, I.; Rowan, J. Natural flood management, land use and climate change trade-offs: The case of Tarland catchment, Scotland. *Hydrol. Sci. J.* **2017**, *62*, 1931–1948. [CrossRef]

48. Gauld, J.; Bell, S.; Nolan, A.; Lilly, A. *Land Capability for Forestry in Eastern Scotland*; The Macaulay Land Use Research Institute: Aberdeen, Scotland, 1989.
49. IPCC. *Climate Change 2014: Synthesis Report. Contribution of Working Groups I, II and III to the Fifth Assessment Report of the Intergovernmental Panel on Climate Change*; IPCC: Geneva, Switzerland, 2014.
50. Kondrup, C.; Mercogliano, P.; Bosello, F.; Mysiak, J.; Scoccimarro, E.; Rizzo, A.; Ebrey, R.; Ruiter, M.D.; Jeuken, A.; Watkiss, P. *Climate Adaptation Modelling*; Springer Nature: Berlin, Germany, 2022; Available online: https://link.springer.com/bookseries/11741 (accessed on 2 July 2024).
51. Buurman, J.; Babovic, V. Adaptation Pathways and Real Options Analysis: An approach to deep uncertainty in climate change adaptation policies. *Policy Soc.* **2016**, *35*, 137–150. [CrossRef]
52. Environment Agency. Estimating the Economic Costs of the 2015 to 2016 Winter Floods. 2018. Available online: www.gov.uk/environment-agency (accessed on 28 June 2024).
53. Woodward, M.; Kapelan, Z.; Gouldby, B. Adaptive flood risk management under climate change uncertainty using real options and optimization. *Risk Anal.* **2014**, *34*, 75–92. [CrossRef]

water

MDPI

Article

Water Management Instructions as an Element of Improving the State of the Pakoski Reservoir (Central–Western Poland)

Bogumił Nowak [1], Grzegorz Dumieński [1] and Agnieszka Ławniczak-Malińska [2,*]

[1] Institute of Meteorology and Water Management—National Research Institute, Podleśna 61, 01-673 Warszawa, Poland; rugosa@op.pl (B.N.); grzegorz.dumienski@imgw.pl (G.D.)
[2] Department of Ecology and Environmental Protection, Poznań University of Life Sciences, Piątkowska 94C, 60-649 Poznań, Poland
* Correspondence: agnieszka.lawniczak@up.poznan.pl; Tel.: +48-61-8466515

Abstract: The management of reservoir dams in the context of observed climate changes and changing environmental conditions is becoming an increasingly significant challenge. Changes in the regimes of rivers feeding the reservoirs, sudden floods, long periods of drought, shallowing of reservoirs, water pollution, and algal blooms create unprecedented threats to the operation of these reservoirs. Among these challenges, the most crucial seems to be the proper management of available water resources, which condition the existence of the reservoir. The location of the reservoir has a significant impact on how water management is conducted. In the case of mountain and upland reservoirs created for flood protection of areas downstream, water management practices differ significantly from those for lowland reservoirs, which primarily serve to retain water for industrial and agricultural needs in the area, with an additional flood protection function. The aim of this study was to assess the factors determining the supply of lowland reservoirs using the example of the Pakoski Reservoir (Central–Western Poland) and to propose actions that would allow more efficient management of water resources in the catchment and reservoir, enabling the preservation of the current morphometric parameters in the face of climate change, adverse environmental phenomena, and increased anthropogenic pressure in the catchment area. This study focused on the Pakoski Reservoir, located in the southern part of the Kuyavian–Pomeranian Voivodeship. It was constructed fifty years ago as a result of damming water in the river systems of the Noteć and Mała Noteć Rivers. For decades, it served its functions, and its management posed no major issues. However, over the past decade, due to environmental changes and human activities in the catchment area, the reservoir has increasingly faced problems with filling.

Keywords: water deficits; water retention; flood protection; levels of impoundment; water transfer

1. Introduction

Managing reservoir dams in the face of observed climate change and environmental transformations is becoming an increasingly challenging task [1–4]. As shown in the last decade, many of these hydrotechnical structures, which have been in place for decades, are encountering more and more problems related to their operation [5–7]. The water management guidelines created for them several decades ago, as well as the water law permits issued based on these guidelines, are becoming increasingly difficult to implement under current conditions and, in some cases, are even harmful to the reservoirs and the areas located downstream [8,9]. The lack of snow cover, long periods without rainfall,

and rainfall events of unprecedented intensity make reservoirs managed according to established schemes fail to meet their role in flood protection and retention. The regime of rivers is also changing, with rivers that were once snow- and rain-fed increasingly becoming solely rain-fed [10]. As a result, many of these rivers, particularly those in the lowland areas, no longer experience a clear winter–spring rise, and the maximum flows now occur in months previously considered winter months [10–13]. On the other hand, events becoming increasingly frequent are heavy, localised rainfalls that cause local flooding [14–16] or extensive, prolonged low-pressure rainfalls, such as those in the Sudetes in September 2024. These events lead to water saturation in the catchment area and widespread, multi-day runoff to lower-lying areas. Additionally, significant changes in land use, particularly urbanisation in cities and smaller towns, result in the loss of natural soil permeability or the intensive irrigation of agricultural land, which drains deeper aquifers [17]. These phenomena and processes contribute to increased water inflow to reservoirs during wet periods and reduced inflow during dry, hot days. As a result, many reservoirs face problems in filling and maintaining stable water levels. Furthermore, in some cases, the flood reserves designed in earlier years are now found to be too small. For lowland reservoirs closing catchments with low water capacity, the first of these issues is especially important, as many of these reservoirs were designed as retention reservoirs primarily for agricultural or industrial water supply. In Poland, this issue is particularly relevant for reservoirs located in regions like Greater Poland and Kuyavia, as these areas experience the lowest rainfall and have the highest groundwater withdrawals for agricultural purposes. Observations show that water reservoirs such as Środa Reservoir on the Maskawa River, Września Reservoir on the Wrześnica River, Kowalskie Reservoir on the Główna River, Słupecki Reservoir on the Meszna River, and Pakoski Reservoir on the Mała Noteć River have faced similar challenges. The inability to capture water from their catchments or the total loss of inflow during the summer months resulted in an inability to reach or maintain normal impoundment levels during the summer half-year. This, combined with poor water quality and high temperatures, contributed to accelerated eutrophication. Consequently, this led to algal blooms, which in shallower reservoirs resulted in massive fish kills. Another negative aspect of prolonged low-water levels in reservoirs was the limitation or complete cessation of feeding the river valleys that pass through these reservoirs. It should be emphasised that this historical catchment was cut off from the reservoir in the 19th century due to drainage works in the upper Noteć River carried out by the Prussian authorities at the time [18,19].

Among all the reservoirs mentioned above, the largest and most economically significant is the Pakoski Reservoir, located in the southwestern part of the Kuyavian–Pomeranian Voivodeship. It is of great importance for the local economy, as it provides water to several industrial plants in the area and serves as a flood protection measure for the towns located in the middle of Noteć River valley. This reservoir has been operational for 50 years, but in its entire history, the past 5 years have proven to be the most challenging, as it has not been able to reach its normal impoundment level even once during this period. The problems described above seem fully justified when the changes in the land use structure and groundwater conditions of the main rivers feeding the reservoir are analysed. In this region, the climatic water balance has significantly worsened, there is no longer snow cover, and the upper parts of catchment areas, especially those with significant lake areas, have become non-drainable. With the constant water demand in the region, increased evaporation from the surface of the reservoir, and water feeding into the Noteć River, it is not surprising that this reservoir has remained only half-filled throughout the year in recent years, despite having the potential to replenish its water. To address the water deficits, it is necessary to modify the water management guidelines created in the 1970s to make them

more flexible and reflect the potential for capturing excess water from both the current catchment of the reservoir and its historical water supply area.

The aim of the study is to assess the factors influencing the water supply to lowland reservoirs in Europe, using the Pakoski Reservoir as a case study, and to identify actions that will enable more efficient water resource management in the catchment and reservoirs, allowing for the maintenance of the current morphometric parameters in the context of climate change, adverse environmental phenomena, and increased anthropogenic pressure occurring in the catchment area. The obtained results can be applied to other lowland reservoirs in Europe in a similar climatic zone.

2. Materials and Methods

The physical–geographical description of the analysed area was based on information from orthophotomaps, topographic and hydrographic maps available on the Geoportal website [20], and raster geological maps at a scale of 1:50,000 provided on the website of the Polish Geological Institute—National Research Institute [21]. Land use forms were determined using data from Corine Land Cover 2021, downloaded from the website of the Chief Inspectorate for Environmental Protection [22]. The historical extent of the Pakoski Reservoir was determined using maps obtained from the Archive of Western Polish Maps [23]. The hydrological and meteorological characteristics of the Pakoski Reservoir catchment were based on data from the Institute of Meteorology and Water Management—National Research Institute (Figure 1), and water level fluctuations in the reservoir were plotted based on data from the State Water Holding Polish Waters. All hydrological and meteorological analyses were conducted using hydrological years, i.e., from 1 November of the previous year to 31 October of the year under analysis. In the development of hydrological characteristics, daily data on water levels and water flows from water gauge stations located in Goryszewo on the Panna River, Gębice on the Mała Noteć River, Pakość on the Noteć River, Kruszwica on Gopło Lake and data from water gauge observations conducted on the Pakoski Reservoir were used. Meteorological characteristics were based on daily data from the climatological station in Kołuda Wielka and the precipitation station in Gębice. Based on daily data, characteristic monthly and annual values were determined and shown in charts presenting trends for individual parameters.

The analysis of the possibility of supplying the Pakoski Reservoir from the Noteć River was carried out based on the location of the water table above the Pakość weir on the Noteć River and in the Pakoski Reservoir. The days on which the water table in the Noteć River was higher than in the Pako Reservoir were indicated as potential periods of water supply to the reservoir from this river. New damming elevations for the Pakoski Reservoir were determined based on the history of elevation changes in the reservoir in relation to changes in flow rates in the Mała Noteć River and the Panna River, as well as climatic trends determined on the basis of analyses carried out at the nearest climatological stations. The descriptions and diagrams of the hydrotechnical structures were based on the current water law permit, which allows for the operation of the Pakoski Reservoir, and the attached water management instruction for the reservoir [24].

The resulting maps were created with reference to the Kronstadt ’86 height reference system and the current Polish State Geodetic Coordinate System 1992.

The analyses of numerical data were carried out in MS Office and the maps were drawn in QGIS.

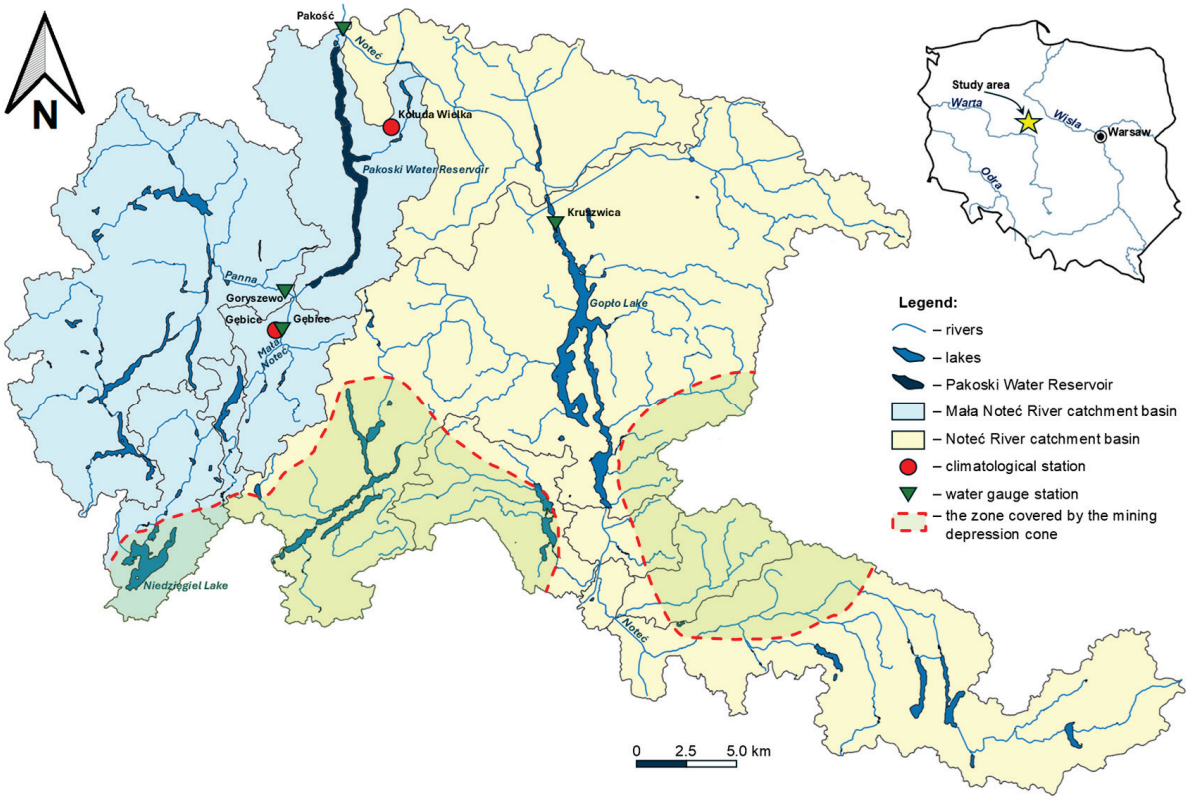

Figure 1. Pakoski Reservoir catchment (source: own elaboration based on IMGW-PIB data).

3. Study Area

The Pakoski Reservoir is located in the Kuyavian–Pomeranian Voivodeship, within the Inowrocław and Mogilno counties, spanning the municipalities of Pakość, Janikowo, Mogilno, and Strzelno. The reservoir begins south of Pakość at kilometre 1 + 825 of the Mała Noteć River, where the main dam is situated, and extends to kilometre 22 + 200 of this river near the village of Nowy Młyn (Figure 1). In addition to the main dam and the reservoir basin, the Pakoski Reservoir's hydrotechnical infrastructure includes the Skalmierowice side dam, which separates the reservoir basin from the old Noteć riverbed, as well as the Pakoski hydrotechnical complex structure with channels distributing water among the Noteć, Mała Noteć, and the reservoir.

The catchment area of the Pakoski Reservoir, calculated as the drainage area of the Mała Noteć River, amounts to a total of $A_{całk}$ = 727.0 km^2, of which the direct catchment area is A_{bezp} = 118.9 km^2. By considering the potential for water diversion into the Pakoski Reservoir from the Noteć River through the Pakoski hydrotechnical complex, the effective catchment area increases by an additional A = 1567.45 km^2. As previously mentioned, the primary river supplying the reservoir is the Mała Noteć, originating from Lake Niedzięgiel. Its largest tributary is the Panna River, which flows into the Mała Noteć 1.3 km upstream of its entry into the Pakoski Reservoir (Figure 1).

The catchment areas of both rivers encompass lakeland regions. They have a sandy–clayey character and are utilised in diverse ways. Larger forest complexes dominate the southern and western parts of these areas, while the central and northern regions are primarily agricultural lands. The direct catchment of the Pakoski Reservoir and its smaller tributaries, forming the northern supply area, mainly consists of fields established on drained clay deposits. This land structure contributes to uneven water supply patterns to the reservoir and its tributaries. During wet periods and the winter–spring thaw, there is a rapid runoff toward local watercourses. These watercourses converge, causing distinct

short-term flow peaks (Figures 2 and 3). This is reflected in unit runoff values during very wet periods, reaching q > 32.0 L s km^{-2} in the Mała Noteć catchment and q > 20.0 L s km^{-2} in the Panna catchment. In contrast, during rainless periods with heightened evapotranspiration, these rivers carry minimal water, with flows of just a few litres per second. This results in unit runoff values in dry months of q = 0.04 L s km^{-2} for Mała Noteć and q < 0.26 Ls km^{-2} for Panna. In the upper sections of these rivers and their tributaries, prolonged episodes of complete flow cessation have been recorded over many years. This issue is particularly severe in the Mała Noteć, where its headwater section has been dry since 2014 [25], and in Panna's spring zone, where significant declines in lake water levels have also been observed [26].

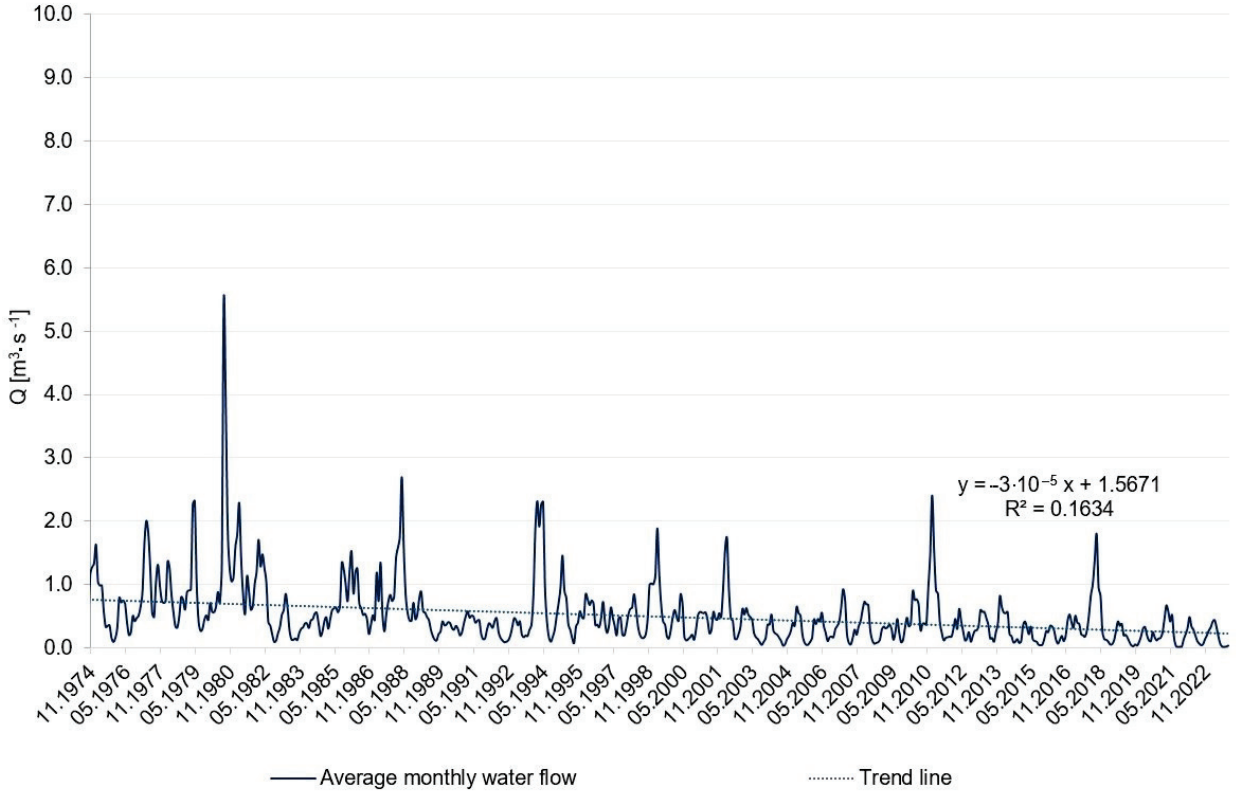

Figure 2. Monthly average water flows in the western Noteć at the Gębice water gauge station (source: own elaboration based on IMGW-PIB data).

According to Kondracki's classification [27], the analysed water body is located within the Gniezno Lakeland, with its catchment area additionally covering the Kuyavian Lakeland and the Inowrocław Plain. This region has long been characterised by some of the lowest precipitation levels in Poland, averaging 500–550 mm per year (Figure 4). An additional factor contributing to the area's low water availability is the long-standing trend of rising temperatures (Figure 4). This warming, combined with the increasing frequency of dry continental air masses with higher vapour pressure deficits, results in an unfavourable climatic water balance [28–30]. Consequently, the reservoir faces limited recharge potential. These adverse atmospheric conditions are exacerbated by significant water withdrawals for agricultural and industrial purposes, creating one of the most severe water deficits in the country [25,31–33].

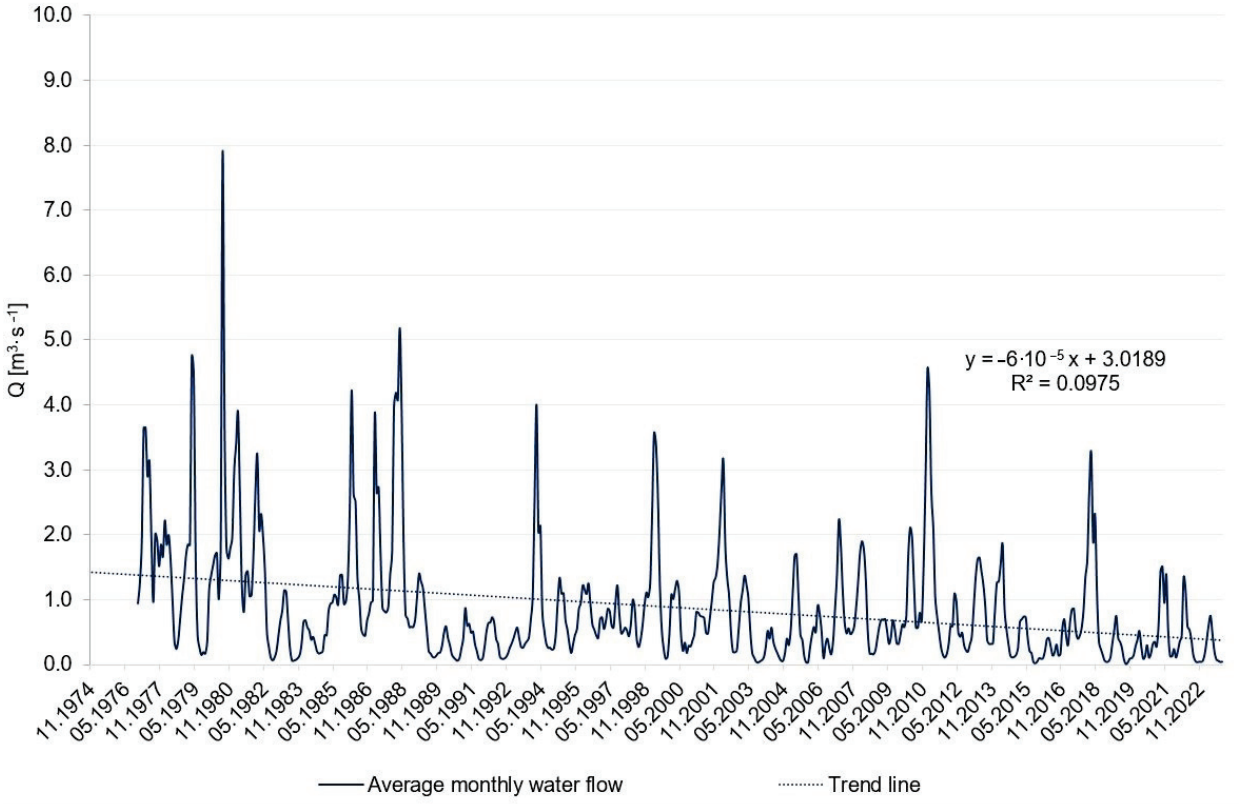

Figure 3. Monthly average water flows in the Panna River at the Goryszewo water gauge station (source: own study based on IMGW-PIB data).

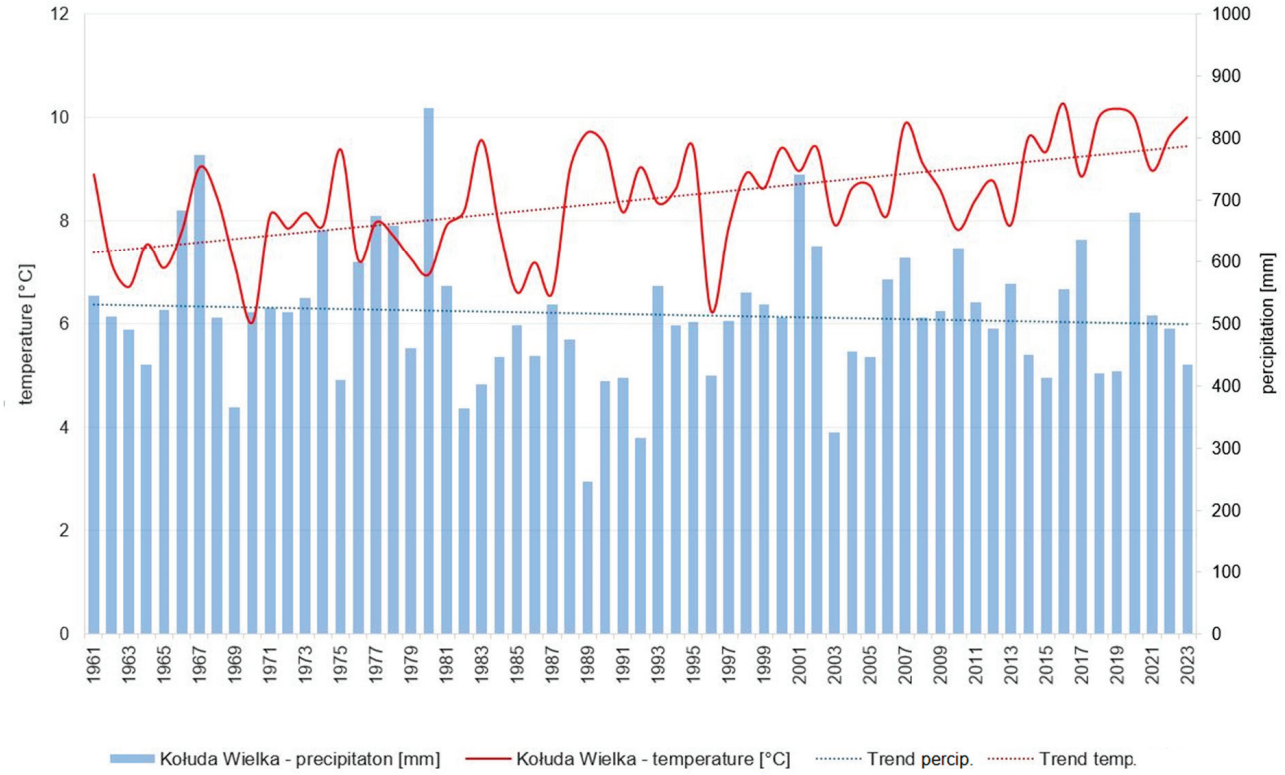

Figure 4. Annual precipitation and average air temperature on climatological station Kołuda Wielka (source: own elaboration based on IMGW-PIB data).

Given the uneven distribution of river flows in the region and the growing industry in the southern part of Kujawy, a decision was made in the second half of the 20th century to construct the Pakoski Reservoir. It was established in 1975 as part of a lake damming programme implemented in the Noteć River basin. The damming aimed to regulate the water balance in the Noteć River basin, which had been disrupted by 19th-century Prussian drainage works; meet the growing demand for water due to the development of nearby industrial facilities; supply water for agriculture; provide flood protection for the middle Noteć valley; and sustain river flow during low-water periods to support navigation. The primary water consumers from the reservoir were intended to be the Soda Works in Janikowo and Mątwy, as well as the aforementioned agriculture and navigation sectors.

The Pakoski Reservoir was created by raising the waters of the Mała Noteć River by 4.5 m in its lower section, encompassing its valley and the basins of three associated lakes (Pakoskie Północne, Pakoskie Południowe, and Bronisławskie). The combined surface area of the bodies of water increased by 60%, from 8.1 km^2 to 13.0 km^2, while the volume grew by 110%, from 40.6 million m^3 to 86.5 million m^3. The maximum water level was limited by the topography of the area and the need to preserve existing infrastructure, primarily a road bridge and a railway line crossing the river valley. The impounding of water caused flooding of the floodplain of the Noteć River between the lakes, as well as a 2.5 km section above Lake Bronisławskie. The flooded areas included the reed belt surrounding the lakes, the adjacent and river-connected peatlands (mainly between the Pakoskie Lake and Lake Bronisławskie), and arable land up to a width of several to 100 m. During the creation of the reservoir, approximately 90,000 trees were planted in its immediate vicinity, including mostly willows (*Salix* sp.), black alders (*Alnus glutinosa*), and linden trees (*Tilia* sp.) [34,35].

The reservoir has an elongated shape, resulting from its location within the subglacial trough of the Skorzęcińsko–Pakoska valley, which divides the Gniezno Upland and the Kuyavian Upland [36]. The depth of the upland cut relative to the trough floor ranges from 20 to 50 m. This form is locally filled with 5–10 m thick lake deposits, including gyttja and peat. The western slopes of the trough are higher but gentler, with a width of about 750 m, while the eastern slopes are narrower, about 250 m wide. The eastern shores often feature cliffs [19,34,35]. The reservoir is divided by three artificial embankments used as roads or railway embankments. As a result, it is divided into four distinct parts, which correspond to the former bodies of water and depressions from which it originated. These include Lake Pakoskie Północne (Janikowskie), Lake Pakoskie Południowe (Trląg), Lake Bronisławskie, and Lake Kunowskie (Figure 5). The morphology of the reservoir bed is very varied, influenced by factors such as the numerous shallows and deep areas of the impounded lakes, the winding and incised channel of the Mała Noteć River, and the flattened areas of the reservoir bed created by flooding the river terraces and historical biogenic accumulation plains associated with the old lake bays. It is also worth noting that the reservoir bed slopes asymmetrically. The eastern slope of the basin is steeper than the western one, as are the depths near the shoreline. The western slope is gentler, with extensive shallow areas along the shoreline. The flooded strip, between elevations 74.9 and 79.4 m above sea level, reaches over 100 m in width with a slope of 6–7°. The reservoir basin's morphology also features two depressions. The first is located in the northern part of Lake Pakoskie Północne, while the second is at the entrance to the Kołudzka Bay in the central part of Lake Pakoskie Południowe.

Figure 5. The range of lakes comprising the Pakoski Water Reservoir in 1940 (**A**) and 2012 (**B**) (source: own elaboration based on materials from the Archive of Maps of Western Poland—http://mapy.amzp.pl/tk25.cgi?11,36,50,103—and the Geoportal website [20]—accessed on 8 November 2024). The reservoir's shores are lined with a strip of woodland, which is periodically submerged. The total shoreline length is approximately 50.6 km, with about 15% of it reinforced with stone riprap. This mainly concerns the dams intersecting the reservoir, including embankments and road and railway

embankments, as well as the front and side dams [19]. Unprotected shores are subject to abrasion, and to a lesser extent, accumulation. The eastern shore, where cliffs rise up to 5 m in height, is more heavily transformed. In the southern part of the reservoir, dense reedbed communities are present, mainly composed of reedbeds overgrown with willows (*Salix* sp.). The shores of the lake are partially forested (Figure 5B). Behind the reedbed and wooded strip, fields and buildings dominate the landscape. The largest settlements located near the reservoir include Pakość to the north, Janikowo and Bronisław on the eastern shore, and Trląg and Głogówiec on the western shore.

According to the valid water permit [24], which defines the operational rules of the reservoir, the damming levels of its water level are as follows:

Absolute Minimum Damming Level (Absolute MinPP) = 74.93 m a.s.l.;

Minimum Damming Level (MinPP) = 75.50 m a.s.l.;

Normal Damming Level (NPP) = 78.85 m a.s.l.;

Maximum Damming Level (MaxPP) = 79.40 m a.s.l.

At the characteristic operational elevations, the surface area and capacity of the reservoir are as follows: P_{MinPP} = 8.35 km^2 and V_{MinPP} = 45.10 million m^3; P_{NPP} = 12.20 km^2 and V_{NPP} = 80.46 million m^3; and P_{MaxPP} = 13.02 km^2 and V_{MaxPP} = 86.46 million m^3. The usable capacity of the reservoir (Vu) is 41.36 million m^3. The remaining morphometric parameters of the reservoir, determined at the NPP level, are as follows:

Maximum length—20.1 km;

Maximum width—2.0 km;

Average width—0.74 km;

Maximum depth—18.6 m;

Average depth—9.2 m;

Length of shoreline—50.55 km.

According to the instructions mentioned above, the Pakoski Reservoir is filled to the elevation of 78.85 m a.s.l. (i.e., NPP) during the period from 16 September to 15 March. In the case of a spring flood event between 16 March and 15 May, it is intended to capture excess water within the flood storage capacity, which operates between NPP and MaxPP, set at the elevation of 79.40 m a.s.l. From 16 May to 15 September, the reservoir undergoes a gradual emptying phase to the MinPP level of 75.50 m a.s.l. In the case of extremely unfavourable hydrological–meteorological conditions and increased water demand from users located downstream of the reservoir, lowering the water level to the Absolute MinPP of 74.93 m a.s.l. is permitted (see Figure 6).

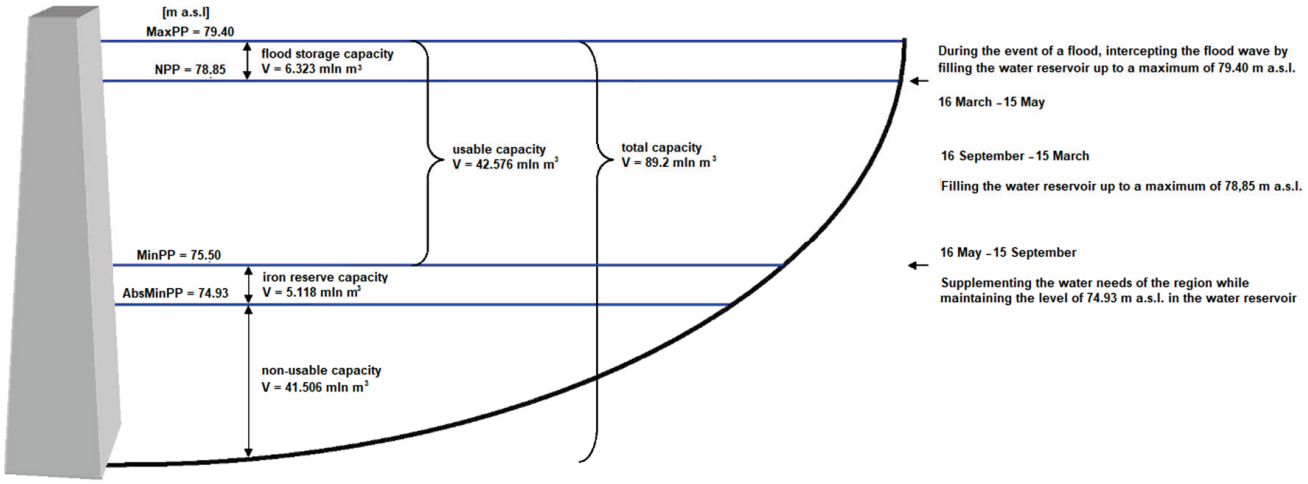

Figure 6. Diagram of water management in the Pakoski Reservoir (source: own elaboration based on data of PGW Wody Polskie).

The recreational functions of the Pakoski Reservoir are limited by its poor water quality, which, according to materials published on the website of the Chief Inspectorate of Environmental Protection [36], has been in poor ecological condition for many years. The poor water quality is a result of long-term contamination from nearby agricultural fields, as well as domestic and industrial sewage. The waters of the reservoir qualify as out of class, among others, due to exceeding the standards for nitrogen and phosphorus compounds. The sediments contained significant amounts of heavy metals, aromatic hydrocarbons, chloride ions, and plant protection products. Despite the poor transparency and frequent algae blooms, the reservoir still has functioning beaches and recreational areas, such as in Janikowo [37]. The reservoir is also an excellent place for fishing, particularly known for its large pike-perch (*Sander lucioperca*). Other fish species found in the reservoir include perch (*Perca fluviatilis*), bream (*Abramis brama*), roach (*Rutilus rutilus*), rudd (*Scardinius erythrophthalmus*), common crucian carp (*Carassius carassius*), silver crucian carp (*Carassius gibelio*), carp (*Cyprinus carpio*), white amur (*Ctenopharyngodon idella*), and eel (*Anguilla anguilla*). The large surface area of the reservoir also makes it suitable for various water sports, such as sailing and windsurfing.

4. Results

The functions performed by the Pakoski Reservoir, along with its operating instructions, dictate the water level regime in the reservoir. During the winter–spring period, meltwater is collected to prevent flooding in the Noteć valley below the reservoir and to store it for industrial purposes. In the summer–autumn period, the stored water is used for field irrigation and to ensure the flow of water in the Noteć River. Due to its functions and the fact that nearly half of the water stored in the reservoir is usable capacity, significant fluctuations in water levels occur throughout the year (Figure 7). According to the operation instructions for the reservoir, the permissible amplitude of water level fluctuations is 3.9 m, ranging from 75.5 m above sea level (0.6 m above the maximum water levels recorded in the lakes before their impoundment) to 79.4 m above sea level. These changes in water levels occur steadily, interrupted only by heavy rainfall episodes directly over the reservoir. In the autumn–winter period, the trend is upward, and in the spring–summer period, it is downward. The water levels change uniformly by one to several centimetres per day. Over the course of the year, there are no periods of prolonged water levels remaining at the same level. After analysing the water level in the reservoir throughout its operational period (Figure 7), it can be concluded that the permissible water levels were only exceeded in critical situations, with the highest water level reached during the flood of July 1980. Water levels were lowered below the permissible minimum only in the first years of operation (1975–1980). The lowest water levels in the full operational range of the reservoir were recorded at the turn of the 1980s and 1990s, in 2003, and in the years 2019–2021, when significant drops in water levels were also observed in central and western Poland [38]. Based on available data, the annual water level amplitudes in the reservoir were determined, averaging H = 2.12 m, and ranging from H = 0.62 m in 2015 to H = 3.83 m in 1977. The difference between the highest and lowest water levels throughout the entire operation period of the reservoir is H = 4.35 m.

Such significant annual water level fluctuations lead to considerable changes in the reservoir's surface area over short periods. During years characterised by extreme wet or dry conditions, with maximum water level amplitudes, the reservoir's surface area can change by 4.7 km^2 and its volume by 42.6 million m^3 within a few months. This means that one-third of the reservoir's basin can be periodically flooded and dried out. In accordance with the water management instructions, high water levels typically occur during the spring–summer transition, while low levels dominate the autumn–winter period.

This operational scheme limits vegetation growth on the reservoir bed by preventing macrophyte colonisation in the lower parts. However, periods of several consecutive years with the reservoir not being filled, coupled with persistently low water levels throughout the year, expose large sections of the reservoir bed during vegetation periods. This fosters accelerated plant succession, which is particularly noticeable in the littoral zone. This process was especially intense during the late 1980s and early 1990s and over the past five years. Exposed sections of the bed were quickly colonised by reed beds and hygrophilous trees, which were subsequently submerged during reservoir refilling. This caused the decomposition of organic matter and an additional influx of nutrients into the reservoir's waters. A reduced water volume also negatively affects the breeding of various fish species and other organisms, particularly those whose life cycles are tied to reed beds and shallow littoral zones. Moreover, low water levels pose potential risks for reservoir users, limit the possibilities for water-based recreation, and hinder activities dependent on stable water availability.

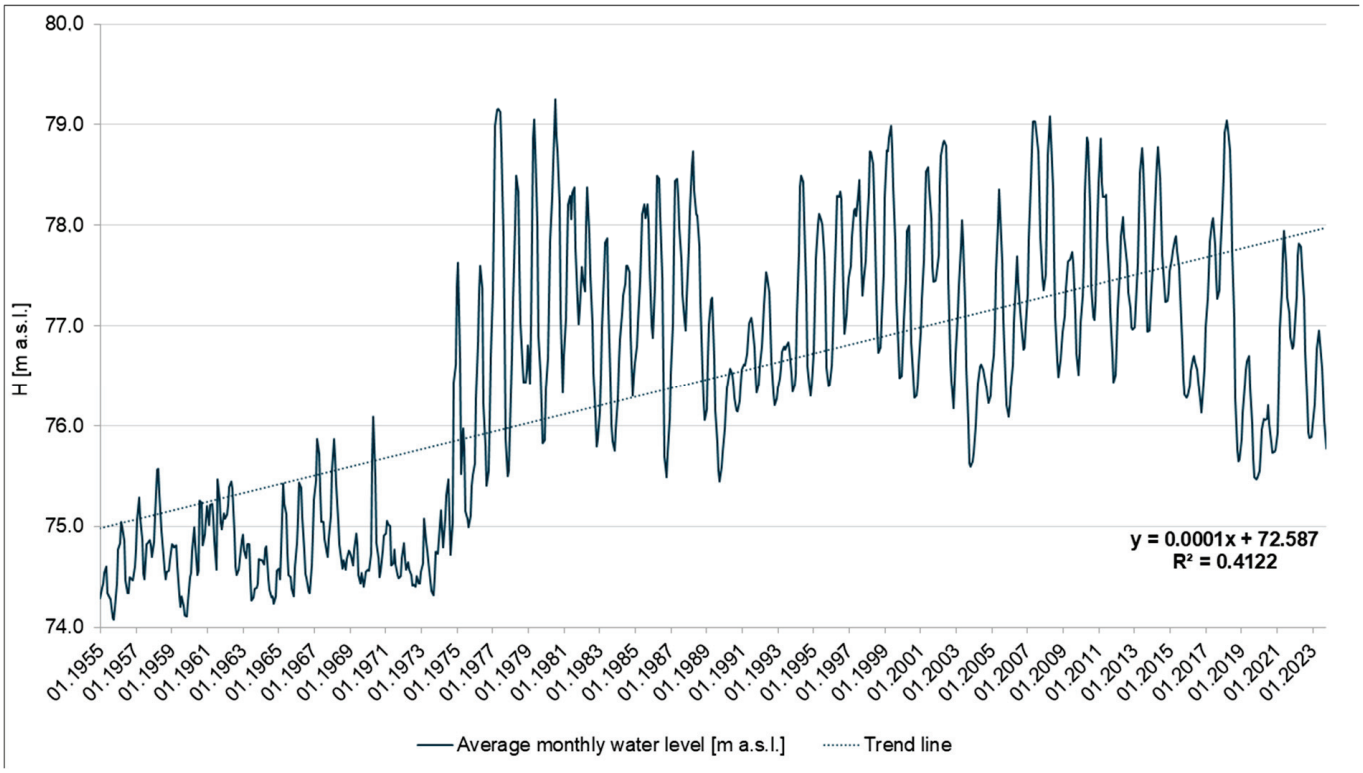

Figure 7. Average monthly water levels in the Pakoski Reservoir (source: own elaboration based on data of IMGW-PIB and PGW Wody Polskie).

Difficulties in filling the Pakoski Reservoir are largely the result of climate change and reduced water inflow. As previously mentioned, the average annual precipitation in the reservoir's catchment does not exceed 550 mm and remains relatively stable both temporally and spatially, with a slight decrease towards the southeast. However, potential evaporation from water surfaces, as well as evapotranspiration responsible for water loss from land, has significantly increased over the past 30 years. From levels of 650–750 mm/year, these values have now consistently exceeded 800 mm/year. The intensified evaporation from water and land surfaces, combined with an extended vegetation period, has led to increased water losses in the catchment and directly from the reservoir. The lack of snow and ice cover further limits water accumulation in the soil during the cold season and prevents winter–spring floods, which historically helped fill the reservoir. Another critical factor in reducing water inflow is the exclusion of upper parts of the catchment area due to

lowered water levels in the lakes feeding the Mała Noteć and Panna rivers and their tributaries. Key examples include the non-flowing lakes Niedzięgiel and Białe, located in the Mała Noteć's source area, and Lake Ostrowickie, part of the Panna Południowa's source area. High evaporation rates, years of low precipitation, and regional groundwater level declines—linked to hydraulic connections with these lakes—have caused their water tables to drop to the extent that their outflow channels have dried up. Consequently, the Pakoski Reservoir's supply area, being the final recipient of waters from these catchments, has shrunk. To illustrate the scale of this problem, comparing the flow rates in the Mała Noteć and Panna at their gauge stations just before the Pakoski Reservoir reveals a declining trend in unit runoff. Despite similar environmental conditions (precipitation, land use, soil composition, and lake coverage), the Mała Noteć basin, more affected by surface water and groundwater declines, shows a more pronounced negative trend. Analysis of runoff trends from 1975 to 2023—the operational period of the reservoir—shows stable unit runoff values during the late 20th century when averaged over wet and dry years. However, in the 21st century, a marked decline has occurred, which is more evident for the Mała Noteć. For instance, at the Gębice water gauge station, the unit runoff decline is approximately 0.8 L s km^{-2} per decade, compared to 0.6 L s km^{-2} per decade at the Goryszewo water gauge station for the Panna River (Figure 8). The decline in groundwater levels, driven by municipal and industrial water withdrawals, long-term mining dewatering associated with lignite extraction in the Konin region, and increasing water use for agricultural irrigation, exacerbates the problem. It not only reduces the inflow from lakes and rivers but also limits the groundwater stream directly feeding the Pakoski Reservoir.

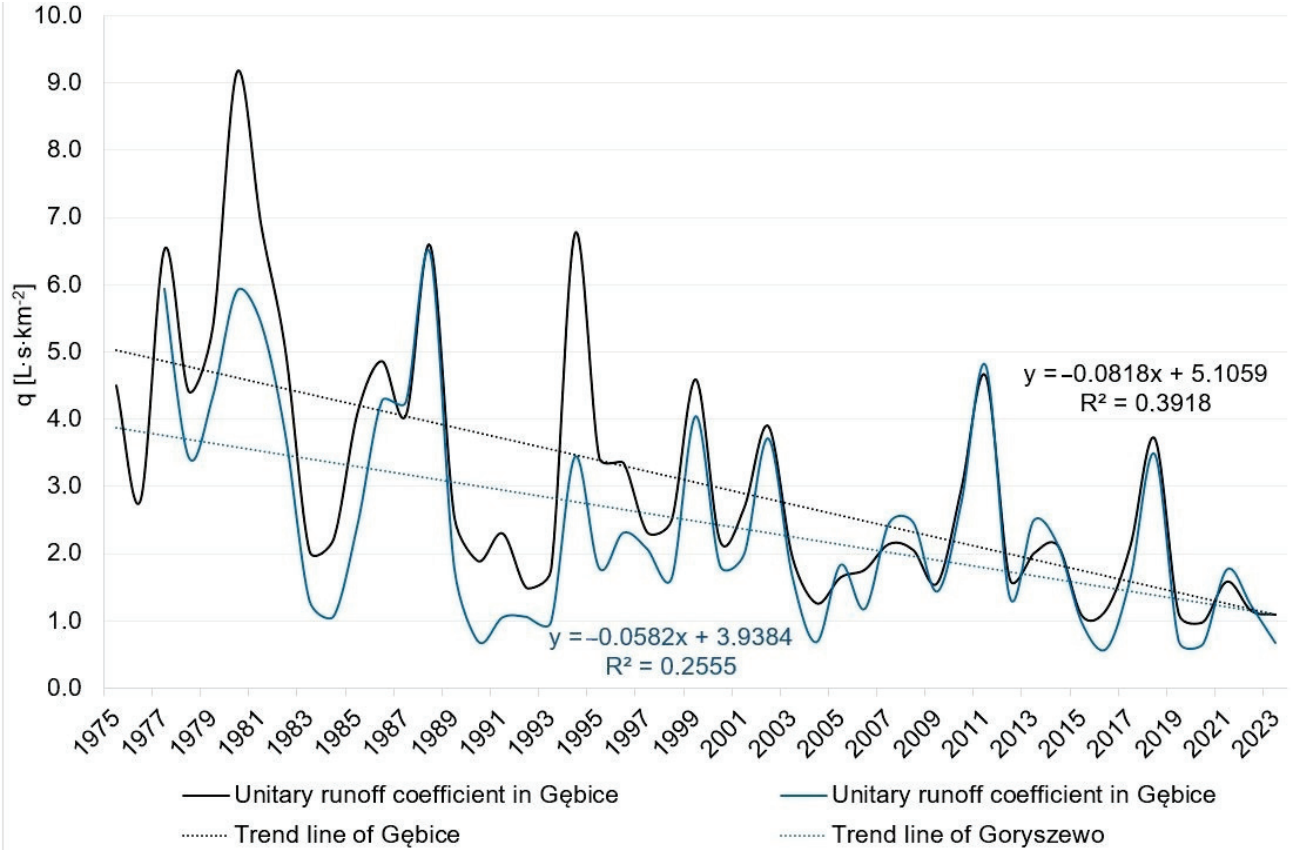

Figure 8. Changes in the unitary runoff coefficient in Mała Noteć and Panna in the period of functioning of the Pakoski Reservoir (source: own elaboration based on IMGW-PIB data).

In addition to contemporary anthropogenic factors affecting the water resources of the Pakoski Reservoir, attention should also be paid to transformations that occurred hundreds

of years ago. At the end of the 18th century and in the mid-19th century, extensive land reclamation works were carried out in this area to canalise the Noteć River and parts of its tributaries and to convert previous wetland areas into arable land [18,38,39]. These works, in addition to improving navigability on the Noteć River and reclaiming thousands of hectares of fertile soil, resulted in the lowering of surface water and groundwater levels across the entire Noteć catchment and adjacent areas, reshaping the river network and disconnecting selected water bodies from their alimentation zones. The Noteć River, which used to flow through northern Lake Pakoskie, was dammed with an embankment and a sluice in Leszczyce, and its waters were diverted to the Noteć Canal, built in 1774. This canal bypassed the Pakoski Reservoir, directing water northward and connecting to the Bydgoszcz Canal in the Toruń–Eberswalde Ice-Marginal Valley to the east and to the main Noteć River to the west. As a result of these modifications, the primary river feeding the Pakoskie Lake became the Mała Noteć, whose recharge area was also reduced due to the construction of the Ostrowo–Gopło Canal, which redirected the southwestern streams that had previously fed it toward Lake Gopło. Consequently, the catchment area of the former Pakoskie Lake was reduced from its original ~2240 km^2 to 727 km^2. Over the next several decades, these works led to a long-term lowering of groundwater levels and the water table in lakes in the region by up to 2.5 m [18,39]. In the former Pakoskie Lake, the water table dropped by 76 cm, and in Lake Bronisław, it dropped by 66 cm [38]. The surface area of the latter decreased by 42%.

Observing such drastic negative changes in the hydrology of the area, the Prussian authorities at the time initiated measures to limit water outflow from selected lakes and rivers, constructing retention and stabilisation structures and simultaneously facilitating flow management during flood periods [19]. This programme also included Lake Pakoskie, whose water level, after stabilisation in the early 20th century, was set at approximately 75.0 m above sea level, with water level fluctuations ranging from 0.5 to 0.6 m.

The next stage of works in the catchment area involved the construction of the Pakoski Reservoir by damming the waters of the Mała Noteć River at the outflow from the northern Pakoskie Lake with a frontal dam and protecting the bed of the Old Noteć River with a side dam to prevent flooding from the impounded lake waters. During this period, the Pakość weir and associated canals were also built, enabling the regulation of water flow and transfer between the Noteć, Mała Noteć, and Pakoski Reservoir (Figure 9). Another function of the weir is to control the water level in Lake Gopło, located about 21.5 km from this hydrotechnical structure.

When describing the Noteć River and Lake Gopło, it is essential to note that significant disruptions have occurred in their hydrological recharge regimes. Due to mining activities associated with open-pit lignite extraction, as well as regional lowering of surface water and groundwater levels, certain areas within the potential recharge zone of Lake Gopło have been periodically or permanently excluded. These areas include the upper parts of the Noteć River catchment [31,32], the catchments of southeastern tributaries of Lake Gopło, the Ostrowo–Gopło Canal catchment located in the Powidzko–Ostrowska trough lake region [40–47], and the catchments of the Skulskie lakes. Partial compensation for the lost water resources has been achieved through the redirection of drainage water from the Lubstów and Tomisławice open-pit mines directly to the Noteć River or its tributaries [31,48] and by supplying the Noteć River through the Gawrony weir, which allows discharges from the summit section of the Ślesiński Canal (Figure 9) [49]. However, it should be noted that in the coming years, as more mines close, discharges of mining water toward the Noteć River will decrease, while the demand for water in areas affected by the mining-induced depression funnel to the east of Lake Gopło will remain constant. A similar situation is currently observed in the Biskupia Struga and Ślesiński Canal catchments, from

which it is becoming increasingly difficult to allocate water to the Noteć system. In the coming years, due to water drainage by flooded pits located near the lakes of the Ostrowo–Gopło Canal, it is expected that reduced water flows in this second-largest tributary of Lake Gopło will persist. For many years, the catchment area of this watercourse, spanning over 300 km^2, has been characterised by the absence of unit runoff. Until the groundwater levels and lake water tables return to their mid-1980s levels, this area is unlikely to contribute to the alimentation of Lake Gopło.

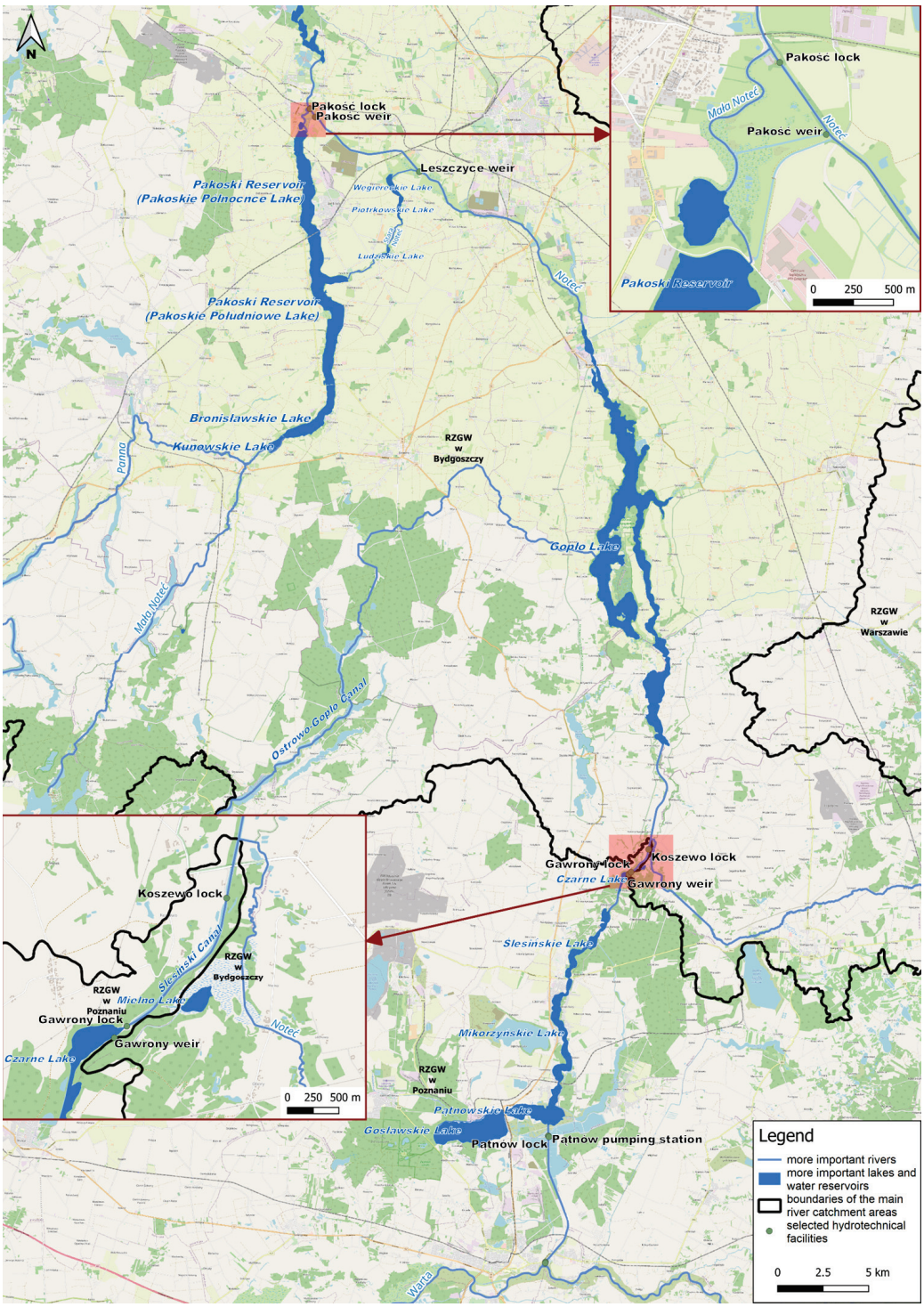

Figure 9. Water availability in the area of potential alimentation of the Pakoski Reservoir (source: own elaboration based on materials of PGW Wody Polskie).

5. Discussion

The intensifying effects of climate change, which result in sudden water surges on one hand and significant water deficits on the other, demand more effective actions in managing water reservoirs [50–52]. These efforts must aim to better utilise water resources within the catchment areas of these bodies of water [53]. Studies of the Pakoski Reservoir have shown that deepening water deficits, particularly severe in central Poland, lead to challenges in filling the reservoir, which in turn impacts its functionality. When revising the reservoir's replenishment and usage scheme, it is crucial to maintain its existing functions, meet the water needs of users reliant on its resources—including those of the upper Noteć River—and ensure the functioning of the Pakoski Reservoir ecosystem. Recent years have demonstrated that the greatest challenge facing the reservoir's management is filling it to the target operational water level (NPP) during the winter–spring period and then maintaining that level while ensuring a minimum outflow during the summer months. Snowless winters, high evapotranspiration, and groundwater withdrawals reduce the inflow of water to the reservoir and its tributaries. Consequently, its retention functions and the ability to supply water to the middle Noteć are becoming increasingly difficult to sustain. The intensifying effects of climate change, which result in sudden water surges on one hand and significant water deficits on the other, demand more effective actions in managing water reservoirs. These efforts must aim to better utilise water resources within the catchment areas of these bodies of water. Studies of the Pakoski Reservoir have shown that deepening water deficits, particularly severe in central Poland, lead to challenges in filling the reservoir, which in turn impacts its functionality.

When revising the reservoir's replenishment and usage scheme, it is crucial to maintain its existing functions [5,51,53], meet the water needs of users reliant on its resources—including those of the upper Noteć River—and ensure the functioning of the Pakoski Reservoir ecosystem. Analyses of the recent years have demonstrated that the greatest challenge facing the reservoir's management is filling it to the target operational water level (NPP) during the winter–spring period and then maintaining that level while ensuring a minimum outflow during the summer months. Snowless winters, high evapotranspiration, and groundwater withdrawals reduce the inflow of water to the reservoir and its tributaries. Consequently, its retention functions and the ability to supply water to the middle Noteć are becoming increasingly difficult to sustain. At the same time, it should be noted that the Mała Noteć River, due to the desiccation of its southern sections and the exclusion of parts of its recharge area (see Figure 1), currently exhibits a very low probability of flooding. Therefore, it is worth considering adjustments to the reservoir's water levels and adopting a more flexible approach to water management during periods of reservoir filling and utilisation.

Considering the above, and particularly to increase the permanent water reserve available to reservoir users and entities in the upper Noteć valley, it is proposed to raise the Absolute Minimum Operating Water Level (MinPP) to the current MinPP level of H = 75.50 m a.s.l., and the MinPP to H = 77.00 m a.s.l. No changes are required for other operational water levels. This approach would reduce the reservoir's water demand during its filling period while maintaining a safe flood reserve. Additionally, a more flexible approach to the dates limiting reservoir filling and utilisation is recommended. Specifically, it is suggested to extend the filling phase until 15 May if the target operating water level (NPP) is not reached by 15 March. This recommendation is driven by changing winter patterns, which no longer feature prolonged snow cover. In earlier years, snowmelt during spring thaws provided a rapid increase in river levels, enabling a swift recovery of the reservoir's water resources while posing a potential flood risk to areas in the upper and middle Noteć valleys. It should also be noted that, during the autumn and winter, if the

Mała Noteć catchment and the reservoir's recharge zone experience significant rainfall and persistent snow cover exceeding 15 cm by the end of February, winter water intake should be limited. In such cases, the reservoir's water level should not rise by more than 1–2 cm per day. If rising temperatures lead to rapid snowmelt and a corresponding surge in inflows to the reservoir's primary tributaries, the Mała Noteć and Panna Rivers, reaching a flow rate of Q = 3.5 m^3/s, measures should be taken to suppress the flood wave passing through the reservoir. During such conditions, an increase in the reservoir's water level of up to 5 cm per day would be permissible.

In the event of a prolonged hydrological drought, when the combined flow rates of the Mała Noteć at the Gębice gauging station and the Panna at the Goryszewo gauging station do not exceed Q = 0.5 m^3/s during the early filling phase of the Pakoski Reservoir, measures should be taken to utilise water from the Notecki Canal (Noteć) to support the reservoir's inundation. As previously demonstrated, until the mid-19th century, Lake Pakoskie Północne, which forms the core of the Pakoski Reservoir, was fed by both the Mała Noteć and the Noteć. The Noteć, with its larger catchment area, is more water-rich. Currently, the Noteć carries mine drainage water from the Tomisławice open-pit mine and benefits from additional discharges from the peak section of the Ślesiński Canal. As a result, water flows in the Noteć at the Pakość weir, particularly during winter and spring, are typically 2–3 times greater than those in the Mała Noteć before its confluence with the Pakoski Reservoir. During these periods, water levels in both the Noteć and Lake Gopło are often higher than in the Pakoski Reservoir (Figures 10 and 11). Over the past six years, such conditions occurred for more than half of the time (1193 days out of a total of 2190).

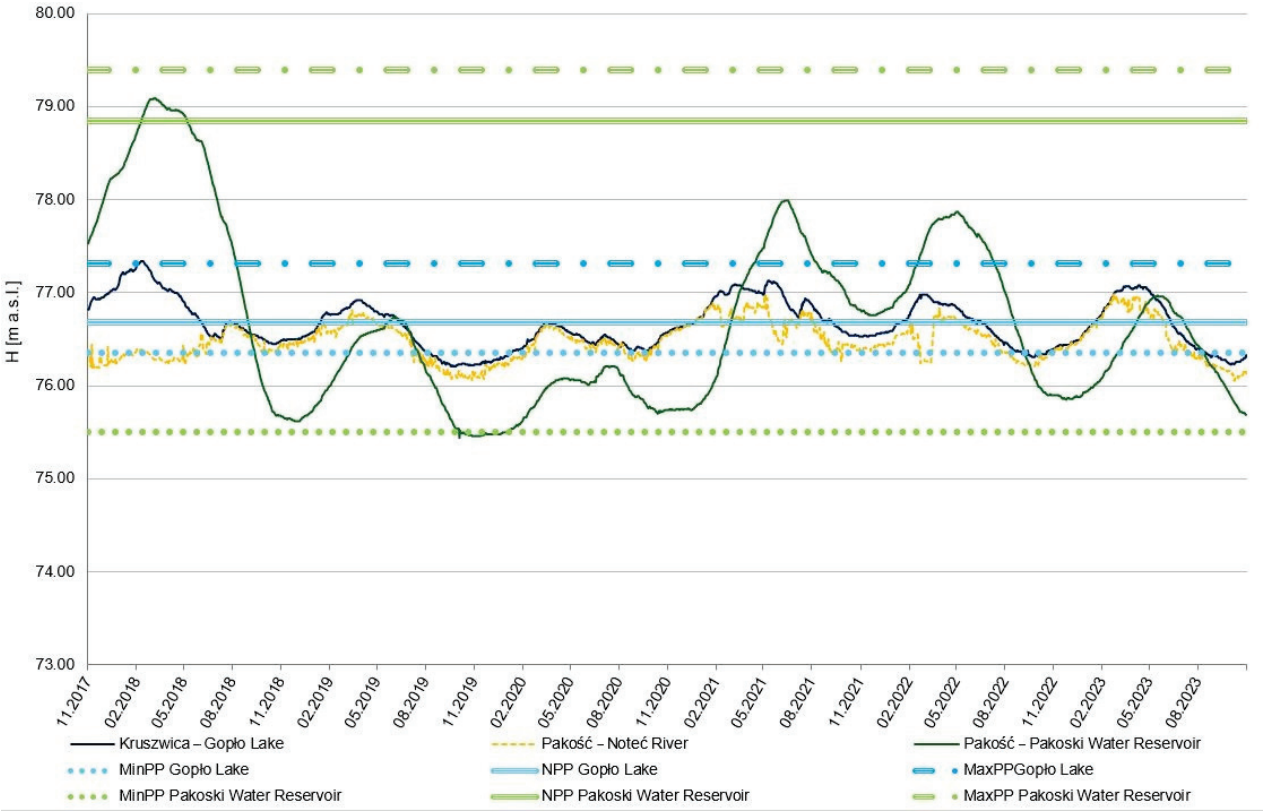

Figure 10. Comparison of water levels in the Noteć River, Pakoski Reservoir, and Lake Gopło against their operational damming levels in 2018–2023 (source: own elaboration based on data from IMGW-PIB and PGW Wody Polskie).

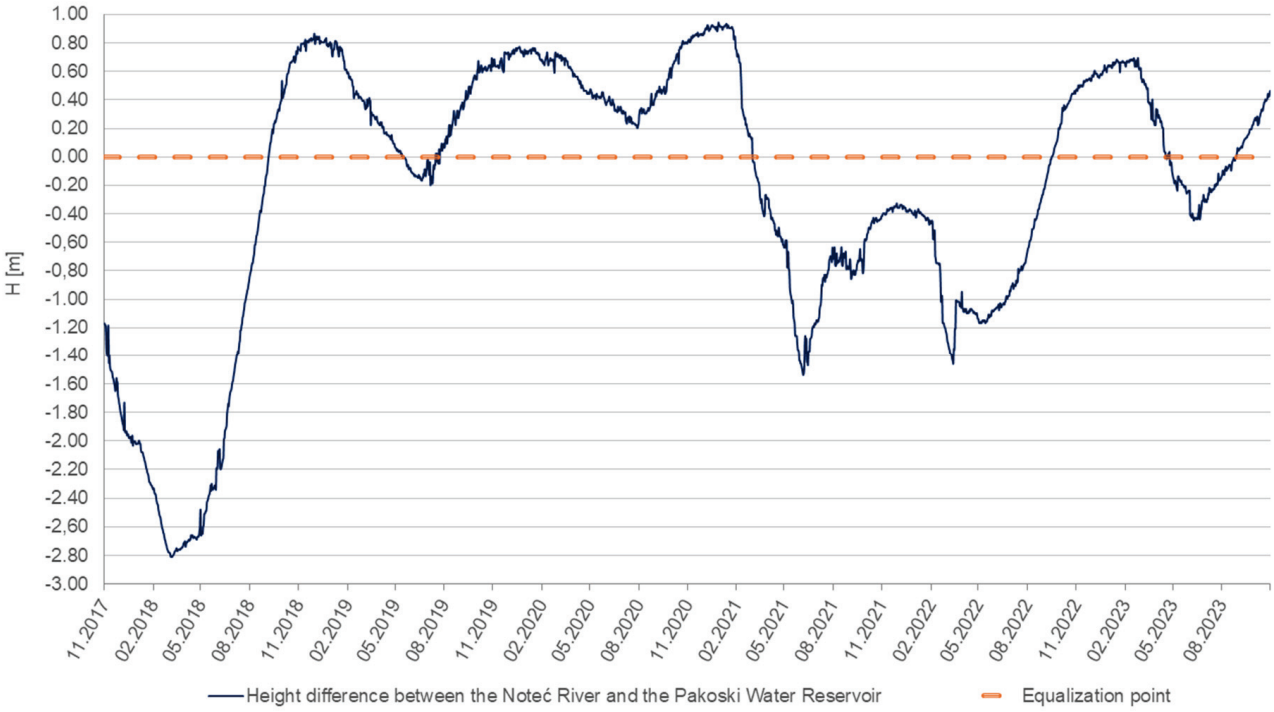

Figure 11. Periods of potential water supply to the Pakoski Reservoir from the Noteć River in 2018–2023 (source: own elaboration based on data from PGW Wody Polskie).

By utilising these additional water resources from the Noteć, along with the distribution of water levels in the Pakoski Reservoir and the Noteć, and considering that the so-called Pakoski hydrotechnical complex allows for the regulation of water management in the lower section of the Mała Noteć and the canalised upper section of the Noteć from the town of Pakość upstream, through Lake Gopło and the Warta–Gopło Canal to the Koszewo lock, it is worth taking steps to redirect part of the water from the Noteć to the Pakoski Reservoir. This can be achieved by using the existing hydrotechnical infrastructure built in the 1970s as part of the Pakoski hydrotechnical complex, which allows such water diversion either through gravitational flow or by means of pumping stations.

Considering the average flows of the Noteć River below Pakość weir, amounting to Q = 5.5 m^3/s (IMGW-PIB data) and the need to maintain water flows in the river at levels that guarantee the water needs of users and preserve the functionality of the waterway on the Noteć, it seems that redirecting Noteć water to the Pakoski Reservoir at a rate of Q = 0.5 m^3/s would not deplete its resources. On the contrary, it would allow for a faster filling of the reservoir, at least until the water levels in the system of the Lake Gopło–Noteć–Pakoski Reservoir are equalised.

In the winter–spring period of the 2023 hydrological year, during which there was a shortfall of nearly 2 m to reach the NPP, this intervention would have allowed an additional 43,200 m^3/day to be introduced into the Pakoski Reservoir. Given the reservoir's morphometric parameters, this would result in a daily water level increase of almost 0.5 cm during periods of low water levels. If the water capture from the Mała Noteć were maintained at the same rate as it was in the considered year, and the reservoir was supplemented with water from the Noteć until the water levels in both systems were equalised, it would ultimately lead to an additional several tens of centimetres of water in the reservoir. It is worth noting that the proposed water extraction of Q = 0.5 m^3/s would constitute 11–44% of the flow in the Noteć River at the Pakość gauge, located downstream of the confluence with the Mała Noteć. Even better results could be achieved with the modernisation of the Pakoski hydrotechnical complex and the installation of new pumps,

which would facilitate water transfer once the water levels in the reservoir and the supply canal equalise. This action would not only increase water resources in the Pakoski Reservoir during drought periods but also enable the storage of water from potential discharges from the peak station of the Ślesiński Canal and mine drainage water from the Tomisławice open pit, which currently flow through the Warta and Oder rivers to the Baltic. Keeping these waters within the river-lake system of the Lake Gopło–Noteć–Pakoski Reservoir would help retain water in a region with the greatest water deficits in Poland [25,26,31–33].

6. Conclusions

In the face of observed changes in river hydrological regimes (snowless winters, heavy rainfall, and late rainy autumns and winters) and increasing challenges related to the operation of reservoirs located on these rivers, there is a need for a serious revision of existing water management instructions for many hydrotechnical facilities. These facilities were designed and have functioned for decades under different hydrological conditions and for different water needs. In many cases, the documentation that has been tested does not foresee actions related to water deficits (drought), focusing primarily on flood control functions. However, currently, especially in the lake districts and the central Polish lowlands, we observe a growing need to address the deficit in the hydrological balance, which is the result of changes in the size and distribution of water inflows to the catchment (intensity and character of rainfall and snowmelt) and water usage (including evaporation, transpiration, and water needs of users). Therefore, there is a need for a "flexible" approach to the operation of hydrotechnical facilities, which will allow for the most efficient use of their retention potential while maintaining their flood control function. Many of these hydrotechnical facilities require consideration of new supply conditions, changes in water needs, and associated functionality of the facilities, as well as the interrelationships between them. A particularly important shift in the approach to water resource management is indicated in the upper Noteć River area, which is characterised by a very unfavourable water balance and is subjected to significant anthropogenic pressure. The results of this pressure are changes in the hydrographic network, high water demand from industry and agriculture, and the impacts of mining (surface lignite mining and underground salt extraction). Water needs resulting from the development of tourism and navigation (e.g., ensuring transit depths and water for lock operation on the Noteć River) as well as the functioning of natural habitats associated with rivers and bodies of water, suffering from water shortages, are also of significant importance. These demands include, among others, the restoration of surface water resources, stabilisation of water levels in reservoirs, and extension of the navigation season. Balancing these often seemingly conflicting interests may seem difficult, but not impossible. An example where such positive effects can be achieved through a change in the current water management approach is the Pakoski Reservoir.

The change in the damming levels, dates of achieving the specified water levels, and the method and scheme of supplying the Pakoski Reservoir, including the redirection of water from the Noteć River (upper Noteć Canal) through the Pakoski hydrotechnical complex during periods of higher water levels in the Noteć River and Lake Gopło, induced by increased supply in the upper Noteć catchment or water discharge from the peak position of the Ślesinski Canal, allows for the achievement of these objectives. The proposed changes will have the following effects:

- Increasing the efficient use of water resources available in the catchment area of the Mała Noteć and upper Noteć Rivers;
- Increasing the water resources of the reservoir while maintaining the safe flood capacity;
- Increasing the capacity for water flow supplementation in the Noteć below the reservoir;

- Securing the water resources of the Mała Noteć and upper Noteć River systems after the closure of the Tomisławice open-pit mine;
- Raising the groundwater levels and improving the condition of wetlands within the reservoir catchment area;
- Improving the habitat conditions for fish and other organisms inhabiting the reservoir's littoral zone;
- Reducing the process of overgrowth in the coastal zones of the reservoir;
- Improving navigation conditions and increasing the reservoir's tourist attractiveness.

Taking into account the challenges associated with maintaining the water level in artificial reservoirs in various parts of the world and the increasing problems with providing water for various industries and agriculture in the light of recorded climate changes [54–64], it seems reasonable to apply the solutions indicated for the Pakoski reservoir to other reservoirs of this type. The solutions developed for the Pakoski Reservoir in terms of increasing the flexibility of water management instructions created decades ago can be applied in particular to other lowland dam reservoirs located in a similar climatic zone, within areas where changes in their water supply regime have been observed in recent years and increasing water deficits have been observed.

Author Contributions: Conceptualisation, B.N.; methodology, B.N.; software, B.N., G.D. and A.Ł.-M.; validation, B.N., G.D. and A.Ł.-M.; formal analysis, B.N.; investigation, B.N.; resources, B.N. and G.D.; data curation, B.N.; writing—original draft preparation, B.N.; writing—review and editing, B.N., G.D. and A.Ł.-M.; visualisation, B.N. and A.Ł.-M.; supervision, B.N. and A.Ł.-M.; project administration, B.N.; funding acquisition B.N. and G.D. All authors have read and agreed to the published version of the manuscript.

Funding: This research received no external funding.

Data Availability Statement: Data are available upon request due to restrictions.

Conflicts of Interest: The authors declare no conflicts of interest.

References

1. Lee, H.; Power, S.B.; Ravindranath, N.H. *Climate Change: Synthesis Report. Contribution of Working Groups I, II and III to the Fifth Assessment Report of the Intergovernmental Panel on Climate Change, Russian Federation*; Intergovernmental Panel on Climate Change (IPCC): Geneva, Switzerland, 2014.
2. Ahn, J.M.; Kwon, H.G.; Yang, D.S.; Kim, Y.S. Assessing environmental flows of coordinated operation of dams and weirs in the Geum River basin under climate change scenarios. *Sci. Total Environ.* **2018**, *643*, 912–925. [CrossRef]
3. Zhang, J.; Shang, Y. Nexus of dams, reservoirs, climate, and the environment: A systematic perspective. *Int. J. Environ. Sci. Technol.* **2023**, *20*, 12707–12716. [CrossRef]
4. Mosaid, H.; Barakat, A.; Bouras, E.H.; Ismaili, M.; El Garnaoui, M.; Abdelrahman, K.; Kahal, A.Y. Dam Siltation in the Mediterranean Region Under Climate Change: A Case Study of Ahmed El Hansali Dam, Morocco. *Water* **2024**, *16*, 3108. [CrossRef]
5. Berga, L. The role of hydropower in climate change mitigation and adaptation: A review. *Engineering* **2016**, *2*, 313–318. [CrossRef]
6. Fluixá-Sanmartín, J.; Escuder-Bueno, I.; Morales-Torres, A.; Castillo-Rodríguez, J.T. Accounting for climate change uncertaintyin Long-Term dam risk management. *J. Water Resour. Plan. Manag.* **2021**, *147*, 04021012. [CrossRef]
7. Wierzbicki, M.; Andrzejak, A.; Piniarska, D.; Sobczyk, B.; Nowak, B. Funkcjonowanie zbiorników retencyjnych Regionalnego Zarządu Gospodarki Wodnej w Poznaniu w kontekście zmian klimatycznych i potrzeb wodnych-wyzwania i problemy eksploatacyjne na przykładzie wybranych obiektów (Functioning of the Regional Water Management Authority in Poznań retentionreservoirs in the context of climate change and water needs-challenges andoperational issues based on the example of selected facilities). *Gospod. Wodna* **2023**, *9*, 32–38.
8. Asadieh, B.; Krakauer, N.; Fekete, B. Historical Trends in Mean and Extreme Runoff and Streamflow Based on Observations and Climate Models. *Water* **2016**, *8*, 189. [CrossRef]
9. Asadieh, B.; Krakauer, N.Y. Global trends in extreme precipitation: Climate models versus observations. *Hydrol. Earth Syst. Sci.* **2015**, *19*, 877–891. [CrossRef]

10. Schneider, C.; Laizé, C.L.R.; Acreman, M.C.; Flörke, M. How will climate change modify river flow regimes in Europe? *Hydrol. Earth Syst. Sci.* **2013**, *17*, 325–339. [CrossRef]
11. IPCC. *Climate Change and Water. Technical Paper of the Intergovernmental Panel on Climate Change*; IPCC: Geneva, Switzerland, 2008.
12. IPCC. *Climate Change: The Physical Science Basis. Contribution of Working Group I to the Fifth Assessment Report of the Intergovernmental Panel on Climate Change*; Cambridge University Press: Cambridge, UK; New York, NY, USA, 2013.
13. Kis, A.; Pongrácz, R. The projected changes of hydrological indicators in European catchments with different climatic conditions. *Hydrol. Sci. J.* **2024**, *69*, 1797–1812. [CrossRef]
14. Blöschl, G.; Hall, J.; Viglione, A.; Perdigão, R.A.P.; Parajka, J.; Merz, B.; Lun, D.; Arheimer, B.; Aronica, G.T.; Bilibashi, A.; et al. Changing climate both increases and decreases European river floods. *Nature* **2019**, *573*, 108–111. [CrossRef]
15. Mohr, S.; Ehret, U.; Kunz, M.; Ludwig, P.; Caldas-Alvarez, A.; Daniell, J.E.; Ehmele, F.; Feldmann, H.; Franca, M.J.; Gattke, C.; et al. A multi-disciplinary analysis of the exceptional flood event of July 2021 in central Europe—Part 1: Event description and analysis. *Nat. Hazards Earth Syst. Sci.* **2023**, *23*, 525–551. [CrossRef]
16. Czarnowska, J.; Bochenek, B.; Pyrc, R. Evaluating extremes in climatology with average value-at-risk measure: Example of precipitation data from upper Vistula region in Poland. *J. Appl. Meteorol. Climatol.* **2024**, *63*, 1311–1326. [CrossRef]
17. Allan, J.D. Landscapes and riverscapes: The influence of land use on stream ecosystems. *Annu. Rev. Ecol. Evol. Syst.* **2004**, *35*, 257–284. [CrossRef]
18. Skarżyńska, K. Gopło-centrum hydrograficzne Polski przed wiekami. *Przegląd Geogr.* **1963**, *8*, 189–201.
19. Grobelska, H. *Ewolucja Strefy Brzegowej Zbiornika Pakoskiego (Pojezierze Gnieźnieńskie) (The Evolution of the Pakośc Reservoir Shore Zone (Gniezno Lakeland))*; Prace Geograficzne IgiPZ, 25; Polska Akademia Nauk Instytut Geografii i Przestrzennego Zagospodarowania im. Stanisława Leszczyckiego: Warszawa, Poland, 2006; pp. 1–173.
20. Available online: https://mapy.geoportal.gov.pl/imap/Imgp_2.html?gpmap=gp0 (accessed on 9 November 2024).
21. Available online: https://geologia.pgi.gov.pl/mapy (accessed on 9 November 2024).
22. Available online: https://clc.gios.gov.pl/index.php/clc-2018/metadane (accessed on 9 November 2024).
23. Available online: http://mapy.amzp.pl/tk25.cgi?11;36;50;103 (accessed on 9 November 2024).
24. Decyzja Marszałka Województwa Kujawsko-Pomorskiego z dnia 25.04.2008 r. nr ŚG.I.ab.6213-11/08 ws Udzielenia Pozwolenia Wodnoprawnego Regionalnemu Zarządowi Gospodarki Wodnej w Poznaniu na Szczególne Korzystanie z Wody w Zakresie Piętrzenia Wody na Kanale Górnonoteckim za Pomocą Jazu Ulgowego i śluzy żeglugowej nr 1 w Pakości Oraz jej Retencjonowanie w Zbiorniku Utworzonym na Rzece i Jeziorze Gopło Oraz Piętrzenia Wody Rzeki Noteci Zachodniej w Przekroju Pakość za Pomocą Obiektów Wchodzących w Skład Zbiornika Zaporowego na Jeziorach Pakoskich Oraz jej Retencjonowanie w tym Zbiorniku; Zwanym Zbiornikiem Pakoskim. 2008. Available online: https://www.gov.pl/web/wody-polskie/ (accessed on 9 November 2024).
25. Nowak, B.; Nadolna, A.; Stanek, P. Evaluation of the potential for the use of lakes in restoring water resources and flood protection; with the example of the Noteć Zachodnia River catchment (Gniezno Lakeland; Poland). *Meteorol. Hydrol. Water Manag.* **2018**, *6*, 45–58. [CrossRef]
26. Nowak, B.; Ptak, M. Możliwości retencyjne jezior w zlewni rzeki Panny na Pojezierzu Gnieźnieńskim (Retention capacities of lakes located in the Panna River catchment area, within the Gniezno Lakeland). *Gospod. Wodna* **2019**, *6*, 7–11.
27. Kondracki, J. *Geografia Regionalna Polski*; Wydawnictwo Naukowe PWN: Warszawa, Poland, 2009; pp. 1–441.
28. Kędziora, A. Bilans wodny krajobrazu konińskich kopalni odkrywkowych w zmieniających się warunkach klimatycznych (Water balance of Konin strip mine landscape in changing climatic conditions). *Rocz. Glebozn.* **2008**, *59*, 104–118.
29. Kędziora, A. Warunki klimatyczne i bilans wodny Pojezierza Kujawskiego (Climatic conditions and water balance of the Kujawy Lakeland). *Rocz. Glebozn.* **2011**, *62*, 189–203.
30. Nowak, B.; Lawniczak-Malinska, A.E. The influence of hydrometeorological conditions on changes in littoral and riparian vegetation of a meromictic lake in the last half-century. *Water* **2019**, *11*, 2651. [CrossRef]
31. Nowak, B.; Szadek, P.; Rosa, J. Analiza możliwości przyspieszenia odbudowy zasobów wodnych w rejonie górnej Noteci i zalewanego wyrobiska końcowego odkrywki Lubstów (Polska środkowo-zachodnia) (Analysis of possibilities to accelerate restoration of water resources in the region of the Upper Noteć River and the flooded Lubstów open-pit working (middle-eastern Poland)). *Gospod. Wodna* **2022**, *8*, 4–17.
32. Habel, M.; Nowak, B.; Szadek, P. Evaluating indicators of hydrologic alteration to demonstrate the impact of open-pit lignite mining on the flow regimes of small and medium-sized rivers. *Ecol. Indic.* **2023**, *157*, 111295. [CrossRef]
33. Wachowiak, G. Potwierdzenie niskiego odpływu średniego w okolicach jeziora Gopło. *Gaz. Obs. IMGW* **1980**, *10*, 13–16.
34. Grobelska, H. Rozwój brzegu abrazyjnego zbiornika wodnego o dużych wahaniach stanów wody (zbiornik pakoski; Noteć Zachodnia). In *Środowisko Przyrodnicze Wobec Zagrożeń Antropogenicznych*; Szczypek, T., Ed.; Prace Wydziału Nauk o Ziemi Uniwersytetu Śląskiego: Sosnowiec, Poland, 2005; Volume 35, pp. 46–58.

35. Grobelska, H. Rozwój strefy brzegowej nizinnego zbiornika wodnego w warunkach dużych wahań stanów wody na przykładzie zbiornika pakoskiego (Noteć Zachodnia). In *Nauka-Przyroda-Technologie*; t.1; z. 2; Melioracje i Inżynieria Środowiska; Wydawnictwo AR w Poznaniu: Poznań, Poland, 2007; pp. 121–130.
36. Available online: https://wody.gios.gov.pl/pjwp/publication/367 (accessed on 9 November 2024).
37. Kaczmarek, H. Zbiornik Pakoski jako część Wielkiej Pętli Wielkopolski i jego zagospodarowanie turystyczne. In *Rewitalizacja Dróg Wodnych Szansą Dla Gospodarki*; Szumińska, D., Ed.; Promotio Geographica Bydgostiensia; Wydawnictwo Uniwersytetu Kazimierza Wielkiego: Bydgoszcz, Poland, 2012; Volume 8, pp. 121–132.
38. Kaniecki, A. Wpływ XIX-wiecznych melioracji na zmiany poziomu wód. In *Wpływ Antropopresji na Jeziora*; Wydawnictwo Homini: Poznań, Poland, 1997; pp. 67–71.
39. Pasławski, Z.; Błaszczyk, B. Charakterystyka hydrologiczna i bilans wodny jeziora Gopło. *Przegląd Geofiz.* **1970**, *15*, 252–266.
40. Ilnicki, P.; Orłowski, W. Klęska ekologiczna w Powidzkim Parku Krajobrazowym. *Aura* **2006**, *10*, 11–14.
41. Ilnicki, P.; Orłowski, W. Rezygnacja z retencjonowania wody na wododziale Noteci i Warty sprzeczna z zasadą zrównoważonego rozwoju (Resignation from collecting water in retention reservoirs in the Noteć and Warta rivers watershed contrary to the principle of sustainable development). *Gospod. Wodna* **2011**, *8*, 322–328.
42. Nowak, B.; Przybyłek, J. Recharge and drainage of lakes in Powidzki Landscape Park in the conditions of increased anthropogenic and environmental pressure (Central-Western Poland). *Geol. Q.* **2020**, *64*, 205–219. [CrossRef]
43. Nowak, B.; Przybyłek, J.; Szadek, P.; Rosa, J. Możliwości odbudowy zasobów wodnych w rejonie odkrywek węgla brunatnego Jóźwin IIB i Kazimierz Północ (Possibilities of restoring water resources in the area of Jóźwin IIB and Kazimierz Północ opencast lignite mines (central Poland)). *Przegląd Geol.* **2024**, *72*, 615–635. [CrossRef]
44. Orłowski, W.; Ilnicki, P. Problemy gospodarowania wodą w otoczeniu Kopalni Węgla Brunatnego Konin (Problems of water management in the surroundings of the Brown Coal Mine Konin). *Gospod. Wodna* **2007**, *9*, 383–386.
45. Przybyłek, J. Środowiskowe uwarunkowania skutków eksploatacji odkrywkowej węgla brunatnego na Pojezierzu Gnieźnieńskim (Environmental conditions of the effects of opencast brown coal exploitation in the Gniezno Lakeland). *Przegląd Geol.* **2020**, *68*, 645–654. [CrossRef]
46. Przybyłek, J.; Nowak, B. Wpływ niżówek hydrogeologicznych i odwodnień górniczych na systemy wodonośne Pojezierza Gnieźnieńskiego (Impact of hydrogeological low flows and groundwater drainage by lignite open cast mine on aquifer systems of Gniezno Lakeland). *Biul. PIG Ser. Hydrogeol.* **2011**, *12*, 513–552.
47. Przybyłek, J.; Gąbka, M.; Kamiński, W.; Wiliński, R. *Analiza Możliwości Zasilania Jezior Powidzkiego Parku Krajobrazowego Zasobami Wodnymi Rzeki Warty Oraz Szczytowego Stanowiska Kanału Ślesińskiego*; Wielkopolskie Biuro Planowania Przestrzennego: Poznań, Poland, 2020; pp. 1–150.
48. Wachowiak, G. Roczniki hydrologiczne i meteorologiczne rejonu odkrywek KWB „Konin" w Kleczewie SA—10 lat badań IMGW dla potrzeb Kopalni. *Węgiel Brunatny* **2005**, *51*, 25–31.
49. Kamiński, W. Modernizacja Kanału Ślesińskiego ze środków Wielkopolskiego Regionalnego Programu Operacyjnego na lata 2007–2013. *Gospod. Wodna* **2009**, *6*, 225–229.
50. Ma, C.; Xu, X.; Yang, J.; Cheng, L. Safety Monitoring and Management of Reservoir and Dams. *Water* **2023**, *15*, 1078. [CrossRef]
51. Ehsani, N.; Vörösmarty, C.J.; Fekete, B.M.; Stakhiv, E.Z. Reservoir operations under climate change: Storage capacity options tomitigate risk. *J. Hydrol.* **2017**, *555*, 435–446. [CrossRef]
52. Badr, A.; Li, Z.; El-Dakhakhni, W. Dam System and Reservoir Operational Safety: A Meta-Research. *Water* **2023**, *15*, 3427. [CrossRef]
53. Huber, M.; Knutti, R. Anthropogenic and natural warming inferred from changes in Earth's energy balance. *Nat. Geosci.* **2012**, *5*, 31–36. [CrossRef]
54. Ahmadi, M.; Haddad, O.B.; Loáiciga, H.A. Adaptive Reservoir Operation Rules under Climatic Change. *Water Resour. Manag.* **2014**, *29*, 1247–1266. [CrossRef]
55. Bednárová, E.; Škvarka, S.; Miščík, M.; Uhorščák, M.; Mackovjak, M. The function of the Veľká Domaša reservoir in the context of observed climate changes. *Gospod. Wodna* **2023**, *9*, 39–43. [CrossRef]
56. Carvalho-Santos, C.; Monteiro, A.T.; Azevedo, J.C.; Honrado, J.P.; Nunes, J.P. Climate Change Impacts on Water Resources and Reservoir Management: Uncertainty and Adaptation for a Mountain Catchment in Northeast Portugal. *Water Resour. Manag.* **2017**, *31*, 3355–3370. [CrossRef]
57. Domingues, L.M.; de Abreu, R.C.; da Rocha, H.R. Hydrologic Impact of Climate Change in the Jaguari River in the Cantareira Reservoir System. *Water* **2022**, *14*, 1286. [CrossRef]
58. Dorchies, D.; Thirel, G.; Perrin, C.; Bader, J.-C.; Thepot, R.; Rizzoli, J.-L.; Jost, C.; Demerliac, S. Climate change impacts on water resources and reservoir management in the Seine river basin (France). *La Houille Blanche* **2016**, *102*, 32–37. [CrossRef]
59. He, S.; Guo, S.; Yang, G.; Chen, K.; Liu, D.; Zhou, Y. Optimizing Operation Rules of Cascade Reservoirs for Adapting Climate Change. *Water Resour. Manag.* **2019**, *34*, 101–120. [CrossRef]

60. Li, Z.; Huang, B.; Yang, Z.; Qiu, J.; Zhao, B.; Cai, Y. Mitigating Drought Conditions under Climate and Land Use Changes by Applying Hedging Rules for the Multi-Reservoir System. *Water* **2021**, *13*, 3095. [CrossRef]
61. Mohammed, R.; Scholz, M. Adaptation Strategy to Mitigate the Impact of Climate Change on Water Resources in Arid and Semi-Arid Regions: A Case Study. *Water Resour. Manag.* **2017**, *31*, 3557–3573. [CrossRef]
62. Savino, M.; Todaro, V.; Maranzoni, A.; D'Oria, M. Combining Hydrological Modeling and Regional Climate Projections to Assess the Climate Change Impact on the Water Resources of Dam Reservoirs. *Water* **2023**, *15*, 4243. [CrossRef]
63. Sen, Z. Reservoirs for Water Supply Under Climate Change Impact—A Review. *Water Resour. Manag.* **2021**, *35*, 3827–3843. [CrossRef]
64. Zhang, L.; Kang, C.; Wu, C.; Yu, H.; Jin, J.; Zhou, Y.; Zhou, T. Optimization of Drought Limited Water Level and Operation Benefit Analysis of Large Reservoir. *Water Resour. Manag.* **2022**, *36*, 4677–4696. [CrossRef]

water

MDPI

Article

Hydrological Monitoring System of the Navío-Quebrado Coastal Lagoon (Colombia): A Very Low-Cost, High-Value, Replicable, Semi-Participatory Solution with Preliminary Results

Andrea Gianni Cristoforo Nardini [1,*], Jairo R. Escobar Villanueva [2] and Jhonny I. Pérez-Montiel [2,*]

[1] Fundación CREACUA-Centro Recuperación Ecosistemas ACUÁticos, Riohacha 440001, Colombia
[2] Grupo de Investigación GISA, Facultad de Ingeniería, Universidad de La Guajira, km 3 + 354 Vía a Maicao, Riohacha 440007, Colombia; jrescobar@uniguajira.edu.co
* Correspondence: nardiniok@gmail.com (A.G.C.N.); jpemon@uniguajira.edu.co (J.I.P.-M.)

Abstract: Like many coastal lagoons in several countries, the "Navío Quebrado" lagoon (La Guajira, Colombia) is a very delicate and precious environment; indeed, it is a nationally recognized Flora and Fauna Sanctuary. Several factors, including climate change, are threatening its existence because of changes in the governing hydro-morphological and biological processes. Certainly, the first step to addressing this problem is to understand its hydrological behavior and to be able to replicate, via simulation, its recent history before inferring likely futures. These potential futures will be marked by changes in the water input by its tributary, the Camarones River, and by modified water exchange with the sea, according to a foreseen sea level rise pattern, as well as by a different evaporation rate from the free surface, according to temperature changes. In order to achieve the required ability to simulate future scenarios, data on the actual behavior have to be gathered, i.e., a monitoring system has to be set up, which to date is non-existent. Conceptually, designing a suitable monitoring system is not a complex issue and seems easy to implement. However, the environmental, socio-cultural, and socio-economic context makes every little step a hard climb. An extremely simple—almost "primitive"—monitoring system has been set up in this case, which is based on very basic measurements of river flow velocity and water levels (river, lagoon, and sea) and the direct participation of local stakeholders, the most important of which is the National Park unit of the Sanctuary. All this may clash with the latest groovy advances of science, such as in situ automatized sensors, remote sensing, machine learning, and digital twins, and several improvements are certainly possible and desirable. However, it has a strong positive point: it provides surprisingly reasonable data and operates at almost zero additional cost. Several technical difficulties made this exercise interesting and worthy of being shared. Its novelty lies in showing how old, simple methods may offer a working solution to new challenges. This humble experience may be of help in several other similar situations across the world.

Keywords: monitoring; coastal lagoons; tidal water exchange; low-cost technology; participatory approach; Colombia

1. Introduction

1.1. Peculiarities of Coastal Lagoons

Coastal lagoons are among the most productive systems in the world [1,2]. Indeed, many species take advantage of the lagoons to feed and reproduce, remaining in these places for part of their life cycle. They provide a significant number of socioeconomic benefits for humans who exploit this productivity, particularly by fishing [3]. Coastal lagoons are characterized by shallow depths, differing greatly in size, morphology, trophic state, and salinity characteristics, which drive the biological structure, species composition, and fishing performance [4]. At its boundaries, the entry of freshwater—typically by rivers—provides hydrological forcing, as does the exchange of water between the lagoon

and the open sea [5]. Due to the above, these ecosystems generate great motivation for researchers to study not only their productivity but also their hydrological and hydrodynamic behavior (inflow, exchange of flows, and water levels).

Coastal lagoons are characterized by a typical annual cycle (Figure 1). This usually starts when the feeding river system is flooding, thus originating a period of "high waters", where the water level rises until the natural sand bar, separating the lagoon from the open sea, breaks down and creates an open mouth ("la boca"; in some cases, local inhabitants contribute to artificially creating an opening to avoid flooding their houses). In these conditions, the outgoing flow of semi-fresh water is felt by sea populations of fish (for Navio-Quebrado: *Litopenaeus schmitti*, *Macrobrachium acanthurus*, *Centropomus undecimalis*, *Elops saurus*, *Micropogonias furnieri*, *Mugil curema*, *Mugil incilis*, *Mugil liza*, *Cathrorops spixii*, *Eugerres plumieri lito*, *Mugil liza*, and *Mugil curema*) and crustaceans, which hence enter the lagoon looking for appropriate zones for reproduction and nursery. While the river freshwater input reduces (often remaining null for several months), the lagoon volume drops, and for a few months, an alternate flow exchange of water into and from the sea is established, according to the tidal pattern. In this period, the fingerlings and grown fish take advantage of this opportunity to exit into the open sea and "look for freedom and a new life". This goes on until the sea waves prevail on this exchange process and recreate a sand bar, closing la boca. From this moment on, until the next cycle starts, the lagoon water evaporates, lowering its level (depth) and area, while salinity strongly increases. All fauna trapped inside are destined to die due to the hypersaline conditions unless a new flood comes in time. Regarding Navío-Quebrado, curious local fishermen collect dead or dying biomass—mostly composed of *Elops saurus* followed by mugilids [6]—as a delicious, although stinky, food (named "cachirra" by the natives of the area).

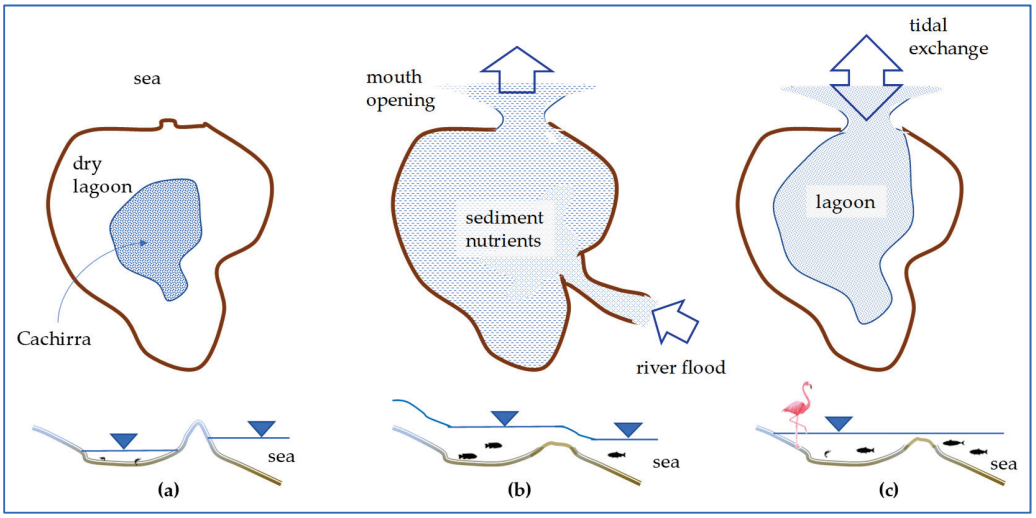

Figure 1. Scheme of the typical hydrological and ecological cycle of a coastal lagoon in La Guajira: (**a**) dry season; (**b**) flood season with opening of la boca and outflow of semi-fresh water; (**c**) sea–lagoon exchange according to the tide.

1.2. The Case of the Navío-Quebrado Lagoon

On the one hand, the interest in the Navío-Quebrado lagoon (Figure 2) stems from its intrinsic environmental value, primarily linked to the presence of a significant population of flamingos (Flamenco Rosado, *Phoenicopterus rube*). Indeed, it is because of this that it is a National Fauna and Flora Sanctuary. On the other hand, it provides important environmental services such as fishery, particularly shrimps (from which the alternate name "Camarones" comes), and is a tourist attraction, both for its scenery and for the observation of local fauna.

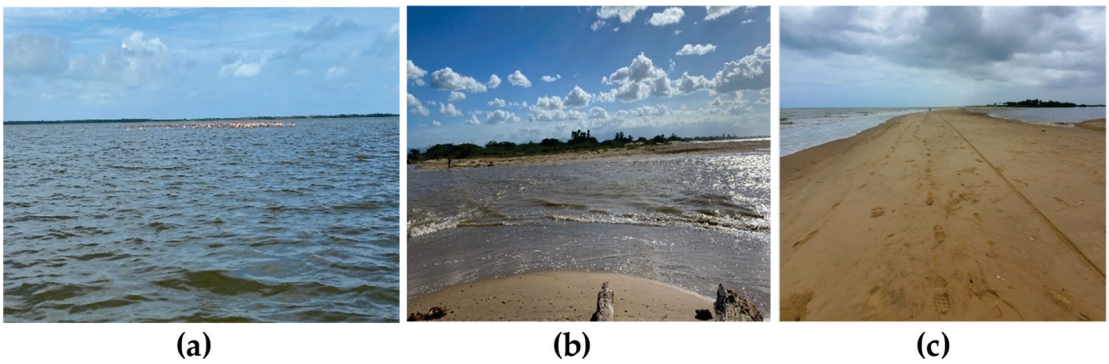

Figure 2. Navío-Quebrado (Camarones) lagoon: (**a**) wet season; (**b**) opening of the mouth ("la boca"); (**c**) the bar between the sea and lagoon (closed mouth).

Threats and Problem Addressed

Since the first River Basin Management Plan (POMCA), developed by the Italian NGO Ricerca e Cooperazione in collaboration with the regional Environmental Authority Corpoguajira and the local Universidad de La Guajira [7] and coordinated by one of us, sedimentation induced by the sediment load of the Camarones River has been identified as a major potential threat. This issue was supposed to be linked to landslides in the headwaters, which transported large amounts of sandy material (as occurred in 1985). This awareness opened the query towards further investigation efforts. Nevertheless, until now, the only additional information acquired refers to a stratigraphic analysis of a nearby sample [8] (but not from the lagoon itself) and a more recent attempt by Parques Nacionales Naturales de Colombia Nacionales (jurisdiction of the *Santuario de Fauna y Flora los Flamencos-SFFF*) to measure the productivity of the lagoon and the fishing effort applied, as well as the counting of the Flamencos Rosados, the emblematic species of the lagoon, usually found mostly between November and March [9]. Fish suffer from a strong anthropogenic pressure given that fishing is the most important livelihood of local inhabitants, which makes rational control problematic. An eco-anthropogenic problem is due to the early capture of fish by locals (many of which are *Wayuu* indigenous people), preventing their growth to commercial size and consequently leading to a virtual income loss [10]. This reality generates a certain level of conflict between different fishermen groups and competition to capture the shrimp population before others can take advantage of it. Although there is scientific information from studies on the fish and insect communities [11,12], no recent information about the hydrology of the lagoon has been generated. There also are other threats due to the use of fertilizers and agro-chemicals in the basin, and also due to direct sewage discharge into the lagoon [13], manifested, for instance, in some episodes of bad water quality [14]. More generally, the Camarones river basin is subject to furious exploitation of its natural resources: industrial agriculture, raising cattle, and clearing the forest to feed the necessary ovens for cooking clay bricks are the major pressure factors affecting the hydrological regime. Finally, pressure from tourism is boosting urbanization and all connected problems.

Another very significant threat is associated with climate change. Rising sea levels, a likely reduction of freshwater supply, and increased evaporation, associated with a possible reduction of the available lagoon volume because of sedimentation, spontaneously raise the question of whether this system will survive as it is or will soon be incorporated into the sea. On the contrary, it could also be transformed into a productive mangrove zone or alternatively a rotten marsh (as seems to have happened in the far past, according to [8].

Therefore, it was decided to undertake a first attempt to set up a hydrological monitoring system. Once established, the data provided by such a system could allow us to set up a hydrological simulation model (water balance). With this model, it may be possible to explore future scenarios, possibly deriving useful indications for action.

1.3. Paper Aim and Structure

This humble paper presents the difficulties encountered in setting up a monitoring system and the solutions adopted. Its aim is to make decision-makers aware of the difficulties inherent in a territory such as La Guajira and, at the same time, to provide practitioners and managers with useful hints to simplify their efforts. It can also stimulate researchers to search for new ideas to overcome our difficulties. Finally, we believe that the whole exercise depicts an interesting scientific process where several potentially viable options are explored and a specific pathway is progressively defined. Its novelty lies in showing how old, simple methods may offer a working solution to new challenges, often in a more appropriate fashion than the more advanced technology.

The Method chapter of this paper is its core. It presents, in a plain fashion, the different attempts performed in order to set up the different components of the monitoring system. Therefore, it may look more like a project report than a paper, as it faces different issues, rather than setting up a particular specific methodology. However, this exercise, in our opinion, has the characteristics of scientific research, where the objective is indeed to set up the monitoring system. The data and graphs presented in each component of the Method chapter are not intended to be results; they are an intrinsic part of the definition of the method itself. Therefore, the Results chapter is simply the display of the data that have been collected during almost a year and a half of monitoring by the system, accompanied by a discussion about their meaningfulness. Strengths and weaknesses of the monitoring system are finally pointed out and indications for future development are established in the Conclusions, where a synthetic overview of the exercise conducted is provided.

As the reader may note, the literature review and discussion section is quite limited. This is due to the fact that we could not find significant contributions facing a similar problem. Many papers discuss specific methods/techniques, which have been carefully considered here, but they proved unsuitable in the end—as clarified—and, hence, a full related discussion would be out of scope and would further extend an already quite lengthy paper.

As the search for a feasible set up of the monitoring system has been a "long trip", the information generated is quite extensive. To help the reader, a summary table is made available in the Conclusions section. This may be consulted, while reading the paper, as a kind of compass.

2. Methods: Practical Challenges and Adopted Solutions to Set Up a Monitoring System for the Camarones Lagoon

A hydrological monitoring system, aimed at feeding a hydrological model (water balance), for a coastal lagoon should include at least the following:

(a) Freshwater inflow by the tributary (the Tomarrazón-Camarones River). The discharge should be measured at a station sufficiently close to the lagoon to represent the whole water basin supply, but at the same time sufficiently far away to be influenced by the backwater effect as little as possible.
(b) Storage and release flows from changes in water volume stored in the lagoon. This implies being able to measure the level of its water surface and to know the morphometric relationships linking such levels to the stored volume (and surface area).
(c) Salty or brackish water exchange between the lagoon and sea (only when the boca is open), as this may be a key component of the water balance. Measuring this variable is not easy, but for systematic monitoring, the idea is to measure essential variables, namely the water surface elevation of the lagoon and of the sea, and to derive a relationship linking them to the exchange flow.
(d) Freshwater inflow from precipitation directly falling on the lagoon itself and from runoff from the local watershed into the lagoon. Both can be estimated from measurements of the precipitation at nearby sites and the area of the two components (the local water basin and lagoon); however, the latter requires data on rainfall–runoff relationships (model).

(e) Evaporation losses from the water surface of the lagoon: this can be calculated from direct estimates of evaporation rates or from indirect estimates based on formulas where the measured variables would be temperature, humidity, etc.

Filtration exchanges with the sea and the nearby area can be neglected at first as the bottom of the lagoon is considered to be basically sealed by fine sediments (silt and clay) and the water head's potential to generate filtration with the sea is very low, while the potential zone of exchange (the mouth) is quite limited.

The physical system is shown in Figure 3, together with key elements.

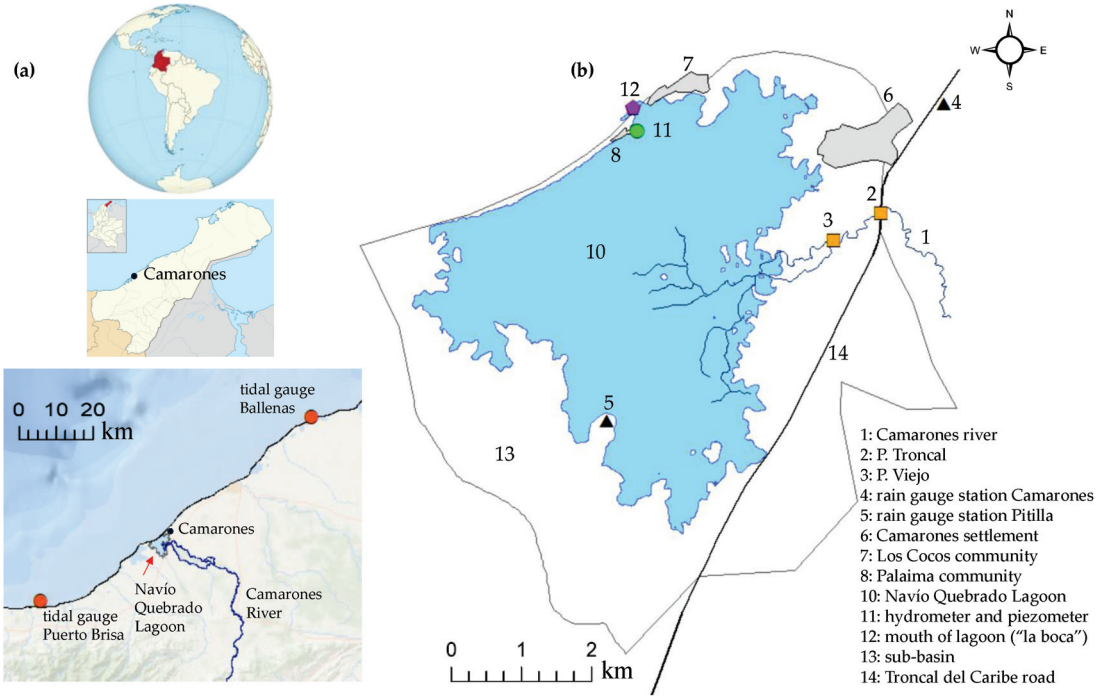

Figure 3. Study area: (**a**) general location; (**b**) location of specific points of interest.

It is spontaneous to think of a (possibly low-cost) technological system to measure several such variables. Low-cost systems are generally modular, thus allowing for the easy replacement of damaged parts. Modularity also allows for a wide freedom in the selection of components, including sensors, recorders, measurement algorithms, communication technology, the feeding source, and other characteristics [15–17]. These systems are suited for a variety of contexts, e.g., water quality monitoring (nutrients, dissolved oxygen, etc.) in a river [15]; environmental monitoring, e.g., the aquifer level, air quality, sediments, or the dynamics of wind-transported sands [16]; management of urban waters [17]; and measurement of water levels in a river [18]. Therefore, we first evaluated this possibility for the different components of the target system.

2.1. River Inflow

No gauging station exists on the Tomarrazón-Camarones River; therefore, the first idea was clearly to set up a new, low-cost monitoring station of the river stage h with automatic measurements (by a pressure or distance sensor) and possibly tele-transmission of data [18,19]. In parallel, the goal was also to set up a suitable stage–discharge relationship Q(h), analogously to what has been achieved by [5].

Unfortunately, our experience in the area led us to immediately discard this idea due to the high probability (or certainty) of rapid robbery of or damage to the devices: very poor people, who are quite numerous in the area, are prone to stealing anything that can reward them with amounts even smaller than a dollar.

Another option was to adopt satellite measurements of water level via-sensors, such as TOPEX/Poseidon, Jason-1, 2, and 3, ERS-1/2, Environmental Satellite-Envisat, ICESat, CryoSat-2, SARAL/AltiKa, and SWOT, with the support of software such as AlTiS, version 2.2.9 [20]. However, analogously, this option was discarded for several reasons. The channel is almost invisible from above owing to the riparian vegetation cover, the channel is too narrow (10–20 m), and the frequency of survey of satellites is too low for our purposes. Nevertheless, these tools have produced data for two decades that can be very useful for studying, for instance, the evolution of water bodies in general [21–24].

As the rainy season was about to start when we were designing the system—and missing it would be a significant loss of data—a very simple but robust and even economic solution was set up. A rule was painted on a fixed vertical part of the wall of the foundation pillar of a bridge. Two rules were set up in the only two bridges in the area (Figure 3b): Puente Troncal, the one selected for the routine measurements, and Puente Viejo, which is some distance upstream. This was conducted to perform a check on data coherence, explore the possible existence of a backwater effect, and provide an alternative calculation of flow based on the gradient of the water level (as explained later in this paper). Details of the rules on both bridges can be observed in Figure 4.

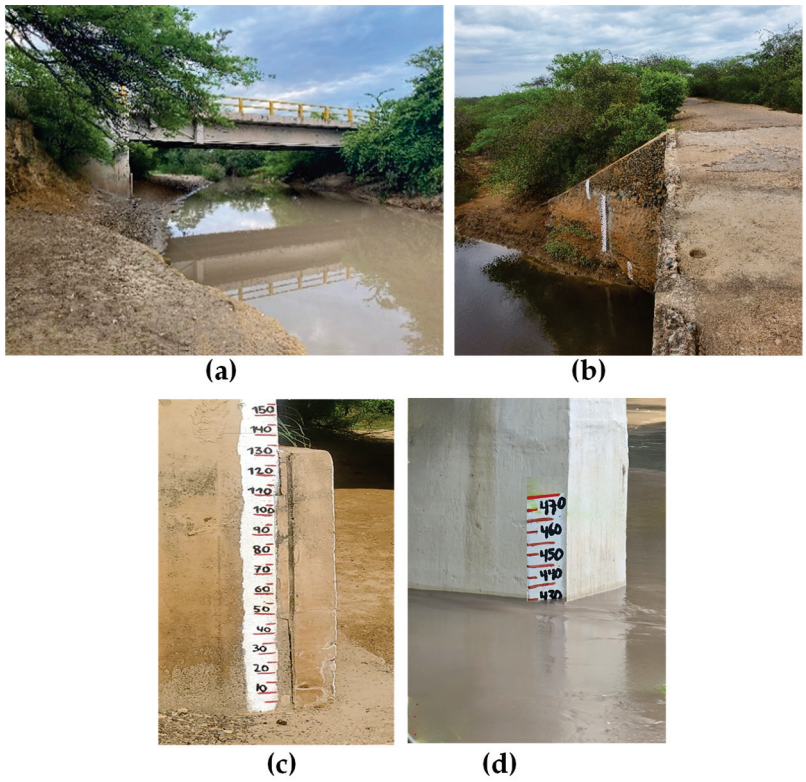

Figure 4. Location of hydrometers: (**a**) view from downstream at Puente Troncal; (**b**) view from the observation point at Puente Viejo; (**c**) rule at Puente Troncal; (**d**) rule at the same site during a flood (this is located on the opposite side of the pillar).

The selected cross-sections are sufficiently stable because the riparian material is mainly organogenic claystone conglomerate, although, of course, a certain level of change in the sediment deposits may take place. With a survey during dry conditions, we determined the geometry of the cross-section so that the relationship A = A(h) was obtained, where A is the area of the wet cross-section for water level h (Figure 5).

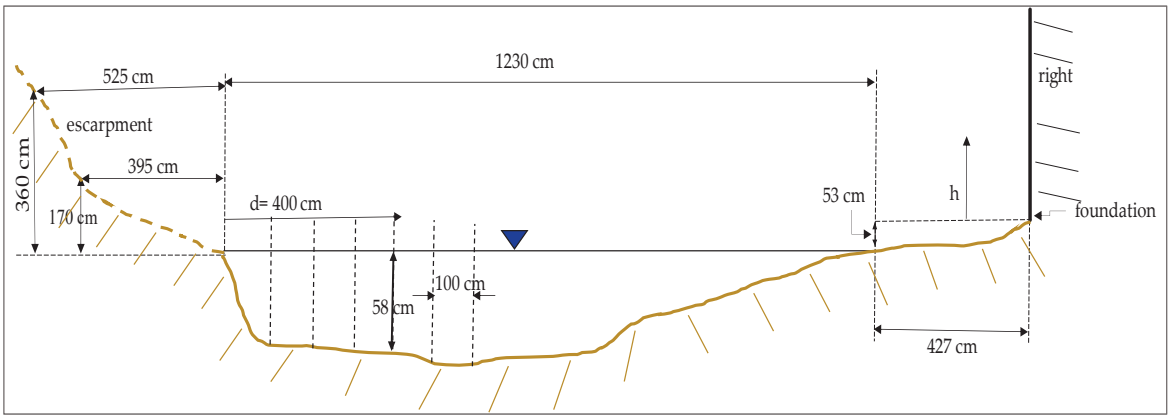

Figure 5. Cross-section at Puente Troncal. It can be noted that the 0 of the hydrometer (on the right) was placed where the water was on the day of installation; however, the water level can be lower (the depth was estimated by directly wading into the section). This means that negative values of the water height h are also possible. The wetted topography was manually surveyed by measuring depth with respect to the water surface every 100 cm, as represented in the figure.

To simplify the routine measurement process as much as possible, we ensured that the water surface and the rule were visible in any condition from a selected site on top of the bridge and opted for just taking a picture, ideally a couple of times each day at (more or less) fixed times (early morning and mid-afternoon). Providentially, we could arrange a formal agreement with the local National Parks office, which immediately and enthusiastically shared the necessity of setting up such a project and accepted the pledge to have one of its staff members pass by the site and take the picture. In addition, we made a private agreement with a local person (*muchacho*) with a motorcycle, who, under a very reasonable payment, would commit to *echar un ojo* (having a look) at the river every day and who, in case of a flood or an emergency (e.g., the impossibility of a Parks servant passing by), would take an additional picture registering the time and immediately send it to us by WhatsApp® version 2.22.7.73. In spite of all these arrangements, in practice, however, most of the time, only one measurement a day was obtained (and some days even that was missing).

Still, the second part of the problem had to be faced: setting up a stage–discharge relationship. This meant gauging the flow rate, particularly during high flows, which is quite a dangerous task. The use of a classic current meter was out of the question because the bridge is too high over the water to hold the device with a long rigid arm, while an ADCP (Acoustic Doppler, Current-meter Profiler; [25]) would require accessing the water body during high water to place a guiding rope/wire, a method that is physically very hard and dangerous owing to the dense vegetation one must cross and the slippery ground (Figure 6). In addition, and most importantly, our University simply had no such device yet. On the other side, wading into the river would certainly be impossible because it becomes very deep and fast with a slippery bottom, while in low water, wading would interfere with the flow we had to measure. Other methods such as salt concentrations or dyes were not viable again because of the impossible access and because the river feeds a natural protected area. This is why we chose the old, somehow "primitive" method of throwing a floater and measuring the time elapsed to cover a fixed, known distance (of 11 m), and averaging amongst several (at least three) launches along different flow lines across the section. Only biodegradable objects such as fruits (ideal because they float but are almost fully immersed, meaning that the wind effect is minimal) or short wooden sticks were used. The flow rate was then obtained by just multiplying the average velocity by the area of the wet section, determined based on the water level h and the known geometric section A = A(h) previously determined in dry conditions (from Figure 5). No correction to

the velocity for the border effect was applied because the velocity field is quite complex and the main flow sometimes occurs on the side rather than in the central sector.

(a) **(b)**

Figure 6. Difficult Access to the measurement sites: (**a**) Puente Troncal; (**b**) Puente Viejo.

This approach would appear to most readers, as it does to us, as quite anachronistic and primitive. Nevertheless, the obtained data after more than one and a half years of observations behave surprisingly well, as shown in Figure 7 (interpolated by a polynomial regression equation).

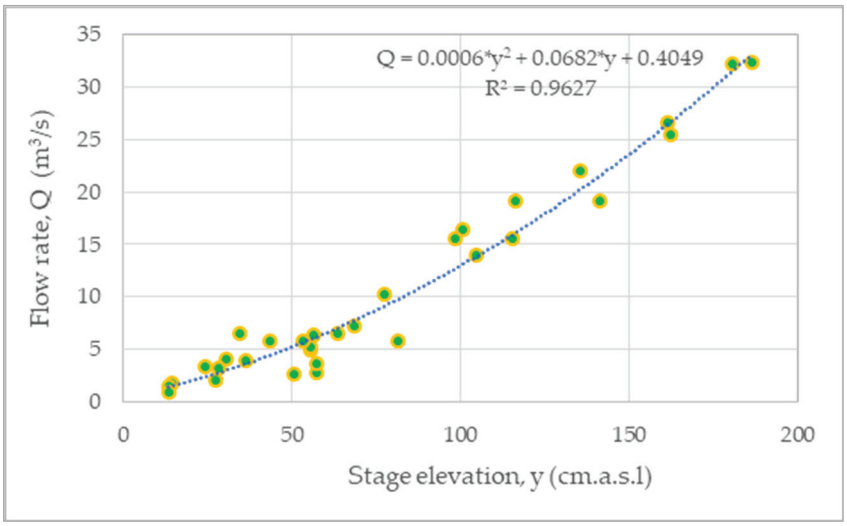

Figure 7. Stage–discharge relationship (polynomial regression) of the Tomarrazon-Camarones River in Puente Troncal with gauging data from 23 April 2022 until 23 October 2023 (y denotes elevation m asl).

It is reasonable to wonder whether these 32 data pairs are sufficient to accurately calculate the relationship. The answer can perhaps be found in the final result, the reasonable consistency of modeled lagoon behavior (depending also on river inputs, estimated through this relationship) with respect to measurements of the lagoon state; however, this is dealt with in another forthcoming paper. Here, to confirm this positive result, and for scientific curiosity, a different method was adopted to estimate the flow rate based on classic hydraulics, i.e., by applying Chezy Manning's Equations (1) and (2) [26], which is often used in current research (e.g., [27–29]). Here, we used the area A = A(h) and wetted perimeter p = p(h) relationships obtained from the cross-section geometry of Figure 5 by points (Figure 8), and for the slopes [m/m] of each measurement (at a given date and time), the water elevation difference Δy between the two bridges monitored (y_T at P.Troncal and

y_V at P.Viejo, see Figure 3), divided by their distance L along the stream axis (L = 1132 m from Google Earth® images), establishes a reference elevation for both (the "IGAC 0"; with IGAC: Instituto Geográfico Agustin Codazzi, the official Colombian entity in charge of geographical issues and maps), so transforming the water depth h of our hydrometer into an elevation y. With this position, the stage–discharge curve at the P.Troncal station, as shown in Figure 9, was obtained by estimating the Manning friction coefficient n from manual trial and error to fit the measured values as far as possible (obtaining the value n = 0.0447 in the SI system). Again, the results are surprisingly nice, as demonstrated by Figure 9. Nevertheless, for the monitoring exercise, the empirical stage–discharge curve (based on our measurements) is preferred simply because this is closer to reality and because more data will be available in time, hopefully making it more reliable gradually.

$$v(h) = 1/n\ R(h)^{2/3}\ s^{1/2} \quad (1)$$

$$Q(h) = V(h)\ A(h) \quad (2)$$

with:

v [m/s]: average velocity in the cross-section
Q [m^3/s]: flow rate
h [m]: water depth in the section
A [m^2]: area of the wetted cross-section
R [m]: hydraulic radius, i.e., R(h) = A(h)/p(h)
s [-]: the river slope
p [m]: wetted perimeter
y [m.a.s.l]: water elevation: y = h + h_0 with h_0 IGAC reference [m.a.s.l].

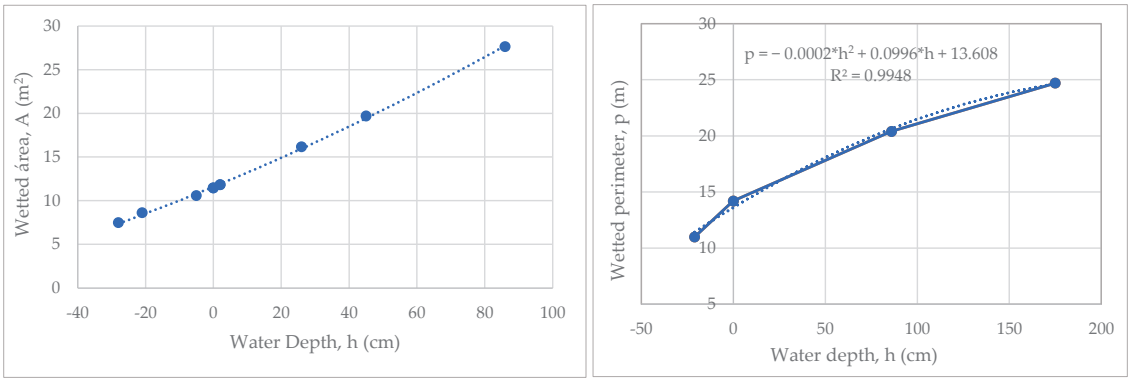

(a) **(b)**

Figure 8. Analytic relationships (approximated) for the cross-section of the river at P.Troncal: (**a**) wetted area A = A(h); (**b**) wetted perimeter p = p(h).

Novelties

However, things are never as smooth as they appear at first sight. While the data collection process was ongoing, we updated the exercise after an additional month (November 2023), when new significant flood events took place. Figure 10 shows the stage–discharge curve with the new data, which shows significantly worse behavior, although it is still not bad.

The suspicion arose then that the deviations detected in the stage–discharge curve of Figure 10 could depend on the backwater effect from the lagoon. Indeed, Figure 11 plots the flow rate deviations (Q measured and Q estimated by the empirically found stage–discharge relationship) as a function of the water surface level of the lagoon, showing a certain tendency to over-estimate Q (i.e., a negative deviation) for increasing values of the water elevation in the lagoon (i.e., towards the right), as expected.

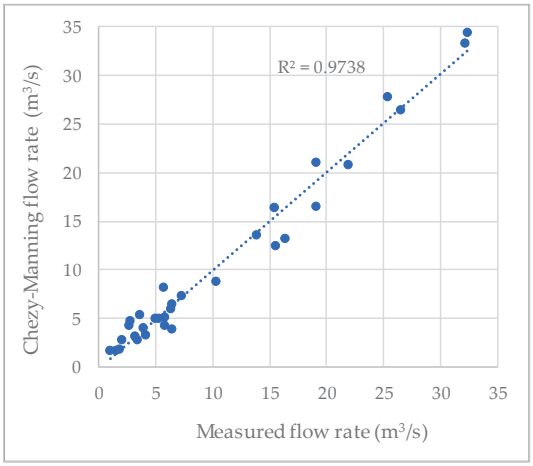

Figure 9. Matching between measured Q and Q estimated via the Chezy–Manning equation (R^2 = 0.9738), with data from 23 April 2022–23 October 2023.

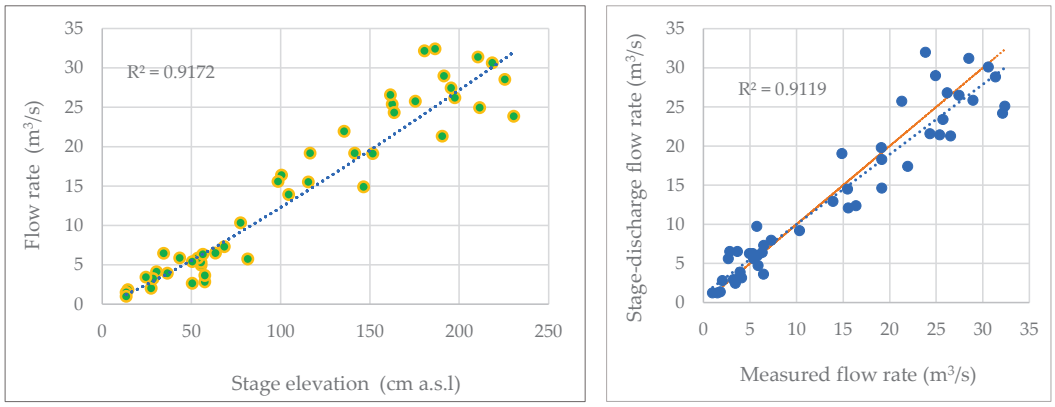

Figure 10. Surprise from new data on the Tomarrazon-Camarones River in Puente Troncal: (**a**) Stage–discharge relationship (power law regression, R^2 = 0.9172) with gauging data from 23 April 2022 until 23 November 2023; (**b**) matching between measured and estimated values (red line: perfect matching, dotted line: linear regression with R^2 = 0.9119).

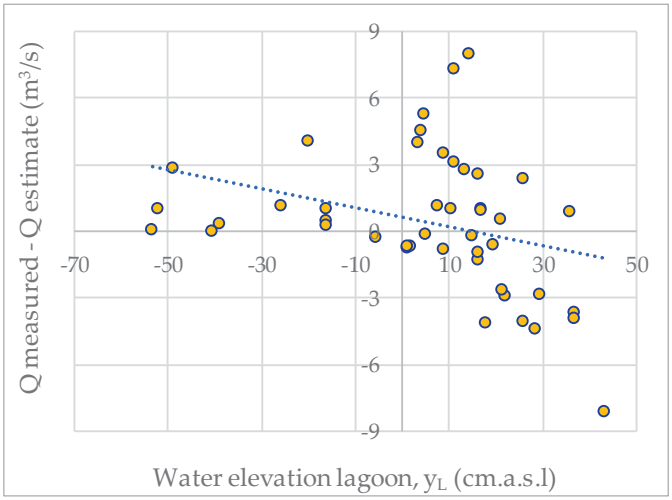

Figure 11. Deviation Q measured vs. Q estimated by the found stage–discharge relationship (m^3/s) as a function of the water elevation y_{Lagoon} (in cm above sea level). The blue dotted line interpolates the points linearly.

Therefore, we sought to improve the found power–law relationship by incorporating a dependency on the water elevation in the lagoon y_L, i.e., $Q = Q(y_T, y_L)$. Specifically, a relationship with a term that would reduce the flow value Q for a lagoon elevation y_L closer to the river stage elevation y_T at P.Troncal (always higher than y_L) was set up, as shown by Equation (3), that simply mathematically expresses this concept. Its four parameter values have been calibrated by trial and error (y in [cm.a.s.l]):

$$Q = a\,(y_T - y_0)^b\,[1 - 1/e^{\theta(y_T - y_L)}]\ [m^3/s] \quad (3)$$

where the parameters "a, b, y_0, and θ" were determined via calibration and assume the following values (Equations (4) and (5)):

$$a = 0.13299;\ b = 1.00927 \quad (4)$$

$$y_0 = -1.900;\ \theta = 0.02600 \quad (5)$$

The result is shown by the corresponding matching graph (Figure 12), where a certain improvement is apparent both in terms of a closer position of the linear tendency line to the perfect matching line (solid red, 45 degrees) and in terms of dots that are closer, in general, to that line (indeed, $R^2 = 0.9335$ overcomes the value obtained by the mono-dimensional regression, Figure 9). The improvement, however, is more relevant for low values of Q; however, this is clearly reasonable as the backwater effect of the lagoon vanishes for high flows as they are associated with high river stages while the lagoon water elevation moves in quite a limited range. It is certainly possible to better calibrate the set of parameters and even to find better functional relationships; however, for the moment, this is the stage–discharge relationship adopted hereafter.

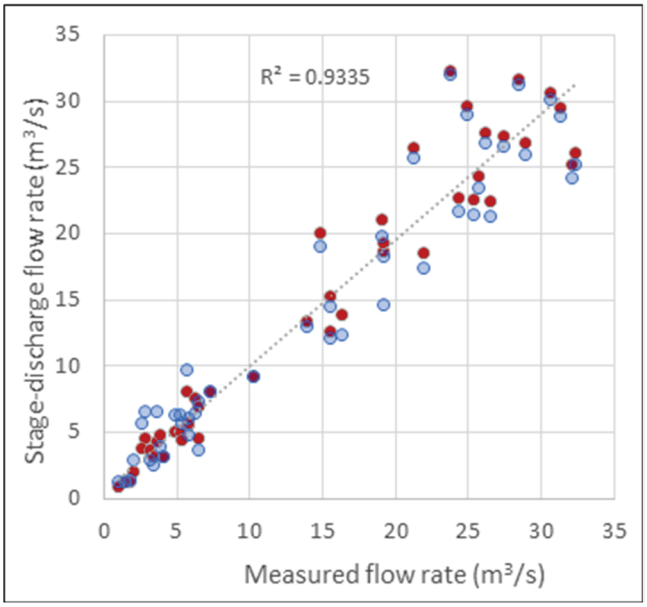

Figure 12. Improvement of the matching between measured Q and Q estimated by the $Q = Q(y_{river}, y_{lagoon})$ relationship (light blue dots are the same as in Figure 9 for ease of comparison). Data until 23 November 2023.

2.2. Sea Level

The sea level is a fundamental variable because it determines the exchange relationship between the lagoon and the sea according to tides and the status of the mouth and, as such, it governs the annual life cycle of the same lagoon.

At first, the idea was to install a dedicated sensor to measure water levels with high frequency (as reported, for instance, in [30]), but this idea was immediately discarded for

the same security reasons already explained above and also for the absence of a suitable installation site. A much simpler solution was hence adopted by simply using existing reported sea elevation data (y_S); in our case, the tide gauge at Puerto Brisa (see Figure 1a) located 39 km away from the mouth of the lagoon is the closest one.

However, getting the data—which are collected and owned by DIMAR (Colombian Dirección General Marítima y Portuaria)—is a process that requires administrative steps and time, as hourly data are not available online; hence, data are always obtained with a delay of a few months and only under explicit request. Another difficulty is the format of the data: they are delivered partly with a dd-mm-yyyy date format and partly with a mm-dd-yyyy format. A harsher difficulty is creating, within a continuous, hourly (Excel® 2019 MSO version 2406) data record sheet, an automatic reference to other sheets where our discontinuous time data of measurements of river flowrate and level, measurements of the lagoon level (usually bi-daily between 7–9 a.m. and 4–6 p.m., but with exceptions), and measurements of the area of the mouth and lagoon–sea exchange flow rate were recorded (by transcription of the physical field data formats). These data are collected at different, irregular times with many missing data ("holes"). To deal with this situation, we developed a specific Excel spreadsheet with suitable algorithms that proved to be indispensable, although far from trivial.

However, another, more serious problem concerned the altimetric consistency of data. According to common sense, the tide should oscillate most of the time around 0 with positive and negative values, although periods of higher or lower moving averages are possible due to particular combinations of astronomic and the meteorological drivers. However, here, almost all of the sea elevation data appeared to be much higher (about 60 cm) than the topographic IGAC 0 (Figure 13), which is impossible because, in those conditions, no flow from the lagoon to the sea could occur, while it is clearly physically expected and was indeed observed in the field. We then asked for formal explanations from the relevant institutions (DIMAR, IGAC, and IDEAM—Instituto de Hidrología, Meteorología y Estudios Ambientales) and understood that the tide gauge, like the entirety of the Colombian national geodesic network managed by IGAC, is referenced to a sea level of 0 located on the Pacific coast in Bonaventura town, which is a completely different water body. Indeed, the average sea level in the Caribbean—where Puerto Brisas and Camarones are located—is in general 28 cm lower (in [31,32]). However, this fact does not solve the mismatch as both the river elevation and that of the lagoon are referenced to the same IGAC 0 and as such should be consistent. Therefore, the final explanation is that a deviation exists between the geoidal and the ellipsoidal models of the Earth's surface in Colombia, as at present, there is no official update of the Colombian model. This is indeed consistent with the results found by [33] when trying to validate geometric leveling points with classic topography and LIDAR data, finding an average difference of 0.63 m.

In order to proceed, it was therefore assumed that the P.Brisa tide gauge utilizes a different (unknown to us) local reference and without searching for that datum, the mismatching was solved by adopting a very operational criterion. As will be detailed in a forthcoming paper, we just imposed that the lagoon–sea flow exchange process was physically meaningful. This means that when the observed flow was outgoing (from the lagoon into the sea), the lagoon water elevation should be higher than that of the sea, and vice versa. Luckily, a meaningful value of a fixed vertical translation of the tide gauge data could be found by trial and error, which could fulfill this condition in all observed cases, except one. Considering that just a tiny level difference (a few centimeters) is involved, and that the tide gauge is 39 km apart and that there are often strong winds, the obtained result (denoted with y_S*) can be considered fully satisfactory.

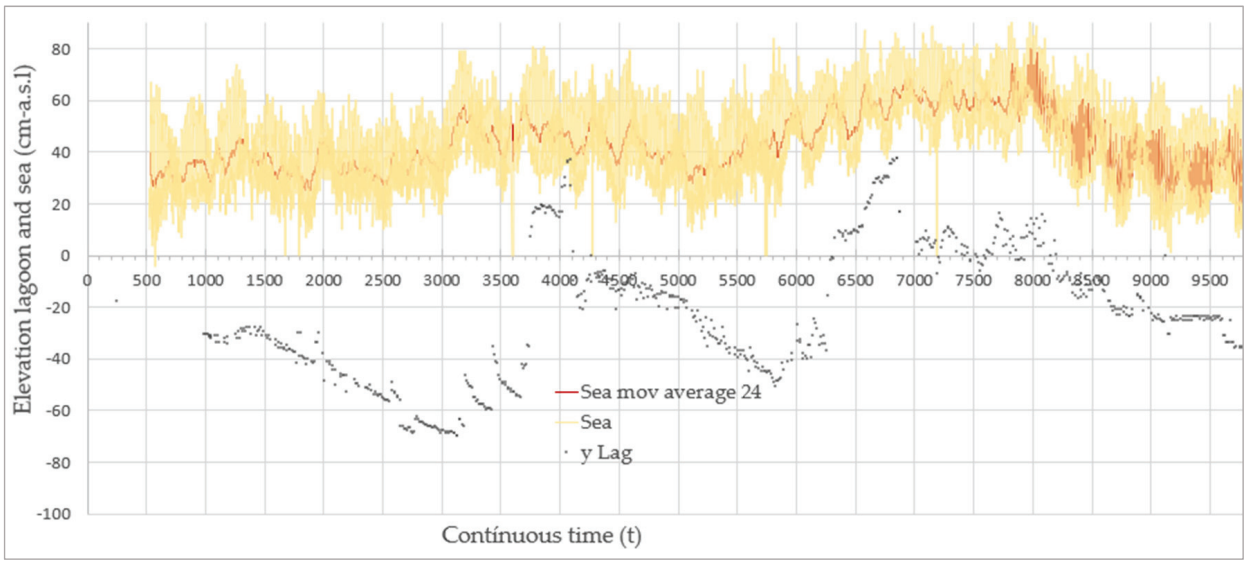

Figure 13. Extract of the time series of recorded data (at hourly time steps) showing the inconsistency between lagoon data and sea data, which are always higher than 0 and higher than the lagoon levels (top: sea elevation data kindly provided by DIMAR: daily moving average indicated by the darker line; bottom: lagoon water elevation data collected by our project).

2.3. Lagoon: Water Level

The most spontaneous solution for the measurement of the water elevation of the lagoon seemed to be the installation of a rule fixed at a pole in a relatively central place in the lagoon so that even for low levels, the rule would still be immersed (as the lagoon is quite shallow and the bottom is characterized by a very gentle slope). Measurements would be taken by the personnel of National Parks from their headquarters on the shore using binoculars. However, this idea was soon discarded because the reflection of sunlight on the water would make remote reading impossible and because wind, the perennial companion of sunlight, generally provokes a high-frequency, irregular wave system with an amplitude of about 5–15 cm, which would severely affect the measurements. Even an automatic sensor, which might allow a certain degree of digital filtering of data, was discarded because of the usual security problem and in line with the idea of creating a very basic system.

Therefore, a manual device installed at the National Parks' headquarters located on the lagoon shore (Figure 1 for general location and Figure 14) was chosen.

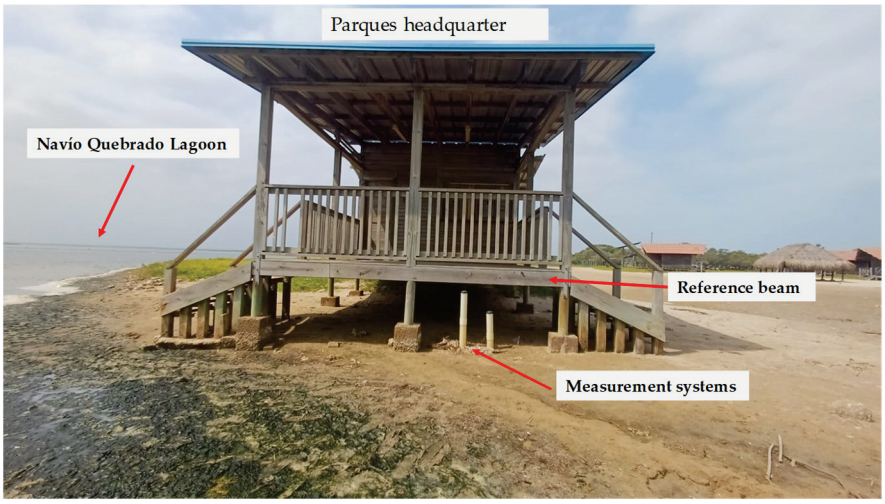

Figure 14. General view of the lagoon water level measurement system.

It is licit to wonder whether the foreseen monitoring frequency of twice a day is sufficient to capture the dynamics of the lagoon. According to Shannon [34], in a linear (linearized) dynamic system, sampling should be carried out with a frequency not lower than T/10, where T is the minimum time constant. This criterion, as will be explained in a forthcoming publication, leads to a very wide range of values; specifically, when the mouth is open, the criterion provides values of 1.6 to about 5 h (depending on the filling status of the lagoon, being quicker when it is low); when the mouth is closed, and the core dynamics are governed by evaporation, values range from a couple of days to three months. Evidently, only in this second case is our monitoring definitely adequate, while, when the mouth is open, our measurements cannot capture the full oscillation process, which is tuned to the tide oscillations. Nevertheless, the data obtained can be very informative, as shown in the rest of this paper.

A mixed solution was eventually preferred, comprising a hydrometer (Figure 15a) on the shore to be used for medium-high levels and a piezometer for situations with lower levels and, consequently, a dry hydrometer (Figure 15b). As water levels can become lower than the local terrain, the hydrometer is enclosed in a typical yellow sewerage pipe set in a vertical position and the reading is performed by manually inserting a rule and reading the depth with respect to a horizontal reference set on the headquarters' structure as indicated. To avoid the disturbance from the high-frequency wave oscillations, the device has a feeding tube with a reduced diameter section of Φ = 1.27 cm (which allows only a very small flow to pass through, according to the change of head from the lagoon surface and local, vertical movement), while the main vertical pipe section is proportionally much larger (Φ = 7.62 cm) so that the water volume input due to a flow increment translates into a much smaller vertical change, so fulfilling the dampening effect ("low-pass filter"). This function, on the other hand, is intrinsically guaranteed for the piezometer as the seepage across the soil cannot accelerate significantly; however, on the opposite side, this may dampen frequent (hourly) oscillations. The important difference is that water enters the hydrometer through the tiny tube, directly governed by the head on top of it, while water enters the piezometer by direct seepage across the soil matrix around it; therefore, the former cannot provide reliable data when the lagoon level drops below the sucking tip of the tube, while the piezometer works improperly when the level overcomes the ground level and even more so when it pours into the pipe from the top of the device.

Figure 15. Construction details of the water surface measurement system: (**a**) sealed inlet of the hydrometer; (**b**) filtering lateral surface of the piezometer covered by a plastic grid and inserted into gravel-filled holes; (**c**) fully installed system.

The implementation of the devices is based on "home-made" very-low-cost technology, as shown in Figure 16).

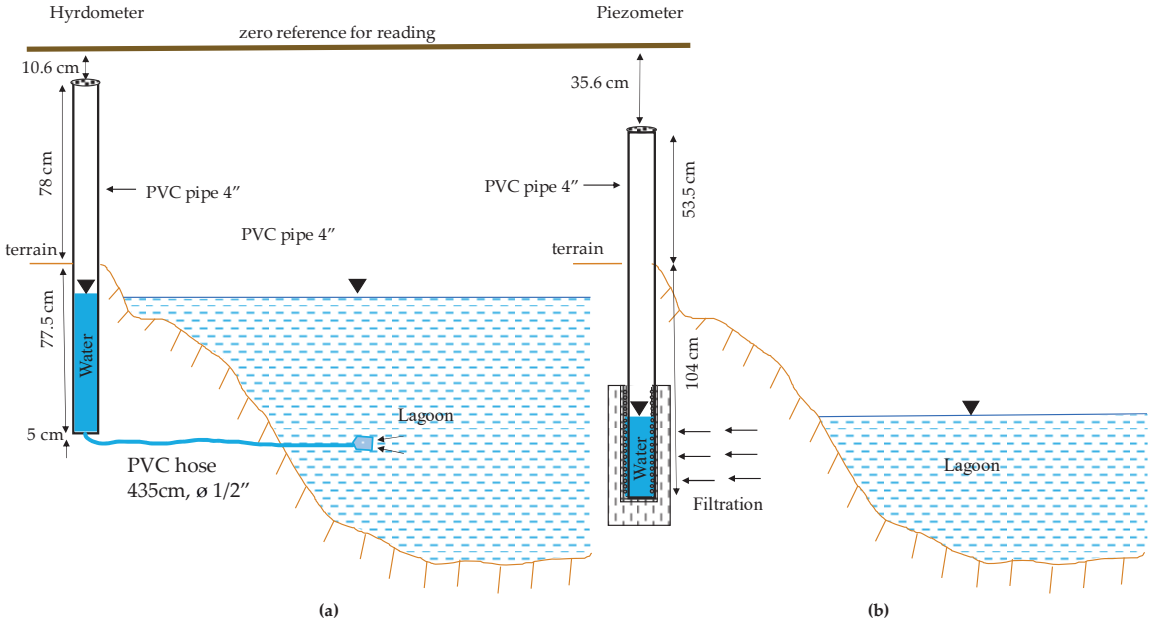

Figure 16. Scheme of the construction details of the measuring systems: (**a**) hydrometer and (**b**) piezometer.

Measurements, after training, were taken by National Parks personnel twice a day, usually around 8 a.m. and 4 p.m. The operation consists of inserting a rigid rule inside the pipe with a block to set on the pipe edge and reading the wetted depth; from this, knowing the elevation of the reference beam edge, the elevation of water inside the pipe is determined. An alternative would have been a transparent cylinder with graduations marked on its external surface; however, the intense sunlight of the site would very soon deteriorate any plastic material, making reading impossible. The method adopted is more robust, but it requires corrections to be made because, as shown in Figure 17, while inserting the rule (with a cross-section a*b), there is a Δh super-elevation that must be removed from the reading.

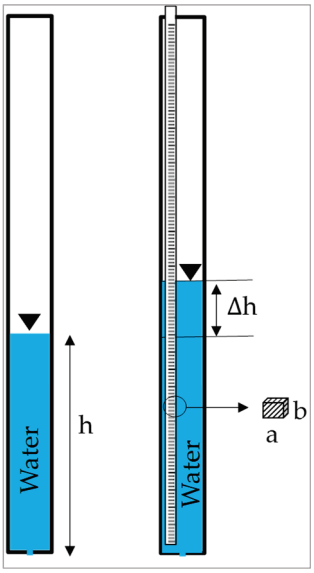

Figure 17. Alteration of the measurement of the water level h because of the volume of the inserted rule.

This correction is determined by imposing that the volume increment inside the pipe be equal to the volume of the piece of wet rule, according to Equation (6):

$$\Delta h\ (A_c - a\ b) = a\ b\ h \tag{6}$$

$A_c = \pi\ D^2/4$: area of the pipe's internal cross-section

D [cm]: internal diameter of the pipe

h [cm]: depth of water inside the pipe already altered by the presence of the partly wet rule (which is the reading effectuated by Parks staff)

Δh [cm]: height difference generated by the rule

a, b: dimensions of the rule stick (specifically: width, a = 3.8 cm; thickness b = 1 cm).

From this, one obtains the correction to be applied to the reading, as shown in Equation (7):

$$\Delta h(h) = a\ b\ h/(A_c - a\ b) \tag{7}$$

2.4. Lagoon: Horizontality Hypothesis

A doubt arose about the fact that the water surface of the lagoon may not be horizontal all the time (or never), mainly because of the effect of wind or due to the hydraulic conditions governing the input and output of water flows when the mouth is open or when the river is flooding.

To ascertain whether the horizontality hypothesis can be acceptable, we adopted two criteria:

- "instantaneous altimetry": The digital elevation model (DEM) we utilized is based on photogrammetry and was generated from an aerial image dataset collected in 2017 (generously provided by a national government agency called 'Fondo de Adaptación). The resulting orthophoto mosaic survey can be assumed to be instantaneous; therefore, the elevation of the water surface border, all around the lagoon, would be constant, were the hypothesis of horizontality verified. Unfortunately, the photo was taken in a dry period, and hence with a low level and small water surface, so that any structural difference cannot be very marked; nevertheless, from Figure 18, a certain non-uniformity is seemingly evident, indicating that there might have indeed been a certain degree of tilt;
- "synchronic monitoring": By measuring the water elevation during the day with a relatively high frequency (every hour or so), both with our installed hydrometer and at the same time at an opposite point, namely the river at P. Viejo (so close to the lagoon that it can be assumed to coincide with its level at that point; see Figure 1), it should be possible to detect any height difference. The results show a systematic elevation difference of approximately 15–20 cm between the two points (Figure 19).

The outcome of these tests is not that straightforward to interpret. The first test is consistent with the conclusion that a certain tilt does exist, meaning that the horizontality hypothesis should be dropped. Possible reasons for this behavior are the sea outlet drawdown effect (as witnessed by our own data on the lagoon–sea exchange process according to hydraulics), the river input hydraulic load (e.g., [35]), and wind seiches, although the latter are more relevant in large water bodies (e.g., [36,37]). However, the three campaigns were conducted on different days with different conditions at the mouth. Only in November was the river inflow really significant, eliminating the first two options; however, this would explain why the difference visible in Figure 19b is smaller, as the river carrying a higher flood rose a bit. In turn, frequent moderate winds are a reality, which would explain the presence of seiches.

However, as visible from Figures 1 and 20, it would be logical that the object with a higher elevation was the site at the river mouth (P.Viejo). However, from Figure 19, it is evidently the reverse, as the river elevation is always lower than the lagoon elevation at its hydrometer. Several explanations can be conceived. One is that the seiche changes periodically and, by chance, all three campaigns resulted in the opposite situation to that of

the satellite image taken in 2017. However, this is very unlikely as our (qualitative) record of wind direction says that the wind was more or less the same in the three conditions in terms of direction and intensity.

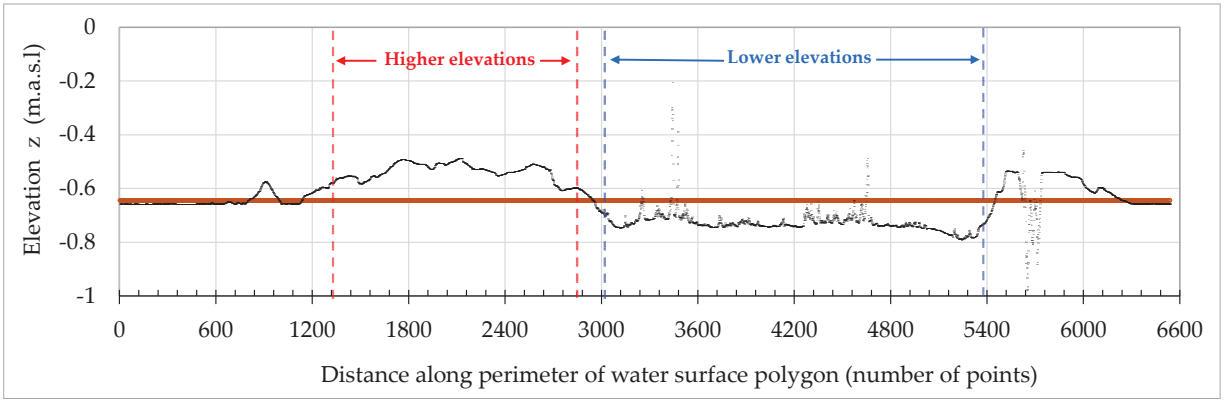

Figure 18. "Instantaneous altimetry" criterion: Elevation pattern of lagoon perimeter according to satellite images taken in 2017 (basis of the adopted DEM). The local peaks ("outliers") are attributed to DEM imperfections, possibly due to imprecision in the definition of the water surface polygon which may create incorrect height values. What counts here, anyway, is the prevailing behavior. The mean elevation is denoted by the brown bar.

Approx time	Day		y_V River (cm.a.s.l)	y_L Lagoon (cm.a.s.l)	Mouth Open/Close
8	19 May 22	1	-3.53	19.54	C
10	19 May 22	2	-3.53	19.26	C
12	19 May 22	3	-3.53	18.99	C
14	19 May 22	4	-3.53	19.08	C
16	19 May 22	5	-3.53	18.90	C
8	8 June 22	6	-28.53	-6.74	O
10	8 June 22	7	-29.53	-7.56	O
12	8 June 22	8	-29.53	-8.10	O
14	8 June 22	9	-30.53	-8.65	O
16	8 June 22	10	-31.53	-10.10	O
8	25 Novemb 22	11	-30.53	-16.19	O
16	25 Novemb 22	12	-20.53	-7.01	O

(a)

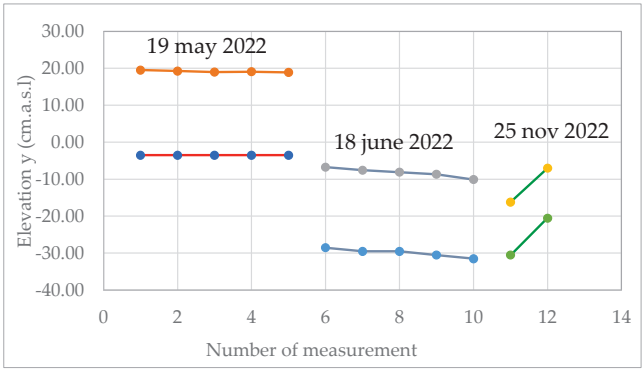

(b)

Figure 19. Horizontality check: synchronic monitoring criterion: (**a**) original data obtained; (**b**) the three sets of curves refer to three different survey days (in May, no exchange with the sea or river inflow and negligible evaporation effect during daytime, so constant values; in June, outgoing flow is emptying the lagoon, although a moderate river inflow was present; in November a significant river inflow is filling the lagoon, in spite of a moderate open mouth); the top curves refer to the lagoon, the bottom ones to the river at the same time: a synchronic behavior is apparent, as well as the existence of an elevation difference of about 12–20 cm.

Another possibility is that the DEM assessment is not reliable; however, this hypothesis is likely to be dropped because we found a relatively reasonable consistency between the elevations and surface areas derived from the DEM and the lagoon elevation measurements (see the paragraph on morphometry). It may be possible, however, that it is reliable on average, but the differences it shows (higher and lower zones) are not, a possibility that could also be due to imprecisions in the definition of the water surface polygon. A third possible explanation is that there is a structural bias in the topographic survey fixing the "zeros" of the hydrometers. Indeed, this seems the most likely option as, although the survey started from official IGAC references in both cases, they were not physically coincidental owing to logistic constraints (absence of signal for the RTK equipment close to the lagoon mouth): an absolute difference between 20 and 40 cm is therefore possible. We

cannot conclude whether there is a tilt or not because according to the instantaneous test (DEM), there seems to be; however, the time pattern test seems to contradict this conclusion as the detected difference has an opposite sign (however, this might be explained by a different topographic reference). More importantly, on all three days (with very different conditions at the mouth and the river), the results kept the same sign and even the same absolute value (which was a little lower in the third case, but this can be reasonably explained by the significant river inflow), which seems less likely and is more consistent with a hypothesis of identical levels (i.e., a horizontal surface or the absence of tilt) plus constant topographic bias.

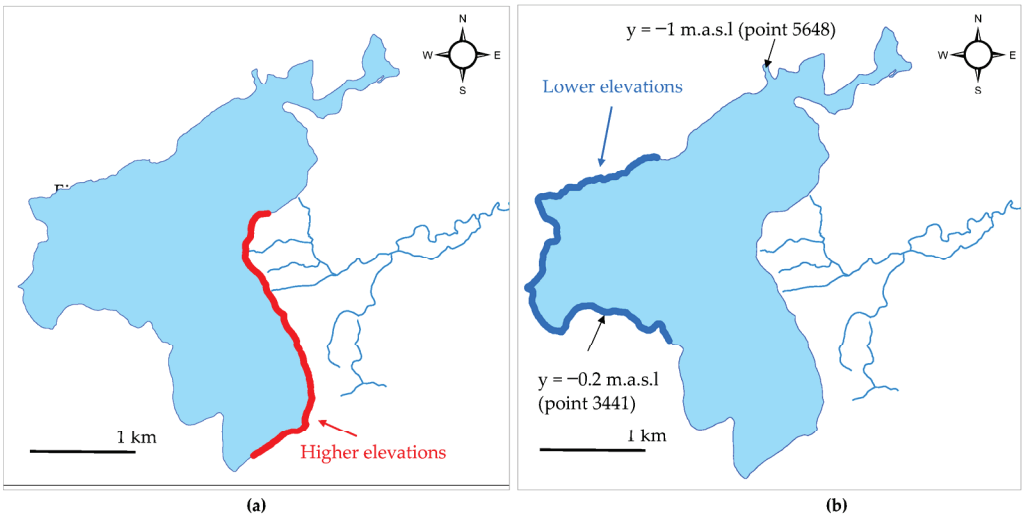

Figure 20. Instantaneous altimetry test based on DEM analysis: Shore affected by lower (**a**) and higher (**b**) elevations; location of anomalous points: the most depressed point (y= −1 m.a.s.l) corresponds to the boca and was most probably captured near the surface of the sea; the highest one, on the other hand, lies in the middle of nowhere and seems to be a local imperfection.

However, it is important to observe that the measurement station of the lagoon level (hydrometer and piezometer) lies outside of the likely affected zones (Figures 1 and 20). Therefore, assuming that the identified conditions (higher and lower zones) do not rotate around the lagoon, the water surface measurements can be considered representative of the real water surface elevation, which is extremely important for monitoring and modeling purposes. In principle, the possible bias between the river hydrometer and the lagoon hydrometer would not affect data acquisition because river elevation is used just to feed the local river stage–discharge relationship (and the relationship with the upstream station at P.Troncal that is using the same reference). However, there may be a subtle influence when the backwater effect is important through Equation (3), but this is negligible for high flows (which are the most important ones). On the other hand, lagoon elevation data are used just in relation to sea elevation data. However, the possible tilt of the lagoon water surface could be affecting hydrodynamic modeling.

In any case, our investigation still goes on to fully understand what is happening there. As a collateral note, it is important to note that the data on which this discussion is based cannot be considered exhaustive and fully representative as the DEM is quite imprecise (see par. 2.6), while our synchronic monitoring did not capture data at nighttime.

2.5. Lagoon: Exchange with the Sea

Being able to measure the exchange flow between the lagoon and the sea is key to setting up a water balance, even more so when water quality is dealt with. The key issue is finding a way to measure (or estimate) this flow in the simplest way.

Normally, there are one or two periods of the year when the lagoon mouth ("la boca") opens and a significant flow of freshwater outgoing occurs; after a few days, the flow alternates twice a day between outgoing and incoming depending on the tide (and possible additional river floods) until the mouth closes again. This is quite a complex phenomenon, which is not easy to measure and hard to predict. Indeed, the opening date depends mainly on the arrival of the first significant river flood. This moment may vary greatly from year to year and may occur twice a year, owing to the bimodal hydrological regime with two wet seasons from April to June and September to November, respectively [38]. Once the mouth is open, its geometry varies depending on the river inflow, the tide pattern, and the average sea level, usually approaching its maximum area in about two weeks. That configuration is usually held for one or two months and then the closure process starts, which is quite slow at the beginning and then accelerates, possibly during an interval of a month. The mouth area also varies during the day. However, this process is clearly different every year. In 2022, the opening lasted 36 days (from May 29 until July 4), and the second opening period, usually stronger, lasted a bit longer than 3 months (from 21 September 2022 until 5 January 2023, a total of 106 days).

The key problem to be addressed at this stage of monitoring is just measuring the water flow in several moments during the open mouth period, for both outgoing and incoming flows, and then setting up a relationship that determines the exchange flow Q_B (positive or negative) as a function of, possibly, the cross section area A, and the height difference between the lagoon water elevation (y_L) and that (y_S) of the sea, as shown in (Equation (8)):

$$Q_B = Q_B(A; y_L, y_S) = Q_B(A; y_L - y_S) \quad (8)$$

Probably, the most suitable manner to carry out such a measurement is by using a digital current meter such as ADCP (Acoustic Doppler, Current-meter Profiler; [25]) guided by a cable through the section. However, several reasons impeded this solution. Firstly, very pragmatically, our institution does not own such a device and the regional environmental authority was reluctant to lend us theirs because it can quickly become spoiled in brackish or salty water. Secondly, the wind can become quite strong and so does the wave surge. Therefore, the device, floating on the surface, would move significantly and irregularly and the data would become very noisy. On the other hand, consistently with the framework adopted, we chose to keep technology very simple and low-cost; therefore, we just pulled a rope as a reference across the section, and onboard a boat driven by hand through poles (an engine would alter measurements and easily get into trouble because of the vertical oscillations and irregular bottom), we measured the depth every 2 or 3 m (detected by colored knots on the rope) with a rule and the velocity with a current meter (two different devices to conduct a quality check on data: Manufacturer General Oceanics Environmental, Model 2030R Mechanical and manufacturer The Geography Specialists, Gepacks brand, model MFP126) at a depth of about 60% of the total depth to be hopefully more representative of the vertical averaged longitudinal velocity (see Figure 21).

By adopting this method, several measurements have been carried out in different conditions, capturing both outgoing and incoming flows. This allowed us to set up a reliable relationship as expected and hoped (as will be described in a forthcoming paper). Therefore, actual systematic monitoring is reduced to components that have already been considered: the lagoon and sea water elevations.

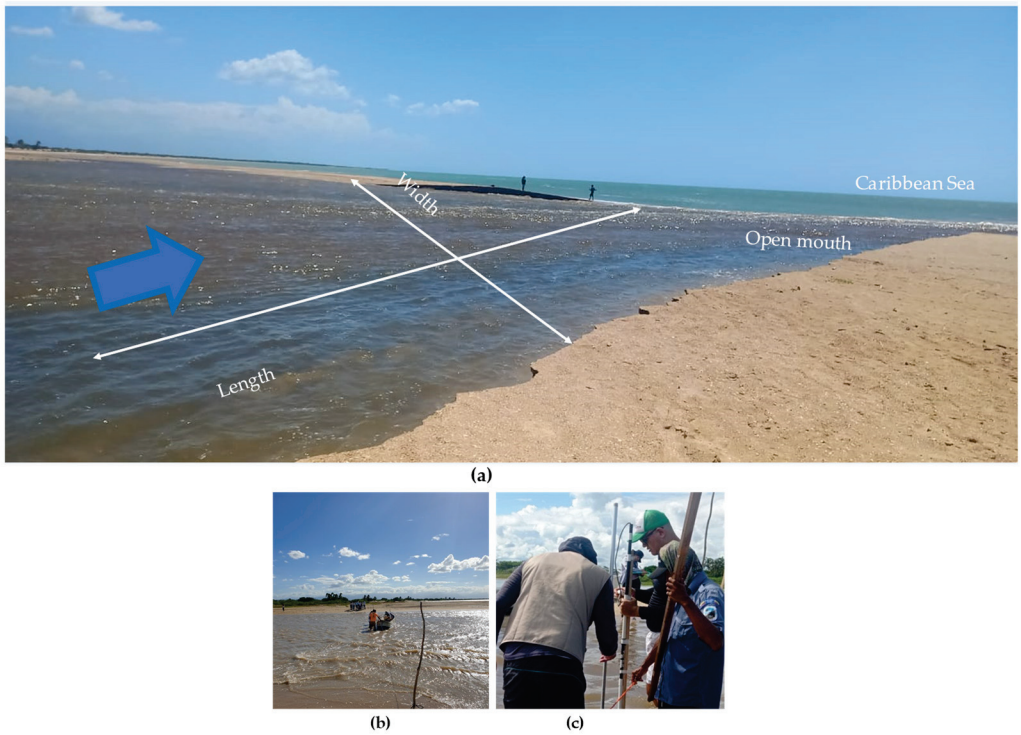

Figure 21. Details of the mouth and velocity measurements: (**a**) lagoon during an "open period"; (**b**) Our vehicle for surveying the cross-section; (**c**) Manual measurement of depth and velocity.

2.6. Lagoon: Morphometric Relationships

As a basis for monitoring the storage changes, it is key to count the functional relationships: elevation–surface area and elevation–volume; these changes are indeed key components for the water balance. The water surface greatly varies with its elevation; this makes it imperative to merge a topographic representation of the zone with a bathymetric one.

We disposed of a set of aerial images taken during the dry season (17 March 2017) by a photogrammetric tripulated flight from an elevation of 1100 m above sea level (size of pixel: 20 cm). By using photogrammetric processing (via the Agisoft Metashape® software version 2.1.2), we generated an orthophoto mosaic of the whole scene and a dense points cloud describing the topography of the surrounding area around the lagoon. These points were manually edited and classified by using the 'Auto-Classify ground points' tool of Global Mapper Pro version 18®.

The bathymetry was reconstructed based on a set of 111 lagoon bottom elevation measurements directly determined by a GNSS-RTK from a boat, during 19, 20 of September 2022, together with an SIG-supported spatial analysis. The spatial pattern of measurement points reflects more operational navigation constraints (wind, depth, and distance) than logical planning (Figure 22).

The adopted GIS strategy (ArcGIS Pro) to generate the bathymetric surface is articulated in 6 steps: (i) Geo-statistical interpolation (Kriging) of acquired points via GNSS-RTK. (ii) Extraction and smoothing of the resulting elevation curves. (iii) Interpolation of curves through TIN. (iv) Rasterization of the TIN generated. (v) Conversion of the bathymetric raster into a cloud points format "*.las" by utilizing the option "Export Layer to New File" in Global Mapper. (vi) Integration and interpolation of the photogrammetric points cloud and bathymetric surface to achieve their connection and thus the final topo-bathymetric DEM. For this last step, we adopted the tool "LAS Dataset to Raster" of ArcGIS Pro.

Independently, measurements of depth were taken by a sonar device (Garmin Striker) during the same bathymetric campaign, while in dry conditions, we carried out point GNSS-RTK measurements in the floodable zone of the lagoon (then in dry conditions). All

of this was to create a database with which validation of the generated topo-bathymetric DEM would be possible.

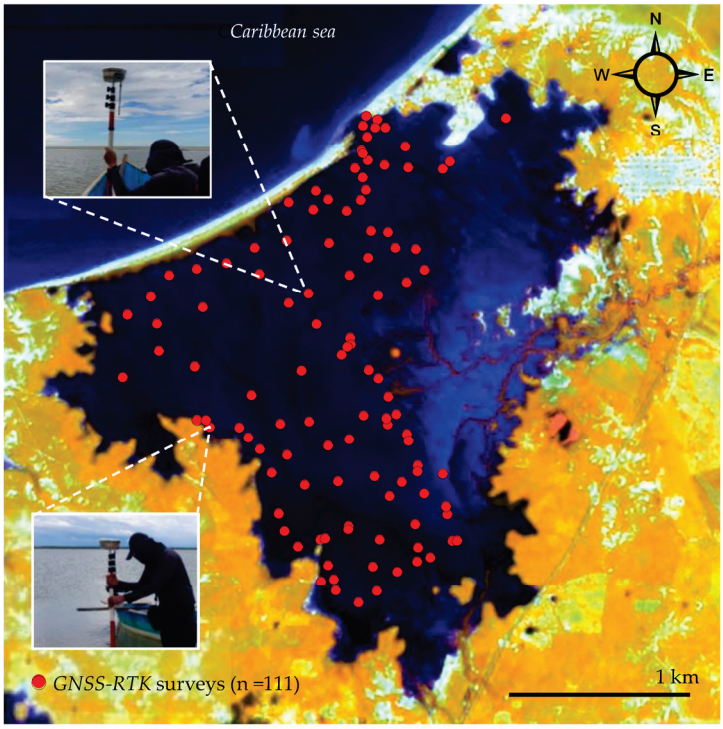

Figure 22. Spatial pattern of 111 GNSS-RTK points (red). The background image is a Landsat 8 of 20 September 2022 when the lagoon was at maximum filling. The false color image identifies water (dark blue tone) under a combination of bands: NIR, SWIR1, and Red.

The key outputs of this activity are the surface area–elevation S(y) and volume–elevation V(y) relationships which have been obtained by points (Figure 23) by means of the r.lake.xy module, a spatial modeling tool hosted in GRASS GIS ® software version 7.8.7. This module fills the water body (topo-bathymetric DEM) from a given elevation until a specified elevation is achieved. This tool requires an input of a raster DEM, a maximum water elevation, and its location coordinates (x,y).

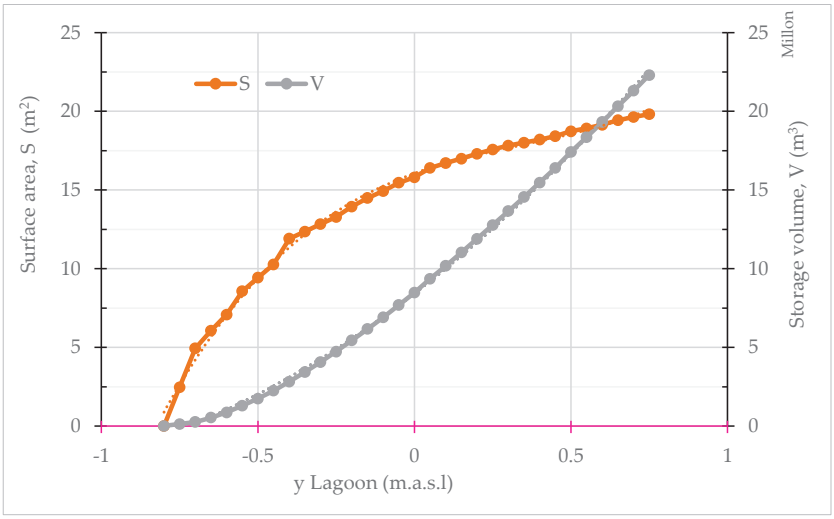

Figure 23. Hypsometric curves: Surface area S = S(y) (m^2); Storage volume V= V(y) (m^3) related to lagoon elevation y_L [masl]. Polynomial curves: $S(y) = 8010914.35\ y^3 - 8335673.88\ y^2 + 7166288.16\ y + 16056191.36$ ($R^2 = 1.00$); $V(y) = 4983114.71\ y^2 + 15272088.13\ y + 8414661.47$ ($R^2 = 1.00$).

A final key check was to ascertain the coincidence of DEM elevation with measurements of the lagoon water surface. More precisely, the idea was to identify some dates with different conditions of the lagoon (at least 4); given the date, we would determine the area S of the water surface from satellite images (transformed into a polygon and eliminating possible "holes"). Then, from the inverse curve y = y(S), we would obtain the elevation y to be compared with the elevation measured that day by the hydrometer/piezometer devices and determine a fitting measure. We obtained an RMSE value of just 8.4 cm (Table 1), which is considered satisfactory. Data from May 31 show the maximum deviation; however, a measurement error seems unlikely because both the piezometer and the hydrometer devices recorded a similar jump between morning and afternoon (a cause for this jump is a possible pressure effect due to stronger winds on the water surface). The significant deviation with respect to the DEM value is probably due to the fact that this value is not associated with a specific time instant, while the measurement is, so they are most probably out of phase.

Table 1. Consistency check between DEM output and measurements of lagoon elevation ("Area" is the area of the surface identified by satellite image after eliminating the holes left by the process; "Y Lagoon Topo-Bati" (third column) is the corresponding elevation determined from the DEM through the y(S) relationship; "when" discerns the two daily measurements of the piezometer ("Y Lag Piezo", fifth column) and of the hydrometer ("Y Lag Hydro"); "Y-Lagoon" is the selection between the two according to the threshold −0.2; "Diff" (Y Lagoon Topo-Bati – Y Lagoon) is the deviation).

Date	Area (m^2)	Y Lagoon Topo-Bati (m.a.s.l)	When	Y Lag Piezo (m.a.s.l)	Y Lag Hydro (m.a.s.l)	Y Lagoon (m.a.s.l)	Diff (cm)
2 May 2023	4,949,302	−0.707	morning	−0.711	−0.770	−0.711	0.4
		−0.707	afternoon	−0.700	−0.772	−0.700	−0.7
15 March 2023	8,484,668	−0.540	morning	−0.593	−0.653	−0.593	5.3
		−0.540	afternoon	−0.596	−0.652	−0.596	5.6
31 May 2022	13,673,330	−0.241	morning	−0.084	−0.089	−0.089	−15.2
		−0.241	afternoon	−0.156	−0.161	−0.161	−8.0
20 September 2022	17,554,393	0.263	morning	0.446	0.367	0.367	−10.4
		0.263	afternoon	0.451	0.365	0.365	−10.2

2.7. Evaporation, Inflow from Runoff, and Direct Precipitation

Evaporation from the lagoon water surface is obtained as surface area S times the evaporation rate e(t) [mm/day]; for the latter, the simplest way is to acquire data about the relevant meteo-climatic variables already monitored in a nearby gauging station (visible in Figure 3) and then apply a suitable formula from the literature. Among the existing stations, the only one with data in our period is Camarones (point in Figure 3). However, it has to be noted that—apart from the rainy days—the meteorological conditions are quite constant in the area, with strong solar radiation, temperature, low cloudiness, and moderate to strong winds. Therefore, evaporation does not vary much (Figure 24).

To determine the direct precipitation input to the lagoon, it is sufficient to know the precipitation itself, which is one of the classic variables already measured in nearby stations. The only issue is ensuring their availability for the period of interest for ex-post simulations and continuous measurements for new monitoring. Luckily, there exists a rainfall gauging station on the official IDEAM network (available at http://dhime.ideam.gov.co/atencionciudadano/, accessed on 18 April 2024) in the nearby town of Camarones (Figure 3).

For the runoff from the local catchment draining into the lagoon, the same discourse holds, although a kind of rainfall runoff model must be developed, which is described in another forthcoming paper.

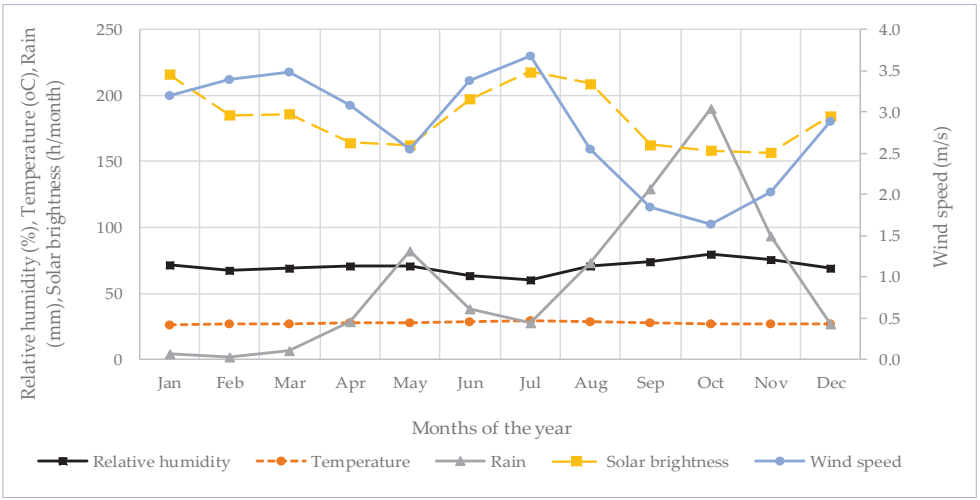

Figure 24. Climatological variables of the study area (from IDEAM data: Rain from Camarones station ID 15050010. All others from Riohacha station ID 15065180).

3. Results

Figure 25 shows the output of the monitoring exercise obtained until this paper was written. The sea data shown are the original ones, without the correction established (see Par. 2.2) to avoid overlapping curves and allow an easier interpretation of the Figure. It is apparent that the hourly tidal cycle is well-hidden behind additional oscillations that are quite complex and irregular; moreover, there appears to be a growing trend (notice that a 500-step interval corresponds to 20.8 days, which is approximately a Moon month).

The data from the piezometer and the lagoon hydrometer are quite consistent in general, although there is a certain unexplained deviation. Many factors can intervene such as wind pressure, which acts more directly on the free water surface than on the underground phreatic surface, or reading errors. Apart from the initial period (until 4 April 2022 when the devices were adjusted and deepened), it can be noted that for low levels, the piezometer provides higher values, while for high levels, in most cases, the opposite occurs. Consistent with the spirit of using the two devices, we decided to utilize the hydrometer data for y (cm.a.s.l) > −20 (cm.a.s.l), which is where the feeding tube is fully immersed, while the piezometer data are utilized below that threshold (see Figure 16).

It is worth noting that, in spite of their numerosity, there are only two measurements a day and this means that it is possible that these data do not capture the maximum and minimum values that actually occurred (i.e., as already noted, the sampling frequency is not high enough to capture the whole phenomenon). This is why they are represented as points with no connecting lines.

The behavior of the lagoon level is fully consistent with the status of the boca: as soon as it opens (fully or partly), the surface starts to oscillate synchronically to the sea tide. As soon as the boca closes, the level starts dropping because of evaporation, unless a flood input comes from the river. It is also apparent, however, that several river inputs are missing or underestimated (top graph), which is unavoidable as the river was measured just once a day.

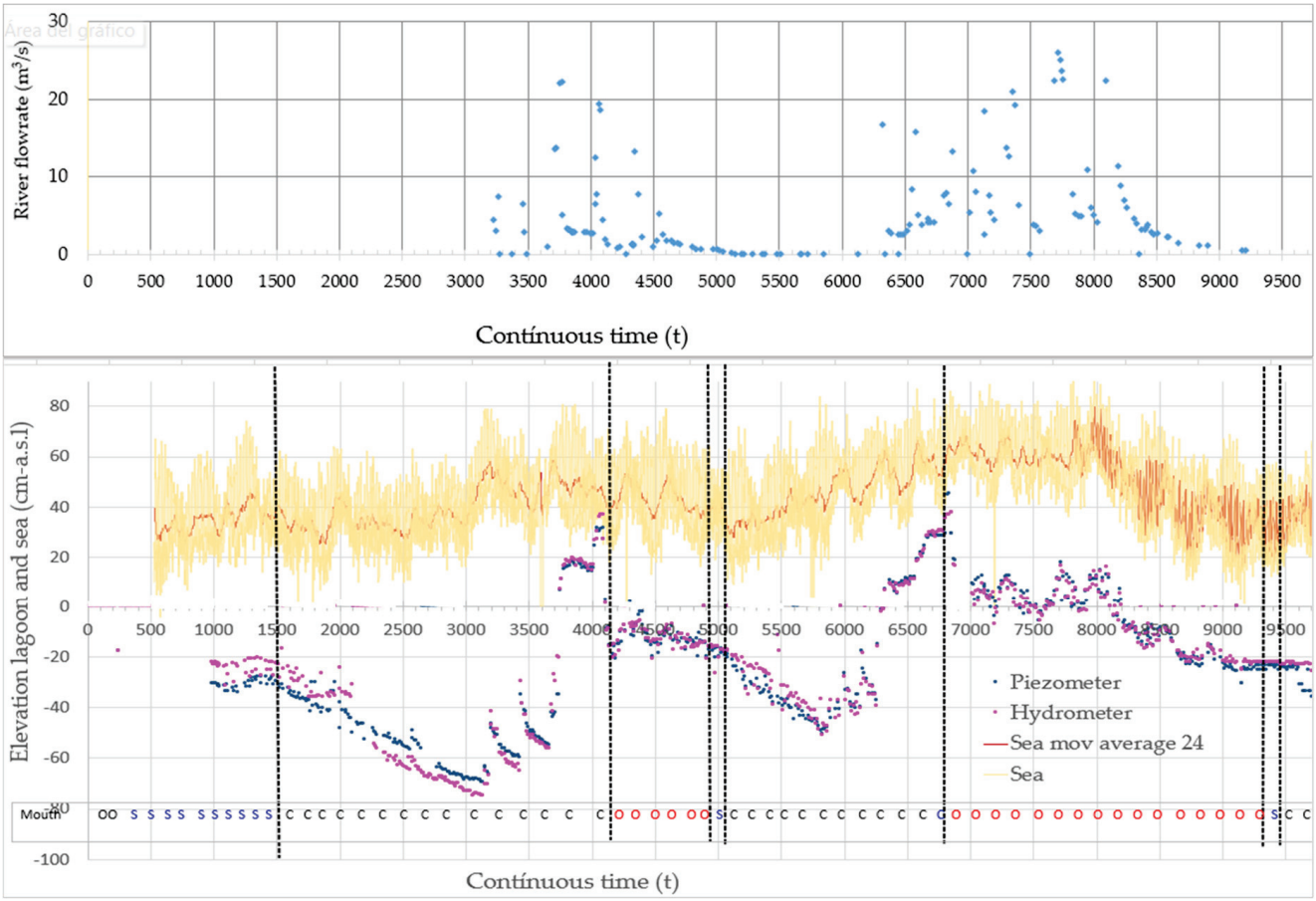

Figure 25. Output of the monitoring system for the period of 10 December 2021 to 14 January 2023 (hourly time step; one square is 500 h), with no correction for the sea level data. At the bottom is the status of the lagoon mouth: C: closed; O: Open; S: Semi-open.

4. Discussion

A system quite similar to ours is described in [5] for some North African coastal lagoons. However, to measure the water level, they adopted both human-read hydrometers (or "stage boards") and a set of automatic sensors (that could not be installed everywhere). Their effort, differently from ours, was not aimed at providing all the variables needed to set up a water balance; in particular, they did not measure the lagoon–sea water exchange, although interesting observations were provided. In addition, they explored how the tidal effect propagates across the lagoon, but they did not show the simultaneous plot of the relevant variables that is illuminating when searching for a cause–effect relationship.

The monitoring system set up for Navío-Quebrado relies on a number of assumptions that may be worth highlighting as they also mark the intrinsic limitations of the output. Concerning river discharge measurements, an underlying assumption is that the river section selected is suitable for capturing the whole flow rate transported by the river and this, rigorously speaking, is not always the case: when the values are very high, part of the flow can occur by direct runoff outside the river channel. However, these are quite exceptional events. Another assumption is that the river section's geometry does not vary with time, but this is quite certain because of the geomorphic character of the site, as already mentioned. The possible dependence on the lagoon level (backwater effect) has been explored and explicitly included, although in an approximate form. However, the greatest limitation is that the manual "once a day" measurement cannot fully capture the relevant flow hydrograph, which is therefore missing several significant inputs. This is made evident by the overall data plotting (Figure 25).

Concerning the lagoon water body, an explicit assumption is that filtration into and from the lagoon is negligible, a fact that could and should be ascertained by installing a number of piezometers capable of detecting filtration fields. We do believe, however, that this flow is quite marginal, based on the type of soil. The horizontality assumption has been explored, but the conclusion cannot be considered final and should be verified by more careful instruments and campaigns; this can be an important element affecting the quality of measurements. A related, implicit, assumption is that the sea level data obtained from the tidal gauging station Puerto Brisa, located about 40 km apart, can be transferred instantaneously and without correction to the lagoon mouth ("la boca"); this can be a serious limitation because of the interplay of winds and water currents and would require thorough study. However, the checks performed in this study seem to affirm that this assumption is acceptable.

Another, quite crude, assumption is that the adopted selection criterion between the piezometer and hydrometer data to provide a water surface elevation, now based just on a water elevation threshold, is appropriate. Perhaps, a different threshold would have worked better, a varying threshold is necessary, or even the explicit representation of some dynamic (currently unidentified) process is needed. Several experiments can be conducted in this sense. Another obliged assumption is that the manual "twice-a-day" reading of water levels is enough to capture the dynamic behavior; this is, in principle, a significant limitation where the rapid variations associated with the tides during open-mouth periods are concerned. However, the overall data obtained still seem sufficient to meaningfully reveal the actual behavior of the lagoon.

Despite all of these doubts, we have a very pragmatic criterion: the data obtained are quite consistent (Figure 25 and comments); moreover, when adopted to feed a simulation model (as explained in a forthcoming paper), the outputs are quite satisfactory.

Last but not least, there is a non-technical issue that deeply characterizes and severely limits the functionality of our system: its participatory dimension, which is simultaneously a strength and a weakness. This is further commented on in the next paragraph.

5. Conclusions

Conceiving and installing a monitoring system for the Camarones lagoon has been a small adventure, through which many doubts have been solved and suitable methods and tools have been tested and applied. Figure 26 summarizes the key components of the whole exercise.

The system is sufficiently reliable, as the various consistency tests (alternative estimation methods and matching graphs) and the observation of outputs demonstrate. Some weaknesses are nevertheless evident, such as the frequent lack of river input data.

Although the project has already provided information suitable for testing a simulation model, which will be described in a forthcoming paper, it is intended to be continued and strengthened. A significant improvement would be the ability to monitor the river inputs continuously (at least hourly); at the moment, the only way to address this need seems to be the installation of a basic automatic station, integrated with the manual monitoring already put in place and with the awareness that the devices will have to be replaced with a certain frequency because of damage and theft. Certainly, an automatic station can also be installed in the lagoon site, which is much more protected, again in parallel with manual monitoring.

This improvement would give us the opportunity to focus on the conformity of the measurement methods adopted; for instance, measurements obtained by standard equipment could be compared with our simpler methods, allowing us to define bias and potentially provide bias correction. Advanced data tests could furthermore be applied such as consistency, homogeneity, stationarity, and randomness, and even concordance checks with some standard data (e.g., satellite data) could be developed.

Component	Activities	Outputs
River discharge Q	• River stage h (two stations: P.Troncal and P.Viejo) (several measurements) • River velocity v (several measurements) • Cross section geometry A (once) • Correction because of backwater effect • Alternative check (with Chezy-Manning and slope s between the two sections)	• Stage-discharge relationship • Measuring protocol defined • Alternative method to estimating Q
Lagoon level	• Lagoon elevation y_L (hydrometer and piezometer) • Correction equation for rule volume effect • Horizontality check of water surface (two criteria) • Construction of morphometric relationships $S(y_L)$, $V(y_L)$ via topo-bathymetric DEM: - Photogrammetry - Validation with sonar depth data - Consistency check with hydrometer measurements and area form satellite images	• Hydrometer and piezometer installed • Measuring protocol defined • Morphometric relationships $S(y_L)$, $V(y_L)$
Lagoon-sea exchange	• Measurement of flowrate Q_B (classic manual velocity, depth measurements across section) • Correction of mareograph data (y_S^*) • Search for a relationship between Q_B and lagoon (y_L) and sea (y_S) elevation difference and cross area A • Check with alternative hydraulic method	• Mathematical relationship Q_B defined to estimate the flow • Information about time changes of the cross section A
Precipitation input	• Use of available precipitation data • Development of (very simple) rainfall-runoff model • Determination of an average evaporation rate	• Rainfall flow input to lagoon • Equation for the evaporation flow

Figure 26. Summary of the whole exercise conducted to set up the hydrological monitoring system.

The highest-level use of the acquired data will eventually be the analysis of the future under climate change by setting up future scenarios of river inflow, evaporation rates, and sea level rise, and hypothesizing about morphological evolution.

A completely different and complementary issue concerns sediment balance and aggradation. During the river flow measurements, a water sample was taken to assess the concentration of suspended solids (SS) with the hope of building a relationship with the flow, i.e., SS = f(Q). Analogous data for the sea in front of the lagoon mouth are available from other entities (although with a much lower frequency). However, the difficulty is measuring the bed load carried by the river and exchanged through the lagoon mouth (in and out). We attempted several methods, but at the moment, our hopes rely on a macro scale, i.e., observing the morphological evolution delta of the Tomarrazón-Camarones River, which seems to be prograding into the lagoon. A direct comparison of satellite images and aerial photos can provide a first estimate, while the analysis of a DEM of differences in the same area might allow us to perform a quantitative estimation. However, much longer times are required to cope with the vertical precision of drone images (at the moment, we have performed a first survey by creating control points where vertical bars of known position and depth have been installed to observe, in the future, possible aggradation of the floodplain). A key element, in addition, will be the coring of the sediment bed and its stratigraphic and dating analysis.

Concerning the future of our system, it must be emphasized that it is based on a participatory basis, thanks to the very nice relationship established with the National Parks institution and its staff. In particular, a number of on-the-field training sessions and office seminars succeeded in motivating the personnel on the usefulness and reliability of the exercise they were involved in. In addition, some local people have been directly involved in providing information and executing some measurements. Therefore, we can state that the exercise has involved a significant participatory dimension. However, systematic long-term monitoring certainly cannot be based on voluntary effort only; the benefits of measuring with such a system will only be evident in the long run and hence cannot be

a sufficiently solid reason to motivate local stakeholders to take charge of operating the system alone. Only National Parks can potentially hold the commitment on a long-term basis, but even this may not be guaranteed as each year, some personnel adjustments take place. This is why a long-term agreement between the local University and National Parks has been proposed and is being considered.

Overall, this experience may clash with the latest groovy advances of science, such as in situ automatized sensors, remote sensing, machine learning, and digital twins. However, it recalls that before the latest technological advances, science may emerge even through old, very simple methods when rooted in a sincere, humble search for insight.

Author Contributions: Conceptualization, A.G.C.N.; methodology, A.G.C.N. and J.I.P.-M.; software (to elaborate DEMs and specific Excel sheets to analyze and plot data), J.R.E.V., A.G.C.N. and J.I.P.-M.; validation, J.I.P.-M. and A.G.C.N.; formal analysis, A.G.C.N.; investigation, J.I.P.-M. and J.R.E.V.; resources, J.I.P.-M. and J.R.E.V.; data curation, J.I.P.-M., J.R.E.V. and A.G.C.N.; writing—original draft preparation, A.G.C.N.; writing—review and editing, J.I.P.-M. and J.R.E.V.; visualization, J.I.P.-M., A.G.C.N. and J.R.E.V.; supervision, A.G.C.N.; project administration, J.I.P.-M.; funding acquisition, J.I.P.-M. All authors have read and agreed to the published version of the manuscript.

Funding: This research was partially funded by Ministerio de Ciencia, Tecnología e Innovación of Colombia, call for proposals 890-2020, project 82511, resources administered by the Colombian Institute of Educational Credit and Technical Studies Abroad–ICETEX, but a self-funding share was necessary at the beginning as the start of the formal project suffered a significant delay.

Data Availability Statement: Data generated within this effort are available under direct request to the corresponding authors.

Acknowledgments: We are grateful to the Universidad de La Guajira for the contributions and the agreement with JIPM to allocate time to the project; the authors also thank CREACUA Foundation (Riohacha, Colombia) for the impulse given to this initiative. A special greeting goes to Parques Nacionales Naturales de Colombia, and particularly to all the public servants of the *Santuario de Fauna y Flora los Flamencos* and their illuminated director Nianza Angulo Paredes. We also want to warmly thank Rosa Rodriguez Fernandez for the support in the installation of the measurement systems as well as Jose Fragozo Arevalo for the help in the topographic surveys. Last, but not least, warm thanks to Yesenia Zuñiga for her help in the preparation of the figures.

Conflicts of Interest: The authors declare no conflicts of interest.

References

1. Kennish, M.J.; Paerl, H.W. *Coastal Lagoons: Critical Habitats of Environmental Change*; CRC Press Taylor & Francis Group: London, UK; New York, NY, USA, 2010; ISBN 9781420088304.
2. Pérez-Ruzafa, A.; Molina-Cuberos, G.J.; García-Oliva, M.; Umgiesser, G.; Marcos, C. Why Coastal Lagoons Are so Productive? Physical Bases of Fishing Productivity in Coastal Lagoons. *Sci. Total Environ.* **2024**, *922*, 171264. [CrossRef] [PubMed]
3. Pérez-Ruzafa, A.; Marcos, C. Fisheries in Coastal Lagoons: An Assumed but Poorly Researched Aspect of the Ecology and Functioning of Coastal Lagoons. *Estuar. Coast. Shelf Sci.* **2012**, *110*, 15–31. [CrossRef]
4. Velasco, A.M.; Pérez-Ruzafa, A.; Martínez-Paz, J.M.; Marcos, C. Ecosystem Services and Main Environmental Risks in a Coastal Lagoon (Mar Menor, Murcia, SE Spain): The Public Perception. *J. Nat. Conserv.* **2018**, *43*, 180–189. [CrossRef]
5. Thompson, J.R.; Flower, R.J.; Ramdani, M.; Ayache, F.; Ahmed, M.H.; Rasmussen, E.K.; Petersen, O.S. Hydrological Characteristics of Three North African Coastal Lagoons: Insights from the MELMARINA Project. *Hydrobiologia* **2009**, *622*, 45–84. [CrossRef]
6. Bedoya Vásquez, C.J. *Caracterización de La Pesquería Artesanal En La Laguna de Navío Quebrado, Departamento de La Guajira, Caribe Colombiano*; Universidad Jorge Tadeo Lozano: Bogotá, Colombia, 2004.
7. Corporación Autónoma Regional de La Guajira [CORPOGUAJIRA]. *Plan de Ordenamiento y Manejo de La Cuenca Del Río Tomarrazón-Camarones*; Corporación Autónoma Regional de La Guajira: Riohacha, Colombia, 2008.
8. Urrego, L.E.; Correa-Metrio, A.; González, C.; Castaño, A.R.; Yokoyama, Y. Contrasting Responses of Two Caribbean Mangroves to Sea-Level Rise in the Guajira Peninsula (Colombian Caribbean). *Palaeogeogr. Palaeoclimatol. Palaeoecol.* **2013**, *370*, 92–102. [CrossRef]
9. Parques Nacionales Naturales de Colombia. Programa de Conservación Del Flamenco En El Santuario de Fauna y Flora Los Flamencos, Departamento de La Guajira, Costa Caribe de Colombia. Ediprint Ltd.: Bogotá, Colombia, 2013; ISBN 978-958-8426-42-6.
10. Rosado Vega, J.R.; Castro Echavez, F.L.; Márquez Gulloso, E.R. Environmental, Biological, and Fishing Factors Influencing Fish Mortality and Development of the Cachirra Event, Navío Quebrao Lagoon. *Tecnura* **2022**, *26*, 17–41. [CrossRef]

11. Cardona, L. Non-Competitive Coexistence between Mediterranean Grey Mullet: Evidence from Seasonal Changes in Food Availability, Niche Breadth and Trophic Overlap. *J. Fish Biol.* **2001**, *59*, 729–744. [CrossRef]
12. Moreno-M., G.P.; Acuña-Vargas, J.C. Caracterización de Lepidópteros Diurnos En Dos Sectores Del Santuario de Flora y Fauna Los Flamencos (San Lorenzo de Camarones, La Guajira). *Bol. Cient. Cent. Museos* **2015**, *19*, 221–234. [CrossRef]
13. Corporación Autónoma Regional de La Guajira [CORPOGUAJIRA]. *Ajuste y/o Actualización Del POMCA Del Río Camarones y Otros Directos Al Caribe—La Guajira*; Corporación Autónoma Regional de La Guajira: Riohacha, Colombia, 2022.
14. INVEMAR. *Concepto Técnico Sobre La Mortandad de Peces Ocurrida En La Laguna Navío Quebrado (Corregimiento de Camarones, Municipio de Riohacha En La Guajira) En Agosto de 2017, CPT-CAM 021-17*; INVEMAR: Santa Marta, Colombia, 2017.
15. Blaen, P.J.; Khamis, K.; Lloyd, C.E.M.; Bradley, C.; Hannah, D.; Krause, S. Real-Time Monitoring of Nutrients and Dissolved Organic Matter in Rivers: Capturing Event Dynamics, Technological Opportunities and Future Directions. *Sci. Total Environ.* **2016**, *569–570*, 647–660. [CrossRef]
16. Chan, K.; Schillereff, D.N.; Baas, A.C.W.; Chadwick, M.A.; Main, B.; Mulligan, M.; O'Shea, F.T.; Pearce, R.; Smith, T.E.L.; van Soesbergen, A.; et al. Low-Cost Electronic Sensors for Environmental Research: Pitfalls and Opportunities. *Prog. Phys. Geogr.* **2021**, *45*, 305–338. [CrossRef]
17. Hamel, P.; Ding, N.; Cherqui, F.; Zhu, Q.; Walcker, N.; Bertrand-Krajewski, J.L.; Champrasert, P.; Fletcher, T.D.; McCarthy, D.T.; Navratil, O.; et al. Low-Cost Monitoring Systems for Urban Water Management: Lessons from the Field. *Water Res. X* **2024**, *22*, 100212. [CrossRef] [PubMed]
18. Kabi, J.N.; wa Maina, C.; Mharakurwa, E.T.; Mathenge, S.W. Low Cost, LoRa Based River Water Level Data Acquisition System. *HardwareX* **2023**, *14*, e00414. [CrossRef]
19. Notter, B.; MacMillan, L.; Viviroli, D.; Weingartner, R.; Liniger, H.P. Impacts of Environmental Change on Water Resources in the Mt. Kenya Region. *J. Hydrol.* **2007**, *343*, 266–278. [CrossRef]
20. Frappart, F.; Blarel, F.; Fayad, I.; Bergé-Nguyen, M.; Crétaux, J.F.; Shu, S.; Schregenberger, J.; Baghdadi, N. Evaluation of the Performances of Radar and Lidar Altimetry Missions for Water Level Retrievals in Mountainous Environment: The Case of the Swiss Lakes. *Remote Sens.* **2021**, *13*, 2196. [CrossRef]
21. Huang, Q.; Long, D.; Du, M.; Zeng, C.; Li, X.; Hou, A.; Hong, Y. An Improved Approach to Monitoring Brahmaputra River Water Levels Using Retracked Altimetry Data. *Remote Sens. Environ.* **2018**, *211*, 112–128. [CrossRef]
22. Tourian, M.J.; Tarpanelli, A.; Elmi, O.; Qin, T.; Brocca, L.; Moramarco, T.; Sneeuw, N. Spatiotemporal Densification of River Water Level Time Series by Multimission Satellite Altimetry. *Water Resour. Res.* **2016**, *52*, 1140–1159. [CrossRef]
23. Biancamaria, S.; Lettenmaier, D.P.; Pavelsky, T.M. The SWOT Mission and Its Capabilities for Land Hydrology. *Surv. Geophys.* **2016**, *37*, 307–337. [CrossRef]
24. Wu, J.; Li, W.; Du, H.; Wan, Y.; Yang, S.; Xiao, Y. Estimating River Bathymetry from Multisource Remote Sensing Data. *J. Hydrol.* **2023**, *620*, 129567. [CrossRef]
25. Mueller, D.S.; Wagner, C.R. *Measuring Discharge with Acoustic Doppler Current Profilers from a Moving Boat*; U.S. Geological Survey Techniques and Methods 3A–22: Reston, VA, USA, 2009.
26. Chow, V.T. *Open-Channel Hydraulic*; McGraw-Hill, Ed.: New York, NY, USA, 1959; ISBN 978-0-07-085906-7.
27. Ferro, V. Comments on "Measurement of Dimensionless Chezy Coefficient in Step-Pool Reach (Case Study of Dizin River in Iran)" by Torabizadeh A., Tahershamsi A., Tabatabai M.R.M. *Flow Meas. Instrum.* **2018**, *64*, 190–193. [CrossRef]
28. Tymiński, T.; Kałuża, T.; Hämmerling, M. Verification of Methods for Determining Flow Resistance Coefficients for Floodplains with Flexible Vegetation. *Sustainability* **2022**, *14*, 6170. [CrossRef]
29. Okhravi, S.; Schügerl, R.; Velísková, Y. Flow Resistance in Lowland Rivers Impacted by Distributed Aquatic Vegetation. *Water Resour. Manag.* **2022**, *36*, 2257–2273. [CrossRef]
30. Boutron, O.; Paugam, C.; Luna-Laurent, E.; Chauvelon, P.; Sous, D.; Rey, V.; Meulé, S.; Chérain, Y.; Cheiron, A.; Migne, E. Hydro-Saline Dynamics of a Shallow Mediterranean Coastal Lagoon: Complementary Information from Short and Long Term Monitoring. *J. Mar. Sci. Eng.* **2021**, *9*, 701. [CrossRef]
31. García, J.; Cuervo, E. *Pronóstico de Pleamares y Bajamares En La Costa Occidental de Colombia Para El Año de 1978.*; Instituto Geográfico Agustín Codazzi (IGAC), Ed.: Bogotá, Colombia, 1978.
32. Álvarez Machuca, M.C.; Pulido Nossa, D.A.; Solano Trullo, L.J.; Oviedo Barrero, F. Construcción de La Superficie Hidrográfica de Referencia Vertical Para Las Bahías de Buenaventura y Málaga, Pacífico Colombiano. *Boletín Científico CIOH* **2018**, *36*, 53–69. [CrossRef]
33. Escobar Villanueva, J.; Nardini, A.; Iglesias Martínez, L. Evaluación Del Uso de Topografía LiDAR En El Modelado de Inundaciones Urbanas Con MODCEL ©. Aplicación a La Ciudad Costera de Riohacha, La Guajira (Caribe Colombiano). In *Humedales y Espacios Protegidos, Libro de actas del XVI Congreso de la Asociación Española de Teledetección*; Asociación Española de Teledetección: Sevilla, Spain, 2015; pp. 383–386.
34. Shannon, C.E. Communication in the Presence of Noise. *Proc. IRE* **1949**, *37*, 10–21. [CrossRef]
35. Wu, Q.; Wang, Z.; Xu, X.; Huang, Z.; Wen, T.; You, W.; Xia, Y. Flood Propagation Characteristics in a Plain Lake: The Role of Multiple River Interactions. *Water* **2024**, *16*, 1447. [CrossRef]
36. Costi, J.; Marques, W.C.; de Paula Kirinus, E.; de Freitas Duarte, R.; Arigony-Neto, J. Water Level Variability of the Mirim—São Gonçalo System, a Large, Subtropical, Semi-Enclosed Coastal Complex. *Adv. Water Resour.* **2018**, *117*, 75–86. [CrossRef]

37. Oliveira, H.; Fernandes, E.; Möller, O.; García-Rodríguez, F. Relationships between Wind Effect, Hydrodynamics and Water Level in the World's Largest Coastal Lagoonal System. *Water* **2019**, *11*, 2209. [CrossRef]
38. Arregocés, H.A.; Rojano, R.; Pérez, J. Validation of the CHIRPS Dataset in a Coastal Region with Extensive Plains and Complex Topography. *Case Stud. Chem. Environ. Eng.* **2023**, *8*, 100452. [CrossRef]

MDPI AG
Grosspeteranlage 5
4052 Basel
Switzerland
Tel.: +41 61 683 77 34

Water Editorial Office
E-mail: water@mdpi.com
www.mdpi.com/journal/water

Academic Open
Access Publishing

mdpi.com

ISBN 978-3-7258-5754-8